A Study of Nanostructuring Effects on Model Heterogeneous Catalysts

Sergey Kozlov

Sergey Kozlov

A Study of Nanostructuring Effects on Model Heterogeneous Catalysts

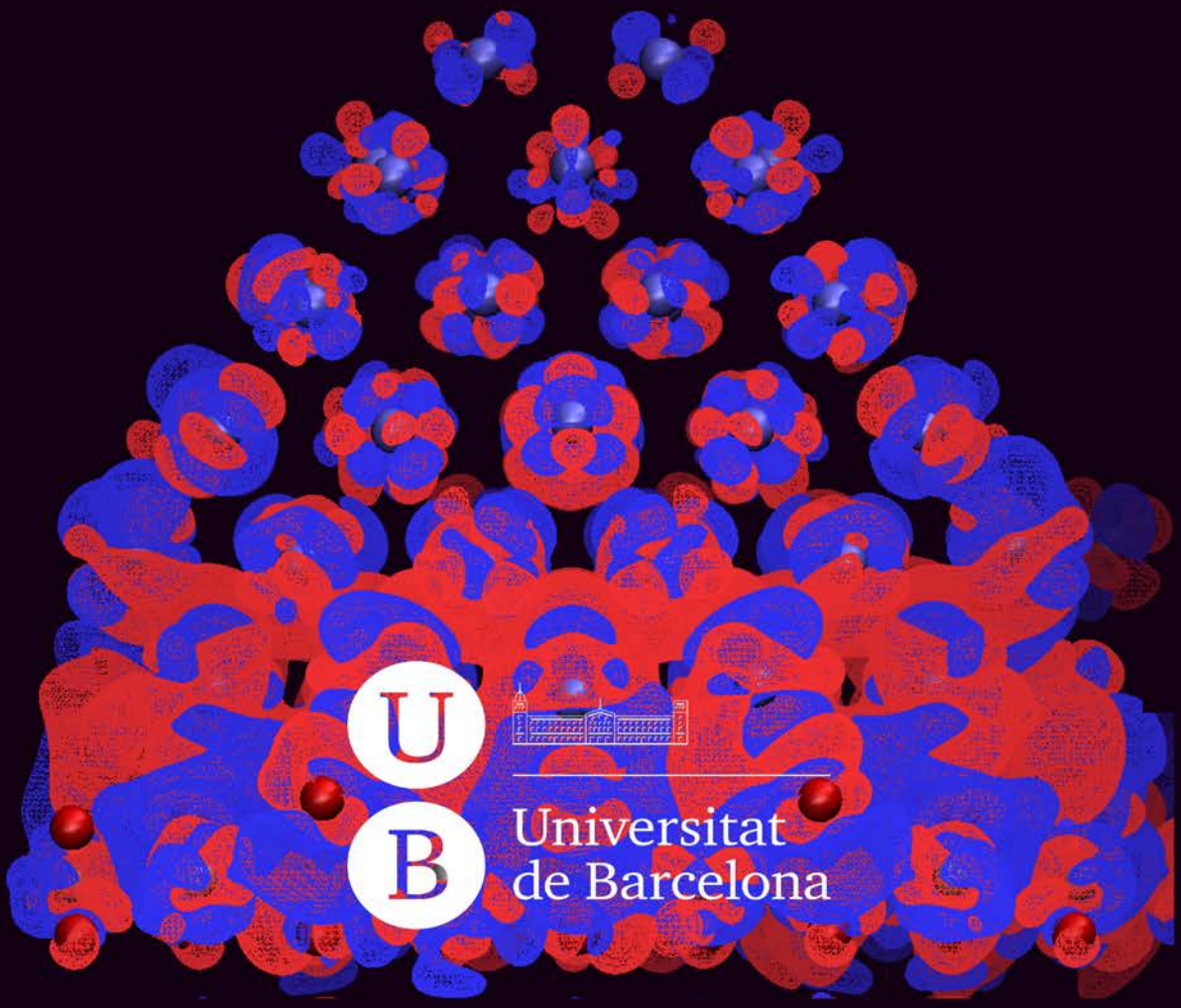

Universitat de Barcelona

Programa de Doctorat de Química Teòrica i Computacional

A Study of Nanostructuring Effects on Model Heterogeneous Catalysts

Presentada por

Sergey Kozlov

Dirigida por

Dr. Konstantin Neyman

Universitat de Barcelona i Institució Catalana de Recerca i Estudis Avançats

Tutor

Dr. Francesc Illas Riera

Universitat de Barcelona

Acknowledgements

Many people have put a lot of effort into making this work and this thesis possible. First of all, I would like to thank my supervisor, Prof. Konstantin Neyman, for his guidance and his help with endless organizational problems during my studies. I have learned many things from him and his vision on investigations and presentation of scientific results. In particular, I appreciate that he was always open for a discussion and allowed me developing and testing my ideas and approaches to problems we were facing. Thanks to him, I was also able to participate in numerous collaborative projects and attend to a great number of conferences, which was a valuable experience for me.

I would like to thank Dr. Francesc Viñes and Dr. Hristiyan Aleksandrov, who taught me the methodology of electronic structure calculations. It was a pleasure to work with them on multiple occasions over the years. I should also thank Prof. Stefan Bromley and Prof. Francesc Illas for many enlightening scientific discussions, which eventually lead to successful collaborations.

The scientific part of this thesis was as difficult to accomplish as the paperwork necessary for my PhD studies. I am in a great debt to everyone who helped me with the latter. In particular, I want to thank Dr. Albert Bruix who spent countless hours struggling with the Spanish bureaucracy on my behalf. Also I would like to thank the director of my PhD program, Prof. Juan Novoa, who was always very understanding and cooperative.

Furthermore, I am very thankful to all people, who helped me with Spanish and Catalan languages over these years. Probably, at some extent this includes everyone in our department, but I would like to especially thank Alberto Figueroba, Daniel Reta, Dr. Marçal Capdevila and Dr. Sergi Vela as well as Oriol Lamiel and Maria Fumanal. I appreciate very much the help of Anna Palacios, Estefanía Lopez, Sergi Posada, Dr. Leny Álvarez, Dr. Jordi Ribas, Isaac Alcon and others in making this thesis better.

Finally, I want to thank Dr. Gábor Kovács, Dr. Kyoung Ko, Almudena Notario, Noelia Pueyo, Sonia Romero, Daniel Jiménez and others for making these years more fun, memorable and fulfilling.

The present work was performed in the Department of Physical Chemistry and the Institute of Theoretical and Computational Chemistry (IQTC) in the University of Barcelona (UB). It was a part of Red Star activities and it was done within the framework of Catalan Reference Network of R+D+i on Theoretical and Computational Chemistry (XRQTC).

These PhD studies were funded mostly by AP2009-3379 FPU fellowship by Spanish Ministry of Education, Culture and Sport and at some part also by the ChipCAT project (Ref. №310191) of European Framework Programme 7.

During this period I have enjoyed multiple conferences and stays abroad organized and financed by the following COST Actions: CM1104 ‘‘Reducible oxide chemistry, structure and functions’’, MP0903 “Nanoalloy”, CM0904 “Intermetallic compounds as catalysts for steam reforming of methanol”, and MP1103 “Nanostructured materials for solid-state hydrogen storage”. One of the stays was financed by the HPC-Europa2 program.

I have to thank the Spanish Supercomputing Network for the provided computational resources. Also I would like to thank Jordi Inglés, Teresa Arenal and Raul Porcel for the help with local computational facilities in the Institute of Theoretical and Computational Chemistry (IQTC).

Contents

List of Key Figures

Front cover: Polarization of electron density upon contact of Pt_{96} nanoparticle with $CeO_2(111)$ surface displayed as CDD plot. Electrons shift from blue areas to red areas.

Back cover: Spin density produced by localized unpaired f-electrons on Ce cations in film of Ce_2O_3 with bixbyite structure.

3. Unsupported Transition Metal Nanoparticles

4. Supported Transition Metal Nanoparticles

5. Steps on Surfaces

6. Nanometer Thick Films

List of Definitions and Abbreviations

1 electronvolt (eV) = 96.485 kilojoules per mol (kJ/mol)
= 23.060 kilocalories per mol (kcal/mol)
= 11604.505 kelvin (K) × $k_{Boltzmann}$

1 nanometer (nm) = 10^{-9} meter (m)
= 10 ångstrom (Å)
= 10^{3} picometer (pm)

β specific step energy measured, e.g., in eV/nm

γ specific surface energy often measured in eV/nm^2 or J/m^2

BEP Brønsted–Evans–Polanyi principle, which postulates that activation energies of similar reactions (anti-)correlate with their exothermicity

CDD charge density difference plot, calculated as an isosurface of the difference between electronic densitites $\Delta\rho = \rho(A + B) - \rho(A) - \rho(B)$ with geometries of subsystems *A* and *B* fixed on those from combined (and optimized) *A* + *B* system

DFT density functional theory or density functional theory methods

DFT+U various density functional theory methods that also include Hubbard U corrections on certain atomic orbitals

DOS density of states

E_F Fermi level; only electronic states with energy less than E_F are occupied

E_f(A) the formation energy of entity A

fcc face centered cubic lattice typical for crystals of many transition metals

GGA generalized gradient approximation in density functional theory or exchange-correlation functionals based on this approximation

HF Hartree-Fock or Hartree-Fock method of calculation

homotops nanoparticles different just by relative arrangement of atoms of different types within a given geometric structure

IP interatomic potentials

IR infrared or infrared spectroscopy

LDA	local density approximation in density functional theory or exchange-correlation functionals based on this approximation
LEED	low-energy electron diffraction
MAPE	mean average percentage error
MSR	methanol steam reforming reaction, $CH_3OH + H_2O \rightarrow CO_2 + 3H_2$, which may yield CO as an undesired product
NP	nanoparticle
O_{vac}	vacancy in a material formed by the removal of a neutral O atom
PAW	projected augmented wave treatment of the interaction between core and valence electrons
STM	scanning tunneling microscopy
SwS	scalable with size
vdW	van der Waals interactions (understood as a complete synonym to dispersive interactions or van der Waals-London interactions)
vicinal surface	surface cut in some misalignment with a low-index Miller plane; such surfaces are typically composed of extended terraces of the low-index plane separated by more or less equally spaced atomic steps
XPS	X-ray photoelectron spectroscopy

Sites on (111) surfaces of fcc metals

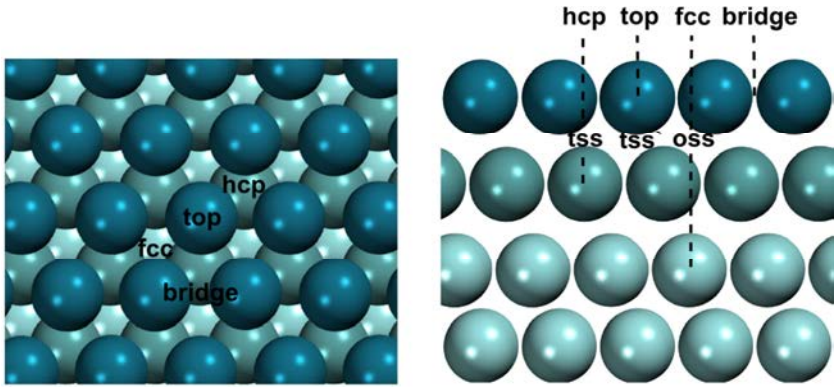

Figure A. Adsorption and subsurface sites on (111) surface of fcc metals. Top sites are above single substrate atom; bridge sites are two coordinated; fcc and hcp are three-fold hollow sites. Tetrahedral tss and tss' interstitial cavities are located below hcp and top sites, respectively; octahedral oss site is below fcc site.

Chapter 1

Introduction

Catalyst is an additional substance that accelerates the rate, k, of a given chemical reaction.[a] In energetic terms, this means that the activation energy, E^a, of the reaction is decreased by the catalyst, often a few times in magnitude (Figure 1.1). Since the reaction rate depends exponentially on the activation energy, $k \sim e^{-E^a/k_{Boltzmann}T}$, as a rule the effect of the catalyst results in an immense speed up of the reaction. In heterogeneous catalysis the reaction occurs on the surface between two phases, most commonly between gas or liquid reactants and a solid catalyst.

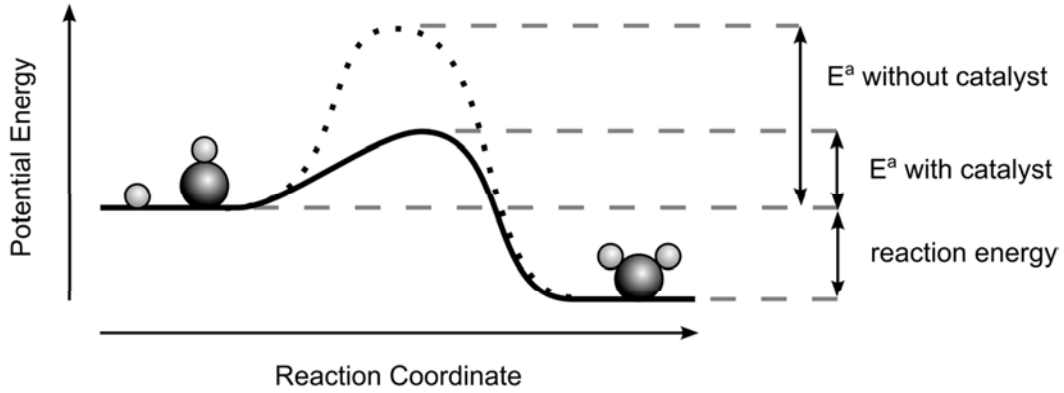

Figure 1.1. Energetic profile of a reaction. The presence of a catalyst lowers the activation energy but keeps the reaction energy the same.

The role of heterogeneous catalysis in society

Heterogeneous catalysis has a great impact on humanity. First, there is simply no way to industrially produce some commonly used materials without heterogeneous catalysis. Second, the utilization of a heterogeneous catalyst usually greatly improves the energy- and cost-efficiency of a reaction, which is decisive for the economical practicability of a given process. Probably, the most influential catalytic reactions of the 20th century were Haber-Bosch process[1] (Nobel prizes[2,3] in chemistry of 1918 and 1931) and petrochemical[4] processes. The first reaction allowed essentially unlimited production of ammonia for fertilizers, which solved the food shortage problem on Earth in the beginning of the 20th century and resulted in the fourfold population increase in the last hundred years. The second group of reactions is responsible for the pervasive role of petroleum in our lives and especially as fuel for cars.

[a] A more precise definition[395] of a catalyst is given by IUPAC: "A substance that increases the rate of a reaction without modifying the overall standard Gibbs energy change in the reaction. The catalyst is both a reactant and product of the reaction."

The 21-st century poses new challenges to science, in general, and to heterogeneous catalysis, in particular.[5] Currently, a lot of scientific attention is devoted to the development of new heterogeneous catalysts that would solve upcoming energy and environmental problems. First, better heterogeneous catalysts with lower content of precious metals are required for fuel cell technologies, which allow more efficient energy extraction from fossil fuels.[6] The usage of more environmentally friendly[b] natural gas in many applications is hindered by the lack of efficient heterogeneous catalysts to oxidize[7,8] it or to convert it to liquid fuels.[9,10] The full-scale application of biofuels also requires development of new catalysts.[11] Finally, the purification of exhaust gases produced upon combustion of fossil fuels in cars or other appliances relies on heterogeneous catalysts.[12] For example, the lack of economically affordable exhaust catalysts limits the application of diesel engines under increasingly stricter exhaust emission criteria.

Such a demand for novel heterogeneous catalysts may be satisfied only by advanced research workflows.[5,13,14] The previously employed "*trial and error*" approach is unlikely to fulfill expectations put by the society on the catalytic community. Instead, new research and development schemes based on the "*rational design*" principle, deep understanding of structure-activity relationships in heterogeneous catalysts and extensive use of simulations to speed up the investigations are urgently needed.

Structure of heterogeneous catalysts

The application of heterogeneous catalysts is often hindered by their significant cost, especially, when they contain noble metals. Thus, the catalyst efficiency per gram of active material becomes a critical factor. The straightforward way to increase the efficiency is to increase catalyst´s surface area, since only atoms on the catalyst surface are accessible by the reactants. In practice this is achieved through a hierarchical structure of industrially employed heterogeneous catalysts (Figure 1.2).

[b] On the one hand, methane itself is a very potent greenhouse gas, which is bad for environment. On the other hand, it has the highest possible hydrogen to carbon ratio, which becomes the highest possible water to CO_2 ratio upon proper combustion resulting in a small environmental footprint.

The active material is typically dispersed in tiny nanoparticles, which have most of their atoms exposed on the surface. In order to prevent the agglomeration of these particles into bigger species accompanied by the loss of surface area and catalytic activity, the active species are supported on a stable high-surface area support. To allow rapid diffusion of reactants to the catalyst (and products from the catalyst) the support has to be at least microstructured. Finally, bits of the porous support with active material are pressed into pellets (possibly with some binding material) with desired mechanical properties and these pellets are put into chemical reactor.

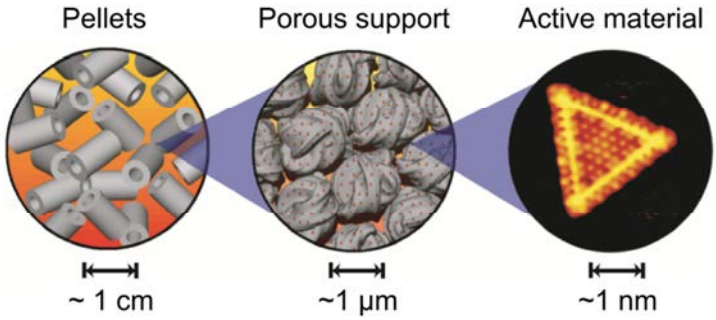

Figure 1.2. Hierarchical structure of a heterogeneous catalyst. The catalyst is put into reactor in the form of hollow pellets, containing nanostructured active material deposited on microstructured (or even nanostructured) porous oxide support. The figure is adapted from Ref. 15.

Effects of nanostructuring on catalytic activity

In principle, all levels of catalyst structure are equally important for its performance. Nevertheless, the work in this thesis is focused only on the nanoscale structure of catalysts. The reason is that in certain cases nanostructuring was shown to *completely alter* catalytic properties of material. This alteration is intimately related to changes in catalyst's electronic structure, which is governed by interactions between quantum wave-like electrons. In this way, the catalytic performance of a nanostructured material becomes dependent on a rich variety of quantum phenomena.

There are many forms of nanostructuring. Such form as nanoparticles (i.e. well separated tiny bits of material) is actively used in heterogeneous catalysis, since it combines very high surface-to-bulk ratio with relatively high thermodynamic stability. It is very common for catalytic properties to be affected by this form of nanostructuring, which is manifested by dependency of properties on the nanoparticle size.[16,17] One of

the most known examples is the pronounced catalytic activity of nanostructured gold in CO oxidation contrasted to the remarkable inactivity of bulky Au samples in almost all chemical processes.[18,19] Also a catalyst may become much more active when nanoparticles of a reducible oxide (e.g. CeO_2) are used as support for transition metal particles.[20]

Depending on the synthesis protocol nanoparticles of catalytically active material may be in supported or solvated state. In some catalysts nanoparticles are agglomerated to form self-supported nanowires or nanoarchitectures.[21-23] These structures are also intensely studied due to their large surface, which is very accessible for reactants.

Steps on surfaces are another ubiquitous form of nanostructuring, since they are naturally present on any but ideally prepared surface.[c] As a rule steps expose low-coordinated atoms with altered chemical activity and in the case of polar or ionic materials they may also have dipole moments.[24] For instance, steps on Ru(0001) surface were shown to be responsible for its catalytic activity in reduction of molecular nitrogen to ammonia.[25] Also, recently the activity of commercial Cu/ZnO catalysts was found to be due to Zn impurities incorporated into steps on Cu surfaces.[26] Finally, the activity of Ru nanoparticles in Fischer-Tropsch synthesis was attributed to steps sites on their surfaces.[27]

Some materials develop new properties when they are reduced to nanoscale only in one dimension, i.e. when they form nanofilms. For example, this can happen in core-shell bimetallic nanoparticles, where one metal forms a thin film covering the nanoparticle core composed of another metal. These nanofilms may have altered properties either due to the electronic interaction with underlying material or just due to the induced mechanical strain. For instance, the latter is thought to be responsible for the catalytic activity of Pt-shell/Co-core nanoparticles in oxygen reduction reaction, which is enhanced compared to pure Pt.[28,29]

[c] Ideally prepared surfaces with high Miller indices would also expose steps arranged in a perfect regular fashion.

Model catalysts

Due to the extremely complex structure of commercial catalysts outlined on Figure 1.2, experimental studies of the effect of nanostructuring on their activity are greatly complicated by a multitude of phenomena taking place at the same time. To tackle this problem model catalysts were developed.[30-32] These systems have a similar degree of nanostructuring as commercial catalysts, but lack any complexity on millimeter and micrometer scales. This is achieved by using single crystal surfaces[d] as a support for nanostructured active materials in experiments instead of sophisticated porous supports in applications. To explore different forms of nanostructuring one may deposit nanoparticles or thin films on single crystal supports, or one may study steps on their surfaces (Figure 1.3). The critical advantage of the model catalyst approach is the ability to precisely control the nanostructuring of the active material, which is seldom achieved in commercial catalysts.

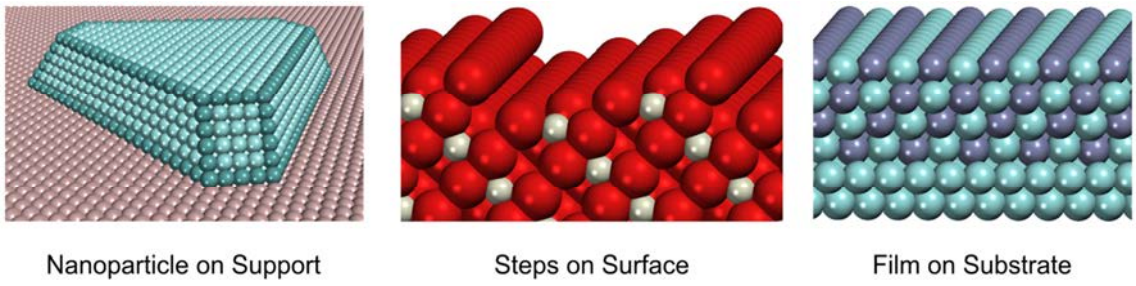

Figure 1.3. Various forms of model catalysts.

The employment of single crystal surfaces as supports for systems under consideration allows exploiting a handful of surface science techniques for investigation of their geometric and electronic structure. The geometric structure can be investigated with scanning tunneling microscopy[31,33,34] (STM), atomic force microscopy[35-37] (AFM) or X-ray reciprocal space mapping.[38-40] In turn, X-ray photoelectron spectroscopy[41-43] (XPS), valence band photoelectron spectroscopy[33,44,45] and scanning tunneling spectroscopy[46,47] (STS) are able to shed light on the electronic structure of model catalysts. The structure of periodic films can be studied with low-energy electron diffraction (LEED) with extreme level of detail when augmented with actual deciphering of I-V curves.[42,48] Also, low-energy ion scattering is used to investigate

[d] Rather often high quality films grown on single crystals are used as supports in model catalysts, instead of single crystals *per se*.

atomic composition and arrangement on surfaces.[28,43] The presence of certain active sites on the surface may be also characterized through adsorption of probe species, e.g. CO molecules, and measurement of their infrared and temperature programmed desorption (TPD) spectra.[49,50] More specialized methods were developed to detect certain particularly important species, like hydrogen atoms[51–53] and Ce^{3+} cations,[54,55] in model catalysts. The application of surface science techniques to catalytic studies has led to multiple breakthroughs in heterogeneous catalysis, which resulted in the Nobel prize award to Ertl in 2007.[56]

Surface Science Approach to Simulations

Following the success of surface science techniques, computational studies of heterogeneous catalysts also started with consideration of perfect single crystal surfaces. In this case, heterogeneous catalysts are modelled either as clusters treated on quantum level embedded in a classically treated environment or as slabs. The latter are sufficiently thick films of material constructed by periodically repeating a certain cell in two lateral dimensions.[e] They have become the working horse of computational studies concerning heterogeneous catalysis.[57-59] Most commonly, such studies focus on adsorption energies of various reactants or products in chemical processes of interest, or reaction and activation energies of the latter. Some examples of these studies are reviewed in Section 11.4. In fact, the slab approach turned out to be not so precise, but still extremely helpful in many cases. Despite that the accuracy of commonly employed electronic structure methods in evaluation of energy profiles is not so high, the precision of pertinent experimental techniques is also far from being perfect. Computational studies have an important advantage compared to experiment – they allow obtaining energetic parameters at each *elementary* reaction step, whereas only *overall* (apparent) energetics are commonly accessible experimentally.

For some purposes even simulation of reaction energy profiles on slabs of catalytically active material is too burdening. One of such tasks is the prescreening of novel potential catalysts for a given reaction, which presents a lot of interest for

[e] Commonly simulation programs based on plane waves require the calculated system to be periodic in three dimensions. In this case, the period of repetition in the third direction is chosen to be sufficiently big to enable the separation of ~ 1 nm between adjacent slabs, where chemical interactions between them become negligible.

industrial companies. During this prescreening the catalytic activity of a few dozens or even hundreds of materials should be evaluated in a reasonable time, which requires less accurate but much faster methods than the one outlined above.

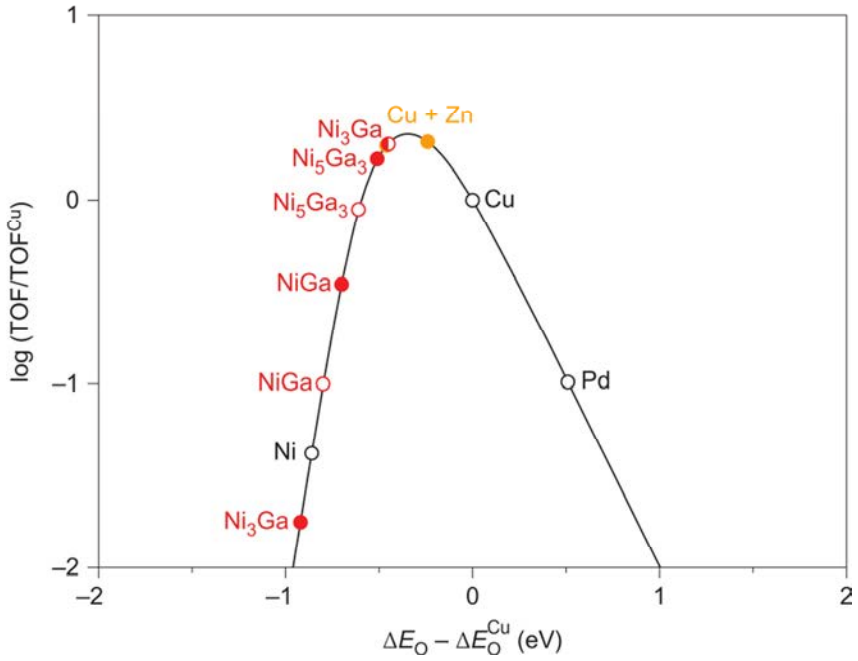

Figure 1.4. Calculated activity of various catalysts for CO_2 reduction to methanol as a function of O binding energy on these catalysts relative to stepped Cu surface. Based on this relation Ni_3Ga was predicted to be a very good catalyst for methanol synthesis, which was verified experimentally.[60]

To deal with this challenge Nørskov et al. proposed using a) Brønsted–Evans–Polanyi principle, b) activity descriptors based on adsorption energies of key moieties, c) the d-band model.[60-62] The first principle postulates correlation between activation energies and reaction energies of elementary steps across structurally similar catalysts of a given type of materials.[63-65] The second notion states that adsorption energies of many reactants, intermediates and products correlate with each other across a set of similar surfaces. That is, it is sufficient to calculate adsorption energies of a few key species to approximately predict reaction energies of pertinent elementary steps (Figure 1.4).[64,66,67] In turn, the latter model introduces correlation between adsorption energies of various species on transition metal surfaces with some parameters of the substrate's electronic structure.[28,68,69] In the simplest form, center of d-band in metal's electronic density of states (DOS) is used as the activity descriptor. In a more advanced version of this method the d-band center is shifted by half of the d-band width to higher energies.[70]

However, the most accurate predictions are obtained when the position of the highest peak in Hilbert transformation of metal's DOS is used as the descriptor,[71] which follows the line of the underlying Newns-Anderson approach. Thus, the combination of all three concepts allows roughly evaluating catalytic properties of a given material based solely on one calculation of its electronic structure.

Most academic studies, however, pursue the opposite goal – to improve the accuracy of conventional slab models by making them more realistic, in spite of concomitant increase of the computational cost of calculations. This can be achieved by a) considering reactions on surfaces covered by reactants, intermediates, products or just "spectator" species and b) accounting for point defects and steps on surfaces.

However, in many cases nanostructuring plays a crucial role for the catalyst activity as discussed before. Only such forms of nanostructuring as steps on surfaces and nanofilms can be simulated using the slab approach. To model catalysts in the form of nanoparticles it is mandatory to go beyond slab models, in particular, when the dependency of catalyst's properties on the nanoparticle size is evident. In fact, due to the present hegemony of slab studies in computational catalysis many basic effects related to nanostructuring of catalytically active materials or their supports remain insufficiently studied with theoretical methods.

1.1. Objectives

The main mission of this thesis is to investigate how various forms of nanostructuring alter properties of materials employed in heterogeneous catalysis through DFT calculations of nanostructured and regular systems. Various nanosized structural features can be classified by the number of dimensions, in which they are extended and in which they are confined to nanoscale. So the following types of nanostructuring are considered in this thesis:

- 0D[f] – unsupported and supported nanoparticles;
- 1D – steps on a surface;
- 2D – thin films.[g]

The goal of this thesis was not to perform systematic studies of a particular material or one or the other type of nanostructuring. Rather this work represents a set of diverse *proof-of-concept* studies aiming at exploration of various ways how nanostructuring may affect catalysts. In particular, the following objectives were identified:

- Quantify differences between physical, adsorptive and catalytic properties of nanoparticle edges, nanoparticle terraces and respective single crystal surfaces for selected representative metal catalysts at different reaction conditions.
- Rationalize the relation between binding in alloy nanoparticles and the most energetically stable structures of bimetallic nanoparticles.
- Estimate the magnitude of changes in properties of metal nanoparticles induced by their interaction with a chemically inert oxide support.
- Investigate how the presence of steps on a surface affects such properties as electronic structure and the energy required to form O vacancies in a reducible oxide.

---

[f] "X" in "XD" means the number of extended dimensions.

[g] This classification does not cover all possible types of nanostructuring. For example, it does not include 1D nanowires and 2D nanogrids composed of 0D ceria nanoparticles considered in this thesis.

- Understand the reasons how and why observed structures of certain thin films differ from bulk structures of respective materials.

Completion of these objectives will broaden the understanding of atomistic mechanisms how nanostructuring may affect catalytic processes. This will be a valuable contribution to the field of computational nanoscience, where many basic concepts are still to be discovered and explored.

1.2. Structure of This Thesis

The introduction to the topics discussed further in the thesis is presented above Chapter 1.

In the following Chapter 2 a brief overview of the theory behind the performed calculations is given. First, the dynamics and the interaction between electrons on quantum level is introduced in Section 2.1. Then a short summary of density functional theory methods (used to obtain results described in Chapters 3–6) is presented in Section 2.2. The performance of popular density functional methods for calculations of solid state transition metals is evaluated in Sections 2.3 and 2.4. Possible ways to account for dispersive (vdW) interactions in DFT are briefly addressed in Section 2.5 and their accuracy for graphene-Ni system is discussed. Section 2.6 outlines studies using slab approach, whereas subsequent Section 2.7 discusses modelling of nanoparticles.

Chapters 3-6 contain results of this work and their discussion. Main results to be defended are presented as articles published in peer-reviewed journals or as articles in preparation. Additional results that were obtained as outcomes of various collaborations are summarized in "Outlook" sections and provided in the Appendix.

The presentation of results is started in Chapter 3 with the discussion of properties of unsupported nanoparticles of transition metals and their alloys. In particular, in Section 3.1 adsorption and infrared spectra of CH_xO_y species on various sites of Pd nanoparticles is discussed. In Section 3.2 the catalytic activity of edges on Pd nanoparticles in methane dissociation analyzed versus that of Pd single crystals. The hydrogenation activity of *terraces* of Pd, Pt, Ni, and Rh nanoparticles in the excess of hydrogen is addressed in Section 3.3. This Chapter is concluded by the presentation of a new method to optimize chemical ordering in bimetallic nanoparticles based on electronic structure calculations in Section 3.4.

Chapter 4 deals with somewhat more complicated structures – transition metal nanoparticles of Pd and Pt on an oxide support, MgO(100). First, in Section 4.1 the most energetically stable shapes of supported nanoparticles and metal-oxide interfaces are investigated. Then the effect of MgO(100) support on the adsorptive and absorptive properties of the supported nanoparticles with respect to single hydrogen atom is

evaluated in Section 4.2. In Section 4.3 a more realistic situation of H absorption into H-covered Pd and Pt nanoparticles supported on MgO(100) is considered.

Such form of nanostructuring as steps on surfaces is discussed in Chapter 5 using CeO_2(111) surface as a practically important example. The discussion is begun with the determination of atomic and electronic structures of steps on CeO_2(111) in combined study using DFT, STM, and STS (Section 5.1). Two novel methods to calculate specific step energies are developed in Section 5.2 and applied to steps on CeO_2(111). In Section 5.3 the ability of the steps to form O vacancies is examined with the help of newly developed procedure to screen the involved O_{vac} + $2Ce^{3+}$ configurations. Section 5.4 outlines the study of water of dissociation on rough CeO_2(111), whereas Section 5.5 deals with the reducibility of nanowires and nanogrids composed of CeO_2 nanoparticles.

Finally, Chapter 6 is devoted to investigations of structures and properties of two-dimensional films. In Section 6.1 the ability of Ce_2O_3 to exhibit different crystal structures in bulk and thin films is discussed. Then in Section 6.2 the reconstruction of PdZn films grown on Pd(111) molecules is investigated with DFT as well as IR spectroscopy and TPD measurements of adsorbed CO species.

The conclusions of this thesis are given in Chapter 7.

Chapter 8 contains the summary of the thesis in Spanish.

The thesis is finished by bibliographic references and list of publications based on the discussion presented herein. As noted before, papers summarized in Outlook sections are provided in the Appendix.

Chapter 2

Methodological Background

2.1. Interaction between Electrons

Wave function of electrons

The probability to encounter an electron in a given point of space is proportional to the electron density in this point, $\rho(r)$. In wave function based methods the density of N electrons is expressed[a] as

$$\rho(r) = N \int |\psi(r_1 = r, r_2 \dots r_N)|^2 dr_2 \dots dr_N \quad (1),$$

where r_i is the three-dimensional vector describing position of each electron and ψ is the normalized wave function of electrons

$$\int |\psi(r_1, r_2 \dots r_N)|^2 dr_1 \dots dr_N = 1 \quad (2).$$

Note that in (1) the integration could be done over any $N-1$ out of N coordinates, because all electrons are equivalent among themselves and are indistinguishable from each other. As a consequence their wave function has a very high symmetry, being anti-symmetric under exchange of any two electron positions r_i and r_j:

$$\psi(r_1 \dots r_i \dots r_j \dots r_N) = -\psi(r_1 \dots r_j \dots r_i \dots r_N) \quad (3).$$

It was proven[72] that such functions may be decomposed into a sum of intrinsically anti-symmetric Slater[73] determinants:

$$\psi(r_1 \dots r_i \dots r_j \dots r_N) = \sum_i C^i \begin{vmatrix} \varphi_1^i(r_1) & \varphi_2^i(r_1) & \cdots & \varphi_N^i(r_1) \\ \varphi_1^i(r_2) & \varphi_2^i(r_2) & \cdots & \varphi_N^i(r_2) \\ \vdots & \vdots & \ddots & \vdots \\ \varphi_1^i(r_N) & \varphi_2^i(r_N) & \cdots & \varphi_N^i(r_N) \end{vmatrix} \quad (4),$$

where each φ is a one-electron function, called orbital.

Schrödinger equation

In the case of low-energy (non-relativistic) electrons the dynamics of this wave function obey Schrödinger[74] equation:

---

[a] For simplicity, here and further in this Chapter spin indexes are omitted.

$$i\hbar\frac{\partial}{\partial t}\psi(r_1 \dots r_N, t) = \widehat{H}\psi(r_1 \dots r_N, t) \quad (5),$$

where $\widehat{H}$ is the Hamiltonian of the system in the form of a linear differential operator acting on the wave function. Eigenfunctions ψ_i with eigenvalues E_i of this Hamiltonian are called stationary states, because they result in electron density, being independent of time t:

$$\psi_i(r_1 \dots r_N, t) = \psi_i(r_1 \dots r_N, 0) * e^{-iE_i t/\hbar} \quad (6),$$

$$\rho_i(r, t) = N \int |\psi(r_1 = r, r_2 \dots r_N, t)|^2 dr_2 \dots dr_N = \rho_i(r, 0) * e^{-iE_i t/\hbar + iE_i t/\hbar} = \rho_i(r, 0).$$

The eigenvalues E_i have a physical nature, being energies of the respective eigenstates. Since any wave function can be decomposed into a sum of eigenfunctions,

$$\psi = \sum C_i \psi_i \quad (7),$$

$$\sum |C_i|^2 = 1 \quad (8),$$

its energy can be written as a sum of eigenvalues,

$$E = <\psi|\widehat{H}|\psi> = \sum |C_i|^2 <\psi_i|\widehat{H}|\psi_i> = \sum |C_i|^2 E_i \quad (9).$$

Thus, if E_0 is the lowest eigenvalue of the Hamiltonian, the energy corresponding to any feasible wave function is higher than E_0. Since often the difference between E_0 and other eigenvalues greatly exceeds room temperature, in many situations it is sufficient to determine ψ_0 (called ground state) and E_0 to describe thermodynamics and behavior of the system.

For a system of interacting electrons in an external potential,[b] $V(r)$, the Hamiltonian has the following form

$$\widehat{H} = -\frac{\hbar^2}{2m}\sum \nabla_i^2 + \sum_{i>j} \frac{e^2}{|r_i - r_j|} + \sum V(r_i) \quad (10),$$

where the first term is due to the kinetic energy of electrons, the second – Coulomb repulsion between electrons.

[b] For example, this external potential may be created by quasi-static atomic nuclei in the Born-Oppenheimer approximation.[396]

Interaction between electrons in the Hartree-Fock method

In the Hartree-Fock method one attempts to calculate the ground state of electronic Hamiltonian in (10) approximating the wave function ψ by a single Slater determinant, ψ_{HF}, in (4). The energy of electrostatic repulsion between electrons in this case is[c]

$$E_{ee} =< \psi_{HF}| \sum_{i \neq j} \frac{e^2}{2|r_i - r_j|} |\psi_{HF} >=$$

$$= \frac{e^2}{2} \sum \left(\int \varphi_i^*(r_1)\, \varphi_j^*(r_2) \frac{1}{|r_1 - r_2|} \varphi_i(r_1)\varphi_j(r_2) \right.$$

$$\left. - \alpha * \varphi_i^*(r_1)\varphi_j^*(r_2) \frac{1}{|r_1 - r_2|} \varphi_i(r_2)\varphi_j(r_1) dr_1 dr_2 \right) \qquad (11).$$

The first term in this integral is the classic electrostatic repulsion between two one-electron charge densities

$$e\rho_i(r) = e\varphi_i^*(r)\varphi_i(r) \qquad (12).$$

The second term, however, does not have any classical equivalent and is caused by the intrinsic asymmetry of the electronic wave function. This way of interaction between electrons is called *exchange* interaction and the second term in (11) is called *Hartree-Fock exchange*.

Naturally, for many electron systems the real ground state wave function cannot be expressed just as one determinant. Consequently, the energy of Hartree-Fock ground state, E_{HF}, is higher than E_0. The difference between two energies is usually defined as the *correlation* energy of the system, $E_{corr} = E_0 - E_{HF}$, which is associated with the so-called *correlation* interaction between electrons. The correlation energy of electrons turns out to be very important in chemical bonding. However, by definition the Hartree-Fock method fails to account for it. At the same time more advanced wave function based methods that succeed in doing this are notoriously computationally expensive for big systems.

[c] The parameter α in the formula is the projection of spin i on spin j, that is, zero for antiparallel spins and one for parallel spins.

2.2. Density Functional Theory

Underlying theory

Kohn (Nobel prize[75] in 1998) and Hohenberg proposed an alternative[76] to methods based on wave functions by proving that the energy (as well as any other observable) of the non-degenerate electronic ground state of (10) should be a universal system-independent Hohenberg-Kohn functional, F_{HK}, of its electron density,

$$E_0 = F_{HK}[\rho] + \int V(r)\rho(r)dr \qquad (13).$$

Later Levy[77] proved that there is a functional that yields the lowest possible energy for a system of interacting electrons for any N-electron density ρ, not necessarily related to a ground state wave function. The exact form of the functional, however, remains unknown.

As a practical solution Kohn and Sham proposed a) to separate known and unknown contributions to F_{HK}, and b) to consider a proxy system of non-interacting electrons in an effective Kohn-Sham potential, V_{KS}, determined by F_{HK}.[78] Namely, the system of N interacting electrons may be represented by a system of N non-interacting electrons[d] with dynamics governed by

$$\widehat{H}_{KS} = -\frac{\hbar^2}{2m}\nabla^2 + V_{KS}(r) \qquad (14),$$

where the effective potential contains the external potential, $V(r)$, and the classical Coulomb interaction between electrons,[e]

$$V_{KS}(r) = V(r) + \int \frac{e^2\rho(r_2)}{|r-r_2|}dr_2 + V_{XC}(r) \qquad (15).$$

[d] Despite the absence of interaction, the electrons still obey the Pauli Exclusion Principle, that is, each state can be populated by at most two electrons with opposite spins.

[e] Thus, V_{KS} depends on the density of the non-interacting electrons. This complicates the search for eigenvalues, ε_i^{KS}, and eigenfunctions, φ_i^{KS}, of $\widehat{H}_{KS}$ in (14), because the form of the latter implicitly depends on φ_i^{KS}.

The remaining part $V_{XC}(r)$ is called *exchange-correlation potential*, which is related to F_{HK} through a set of equations:

$$F_{HK}[\rho] = T_s[\rho] + \int \frac{e^2\rho(r_1)\rho(r_2)}{|r_1 - r_2|} dr_1 dr_2 + E_{XC}[\rho] \quad (16),$$

where T_s is the kinetic energy of the system of non-interacting electrons explicitly accounted for in (14) and E_{XC} is the so-called *exchange-correlation functional*. When the latter is expressed as

$$E_{XC}[\rho] = \int \rho(r)\varepsilon_{xc}(\rho(r))dr \quad (17),$$

the expression for the exchange-correlation potential becomes

$$V_{KS}(r) = \frac{\partial}{\partial\rho}\rho(r)\varepsilon_{xc}(\rho(r)) \quad (18).$$

On the one hand, finding the exact form of E_{XC} is probably as complicated as finding the exact form of F_{HK}. On the other hand, $E_{XC}[\rho]$ is much smaller in magnitude than $F_{HK}[\rho]$, which is dominated by the kinetic energy of non-interacting electrons and their Coulomb repulsion. Thus, any approximations made to E_{XC} would have a smaller effect on the resulting ground state compared to approximations made to F_{HK}.

Tiers of exchange-correlation functionals[f]

Naturally, the predictive ability of Kohn-Sham formulation of density functional theory depends on the accuracy and complexity of the employed E_{XC} or ε_{xc}.[g] In the simplest version, called *local density approximation*[78] or *LDA*, ε_{XC} is fitted to reproduce properties of homogeneous electron gas. Namely, if ε_{XC} is decomposed to separate contributions from electron exchange, ε_X, and correlation, ε_C, then according to Dirac[79]

$$\varepsilon_X = -\left(\frac{81}{64\pi}\rho\right)^{1/3} \quad (19),$$

[f] Functionals of Minnesota family are touched in Section 11.2 and a brief discussion of available methods to account for van der Waals interactions in DFT are outlined in Section 2.5.

[g] Similarly to Section 2.1, the extension of density functional theory to spin-polarized systems is not considered here for simplicity. Recently, the complexity associated with spins in DFT was reviewed by Jacob and Reiher.[397]

and ε_C can be obtained not analytically but through quantum Monte-Carlo calculations.[80]

Local density approximation offers almost perfect description of the homogeneous electron gas; however, electron density of atoms is far from being homogeneous. To account for spatial variations of the electron density one may consider the dependency of ε_{XC} also on gradient of electron density, $\nabla\rho$. This leads to the *generalized gradient approximation* or *GGA*. There is no single possible way to include the dependency on $\nabla\rho$ in the exchange-correlation functional. GGA functionals used nowadays such as PBE[81], RPBE[82] usually aim to reproduce as many of established properties[83-85] of exact E_{XC} as possible. In particular, such functionals as RGE,[86] SOGGA[87] and PBEsol[88] intend to reproduce the correct second-order behavior of exact exchange correlation functional, which could be beneficial for solid-state calculations.

Both LDA and GGA functionals suffer from self-interaction error, that is, in these calculations each electron is repulsed by its own electrostatic field.[89] Partially, this error may be corrected by more flexible exchange-correlation functionals from the next tier, called *meta-GGA*. These functionals take into account not only the density gradient, $\nabla\rho$, but also its second derivative $\Delta\rho$ or kinetic energy density[h]

$$\tau(r) = \frac{\hbar^2}{2m}\sum\left|\nabla\varphi_i^{KS}(r)\right|^2 \qquad (20),$$

where φ_i^{KS} are Kohn-Sham one-electron states defined as eigenfunctions of $\widehat{H}_{KS}$ in (14). In particular, the TPSS[90] functional of meta-GGA family is able to eliminate self-interaction error for systems with one and two electrons (i.e. single occupied φ_i^{KS}). Also unlike many GGA functionals TPSS has correct asymptotic behavior in the vicinity of atomic nuclei. Note that meta-GGA functionals not always follow the Kohn-Sham scheme exactly, since it may be very hard to take the derivative in (18) in order to calculate V_{KS}.[91]

Another way of (partially) correcting the self-interaction error is the introduction of explicit Hartree-Fock exchange between φ_i^{KS} into the exchange-correlation

[h] The latter is interrelated with $\Delta\rho$ through $\tau(r) = \sum\varepsilon_i^{KS}\left|\nabla\varphi_i^{KS}\right|^2 - V_{KS}\rho(r) + \frac{1}{4}\Delta\rho(r)$ in atomic units, where ε_i^{KS} are eigenvalues of $\widehat{H}_{KS}$ (14). [398]

functional. This leads to *hybrid* exchange-correlation functionals, which are significantly more computationally expensive than LDA or GGA functionals. The reason is the necessity to explicitly calculate interaction between each pair of electrons, which is done through orbital-independent effective potential in other methods.

The design of hybrid functionals is also not straightforward. Typically they have a form

$$E_{XC} = \alpha E_X^{HF} + \beta E_X^{DF} + \gamma E_C^{DF} \quad (21),$$

where E_X^{HF} is the Hartree-Fock exchange, E_X^{DF} and E_C^{DF} are exchange and correlation part of a given exchange-correlation density functional and α, β, and γ are some coefficients. Naively one could think that $\alpha = \gamma = 1$ and $\beta = 0$ (i.e. direct substitution of approximate DFT exchange by the exact Hartree-Fock exchange) would yield the highest accuracy.[i] However, it turns out that there is a very big error compensation between known forms of E_X^{DF} and E_C^{DF}. Hence, the combination of $\beta = 0$ with $\gamma = 1$ leads to a very poor description of many systems. In fact, it was shown that the amount of the exact exchange, α, should be different for different systems.[92] Namely, molecular systems were suggested to be best described with 25% of Hartree-Fock exchange, adopted in such hybrid functionals as PBE0,[93] HSE[94,95] and B3LYP[96] (the latter has $\alpha = 0.2$). At the same time, metals do not seem to require any Hartree-Fock exchange at all, which actually was shown detrimental for the description of conductors.[97]

Due to the high computational cost of hybrid functionals there have been some attempts to make it more affordable via so-called range separation. That is, to calculate the Hartree-Fock exchange only for orbitals located close to each other and to consider only not so computationally expensive E_X^{DF} for well-separated orbitals. This scheme seems to be particularly advantageous for solid state calculations, which have an enormous amount of distant atoms. For example, HSE exchange-correlation functional[94,95] contains range-separated exchange.

Note that some functionals, like TPSSh,[98] combine both ingredients of meta-GGA and hybrid functionals.

---

[i] Note that $\alpha = 1$ is necessary to fully correct the self-interaction error.[399]

The next rung of density functionals methods is based on random phase approximation (RPA) to the exact electron correlation.[99-101] Although RPA calculations are very computationally expensive, they correct some *qualitatively* wrong predictions of other DFT approaches.[102,103]

Hubbard and Dudarev approach to the electron localization problem

Many contemporary density functional methods suffer from the electron localization problem, i.e. they overestimate the energetic stability of electronic configurations with some electrons delocalized over two or more atoms.[104] This problem is related to the already mentioned (many-electron) self-interaction error.[89] At some degree, the electron localization problem may be solved by introduction of the Hartree-Fock exchange into E_{xc} as in hybrid functionals. On the one hand, the consideration of Hartree-Fock exchange will dramatically increase the computational cost of pertinent calculations. On the other hand, the Hartree-Fock exchange has a potential to overcorrect the electron localization problem and to lead to overlocalized solutions.[105]

A similar problem of too delocalized electrons also exists in the conventional band structure theory, which predicts certain well-known insulators to be conducting. There, the practical solution was proposed by Hubbard through the consideration of model Hamiltonians with explicit contributions from on-site intra-atomic Coulomb interactions to the total energy.[106] Several authors[107-109] tried to introduce similar corrections to the Kohn-Sham framework, hoping that it will alleviate the electron localization problem. Among various methods the rotationally invariant scheme by Dudarev et al. became the most common due to its relative simplicity.[110] Roughly speaking[j] in this approach the total energy is a sum of DFT-energy, E^{DFT}, and Hubbard corrections

$$E = E^{DFT} + \frac{U_{eff}}{2}\sum n_i(1 - n_i) \qquad (22),$$

[j] More precise formulas are written in terms of density matrices or creation-destruction operators.

where U_{eff} is the effective energy of on-site Coulomb interaction and n_i is the occupation of *atomic* orbitals,[k] to which this correction is applied. As one can see, the corrections are zero for fully occupied and fully unoccupied orbitals, whereas the partial occupation of atomic orbitals by delocalized electrons is disfavored by ~$U_{eff}/8$, where U_{eff} is typically of the order of few eV. Note that these corrections also affect the energies of one-electron Kohn-Sham states by

$$\Delta\varepsilon \sim \frac{\partial}{\partial n_i}\frac{U_{eff}}{2}\sum n_i(1-n_i) = U_{eff}(\frac{1}{2}-n_i) \qquad (23).$$

That is, full occupied one-electron states are stabilized by $U_{eff}/2$, while fully unoccupied states are destabilized by the same value.

The downside of this method is the difficulties associated with the determination of U_{eff} values for each system, caused by not clearly understood electron screening in the solid state.[111-113] In practice U_{eff} is often chosen empirically to reproduce certain experimental observables.[114]

[k] This approach can be also extended to molecular orbitals.[400-402]

2.3. Transition Metals Calculated with LDA and GGA Functionals (Outlook)

One of the advantages of the wave function based methods compared to DFT is the ability to gradually increase their accuracy. Indeed, by increasing the size of the basis set and by including more determinants in the multi-configurational methods one can approximate the *exact* wave function increasingly better. In contrast, Kohn-Sham DFT is inherently a single-determinant approach and its accuracy is limited by the approximate form of E_{XC}, which cannot be improved at will.

It is very important to assess the accuracy of various approximate exchange-correlation functionals for calculations of specific systems. Such assessments are common for molecular or cluster systems,[115-117] but relatively seldom for solid state.[85,118,119] Partially, this is because computational studies dealing with molecules are more widespread than investigations concerning modelling of solid state systems. However, partially this is also due to the abundance of precise experimental measurements of various properties of molecular systems, which is not the case for many crystalline materials.[120,121] Since Chapters 3 and 4 as well as Section 6.2 of this thesis deal with nanostructured Pd, Pt and other transition metals, it seemed necessary to understand the degree of accuracy of DFT for this kind of materials.

In Section 11.1 a study of bulks of all 30 transition metals with PW91, PBE, RPBE and PBEsol functionals of GGA type as well as CA and VWN variations of LDA is presented. The calculated interatomic distances, cohesive energies and bulk moduli were compared to the available experimental data. Calculations of many of these transition metals (e.g. Re, Hf, Cd, Zn, Sc, Hg, La, and Mn) were presented in a systematic manner for the first time.[l]

Some findings in this study were well expected, while others appeared rather surprising (Figure 2.1). For example, it was found that GGA functionals on average yield more accurate interatomic distances than functionals of LDA family. Also the PBEsol functional, which was designed to yield improved lattice constants of crystals,[88] actually resulted in less accurate interatomic distances than the original version of PBE.

[l] Despite that DFT calculations of periodic systems have been possible for ~20 years, the absolute majority of them focused on Cu, Rh, Pd, and Ag, while many metals did not get any scientific attention.

As for cohesive energies, LDA exchange-correlation functionals expectedly yielded too strong metal-metal bonding. Rather surprisingly, PW91 and PBE functionals were found to neither systematically underbind nor overbind transition metals. All the considered functionals except RPBE overestimated the experimental values of bulk moduli. All in all, among the considered functionals PW91 and PBE were found to be the most accurate for calculations of transition metal bulks and LDA functionals the least accurate.

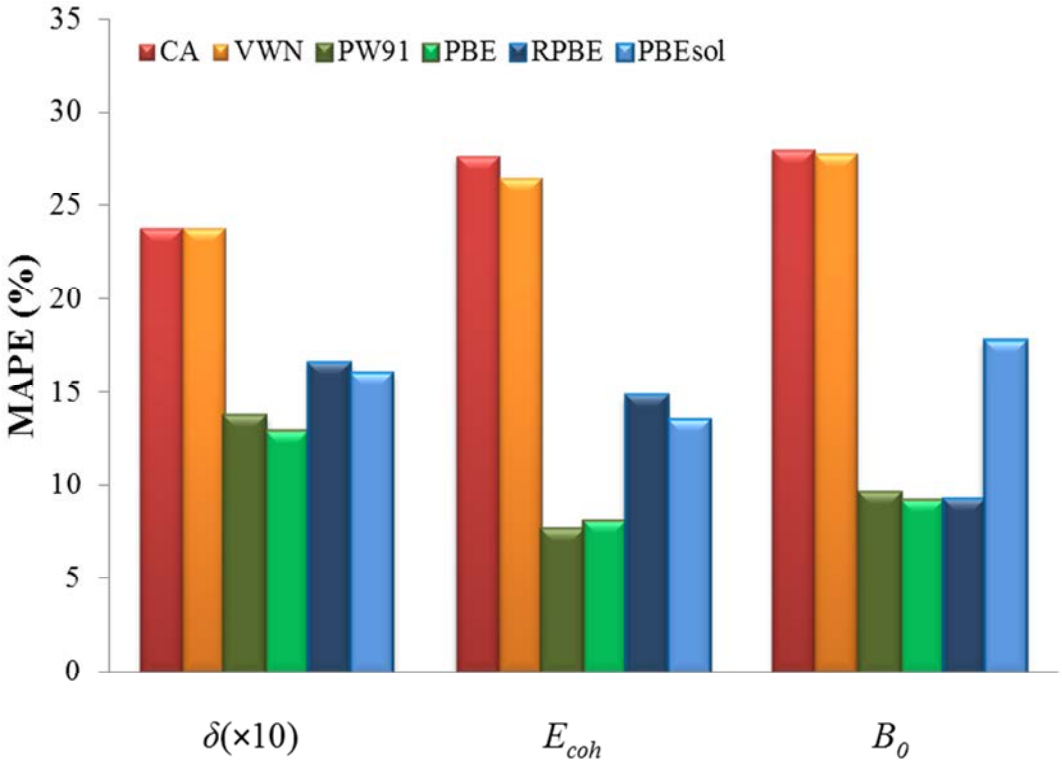

Figure 2.1. Performance of LDA and GGA functionals for transition metals. Mean average percentage errors (MAPE) for the closest interatomic distances, δ, cohesive energies, E_{coh}, and bulk moduli, B_0, of transition metal bulks (except Mn, La, and Hg) are presented.

Nevertheless, this trend changed when specific energies of (111) surface of fcc metals were considered. Namely, all the LDA and GGA functionals underestimated the experimental surface energies. However, the inherent underestimation of surface energies was partially compensated by the overestimated strength of metal-metal bonds by LDA functionals and at a lesser extent by PBE_{sol}. Such GGA functionals as PW91 and PBE, which are quite accurate (but not precise) in the prediction of cohesive

energies, lead to underestimated surface energies. Finally, the RPBE functional yields the lowest and the worst surface energies, since it underbinds transition metals.

Interestingly, RPBE is reported to yield rather accurate adsorption energies[82,122] accompanied by the lowest surface energies. In contrast, LDA functionals are the most accurate for surface energies but commonly overestimate energies of adsorption. Other functionals are in between these two extremes in both respects. Thus, for the considered LDA and GGA functionals it seems impossible to predict both adsorption and surface energies with the same degree of accuracy. Only more advanced TPSS and M06-L meta-GGA functionals or significantly more time consuming RPA method are reported to succeed in this.[102,122]

2.4. Hybrid and Meta-GGA Functionals for Transition Metals (Outlook)

The accuracy of DFT for molecular calculation can be improved by advancing the employed functionals to meta-GGA or hybrid level. These functionals yield better description of strong variations of electron density within molecules and/or the intrinsically non-local nature of exchange interaction, which is necessary to correct the self-interaction error. The situation in transition metal bulks, however, differs in the following respects: 1) the density of valence electrons varies rather smoothly in infinite periodic single crystals; 2) Hartree-Fock exchange is screened by electron correlation; 3) the self-interaction problem is not so critical for electrons delocalized over the whole periodic structure. Thus, it is not clear if meta-GGA and hybrid functionals would be as advantageous for calculations of solid state transition metals as for molecular moieties.

Additional complications arise from the well-known poor performance of the Hartree-Fock method and hybrid functionals for transition metal systems.[97,123] Apparently, the addition of HF exchange ruins the ability of LDA and GGA exchange correlation functionals to account for static correlation, which is of utmost importance in transition metals. [116,117,124] Also the consideration of HF exchange is not advisable for conducting metallic systems, because it leads to incorrect density of states at the Fermi level.[m]

Many common meta-GGA and hybrid functionals belong to the so-called Minnesota family of functionals developed by Truhlar et al.[125-127] These functionals may contain dozens of empirical parameters, which are fitted in order to reproduce certain experimental observables. Naturally, one may question the reliability of such a fitting and the applicability of these functionals outside of their fitting sets. These fitting sets consisted mostly of various properties of molecular species. Only in some cases they also included relatively few data points regarding transition metal complexes and solid state systems.[87,128] Thus, it is very interesting to examine the performance of Minnesota functionals for calculations of single crystals of transition metals, since the latter are very different from the systems used for the fitting of the functionals.

[m] The correct behavior should be, of course, recovered, when the exact correlation functional is used.

A study assessing the performance of various meta-GGA and hybrid functionals including those by Truhlar et al. for calculations of solid transition metals is presented in Section 11.2. Similarly to Section 11.1 interatomic distances, cohesive energies and bulk moduli of 27 transition metals[n] were calculated with the following functionals:

GGA – SOGGA11, N12[o] (+data calculated with PBE from Section 11.1);

meta-GGA – TPSS, revTPSS, M06-L, MN12-L[o];

hybrid – PBE0, HSE06, B3LYP.

In variation with the analysis performed in Section 11.1, in Section 11.2 results of calculations are compared to the respective experimental data corrected for finite temperature and zero-point vibrations. These corrections were computed to be 0.3 – 2.2 pm for interatomic distances, 0.01 – 0.06 eV for cohesive energies, and 1–17 GPa for bulk moduli by Lejaeghere et al. Although not being critical, these corrections shift the experimental values closer to the results of the discussed DFT calculations.

Rather surprisingly, it was found that hybrid functionals HSE06 and PBE0 yield the most accurate interatomic distances, despite certain doubts of their applicability to conductors and systems containing transition metals (Figure 2.2). In terms of the predictive power for structural parameters these two functionals are followed by non-parameterized PBE, TPSS and revTPSS exchange-correlation functionals. For cohesive energies fitted nonseparable N12 functional was found to be the most accurate, followed by TPSS functional and then by fitted M06-L and finally by PBE. Hybrid functionals underestimated cohesive energies by ~1 eV and were concluded to be the least accurate. The most accurate bulk moduli were calculated by PBE, followed by hybrid HSE06 and meta-GGA functional TPSS.

---

[n] Out of all 30 transition metals Mg, La, and Hg were not considered, because in Section 11.1 it is shown that DFT describes these method in an unsatisfactory way. Therefore, these rather special cases should be considered apart from the rest of transition metals.

[o] NGA and MN12-L functionals employ the so-called nonseparable approximations, where no clear distinction is made between exchange and correlation parts of E_{xc}.

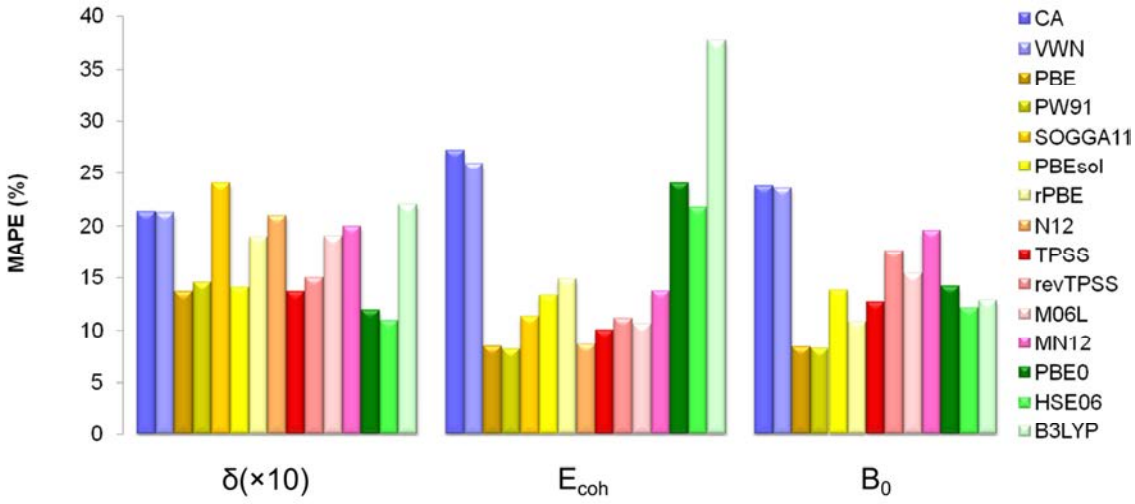

Figure 2.2. Performance of LDA, GGA, meta-GGA and hybrid functionals for transition metals. MAPE for calculation of the closest interatomic distances, δ, cohesive energies, E_{coh}, and bulk moduli, B_0, of transition metal bulks (except Mn, La, and Hg) are displayed.

Overall, PBE and TPSS were concluded to be the most suitable functionals for studies of transition metals. Despite that PBE yields the best accuracy only for bulk moduli and TPSS is not the most accurate functional for any particular property, their performance for all considered observables as a whole is superior to other functionals. The considered Minnesota functionals were shown to be quite appropriate for description of transition metal bulks, despite that they were not included in the fitting sets for these functionals. Most often their performance was not superior to the performance of non-parameterized PBE and TPSS functionals, but also it was not much worse than the latter. This suggests that many meta-GGA functional, in particular TPSS, can be applied to modelling of systems containing solid state transition metals. This may be very advantageous for systems composed of both organic molecules and metal particles or surfaces, since meta-GGA functionals could describe the organic part of the system much better than PBE does. Interestingly, the B3LYP exchange-correlation functional, still very popular in molecular studies,[129] yields the lowest accuracy for interatomic distances and cohesive energies of transition metals. Previously, this was rationalized by the wrong description of homogeneous electron gas by B3LYP, which is not important for molecular species but is crucial for modelling of solid state systems.[123]

2.5. Taking Dispersive Interactions into Account within DFT (Outlook)

Dispersive interactions are very important in certain systems, especially where the immediate chemical interactions between adjacent atoms do not play a decisive role. For example, these interactions are of utmost importance in biochemistry due to the mere size of considered moieties.[130] However, van der Waals (vdW) interactions[p] may be important also in other cases, such as adsorption on a substrate without the formation of strong chemical bonds.[131] One of such cases is the interaction of graphene with transition metal surfaces or adsorbates, which manifests interesting interplay between van der Waals attraction and Pauli repulsion.[132,133] Since many scientists study graphene on transition metal surfaces for a handful of practical reasons,[134-136] it is important to determine which of the available computational methods is the most suitable for modelling of this system.

In fact, a few methods have been proposed to augment density functional theory with dispersive interactions. The simplest methods developed by Ortmann[137] or Grimme[138,139] just include a vdW contribution as an additional empirical term to energy (and interatomic forces)

$$E = E^{DFT} + \sum \varepsilon_{ij}^{vdW} \tag{24}.$$

There ε_{ij}^{vdW} is the dispersive interaction between a pair of atoms at positions R_i and R_j given by the asymptotically correct formula:

$$\varepsilon_{ij}^{vdW} = -f_{ij}(|R_i - R_j|)\frac{C_6^{ij}}{|R_i - R_j|^6} \tag{25},$$

where empirical coefficients C_6^{ij} may be approximated in various ways, starting from the original formulas by London, or by fitting to the available experimental data. In turn, f_{ij} is the damping function, which smoothly increases from 0 to 1 as its argument changes of 0 to ∞ (Figure 2.3). This function is necessary because these vdW corrections are required only to correctly describe the *long-range* dispersive interaction between atoms. Since dispersive interactions are just a manifestation of non-local

[p] In this Chapter "van der Waals" interaction is used in the meaning of "van der Waals-London" interaction, that is, as a complete synonym to "dispersive" interaction.

electron correlation, at short interatomic distances they are taken into account by the correlation part of the employed density functional. The differences between various methods of this family are mainly limited to different values of the employed C_6^{ij} and different forms of f_{ij}. Partially, rather satisfactory accuracy of these methods is due to the fact that equation (24) is actually a pretty good approximation for the exact van der Waals interaction computed by high-level wave function based techniques.

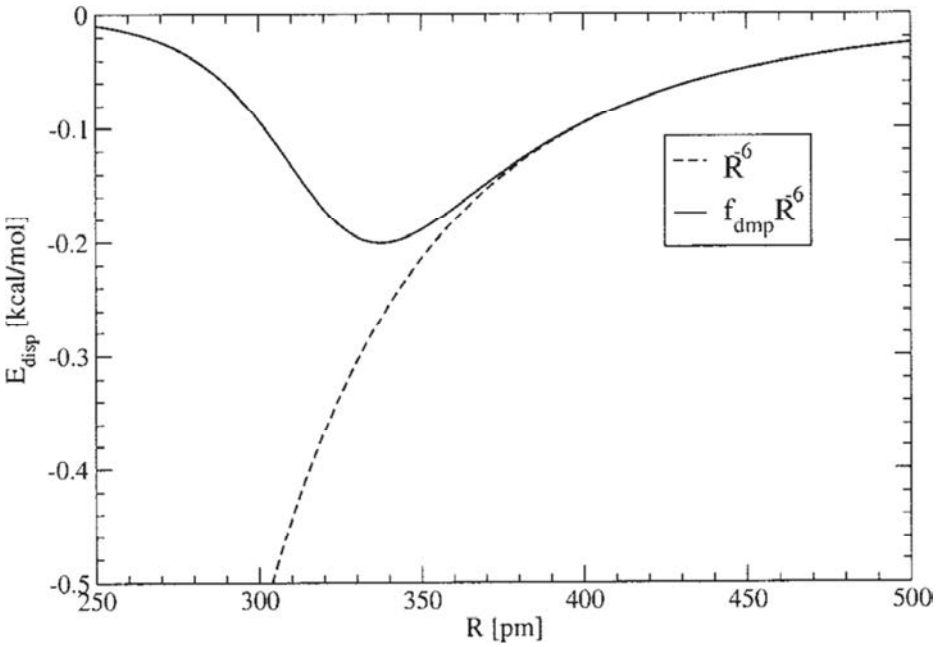

Figure 2.3. Empirical corrections for the attractive part of dispersive interactions before damping (dashed line) and after damping in the method by Grimme.[138]

Recent methods to account for dispersive interactions in DFT framework developed by Tkatchenko and Scheffler are more sophisticated. In the simplest version[140] they follow equations (24) and (25), but with coefficients C_6^{ij} calculated individually for each atom in each particular system

$$C_6^{eff} = C_6^{free}(V^{eff}/V^{free})^2 \qquad (26).$$

In this formula C_6^{free} is the coefficient for the free atom and V^{free} and V^{eff} are volumes of free atom and the same atom in the molecule calculated via the Hirshfeld method. In this way it is possible to account for the changes in electronic structure of every atom depending on its chemical environment and the charge state. The latter is

particularly important for modelling of ionic materials, for which the reliable empirical values of C_6^{ij} are often not yet established.

In the more advanced version[141] of this method an even more sophisticated method to determine C_6^{ij} is used. This method is based on the theory developed by Tkatchenko et al. who found a way through the determination of C_6^{ij} in a self-consistent manner to account for the *screening* between instantaneous dipoles causing the attraction. In order to perform these calculations equations analogous to quantum harmonic oscillator model for coupled fluctuating dipoles should be solved. Despite this complication, the computational cost of this method is still much lower than the computational cost of the DFT part. This method is supposed to yield increased accuracy for solid state systems, where van der Waals interactions may be effectively screened by surrounding atoms.

The final group of methods is based on the work by Dion et al.[142] to express the dispersive interaction as a function of density in the form of

$$E^{corr-vdW}[\rho] = \frac{1}{2}\int \rho(r_1)\varphi(r_1, r_2)\rho(r_2)dr_1 dr_2 \qquad (27),$$

where the kernel $\varphi(r_1, r_2)$ is derived approximately from the response function of the electron density and from its dielectric function. Additional complications come from the fact that $E^{corr-vdW}$ represents only a part of exchange-correlation functional. So it is not very clear what should be the form of its other parts to be consistent with such a correlation. In the original publication the authors suggest to use revPBE for the description of semi-local parts of exchange and correlation. Later, however, some of them proposed to use rPW86.[143] Other authors assessed the performance of a multitude of functionals augmented by (27) for description of various molecular and solid state systems and proposed alternative versions of vdW functionals, more accurate than rPW86-vdW.[144,145]

Note that all these methods were developed based on the theoretical background for molecular or semiconducting systems. The application of these methods to conductors, such as metallic solids, should be done with caution. However, there are certain arguments that even the simplest empirical methods may be used in this case, since they result in the correct asymptotic behavior for conducting surfaces (if

parameterized properly).[103,146] The self-consistent method by Tkatchenko, Scheffler et al. appears to be even more reliable, since it takes the screening between instantaneous dipoles into account. Finally, the vdW density functional, $E^{corr-vdW}$, by Dion et al. should give the correct (zero) non-local dispersive energy for (conducting) homogeneous electron gas and so it may be also applied to metals.

In Section 11.3 the discussed approaches are applied to graphite and graphene sheet adsorbed on Ni(111) surface (Figure 2.4). These systems are used for benchmarks since they are very representative of graphene containing systems and also well-characterized. In particular, it is known that on Ni(111) graphene may chemisorb in two modes: 1) top-fcc with a half of C atoms above top sites and another half above fcc sites and 2) bridge-top, where centers of every second C-C bond are located above top sites.[69,147] In both these adsorption modes the graphene-Ni distance should be 190-220 pm. At the same time only physisorption of graphene is possible in the hcp-fcc adsorption mode with graphene-Ni distance of >300 pm. Also the energy of the interaction between graphene and Ni(111) has been estimated experimentally and it was clearly shown to exceed the interaction energy between graphene layers in graphite.

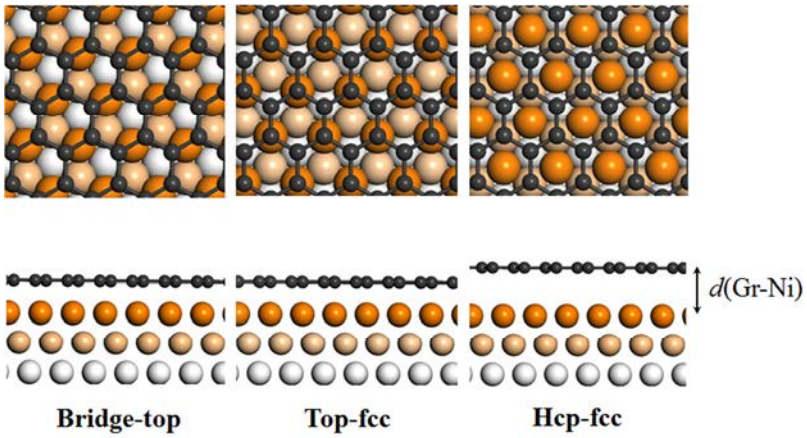

Figure 2.4. Adsorption modes of graphene (grey) on Ni(111) (shades of orange).

Among all the considered functionals only optB86b-vdW version of density functional and PBE exchange correlation functional augmented by dispersive corrections by Grimme were able to provide realistic description of both graphite and graphene-Ni system. Hence, dispersive interactions in graphene-containing systems may be described by various approaches based on completely different principles. At the same time, the method by Tkatchenko et al. showed somewhat unsatisfactory results

because of the following: 1) it lead to underestimation of the lattice constant of bulk Ni, 2) it predicted the interaction between graphene sheets in graphite to be stronger than the interaction between graphene sheet and Ni(111) surface.

2.6. Studies of Catalysts Using Conventional Slab Approach (Outlook)

Presently the majority of computational catalytic studies are performed using slab[q] approach, which is able to grasp many phenomena important for catalyst's activity. For example, using slab approach it is possible to investigate 1) detailed reaction mechanism and each elementary step of the reaction, 2) trends in catalytic activity across various materials, 3) how the catalytic activity depends on the type of exposed surface, 4) how the catalytic activity changes with surface coverage and/or coadsorbates, 5) the effect of impurities, absorbed moieties and alloying on the catalytic activity. Thus, even within the slab approach there is a plenty of room for basic investigations.

Some topics extensively investigated in such a way are reviewed in Section 11.4. First, ethylene and acetylene hydrogenations on noble metals are scrutinized as model reactions for industrially important hydrogenations of double C=C and triple C≡C bonds. Second, exhaustive analysis of literature available on methanol decomposition and methanol steam reforming on Cu, Pd, and PdZn surfaces is presented. These interrelated reactions have attracted so much attention because 1) they are very important for prospective hydrogen-based energy production and 2) they present a curious case where catalyst's activity and selectivity are determined by two different elementary steps. Then the ability of DFT calculations to predict the selectivity of a catalyst is discussed for selective hydrogenation of unsaturated aldehydes, which is important for synthesis of pharmaceutical compounds. The selectivity was found to be very sensitive to the calculated activation energies, which limited the predictive power of DFT for this system. Finally, the effect of low-coordinated atoms and Ag impurities on the catalytic activity of Au in CO oxidation was reviewed to show how complex could be the structure of an active site on a heterogeneous catalyst.

Despite its widespread application the slab approach has one major deficiency; it is not able to account for nanoscopic structural features often present in commercial catalysts. Hence, in the cases when these features actually determine the catalyst's activity or selectivity, insights obtained using the slab approach may become irrelevant or even misleading.

---

[q] A typical slab is displayed on Figure 2.4.

2.7. Modelling of Nanoparticulate Catalysts

As pointed out in the Introduction, the majority of catalysts studied experimentally and/or employed in industry contain the active material in nanoparticulate phase in order to increase the reacting surface area. Often these nanoparticles have the size around tens of nanometers and contain thousands of atoms. Thus, their direct calculation using electronic structure methods remains practically impossible with contemporary computational methods and so dedicated modelling approaches are often required.

There is a variety of active sites on nanoparticulate catalysts. Among these sites surface terraces are relatively easy to investigate, because they are composed of the same sites as regular periodic surfaces defined by low Miller indexes. Hence, they can be represented by conventional slab models. The remaining areas on the surface of NPs involve under-coordinated edge or corner metal atoms and feature the sites different from those on the single-crystal surfaces (Figure 2.5). Such sites partially composed of low-coordinated atoms are often considered to be notably more reactive than the regular surface sites.[148-150] Thus, their proper account in theoretical studies is necessary already for very well-ordered model catalysts. The importance of the inherently nanoparticulate sites is expected to be even higher for industrial catalysts than for model systems, because the former feature more disordered NPs with much higher proportion of low-coordinated atoms and adjacent areas.

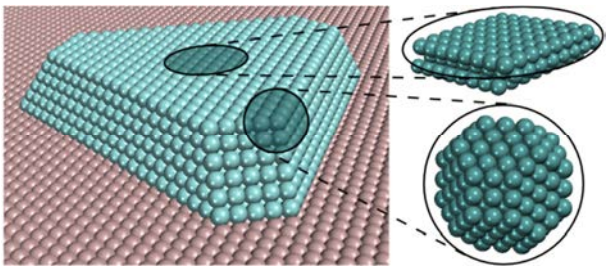

Figure 2.5. Schematic representation of the experimentally studied model catalysts with a well-defined metal NP (cyan) supported on an oxide film (redwood). The insets (turquoise) encompass active sites on the planar and the edge-corner zones of the NP inherent to the slab and particle models, respectively.

To simulate edge, corner and related surface irregular active sites of NPs one has to not only reproduce their local structure in calculations, but also adequately describe

the surrounding ensemble of atoms (environment). In ionic and covalent materials it is sufficient to account for relatively few adjacent atoms to describe the chemical properties of a certain site (also typical for homogeneous catalysts). At the same time, due to delocalized electronic states, the number of atoms required to properly mimic the environment in a metallic system may be rather large and depend on particular system or reaction. A practical way to efficiently calculate the environment part of the system is to exclude from it atoms that do not critically affect the investigated properties.

As a consequence, the electronic structure modelling of oxide-supported transition metal NPs usually relies on accounting for only a fraction of metal atoms surrounding the active site and neglects direct effects of the oxide component.[151,152] The latter assumption of the negligible support effect is expected to be valid for big nanoparticles on relatively unreactive and non-reducible oxide supports, because in this case only a small fraction of nanoparticle atoms has contact with the support. The validity of this assumption is assessed and discussed in due detail in Chapter 4. At the same time, to describe the interaction of metal nanoparticles with such supports as TiO_2 and CeO_2 it may be necessary to use more complicated models,[55,153,154] which explicitly include support and may be also its nanoscale features.[r]

Existing ways to simulate nanoparticles and their drawbacks

Three cluster-type models are employed in first-principles theoretical studies of surface reactivity of metals: (*i*) so-called, two-dimensional (2D) cluster models cut from surface layers;[155] (*ii*) sub-nanometer size particles, either at the true global minimum or the lowest-energy isomers found;[156] (*iii*) three-dimensional (3D) NPs (mainly, truncated octahedral-like) cut from the bulk by low-index Miller planes and subsequently structurally optimized to the closest local minimum (Figure 2.6).[157] Models (*i*) typically consist of two or three varying in the lateral size layers of a surface under scrutiny, which are fixed at the bulk structure.[155,158,159] Nowadays, the non-embedded version of method (*i*) is rarely used for metals, because it results in adsorption energies considerably fluctuating upon cluster size variations.[160] However, the energetics may be improved if adsorption on clusters in (slightly) excited electronic configuration is

[r] The effect of nanostructuring on properties of ceria is at varying extent touched in Chapter 5.

considered by means of a rather involving bond preparation method.[161] Note that cluster-based modelling of non-metallic systems is widely used when augmented with cluster embedding techniques; however, the application of these techniques to metals is complicated and not so common.[162-164] Approach (*ii*) is limited to clusters with up to several dozens of atoms, for which it is still feasible to calculate global minimum structures.[165-167] For any given small cluster size, this strategy is perfectly adequate (leaving aside the seldom considered[168,169] issue of the support treatment). However, it yields observables specific for each particular cluster size,[170,171] which cannot be extrapolated to the observables of bigger NPs typical for model catalysts (because of the so-called "every atom counts" regime).[167,172] Nevertheless, this approach is widely used, when properties of sub-nanometer clusters are subject of interest,[173] as, for instance, in the case of small Au particles.[170,171,174]

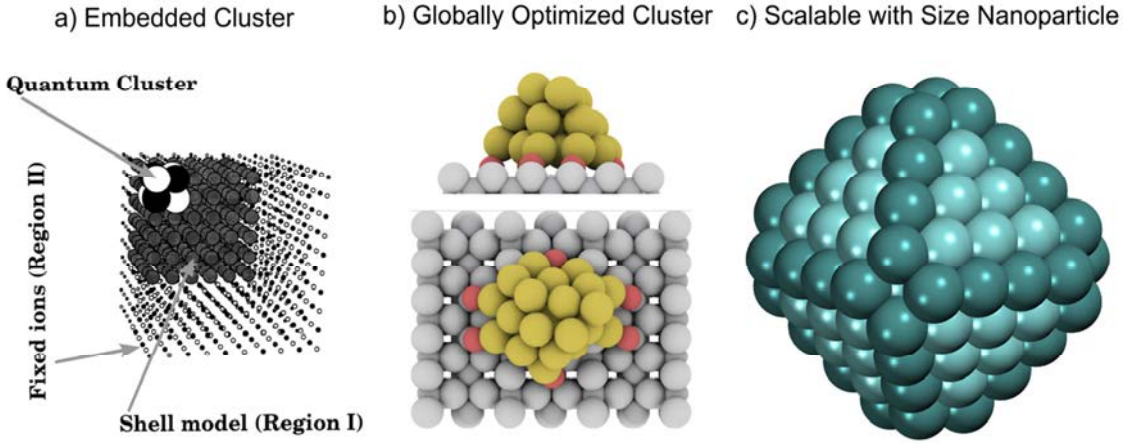

Figure 2.6. Models of nanoparticulate materials: a) embedded cluster model of MgO nanoparticle corner, adapted from Ref. 163 b) globally optimized Au_{24} cluster on TiO_2(110) slab with adsorbed oxygen;[175] c) Pd_{140} scalable with size nanoparticle with fcc structure and truncated octahedral shape. Au atoms are displayed in gold; adsorbed O – red, TiO_2 – grey, Pd – cyan. Darker atoms are located on NP edges.

Scalable with size nanoparticles

Studies described in Chapters 3 and 4 are performed within the third approach, i.e. by calculating 3D NPs of (mainly) truncated cuboctahedral shape, cut from the bulk and then optimized. The model NPs designed in such a manner have the bulk-like atomic arrangement and are terminated by (111) and (100) Miller surfaces, just as the bigger experimentally observed NPs.[33,176] Because of that, the structures of terrace, edge and

corner adsorption sites on these NPs closely mimic respective sites on model catalysts. On the one hand, the so constructed NP models may not be global minima at respective particle sizes. On the other hand, global minima of these moieties may not feature the bulk-like atomic arrangement, surface sites and electronic structure closely resembling those of model catalysts. Thus, calculations using global minima structures of NPs may yield results prone to changes upon NP size variations, which cannot be extrapolated to bigger NPs.

In contrast, the main advantage of 3D transition metal NP models with bulk like structures is that despite their computationally tractable size they feature the so-called "scalability with size" property. That is, observable properties of sufficiently big NPs vary smoothly and monotonically with the NP size.[151,177,178] Customary 2D cluster models (*i*) lack this property because of higher proportion of under-coordinated atoms in comparison with 3D models (*iii*). In fact, such properties as cohesive energy, average interatomic distance of (cub-)octahedral Pd_N, Cu_N, Ag_N and Au_N NPs[179–181] as well as the *d*-band centre of Pd_N NPs[182] were shown to depend linearly on the inverse effective radius of the nanoparticle, $N^{-1/3}$. Also CO adsorption energies on terraces of 3D Pd_N nanoparticles were shown to mildly vary with their size for $N \geq 70$ (Figure 2.7).[157,182] Thus, knowing the scaling relationships one can extrapolate properties of computationally tractable NPs of 100–200 atoms to those of bigger ones consisting of few thousand atoms, typically present in model catalysts. Nevertheless, the results calculated on scalable with size nanoparticle models should be compared to those measured on model catalysts with some caution, because oxide support and reaction atmosphere may still be unaccounted for in the computational treatment. Note that the indispensable scalability with size property has not yet been established for the interaction of metal nanoparticles with an oxide support or for adsorption of a given species at high coverage.[s]

Only sufficiently big 3D NPs feature scalable with size properties, while NPs below certain critical size belong to the "every atom counts" regime.[167,172] In turn, the critical size of the conversion from one regime to the other depends on a property and material under investigation and should be determined before large scale studies of a given system. Studies of 3D transition metal NPs have ascertained that the scalability

[s] Certain advances made in this direction are taken in Chapter 4 and Section 3.3.

with size regime is often achieved already on computationally rather undemanding models. This regime was found for cohesive energies of Cu, Ag, Au, and Pd clusters with the size exceeding 38 atoms.[179,181] Average interatomic distances in M_N species linearly depend on the average coordination numbers for NPs exceeding 38 (Pd), 44 (Cu), and 79 (Ag) atoms.[157,179,180] Centres of *d*-bands also vary smoothly with the size for Cu and Ag NPs with more than ~79 atoms,[179] and Pd NPs with more than 50 atoms.[182] Somewhat bigger NPs are usually required for calculated adsorption energies to be scalable with size. For example, the models of 79 atoms were required to calculate scalable with size adsorption energies of CO on terraces[157,180,182] (Figure 2) and NO on edges[49] of Pd NPs. However, more strongly bound adsorbates, such as atomic C, require Pd and Pt NPs of 140 atoms to obtain scalable with size adsorption energies.[183,184] Comparably large or even bigger NPs may be required for modelling structure and bonding of subsurface atomic impurities in them.[185,186] Somewhat bigger nanoparticles of 147 atoms were found to be necessary to calculate size-converged adsorption energies of CO molecules and O atoms on Pt species.[187] It was even harder to achieve size-convergence for adsorption properties of Au nanoparticles. A detailed analysis of O_2 adsorption and dissociation on neutral and charged species from Au_5 to Au_{79} revealed no signs of convergence.[188] Only much bigger Au species of 561 atoms yielded the same adsorption energies towards CO and O as Au(111) surfaces.[189] Even bigger Au_{923} nanoparticles were found to be necessary to obtain size-converged adsorption energies of O atoms on NP edges.

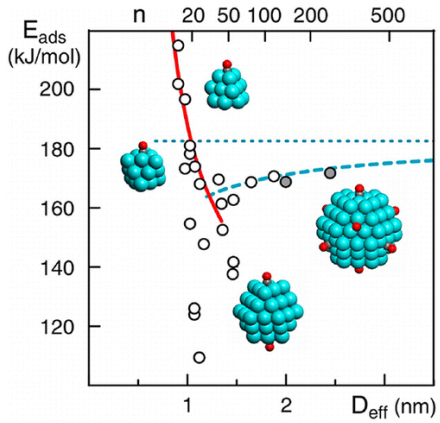

Figure 2.7. The dependency of CO adsorption energies on {111} facets of Pd nanoparticles as a function of nanoparticle size.[182] Pd is displayed in cyan, C – grey, O – red.

Only few studies comparing properties of NP and slab models obtained using similar computational techniques have been published so far.[t] Because differences between electronic structures and interatomic distances of slabs and NPs are well understood, these studies focused on less obvious differences between adsorptive properties of extended terraces on slabs and NP facets, which resemble them. Based on the scarcely available data, one is tempted to think that observables calculated on {111} terraces of scalable with size metal NPs do not exactly reproduce the respective numbers obtained on slab models, but can be extrapolated to them. For example, the adsorption energies of NO on terraces of Pd_{79} NP and on Pd(111) surface differ merely by up to 0.17 eV (8.8% of the overall adsorption energy);[49] the adsorption energies of atomic C on M_{140} and M(111) differ by 0.29 eV (4.2%) for Pd[186] and 0.25 eV (3.7%) for Pt.[184] Also, the energies of subsurface absorption of atomic C in Pd_{140} and Pd(111) models are different by only 0.16 eV (2.2%).[186] The nano-effect is, however, very large for the activated migration of a surface C atom into the subsurface region. The barrier of the subsurface migration is calculated by up to 0.35 eV (71%) smaller on Pd_{140} than on Pd(111).[186] Most of the aforementioned differences in adsorption and migration energies may be assigned to either *a*) higher flexibility of metal atoms in the NPs or *b*) smaller interatomic distances in them (in agreement with the scalability of the NP properties). Note that despite that effects *a*) and *b*) express themselves differently with different consequences for the surface reactivity, they both have inherently nanoscale origin.

For most of the other (e.g., non-metallic) nanoparticulate materials the scalability with size is yet to be established, with only few studies present in the literature. For example, cohesive energies of global minima of $(ZnO)_N$ and $(SiO_2)_N$ clusters show linear dependency on $N^{-1/3}$ for $N \geq 13$, while other properties exhibit no convergence up to $N \sim 30$. Studies of 3D CeO_{2-x} NPs revealed that their interatomic distances and cohesive energies depend monotonously on the NP diameter and the average coordination number of Ce atoms, respectively, for NPs bigger than ~$Ce_{40}O_{80}$.[190,191] Thorough studies of global minima of $(CeO_2)_N$ NPs have shown that their binding energies (per CeO_2 unit) depend linearly on $N^{-1/3}$ already for $N \geq 10$.[192] Also, modest

[t] Sections 3.2, 3.3, 4.2, 4.3 as well as 5.3 and 11.7 provide important reference points in this respect.

variations (≤ 0.15 eV) of the CO adsorption energy on Ce_NO_{2N-x} NPs for $N \geq 38$ with the size of the latter are reported.[193] At the same time the formation energy of O vacancies in ceria nanoparticles were found to have a complex dependency on the nanoparticle size and to be strongly affected by the presence of four-coordinated Ce cations on the NP corners (Section 11.7).

Additional studies performed with the scalability with size approach are reviewed in Section 11.5. For example, critical comparison of adsorption properties of Pd, Pt, Cu, Ag, and Au nanoparticles to those of (111) single crystals performed by Henkelman et al.[194] is discussed. The increased activity of edges of SwS Pt nanoparticles in methane dissociation compared to the activity of Pd(111) surfaces investigated by Viñes et al.[150] is analyzed. This study motivated the study of methane dissociation on Pd nanoparticles and Pd(111) presented in Section 3.2. The very important issue of higher flexibility of nanoparticles compared to bulky samples is illustrated using the migration of C atoms into the subsurface region of Pd NPs[186] as an example. Finally, the possible role of nanostructured reducible oxide supports on the properties of supported metal clusters is discussed for Pt-ceria system.[55]

Experimental studies of scalability with size

It has been known for many years that physical properties of small metal clusters vary abruptly with the cluster size,[156,195,196] but the size-dependency is smooth for bigger nanoparticles.[197] Smooth variation of catalytic properties with the nanoparticle size is also well documented experimentally for sizeable species.[198-200] Finally, some laboratory studies of catalytic activity of small size-selected clusters confirmed its strong variation with the cluster size.[172,201] However, since studies of catalytic properties measured the overall activity, it was impossible to quantify the effect of nanostructuring on a particular elementary reaction step. Some of such elementary steps that are very important in any reaction are the adsorption of reactants on the catalyst surface and the desorption of products. Surprisingly, the dependency of adsorptive properties on the size of catalytically active nanoparticles is not well studied experimentally, because of the complexity of involved measurements.

The recently built experimental setup in Fritz Haber Institute (Berlin) is one of the few apparatus that allow direct calorimetric measurements of adsorption energies of

very small doses of molecules on model catalysts composed of oxide supported metal NPs.[46,202] For example, it allowed Schauermann et al. to measure the adsorption energies of CO molecules on Pd nanoparticles grown on Fe_3O_4 films.[203,204] It was found that the adsorption energy of CO, indeed, varies smoothly with the nanoparticle size starting from the smallest considered species of ~1.8 nm (Figure 2.8). However, conversely to the theoretical predictions,[u] the smaller Pd nanoparticles were the weaker they adsorbed CO molecules at low CO coverage. Moreover, the adsorption energy of CO on Pd(111) single crystal was found to exceed that on Pd nanoparticles for all NP sizes. In the original article[203] two concepts were invoked to account for this finding: 1) shorter interatomic distances in smaller Pd NPs, which caused weaker interaction with CO; 2) weaker van der Waals attraction between CO and smaller Pd nanoparticles. Interestingly, the data presented in the same article reveals that at high CO coverage the adsorption energies were roughly the same for Pd(111) and all Pd nanoparticles, which does not seem consistent with the proposed explanations. Moreover, further experiments on CO adsorption on O-precovered Pd revealed the same strength of interaction (~1 eV) of CO with Pd nanoparticles and Pd(111) single crystals.[205] This value of CO adsorption energy on O-precovered Pd turns out to be very close to the adsorption energy measured on the smallest considered *bare* ~1.8 nm Pd nanoparticles supported on Fe_3O_4. Finally, in later articles by the same group the strong metal-support interaction between *reducible* iron oxide films and deposited nanoparticles is discussed.[31,34,206] Thus, there is a certain possibility that complex metal-support interaction interfered in the measurements. Hence, properties of Fe_3O_4-supported Pd nanoparticles may be not representative of intrinsic properties of unsupported Pd NPs.

Similar studies of the dissociative adsorption of O_2 on Fe_3O_4 supported Pd nanoparticles revealed somewhat more complicated dependency of the adsorption energies on the nanoparticle size.[149] The adsorption energies grew from ~2.1 eV per O_2 molecule to ~2.9 eV when the NP size increased from ~2 nm to ~4 nm. Then the adsorption energies decreased to ~2.6 eV on ~7-8 nm NPs and back to ~2.1 eV on Pd(111) surfaces. This behaviour was explained by the same arguments as in the case of CO molecules extended by the fact that O atoms adsorb significantly stronger on the

[u] CO adsorption on *terraces* of Pd nanoparticles is calculated to be weaker than the adsorption on Pd(111).[182] Nevertheless, the adsorption on the *edges* of Pd nanoparticles is predicted to be more exothermic compared to Pd(111) single crystal.[209]

edges of Pd nanoparticles that on their terraces. The latter finding was confirmed by IR spectroscopy of CO molecules adsorbed on Pd nanoparticles with preadsorbed oxygen. Nevertheless, similarly to the previous case one may wonder about the role of the support in these experiments.

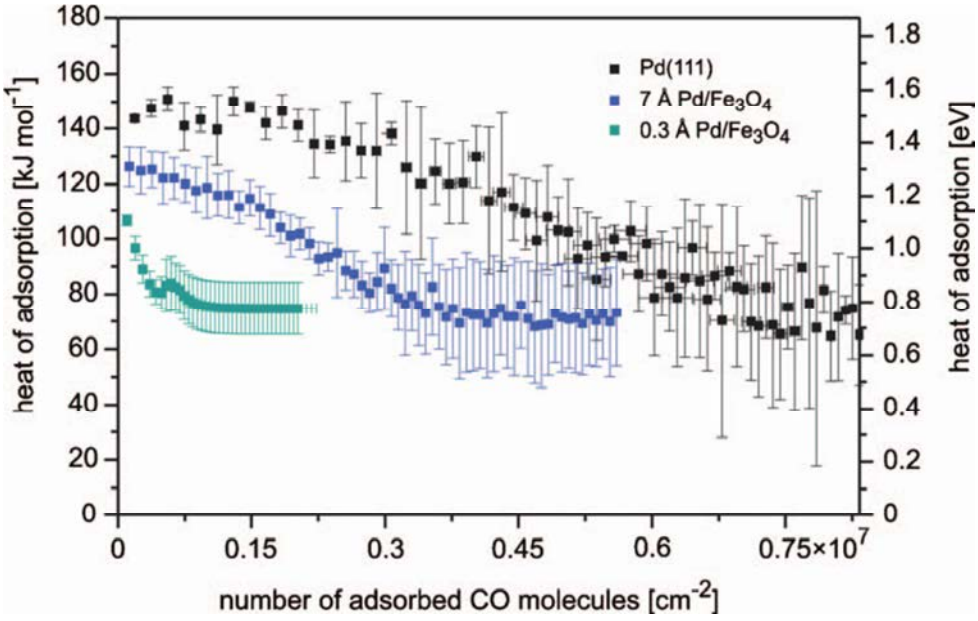

Figure 2.8. Experimentally measured adsorption energies of CO molecules on Pd(111) and Pd nanoparticles as a function of the number of adsorbed species. The deposition of 0.3 Å of Pd yields 1.8 nm big nanoparticles; in turn, 7 Å of Pd correspond to 8 nm big nanoparticles.[203]

To conclude, despite certain progress in measurements of adsorptive properties of nanoparticles as a function of their size, the direct comparison between experimental and theoretical results does not seem to be straightforward. The reason is rather complex nature of experimentally prepared systems that does not allow disentangling effects of the nanoparticle size from other factors.

Shape of scalable with size nanoparticles (Wulff and Wulff-Kaischev constructions)

Chemical properties of scalable with size nanoparticles are determined not only by their size, but also by their shape. The latter governs the arrangement of atoms on the nanoparticle facets and the abundance of different types of active sites on the nanoparticle surface. In principle, the shape of employed nanoparticle model should

resemble the prevailing shape of nanoparticles in a particular experiment.[v] In turn, in experiment the shape of nanoparticles could be governed either by the particular preparation protocol[148] or by thermodynamics.

According to Gibbs, the most thermodynamically stable shape of a nanoparticle is the one that minimizes its surface energy:

$$\Delta G = \sum \gamma_i A_i \quad (28),$$

where ΔG is the excess Gibbs energy compared to the same amount of bulk material, γ_i – the specific surface (Gibbs) energy of a given facet i and A_i – the surface area of the facet. The solution to the problem of the minimization of ΔG was first proposed by Wulff and so it is called Wulff construction. According to this method in the most thermodynamically stable shape there is a certain point (usually NP centre) such that for each facet at the distance[w] h_i from this point

$$\frac{\gamma_i}{h_i} = const \quad (29).$$

According to this rule, surfaces with higher specific energies are located farther from the nanoparticle center, which in lower surface area of the corresponding facets. More or less elegant proofs that nanoparticles created following this rule, indeed, yield the lowest possible ΔG for a given volume of material were proposed by several scientists many years after the pivotal work by Wulff.

Note that since γ_i may change depending on the experimental and reaction conditions, the most thermodynamically stable nanoparticle shape will vary accordingly. [38,198,207] Typically such changes may be introduced by a) temperature, b) reaction atmosphere and c) the interaction with a support. In the latter case, the nanoparticle facet that interacts with the support is stabilized by the latter and so its surface energy changes to

$$\gamma_{int} = \gamma_i + E_{adhesion} \quad (30),$$

[v] The shapes could be somewhat different if supported nanoparticles are studied experimentally and unsupported species are addressed computationally.

[w] To be more precise, h_i is the distance between this point and a plane containing the given facet.

where the specific nanoparticle-support interaction energy $E_{adhesion} < 0$. The design of a nanoparticle shape taking (30) into account is called Wulff-Kaischev construction. As a rule, it leads to the spatial extension of the facet stabilized by the substrate compared to other facets of the same surface type.

Chapter 3

Unsupported Transition Metal Nanoparticles

It seems suitable to begin the presentation with the discussion of results obtained on unsupported nanoparticle models because there is no much uncertainty regarding their atomic structure.[a] This follows from the notion of scalability with size outlined in the Section 2.7 – only species with bulk-like arrangement of atoms and shape in line with Wulff construction may be SwS. In practice, these two conditions are sufficient to create nanoparticle models that represent metal particles in catalysts.

From the earliest to contemporary studies of SwS nanoparticles

Notker Rösch and Konstantin Neyman were among the first who started systematic investigations of scalability in transition metal nanoparticles. The first study by Rösch et al. dates back to 1994 and concerns only physical properties of Ni clusters, such as cohesive energies, ionization potentials and magnetization.[177] Later, in early 2000´s, similar studies were performed for Pd nanoparticles, including investigation of adsorptive properties of their terraces and edges with respect to CO molecules.[157,208,209] The first study of transition states on scalable with size nanoparticles appeared in 2004 and concerned migration of atomic H, C, N, and O from the surface to subsurface region of Pd.[185] Finally, in 2010 the catalytic ability of edges of Pt nanoparticles to decompose methane was studied Viñes et al.[150] and found to greatly exceed that of extended Pt(111) surface.

Recently, increasingly more scientific groups have been starting to work using scalable with size nanoparticle models in electronic structure calculations. For example, in 2011 Nørskov et al. calculated adsorptive properties of edges and {111} terraces of Au_n nanoparticles with respect to CO and atomic O to converge to those of extended Au(111) and Au(211) surfaces at n = 561.[189] The same year Henkelman et al. investigated ethylene adsorption on various sites of sizeable Au, Ag, Cu, and Pt nanoparticles and compared it to the adsorption on terrace, step, and kink sites on the respective surfaces.[194] Again in 2011 Neurock et al. investigated activity of SwS Pt nanoparticles in CO oxidation at high CO coverage and found it to be very similar to that of Pt(111) single crystals.[210] In 2013 Mamatkulov and Filhol found that CO adsorption on Pt nanoparticles is affected not only by compressed interatomic distances in the nanoparticulate substrate but also by distribution of electrostatic field around the

[a] At least for nanoparticles composed of one element.

NPs.[211] Later, in 2014, Loffreda et al. by analyzing binding energies of H_xO_y compounds to Pt nanoparticles and extended surfaces suggested "generalized coordination number" of a binding site as a descriptor of its reactivity.[212] Also the same year Ho et al. calculated N_2 dissociation on twinned octahedral Ru_{79} nanoparticles.[213]

Objectives of this Chapter

As one can see, even now there are only a limited number of theoreticians working on the understanding of nanoeffects in the framework of scalable with size nanoparticles, so there are still many basic effects to be discovered. On the other hand, despite that the outlined studies have led to conceptual advances in this field, most of these studies were exemplary or proof-of-concept investigations, that is, lacked systematicity. Therefore, it is also timely to examine at which degree already discovered concepts are transferable to other systems and other processes. These two aspects, exploration of new ways how nanostructuring may affect properties of unsupported SwS NPs as well as more systematic studies of already discovered nanoeffects are the main objectives of investigations presented in this Chapter.

Among many possibilities nanoparticulate Pd was chosen for a detailed investigation since this metal and its alloys are indispensable in heterogeneous catalysis. For instance, Pd catalyzes water gas shift,[214] C-C coupling[215] and various hydrogenation / dehydrogenation reactions.[216] Also Pd is able to catalytically mediate decomposition or oxidation of hydrogen reach molecules, such as methane[7,217] or methanol,[218] which is very important for their applications as energy carriers. Due to such a wide range of catalytic applications of Pd its properties (in the absence of nanostructuring) were already addressed computationally in certain studies, which could be used as a reference. Another important feature of Pd is that even relatively small truncated octahedral Pd_{79} nanoparticles seem to be scalable with size,[152,182] which makes studies of chemical activity of Pd NPs particularly computationally efficient.

Adsorption on nanoparticle edges

Possibly the most obvious difference between Pd nanoparticles and extended Pd surfaces is the presence of the low-coordinated Pd atoms on edges of the former. In principle, one may expect edge atoms to form stronger bonds with adsorbed species than terrace atoms, due to a higher number of something analogous to "dangling

bonds". However, until few years ago only adsorption of CO and NO on edges of Pd nanoparticles was investigated. The former molecule, CO, was calculated to adsorb ~0.2 eV stronger on edge bridge sites than on the most stable fcc sites on {111} terraces.[209] Confirming this finding, IR peak characteristic for bridge adsorbed species was observed when Pd nanoparticles were exposed to a very low CO pressure. In a similar manner it was possible to distinguish NO molecules on edges of Pd NPs in a combined DFT and IR spectroscopy study.[49] However, it was found that NO adsorption on the edges is slightly less energetically favorable than on {111} facets.

Naturally, the aforementioned studies of CO and NO on Pd nanoparticles provoked some questions. First, what other species are more energetically stable on edges of Pd NPs than on their terraces? Second, how common is for edge-adsorbed species to have IR fingerprints distinguishable the respective terrace adsorbed species? In order to answer these questions a comprehensive study of adsorption of intermediates in methanol decomposition, i.e. CH_xO_y species (x = 1 – 3, y = 0 – 1), on various sites of scalable-with-size Pd_{79} nanoparticles was performed (Figure 3.1 and Section 3.1). For each adsorbate vibrational frequencies were calculated and for some of them also intensities of IR peaks were quantified. This particular set of adsorbed compounds was chosen because of the following: 1) they appear in many reactions catalyzed by Pd, 2) a less detailed computational study of these species on Pd_{79} was performed earlier (using the Paragauss code) and could be used as a reference.[219] Particularly advantageous was that some optimized geometries were provided in supplementary information to Ref. 219.

It was found that most of the CH_xO_y species are, indeed, stabilized on edges of Pd_{79} compared to {111} terraces of the nanoparticle. The only exception was CH radical, which binds to three-fold hollow sites on terraces by 0.12 eV stronger than to the same sites on the edges. The strongest stabilization on the edges was calculated for compounds forming O-Pd bonds, CH_3O, CH_2O and CHO, and amounted to 0.35 – 0.55 eV. Methoxy species also changed their preferential sites from three-fold hollow on terraces to bridge sites on edges of Pd_{79}. The stabilization for species chemisorbing via C-Pd bonds was ~0.2 eV for CH_2OH, CH_3, and CH_2. This magnitude of stabilization can significantly affect energy profiles of various reactions taking place on nanostructured Pd catalysts.

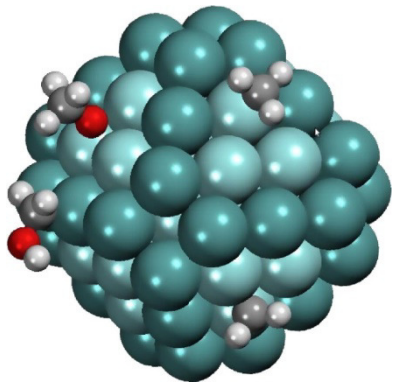

Figure 3.1. Pd_{79} nanoparticle with CH_2, CH_3, CH_2OH, and CH_3O adsorbed on it. Pd is displayed in cyan, H – white, C – grey, O – red. Darker atoms are located on NP edges.

There were notable differences between infrared spectra of some considered species adsorbed on edges and terraces. Namely, some vibrational frequencies of CH_2OH, CHO, CH_2 and CH changed by more than 30 cm^{-1} depending on location of the species, which significantly exceeds the resolution of contemporary experimental setups. At the same time positions of IR peaks of methoxy, formaldehyde and methyl groups were almost the same on terraces and edges of Pd_{79} nanoparticles. However, even for these compounds one could find differences between IR spectra of species adsorbed on edges and terraces due to altered relative intensities of some spectral peaks. The latter are governed by the surface selection rule, which postulates that molecular vibrations are IR-active only if they change molecular dipole moment in the direction perpendicular to the surface. Since edge-adsorbed species as a rule had a different tilting angle with respect to a NP surface compared to terrace adsorbed species, the surface selection rule noticeably affected IR intensities of their vibrations. Hence, vibrations that were inactive in infrared spectroscopy for adsorbates on terraces could become IR-active, when the same species were located on the edges and vice versa.

Catalytic activity of nanoparticle edges

Of course, one could expect nanoparticle edges not only to feature altered adsorptive properties but also modified catalytic activity with respect to nanoparticle terraces or respective single crystal surfaces. However, since studies involving location of transition states are significantly more computationally expensive than similar studies of locally stable structures, there are still only few computational studies of catalytic properties of edges of sizeable NPs. Namely, Jennings et al.[220] explored O_2 dissociation

on different sites of Pt and Pt-Ti nanoparticles as well as Pt(111) single crystals. The authors were able to demonstrate that terraces and edges of Pt NPs are much more active in this reaction than Pt(111) due to the significantly increased flexibility of the former. Another study comes from Viñes et al. who investigated methane decomposition on edges of Pt_{79} NPs and extended Pt(111) surfaces.[150] Again the catalytic activity of edges of Pt nanoparticles was found to be significantly higher than that of Pt(111) surface, which was confirmed by molecular beam experiments.

One of the reactions catalyzed by Pd is the oxidation of methane, a potent greenhouse gas. This reaction is widely used in stationary power generators working on natural gas to abate emission of methane together with the exhaust. Unfortunately, the existing Pd catalysts are active in methane oxidation only at specific reaction conditions, which impedes their application in mobile vehicles. In turn, this limits the usage of very abundant natural gas as a fuel for cars. The situation is complicated by the fact that the reaction mechanism, the active site and even the active phase of Pd catalysts in this reaction has been under debate for more than 50 years.[7,8,217,221]

Curiously, the activities of Pd and Pt NPs in methane oxidation depend very differently on the size of respective nanoparticles.[200] While the turnover frequency on Pt nanoparticles remains constant for nanoparticles bigger than 3 nm, the turnover frequency on Pd nanoparticles continues to grow with the NP size until they are at least 22 nm big. It appeared very interesting to investigate if Pd and Pt nanoparticles will behave differently also in a simpler reaction of methane decomposition,[b] which may also take place during Pd-catalyzed methane combustion.[222] To answer this question a computational study of this reaction on edges of Pd_{79} nanoparticles and extended Pd(111) surface was performed (Section 3.2) and its results were compared to those obtained on Pt by Viñes et al.[150] The computational parameters were chosen to be very similar in both studies, which allowed for quantitative comparison of the calculated reaction energy profiles. This study allows one to single out the difference between effects of nanostructuring on catalytic properties of Pd and Pt.

[b] Note that it is likely that both methane decomposition and oxidation share the same rate-limiting step – from methane to methyl.

The calculations presented in Section 3.2 revealed much higher activity of edges of Pd nanoparticles in methane activation. The barrier for the first reaction step decreased from 0.98 eV on Pd(111) single crystals to 0.57 eV on edges of Pd_{79} nanoparticles (Figure 3.2). This finding is very important since methane activation is the rate-limiting step in methane decomposition and many other reactions. Nanoparticle edges were also more active than Pd(111) single crystals in decomposition of methyl and CH groups, whose activation energies decreased by 0.24 and 0.34 eV, respectively. The barrier for decomposition of CH_2 species, however, slightly increased from 0.24 to 0.37 eV on nanoparticle edges due to the higher stability of the initial state. Thus, this study corroborated the notion of higher catalytic activity of edges of Pd nanoparticles.

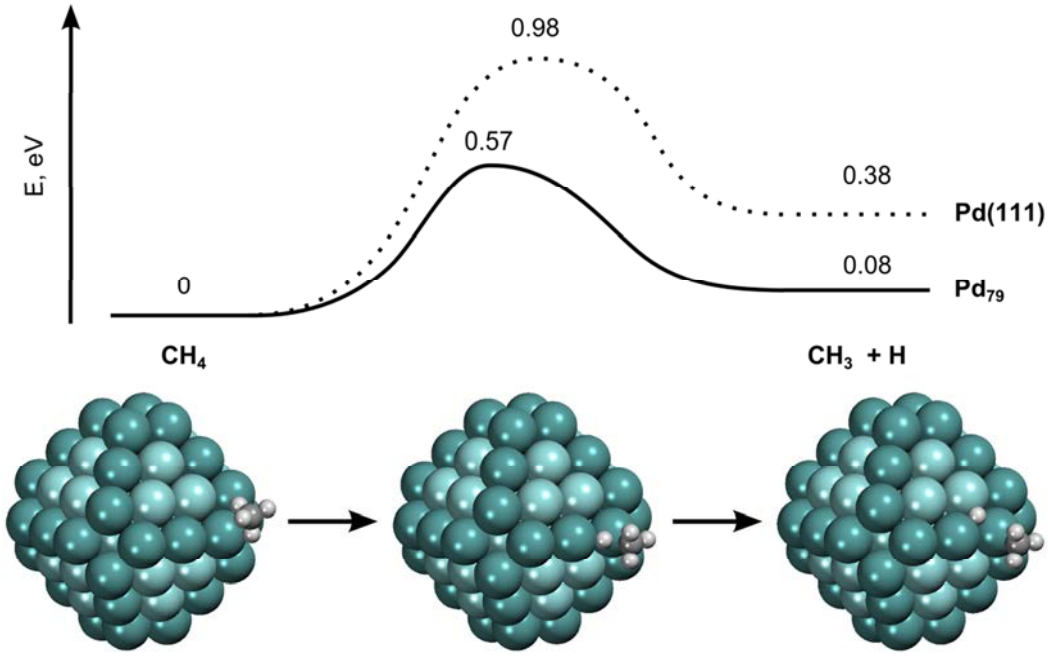

Figure 3.2. Energetic profile and initial, transition, and final step in the first elementary step of methane dissociation. Pd is displayed in cyan, H – white, C – grey. Darker atoms are located on NP edges.

Interestingly, the reaction energy profile calculated for methane decomposition on Pd(111) was quite similar to that calculated by Viñes et al. on Pt(111).[150] In particular, the difference between barriers for the rate-limiting step from methane to methyl was only 0.05 eV with Pt being slightly more active than Pd. Other activation energies are also slightly, by up to 0.1 eV, lower on Pt(111) than on Pd(111). Despite the apparent similarity between catalytic activities of {111} terraces of Pd and Pt, there was a significant difference between reaction energy profiles calculated on edges of

Pd_{79} and Pt_{79}. Activation energies for the first two reaction steps decreased from ~0.55 eV on edges of Pd_{79} to ~0.3 eV on Pt_{79} edges. The last two barriers in methane decomposition in contrast are by 0.23 and 0.07 eV higher on Pt_{79} than on Pd_{79} nanoparticles. Thus, the nanostructuring affected catalytic activity of both metals is qualitatively similar (both NPs are more active than (111) single crystals), but quantitatively different way. This investigation contributed to the understanding of the different dependency of the activity of Pd and Pt nanoparticles on their size in methane oxidation.[200]

Catalytic activity of nanoparticles as a function of reaction conditions

Another relevant question concerning scalable with size NPs is if properties of nanoparticle facets are always the same as those of respective single crystal terraces or they may change under certain conditions. In principle, the definition of scalability with size requires the possibility to *extrapolate* properties of NP facets to those of single crystals, not the quantitative similarity between their properties. In turn, if the calculated difference between facets of e.g. ~1.5 nm NPs and respective single crystals is rather significant (but still monotonously decays with the NP size), this difference may remain notable for NPs of few nm, i.e. those present in common catalytic processes.

One of the phenomena that may cause such big differences between NP facets and single crystals is the formation of near-surface hydrides, [66,223,224] carbides, [186,225,226] (as well as their mixtures[52,227,228]) and oxides[221,229,230] or respective subsurface impurities.[185,231] All these processes happen readily in Pd catalysts under different reaction conditions and are known to be facilitated by the nanostructuring of Pd.[186,232] In particular, sustainable hydrogenation of alkenes (especially, the second half-hydrogenation step) was found to be possible only on Pd nanoparticles containing subsurface H.[52] Since edges of these nanoparticles were saturated with subsurface C in order to promote the kinetics of subsurface H formation[233] and the immediate presence of subsurface C is detrimental for hydrogenation of C-C double bonds,[227,228,234] the reaction probably took place on the NP facets. At the same time, this reaction could not be maintained on Pd(111) single crystals in the same experimental conditions, suggesting that the activity of facets of Pd NPs was somehow altered.

In order to get an atomistic understanding of the involved chemistry a systematic study of ethyl hydrogenation on {111} terraces of Pd_{79} and Pd(111) surface was performed at different amounts of adsorbed and absorbed H present in the system (Figure 3.3 and Section 3.3). Since not only Pd, but also nanoparticles of Pt[235] and Rh[236] as well as Ni[237] surfaces were reported to be able to absorb hydrogen, the effects of subsurface hydrogen on nanoparticles and slabs of these metals were also explored but in a less detail. Hence, this study also shed light on how different types of H-metal bonds lead to different activities of transition metals in hydrogenation reactions.

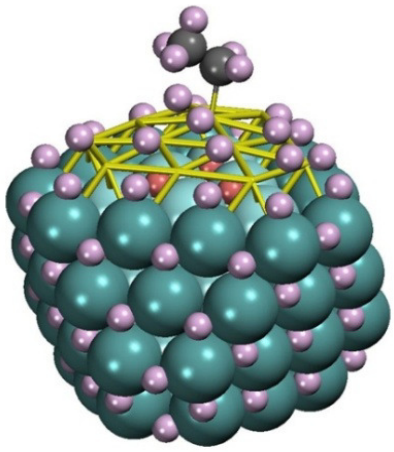

Figure 3.3. Ethyl species adsorbed on Pd_{79} nanoparticle with surface covered by adsorbed H and with some H atoms located also in the subsurface region of the Pd NP. Pd atoms are displayed in cyan, H adsorbed on Pd or composing ethyl – pink, absorbed H – red, C – grey.

At low hydrogen coverage the hydrogenation of ethyl on Pd(111) single crystals was calculated to pass through the (Gibbs) barrier of 0.5 eV, which resulted in the reaction rate constant of $k_{298} = 2\times10^4$ s^{-1}. The saturation of surface sites with H increased the constant to 2×10^7 s^{-1} and addition of a hydrogen atom in every subsurface tss' site increased it further to 2×10^8 s^{-1}. When more absorbed H was put into second subsurface layer k_{298} continued to increase to 4×10^9 s^{-1}. Thus, even on Pd(111) surface the reaction rate strongly depended on H concentration in the system. On Pd_{79} nanoparticles there is a similar but much stronger dependency of k_{298} on the H content present in the system. The reaction rate constant grew as $2\times10^4 \rightarrow 5\times10^7 \rightarrow 8\times10^{11}$ s^{-1} for nanoparticles with low H coverage → complete surface coverage of {111} facets by H → filling of subsurface layer by H. Note how similar are the reaction rate constants on Pd_{79} and

Pd(111) without subsurface H and how the formation of near-surface hydride eliminates the resemblance. First, this means that the difference between calculated catalytic activities of Pd single crystals and Pd nanoparticles is not just an artifact in the simulations. Second, this shows high sensitivity of nanoparticle properties on the reaction conditions, which may be used to tune the catalytic activity.

The mechanism how the presence of absorbed hydrogen modifies the surface activity was also examined in detail. Despite that subsurface H species have lower thermodynamic stability than adsorbed H atoms,[c] the former did not act as attacking species as they might do on Ni surfaces.[237,238] Rather high-energy subsurface H species were stabilized on the surface upon emergence and converted into regular adsorbed hydrogen atoms, H^{ads}. Instead, it is the effect of subsurface H on the electronic structure of the catalyst that triggered the enhanced hydrogenation activity of Pd. This effect was reflected in the densities of states projected on adsorbed H and surface Pd atoms at the reaction site. The increasing concentration of adsorbed and absorbed H on Pd(111) surface and Pd nanoparticles shifted the DOS of surface Pd atoms to lower energies (with respect to E_F), making the metal more noble and lowering its reactivity with respect to surface H. Since binding energies of surface H on various Pd substrates were found to strongly anticorrelate with activation energies of ethyl hydrogenation, the destabilization of H^{ads} resulted in strong acceleration of the reaction. In particular, when subsurface H was added to Pd_{79} nanoparticles the shift of DOS to low-energy region was so pronounced that it lead to a partial occupation of antibonding H^{ads}-Pd states. In turn, this decreased thermodynamic stability of reacting surface H species and made them very active in hydrogenation reactions. This mechanism of H activation was found to be feasible only on Pd nanoparticles. On Pd(111) single crystals a much higher concentration of absorbed H would be required to cause the occupation of antibonding H^{ads}-Pd states due to a much lower surface-to-bulk ratio (i.e. lower H to Pd ratio) on extended surfaces compared to nanoparticulate systems. Such concentration of subsurface H would be very difficult to maintain experimentally, which explains the absence of long-term hydrogenation activity of extended Pd(111) surfaces.[52]

[c] So reactions involving subsurface H atoms would be more exothermic than those with adsorbed H. In turn, according to Brønsted–Evans–Polanyi principle this should lead to lower activation energies in various chemical reactions.

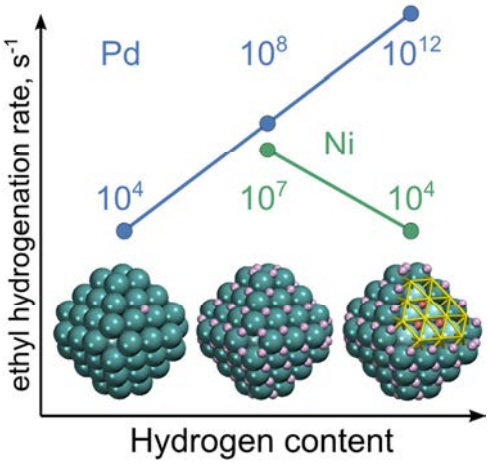

Figure 3.4. Reaction rate of ethyl hydrogenation depending on the hydrogen content in Pd and Ni nanoparticles. Pd atoms are displayed in cyan, adsorbed H – pink, absorbed H – red.

On Pt nanoparticles and extended (111) surfaces adsorbed H was found to be activated by the presence of absorbed H species in a very similar manner. Binding energies of hydrogen decreased by ~0.35 and ~0.1 eV in the presence of subsurface H on Pt_{79} and Pt(111), respectively, just like on Pd. In contrast, on nanoparticles and surfaces of Ni and Rh subsurface H lead to *weaker* binding of H^{ads} and concomitantly *lower* hydrogenation activity (Figure 3.4). This finding was attributed to the polar character of H-Ni and H-Rh bonds. According to Bader analysis each H atom on Ni and Rh accumulates around 0.2 extra electrons, whereas the charge on surface metal atoms was determined essentially by the amount of H present in the system. That is, the more H there was in the system, the higher was the compensating charge on metal atoms and so the stronger were H-M bonds and the slower were hydrogenation reactions. Despite that mechanisms how subsurface H affects hydrogenation activity of Ni/Rh and Pd/Pt catalysts were very different, in both cases the magnitude of their effects was higher for nanoparticulate metals than for respective single crystals. Whereas on Ni(111) subsurface hydrogen decelerates the reaction only by 30% on Ni_{79} it leads to ~1000 times lower reaction rate constant. Therefore, one may assume that the synergy between nanostructuring and surface modification by adsorbates is present in a variety of reactions and processes. For example, very recently it was shown that covering surface of Pd nanoparticles by a metal-organic framework strongly promotes H absorption into Pd.[239]

Structure of bimetallic nanoparticles

Another common way to modify various properties of transition metal catalysts is to alloy them with another metal (keeping the system nanostructured). The ratio between the two components adds another degree of freedom to the system and allows to tune activity and/or selectivity of the nanoalloy catalyst in a particular process.[67,240] In some other cases, the second component is chosen to be just an inexpensive and abundant metal in order to decrease the overall cost of a catalyst. Anyways, it may be helpful to know the chemical ordering (distribution) of both atomic components within a bimetallic nanoparticle and, in particular, the structure and composition of surface sites available for a reaction. Without this knowledge it is hard to perform a computational study of nanoalloy's chemical and catalytic activity with common computational techniques. The most widespread forms of chemical ordering are core-shell structures as well as random or ordered alloys, with asymmetric core-shell or Janus-like nanoparticles being less common.[241,242] Typically, segregated structures form when two metals have very different atomic sizes or surface energies, while strong and/or polar heteroatomic bonds between metals favor the formation of well-mixed structures. A method to analyze these tendencies in a quantitative fashion could shed light onto the nature of binding in different alloys.

Computational attempts to determine the most energetically stable atomic structure of a bimetallic nanoparticle or at least the most energetically stable chemical ordering within a NP with fixed geometric structure are extremely computationally expensive. Presently, such studies are performed using interatomic potentials and in some studies also the low-energy structures predicted by interatomic potentials are recalculated using more reliable DFT methods.[243–245] However, even the most sophisticated contemporary interatomic potentials do not seem to provide satisfactory description of alloys forming ordered structures or involving polar heteroatomic bonds. Thus, there is a demand for an efficient method to optimize chemical ordering in bimetallic nanoparticles based just on the results of a limited number of trustworthy electronic structure calculations. This method would greatly improve the reliability of optimization of chemical ordering in bimetallic nanoparticles and allow such studies for systems, for which no reliable interatomic potentials yet exist.

In order to deal with the problems outlined in the previous two paragraphs a novel method based on topological Hamiltonians, H_{TOP}, was proposed (Section 3.4). In the simplest form these Hamiltonians take into account segregation of one or the other metals to terraces, edges, and corners as well as the formation of heteroatomic bonds. However, H_{TOP} may be extended to explicitly account for the presence of different kinds of NP terraces, edges and corners as well as nanoparticle support in a rather straightforward fashion. Energetic parameters in these Hamiltonians (later referred to as *descriptors*) were fitted individually for each particular system under scrutiny based on results of electronic structure DFT calculations for NPs with a particular size, shape and composition. This resulted in much higher precision[d] of topological Hamiltonians compared to interatomic potentials with many more fitting parameters. The downside of this approach is the absence of a single topological Hamiltonian for a given material.

Probably, the key advantage of H_{TOP} is its simple structure that does not explicitly depend on Cartesian coordinates of involved atoms. On the one hand, it allows intuitive physical interpretation of all calculated descriptors defining such a Hamiltonian, which sheds light onto binding in different compounds. On the other hand, this makes optimization of chemical ordering with H_{TOP} particularly computationally efficient. Indeed, using the established fitting parameters it was possible to perform $>10^7$ Monte-Carlo steps per hour in simulations of nanoparticles with almost 1500 atoms on a single 2.66 GHz processor. This computational speed is hardly achievable with sophisticated interatomic potential schemes.

The method of topological Hamiltonians was applied to optimization of chemical ordering in $Pd_{70}X_{70}$ nanoparticles (X = Au, Ag, Cu, and Zn) as well as Pd_YAu_{79-Y} and Pd_YAu_{140-Y} NPs of ~1.6 nm in size. Pd-Au and Pd-Ag alloys preferred to form core-shell structures with bulk segregation of Pd (Figure 3.5). The major contributions to the binding in these nanoalloys come from the higher stability of Au or Ag atoms on low-coordinated sites (NP corners and edges), as revealed by the values of respective descriptors. Heteroatomic bonds were of less importance for the chemical ordering. In variation, Cu atoms are more stable in the interior of Pd-Cu nanoparticles than on their surface. Nevertheless, the energy of heteroatomic Pd-Cu bonds is

[d] Precision was estimated as twice the standard deviation of residuals between H_{TOP} and DFT calculated energies of >10 NP configurations *not* included in the fitting set.

sufficient to drive a significant fraction of Cu atoms to corner, edge and terrace positions. The resulting most energetically stable homotop of $Pd_{70}Cu_{70}$ had matryoshka or onion structure with Pd-rich surface shell, Cu-rich subsurface shell and again NP core almost entirely composed of Pd. The final case, Pd-Zn, features very strong heteroatomic bonds, which essentially define the chemical ordering in this compound. The homotop of $Pd_{70}Zn_{70}$ with the maximum possible number of heteroatomic bonds had the structure with Pd and Zn atoms arranged in layers perpendicular to [001] directions like in PdZn bulk crystals. Also, similarly to bulk crystals the nanoparticle exhibits tetragonal distortion of its lattice – its size is 1.6 nm in [100] and [010] directions, but only 1.3 nm in [001] direction. To account for this distortion it was necessary to include an additional term in the topological Hamiltonians for PdZn particles. This term accounted for 16% of the binding energy and improved the precision of the H_{TOP} almost fourfold.

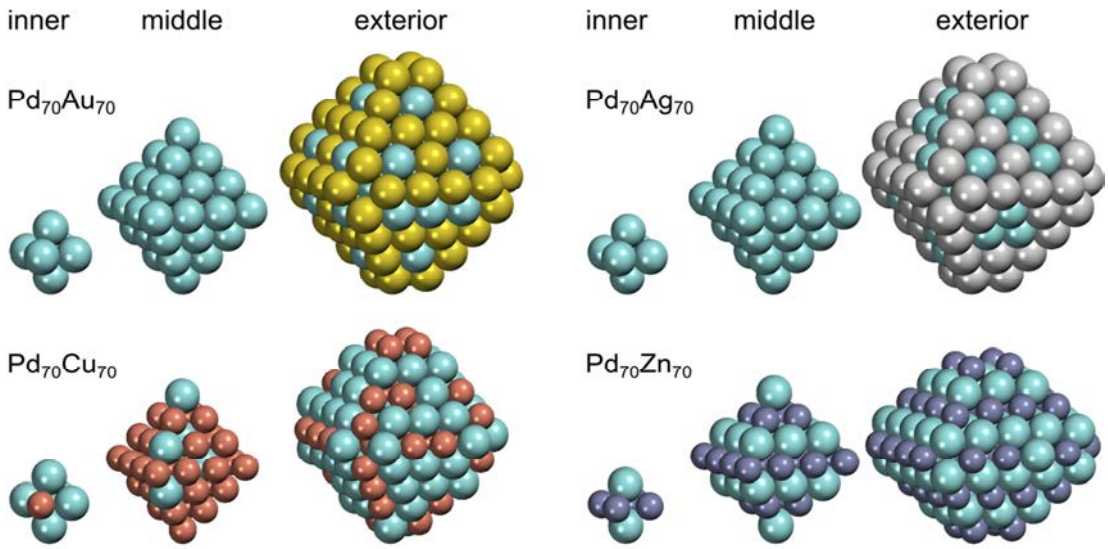

Figure 3.5. Inner, middle and exterior shells of $Pd_{70}X_{70}$ nanoparticles with optimized chemical ordering. Pd atoms are displayed in cyan; Au – gold, Ag – silver, Cu – copper, Zn – stale blue.

Speaking of the precision of the calculated H_{TOP}, it was found to be better than 150 meV (<1.1 meV per atom) for the considered Pd-Au and Pd-Ag nanoparticles and better than 360 meV (<2.6 meV per atom) for Pd-Cu and Pd-Zn. Such a precision reflects the topological Hamiltonians were able to grasp energetics of some interactions in these systems and partially due to the fitting of individual H_{TOP} for each particular structure. To put the precision of H_{TOP} into perspective one may compare it to thermal

energies accumulated by chemical (dis-)ordering at finite temperatures. Thermal energies of $Pd_{70}X_{70}$ (X = Au, Ag, Cu) nanoparticles would reach the precisions of the respective topological Hamiltonians at temperatures of 140 – 360 K. That is, at these or higher temperatures the entropic contributions to relative stabilities of various chemical orderings would surpass in magnitude the precision of H_{TOP}. Since in some applications bimetallic systems are expected to work at room or higher temperatures, one may conclude that the precision achieved by the proposed method is sufficient for practical purposes.

To examine how descriptors in topological Hamiltonians depend on nanoparticle size and composition they were tailored for a set of Pd_YAu_{79-Y} and Pd_YAu_{140-Y} nanoparticles. It was shown that the dependency of descriptors on the NP size is weaker than on the NP composition. Thus, descriptors calculated for smaller nanoparticles can be used to simulate bigger species without a substantial loss of accuracy as long as the ratio between both alloy components does not change too much.

All in all, the proposed topological Hamiltonian approach seems to be able to predict chemical orderings in sizeable bimetallic nanoparticles. This method is expected to allow one extending the scalability with size concept to nanoalloys and to make systematic studies the latter as feasible as the studies of monometallic NPs.

Section 3.1

Chemical Physics Letters 506 (2011) 92–97

Contents lists available at ScienceDirect

Chemical Physics Letters

journal homepage: www.elsevier.com/locate/cplett

Bonding and vibrations of CH_xO and CH_x species (x = 1–3) on a palladium nanoparticle representing model catalysts

Sergey M. Kozlov [a], Gabriela F. Cabeza [b,*], Konstantin M. Neyman [a,c,*]

[a] Departament de Química Física, Institut de Química Teòrica i Computacional (IQTCUB), Universitat de Barcelona, 08028 Barcelona, Spain
[b] Departamento de Física, Universidad Nacional del Sur, 8000 Bahía Blanca, Argentina
[c] Institució Catalana de Recerca i Estudis Avançats (ICREA), 08010 Barcelona, Spain

ARTICLE INFO

Article history:
Received 5 January 2011
In final form 27 February 2011
Available online 2 March 2011

ABSTRACT

This computational study deals with the adsorption of CH_3, CH_2, CH, CH_2OH, CH_3O, CH_2O and CHO species on a nanoparticle Pd_{79} that mimics experimentally investigated model Pd catalysts. We quantify structural, energetic and vibrational parameters of these adsorption complexes and analyse their dependence on the adsorption site. Most of the considered low coordinated adsorption sites are found to be favoured by 20–50 kJ/mol over the sites on (1 1 1) facets. Some of the studied species have distinguishable vibrational parameters at different adsorption sites of the model nanoparticle, making possible spectroscopic characterization of respective adsorption complexes.

1. Introduction

Recent advances in surface science provided deep insights into the energetics, kinetics and mechanisms of reactions at solid surfaces [1]. Studies on well-defined model surfaces in ultrahigh vacuum also illuminated important details of many processes in heterogeneous catalysis ([2,3] and references therein). However, it is well recognized nowadays that profound understanding of processes on single crystal surfaces cannot be automatically translated into an equally good understanding of heterogeneous catalysis. One of the main reasons for that is a high structural disorder and heterogeneity of the real catalysts vs. the single crystal surfaces, which has been denoted as the 'material gap' [4]. Experimentalists made attempts to bridge this gap quite early, by preparing model catalysts consisting, e.g. of well-characterised metal nanoparticles deposited on metal–oxide films [5,6]. Appropriate high-level computational efforts were notably delayed [7,8].

The simplest organic molecules and radicals with just one carbon atom, e.g. CH_xO and CH_x (x = 1–3), are ubiquitous intermediates and reactants in a variety of important catalytic processes, including chemical transformations of methanol (CH_3OH) [9], methane (CH_4) [10] and other chemicals. The progress in identification of reaction intermediates and catalytically active sites through in situ characterization techniques, including vibrational spectroscopy, has been recently reviewed [11–13] and considerable differences due to catalyst nanostructuring have been documented. Also, first density-functional (DF) computational investigations clearly revealed notable nano-effects for transition and noble metal catalysts with respect to their adsorption properties and reactivity [7,14–20]. So far the DF modeling of the CH_xO and CH_x species interacting with Pd has been mainly limited to single-crystal surfaces ([21] and references therein). The most relevant DF studies [15,16] were related to methanol decomposition on nanocrystalline Pd catalysts and focused on the CH_x intermediates and transition states involved in the slow C–O bond scission path of methoxide. In these studies, localized Gaussian-type basis sets were employed and, due to symmetry restrictions, eight adsorbed species – one per each (1 1 1) facet – had to be accommodated on the model cub-octahedral Pd nanoparticles.

The main goal of the present DF study is to determine and possibly quantify the distinctive characteristics of the adsorption complexes of various above-mentioned C_1 species involved in chemical reactions on Pd catalysts and caused by nano-structuring of the latter. In particular we (i) inspect whether the low-coordinated edge/corner sites of Pd nanoparticles are energetically favourable for the adsorption of the C_1 species and (*ii*) search for the opportunities to spectroscopically characterise the adsorbates and differentiate between locations on the regular terrace and edge/corner sites of the Pd catalysts, for instance, employing differences in the vibrational fingerprints. This information is useful to gain new insights into the mechanisms of a broad spectrum of industrially-relevant reactions on such an indispensable catalytic material as palladium.

2. Computational details and models

Calculations were carried out with the help of the VASP code [22,23], in which Kohn–Sham functions are expanded in a basis

* Corresponding authors. Address: Departament de Química Física and Institut de Química Teòrica i Computacional (IQTCUB), Universitat de Barcelona, 08028 Barcelona, Spain (K.M. Neyman).
E-mail addresses: gcabeza@uns.edu.ar (G.F. Cabeza), konstantin.neyman@icrea.es (K.M. Neyman).

0009-2614/$ - see front matter © 2011 Elsevier B.V. All rights reserved.
doi:10.1016/j.cplett.2011.02.061

of periodic plane waves. The core–valence interaction was treated using the projector augmented wave (PAW) method [24] with the cut-off energy for plane waves of 415 eV. The RPBE [25] form of the Generalized Gradient Approximation (GGA) was employed. The total energy tolerance defining self-consistency of the electron density was 10^{-4} eV. To speed up convergence of the Kohn–Sham self-consistent process, a first-order Methfessel–Paxton smearing of 0.1 eV has been applied and then total energies were extrapolated to 0 K (no smearing). Structures were optimised until the maximum forces acting on each atom became less than 0.01 eV/Å. Only spin-restricted calculations of the adsorption systems have been performed, which are considered accurate enough for the purposes of the present model study [26]. Calculations of the reference gas-phase C_1 species were performed using the spin-polarized approach, which yielded the following ground states: CH – doublet, CH_2 – triplet, CH_3 – doublet, CH_2OH – doublet, CH_3O – doublet, CH_2O – singlet, CHO – doublet. Only the Γ point was used for sampling the Brillouin zone of the discrete nanoparticles.

A cub-octahedral nanoparticle Pd_{79} [7] is a cut out of bulk structure that exhibits only low-index (1 1 1) and (1 0 0) Miller planes on the surface. Its (1 1 1) facets were shown to be in the so-called 'scalable-to-bulk' regime (e.g. [14–17]), i.e. their structural and adsorption properties scale with increasing particle size to those of bulk-like samples [27,28]. However, the (1 0 0) nanofacets of the Pd_{79} particle, consisting of only four atoms, (and their edges) appear to be too small to adequately represent (1 0 0) facets (and edges) of larger metal nanoparticles commonly dealt with in catalytic experiments [5,14]. That is why we deliberately refrained from considering interactions with the sites at the (1 0 0) facets by means of the present model Pd_{79}. The supercell approach is used; the nanoparticle with the adsorbate under scrutiny C_1/Pd_{79} located in a cubic cell $2.4 \times 2.4 \times 2.4$ nm is separated from its images by at least 1 nm. Thus, artificial interactions between periodically repeated images are avoided. Only the lowest-coverage limit with just one C_1 species per Pd_{79} nanoparticle is considered. For brevity, all studied structures for each adsorbate are grouped together in one panel of Figure 1.

While we always fully optimised atomic positions of the adsorbates, three types of models were considered for the Pd_{79} nanoparticle interacting with CH_x (Table 1): **1** – all Pd atoms were kept at the experimental positions as in bulk Pd with r(Pd–Pd) = 275 pm, **2** – all Pd atoms were kept at the RPBE optimised positions of bare Pd_{79} and the optimization was restricted to atoms of the adsorbed CH_x, **3** – Pd_{79} fully optimised together with the adsorbates. Optimization of bare Pd_{79} with the gradient-corrected RPBE functional and PAW technique to treat core electrons yields a somewhat rounded structure [7,26,29], which exhibits on its (1 1 1) nanofacets Pd–Pd distances from 272 pm (between atoms on the long edges) to 277 pm (between Pd atoms on the edges and on the terrace), notably shorter than the bulk-optimised Pd–Pd distance of 282 pm. Only the approach **2** has been used for the CH_xO/Pd_{79} complexes. According to vibrational analysis, all calculated structures (except CH_2 adsorbed at site **A**, see below) represented local minima on the potential energy surface. Harmonic vibrational frequencies (for the anharmonicity corrections of the free C_1 species addressed here we refer to [30]) were calculated with the finite difference method, in which Hessian matrix was obtained by displacing all atoms of the adsorbates by ±2 pm from the equilibrium positions in all three Cartesian directions. We illustrate the accuracy of the RPBE calculated harmonic vibrational frequencies for

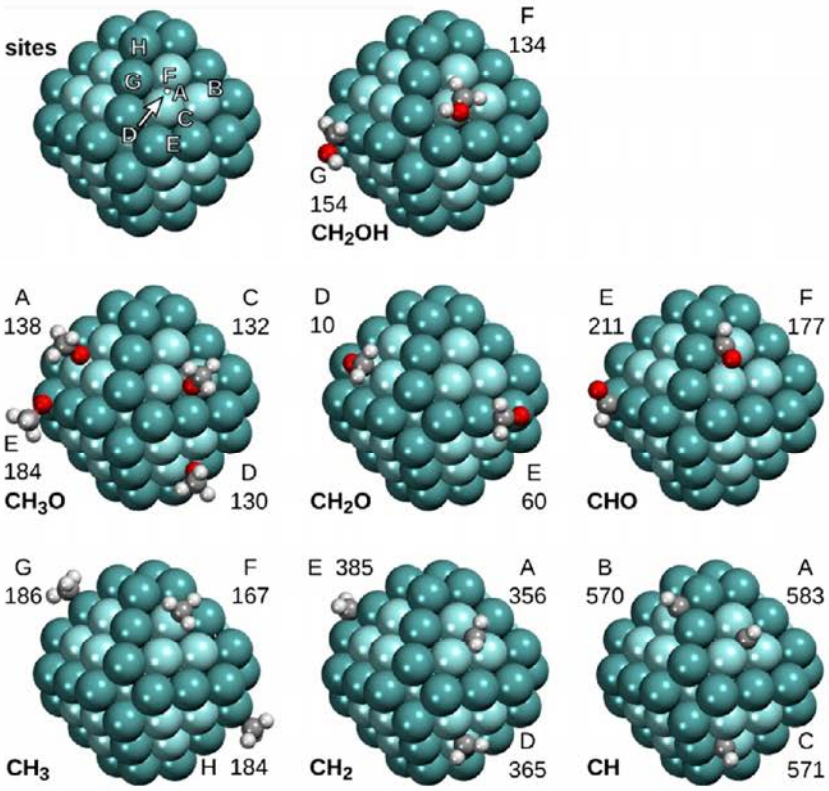

Figure 1. Calculated adsorption complexes of the CH_xO and CH_x species (x = 1–3) on various sites of Pd_{79} nanoparticle: structures and adsorption energies (in kJ/mol). See the upper left-hand side panel for the notations of the adsorption sites: **A** – μ_3 (three-fold hollow) inside a (1 1 1) facet; **B** and **C** – μ_3 on a (1 1 1) facet near edges; **D** – μ_2 inside a (1 1 1) facet; **E** – μ_2 bridging two Pd atoms of a long edge; **F** – μ_1 (on-top) inside a (1 1 1) facet; **G** – μ_1 on a Pd atom in the middle of a long edge; **H** – μ_1 on a Pd atom of a short edge. μ_i defines the bonding mode of the C atom, except for CH_3O and CHO, where the O atom is referred to. Darker large spheres – Pd atoms at the edges, lighter large spheres – Pd atoms inside the (1 1 1) facets, dark medium size spheres – C atoms, light medium size spheres – O atoms, small spheres – H atoms.

formaldehyde molecule CH_2O by comparing with the experimental values [31]] (in parentheses), in cm^{-1}: asymm. stretch σ_{CH_2} – 2863 (2843), symm. stretch σ_{CH_2} – 2816 (2782), stretch $\sigma_{C=O}$ – 1758 (1746), $sciss_{CH_2}$ – 1496 (1500), $rock_{CH_2}$ – 1227 (1250), $wagg_{CH_2}$ – 1154 (1167). Only the frequencies around and above 400 cm^{-1} are listed and discussed in the following. The dipole moment of each system along the direction z perpendicular to the (1 1 1) facet interacting with the adsorbate was calculated for all displacements and used to compute intensities of the infrared (IR) vibrations as described elsewhere [32–34]. The IR spectra computed in such a way account for cancellation of the dipole moment components parallel to the nanoparticle facet under scrutiny, i.e. obey the surface selection rules.

The adsorption energy of CH_xO or CH_x adsorbate on the Pd_{79} nanoparticle, E_{ad}, is defined as the total energy difference $E_{ad} = E(Pd_{79}) + E(\text{adsorbate}) - E(\text{adsorbate}/Pd_{79})$, with adsorbate/$Pd_{79}$ being the adsorption structure. Positive E_{ad} values characterise stabilization of the adsorption structure with respect to isolated adsorbate and substrate species.

3. Results and discussion

3.1. Adsorption sites and vibrational frequencies of CH_3, CH_2 and CH on Pd_{79}

Let us start with the results for adsorption complexes of the three CH_x species, which were considered most comprehensively, i.e. employing all three approaches **1**–**3** for the atomic positions in the substrate Pd_{79} nanoparticle, as outlined in the previous section (Table 1). Some pertinent calculated geometric parameters of the adsorption complexes (also for CH_xO adsorbates) are presented in the Supplementary Information (Table S1).

In the Pd_{79} nanoparticle that was cut from the metal bulk at its experimental geometry and was kept frozen (model **1**), the Pd–Pd bond lengths are the same as on Pd surfaces; also, the small (1 1 1) facets of Pd_{79} are entirely planar similar to terraces on the Pd(1 1 1) surface. Thus, the surface sites in the interior of the (1 1 1) facets could be thought as a rather realistic representation of the corresponding sites on extended surfaces and terraces [7,17,35]. CH_3, CH_2 and CH species bind strongly to the terrace sites with adsorption energies of 155, 347 and 557 kJ/mol, respectively (Table 1). These values are slightly (by up to 3%) higher than the respective adsorption energies calculated previously on a Pd(1 1 1) slab [36]] using a functional by Becke and Perdew (BP86) [37,38]. However, for the adsorbed CH_3 and CH_2 species the (1 1 1) facets are not the most strongly bound places, whereas CH reveals quite similar binding on all studied sites, in close agreement with previous DF calculations on the Pd_{79} model [16]. Note, that the three-fold hollow terrace site **A** is a saddle point for the adsorption of CH_2 species and thus is not discussed further.

Upon relaxation of the Pd_{79} substrate (model **2**) a strengthening of the adsorption bonds is observed in most cases, by up to 12 kJ/mol for CH_3 and by 26 kJ/mol for CH. The most favourable adsorption position for CH is also changed from site **C** near the edge to site **A** in the centre of (1 1 1) nanofacet. The adsorption energy further slightly increases (by 16 kJ/mol at most) when all degrees of freedom are allowed to relax (model **3**). Thus, one can conclude that the intermediate (computationally moderately demanding) model **2** is suitable not only for the qualitatively correct DF description of the preferred adsorption sites of CH_x species on Pd particles with a diameter over 1 nm, but the energy uncertainty it introduces is quite small, around 15 kJ/mol or less. In fact, the calculations show that CH_3 strongly prefers on-top (μ_1) edge sites **G** and **H**, CH_2 is most stable on the site **E** bridging (μ_2) two Pd atoms on the edge and CH binds to three-fold hollow (μ_3) sites revealing a slight preference to the position **A** in the centre of the (1 1 1) facet. These data are in complete agreement with the finding of previous DF calculations (performed using the BP86 functional [37,38] for the energetics and localized Gaussian basis sets), where the coordination preferences of the CH_x adsorbates were rationalized in terms of the sp^3 hybridisation of the carbon atom [16].

What about vibrational frequencies of the adsorption complexes just addressed? To the best of our knowledge, there is no DF data on interactions of CH_x with nanostructured Pd. Reflection absorption IR spectroscopy (RAIRS) studies of methanol dehydrogenation on model catalysts consisting of Pd nanoparticles supported on Al_2O_3/NiAl(1 1 0) revealed two weak adsorption bands at 2945 and 2830 cm^{-1} attributed to CH_x adsorbates on Pd [39]. Even for the most studied Pd(1 1 1) surface, experimental vibrational spectroscopy data for adsorbed CH_x are scarce [40], thus preventing a detailed comparison with the calculated data listed in Table 1. We can see, that the calculated frequencies of the CH_x adsorbates are rather slightly affected by the model type **1**, **2** or **3** employed and the differences in the results from these three models hardly exceed 20–30 cm^{-1}. This means that also for computed frequencies the model **2** appears to be appropriate and only this model will be discussed in the following.

The first question is whether the computed vibrational frequencies (after a thorough calibration against the experimental frequencies of the most relevant model systems) could help in discriminating between the adsorbed CH_3, CH_2 and CH species on Pd. To this end, the following observation are pertinent: (*i*) the highest, C–H stretching frequencies at 2980–3090 cm^{-1} gradually shift along the series of the adsorbates to lower values and, obviously, the number of the C–H modes decreases with the number of the C–H bonds; (*ii*) the CH_3 species exhibits single characteristic mode around 1100 cm^{-1} together with 2 modes at 1380–1390 cm^{-1} that may be IR active or inactive depending on adsorption site (see Section 3.3); (*iii*) adsorbed CH_2 reveals a vibration at 1280–1310 cm^{-1}, which is notably lower than in the CH_3; (*iv*) finally, the highest vibrational mode of the adsorbed CH different from the C–H stretch, should appear only at 720 cm^{-1} or lower. Inspection of Table 1 shows that only for the CH_2 species, for which an asymmetric C–H stretching frequency on site **D** is by 53 cm^{-1} different from that on site **E**, one should be able to distinguish between the adsorption on terraces and edges. The vibrational frequencies of CH on terrace site **A** are systematically higher by 20–30 cm^{-1} than those on sites **B** and **C** closer to the edge; however, the difference is comparable with accuracy of our calculations. Finally, the frequencies of the CH_3 species that are above 1000 cm^{-1}, vary only slightly from one adsorption site to the other, by less than 10 cm^{-1}. However, if the considerations of the IR intensity change depending on the adsorption site are invoked (see Section 3.3) more information practically useful for the characterization of the adsorption complexes could be extracted from the calculated data.

3.2. Adsorption and vibrational frequencies of CH_2OH, CH_3O, CH_2O and CHO on Pd_{79}

The results of calculations for the adsorption complexes CH_xO/Pd_{79} are shown in Figure 1 and Table 2; the geometrical characteristics of the calculated structures are listed in Table S1 in Supplementary Materials. Hydroxymethyl, CH_2OH, is 20 kJ/mol more stable on the edge on-top site **G** of Pd_{79} than at site **F** inside the (1 1 1) facet. The preference of methoxy, CH_3O, to occupy an edge μ_2 site **E** with respect to the μ_2 **A** and **C** and μ_3 **D** sites of Pd_{79} is even stronger, by about 50 kJ/mol. Formaldehyde, CH_2O, binds to (1 1 1) facets of Pd_{79} (μ_2 site **D**) weakly, with the adsorption energy of only 10 kJ/mol, in line with the observations for the Pd(1 1 1) surface [9,40]. The adsorption is notably stronger, 60 kJ/mol, on

Table 1
Calculated adsorption energies E_{ads} and harmonic vibrational frequencies ω of the optimised CH_x species adsorbed on various sites of a Pd_{79} nanoparticle (see Figure 1). Italic font – Pd atoms are kept fixed at the experimental positions in Pd bulk (approach **1**, see text); straight font – Pd atoms are kept fixed at the optimised positions of bare Pd_{79} (approach **2**, gray background); in parentheses – fully optimised structures CH_x/Pd_{79} (approach **3**). Assignment of the vibrations is also given for the most stable structures.[a]

Adsorbate	Site	E_{ads} kJ/mol	ω cm^{-1}								
CH_3	**F**	*155*	*3084*	*3075*	*2974*	*1385*	*1383*	*1091*	*658*	*649*	*432*
		167	3085	3080	2977	1388	1383	1096	660	657	448
		(178)	(3090)	(3087)	(2981)	(1390)	(1384)	(1100)	(671)	(664)	(472)
	G	*182*	*3090*	*3069*	*2971*	*1398*	*1382*	*1101*	*651*	*633*	*459*
		186	3094	3076	2977	1397	1384	1101	656	639	457
		(190)	(3095)	(3079)	(2977)	(1398)	(1383)	(1102)	(656)	(646)	(467)
	H	*183*	*3096*	*3076*	*2974*	*1392*	*1390*	*1101*	*644*	*630*	*466*
		184	3094	3076	2973	1392	1391	1102	648	631	463
		(187)	(3097)	(3075)	(2972)	(1390)	(1390)	(1104)	(646)	(632)	(469)
			σ_{CH_3}	σ_{CH_3}	σ_{CH_3}	def	def	umbr	δ	δ	σ_{Pd}
CH_2	**A**[b]	*316*	*2997*	*2921*	*1311*	*800*	*573*	*505*	*501*	*376*	
		356	2910	2869	1291	749	511	449	355	316	
		(345)	(3027)	(2945)	(1312)	(830)	(612)	(546)	(531)	(412)	
	D	*347*	*3008*	*2934*	*1307*	*794*	*570*	*505*	*489*	*377*	
		365	3012	2937	1308	807	585	528	500	392	
		(377)	(3039)	(2956)	(1309)	(821)	(608)	(532)	(530)	(405)	
	E	*386*	*3061*	*2964*	*1289*	*791*	*595*	*544*	*520*	*425*	
		385	3065	2967	1286	795	601	552	527	413	
		(393)	(3060)	(2963)	(1289)	(811)	(602)	(556)	(533)	(417)	
			σ_{CH_2}	σ_{CH_2}	sciss	wagg	rock	σ_{Pd}	twist	σ_{Pd}	
CH	**A**	*557*	*3008*	*720*	*718*	*576*	*461*	*458*			
		583	3010	720	716	603	471	467			
		(599)	(3042)	(706)	(704)	(587)	(473)	(471)			
	B	*564*	*2985*	*710*	*691*	*573*	*465*	*444*			
		570	2984	702	688	577	460	443			
		(584)	*(2961)*	*(709)*	*(693)*	*(555)*	*(483)*	*(451)*			
	C	*561*	*2995*	*721*	*719*	*573*	*467*	*457*			
		571	2988	717	713	576	459	453			
		(585)	(2973)	(739)	(734)	(546)	(491)	(469)			
			σ_{CH}	δ	δ	σ_{Pd}	σ_{Pd}	σ_{Pd}			

[b] **A** is a saddle point structure for the diffusion of CH_2 on Pd_{79}.
[a] σ_{CHx} – C–H stretching (in all cases asymmetric vibrations have higher frequencies than the symmetric one); σ_{Pd} – Pd–C stretching; δ – bending with respect to the substrate; def – deformation of CH_3; umbr – umbrella mode of CH_3; sciss, wagg, rock, twist – scissor, wagging, rocking and twisting vibrations of CH_2, respectively.

Table 2
Calculated adsorption energies E_{ads} and harmonic vibrational frequencies ω of the adsorbed CH_xO species optimised on various sites of a bare Pd_{79} nanoparticle (model **2**, see Table 1, Figure 1). Assignments of the vibrations are also given for the most stable structures.[a]

Adsorbate	Site	E_{ads} kJ/mol	ω cm^{-1}									
CH_2OH	**F**	134	3654	3092	2986	1426	1330	1135	1070	962	685	458
	G	154	3700	3063	2958	1428	1333	1132	1069	1003	673	460
			σ_{OH}	σ_{CH_2}	σ_{CH_2}	sciss	δ_{OCH}	σ_{CO}	δ_{OCH}	wagg	σ_{Pd}	σ_{Pd}
CH_3O	**A**	138	3015	3013	2936	1441	1441	1413	1110	1108	977	
	C	132	3022	3016	2940	1443	1436	1413	1101	1098	966	
	D	130	3023	3006	2932	1439	1438	1410	1108	1099	962	
	E[b]	184	3012	2999	2927	1450	1437	1412	1128	1115	986	
			σ_{CH_3}	σ_{CH_3}	σ_{CH_3}	umbr	def	def	σ_{CO}	δ_{OCH}	δ_{OCH}	
CH_2O	**D**	10	2929	2851	1452	1231	1147	918	516	415		
	E	60	2944	2865	1444	1235	1151	929	490	429		
			σ_{CH_2}	σ_{CH_2}	σ_{CO}	sciss	rock	wagg	σ_{Pd}	σ_{Pd}		
CHO	**E**[b]	211	2755	1584	1090	591	398					
	F[c]	177	2855	1376	1123	670	449					
			σ_{CH}	σ_{CO}	δ_{OCH}	σ_{Pd}	σ_{Pd}					

[a] σ_{OH} – O–H stretching; σ_{CHx} – C–H stretching (in all cases asymmetric vibrations have higher frequencies than the symmetric one); σ_{Pd} – Pd–C or Pd–O stretching; δ_{ABC} – bending of A–B–C bonds; def – deformation of CH_3; umbr – umbrella mode of CH_3; sciss, wagg, rock – scissor, wagging and rocking vibration modes of CH_2, respectively.
[b] CH_3O and CHO spontaneously move from site **B** to site **E** during geometry optimisation.
[c] CHO is adsorbed in μ_1–μ_2 fashion on the site **F** with O coordinated by one Pd atom and C by two Pd atoms.

the edge μ_2 site **E**. This considerable increase in the binding strength of formaldehyde through an interaction with low-coordinated Pd atoms of Pd_{79} is in accord with the findings of earlier DF studies on stepped extended surfaces [41,42] as well as on sub-nanometer Pd clusters [43]. Thus, nanostructuring of Pd surfaces stabilizing adsorbed formaldehyde is also expected to dramatically affect its reactivity under specific conditions. The formyl species CHO reveals rather strong adsorption interactions,

but its most stable position on Pd_{79} with the adsorption energy 211 kJ/mol is a μ_2 site **E** bridging two edge Pd atoms. Thus, all the CH_xO adsorbates under consideration show a strong propensity to be located at the edges of Pd nanoparticles, which implies a considerably different reactivity on nanostructured Pd versus that on single crystal surfaces when the CH_xO species take part in the reactions. Note that calculations on CH_xO species adsorbed at (1 1 1) facets of the Pd_{79} nanoparticle performed using another common gradient-corrected exchange–correlation functional BP86 [37,38] revealed systematically higher (by up to 15%) adsorption energies [16].

The following IR spectroscopy data are available in the literature for the CH_xO/Pd(1 1 1) adsorption complexes: trace amounts of methoxy (CH_3O) are detected at 2900 cm^{-1}; formaldehyde (CH_2O) manifests itself by the modes at 1305 and 1255 cm^{-1} assigned to two different adsorption geometries; formyl (CHO) reveals a peak at 1200 cm^{-1}, which is either bending δ_{OCH} or stretching σ_{CO} mode [12,40]. On a model catalyst $Pd/Al_2O_3/NiAl(1\ 1\ 0)$ two RAIRS shoulders at 2905 and 2800 cm^{-1} are tentatively assigned to methoxy species adsorbed on Pd nanoparticles [39]. Missing spectroscopic indications of any intermediates of methoxy dehydrogenation on the model catalyst imply that the subsequent decomposition steps are fast [44]. The calculated vibrational frequencies of CH_xO/Pd_{79} in Table 2 show (*i*) that similarly to the CH_x/Pd_{79} systems (see Section 3.1), some of the discussed species exhibit a pronounced change in vibrational frequencies at different adsorption sites, e.g. CH_2OH and CHO, while others show no change in frequencies, e.g. CH_3O and CH_2O; (*ii*) there is a quite substantial systematic frequency shift of the highest stretching mode to lower values in the series of adsorbed CH_2OH (3700 cm^{-1}, O–H stretch) > CH_3O (3012 cm^{-1}, O–H stretch) > CH_2O (2944 cm^{-1}, O–H stretch) > CHO (2755 cm^{-1}, O–H stretch). There are also other less pronounced trends in the calculated frequencies, which could be used for characterization of the species. Additional useful information comes from the analysis of the IR intensities computed for selected surface complexes and discussed in the following section.

3.3. Positions of the adsorbates and IR intensities

Before closing the discussion, let us briefly comment how IR intensities may give indication about the preferred adsorption positions of certain species. Most of the studied CH_xO and CH_x species orient differently orientations with respect to a (1 1 1) facet when adsorbed on the sites inside the facet and at an edge of the corresponding (1 1 1) facet of Pd_{79} nanoparticle (Figure 1). In turn, (1 1 1) facets of larger transition metal nanoparticles prepared by deposition on conducting oxide films are often parallel to the substrate plane [39]. Thus, C_1 species adsorbed on the terraces and at the edges of the nanoparticles may reveal substantially different peak intensities in their IR spectra due to electrostatic interactions with the substrate. Vibrations that do not manifest themselves in the IR spectra of the species adsorbed on terraces due to surface selection rules may become visible when the molecule is adsorbed at an edge. And vice versa, the intensities of vibrations normal to (1 1 1) facets may be decreased or even reduced to zero. Indeed, Figure 2 illustrates these considerations for selected adsorbates at selected positions.

For example, the CH_2 scissor mode of CH_2OH at ~1430 cm^{-1} should be visible in the IR spectra (provided that the species does not decompose) only in the case of adsorption at an edge (site **G**). In contrast, the C–O–H bending mode at ~1330 cm^{-1} should be IR-visible only when CH_2OH is adsorbed at a nanoparticle terrace (site **F**). This implies that adsorption at sites **G** and **F**, energetically apart by only 20 kJ/mol, could be distinguishable via a strong intensity alteration of the IR peaks separated by ~100 cm^{-1} and thus be eventually detectable.

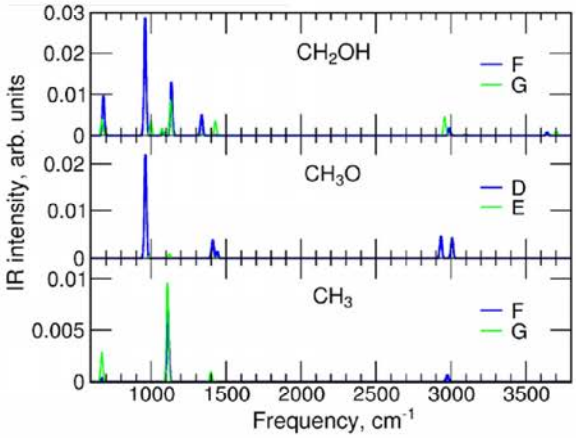

Figure 2. Calculated IR spectra for adsorption complexes of CH_2OH, CH_3O and CH_3 on selected sites of the optimised Pd_{79} nanoparticle. See Figure 1 for the definition of the sites.

Likewise, the adsorbed CH_3 and CH_3O species have three vibrational modes associated with the stretching of C–H bonds. However, not all of these modes are always visible in the IR spectra due to their different symmetry. Whereas on the (1 1 1) terrace (site **F**) only a symmetric stretch of three C–H bonds in CH_3 is IR-active, in the case of adsorption at an edge (site **G**) there is also another IR peak at a higher frequency, associated with the asymmetric CH_3 stretching. In this case, a peak that appears near 1400 cm^{-1} is caused by an asymmetric bending of the C–H bonds.

The CH_3O species adsorbed on a (1 1 1) terrace of Pd nanoparticle are tilted, so that the symmetric and one of asymmetric modes are IR-visible. However, when CH_3O is adsorbed on the edge of nanoparticle (the notably preferred site **E**) the CH_3 group is oriented nearly perpendicularly to one of (1 1 1) facets, resulting in the negligible IR intensities of the CH_3 vibrations in the frequency regions around 3000 cm^{-1} and 1400 cm^{-1} (Figure 2). Thus, also for the methoxide adsorbate its spectroscopic detection and characterisation on Pd nanoparticles could be facilitated with the help of our computationally predicted IR intensity features.

4. Summary

The main results of this study can be summarized as follows:

- All studied C_1 adsorbates except CH are computed to be stabilized on the edge sites of the nanoparticle Pd_{79} with respect to the sites in the interior of the (1 1 1) facets, the latter serve in our models to represent Pd(1 1 1) terraces. The stabilization is quite significant, 20–50 kJ/mol, which implies a notable effect of low-coordinated atoms exposed by Pd catalyst particles on the thermodynamics and kinetics of the processes involving the C_1 species as reactants, intermediates or products. The largest stabilization on edges is observed for formaldehyde, whose adsorption energy increases from 10 kJ/mol on terraces to 60 kJ/mol on edges.
- Some of the studied species do not show a significant dependence of their vibrational frequencies on the adsorption site (~15 cm^{-1} for CH_3O, CH_2O, CH_3) whereas the frequencies of several other adsorbates (CH_2OH, CHO, CH_2, CH) do change by 30 cm^{-1} or more. The frequency variations appear to be rather modest compared to the pronounced changes in the adsorption energies and structural changes at different adsorption sites.
- The spatial orientations of various C_1 species adsorbed on nanoparticle edges are changed with respect to adsorption on flat terraces, yielding pronounced changes in the IR intensities.

Vibrations that cannot be observed on extended surfaces due to the surface selection rule could manifest themselves in the IR spectra taken on nanoparticles, while the intensities of other IR peaks detectable on flat surfaces may be dramatically reduced. These findings together with the frequency shifts associated with the adsorption on nanoparticle edges may help to characterise usually elusive C_1 adsorption species formed and disappearing rapidly in pertinent reactions on Pd catalysts.

Acknowledgements

SMK is grateful to the Spanish *Ministerio de Educación* for a predoctoral FPU grant. GFC thanks CONICET and ANPCyT (PICT N° 02419) of Argentina for financing her stay in Barcelona. Financial support has been provided by Spanish MICINN (grants FIS2008-02238) and by *Generalitat de Catalunya* (grants 2009SGR1041 and XRQTC). Computational time on MARENOSTRUM supercomputer granted by the Barcelona Supercomputing Center is also acknowledged.

Appendix A. Supplementary data

Supplementary data associated with this article can be found, in the online version, at doi:10.1016/j.cplett.2011.02.061.

References

[1] G. Ertl, Reactions at Solid Surfaces, second ed., J. Wiley, Hoboken, 2009. p. 208.
[2] M. Bowker, ACS Nano 1 (2007) 253.
[3] H.-P. Steinrück, J. Libuda, D.A. King, Chem. Soc. Rev. 37 (2008) 2152.
[4] R. Imbihl, R.J. Behm, R. Schlögl, Phys. Chem. Chem. Phys. 9 (2007) 3459.
[5] M. Bäumer, H.-J. Freund, Prog. Surf. Sci. 61 (1999) 127.
[6] H.-J. Freund, Chem. Eur. J. 16 (2010) 9384.
[7] I.V. Yudanov, R. Sahnoun, K.M. Neyman, N. Rösch, J. Chem. Phys. 117 (2002) 9887.
[8] K.M. Neyman, F. Illas, Catal. Today 105 (2005) 2.
[9] M. Bäumer, J. Libuda, K.M. Neyman, N. Rösch, G. Rupprechter, H.-J. Freund, Phys. Chem. Chem. Phys. 9 (2007) 3541.
[10] T. Fuhrmann, M. Kinne, B. Tränkenschuh, C. Papp, J.F. Zhu, R. Denecke, H.-P. Steinrück, New J. Phys. 7 (2005) 107.
[11] F. Zaera, Prog. Surf. Sci. 69 (2001) 1.
[12] G. Rupprechter, C. Weilach, J. Phys.: Condens. Matter 20 (2008) 184019.
[13] A.J. Foster, R.F. Lobo, Chem. Soc. Rev. 39 (2010) 4783.
[14] I.V. Yudanov et al., J. Phys. Chem. B 107 (2003) 255.
[15] I.V. Yudanov, K.M. Neyman, N. Rösch, Phys. Chem. Chem. Phys. 8 (2006) 2396.
[16] I.V. Yudanov, A.V. Matveev, K.M. Neyman, N. Rösch, J. Am. Chem. Soc. 130 (2008) 9342.
[17] F. Viñes, A. Desikusumastuti, T. Staudt, A. Görling, J. Libuda, K.M. Neyman, J. Phys. Chem. C 112 (2008) 16539.
[18] F. Viñes, C. Loschen, F. Illas, K.M. Neyman, J. Catal. 266 (2009) 59.
[19] F. Viñes et al., Chem. Eur. J. 16 (2010) 6530.
[20] K.M. Neyman, S. Schauermann, Angew. Chem. Int. Edit. 49 (2010) 4743.
[21] Z.-J. Zhao, L.V. Moskaleva, H.A. Aleksandrov, D. Basaran, N. Rösch, J. Phys. Chem. C 114 (2010) 12190.
[22] G. Kresse, J. Furthmuller, Phys. Rev. B 54 (1996) 11169.
[23] G. Kresse, J. Hafner, Phys. Rev. B 47 (1993) 558.
[24] G. Kresse, D. Joubert, Phys. Rev. B 59 (1999) 1758.
[25] B. Hammer, L.B. Hansen, J.K. Nørskov, Phys. Rev. B 59 (1999) 7413.
[26] F. Viñes, F. Illas, K.M. Neyman, J. Phys. Chem. A 112 (2008) 8911.
[27] F. Baletto, R. Ferrando, Rev. Mod. Phys. 77 (2005) 371.
[28] S.T. Bromley, I. de P.R. Moreira, K.M. Neyman, F. Illas, Chem. Soc. Rev. 38 (2009) 2657.
[29] F. Viñes, F. Illas, K.M. Neyman, Angew. Chem. Int. Ed. 46 (2007) 7094.
[30] G. Herzberg, Molecular Spectra and Molecular Structure: II. Infrared and Raman Spectra of Polyatomic Molecules, Krieger, Malabar, 1991.
[31] R.J. Bouwens, J.A. Hammerschmidt, M.M. Grzeskowiak, T.A. Stegnik, P.M. Yorba, W.F. Polik, J. Chem. Phys. 104 (1996) 460.
[32] R.D. Amos, Adv. Chem. Phys. 67 (1987) 99.
[33] K.M. Neyman, N. Rösch, Ber. Bunsenges. Phys. Chem. 96 (1992) 1711.
[34] A. Valcárcel, J.M. Ricart, F. Illas, A. Clotet, J. Phys. Chem. B 108 (2004) 18297.
[35] I.V. Yudanov, M. Metzner, A. Genest, N. Rösch, J. Phys. Chem. C 112 (2008) 20269.
[36] J.-F. Paul, P. Sautet, J. Phys. Chem. B 102 (1998) 1578.
[37] A.D. Becke, Phys. Rev. A 38 (1988) 3098.
[38] J.P. Perdew, Phys. Rev. B 33 (1986) 8822.
[39] S. Schauermann, J. Hoffmann, V. Johánek, J. Hartmann, J. Libuda, Phys. Chem. Chem. Phys. 4 (2002) 3909.
[40] M. Borasio, O. Rodríguez de la Fuente, G. Rupprechter, H.-J. Freund, J. Phys. Chem. B 109 (2005) 17791.
[41] Z.-X. Chen, K.H. Lim, K.M. Neyman, N. Rösch, J. Phys. Chem. B 109 (2005) 4568.
[42] K.H. Lim, Z.-X. Chen, K.M. Neyman, N. Rösch, J. Phys. Chem. B 110 (2006) 14890.
[43] F. Mehmood, J. Greeley, L.A. Curtiss, J. Phys. Chem. C 113 (2009) 21789.
[44] S. Bertarione et al., J. Catal. 223 (2004) 64.

Section 3.2

Methane decomposition on edges of Pd nanoparticles

Sergey M. Kozlov,[1] Konstantin M. Neyman[1,2]

[1] Departament de Química Física and Institut de Química Teòrica i Computacional (IQTCUB), Universitat de Barcelona, c/ Martí i Franquès 1, 08028 Barcelona, Spain

[2] Institució Catalana de Recerca i Estudis Avançats (ICREA), 08010 Barcelona, Spain

Abstract

Full-scale employment of methane as an environmentally friendly source of energy, hydrogen or higher hydrocarbons faces the challenge of methane activation for further chemical transformations. In particular, activity of Pd-containing catalysts with respect to methane is intensely discussed due to their application for methane abatement in exhaust gases. Herein, we investigate computationally the activity of edges of scalable with size 1.2 nm big Pd_{79} nanoparticles to activate and dissociate methane and compare it to the activity of extended Pd(111) surfaces. Activation energy for the rate-limiting step, methane to methyl, was found to be 40 kJ/mol lower on the edges of Pd nanoparticles than on Pd(111), suggesting significantly higher activity of the former.

Introduction

Methane is not only a naturally abundant fuel but also a very potent and chemically inert greenhouse gas. This limits its usage in many applications, e.g. acetic acid production,[1] NO reduction,[2] as well as CO_2[3,4] and steam[5] reforming. Even the most common and the most important reaction involving methane, its combustion, is complicated by the necessity to catalytically remove traces of methane from the exhaust gases to lower the environmental fingerprint. The ability of Pd-based catalysts for methane abatement has been intensely studied since early 60s.[6–8] However, due to the very complex phase diagram[7,9,10] of nanostructured Pd in oxidative conditions the structure of the active site for methane oxidation is still controversially discussed.[11–13] Some studies concluded that methane activation on metallic Pd is a feasible process.[13–15] Since closed packed surfaces of Pd are rather inert towards methane,[13,16,17] it is particularly interesting to investigate methane dissociation on low-coordinated metal atoms formed on nanoparticle (NP) edges. Previously, NP edges were shown to yield

much higher activity than extended NP terraces in many reactions,[18,19,20] including methane dissociation on Pt.[21]

Activity of nanoparticle edges can be reliably studied using scalable with size NP models.[22–24] These nanoparticles are chosen in such a way that their properties (including interaction with adsorbates) can be extrapolated to those of much bigger NPs typically dealt with in experiment.[25–27] In order to be scalable with size, NPs should have bulk-like lattice structure (like bigger species), a shape in line with Wulff-construction and be above certain size. For Pd already truncated octahedral Pd_{79} NPs fulfill all these criteria, which explains their numerous applications in computational studies.[28–30] Recently it was also shown that unsupported scalable with size nanoparticles closely mimic the nanoparticles on chemically inert supports, such as MgO(100).[26,31]

In this work we calculate reaction energy profile for methane activation and decomposition on edges of Pd_{79} and compare it to the activity of extended Pd(111) surface. It is found that the rate-limiting step, dissociative adsorption of methane, has twice lower activation energy on the NP edges compared to Pd(111). Since computational parameters adopted in this work closely mimic those in a previous work on methane dissociation on Pt_{79} NPs and Pt(111)[21] we were also able to quantitatively compare the activity of Pd and Pt catalysts. It was found that the reaction energy profiles for methane dissociation on Pd(111) and Pt(111) are quite similar, while the activities of Pd_{79} and Pt_{79} NPs are markedly different. This study clarifies the role of nanostructured metallic Pd in methane activation, which is important for understanding of complex reaction network during methane oxidation on Pd-based catalysts.

Computational Details

The computational parameters employed in this paper were chosen to be as similar as possible to Ref [21]. VASP software[32] was used to perform periodic calculations with rPBE exchange-correlation functional,[33] which was shown to yield reasonable results at least for H interaction with Pd.[26] Eigenstates of valence electrons were calculated using plane-wave basis set was with the cut-off of 415 eV and 0.1 eV Methfessel-Paxton smearing was applied to the occupation numbers.[34] The presence of core electrons was modelled via projector augmented wave technique.[35] All calculations

except those for gas phase CH_x species were performed in spin unpolarized fashion, which does not introduce any significant inaccuracy.[36] For slab calculations the 5×5×1 Monkhorst-Pack mesh of k-points was used to sample the reciprocal space.

Geometry optimization was performed until forces on atoms became less than 0.2 eV/nm. All C and H atoms as well as all metal atoms in Pd_{79} NP were relaxed. Extended p(3×3) Pd(111) slab consisted of six atomic layers with four top relaxed layers and two bottom layers fixed on bulk-optimized lattice parameter, r(Pd-Pd) = 282 pm. The separation between adjacent NPs exceeded 0.7 nm (which leads to negligible interaction between adjacent species),[31,37] while the separation between slabs was larger than 1 nm. Transition states were pre-optimized with nudged elastic band method[38] and converged using dimer method.[39] Vibrational frequencies were calculated using finite differences method with 3 pm displacements. All transition states featured exactly one imaginary vibrational frequency.

Adsorption energies of CH_x species on Pd, $E_{ads}[CH_x]$, were calculated from their total energies $E[CH_x/substrate]$ as $E_{ads}[CH_x]=E[CH_x/substrate]-E[CH_x]-E[substrate]$, where $E[CH_x]$ is the energy of respective gas phase species and E[substrate] is the energy of the substrate. Relative energies of CH_x species, $E_{rel}[CH_x]$, with respect to the energy of gas phase methane, $E[CH_4]$, and 4-x adsorbed H atoms using the following formula: $E_{rel}[CH_x] = E[CH_x/substrate] + (4-x)\times E[H_{ads}] - E[CH_4] - E[substrate]$, where $E[H_{ads}] = E[H/substrate] - E[substrate]$ is the energy of adsorbed H atom. Relative energies of transition states were calculated in a similar way. All relative energies presented in the manuscript include zero-point energy corrections (ZPE) and correspond to 0 K temperature; data without ZPE can be found in the supplementary information.

Results and Discussion

We begin the discussion by comparing adsorption energies of various CH_x intermediates on terraces and edges of Pd_{79} nanoparticles and extended Pd(111) surface. As one can see from Table 1, adsorption energies of various species on {111} terraces of Pd_{79} are higher than those on extended Pd(111) surface by ~7 % for CH_3, by ~5% for CH_2, CH, and C species and by only 2% for H atoms. However, this relatively small relative increase of E_{ads} results in a change of absolute values by up to 30 kJ/mol for strongly bound species such as C or CH. The most probable reason for the stronger

binding of the adsorbates is higher flexibility of NP terraces compared to extended surfaces. As was noted before,[40] the stabilization of various species on the edges of Pd NPs correlates with their adsorption sites. Namely, CH_2 species adsorbed on bridge sites on edges of Pd_{79} by 17 kJ/mol stronger than on the terrace bridge sites. For top adsorbed CH_3 species the stabilization on the edges is only 9 kJ/mol. In contrast, CH, C and H species, which adsorb on three-fold hollow sites, are a bit more stable on the terraces compared to the edges. A similar stability of H and C atoms on edges and terraces of Pd NPs was also found in previous studies. [26,29,41]

In variation with other species, CH_4 is calculated to interact very weakly with Pd. This is, however, due to the neglect of dispersive interactions in the employed computational approach. Correcting for this would result in small but measurable physisorption energy of methane on Pd. Systematically accounting for dispersive corrections would slightly increase adsorption energies of all the adsorbates. However, it would affect the shape of reaction energy profile for methane decomposition in a negligible way, since all the intermediates are located at roughly the same distance from the substrate.

Table 1. Adsorption energies of CH_x species (eV) calculated on Pd(111) slabs and Pd_{79} nanoparticles.

	Pd(111)	Pd_{79} terrace	Pd_{79} edge
CH_4	-24	-24	-26
CH_3	127	137	147
CH_2	312	330	345
CH	553	582	566
C	633	661	662
H[a]	245 (37)	251 (44)	248 (41)

[a] In parentheses are adsorption energies of H atom with respect to ½ of gas phase H_2 molecule.

Extended Pd(111) surface is calculated to be rather inactive in methane activation, with the first dissociation barrier being almost 100 kJ/mol (Table 2). Since this barrier greatly exceeds methane desorption energy from Pd, the first step of methane dehydrogenation is the rate-limiting step of methane decomposition. Also this elementary step is fairly endothermic, which makes the reverse reaction very probable. The next barrier for methyl hydrogenation is also significant, 82 kJ/mol, while dehydrogenation of CH_2 species is facile with the barrier of only 23 kJ/mol. This small value of the latter activation energy is consistent with the fact that CH_2 is hardly observed experimentally on Pd. The highest barrier is for CH dehydrogenation to atomic C and H, the process that happens only at rather high T.[42] Note that the activation energy for CH decomposition greatly exceeds the migration barrier of adsorbed C atom into subsurface region of Pd(111).[43]

Table 2. Reaction energies, ΔE, and activation energies, $E^{\#}$, (kJ/mol) of elementary steps in methane decomposition on Pd.

	$E^{\#}\|Pd(111)$	$E^{\#}\|Pd_{79}$	$\Delta E\|Pd(111)$	$\Delta E\|Pd_{79}$
$CH_4 \rightarrow CH_3$	95	55	37	8
$CH_3 \rightarrow CH_2$	82	59	10	-11
$CH_2 \rightarrow CH$	23	36	-55	-42
$CH \rightarrow C$	125	92	25	2

The activation of methane is significantly easier on the edges of Pd_{79} NPs with the barrier reduced by 40% and also the endothermicity of this step is decreased to only 8 kJ/mol. This suggests a greatly improved activity of Pd NPs compared to extended Pd(111) surface in processes involving methane, since C-H bond scission in methane is the rate-limiting step in many processes. Note that the increased catalytic activity of the edges is not unique – a similar activity with respect to methane was calculated with PBE functional[44] on stepped Pd(211) surface.[13,45] However, in this case the first elementary step is calculated to be exothermic by ~25 kJ/mol, whereas on Pd_{79} edges this step is almost energy neutral. The activation energy of the second elementary step $CH_3 \rightarrow CH_2$

is also decreased by more than 20 kJ/mol on edges of Pd_{79}, where this step becomes exothermic. In variation, the dehydrogenation of CH_2 species is hindered on the edges, because the initial state, CH_2, is somewhat stabilized in this case. Nevertheless, this barrier of 36 kJ/mol still remains insignificant in the overall course of the reaction. The activation energy and the endothermicity of the final dehydrogenation step, CH→C, are also decreased by 32 and 23 kJ/mol, respectively. Note that when C atoms form on the edges of Pd_{79} NPs they can migrate into subsurface region without crossing any significant barrier.[41]

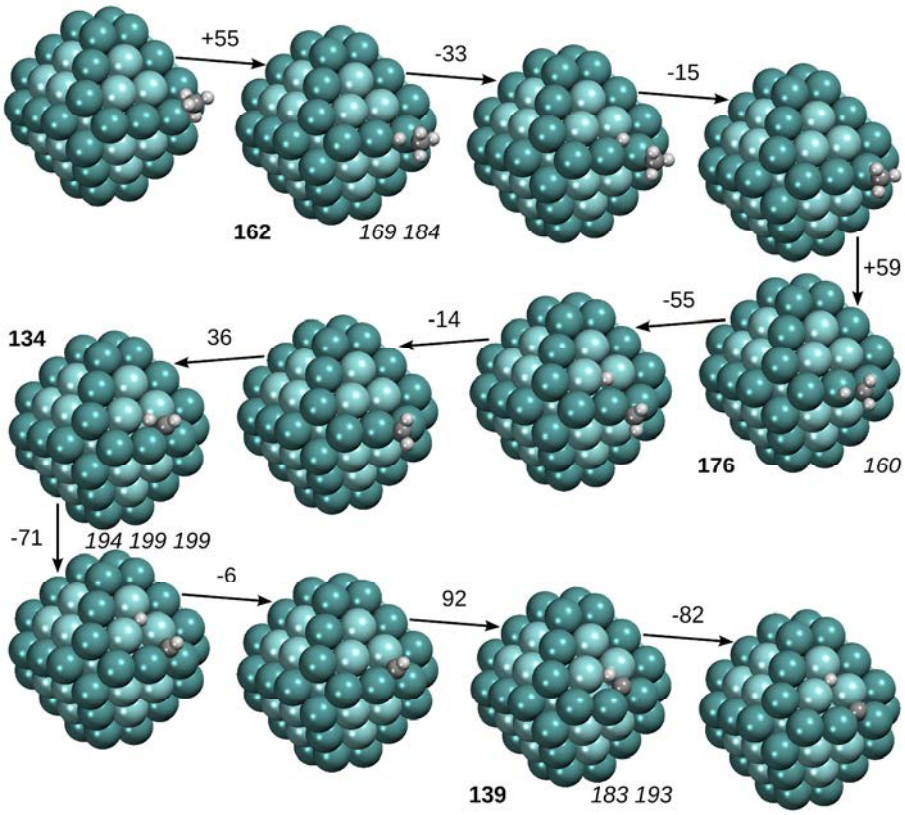

Figure 1. Methanol dissociation at edges and corners of the Pd_{79} NP. Energy cost of each transformation is given above the arrows. Interatomic C-H and H-Pd distances in transition states are given in bold and italic, respectively.

Transition states for CH_4 decomposition calculated on edges of Pd_{79} are displayed on Figure 1. In the first two transition states H-C distances are 162 and 176 pm, which is much longer than in the last two transition states with r(H-C) around 135 pm. (The C-Pd distance in the transition state of methane dehydrogenation is 215 pm.) Distances between dissociating H atom and Pd substrate may vary from 160 to 199 pm and depend on H-Pd coordination in the transition state. In general, H tends to form

shorter H-Pd bonds, when it is coordinated by fewer Pd atoms. The transition states for CH_4, CH_3 and CH_2 dehydrogenation on Pd(111) are similar to those on Pd_{79}. The differences are limited to 3 pm for respective H-C distances, and to 8 pm for H-Pd distances. At the same time the transition state for CH dissociation is different on Pd(111) single crystals and edges of Pd_{79}. Namely, in the former case H forms only one H-Pd bond of 160 pm, whereas H-C distance is 175 pm. The reason for such difference is probably better accommodation of strongly bound C atoms on flexible NP edges,[41] which affects both transition and final states.

It is very instructive to compare our results with the previous study by Viñes et al.[21] performed using very similar computational parameters. On Figure 1 one can see that the reaction energy profiles for Pd(111) and Pt(111) are quite close to each other. The differences between respective reaction energies of various steps on Pd(111) and Pt(111) do not exceed 20 kJ/mol, while for the activation energies they are even less than 10 kJ/mol. In particular, activation energies for the rate-limiting step, methane activation, differ by 5 kJ/mol only.

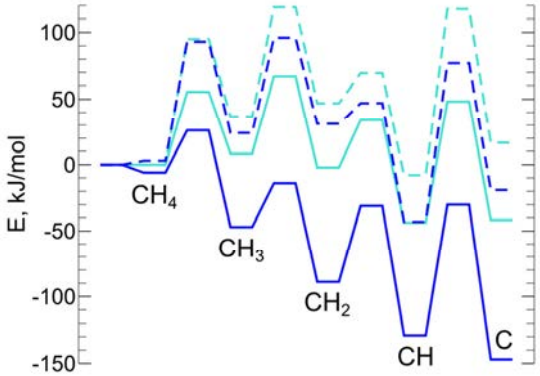

Figure 2. Reaction profiles of methane decomposition on edges of M_{79} nanoparticles (solid line) and M(111) surfaces (dashed line) of Pd (cyan) and Pt (blue). The data for Pt is adapted from Viñes et al.[21]

Differences between the two reaction energy profiles on edges of Pd_{79} and Pt_{79} are markedly bigger. The activation energies for the first two dehydrogenation steps are decreased from ~55 kJ/mol on Pd_{79} to ~30 kJ/mol on Pt_{79}. Besides, the respective reaction energies become exothermic by 40 kJ/mol on Pt_{79} compared to almost isoenergetic situation on Pd_{79} edges. Finally, the overall exothermicity of methane

decomposition on the edges of Pd_{79} is around 40 kJ/mol, while for Pt_{79} it almost reaches 150 kJ/mol.

As one can see, whereas the activities of Pd(111) and Pt(111) surfaces in methane decomposition are quite similar, the respective NPs may behave very differently in this process. This finding illustrates that nanostructuring may affect properties of seemingly similar materials in very different ways. Therefore, effects of nanostructuring should be considered very carefully in every particular case without making unjustified assumptions.

Conclusions

In summary, electronic structure calculations show that edges of Pd nanoparticles are significantly more active in methane activation than Pd(111) surfaces. Namely, the activation energy for the rate-limiting step, methane dehydrogenation to methyl, is predicted to decrease from 95 to 55 kJ/mol. The reaction energy profile for methane dissociation on Pd(111) was found to be rather close to that on Pt(111) calculated by Viñes et al.[21] At the same time, the reaction energy profiles on the edges of Pd_{79} and Pt_{79} nanoparticles were found to be markedly different, indicating that nanostructuring affects these two apparently similar metals in distinct ways. These findings help to assess the role of metallic Pd in methane oxidation and to explain why properties of Pd and Pt catalysts depend differently on the NP size in e.g. methane oxidation.[46]

References

(1) Periana, R. A.; Mironov, O.; Taube, D.; Bhalla, G.; Jones, C. J. Catalytic, Oxidative Condensation of CH_4 to CH_3COOH in One Step via CH Activation. *Science* **2003**, *301*, 814–818.

(2) Li, N.; Wang, A.; Li, L.; Wang, X.; Ren, L.; Zhang, T. NO Reduction by CH_4 in the Presence of Excess O_2 over Pd/sulfated Alumina Catalysts. *Appl. Catal. B Environ.* **2004**, *50*, 1–7.

(3) Zhang, Z.; Verykios, X. E.; Macdonald, S. M.; Affrossman, S. Comparative Study of Carbon Dioxide Reforming of Methane to Synthesis Gas over Ni/La_2O_3 and Conventional Nickel-Based Catalysts. **1996**, 744–754.

(4) Chen, Y.; Tomishige, K.; Yokoyama, K.; Fujimoto, K. Promoting Effect of Pt, Pd and Rh Noble Metals to the $Ni_{0.03}Mg_{0.97}O$ Solid Solution Catalysts for the Reforming of CH_4 with CO_2. *Appl. Catal. A Gen.* **1997**, *165*, 335–347.

(5) Mukainakano, Y.; Li, B.; Kado, S.; Miyazawa, T.; Okumura, K.; Miyao, T.; Naito, S.; Kunimori, K.; Tomishige, K. Surface Modification of Ni Catalysts with Trace Pd and Rh for Oxidative Steam Reforming of Methane. *Appl. Catal. A Gen.* **2007**, *318*, 252–264.

(6) Anderson, R. B.; Stein, K. C.; Feenan, J. J.; Hofer, L. J. E. Catalytic Oxidation of Methane. *Ind. Eng. Chem.* **1961**, *53*, 809–812.

(7) Chenakin, S. P.; Melaet, G.; Szukiewicz, R.; Kruse, N. XPS Study of the Surface Chemical State of a $Pd/(SiO_2+TiO_2)$ Catalyst after Methane Oxidation and SO_2 Treatment. *J. Catal.* **2014**, *312*, 1–11.

(8) Gélin, P.; Primet, M. Complete Oxidation of Methane at Low Temperature over Noble Metal Based Catalysts: A Review. **2002**, *39*, 1–37.

(9) Chen, X.; Schwank, J. W.; Fisher, G. B.; Cheng, Y.; Jagner, M.; McCabe, R. W.; Katz, M. B.; Graham, G. W.; Pan, X. Nature of the Two-Step Temperature-Programmed Decomposition of PdO Supported on Alumina. *Appl. Catal. A Gen.* **2014**, *475*, 420–426.

(10) Senftle, T. P.; van Duin, A. C. T.; Janik, M. J. Determining in Situ Phases of a Nanoparticle Catalyst via Grand Canonical Monte Carlo Simulations with the ReaxFF Potential. *Catal. Commun.* **2014**, *52*, 72–77.

(11) Choudhary, T. V; Banerjee, S.; Choudhary, V. R. Catalysts for Combustion of Methane and Lower Alkanes. **2002**, *234*, 1–23.

(12) Carstens, J. N.; Su, S. C.; Bell, A. T. Factors Affecting the Catalytic Activity of Pd/ZrO_2 for the Combustion of Methane. **1998**, *142*, 136–142.

(13) Hellman, A.; Resta, A.; Martin, N. M.; Gustafson, J.; Trinchero, A.; Carlsson, P.-A.; Balmes, O.; Felici, R.; Rijn, R. Van; Frenken, J. W. M.; et al. The Active Phase of Palladium during Methane Oxidation. *J. Phys. Chem. Lett.* **2012**, *3*, 678–682.

(14) Peskov, N. V; Slinko, M. M.; Bychkov, V. Y.; Korchak, V. N. Mathematical Modelling of Oscillatory Behaviour during Methane Oxidation over Palladium Catalysts. *Chem. Eng. Sci* **2012**, *84*, 684–694.

(15) Lyubovsky, M.; Pfefferle, L. Complete Methane Oxidation over Pd Catalyst Supported on α-Alumina. Influence of Temperature and Oxygen Pressure on the Catalyst Activity. **1999**, *47*, 29–44.

(16) Zhang, C. J.; Hu, P. Methane Transformation to Carbon and Hydrogen on Pd(100): Pathways and Energetics from Density Functional Theory Calculations. *J. Chem. Phys.* **2002**, *116*, 322.

(17) Tait, S. L.; Dohnálek, Z.; Campbell, C. T.; Kay, B. D. Methane Adsorption and Dissociation and Oxygen Adsorption and Reaction with CO on Pd Nanoparticles on MgO(100) and on Pd(111). *Surf. Sci.* **2005**, *591*, 90–107.

(18) Jennings, P. C.; Aleksandrov, H. A.; Neyman, K. M.; Johnston, R. L. A DFT Study of Oxygen Dissociation on Platinum Based Nanoparticles. *Nanoscale* **2014**, *6*, 1153–1165.

(19) Bruix, A.; Rodriguez, J. A.; Ramírez, P. J.; Senanayake, S. D.; Evans, J.; Park, J. B.; Stacchiola, D.; Liu, P.; Hrbek, J.; Illas, F. A New Type of Strong Metal-Support Interaction and the Production of H_2 through the Transformation of Water on Pt/CeO_2(111) and Pt/CeO_x/TiO_2(110) Catalysts. *J. Am. Chem. Soc.* **2012**, *134*, 8968–8974.

(20) Roldán, A.; Ricart, J. M.; Illas, F. Origin of the Size Dependence of Au Nanoparticles toward Molecular Oxygen Dissociation. *Theor. Chem. Acc.* **2010**, *128*, 675–681.

(21) Viñes, F.; Lykhach, Y.; Staudt, T.; Lorenz, M. P. A.; Papp, C.; Steinrück, H.-P.; Libuda, J.; Neyman, K. M.; Görling, A. Methane Activation by Platinum: Critical Role of Edge and Corner Sites of Metal Nanoparticles. *Chem. A Eur. J.* **2010**, *16*, 6530–6539.

(22) Kozlov, S. M.; Neyman, K. M. Catalysis from First Principles: Towards Accounting for the Effects of Nanostructuring. *Top. Catal.* **2013**, *56*, 867–873.

(23) Yudanov, I. V.; Genest, A.; Rösch, N. DFT Studies of Palladium Model Catalysts: Structure and Size Effects. *J. Clust. Sci.* **2011**, *22*, 433–448.

(24) Häberlen, O. D.; Chung, S.-C.; Stener, M.; Rösch, N. From Clusters to Bulk: A Relativistic Density Functional Investigation on a Series of Gold Clusters Au_n, n=6,…,147. *J. Chem. Phys.* **1997**, *106*, 5189–5201.

(25) Yudanov, I. V; Genest, A.; Schauermann, S.; Freund, H.-J.; Rösch, N. Size Dependence of the Adsorption Energy of CO on Metal Nanoparticles: A DFT Search for the Minimum Value. *Nano Lett.* **2012**, *12*, 2134–2139.

(26) Kozlov, S. M.; Aleksandrov, H. A.; Neyman, K. M. Adsorbed and Subsurface Absorbed Hydrogen Atoms on Bare and MgO(100)-Supported Pd and Pt Nanoparticles. *J. Phys. Chem. C* **2014**, *118*, 15242–15250.

(27) Kleis, J.; Greeley, J.; Romero, N. A.; Morozov, V. A.; Falsig, H.; Larsen, A. H.; Lu, J.; Mortensen, J. J.; Dułak, M.; Thygesen, K. S.; et al. Finite Size Effects in Chemical Bonding: From Small Clusters to Solids. *Catal. Letters* **2011**, *141*, 1067–1071.

(28) Kozlov, S. M.; Cabeza, G. F.; Neyman, K. M. Bonding and Vibrations of CH_xO and CH_x Species (x=1–3) on a Palladium Nanoparticle Representing Model Catalysts. *Chem. Phys. Lett.* **2011**, *506*, 92–97.

(29) Aleksandrov, H. A.; Viñes, F.; Ludwig, W.; Schauermann, S.; Neyman, K. M. Tuning the Surface Chemistry of Pd by Atomic C and H: A Microscopic Picture. *Chem. A Eur* **2013**, *19*, 1335–1345.

(30) Yudanov, I. V; Neyman, K. M.; Rösch, N. Density Functional Study of Pd Nanoparticles with Subsurface Impurities of Light Element Atoms. *Phys. Chem. Chem. Phys.* **2004**, *6*, 116–123.

(31) Kozlov, S. M.; Aleksandrov, H. a; Goniakowski, J.; Neyman, K. M. Effect of MgO(100) Support on Structure and Properties of Pd and Pt Nanoparticles with 49-155 Atoms. *J. Chem. Phys.* **2013**, *139*, 084701.

(32) Kresse, G.; Furthmüller, J. Efficient Iterative Schemes for Ab Initio Total-Energy Calculations Using a Plane-Wave Basis Set. *Phys. Rev. B. Condens. Matter* **1996**, *54*, 11169–11186.

(33) Hammer, B.; Hansen, L.; Nørskov, J. Improved Adsorption Energetics within Density-Functional Theory Using Revised Perdew-Burke-Ernzerhof Functionals. *Phys. Rev. B* **1999**, *59*, 7413–7421.

(34) Methfessel, M.; Paxton, A. T. High-Precision Sampling for Brillouin-Zone Integration in Metals. **1989**, *40*, 3616–3621.

(35) Kresse, G.; Joubert, D. From Ultrasoft Pseudopotentials to the Projector Augmented-Wave Method. **1999**, *59*, 11–19.

(36) Fajín, J. L. C.; Nata, M.; Cordeiro, D. S.; Gomes, J. R. B.; Illas, F. On the Need for Spin Polarization in Heterogeneously Catalyzed Reactions on Nonmagnetic Metallic Surfaces. **2012**.

(37) Viñes, F.; Illas, F.; Neyman, K. M. On the Mechanism of Formation of Metal Nanowires by Self-Assembly. *Angew. Chem. Int. Ed. Engl.* **2007**, *46*, 7094–7097.

(38) Mills, G.; Jónsson, H.; Schenter, G. K. Reversible Work Transition State Theory : Application to Dissociative Adsorption of Hydrogen. *Surf. Sci.* **1995**, *324*, 305-337.

(39) Henkelman, G.; Jónsson, H. A Dimer Method for Finding Saddle Points on High Dimensional Potential Surfaces Using Only First Derivatives. *J. Chem. Phys.* **1999**, *111*, 7010.

(40) Kozlov, S. M.; Cabeza, G. F.; Neyman, K. M. Bonding and Vibrations of CH_xO and CH_x Species (x=1–3) on a Palladium Nanoparticle Representing Model Catalysts. *Chem. Phys. Lett.* **2011**, *506*, 92–97.

(41) Viñes, F.; Loschen, C.; Illas, F.; Neyman, K. M. Edge Sites as a Gate for Subsurface Carbon in Palladium Nanoparticles. *J. Catal.* **2009**, *266*, 59–63.

(42) Schauermann, S.; Hoffmann, J.; Johánek, V.; Hartmann, J.; Libuda, J.; Freund, H.-J. Catalytic Activity and Poisoning of Specific Sites on Supported Metal Nanoparticles. *Angew. Chem. Int. Ed. Engl.* **2002**, 2532–2535.

(43) Kozlov, S. M.; Yudanov, I. V; Aleksandrov, H. A.; Rösch, N. Theoretical Study of Carbon Species on Pd(111): Competition between Migration of C Atoms to the Subsurface Interlayer and Formation of Cn Clusters on the Surface. *Phys. Chem. Chem. Phys.* **2009**, *11*, 10955–10963.

(44) Perdew, J.; Burke, K.; Ernzerhof, M. Generalized Gradient Approximation Made Simple. *Phys. Rev. Lett.* **1996**, *77*, 3865–3868.

(45) Trinchero, A.; Hellman, A.; Grönbeck, H. Methane Oxidation over Pd and Pt Studied by DFT and Kinetic Modeling. *Surf. Sci.* **2013**, *616*, 206–213.

(46) Stakheev, A. Y.; Batkin, A. M.; Teleguina, N. S.; Bragina, G. O.; Zaikovsky, V. I.; Prosvirin, I. P.; Khudorozhkov, A. K.; Bukhtiyarov, V. I. Particle Size Effect on CH_4 Oxidation Over Noble Metals: Comparison of Pt and Pd Catalysts. *Top. Catal.* **2013**, *56*, 306–310.

Section 3.3

Surface Chemistry

DOI: 10.1002/anie.201405738

How Absorbed Hydrogen Affects the Catalytic Activity of Transition Metals**

*Hristiyan A. Aleksandrov, Sergey M. Kozlov, Swetlana Schauermann, Georgi N. Vayssilov, and Konstantin M. Neyman**

Abstract: *Heterogeneous catalysis is commonly governed by surface active sites. Yet, areas just below the surface can also influence catalytic activity, for instance, when fragmentation products of catalytic feeds penetrate into catalysts. In particular, H absorbed below the surface is required for certain hydrogenation reactions on metals. Herein, we show that a sufficient concentration of subsurface hydrogen, H^{sub}, may either significantly increase or decrease the bond energy and the reactivity of the adsorbed hydrogen, H^{ad}, depending on the metal. We predict a representative reaction, ethyl hydrogenation, to speed up on Pd and Pt, but to slow down on Ni and Rh in the presence of H^{sub}, especially on metal nanoparticles. The identified effects of subsurface H on surface reactivity are indispensable for an atomistic understanding of hydrogenation processes on transition metals and interactions of hydrogen with metals in general.*

For a long time scientists have been studying the interaction of hydrogen with transition metals, in particular with Pd. The latter is highly permeable for H and widely used as a hydrogenation catalyst.[1,2] Despite strong research efforts, it is still controversially discussed in which way H^{sub} atoms absorbed just beneath the top metal layer affect surface reactions. For instance, it is uncertain whether H^{sub} species directly participate in the hydrogenation of alkyls on Pd, as also discussed for Ni catalysts.[3,4] As a touchstone reaction we have chosen the alkyl to alkane hydrogenation step, which on Pd catalysts is known to be critically affected by the H^{sub} content.[5–7] (See also our experimental data in the Supporting Information (SI) and in Figure S1.) Importantly, the hydrogenation activity of Pd is qualitatively different on single-crystal and nanoparticle (NP) samples.[6] Thus, to account for a part of the complexity of the subsurface chemistry[8] and the involvement of H^{sub} in the hydrogenation on metal catalysts, we go beyond the consideration of only single-crystal surfaces and explore NP models as well. After an in-depth analysis of the processes on Pd we critically compare it with three other transition metals, Pt, Ni, and Rh, whose bulk or NP forms were experimentally shown to absorb H.[4,9]

Our density functional calculations of Pd catalysts are performed for Pd(111) extended (slab) and unsupported Pd_{79} NP models with different arrangements and concentrations of H atoms (Figure 1 a). Note that bare Pd NPs of a similar size sufficiently accurately mimic the NPs deposited on inert metal-oxides.[10] We consider the reactivity of terrace sites on {111} facets of the Pd_{79} NP, which is representative for larger Pd NPs commonly employed in catalytic experiments.[11] Edge sites are not discussed here because we did not find them to be more active than the terrace sites in the reaction under scrutiny. Theoretical studies reveal that H^{sub} is bound weaker than H^{ad} on Pd[12] and other transition metals,[13] implying that at equilibrium conditions H occupies subsurface positions only after filling most of the surface positions.[5,12,14] In some papers the effect of the H^{ad} atoms on the H^{sub} was considered for transition metal slabs,[15] whereas the influence of H^{sub} on H^{ad} reactivity analyzed in the present paper was not explored in due detail. Thus, for both Pd_{79} NP and Pd(111) slab different hydrogen contents were represented by three types of models: 1) low-coverage models with just one adsorbed H^{ad} atom, $H_1^{ad}H_0^{sub}$/Pd(NP) and $H_1^{ad}H_0^{sub}$/Pd(111); 2) surface-saturated[16] models, $H_{78}^{ad}H_0^{sub}$/Pd(NP) and $H_7^{ad}H_0^{sub}$/Pd(111); and 3) subsurface-saturated models, $H_{78}^{ad}H_{24}^{sub}$/Pd(NP) and $H_7^{ad}H_9^{sub}$/Pd(111). High exposure of Pd to H_2 under experimental hydrogenation conditions.[5,7] corresponds to the

[*] Dr. H. A. Aleksandrov, S. M. Kozlov, Prof. Dr. K. M. Neyman
Departament de Química Física and
Institut de Química Teòrica i Computacional (IQTCUB)
Universitat de Barcelona
Martí i Franquès 1, 08028 Barcelona (Spain)
Homepage:
http://www.icrea.cat/Web/ScientificForm.aspx?key=292
Dr. H. A. Aleksandrov, Prof. Dr. G. N. Vayssilov
Faculty of Chemistry and Pharmacy, University of Sofia
1126 Sofia (Bulgaria)
Dr. S. Schauermann
Department of Chemical Physics
Fritz-Haber-Institut der Max-Planck-Gesellschaft
14195 Berlin (Germany)
Prof. Dr. K. M. Neyman
Institució Catalana de Recerca i Estudis Avançats (ICREA)
08010 Barcelona (Spain)
E-mail: konstantin.neyman@icrea.cat

[**] We thank Prof. H.-J. Freund, Dr. S. Shaikhutdinov, and Dr. L. V. Moskaleva for valuable discussions and critical reading of the manuscript. We acknowledge financial support provided by the EU (FP7-NMP.2012.1.1-1, project ref. no. 310191), the Spanish MINECO (grant CTQ2012-34969), the MEDU (grants SB2010-0172 for H.A.A. and AP2009-3379 for S.M.K.) and Generalitat de Catalunya (grants 2014SGR97 and XRQTC). H.A.A. and G.N.V. are grateful to the Bulgarian Science Fund (grant DCVP 02/1) and the FP7 programme (project Beyond Everest). S.S. thanks the Verband der Chemischen Industrie for a Dozentenstipendium. We gratefully acknowledge the computer resources provided by the Red Española de Supercomputación.

Supporting information for this article is available on the WWW under http://dx.doi.org/10.1002/anie.201405738.

regimes (2) or (3). We study ethyl hydrogenation to ethane, $C_2H_5 + H \rightarrow C_2H_6$, (Figure S6) as a representative surface reaction because alkyl hydrogenation on Pd was observed to be particularly sensitive to the presence of H^{sub} (see SI and Figure S1); our benchmark calculations of butyl hydrogenation on Pd NPs revealed very similar trends in the reactivity (see Table 1). Note, however, that for the examined reaction the surface concentration of the alkyl intermediate hardly depends on the concentration of the H^{sub} species (see SI).

The hydrogenation of ethyl is exothermic by 50–140 kJ mol^{-1} (Table 1) for all catalyst models addressed, implying that only kinetic aspects need to be investigated in depth. We first examined possible reaction paths of ethyl recombination directly with a H^{sub} atom (see Figure S2). However, the attacking H^{sub} emerging from the subsurface area of Pd was inevitably stabilized on the surface and converted to H^{ad}, which subsequently acted as a reactant, similarly to methyl hydrogenation on Ni(111).[3,4] Therefore, in the following only the attack of alkyl species by a surface H^{ad} atom is discussed.

Results in Figure 1 predict that increasing the hydrogen content should accelerate the reaction on Pd NPs as well as on the Pd(111) single-crystal surface. As one moves from the bare NP with just one H^{ad} to the surface-saturated NP, the Gibbs activation energy of hydrogenation decreases by 19 kJ mol^{-1} (Table 1). This corresponds to a three orders of magnitude higher hydrogenation rate at 298 K. The activation barriers for the low-coverage and surface-saturated single-crystal models agree within 2 kJ mol^{-1} with those for the corresponding NP models. This observation corroborates the suitability of the employed NP models to represent bigger Pd NPs studied experimentally.

The prominent difference between NPs and single crystals

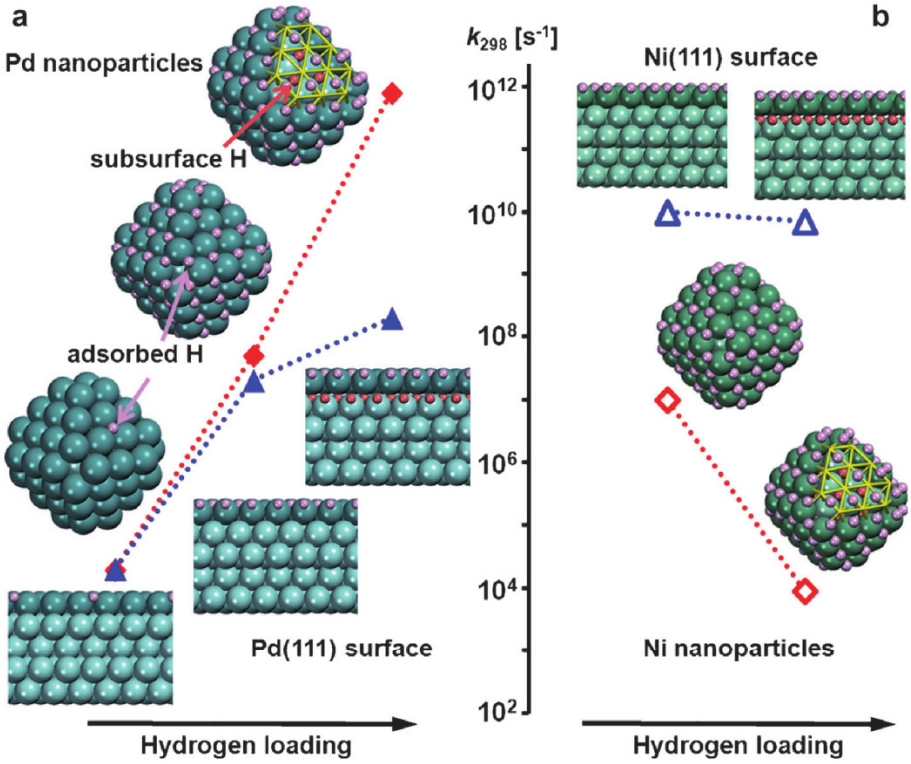

Figure 1. Calculated rate constant k_{298} of ethyl hydrogenation on a) Pd and b) Ni at 298 K as a function of hydrogen loading and nanostructuring of the catalyst. Data for metal nanoparticles (red diamonds) and (111) single-crystals (blue triangles) are shown together with the sketches of the models.

Table 1: Calculated data for ethyl hydrogenation catalyzed by Pd and Ni. Rate constant, activation, and reaction Gibbs free energies at temperature $T = 298$ K (k_{298}, $\Delta G^{\neq}_{298}$, and ΔG_{298}, respectively), binding energies (E_b) of atom H^{ad} as well as those of initial state (IS) and transition state (TS) structures on various forms of the catalysts.[a]

Model[b]	k_{298}[c] [s^{-1}]	$\Delta G^{\neq}_{298}$ [kJ mol^{-1}]	ΔG_{298} [kJ mol^{-1}]	$E_b^{IS}(C_2H_5+H)$ [kJ mol^{-1}]	$E_b^{TS}(C_2H_5+H)$ [kJ mol^{-1}]	$E_b(H)$ [kJ mol^{-1}]
Pd nanoparticle						
low-coverage	2×10^{4}	48	−51	−219	−165	−61
surface-saturated[d]	5×10^{7} (2×10^{6})	29 (37)	−100 (−106)	−178	−133	−51
subsurface-saturated[d]	8×10^{11} (7×10^{9})	5 (17)	−142 (−142)	−134	−119	−15
Pd single crystal						
low-coverage	2×10^{4}	48	−58	−205	−155	−56
surface-saturated	2×10^{7}	31	−103	−174	−133	−43
subsurface-saturated	2×10^{8}	26	−126	−152	−115	−34
Ni nanoparticle						
surface-saturated	1×10^{7}	33	−105	−176	−132	−66
subsurface-saturated	9×10^{3}	51	−52	−207	−149	−69
Ni single crystal						
surface-saturated	1×10^{10}	16	−137	−147	−122	−51
subsurface-saturated	7×10^{9}	17	−126	−165	−133	−60

[a] E_b is the binding energy to the metal substrate of either the co-adsorbed species $C_2H_5 + H$ (with respect to the energy of free $C_2H_5 + {}^1/_2\ H_2$) or the atom H^{ad} involved in the hydrogenation (calculated without co-adsorbed ethyl, with respect to the energy of ${}^1/_2\ H_2$). [b] See Figure 1. [c] $k_T = (k_B T/h) \times \exp(-\Delta G^{\neq}_T/RT)$, where k_B, h, and R are the Boltzmann, Planck, and ideal gas constant, respectively. [d] In parentheses, the data for butyl hydrogenation is shown.

becomes evident when H is introduced into the subsurface region of Pd. For the subsurface-saturated NP it causes a further strong reduction of the Gibbs activation energy by 24 kJ mol^{-1} (Table 1). Such barrier lowering should increase the reaction rate by four orders of magnitude compared to the surface-saturated NP without H^{sub}. At the same time, the addition of H^{sub} atoms to the surface-saturated single crystal decreases the barrier by only ca. 5 kJ mol^{-1} and accelerates the reaction tenfold. Hence, we conclude that a significantly accelerated hydrogenation on Pd can be achieved through the synergy of high H^{sub} content and catalyst nanostructuring.[17]

To further evaluate the contributions to the barrier lowering by various H^{ad} and H^{sub} atoms surrounding the reacting species, we considered two more models derived from the most reactive subsurface-saturated NP model $H^{ad}_{78}H^{sub}_{24}$/Pd(NP). First, the most distant H^{ad} and H^{sub} atoms were removed from the {111} NP facet that accommodates the ethyl reactant, giving the $H^{ad}_{38}H^{sub}_{12}$/Pd(NP) model. Subsequent removal of the H atoms most distant from the reaction site results in the model $H^{ad}_{23}H^{sub}_{3}$/Pd(NP) (see Figure S3). For the $H^{ad}_{38}H^{sub}_{12}$/Pd(NP) model, the Gibbs activation barrier of the hydrogenation is 9 kJ mol^{-1}, close to that of the subsurface-saturated NP containing about twice as many H^{ad} and H^{sub} atoms. The model with only three H^{sub} atoms located below the reaction site, $H^{ad}_{23}H^{sub}_{3}$/Pd(NP), features a barrier height of 28 kJ mol^{-1}, the same as on the surface-saturated NP without any H^{sub} atoms. Thus, solely the H^{sub} atoms right beneath the hydrogenation sites on Pd NP are likely insufficient to notably lower the barrier. Rather, the effect of the overall concentration of H^{sub} on the barrier height appears to be gradual. Indeed, the Pd NPs with increasing number of H^{sub} atoms, $H^{ad}_{78}H^{sub}_{0}\rightarrow H^{ad}_{23}H^{sub}_{3}\rightarrow H^{ad}_{38}H^{sub}_{12}\rightarrow H^{ad}_{78}H^{sub}_{24}$ exhibit decreasing activation barriers 29→28→9→5 kJ mol^{-1}. A similar, but much weaker effect could also be seen on Pd(111) models: the barrier drops from 31 to 26 kJ mol^{-1} when switching from the surface-saturated to the subsurface-saturated single-crystal model. Doubling the H^{sub} concentration in the subsurface-saturated single-crystal model (by filling the second subsurface layer) further decreases the Gibbs activation barrier from 26 to 18 kJ mol^{-1}. In line with the experimental observations (Figure S1 and the second paragraph in SI), this finding suggests that Pd(111) single crystal can be as active as Pd NPs in hydrogenation of alkyls, but only at a rather high concentration of H^{sub}, which may be difficult to maintain in the steady state reaction regime.

What are the fundamental reasons for the enhanced hydrogenation activity of Pd NPs in the presence of H^{sub} species and why is the activation less efficient on the extended Pd(111) surface? To answer these questions, we analyze the energy contributions that determine the barrier heights. From the binding energy of ethyl + H considered as the initial state (IS) of the process, E_b^{IS} (Table 1), one notices that the increase in the H content gradually destabilizes the IS structures on NP and, to a lesser extent, on single-crystal models. The transition state (TS) destabilization caused by H^{sub} atoms is not so strong, as seen from its binding energy, E_b^{TS} (Table 1). The different destabilization of the IS and TS structures by H^{sub} atoms determines the activation energies, which are lowered by 24 kJ mol^{-1} on the NP and by 5 kJ mol^{-1} on the single crystal when changing from the surface-saturated to the subsurface-saturated model.

The data presented in Table 1 suggest that the binding energy of an attacking H^{ad} (without co-adsorbed ethyl) is a descriptor of the surface hydrogenation reactivity. The adsorption energies of the probe atom H, E_b(H), correlate with the activation energies of ethyl hydrogenation (Figure 2): lowering of E_b(H) is accompanied by a decrease of the Gibbs activation barrier by almost the same amount. Thus, a destabilization of H^{ad} by H^{sub}, consistent with experimental observations,[18] appears to be the main reason for the activation of Pd catalysts by subsurface H, which is particularly strong on Pd NPs.

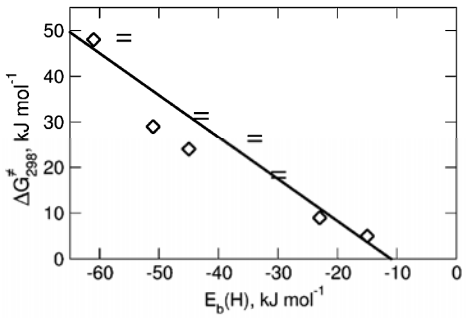

Figure 2. Correlation of activation barriers with adsorption energies of hydrogen. Activation Gibbs free energies of ethyl hydrogenation, $\Delta G^{\neq}_{298}$, as a function of H binding energies in IS, E_b(H), calculated on Pd NP (◇) and Pd(111) single crystal (=) models.

Examining the electronic structure of Pd with a varying number of H^{ad} and H^{sub} atoms is the key to understanding the origin of the weakened adsorption of H atoms and their enhanced reactivity. Two effects are manifested in densities of states (DOS) projected on H s and Pd d states of atoms forming three-fold hollow hydrogenation sites $H^{ad}Pd_3$ (Figures 3, S3 and S4). First, a shift of the Pd 4d states to lower energies with increasing H content notably reduces the number of states at the Fermi level. The magnitude of these H-induced DOS shifts, ca. 0.3 eV, is comparable to differences between d-band centers of such distinct metals as Cu and Pt,[19] explaining the significant change in catalytic properties of Pd upon saturation with H. The second effect is related to the DOS of the subsurface-saturated NP model, for which the lowest hydrogenation activation energy is computed. The H s-projected DOS reveals a small feature just below the Fermi level corresponding to a partial occupation of the antibonding H^{ad}–Pd_3 states (see asterisks in Figure 3). The latter, in line with the reactivity analysis of different late transition metals with respect to H,[20] results in a notably weaker interaction between H^{ad} and Pd. Both effects on DOS plots described above are significantly stronger for NPs than for single-crystal models. Filling of subsurface sites by H atoms in the subsurface-saturated single crystal does not lead to any noticeable occupation of the antibonding H^{ad}–Pd states, consistent with the substantial ethyl hydrogenation barrier of 26 kJ mol^{-1}. Thus, a high sensitivity of NPs to changes in the electronic structure upon interaction with hydrogen is crucial for the

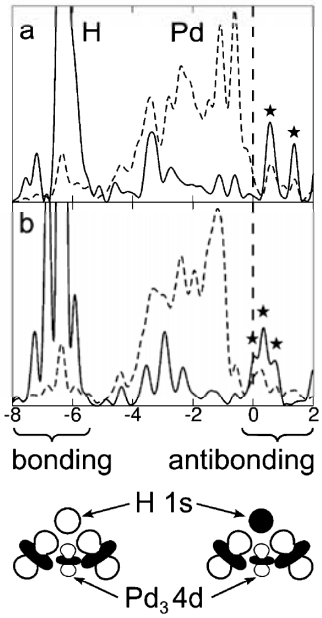

Figure 3. Dependence of the electronic structure of nanoparticulate Pd–H systems on the hydrogen content: a) Pd_{79} NP saturated with adsorbed hydrogen H^{ad}, b) Pd_{79} NP saturated with both adsorbed H^{ad} and subsurface H^{sub} hydrogen (see Figure 1 a). The density of states (DOS) projected on: solid line: s states of the reacting H^{ad} atom (×50); dashed line: d states of the atoms forming the hollow site Pd_3, where the atom H^{ad} is located. DOS is given in arbitrary units, with respect to the Fermi energy $\varepsilon_F = 0$ eV. The H–Pd_3 antibonding states (marked by asterisks) approach the Fermi level with increasing H content, resulting in their partial occupation in subsurface-saturated NP (panel b).

activation of Pd by H^{sub}. This explains why both subsurface hydrogen and nanostructuring of Pd catalysts are necessary for the high observed steady state hydrogenation activity. Note that changes in the geometric structure of Pd catalysts induced by H^{sub} cannot explain the increase in the hydrogenation activity (see SI).

Having analyzed the interplay between H^{sub} content and hydrogenation catalytic activity for Pd, we explored to what extent the trends identified for Pd are inherent to transition metals in general. To this end we investigated other catalytically relevant metals, namely Pt, Ni, and Rh, using the same models as for Pd and calculated binding energies of adsorbed hydrogen, E_b(H), as a descriptor of the hydrogenating activity, and its dependence on the content of subsurface hydrogen. For one of the metals, Ni, we also calculated hydrogenation rates (Figure 1 b), which are shown to be related to E_b(H), as discussed above for Pd.

The results collected in Table 2 suggest that Pt behaves similarly to Pd; the binding energy of H^{ad} is decreased in magnitude from -49 kJ mol^{-1} on the low-coverage Pt NP to -13 kJ mol^{-1} on the subsurface-saturated NP. Again this sharp weakening of H^{ad} binding is related to changes in the electronic structure and partial occupation of antibonding H–Pt states (Figure S5). On the single-crystal Pt(111) surface the weakening of H^{ad} binding is much more modest, only to -30 kJ mol^{-1} for the subsurface-saturated model.

In contrast, the binding nature of hydrogen to Ni and Rh appears to be remarkably different from that to Pd and Pt due to distinctively polar H–Ni and H–Rh bonds with significantly larger electron density accumulated on hydrogen and concomitantly increased positive charge on metal atoms (Table 2). Addition of H^{sub} to hydrogen-loaded Ni and Rh systems is predicted to lead to further electron depletion from the surface metal atoms and increase their electrostatic attraction to the adsorbed (noticeably negatively charged) H^{ad} atoms. Thus, in striking variance with Pd and Pt, the presence of H^{sub} in Ni and Rh makes H^{ad} atoms more strongly bound to the metal. Keeping in mind our findings for Pd, one could expect that this stabilization results in a decreased activity of H^{ad} in the presence of H^{sub}. Indeed, we calculated (Table 1, Figure 1 b) that on Ni nanoparticles H^{sub} slows down ethyl hydrogenation by three orders of magnitude.

In summary, we determined two mechanisms by which subsurface H may affect the activity of transition metals, in particular, in hydrogenation reactions. On Pd and Pt subsurface H destabilizes adsorbed H by changing the electronic structure of metals, causing occupation of antibonding H^{ad}–Pd or H^{ad}–Pt electronic states. This effect is stronger on metal

Table 2: Results for nanoparticle and (111) single-crystal models of transition metals interacting with a different number of hydrogen atoms. Binding energies of adsorbed hydrogen atoms, E_b(H), and calculated Bader charges, q, of selected atoms.

Model[a]	E_b(H),[b] [kJ mol^{-1}]				q(H),[c] [|e|]				q(M),[d] [|e|]			
	Ni	Rh	Pd	Pt	Ni	Rh	Pd	Pt	Ni	Rh	Pd	Pt
Nanoparticle												
low-coverage	−63	−49	−61	−49	−0.27	−0.21	−0.11	−0.04	0.10	0.07	0.03	0.02
surface-saturated	−66	−37	−51	−47	−0.22	−0.16	−0.09	−0.02	0.17	0.11	0.08	0.01
subsurface-saturated	−69	−66	−15	−13	−0.28	−0.20	−0.11	−0.04	0.29	0.19	0.11	0.05
					(−0.27)	(−0.15)	(−0.08)	(0.00)				
Single crystal												
low-coverage	−54	−56	−56	−47	−0.28	−0.22	−0.13	−0.08	0.07	0.03	0.03	−0.02
surface-saturated	−51	−47	−43	−39	−0.25	−0.20	−0.12	−0.05	0.19	0.13	0.09	0.03
subsurface-saturated	−60	−52	−34	−30	−0.27	−0.20	−0.13	−0.06	0.27	0.15	0.12	0.01
					(−0.29)	(−0.17)	(−0.11)	(−0.01)				

[a] See models depicted in Figure 1. [b] E_b(H) is the binding (adsorption) energy of the H^{ad} atom involved in the hydrogenation (calculated without co-adsorbed ethyl species) versus free $^1/_2$ H_2. [c] Average charges of all adsorbed atoms H^{ad}, or, in parentheses, of all subsurface atoms H^{sub}. [d] Average charges of the three metal atoms M, to which the attacking atom H^{ad} is coordinated.

NPs than on single crystals and is sufficient to accelerate alkyl hydrogenation by several orders of magnitude on Pd NPs. Moreover, the hydrogenation rate is found to increase gradually with increasing H^{sub} content even at a distance from the reaction site. Thus, the structure of active sites alone (similar in NPs and single crystals) does not yet determine the reactivity. Our findings help to clarify a long-standing puzzle why both subsurface hydrogen and nanostructuring of Pd catalysts are necessary for the observed high steady-state olefin hydrogenation activity. Importantly, the outlined mechanism of H^{ad} activation is inherent to H–Pd and H–Pt interactions and, thus, should affect various hydrogenation (and dehydrogenation) reactions on these catalysts. In a very remarkable contrast, on Ni and Rh we have found another mechanism of interplay between adsorbed and subsurface H, which leads to the stabilization of adsorbed H. This behavior is due to the more polar character of H–Ni and H–Rh bonds, which leads to an increased positive charge of surface metal atoms due to the presence of H^{sub} and consequently stronger electrostatic attraction of (negatively charged) H^{ad} to the surface. Notable deactivation of adsorbed H by subsurface H on Ni NPs is manifested by decreased reaction rates for ethyl hydrogenation. At the same time, desorption of surface H should also be hindered by subsurface H on Ni and Rh, which may be beneficial for certain reactions. From a practical point of view, the discussed mechanisms of destabilization or stabilization of adsorbed H by absorbed H may be used to tune the catalytic activity of transition metals.

Received: May 29, 2014
Revised: August 25, 2014
Published online: October 7, 2014

Keywords: density functional calculations · heterogeneous catalysis · hydrogenations · nanoparticles · surface chemistry

[1] *Handbook of Heterogeneous Catalysis* (Eds.: G. Ertl, H. Knözinger, J. Weitkamp), Wiley-VCH, Weinheim, **1997**.
[2] D. Teschner, J. Borsodi, A. Wootsch, Z. Révay, M. Hävecker, A. Knop-Gericke, S. D. Jackson, R. Schlögl, *Science* **2008**, *320*, 86–89.
[3] a) A. D. Johnson, S. P. Daley, A. L. Utz, S. T. Ceyer, *Science* **1992**, *257*, 223–225; b) G. Henkelman, A. Arnaldsson, H. Jónsson, *J. Chem. Phys.* **2006**, *124*, 044706.
[4] S. T. Ceyer, *Acc. Chem. Res.* **2001**, *34*, 737–744.
[5] M. Wilde, K. Fukutani, W. Ludwig, B. Brandt, J.-H. Fischer, S. Schauermann, H.-J. Freund, *Angew. Chem. Int. Ed.* **2008**, *47*, 9289–9293; *Angew. Chem.* **2008**, *120*, 9430–9434.
[6] A. M. Doyle, S. K. Shaikhutdinov, S. D. Jackson, H.-J. Freund, *Angew. Chem. Int. Ed.* **2003**, *42*, 5240–5243; *Angew. Chem.* **2003**, *115*, 5398–5401.
[7] a) W. Ludwig, A. Savara, K.-H. Dostert, S. Schauermann, *J. Catal.* **2011**, *284*, 148–156; b) W. Ludwig, A. Savara, S. Schauermann, H.-J. Freund, *ChemPhysChem* **2010**, *11*, 2319–2322.
[8] M. Armbrüster, M. Behrens, F. Cinquini, K. Föttinger, Y. Grin, A. Haghofer, B. Klötzer, A. Knop-Gericke, H. Lorenz, A. Ota, S. Penner, J. Prinz, C. Rameshan, Z. Révay, D. Rosenthal, G. Rupprechter, P. Sautet, R. Schlögl, L. Shao, L. Szentmiklósi, D. Teschner, D. Torres, R. Wagner, R. Widmer, G. Wowsnick, *ChemCatChem* **2012**, *4*, 1048–1063.
[9] a) M. Yamauchi, H. Kobayashi, H. Kitagawa, *ChemPhysChem* **2009**, *10*, 2566–2576; b) H. Kobayashi, H. Morita, M. Yamauchi, R. Ikeda, H. Kitagawa, Y. Kubota, K. Kato, M. Takata, *J. Am. Chem. Soc.* **2011**, *133*, 11034–11037.
[10] a) S. M. Kozlov, H. A. Aleksandrov, J. Goniakowski, K. M. Neyman, *J. Chem. Phys.* **2013**, *139*, 084701; b) S. M. Kozlov, H. A. Aleksandrov, K. M. Neyman, *J. Phys. Chem. C* **2014**, *118*, 15242–15250.
[11] I. V. Yudanov, R. Sahnoun, K. M. Neyman, N. Rösch, *J. Chem. Phys.* **2002**, *117*, 9887–9896.
[12] H. A. Aleksandrov, F. Viñes, W. Ludwig, S. Schauermann, K. M. Neyman, *Chem. Eur. J.* **2013**, *19*, 1335–1345.
[13] P. Ferrin, S. Kandoi, A. U. Nielekar, M. Mavrikakis, *Surf. Sci.* **2012**, *606*, 679–689.
[14] K. M. Neyman, S. Schauermann, *Angew. Chem. Int. Ed.* **2010**, *49*, 4743–4746; *Angew. Chem.* **2010**, *122*, 4851–4854.
[15] a) J. Greeley, M. Mavrikakis, *Surf. Sci.* **2003**, *540*, 215–229; b) J. Greeley, W. P. Krekelberg, M. Mavrikakis, *Angew. Chem. Int. Ed.* **2004**, *43*, 4296–4300; *Angew. Chem.* **2004**, *116*, 4396–4400.
[16] Leaving vacant only surface sites required for modeling adsorption and hydrogenation of olefin reactant.
[17] Not only the activation barriers can be affected by co-adsorbed species, such as H^{sub} or hydrocarbons. Also, the binding energies of the intermediates can be influenced, which might modify the concentrations and the relative distribution of all surface species in a complex way. Description of this complicated interplay using extensive electronic structure and kinetic Monte–Carlo calculations is beyond the scope of this communication.
[18] E. C. H. Sykes, L. C. Fernández-Torres, S. U. Nanayakkara, B. A. Mantooth, R. M. Nevin, P. S. Weiss, *Proc. Natl. Acad. Sci. USA* **2005**, *102*, 17907–17911.
[19] A. Ruban, B. Hammer, P. Stoltze, H. L. Skriver, J. K. Nørskov, *J. Mol. Catal. A* **1997**, *115*, 421–429.
[20] B. Hammer, J. K. Nørskov, *Nature* **1995**, *376*, 238–240.

Section 3.4

How to Determine Accurate Chemical Ordering in Several Nanometer Large Bimetallic Particles from Electronic Structure Calculations

Sergey M. Kozlov,[a] Gábor Kovács,[a] Riccardo Ferrando,[b] Konstantin M. Neyman[a,c*]

Chemical and physical properties of binary metallic nanoparticles (also known as nanoalloys) are to a great extent defined by their chemical ordering, i.e. the pattern in which the elements are arranged within the nanoparticle. The reliable determination of the optimal chemical ordering is a challenge that impedes studies of bimetallic particles of a few nm. We propose a method to efficiently optimize the chemical ordering based solely on results of electronic structure (density functional) calculations. We demonstrate that the accuracy of this method is very close to the accuracy of the underlying quantum mechanical approach. This method immediately reveals why this or another chemical ordering is preferred and unravels the nature of the binding within the nanoparticles. For instance, our data explain why gold and silver segregate on low-coordinated sites in $Pd_{70}Au_{70}$ and $Pd_{70}Ag_{70}$ nanoparticles, while $Pd_{70}Cu_{70}$ exhibits matryoshka structure and $Pd_{70}Zn_{70}$ features Zn and Pd atoms arranged in layers. To illustrate the power of the new method we optimized chemical ordering in much larger $Pd_{732}Au_{731}$, $Pd_{732}Ag_{731}$, $Pd_{732}Cu_{731}$, and $Pd_{732}Zn_{731}$ species, whose size ~4.4 nm is common in catalytic experiments and applications.

Introduction

Multicomponent metallic nanoparticles (NPs), often referred to as nanoalloys, represent a lively research subject, thanks to their usage in catalysis, magnetism, optics and nanomedicine.[1] The properties of nanoalloys depend both on the size and the composition, making them much more tunable for tailored applications compared to single-component NPs.

Properties of bimetallic NPs strongly depend on their geometric structure, size, and composition. The latter two features are determined by the preparation conditions in each particular experiment. At the same time the geometric structure of bimetallic NPs is affected by the relative thermodynamic stability of conceivable atomic arrangements of the two components with the more stable structures being easier to obtain. Computational search for the geometric structure and shape that yield the lowest energy for a given NP size and composition is part of the so-called global optimization problem.[2,3] Even though numerous techniques have been developed to treat this extremely difficult problem, even nowadays global optimization of only relatively small clusters is feasible.

Another part of the global optimization problem is the search for the lowest-energy chemical ordering, that is, the pattern in which atoms of different elements are arranged within a fixed geometric structure. Chemical ordering governs such NP properties as surface composition and electronic structure, which are crucial for surface reactivity and heterogeneous catalysis.[4] A rich variety of chemical ordering patterns can be found in nanoalloys: from ordered phases and solid solutions through core-shell and multishell arrangements to phase-separated quasi-Janus particles. As a rule, strong heteroatomic bonds and charge transfer between different metals tend to favor well-mixed structures, while big differences between atomic sizes and surface energies of the two components facilitate surface segregation.2 Despite that recent advances in electron microscopy techniques have allowed the visualization of individual atoms in bimetallic NPs, it is still hard to derive *three-dimensional* chemical ordering solely based on experimental data. Therefore, predicting the most thermodynamically stable way of chemical ordering theoretically is of great importance.

This task is extremely difficult, because the number of possible inequivalent arrangements of atoms of different types within a given geometric structure (*i.e.* the number of the so-called homotops) is simply enormously big.[2] For instance, for a binary alloy particle consisting of N atoms, A_YB_{N-Y} the total number of homotops is $\frac{N!}{Y!(N-Y)!}$, which for Y = N/2 is approximately $2^{N+1/2}/\sqrt{\pi N}$. This renders the complete exploration of the homotop landscape unfeasible already for NPs of a few dozens of atoms. At the same time, NPs that are relevant to chemical experiments and practical applications very often contain from hundred to several thousand atoms.

In order to deal with this formidable problem, intelligent search algorithms combined with reliable energetic models are required. Efficient search algorithms that can explore the low-energy part of the homotop landscape have been developed recently.[5-8] However, these algorithms can be used in the relevant size range only within simplified energetic models,[9,10] since ab-initio search procedures are by far too tedious. Nowadays, state-of-the-art ab-initio searches are still limited to nanoalloys with a few dozens of atoms,3 despite that much bigger NP structures can be routinely calculated by density functional theory methods (DFT).[11-13]

Simplified energetic approaches comprise atomistic interaction potentials and lattice models. Reliable interatomic potentials are now available for some phase-separating systems[14-18] and for certain systems making solid solutions,[19,20] while their accuracy is often limited when dealing with systems forming ordered phases.[21] Generally speaking, the reliability of atomistic approaches for nanostructured materials is system-dependent and cannot be predicted *a-priori*. Rather, it needs to be examined for each case against higher-level calculations. On the other hand, lattice models depend on a set of energetic parameters that are often fitted on bulk or surface quantities obtained by experiments or ab-initio calculations by ad-hoc procedures.[22-24]

Here we propose a general and systematic method for developing lattice models that aims at transferring ab-initio or DFT level of accuracy to NP sizes that are relevant to experiments and practical applications. This novel method is based on robust concept of topological Hamiltonian, H_{TOP}. Topological Hamiltonians used in this paper take into account 1) the formation of heteroatomic bonds, 2) the different coordination of atoms in different positions of a NP, and 3) the possible tetragonal distortion in $L1_0$ alloys. The parameters in the topological Hamiltonian for each particular NP size and composition are derived by a rigorous fitting procedure based on energies, E_{ES}, from a limited set of density functional (electronic structure) calculations for NPs of the same size and composition. The inherently physical origin of the fitted parameters allows one to directly rationalize the nature of binding in the considered bimetallic alloys. The accuracy and precision of the employed Hamiltonians were carefully assessed and in most cases they were found to be sufficient to obtain models realistic at mild temperatures.

Herein, the chemical ordering in $Pd_{70}X_{70}$ NPs of truncated octahedral *fcc* structure for X = Au, Ag, Cu and tetragonal $L1_0$ structure for X = Zn, which are interesting for heterogeneous catalysis applications, has been optimized employing the proposed method.[‡] Note that unsupported transition metal NPs of this size were shown to be representative models for catalytic studies.[25-27] In order to ensure the finding of the lowest-energy homotops, we used a novel multiple exchange algorithm, which allowed us to overcome very big energy barriers in the configurational space of certain NPs. In principle, one would expect bulk segregation of Pd in all these structures, since Pd has the highest surface energy among the

considered metals.[28,29] Nevertheless, only for Pd-Au and Pd-Ag we found high stability of the segregated structures, while Pd-Cu and Pd-Zn exhibited more complex morphologies. We also performed the fitting of topological Hamiltonians for $Pd_{79-Y}Au_Y$ and $Pd_{140-Y}Au_Y$ and found that the fitting parameters in H_{TOP} depend much more strongly on the NP composition than on its size. This observation allowed us to apply the topological Hamiltonians obtained for $Pd_{70}X_{70}$ NPs (X = Au, Ag, Cu, and Zn) to the optimization of chemical ordering in the respective 4.4 nm big $Pd_{732}X_{731}$ NPs, illustrating the power of the proposed approach.

One should note here that the proposed Hamiltonians are also extendable to account for other contributions to the energy, *e.g.* NP-support or NP-adsorbate interactions. This makes the presented method very promising for studies of bimetallic NPs with experimentally accessible sizes in experimentally relevant conditions.

Results and discussion

Optimization of chemical ordering in nanoalloys: Outline of the proposed methodology

The idea of topological Hamiltonians was inspired by the observation that in bimetallic NPs *A*-*B* atoms of one element often prefer to occupy bulk sites in the most stable structures, while atoms of the other element prefer to be located at low-coordinated sites.2,[30] The formation of heteroatomic bonds during the alloying process is also known to be important. To quantify these trends we considered the following form of topological Hamiltonians, H_{TOP}, that depend only on the mutual positions of atoms of types *A* and *B* within a predetermined lattice. The energy of a given structure with this Hamiltonian is

$$E_{TOP} = E_0 + \varepsilon^{A-B}_{BOND} N^{A-B}_{BOND} + \varepsilon^{A}_{CORNER} N^{A}_{CORNER} + \varepsilon^{A}_{EDGE} N^{A}_{EDGE} + \varepsilon^{A}_{TERRACE} N^{A}_{TERRACE} \quad (1).$$

In this formula E_0 is a constant, not important for practical purposes; N^{A-B}_{BOND} – number of heteroatomic bonds in the considered structure; N^{A}_{CORNER}, N^{A}_{EDGE}, and $N^{A}_{TERRACE}$ numbers of atoms of type *A* on corners, edges and terraces, respectively. Other parameters, such as N^{A-A}_{BOND}, N^{B-B}_{BOND} or N^{B}_{CORNER}, N^{B}_{EDGE}, and $N^{B}_{TERRACE}$ as well as N^{A}_{BULK} depend linearly on the employed parameters for a given NP size and composition. Hence, they were not included in the Hamiltonians.

In (1) ε_i are energetic parameters associated with each characteristic N_i considered in the topological Hamiltonians. They will be referred to as *descriptors* from now on. In contrast to parameters in many empirical methods, each descriptor ε_i has a clear physical meaning. For instance, ε^{A-B}_{BOND} is related to the energy gain caused by the mixing of two metals. For example, the formation energy of ordered $L1_0$ $A_{0.5}B_{0.5}$ bulk alloy from separated bulk *A* and bulk *B* is $4\varepsilon^{A-B}_{BOND}$ per atom, since in this alloy each atom forms 8 heteroatomic bonds and each bond connects two atoms. In turn, ε^{A}_{CORNER} is the energy required for or gained from the exchange of an atom of type *A* on the corner with an atom of type *B* in the NP bulk (given that the number of heteroatomic bonds remains constant).

For each NP structure with a given shape, size and composition, an individual Hamiltonian H_{TOP} is tailored via fitting the descriptors ε_i to the DFT total energy E_{ES} values of various homotops of this particular NP. This way of fitting leads to a rather high accuracy of the H_{TOP} compared to *e.g.* interatomic potentials despite the more complex structure of the latter with many more fitting parameters. Also, this way of fitting leads to different topological Hamiltonians for different structures. However, since each of these descriptors ε_i determines certain interactions, changes in their values from system to system directly reflect the underlying changes in material's properties.

In this work we calculated DFT energies E_{ES} of 22 to 127 structures to fit H_{TOP} for every considered NP shape and composition via multiple linear regression.[31] When several structures with the same set of N_i characteristics were present in the fitting set, only the structure with the lowest E_{ES} was actually added to the fitting. The electronic structure calculations of E_{ES} for NP structures used for the fitting is the most computationally demanding part of the method. Therefore, one should aim to keep the number of DFT calculations to a minimum. Nevertheless, we have to point out that insufficient size of the fitting set would lead to overfitting and poor statistical accuracy of the obtained coefficients ε_i. The accuracy can be estimated as 95 % confidence intervals via the bootstrap method.[32] This method was applied since it seamlessly takes into account that ε_i are not independent statistical quantities and may strongly correlate with each other. In practice, descriptors that contribute strongly to E_{TOP} have rather small inaccuracies, while those that are not crucial for the fitting are determined less accurately. So the inaccuracy of the coefficients does not reflect the inaccuracy of H_{TOP} as a whole.

The precision of the topological Hamiltonians themselves was estimated as twice the residual standard deviation (RSD) between E_{ES} and E_{TOP} energies for a set of $N_{TEST} \geq 10$ structures *not* included in the fitting procedure

$$\delta = 2\sqrt{\frac{\sum(E_{ES}-E_{TOP})^2-(\sum(E_{ES}-E_{TOP}))^2}{N_{TEST}-1}}.$$

According to this definition, (relative) E_{TOP} values are within δ from the respective (relative) E_{ES} values with > 95 % probability. In turn, the accuracy (trueness) of the topological Hamiltonians, ΔE, was estimated as the energy difference between the lowest-energy structure according to the ES calculations and the global minimum within the topological Hamiltonian calculations. Since many homotops yield the same E_{TOP} but somewhat different E_{ES}, the energy difference ΔE was calculated by the topological Hamiltonians to avoid any arbitrariness.

Once a topological Hamiltonian for a given system is established, one may use it to perform efficient optimization of chemical ordering within the predetermined lattice. In this work, we carried out Monte-Carlo simulations with only one kind of moves – simultaneous exchange of *n* random atoms of element *A* with *n* random atoms of element *B*. The number of atoms to be exchanged was chosen randomly with the probability $p(n) \sim n^{-3/2}$, which yields the probability of single exchange moves for big NPs around $1/\zeta(3/2) \sim 38\%$, where ζ is the Riemann zeta function. This method makes it possible to overcome very big energy barriers that exist in the configurational space of Pd-Zn NPs (see the respective discussion in Pd-Zn section below).

The temperature in a Monte-Carlo simulation was chosen in such a way that a system spends < 50 % of time in the lowest-energy configuration. A configuration of A_YB_{N-Y} NP was considered a global minimum if a move from it to a lower energy structure failed after $10 * Y(N-Y)$ multiple exchange moves. This means that we applied every possible out of $Y(N-Y)$ single exchange moves for the global minimum search with probability of

$$1-\left(1-\frac{1}{Y(N-Y)}\right)^{0.38*10*Y(N-Y)} \sim 1-e^{-3.8}=98\%$$

and we could not find a structure of lower energy.

The code that performs Monte-Carlo simulations was written in a way that whenever it finds a structure with lower energy than the previously calculated ones, the geometry is recorded. Out of these structures N_{TEST} structures with the lowest E_{TOP} energies were calculated by the chosen ES technique, and their ES energies were used to estimate the precision of the H_{TOP} employed in the Monte-Carlo simulation. Thus, the test sets included rather diverse low-energy structures ranging from the predicted global minimum to structures located ~N_{TEST} multiple exchange moves far from it in the configurational space. If the precision of a topological Hamiltonian estimated using this test set was found unsatisfactory, then the test set was added to the fitting set and a new topological Hamiltonian was generated. As a result of the global optimization with the new Hamiltonian, a new test set was generated in the fashion described above and the precision of the new Hamiltonian was estimated on the new test set, which had not yet been included in the fitting.

The Monte-Carlo scheme also allows one to estimate thermal energy associated with the Boltzmann population of different homotops for a given NP structure. Thermal energies calculated in such a way (with fixed atomic positions) are used only to inspect the magnitude of chemical disorder at finite temperature and to put precision δ of the topological Hamiltonians into perspective. Other contributions to the thermal energy may be much bigger and, thus, more important. Nevertheless, they are not relevant to the analysis performed herein.

In the present work we applied the just outlined method to the optimization of chemical ordering in PdAu, PdAg and PdCu NPs with *fcc* lattices. In order to make the method applicable to more complex lattices one may need to modify the Hamiltonian appropriately. For example, unlike other considered alloys, bulk PdZn has tetragonally distorted $L1_0$ crystal structure with experimental interatomic distances r(Zn-Zn) = r(Pd-Pd) = 289 pm and r(Pd-Zn) = 222 pm.[33] Hence, Zn and Pd atoms are arranged in layers normal to [001] direction in a *fcc*-like lattice and the distance between adjacent atoms from different layers is smaller than the distance between adjacent atoms within the same layer. To account for the tetragonal distortion and the energy associated with it, the term $\varepsilon_{LAYER}\sum_{LAYERS}\left|N_i^A - N_i^B\right|$ was added to the topological Hamiltonian, where N_i^A and N_i^B are the numbers of atoms of element *A* and element *B* in layer *i* of a NP and the sum is taken over all layers. The term $\left|N_i^A - N_i^B\right|$ is the biggest for layers composed entirely of an element *A* or *B* and is close to zero for layers composed of both elements in equal proportions. Therefore, if $\varepsilon_{LAYER} < 0$, the formation of layered structures is favored.

It is important to emphasize that having slightly changed H_{TOP} and/or electronic structure calculations one may apply the proposed method to a rich variety of materials, structures and reaction conditions. For instance, one may substitute $\varepsilon^A_{TERRACE}N^A_{TERRACE}$ in (1) by $\varepsilon^A_{\{111\}}N^A_{\{111\}}$ and $\varepsilon^A_{\{100\}}N^A_{\{100\}}$ to account separately for segregation on {111} and {100} NP facets in NPs of certain shapes. The same can be done to distinguish different kinds of edges and corners. Also to account for NP-support interactions one may add the term $\varepsilon^A_{interface}N^A_{interface}$ to H_{TOP} to consider support-induced segregation on the interface. In order to account for the reaction atmosphere there is no need to change H_{TOP} at all: It is sufficient to include the presence of adsorbates in the respective electronic structure calculations.

Table 1 Descriptors[a] ε_i in the topological Hamiltonians for the $Pd_{70}X_{70}$ NPs (see Methodology) with their precision and inaccuracy values (in meV) and number of structures used for the fitting, N_{FIT}.

X	Au	Ag	Cu	Zn
$\varepsilon^{Pd-X}_{BOND}$	-13^{+4}_{-6}	-1^{+2}_{-2}	-26^{+5}_{-5}	-160^{+52}_{-40}
ε^{X}_{CORNER}	-404^{+76}_{-72}	-361^{+50}_{-68}	95^{+36}_{-33}	-251^{+316}_{-342}
ε^{X}_{EDGE}	-301^{+52}_{-77}	-289^{+78}_{-129}	147^{+46}_{-45}	-205^{+280}_{-243}
$\varepsilon^{X}_{TERRACE}$	-200^{+52}_{-64}	-163^{+43}_{-64}	183^{+42}_{-40}	-90^{+231}_{-234}
ε_{LAYER}	–	–	–	-105^{+29}_{-38}
N_{FIT}	32	53	127	28
precision, δ	115	150	360	348
inaccuracy, ΔE	26	29	171	0

[a] 95% confidence intervals of ε_i are also given, *e.g.* -13^{+4}_{-6} means that the interval is -19 ÷ -9.

The chemical ordering of the lowest-energy homotop found for $Pd_{70}Au_{70}$ nicely reflects the magnitude of different terms in the topological Hamiltonian (see Figure 2). There, Au atoms occupy all the most energetically stable corner and edge positions and the remaining Au atoms occupy surface terrace positions. The configuration of Au atoms on terraces may vary from facet to facet tending to maximize the number of Pd-Au bonds. Note, however, that in the lowest-energy structure found by DFT there is only 260 heteroatomic bonds, while in the global minimum according to the topological Hamiltonian N^{Pd-Au}_{BOND} is 262 (Table 2). This finding reflects the expected presence of other minor contributions (of the order of δ = 115 meV) to the E_{ES} that are not accounted for by the topological Hamiltonian.

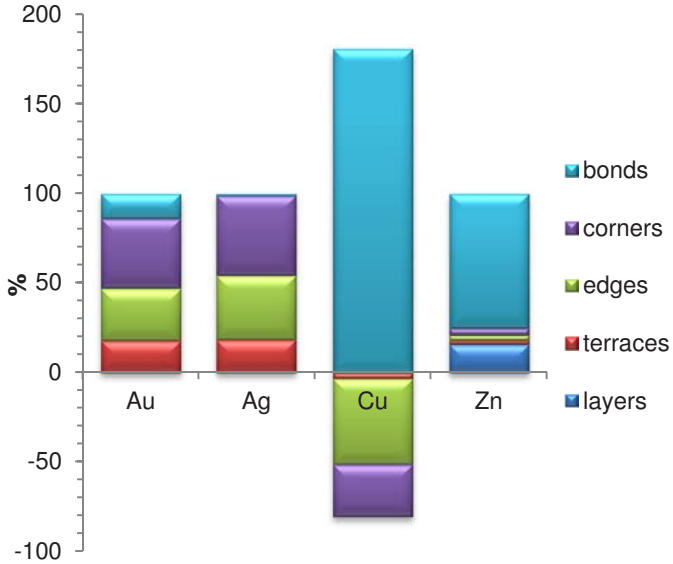

Fig. 1 Relative energy contributions (%) to the global minima structures of $Pd_{70}X_{70}$ NPs according to the topological Hamiltonians calculated as $\varepsilon_i N_i / \sum \varepsilon_i N_i$. Since in Pd-Cu the only negative term is $\varepsilon^{Pd-Cu}_{BOND}$, the value of $\varepsilon^{Pd-Cu}_{BOND}N_{BOND}/\sum \varepsilon_i N_i$ exceeds 100 %.

Pd-Au

Alloys of Au and Pd have been intensively studied[34,35] due to their numerous actual and potential applications in heterogeneous catalysis. They include H_2O_2 synthesis,[36] CH_4 conversion to methanol,[37] C-C coupling,[38] oxygen reduction reaction,[39] and various hydrogenation[40] and oxidation[41,42] reactions. According to theoretical predictions the Au-shell Pd-core structure is the most thermodynamically favorable for Pd-Au NPs,[43] while a rich variety of Pd-Au NP structures has been detected in experiment.[44-46] It is important to note that the surface composition of Pd-Au systems may be altered by adsorbates such as CO and that even single Au or Pd atoms or dimers on the surface may significantly affect the overall catalytic performance of the system.[47-49]

According to our analysis, the most significant contributions to the H_{TOP} for $Pd_{70}Au_{70}$ NP come from strong stabilization of Au atoms on low-coordinated sites (Table 1). The lower coordination number of the site, the bigger is the energy gain: 200 meV for 9-coordinated terrace atoms of Au, 301 meV for 7-coordinated edge atoms, and 404 meV for 6-coordinated corner atoms. The respective relative contributions to the global minimum energy calculated with the H_{TOP} are 18%, 29%, and 39% (Figure 1). The energy of a heteroatomic bond is calculated by H_{TOP} to be only ~13 meV; however, due to the large overall number of heteroatomic bonds their contribution to the energy is sizeable, 14%.

Pd-Ag

Pd-Ag alloys are studied mostly because of their potential application as hydrogenation,[50-53] fuel cell[54] and other catalysts,[55-57] sensors[58] and biosensors.[59] Similarly to Pd-Au NPs, theoretical studies8.[60] predict Pd-core/Ag-shell structure of Pd-Ag NPs and surface segregation of Ag was also observed in experiment.[52,53,56] At the same time, several experimental studies report homogeneous Pd-Ag alloys[55,58,61] or even Pd-shell/Ag-core structures.[54] It was also found that the surface segregation may be affected by the presence of adsorbates such as atomic H.[53,62]

We have found interactions in $Pd_{70}Ag_{70}$ to be quite similar to those in $Pd_{70}Au_{70}$: the lower the coordination number of a site is, the more energy is gained when it is occupied by an Ag atom. The most

prominent contributions to the energy in the topological Hamiltonian come from Ag atoms on corners (45%), edges (36%) and terraces (18%). The energy of heteroatomic bonds is calculated to be essentially zero (-1±2 meV); thus, their contribution to E_{TOP} does not exceed 1%.

In line with the form of the topological Hamiltonian, the structure of $Pd_{70}Ag_{70}$ with the lowest E_{ES} has all corner and edge positions occupied by silver atoms. The remaining Ag atoms are located on terraces, whereas the NP core is composed of solely Pd (Fig. 2). The number of heteroatomic bonds in this structure is only 234, *i.e.* significantly lower than 262 in the global minimum of the respective topological Hamiltonian. The reason for this structural difference is the negligible energy associated with N_{BOND}^{Pd-Ag}, which probably compares in magnitude with other contributions to the E_{ES}, not accounted for by the topological Hamiltonian. Similarly to these results, previous DFT studies found surface segregation of Ag on extended Pd-Ag(111) surfaces.[62]

Pd-Cu

A lot of scientific effort has been devoted to Pd-Cu alloys since they catalyze oxygen reduction reaction,[63,64] O-enhanced water-gas shift reaction (when supported on ceria),[65,66] formic acid oxidation,[67] water denitrification[68-70] and hydrogenation reactions.[51,71,72] Early interatomic potential studies pointed out two competing effects governing the structure of Pd-Cu NPs: the tendency to maximize the number of heteroatomic bonds and the tendency of Pd[73] or Cu[74] to segregate on the surface. In some studies the enrichment of the surface by Cu or Pd was found to depend on their concentration.[75] In those studies the most energetically stable NP structures also featured higher concentration of surface Cu atoms on corner and edge sites rather than on terrace sites. Experimentally Pd-Cu NPs with Cu-rich surfaces[68,76] and well mixed ordered or disordered Pd-Cu alloys[67,71,77] were characterized. Note that CO-induced surface segregation of Pd was documented for Pd-Cu.[76]

We consider chemical ordering in Pd-Cu with *fcc* structure since for NPs of few nm it is more stable than *bcc* structure observed in Pd-Cu bulk.[74,78] The energetic stability of Pd-Cu NPs comes mainly from the energy of heteroatomic bonds, which is twice of that in Pd-Au NPs (Table 1). Unlike the cases of Pd-Au and Pd-Ag nanoparticles, Cu prefers to stay inside the NP, whereas the surface of $Pd_{70}Cu_{70}$ is enriched by Pd. The reason is that Pd atoms are bigger than Cu atoms and, therefore, tend to segregate on the surface, where a part of the elastic stress is relieved.[73] Note, however, that the employed density functional (as well as other local and gradient-corrected functionals) also favors Pd segregation to the surface, since it predicts the surface energy of Pd(111) to be slightly smaller than the surface energy of Cu(111) in disagreement with experiments.[29,104] Curiously, the order of stability of Cu in different positions, bulk > corner > edge > terrace, does not correlate with the coordination number of Cu in these sites. Since descriptors corresponding to Cu atoms on corner, edge and terrace positions are positive (reflecting that these positions are unstable with respect to bulk), their destabilizing contributions to the E_{TOP} of the global minimum are -29, -47 and -3%. Hence, the contribution of the heteroatomic bonds to E_{TOP} formally exceeds 100%. The value of the descriptor for heteroatomic bonds, -26_{-5}^{+5} meV/bond, corresponds to the binding energy of -104_{-20}^{+20} meV per atom in (*fcc* or *bcc*) Pd-Cu bulk, which agrees nicely with the experimental value of -114 meV per atom for the *bcc* alloy.[79]

The homotop with the lowest E_{ES} of the $Pd_{70}Cu_{70}$ NP exhibits matryoshka (also called onion or multishell) arrangement with Pd-rich surface shell, Cu-rich subsurface shell and Pd-rich core. This chemical ordering allows formation of 358 heteroatomic bonds, while number of Cu atoms is kept low on the surface, especially on terraces. The structure of the global minimum according to the topological Hamiltonian features even more heteroatomic bonds, 382, more Cu atoms on terraces and less Cu on edges and corners.

Pd-Zn

Intermetallic Pd-Zn compounds are actively studied[80-82] (often in the form of surface alloys[83-85]) because of their catalytic activity in (reverse) water-gas shift[86-88] and hydrogenation reactions[89] as well as potential application as selective and highly stable[90,91] catalysts for methanol steam reforming.[92-94] However, the employment of Pd-Zn catalysts is complicated by significant dependence of their properties on the Zn/Pd ratio,[87,95] NP size[88] and composition of catalyst's subsurface region.[94] Both bulk and nanoparticulate Pd-Zn are known to have $L1_0$ structure[33,96] without pronounced segregation of one or the other component to the surface or edges.[83,90] Additional complications come from strong dependence of the structure and composition of Pd-Zn systems on environmental conditions.[81,85,97]

In order to account for the $L1_0$ structure of the bulk Pd-Zn we introduced an additional term, $\varepsilon_{layer}\sum_{layers}\left|N_i^A - N_i^B\right|$, in the respective Hamiltonian. Such augmentation of H_{TOP} increased its precision, δ, from 1294 meV to 348 meV. For smaller octahedral $Pd_{22}Zn_{22}$ NPs with *fcc* structure (data not shown) this term was also necessary to improve the accuracy (ΔE) of the topological Hamiltonian from 472 meV to 141 meV.

Table 2 Structural properties of the homotops with the lowest energies E_{ES} or E_{TOP}. Average coordination numbers of X by X, N^{X-X}, X by Pd or Pd by X, N^{Pd-X}, and Pd by Pd, N^{Pd-Pd} are also given to facilitate comparison with experimental (*e.g.* EXAFS) data.

X		N_{BOND}^{Pd-X}	N_{CORNER}^{X}	N_{EDGE}^{X}	$N_{TERRACE}^{X}$	N^{X-X}	N^{Pd-X}	N^{Pd-Pd}
Au	ES	260	24	24	22	3.57	3.71	7.17
	TOP	262	24	24	22			
Ag	ES	234	24	24	22	3.94	3.34	7.54
	TOP	262	24	24	22			
Cu	ES	358	16	17	1	4.20	5.11	3.69
	TOP	382	12	14	8			
Zn[a]	ES=TOP	422	16	14	16	2.57	6.03	3.54

[a] The same structure yields both the lowest E_{ES} and E_{TOP} for $Pd_{70}Zn_{70}$; in this structure $\sum_{LAYERS}\left|N_i^{Zn} - N_i^{Pd}\right|$ equals to 136.

Heteroatomic bonds in Pd-Zn NPs are found to be an order of magnitude stronger than those in the other investigated alloys. The reason is that composites of Au, Ag, Cu with Pd are alloys of d-elements, while Zn is an sp-element that interacts much stronger with Pd. The very strong heteroatomic Pd-Zn bonds of polar character[33,98] result in the prevalence of ordered structures of Pd-Zn in the phase diagram.[81] On the contrary, alloys of d-elements often prefer random structures, where the number of heteroatomic bonds is not maximal. Hence, Pd-Zn is better classified as an intermetallic compound rather than a bimetallic alloy.

In line with these considerations, the dominant contribution to the topological Hamiltonian for $Pd_{70}Zn_{70}$ is given by heteroatomic Pd-Zn bonds. The value of the obtained descriptor, $\varepsilon_{BOND}^{Pd-Zn} = -160^{+52}_{-40}$ meV, yields the alloy formation energy of -640^{+208}_{-160} meV per atom, which is in agreement with the measured value of -520 meV per atom.[99] Hence, heteroatomic bonds define 75% of the E_{TOP} of the global minimum, while the rest comes mostly from the energy associated with the formation of the layered structure (16%). Despite that the energies of Zn atoms on low-coordinated sites are only somewhat smaller than the respective energies of Ag atoms in $Pd_{70}Ag_{70}$, their overall contribution is tiny (2-4%) compared to that of Pd-Zn bonds. Since the relative energies of $Pd_{70}Zn_{70}$ NPs do not strongly depend on the number of low-coordinated Zn atoms (compared to other characteristics), it is hard to obtain an accurate estimate of the respective descriptors from the fitting. Consequently, the formal statistical inaccuracy of $\varepsilon_{CORNER}^{Zn}$, ε_{EDGE}^{Zn}, and $\varepsilon_{TERRACE}^{Zn}$ exceeds 100%. However, this finding does not seem to affect the overall accuracy of H_{TOP}, because these descriptors appear to be quite unimportant for an appropriate description of Pd-Zn systems.

The structures with the lowest E_{ES} and E_{TOP} are the same for $Pd_{70}Zn_{70}$ NPs due to the high accuracy of the topological Hamiltonian. They feature the maximum possible number of heteroatomic bonds, 422, for the $A_{70}B_{70}$ NP of the considered shape. The value of $\sum_{LAYERS}\left|N_i^A - N_i^B\right|$ is also maximum possible, 136, for this particular stoichiometry and shape. The energies of Zn atoms on the low-coordinated sites are of minor importance for the determination of the most stable $Pd_{70}Zn_{70}$ structure. Hence, the amounts of Zn atoms on various types of low-coordinated sites have intermediate values. All in all, the most energetically stable homotop exhibits the layered $L1_0$ structure, similar to PdZn bulk. Nevertheless this structure also exposes some Pd atoms located on Zn-composed edges, due to the slight excess of Pd for the formation of perfect layered structure. Unlike monolayer thick Pd-Zn films on Pd(111), no zigzag-like arrangements are observed on {111} facets of $Zn_{70}Pd_{70}$.[85]

Note that for $Pd_{70}Zn_{70}$ NP one could construct a homotop apparently very similar to the obtained global minimum by exchanging all Zn atoms with all Pd atoms at once. This homotop has the same number of heteroatomic bonds and the same layered structure as the global minimum, but less Zn atoms on corners and edges and more Zn atoms on terraces. Therefore, its E_{ES} (E_{TOP}) is 1765 meV (1389 meV) higher than that of the global minimum displayed in Figure 2. Despite the apparent similarity, for the simulation code this homotop looks absolutely different compared to the global minimum, since the position of *every* atom has changed. The transition from one homotop to another via exchange of one random Zn atom with a random Pd atom at a time would go through the configurations with rather small amount of Pd-Zn bonds and, therefore, very high relative energy. In practice, it was impossible to overcome the transition state between these two homotops via single exchange moves even at Monte-Carlo simulation temperatures as high as 10000 K. However, the transformation between the discussed homotop and the global minimum does not pose any difficulty when multiple exchange moves are applied, that is, n random atoms are exchanged at a time (see Methodology part). This illustrates the efficiency of the employed computational scheme, which we believe is sufficient to ensure that the lowest energy structures obtained during the Monte-Carlo simulations with H_{TOP} are, indeed, the global minima within the considered framework.

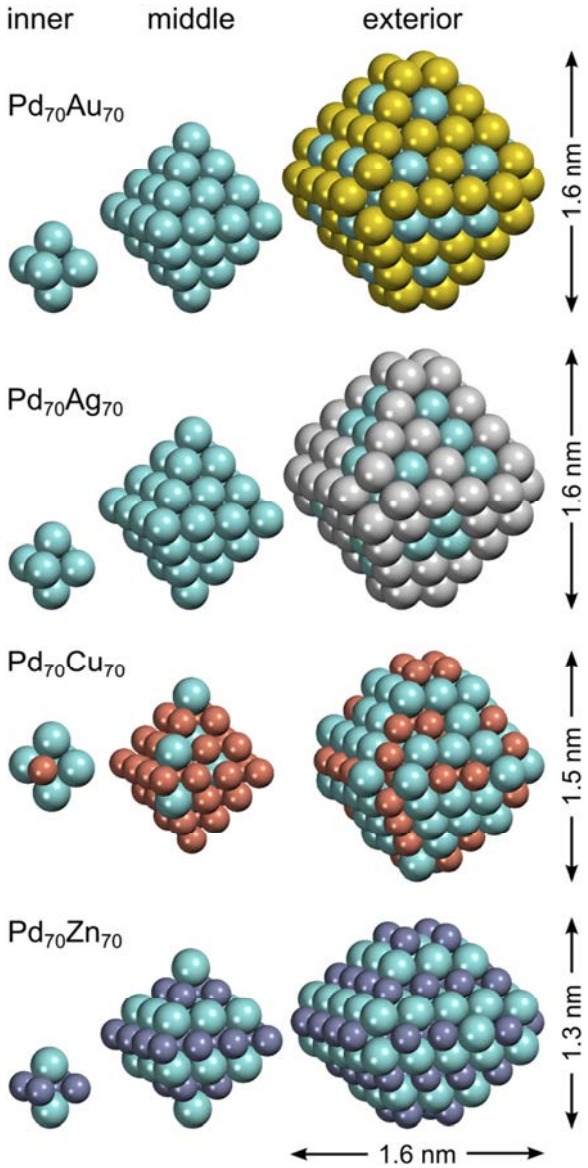

Fig. 2 Inner, middle and exterior shells of the lowest-energy structures of the $Pd_{70}X_{70}$ (X = Au, Ag, Cu, Zn) NPs according to density functional calculations. Spatial dimensions of the NPs are also given (for $Pd_{70}Zn_{70}$ the dimensions are given in two directions). Pd atoms are displayed as cyan spheres; elements X – as spheres of other colors.

Thermal energies

Naturally, a system in thermodynamic equilibrium adopts solely its global minimum configuration only at zero Kelvin, while at any finite temperature the presence of other homotops is also possible with a probability determined by the Boltzmann factor. The configurational space of $Pd_{70}Au_{70}$, $Pd_{70}Ag_{70}$ and $Pd_{70}Cu_{70}$ NPs features many homotops different from the respective global minima only by the number of heteroatomic bonds. The energies of these homotops are only slightly higher than the energies of the global minima and so the population of these homotops is considerable even at relatively low temperatures. Consequently, these homotops can contribute to the thermal energy.

It is very instructive to compare the thermal energy accumulated by chemical (dis-)ordering to the precision of topological Hamiltonians (Table 1). For example, the $Pd_{70}Au_{70}$ NP obtains (homotopic) thermal energy of 115 meV already at ~140 K. (That is, at this temperature the average energy of the system in our Monte-Carlo simulations is 115 meV above the energy of the global minimum.) Therefore, despite that the structure of $Pd_{70}Au_{70}$ with the lowest found E_{ES} (Figure 2) may not yet be the global minimum for the chosen ES computational scheme, it is certainly feasible at 140 K

and may serve as a representative model for the NP at this and higher temperatures. In a similar way one gets that the considered lowest-energy structure of the $Pd_{70}Ag_{70}$ is a representative homotop at ~360 K, while for $Pd_{70}Cu_{70}$ this temperature is ~220 K.

Unlike the aforementioned three alloys, PdZn features strong heteroatomic bonds with $\varepsilon_{BOND}^{Pd-X}$ of 160 meV. As a consequence, there are not many low-energy homotops around the global minimum. In fact, the second most stable structure has the energy E_{TOP} ~205 meV higher than the global minimum. Therefore, below 500 K essentially the global minimum structure alone has to be present in the thermodynamic ensemble. Much higher temperatures are required to populate less stable homotops, so the (homotopic) thermal energy reaches the precision of the topological Hamiltonian, 348 meV, only at ~1300 K. Thus, this high temperature is related mostly to the propensity of Pd-Zn to form regular nanostructures and to avoid any disorder, rather than to the low precision of the topological Hamiltonian for this system. Note that Zn evaporates from Pd-Zn surface alloys at temperatures above 800 K.[100] Therefore, it is safe to assume a very small degree of disorder in experimental samples of Pd-Zn close to the thermodynamic equilibrium.

Mixing energies

Another way to quantify the binding strength of the two metals in A_XB_{N-Y} NPs is by means of their mixing energy, E_{MIX}. The following formula was applied to calculate the mixing energies per atom: $E^{MIX} = (Y * E[A_N] + (N - Y) * E[B_N] - N * E[A_Y B_{N-Y}])/N^2$, where $E[A_XB_{N-Y}]$ is the total energy of the A_YB_{N-Y} NP and $E[A_N]$, $E[B_N]$ are the energies of respective monometallic NPs with the same structure calculated with the same plane-wave basis cut-off as for A_YB_{N-Y} NP. Thus, Zn_{140} NP with *fcc* structure was considered as the energy reference for $Pd_{70}Zn_{70}$. According to this definition positive values of E_{MIX} mean exothermic interaction.

Table 3 Mixing energies per atom (in meV) of the homotops with the lowest E_{ES} calculated for $Pd_{70}X_{70}$ NPs.

NP	$Pd_{70}Au_{70}$	$Pd_{70}Ag_{70}$	$Pd_{70}Cu_{70}$	$Pd_{70}Zn_{70}$
E_{ES}^{MIX}	109	108	119	498
E_{TOP}^{MIX}	82	55	89	484

The mixing energies of the homotops with the lowest E_{ES} calculated by the respective topological Hamiltonian and using DFT are given in Table 3 (see also Table S1). The ES mixing energies are found to be ~110 meV per atom for Pd-Au, Pd-Ag and Pd-Cu, while the mixing energy of Pd-Zn is almost 500 meV per atom due to the very strong Pd-Zn bonds. The mixing energies obtained by means of the topological Hamiltonians resemble the respective ES mixing energies, except the Pd-Ag case, for which E_{TOP}^{MIX} is almost twice smaller than E_{ES}^{MIX}. The reason is that the topological Hamiltonian for Pd-Ag predicts almost zero energy of the heteroatomic Pd-Ag bonds and consequently their essentially non-existing contribution to the mixing energy. In the rather similar $Pd_{70}Au_{70}$ NP heteroatomic bonds are responsible for 30% of the mixing energy calculated with the topological Hamiltonian, which can explain the 33% difference between E_{TOP}^{MIX} for Pd-Au and Pd-Ag.

Dependency of descriptors on the composition and the size of nanoparticles

For practical purposes it is very important to know if descriptors obtained for one system also can be used to represent a slightly different system. For instance, one may wonder if descriptors calculated for smaller NPs yield reasonable results when applied to bigger species, for which ES calculations are already unfeasible. To evaluate the dependency of descriptors on the size and the composition of NPs we constructed H_{TOP} and performed optimization of chemical ordering in Pd_YAu_{79-Y} (Y = 6, 28, 40, 53, 71) and Pd_YAu_{140-Y} (Y = 11, 20, 30, 35, 40, 49, 70, 91, 126) NPs. The results are summarized in Figure 3, where the error bars represent 60% confidence intervals of the ε_i calculated via the bootstrap analysis. Note that if such confidence intervals for two ε_i values do not overlap, the probability that these descriptors are not different is less than $((1 - 0.6)/2)^2 = 4$ %.

The first observation is that the descriptors (and, expectedly, the mixing energies) strongly depend on the composition of the NPs. That is, the binding in Pd-rich Pd-Au NPs is quite different from that in Au-rich NPs. The latter feature stronger heteroatomic bonds but less stable gold atoms on low-coordinated sites compared to the Pd-rich NPs. These differences are probably related to the gradual changes in the overall electronic structure and average interatomic distances in the NPs with growing Au content. In most of the cases, quantitative changes of the descriptors do not lead to qualitative changes in the NP structure. The only exception is that at very low Au concentrations Au atoms seem to prefer to occupy edges of the Pd-Au NPs rather than corners. This effect is more pronounced for Pd_YAu_{79-Y} than for Pd_YAu_{140-Y} NPs. The change in the relative stability of corner and edge positions for Au is reflected in the structure of the respective global minima.

A similar phenomenon was described in a previous study of Pd_YAu_{79-Y} NPs.[30] Nevertheless, Pd-Au NPs prepared by galvanic displacement expose Au atoms on corners rather than on edges.[46] However, according to our calculations corners are the most stable positions for Au only at moderate and high Au concentrations. The inconsistency between the presented and experimental results may be due to kinetic limitations in the experimental setup or deficiencies of the employed exchange-correlation functional.

One notices a rather limited dependency of the descriptors and the mixing energies per atom on the NP size. Especially at high Au concentrations, differences between ε_i values for Pd_YAu_{79-Y} and Pd_YAu_{140-Y} are barely noticeable and they are often within the statistical accuracy of the calculations. However, at lower Au content the binding was found to be slightly stronger in the smaller NPs. In numerous cases it was shown that many (physical) properties of NPs bigger than 1.5 nm already depend rather smoothly on their size and start to converge to a certain value.[26,27,101] Hence, it is probable that the descriptors calculated for Pd_YAu_{140-Y} as well as for $Pd_{70}X_{70}$ NPs may serve as a reasonable approximation for descriptors for bigger NPs or, at least, that they will lead to qualitatively correct structures, when applied to bigger NPs. Our findings suggest that it is much more important to tailor descriptors for the particular composition of a NP rather than to its size.

Extrapolation to the 4.4 nm large nanoparticles

Since we have established a rather moderate dependency of descriptors on nanoparticle size, we can apply the descriptors calculated for $Pd_{70}X_{70}$ NPs to bigger ~4.4 nm $Pd_{732}X_{731}$ NPs as an illustrative example (see Figure 4). The shape of these NPs is chosen to be very similar to the shape of $Pd_{70}X_{70}$ NPs and hence it features very small {100} facets composed of only four atoms. To simulate NPs with bigger {100} facets one would need to calculate the descriptor for X atoms on the {100} terraces, which are absent in the M_{140} models. Mind that using the proposed topological Hamiltonians we were able to perform efficient simulations of such ~4.4 nm NPs with the speed of $>10^7$ Monte-Carlo steps per hour on one Intel 2.66 GHz processor.

Both $Pd_{732}Au_{731}$ and $Pd_{732}Ag_{731}$ NPs have surfaces covered by Au and Ag, respectively. In turn, their subsurface shells are composed mostly of Pd atoms and only two Au or three Ag atoms, which allows the maximization of the number of heteroatomic bonds. Consequently, the cores of the NPs have stoichiometries of $Pd_{332}Au_{157}$ and $Pd_{333}Ag_{156}$. In order to maximize the number of heteroatomic bonds these $Pd_{0.68}X_{0.32}$ cores also develop $L1_0$-like structure with partially formed layers of Au or Ag in Pd. The structure of the Pd-Cu NPs is more complicated due to the presence of two competing tendencies: maximization of N_{BOND}^{Pd-Cu} and bulk

segregation of Cu. As a result, the surface shell has stoichiometry of $Pd_{412}Cu_{160}$ and exhibits abundant Cu monomers as well as occasionally present Cu dimers on terraces and edges. Each corner of the NP has two Cu atoms on the opposite vertices of the small {100} facet. The subsurface shell of the NP is enriched in Cu and has the stoichiometry of $Pd_{87}Cu_{315}$. Finally, the core of the NP is almost stoichiometric, $Pd_{233}Cu_{256}$, and again features layer-like structure. As for the global minimum of $Pd_{732}Zn_{731}$, quite expectedly, it has almost a bulk-cut structure similarly to the $Pd_{70}Zn_{70}$ case.

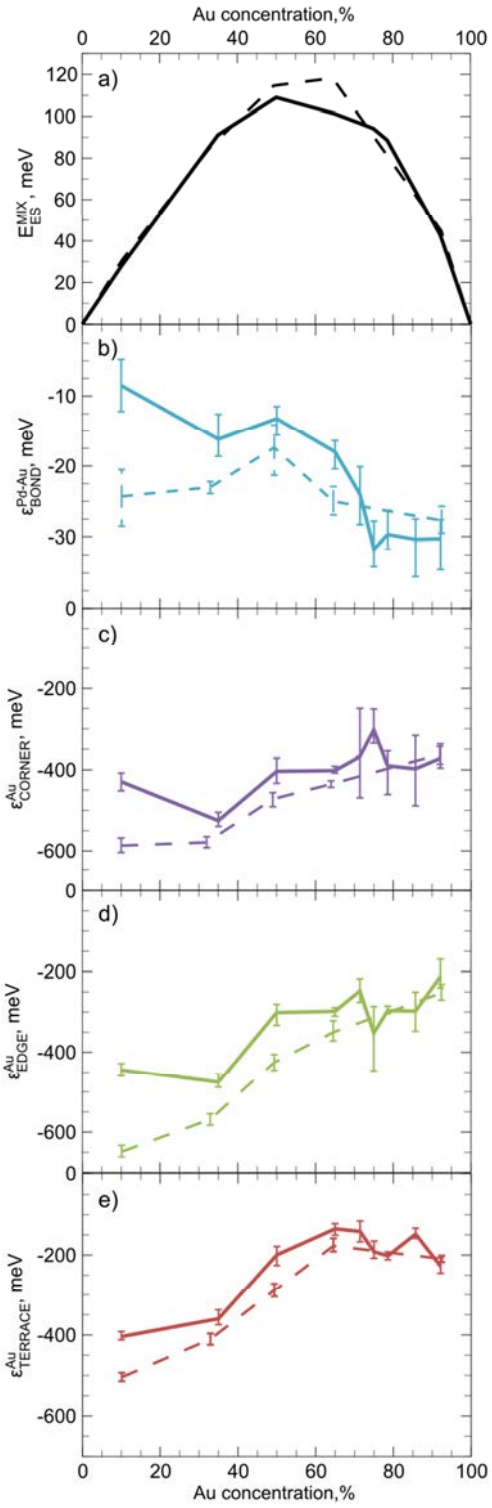

Fig. 3 Dependency on the NP composition of a) ES calculated mixing energy per atom, and of the descriptors b) $\varepsilon_{BOND}^{Au-Pd}$, c) $\varepsilon_{CORNER}^{Au}$, d) ε_{EDGE}^{Au}, e) $\varepsilon_{TERRACE}^{Au}$ in H_{TOP} for $Pd_{140-Y}Au_Y$ (solid line) and $Pd_{79-Y}Au_Y$ (dashed line) NPs. Error bars represent 60% confidence intervals.

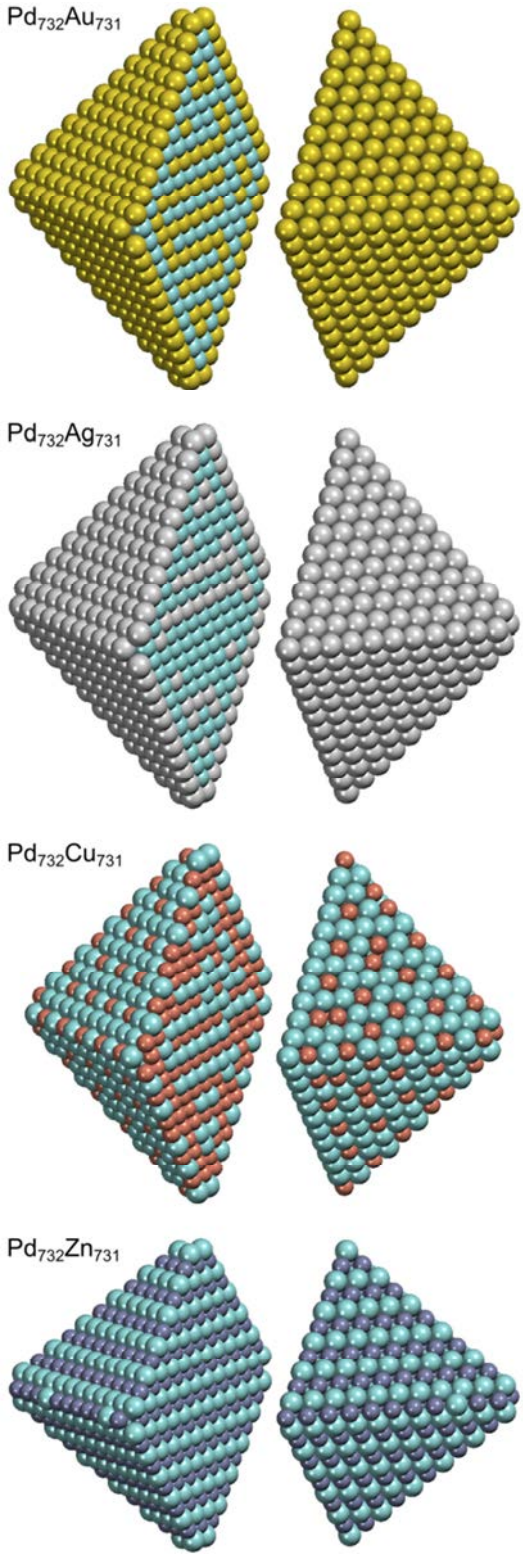

Fig. 4 Structures of $Pd_{732}X_{731}$ (X = Au, Ag, Cu, and Zn) NPs with optimized chemical ordering. Pd atoms are displayed as cyan spheres; elements X – as spheres of other colors.

Conclusions

Herein, we propose a method to optimize chemical ordering in bimetallic and intermetallic NPs using topological Hamiltonians, H_{TOP}. These Hamiltonians depend on the topology of bonds between atoms composing the NP, but not on the explicit coordinates of these atoms. Using this approach we optimized chemical ordering in truncated octahedral Pd_YAu_{79-Y} and Pd_YAu_{140-Y} NPs as well as in $Pd_{70}Ag_{70}$ and $Pd_{70}Cu_{70}$ NPs with *fcc* lattices and $Pd_{70}Zn_{70}$ with ordered $L1_0$ structure.

For every NP size and composition the energetic parameters (descriptors) in H_{TOP} were fitted to the energies of more than 20 NP structures obtained via density functional calculations. The precision of the H_{TOP} tailored in such a way (*i.e.* their ability to predict results of the electronic structure calculations) was 115 – 360 meV for $Pd_{70}X_{70}$ NPs (X = Au, Ag, Cu and Zn) and the accuracy (trueness) of the H_{TOP} was at least twice better. For the Pd-Au, Pd-Ag, and Pd-Cu NPs the precision of the respective H_{TOP} is already comparable to the thermal energy associated with the population of low-energy homotops at temperatures of 140 – 360 K. Therefore, even if the lowest-energy structures located in this study are not exactly the lowest-energy homotops (according to electronic structure calculations), they are highly probable representative NP structures at very moderate temperatures.

A very useful advantage of the proposed approach is that the energetic parameters of H_{TOP} have a clear physical meaning, *e.g.* the energy of heteroatomic bonds or the relative energy of X atom on terrace, edge or corner positions of the NP (bulk positions being the reference). Thus, the overall binding energy is inherently a sum of contributions from particular structural features. In turn, changes of these contributions from system to system reflect changes in their physical properties. Thus, analyzing the structure of topological Hamiltonians we were able to get valuable insights into binding in Pd-Au, Pd-Ag, Pd-Cu, and Pd-Zn nanoalloys. Note that for Pd-Cu and Pd-Zn the obtained energies of heteroatomic bonds agree with experimental formation energies of the respective bulk alloys. The analysis of descriptors for Pd_YAu_{79-Y} and Pd_YAu_{140-Y} NPs showed a rather strong dependency on the composition of the NPs and much smaller dependency on their size. The latter allows one to use descriptors based on electronic structure calculations of relatively small NPs of *e.g.* 140 atoms to optimize chemical ordering in bigger species with thousands of atoms. Hence, we applied our method to describe the chemical ordering in large $Pd_{732}X_{731}$ (X = Au, Ag, Cu and Zn) NPs, which are beyond the scale of conventional density functional calculations.

The H_{TOP} for Pd-Au and Pd-Ag NPs predict Au and Ag atoms to be more stable in positions with lower coordination numbers. Consequently, in the lowest-energy homotops of $Pd_{70}Au_{70}$ and $Pd_{70}Ag_{70}$ NPs all corner and edge sites are occupied by Au and Ag respectively, while the rest of Au or Ag atoms are located on terrace sites. The energy gain due to the formation of heteroatomic bonds is rather small for these materials and plays a secondary role in the determination of the NP structure. On the contrary, the energy of heteroatomic bonds is the driving force for binding between Cu and Pd. In this case, the stability of Cu is the highest inside the nanoparticle and the lowest on NP terraces. These two effects lead to the matryoshka structure of the lowest-energy homotop of $Pd_{70}Cu_{70}$ NPs, which has the surface shell enriched with Pd, the subsurface region enriched with Cu and the core composed mostly of Pd.

Unlike bimetallic Pd-Au, Pd-Ag, and Pd-Cu alloys formed by d-elements, the binding in intermetallic Pd-Zn involves the interaction of a noble d-metal with an sp-element. The result is a much higher energy gain due to the formation of Pd-Zn bonds and a much higher mixing energy of Pd-Zn NPs compared to the other considered nanoalloys. The preferential occupation of any particular type of sites by Zn atoms is much less important for the NP structure and energy in this case. The structure of the most energetically stable homotop is very close to the cut from bulk Pd-Zn with $L1_0$ alloy structure. Like the bulk, it features tetragonal distortion, *i.e.* different lattice parameters in different directions. To account for the tetragonal distortion, we added to the H_{TOP} a term related to the formation of layered structure, which turned out to be responsible for 16 % of the binding energy in Pd-Zn NPs.

The proposed method for the optimization of chemical ordering in bimetallic NPs via the topological Hamiltonians paves the way to atomistic studies of a few nm big bimetallic species with known lattice structure. Fortunately, the latter can be determined with rather moderate effort by contemporary experimental techniques. Finally, note that the present approach may be straightforwardly augmented to be applicable to NPs on a support or in a reaction atmosphere.

Acknowledgements

This study was supported by the European Commission (FP7-NMP.2012.1.1-1 project ChipCAT, Ref. Nº310191 and COST Actions MP0903 "Nanoalloy" and CM0904 "Methanol to Hydrogen"), the Spanish MINECO (grant CTQ2012-34969) and the Generalitat de Catalunya (projects 2014SGR97 and XRQTC). Financial support from the Spanish MEDU is gratefully acknowledged by SMK (FPU grant AP2009-3379). The authors thank the Red Española de Supercomputación for provided computer resources and technical assistance.

Methods

Electronic structure calculations were performed with the periodic plane wave code VASP[102] using the PBE[103] exchange-correlation functional, which was found to be the most appropriate among common functionals for the description of transition metal bulks.[104] The interaction between valence and core electrons was treated within the projector augmented wave (PAW) approach. To moderate computational expenditures we carried out calculations with the 250-280 eV energy cut-off of plane wave basis sets, which yielded results very close to those obtained with the cut-off of 415 eV (Table S1). The electron density was smeared by 0.1 eV using the first-order method of Methfessel and Paxton;[105] finally, converged energies were extrapolated to the zero smearing. All calculations were performed only at the Γ-point in the reciprocal space. All atoms were allowed to move (relax) during the geometry optimization until forces on them became less than 0.2 eV/nm. The minimal separation between NPs exceeded 0.7 nm, at which the interaction between adjacent NPs was found to be negligible.[25,106]

Notes and references

[a] Departament de Química Física and Institut de Química Teòrica i Computacional (IQTCUB), Universitat de Barcelona, c/ Martí i Franquès 1, 08028 Barcelona, Spain

[b] Dipartimento di Fisica and CNR-IMEM, Via Dodecaneso 33, 16146 Genova, Italy

[c] Institució Catalana de Recerca i Estudis Avançats (ICREA), 08010 Barcelona, Spain

† Electronic supplementary information (ESI) available: Data on the sensitivity of calculated density functional energies on the quality of the employed plane-wave basis sets.

‡ For the sake of brevity, in the following we refer to the optimization of chemical ordering within a fixed nanoparticle lattice as global optimization and to the ordering that yields the lowest energy within this lattice as the global minimum.

1 F. Calvo, *Nanoalloys from Fundamentals to Emergent Applications*, Elsevier, Amsterdam, 2013.

2 R. Ferrando, J. Jellinek and R. L. Johnston, *Chem. Rev.*, 2008, **108**, 845-910.

3 S. Heiles and R. L. Johnston, *Int. J. Quantum Chem.*, 2013, **113**, 2091-2109.

4 D.Wang, H. L. Xin, R. Hovden, H. Wang, Y. Yu, D. A. Muller, F. J. DiSalvo and H. D. Abruña, *Nat. Mater.*, 2013, **12**, 81-87.

5 D. Bochicchio and R. Ferrando, *Phys. Rev. B*, 2013, **87**, 165435.

6 D. Schebarchov and D. J. Wales, *J. Chem. Phys.*, 2013, **139**, 221101.

7 F. Calvo, *Faraday Discuss.*, 2008, **138**, 75-88.

8 G. G. Rondina and J. L. F. Da Silva, *J. Chem. Inf. Model.*, 2013, **53**, 2282-2298.

9 R. Marchal, A. Genest, S. Krüger and N. Rösch, *J. Phys. Chem. C*, 2013, **117**, 21810-21822.

10 F. Calvo and C. Mottet, *Phys. Rev. B*, 2011, **84**, 035409.

11 S. M. Kozlov, G. F. Cabeza and K. M. Neyman, *Chem. Phys. Lett.*, 2011, **506**, 92–97.

12 J. Kleis, J. Greeley, N. A. Romero, V. A. Morozov, H. Falsig, A. H. Larsen, J. Lu, J. J. Mortensen, M. Dułak, K. S. Thygesen, J. K. Nørskov and K. W. Jacobsen, *Catal. Lett*., 2011, **141**, 1067-1071.

13 G. Barcaro, A. Fortunelli, M. Polak and L. Rubinovich, *Nano Lett.*, 2011, **11**, 1766-1769.

14 M. Alcantara Ortigoza and T. S. Rahman, *Phys. Rev. B*, 2008, **77**, 195404.

15 M. Molayem, V. G. Grigoryan and M. Springborg, *J. Phys. Chem. C*, 2011, **115**, 7179-7192.

16 D. Bochicchio and R. Ferrando, *Nano Lett.*, 2010, **10**, 4211-4216.

17 K. Laasonen, D. Bochicchio, E. Panizon and R. Ferrando, *J. Phys. Chem. C*, 2013, **117**, 26405-26413.

18 Y. Wang and M. Hou, *J. Phys. Chem. C*, 2012, **116**, 10814-10818.

19 L. O. Paz-Borbón, R. L. Johnston, G. Barcaro and A. Fortunelli, *J. Phys. Chem. C*, 2007, **111**, 2936-2941.

20 F. R. Negreiros, Z. Kuntova, G. Barcaro, G. Rossi and A. Fortunelli, *J. Chem. Phys.*, 2010, **132**, 234703.

21 G. Barcaro, R. Ferrando, A. Fortunelli and G. Rossi, *J. Phys. Chem. Lett.*, 2010, **1**, 111-115.

22 M. Polak and L. Rubinovich, *Phys. Chem. Chem. Phys.*, 2014, **16**, 1569-1575.

23 M. Mueller, P. Erhart and K. Albe, *Phys. Rev. B*, 2007, **76**, 155412.

24 F. Lequien, J. Creuze, F. Berthier, I. Braems and B. Legrand, *Phys. Rev. B*, 2008, **78**, 075414.

25 S. M. Kozlov, H. A. Aleksandrov, J. Goniakowski and K. M. Neyman, *J. Chem. Phys.*, 2013, **139**, 084701.

26 S. M. Kozlov, H. A. Aleksandrov and K. M. Neyman, *J. Phys. Chem. C*, 2014, **118**, 15242−15250.

27 S. M. Kozlov and K. M. Neyman, *Top. Catal.*, 2013, **56**, 867-873.

28 L. Vitos, A. V. Ruban, H. L. Skriver and J. Kollár, *Surf. Sci.*, 1998, **411**, 186–202.

29 F. R. de Boer, R. Boom, W. C. M. Mattens, A. R. Miedema and A. K. Niessen, *Cohesion in Metals*, North-Holland, Amsterdam, 1988.

30 I. V. Yudanov and K. M. Neyman, *Phys. Chem. Chem. Phys.*, 2010, **12**, 5094-5100.

31 P. Wessa, Free Statistics Software, Office for Research Development and Education, version 1.1.23-r7, 2014, URL http://www.wessa.net/

32 A. C. Davison and D. V. Hinkley, *Bootstrap Methods and their Application*, Cambridge University Press, Cambridge, 1997.

33 M. Friedrich, A. Ormeci, Y. Grin and M. Z. Armbrüster, *Anorg. Allg. Chem.*, 2010, **636**, 1735-1739.

34 A. Wang, X. Y. Liu, C.-Y. Mou and T. Zhang, *J. Catal.*, 2013, **308**, 258–271.

35 G. J. Hutchings and C. J. Kiely, *Acc. Chem. Res.*, 2013, **46**, 1759-1772.

36 J. K. Edwards, B. Solsona, A. F. Carley, A. A. Herzing, C. J. Kiely, E. N. N and G. J. Hutchings, *Science*, 2009, **323**, 1037-1041.

37 M. H. Ab Rahim, M. M. Forde, R. L. Jenkins, C. Hammond, Q. He, N. Dimitratos, J. A. Lopez-Sanchez, A. F. Carley, S. H. Taylor, D. J. Willock, D. M. Murphy, C. J. Kiely and G. J. Hutchings, *Angew. Chem. Int. Ed.*, 2013, **52**, 1280–1284.

38 R. Nath Dhital, S. Karanjit, C. Kamonsatikul and H. Sakurai, *J. Am. Chem. Soc.*, 2012, **134**, 20250-20253.

39 M. Nie, P. K. Shen and Z. Wei, *J. Power Sources*, 2007, **167**, 69–73.

40 N. E. Kolli, L. Delannoy and C. Louis, *J. Catal.*, 2013, **297**, 79–92.

41 M. Nie, H. Tang, Z. Wei, S. P. Jiang and P. K. Shen, *Electrochem. Comm.*, 2007, **9**, 2375–2379.

42 D. I. Enache, J. K. Edwards, P. Landon, B. Solsona-Espriu, A. F. Carley, A. A. Herzing, M. Watanabe, C. J. Kiely, D. W. Knight and G. J. Hutchings, *Science*, 2006, **311**, 362-365.

43 L. O. Paz-Borbón, R. L. Johnston, G. Barcaro and A. Fortunelli, *J. Chem. Phys.*, 2008, **128**, 134517.

44 R. C. Tiruvalam, J. C. Pritchard, N. Dimitratos, J. A. Lopez-Sanchez, J. K. Edwards, A. F. Carley, G. J. Hutchings and C. J. Kiely, *Faraday Discuss.*, 2011, **152**, 63-86.

45 A. Bruma, R. Ismail, L. O. Paz-Borbón, H. Arslan, G. Barcaro, A. Fortunelli, Z. Y. Li and R. L. Johnston, *Nanoscale*, 2013, **5**, 646-652.

46 H. Zhang, T. Watanabe, M. Okumura, M. Haruta and N. Toshima, *Nat. Mater.*, 2012, **11**, 49-52.

47 F. Gao, Y. Wang and D. W. Goodman, *J. Phys. Chem. C*, 2010, **114**, 4036–4043.

48 P. Han, S. Axnanda, I. Lyubinetsky and D. W. Goodman, *J. Am. Chem. Soc.*, 2007, **129**, 14355-14361.

49 F. Gao, Y. Wang and D. W. Goodman, *J. Phys. Chem. C*, 2009, **113**, 14993–15000.

50 Q. Zhang, J. Li, X. Liu and Q. Zhu, *Appl. Catal. A: Gen.*, 2000, **197**, 221–228.

51 S. K. Kim, J. H. Lee, I. Y. Ahn, W.-J. Kim and S. H. Moon, *Appl. Catal. A: Gen.*, 2011, **401**, 12–19.

52 A. Pachulski, R. Schödel and P. Claus, *Appl. Catal. A: Gen.*, 2011, **400**, 14–24.

53 A. Yarulin, I. Yuranov, F. Cárdenas-Lizana, D. T. L. Alexander and L. Kiwi-Minsker, *Appl. Catal. A: Gen.*, 2014, **478**, 186–193.

54 K. Tedsree, T. Li, S. Jones, C. W. A. Chan, K. M. K. Yu, P. A. J. Bagot, E. A. Marquis, G. D. W. Smith and S. C. E. Tsang, *Nat. Nanotech.*, 2011, **6**, 302–307.

55 Y. Lu and W. Chen, *ACS Catal*., 2012, **2**, 84-90.

56 H. Rong, S. Cai, Z. Niu and Y. Li, *ACS Catal.*, 2013, **3**, 1560-1563.

57 L. Li, M. Chen, G. Huang, N. Yang, L. Zhang, H. Wang, Y. Liu, W. Wang and J. A. Gao, *J. Power Sources*, 2014, **263**, 13–21.

58 Q. Wang, J. Zheng and H. Zhang, *J. Electroanal. Chem.*, 2012, **674**, 1–6.

59 H. Wang, Y. Zhang, H. Li, B. Du, H. Ma, D. Wu and Q. Wei, *Biosens. Bioelectron.*, 2013, **49**, 14–19.

60 F. R. Negreiros, G. Barcaro, Z. Kuntová, G. Rossi, R. Ferrando and A. Fortunelli, *Surf. Sci.*, 2011, **605**, 483–488.

61 W. He, X. Wu, J. Liu, W. Zhou, X. Hu and S. Xie, *Chem. Mater.*, 2010, **22**, 2988–2994.

62 S. González, K. M. Neyman, S. Shaikhutdinov, H.-J. Freund and F. Illas, *J. Phys. Chem. C*, 2007, **111**, 6852–6856.

63 F. Fouda-Onana, S. Bah and O. Savadogo, *J. Electroanal. Chem.*, 2009, **636**, 1–9.

64 L. Zhang and G. Henkelman, *J. Phys. Chem. C,* 2012, **116**, 20860-20865.

65 J. Kugai, J. T. Miller, N. Guo and C. Song, *Appl. Catal. B: Environ.*, 2011, **105**, 306–316.

66 J. Kugai, J. T. Miller, N. Guo and C. Song, *J. Catal.*, 2011, **277**, 46-53.

67 L. Lu, L. Shen, Y. Shi, T. Chen, G. Jiang, C. Ge, Y. Tang, Y. Chen and T. Lu, *Electrochem. Acta*, 2012, **85**, 187-194.

68 U. Matatov-Meytal and M. Sheintuch, *Catal. Commun.*, 2009, **10**, 1137–1141.

69 O. S. G. P. Soares, J. J. M. Órfão and M. F. R. Pereira, *Appl. Catal. B: Environ.,* 2009, **91**, 441–448.

70 Q. Zhang, L. Ding, H. Cui, J. Zhai, Z. Wei and Q. Li, *Appl. Surf. Sci.*, 2014, **308**, 113-120.

71 M. Friedrich, S. A. Villaseca, L. Szentmiklósi, D. Teschner and M. Armbrüster, *Materials*, 2013, **6**, 2958-2977.

72 G. Kyriakou, M. B. Boucher, A. D. Jewell, E. A. Lewis, T. J. Lawton, A. E. Baber, H. L. Tierney, M. Flytzani-Stephanopoulos and E. C. H. Sykes, *Science*, 2012, **335**, 1209-1211.

73 J. M. Montejano-Carrizales, M. P. Iniguez and J. A. Alonso, *Phys. Rev. B*, 1994, **49**, 16649-16658.

74 L. Zhu, K. S. Liang, B. Zhang, J. S. Bradley and A. E. DePristo, *J. Catal.*, 1997, **167**, 412–416.

75 L. Yang, *Philos. Mag. A*, 2000, **80**, 1879-1888.

76 J. S. Bradley, E. W. Hill, B. Chaudret and A. Duteil, *Langmuir*, 1995, **11**, 693-695.

77 M. Friedrich and M. Armbrüster, *Chem. Mater.*, 2009, **21**, 5886–5891.

78 V. Shah and L. Yang, *Philos. Mag. A*, 1999, **79**, 2025-2049.

79 R. Hultgren, P. D. Desai, D. T. Hawkins, M. Gleiser and K. Kelley, *Selected Values of Thermodynamic Properties of Binary Alloys*, American Society for Metals, Russell Township, 1973.

80 K. Föttinger, *Catal. Today*, 2013, **208**, 106–112.

81 M. Armbrüster, M. Behrens, K. Föttinger, M. Friedrich, É. Gaudry, S. K. Matam and H. R. Sharma, *Catal. Rev.*, 2013, *55*, 289-367.

82 S. M. Kozlov, H. A. Aleksandrov, L. V. Moskaleva, M. Bäumer and K. M. Neyman, in *Comprehensive Inorganic Chemistry (2nd edition),* eds. J. Reedijk and K. Poeppelmeier, Elsevier, Amsterdam, 2013; *vol. 7: Surface Inorganic Chemistry and Heterogeneous Catalysis, eds.* R. Schlögl and J. W. Niemantsverdriet, pp. 475-503.

83 Z.-X. Chen, K. M. Neyman and N. Rösch, *Surf. Sci.*, 2004, **548**, 291–300.

84 A. Bayer, K. Flechtner, R. Denecke, H.-P. Steinrück, K. M. Neyman and N. Rösch, *Surf. Sci.*, 2006, **600**, 78–94.

85 C. Weilach, S. M. Kozlov, H. H. Holzapfel, K. Föttinger, K. M. Neyman and G. Rupprechter, *J. Phys. Chem. C*, 2012, **116**, 18768−18778.

86 R. A. Dagle, A. Platon, D. R. Palo, A. K. Datye, J. M. Vohs and Y. Wang, *Appl. Catal. A: Gen.*, 2008, **342**, 63–68.

87 L. Bollmann, J. L. Ratts, A. M. Joshi, W. D. Williams, J. Pazmino, Y. V. Joshi, J. T. Miller, A. J. Kropf, W. N. Delgass and F. H. Ribeiro, *J. Catal.*, 2008, **257**, 43–54.

88 V. Lebarbier, R. Dagle, A. Datye and Y. Wang, *Appl. Catal. A: Gen.*, 2010, **379**, 3–6.

89 M. W. Tew, H. Emerich and J. A. van Bokhoven, *J. Phys. Chem. C*, 2011, **115**, 8457–8465.

90 T. Conant, A. M. Karim, V. Lebarbier, Y. Wang, F. Girgsdies and A. Datye, *J. Catal.*, 2008, **257**, 64–70.

91 Q. Zhang and R. J. Farrauto, *Appl. Catal. A. Gen.*, 2011, **395**, 64-70.

92 N. Iwasa, S. Masuda, N. Ogawa and N. Takezawa, *Appl Catal. A: Gen.,* 1995, **125**, 145-157.

93 N. Iwasa and N. Takezawa, *Top. Catal.*, 2003, **22**, 215-216.

94 C. Rameshan, W. Stadlmayr, C. Weilach, S. Penner, H. Lorenz, M. Hävecker, R. Blume, T. Rocha, D. Teschner, A. Knop-Gericke, R. Schlögl, N. Memmel, D. Zemlyanov, G. Rupprechter and B. Klötzer, *Angew. Chem. Int. Ed.*, 2010, **49**, 3224–3227.

95 M. Friedrich, D. Teschner, A. Knop-Gericke and M. Armbrüster, *J. Catal.*, 2012, **285**, 41-47.

96 S. Penner, B. Jenewein, H. Gabasch, B. Klötzer, A. Knop-Gericke, R. Schlögl and K. Hayek, *J. Catal.*, 2006, **241**, 14–19.

97 K. Föttinger, J. A. van Bokhoven, M. Nachtegaal and G. Rupprechter, *J. Phys. Chem. Lett.*, 2011, **2**, 428–433.

98 According to the Bader analysis the charge distribution in the bulk material corresponds to Pd-0.4Zn+0.4. So some researchers find the notation Zn-Pd (with the positively charged atom mentioned first) to be more appropriate than Pd-Zn.

99 S. Kou and Y. A. Chang, *Acta Metall.*, 1975, **23**, 1185–1190.

100 H. Gabasch, A. Knop-Gericke, R. Schlögl, S. Penner, B. Jenewein, K. Hayek and B. Klötzer, *J. Phys. Chem. B*, 2006, **110**, 11391–11398.

101 A. Roldán, F. Viñes, F. Illas, J. M. Ricart and K. M. Neyman, *Theor. Chem. Acc.*, 2008, **120**, 565–573.

102 G. Kresse and J. Furthmuller, *Phys. Rev. B*, 1996, **54**, 11169−11186.

103 J. P. Perdew, K. Burke and M. Ernzerhof, *Phys. Rev. Lett.*, 1996, **77**, 3865−3868.

104 P. Janthon, S. M. Kozlov, F. Viñes, J. Limtrakul and F. Illas, *J. Chem. Theory Comput.*, 2013, **9**, 1631−1640.

105 M. Methfessel and A. T. Paxton, *Phys. Rev. B,* 1989, **40**, 3616-3621.

106 F. Viñes, F. Illas, and K. M. Neyman, *Angew. Chem. Int. Ed.*, 2007, **46**, 7094 –7097.

Chapter 4

Supported Transition Metal Nanoparticles

In laboratory experiments and in applications often nanoparticulate species are stabilized on a support or in a solution. The practical interest in nanoparticles on solid supports is because they allow making use of features of heterogeneous catalysis in chemical applications and making the engineering layout of physical appliances less complex. Presently, a variety of supports is available for transition metal nanoparticles, some of them are based on high-area carbon or oxide frameworks. The latter are particularly suitable for oxidizing reaction conditions.

Introduction to metal catalyst-oxide support interactions

It has been known that the performance of a transition metal catalyst depends strongly on the type of support used in the preparation (Figure 4.1). [19,246,247] However, exact reasons for altered catalyst's properties is often very hard to identify. In some cases it could be just the effect of a support on the dispersion and stability of the metal nanoparticles or on the diffusion of reactants (products) towards (from) the catalyst. Many studies ascribe the role of support to increased catalytic activity of sites at metal-oxide interface;[19,246] however, only in a few studies this was shown conclusively.[18,153] Other authors suggest that support may modify electronic structure and concomitantly catalytic properties of supported metals.[168,248,249] Sometimes the effect of support cannot be ascribed to any of these mechanisms. For example, certain supports facilitate oxidation of Pd catalysts deposited on them and so they affect the catalytic activity of Pd at high temperatures.[247,250,251] Also, the favorable influence of ZnO support on the activity of Cu catalysts in methanol steam reforming was assigned to the formation of Zn impurities on steps of Cu surfaces,[26] which exemplifies yet another way of NP-support interaction. Finally, one should mention the well-known phenomenon of "strong metal-support interaction", when it is thermodynamically favorable for the oxide to form a film around the metal nanoparticle covering it completely.[32,34,206]

Among common supports, usually it is reducible oxides, such as CeO_2,[252–254] TiO_2[154,255,256] or Fe_2O_3,[32,34,206] that strongly modify properties of supported nanoparticles. Other common oxide supports, MgO, Al_2O_3 and at a lesser extent SiO_2, have been concluded to have a minor direct influence on catalytic processes.[246,257,258] However, some authors challenge the assignment of magnesia and alumina to innocent catalyst supports.[259] Naturally, the only direct way to verify or disprove this attribution is to compare activity of nanoparticles supported on MgO or Al_2O_3 to that of

unsupported NPs of the same size. Some industrially relevant processes, however, have not yet been studied experimentally on realistic unsupported nanoparticles and only computational data is available (see Chapter 3).

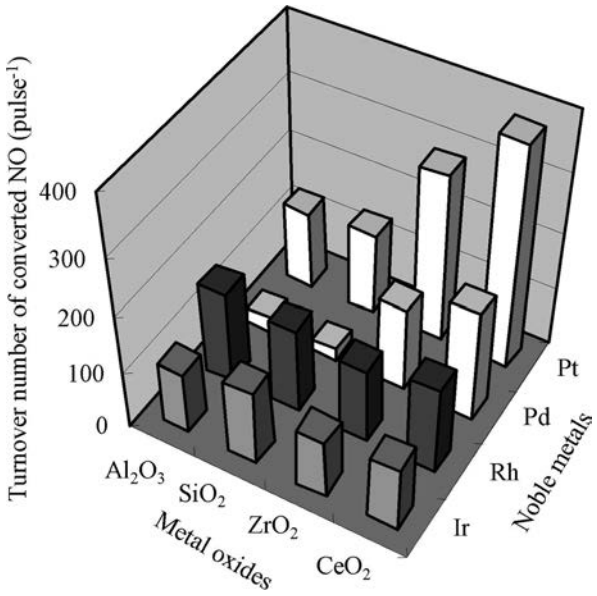

Figure 4.1. The effect of various oxide supports on catalytic activity of transition metals in NO reduction.[248] Al_2O_3 and SiO_2 are attributed to inactive supports, whereas ZrO_2 and CeO_2 are able to alter the activity of some metals.

Simulations of supported nanoparticles are essentially limited by their significant computational cost. Hence, supported nanoparticles with the size of > 1 nm (potentially SwS) are commonly studied only using interatomic potentials. [244,260] This approach may shed light onto the effect of a support on the structure and the shape of metal nanoparticles, but it is not able to provide detailed information about the effect on electronic structure and chemical activity. Various electronic structure investigations considered supported clusters.[168,261,262] However, most of these studies again focused on the effect of a support on the structure of adsorbed clusters, since the latter are rather fluxional and may adapt to the substrate's geometry.[261,263,264] Only in the last years studies of reactions on supported transition metal clusters became more numerous.[169,175,265] In these studies the effect of support on clusters' properties was found to be notable.[266–268] This comes as no surprise, since small clusters exhibit very high fractions of atoms not only on their surface but also on the interface with the substrate. These fractions are smaller in sizeable nanoparticles, dealt with in pertinent

catalytic experiments. So one should be careful extrapolating results obtained for supported clusters to industrial catalysts.

Objectives of this Chapter

On the atomistic level it is possible to divide different mechanisms of nanoparticle-support interaction into a) creation of new active sites and b) modification of the existing active sites. The former is very specific to a particular combination of materials, while the latter may be present for all nanoparticles and all substrates at some varying (and possibly often negligible) extent. Quantify this extent could help to answer the following interrelated questions: Is the consideration of a support always a must in computational studies of nanoparticles? How suitable are unsupported SwS nanoparticles to represent model catalysts in the form of supported NPs?

Studies presented in this Chapter attempt to assess the role of oxide supports on physical, adsorptive and absorptive properties of sizeable noble metal nanoparticles at the perimeter of metal-oxide interface and far from it. Following the general strategy adopted in this thesis we focus on nanoparticles of the size of around 1 nm or more with bulk-like structures, because only such species may be scalable with size.

In this Chapter we consider not only Pd NPs addressed in Chapter 3, but also Pt nanoparticles. The reason is that in Section 3.3 unsupported Pt nanoparticles were shown to be quite similar to unsupported Pd NPs in ethyl hydrogenation, whereas in Section 3.2 the difference between the activities unsupported Pd and Pt NPs in methane decomposition was discussed. Hence, it is unclear if NPs of these two materials would be affected in the same or in different ways by the presence of an oxide support. Moreover, similarly to Pd, platinum is used in heterogeneous catalysis applications,[214,269,270] e.g. in fuel cells.[271–273] Since H may be present in reactions catalyzed by Pd and Pt, it is especially important to study H adsorption and absorption on these metals (especially in view of Section 3.3). Hence, studies in Sections 4.2 and 4.3 attempt to clarify the role of different effects on H interaction with Pd and Pt nanoparticles supported on MgO(100), which is also one of the objectives of this Chapter.

MgO(100) surface was chosen as a nanoparticle support because of the following: 1) The effect of MgO(100) on properties of supported NPs was concluded to be minor in some experimental studies, so this oxide may serve as a reference for other support materials; 2) MgO has only one crystalline phase and its stable and unipolar (100) surface is characterized sufficiently for the purposes of the following studies, which is not the case for e.g. Al_2O_3 or SiO_2; 3) Experimental effort has been put into studies of shapes of Pd and Pt nanoparticles on MgO(100) as well as the respective metal-oxide interfaces.[38,40,274]

Effect of support on structure and physical properties of metal nanoparticles

The first step in studies of scalable with size Pd and Pt nanoparticles on MgO(100) was determination of their atomic structures (Section 4.1). Unlike unsupported nanoparticles discussed in Chapter 3, whose structure was created via Wulff construction, the structure of sufficiently big supported nanoparticles should be governed by Wulff-Kaischev construction. In practice, however, the latter may be used only as a rough estimate, unsuitable for building atomistic models, because it requires one to know the specific surface energy of nanoparticle-oxide interface. First, this may be not straightforward to obtain either experimentally or theoretically, in part due to possibly uncertain atomic structure of the interface. Second, this energy does not seem to be constant,[274–276] because of the gradual accumulation of stress at the interface with the increasing interface size, caused by the mismatch between NP and oxide lattices. The stress results in the gradual destabilization of the contact for bigger nanoparticles. Consequently, the most thermodynamically favorable shape of smaller supported nanoparticles may not be exactly the same from that of bigger species – the effect, which is not accounted for by the Wulff-Kaischev construction. Hence, a dedicated DFT study of relative stabilities of Pd and Pt nanoparticles with different shapes on MgO(100) had to be performed.

As mentioned before, nowadays, it is still too costly to perform a global optimization of big metallic species on a support, so interatomic potentials from Ref. 276 were used for this purpose. After a thorough screening of various cluster structures with interatomic potentials, low-energy nanoparticles of 49 – 155 atoms that kept fcc

lattice arrangement without any stacking faults were recalculated with DFT.[a] The reason is that only these nanoparticles may comply with all the requirements to be scalable with size. Smaller nanoparticles were not investigated for the same reason.[182] The maximum size of the nanoparticles was limited by the necessity to keep the separation of at least 0.5 nm between the adjacent species to prevent any noticeable interaction[277] between them in the employed 2.08 × 2.08 nm MgO(001) support supercell. These nanoparticles featured not only the most energetically favored shapes according to the interatomic potentials, but also the most energetically favored Pd||MgO or Pt||MgO interface structures, which would be also very computationally costly to obtain using just DFT. Overall, the agreement between IP and DFT results was found to be quite good for supported and unsupported Pd nanoparticles and rather moderate for the Pt species. However, in both cases it was concluded that interatomic potentials are accurate enough for screening purposes. In this way representative models of Pd and Pt nanoparticles on MgO(100) energies were obtained (Figure 4.2).

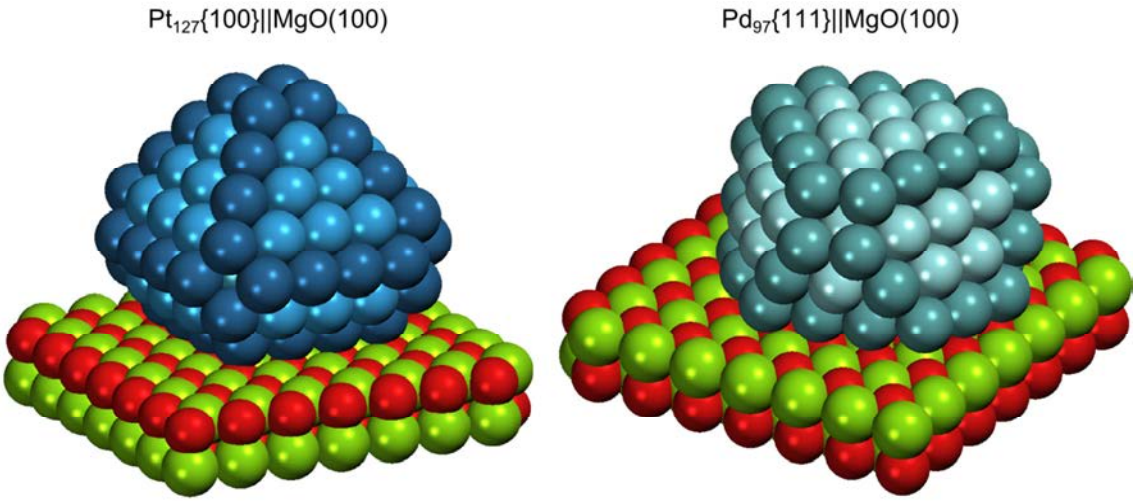

Figure 4.2. Selected energetically favorable structures of Pd and Pt nanoparticles on MgO(100) support. Pd atoms are displayed in cyan, Pt – blue, Mg – green, O – red. Darker atoms are located on NP edges.

Shapes of calculated low-energy nanoparticles were quite similar to shapes of much bigger experimentally observed Pd and Pt nanoparticles on MgO(100).[38,278,279] They both featured a truncated octahedral shape like unsupported nanoparticles, but

[a] Hence, they may not be the global minima structures at respective nanoparticle sizes. Nevertheless, they appear to be at least more stable than decahedral nanoparticles.[276]

with one facet extended to form a larger interface with MgO(100). The formation of Pd{100}||MgO(100) was found to be energetically favored compared to that of Pd{111}||MgO(100) interface. This finding is in line with the pertinent experimental observations, where the former interface is encountered more often than the latter.[39,280,281] Both types of Pt||MgO interfaces were calculated to be similar in energy, in line with the occurrence of both contact structures in experiment.[274,279] In all considered interface structures of Pd and Pt nanoparticles on MgO(100) transition metal atoms preferred to be located above O anions. In the case of (small) M{100}||MgO(100) interfaces this epitaxy was easy to achieve, since both surfaces had the same square symmetry. In the case of M{111}||MgO(100) contact only a part of metal atoms could bind to O anions on the interface, due to the different surface symmetries. In turn, this resulted in much lower interaction energy. The weaker binding between the metal and the oxide in this case was, however, compensated by the higher intrinsic energetic stability of {111} facets on Pt nanoparticles compared to {100} facets.

Having determined the realistic models of MgO(100)-supported Pd and Pt nanoparticles, it was possible to perform analysis of their physical properties and inspect how they were affected by the interaction with the support. Among many considered structures, M_{119} and M_{127} species with bottom[b] {111} and {100} facets were chosen for a more detailed investigation because of their high relative energetic stability and rather similar size of ~1.6 nm. First, it was shown that the support does not affect the geometric structure of the nanoparticle species – the differences between respective distributions of interatomic distances in supported and unsupported NPs were barely visible. Thus, not only the presence of the support did not change average interatomic distances within NPs, it also did not lead to the appearance of unusually short or long metal-metal bonds at the interface. Second, the effect of MgO on the electronic structure of supported Pd and Pt nanoparticles appeared to be negligible – even densities of states projected on atoms on bottom NP edges (that feel immediate presence of the support) were almost the same for supported and unsupported nanoparticles. Finally, if one had a look on the effect of the support on the distribution of electron density in the nanoparticles via CDD plots, one could find that it can be explained by simple electrostatic considerations. That is, electrons in nanoparticles moved from the regions

[b] That is, the facets in contact with the support.

above negatively charged O anions towards the regions above positively charged Mg cations of the substrate and the polarization of the charge density decreased rapidly with the growing distance from the substrate. All in all, the effect of MgO(100) support on physical properties of Pd and Pt nanoparticles was found to be quite small. In turn, this suggests that these properties may be reliably simulated using unsupported nanoparticle models.

Effect of oxide on adsorptive and absorptive properties of supported nanoparticles

Usually adsorptive properties of a surface site are more sensitive to the environment than its physical properties, such as densities of states of atoms composing the site and distances between them. For example, the smooth monotonous dependency of adsorption energies on the growing NP size, N, is achieved only for relatively big nanoparticles, while interatomic distances, cohesive energies or d-band centers depend linearly on $N^{-1/3}$ even for smaller species.[179,182,189] Thus, the small effect of MgO(100) on physical properties of Pd and Pt nanoparticles described in Section 4.1 does not necessarily mean that the effect of the support on adsorptive properties of the nanoparticles is also negligible.

The ability of MgO(100) support to modify the adsorptive and absorptive properties of 1.5 nm big Pd_{127} and Pt_{127} nanoparticles was addressed in Section 4.2 using H-Pd and H-Pt interactions as an example. Hydrogen was chosen for a detailed investigation because it participates in many reactions catalyzed by these two metals, for example in those discussed in Sections 3.2 and 3.3. In particular, in Section 3.3 it was shown that H absorption into subsurface region of Pd and Pt nanoparticles and single crystals can alter their activity in hydrogenation reactions. Therefore, it is very important also to investigate the formation of subsurface hydrogen in Pd and Pt. Hydrogen absorption in Pd has been studied both by theoretical[185,233,282] and experimental[223,227,239] means, partially because Pd has been considered as a potential hydrogen storage medium for energy applications. It was observed that Pd nanoparticles become hydrided more rapidly than Pd single crystals. [235,283,284] Only negligible concentration of subsurface H was measured on Pt(111)[53] and there is only one experimental paper reporting significant H absorption into Pt nanoparticles.[235] The presence of subsurface H in Pt was also suggested based on interpretation of some electrochemical measurements.[285,286] In line with the experimental findings,

computational studies[287,288] of H on Pt(111) predicted this process to be rather endothermic and, therefore, unlikely. To the best of my knowledge, H interaction with scalable-with-size Pt nanoparticles had not yet been addressed with the help of DFT calculations.

Similarly to other computational studies, hydrogen atoms were calculated to adsorb on Pd and Pt nanoparticles and single crystals with binding energies of around 0.3 eV with respect to a half of H_2 molecule. Pd_{127} nanoparticles were found to adsorb hydrogen by up to 0.08 eV stronger than Pd(111) surfaces.[c] For Pt the difference between binding strength of nanoparticles and single crystals was 0.18 eV. Binding of H absorbed into subsurface region of Pd was calculated to be almost isoenergetic with respect to $½H_2$ and by 0.04 eV stronger on Pd_{127} than on Pd(111). The absorption of H on Pt(111) was calculated to be notably endothermic, by -0.43 eV, whereas the energy required for H absorption was by 0.13 eV lower on Pt nanoparticles. This stabilization of absorbed H was partially attributed to the higher flexibility of nanostructured Pt compared to Pt(111), which allowed for better accommodation of H impurities in interstitial sites. Note that again the nanostructuring was found to be more important for Pt than for Pd in line with the results of Section 3.2.

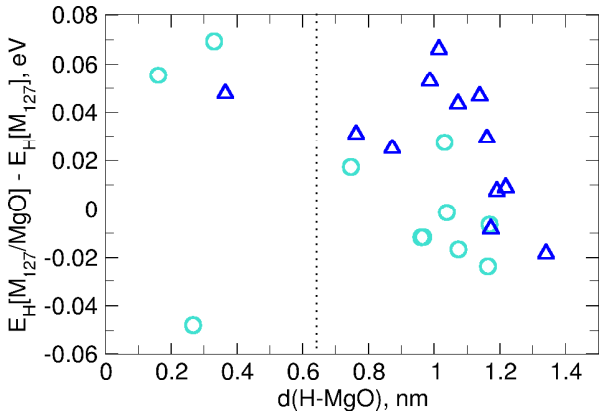

Figure 4.3. The effect of MgO(100) support on adsorption and absorption energies of hydrogen atoms in Pd_{127} (circles) and Pt_{127} (triangles) nanoparticles depending on the H-MgO distance. Dotted line separates the data calculated on bottom and top facets of the nanoparticles.

[c] In this paragraph binding energies on the most energetically stable sites are compared.

Interestingly, in most of the cases subsurface interstitial sites at the nanoparticle edges were found to be locally unstable for H absorption. Instead H escaped spontaneously from these sites to more stable surface sites, which did not happen on {111} terraces of the NPs or (111) single crystals. This indicates a lowered barrier for surface ↔ subsurface migration at the nanoparticle edges, which may result in facilitated H absorption into metal nanoparticles due to the kinetic considerations.

The effect of MgO(100) support on adsorptive and absorptive properties of Pd and Pt nanoparticles was found to be rather small, at most 0.07 eV (Figure 4.3). For Pd nanoparticles the effect of support on H binding was found to decrease in magnitude with the growing distance from the support. This finding is in line with the rapidly decaying effect of MgO(100) on distribution of electronic density in the supported Pd nanoparticles documented in Section 4.1. At variance, for Pt certain differences between H binding energies on supported and unsupported nanoparticles were calculated even at H-MgO(100) distances of ~1 nm. In many cases the effect of the support was limited to the local destabilization of sites at the NP-oxide interface caused by the steric repulsion between H and MgO(100). All in all, the effect of MgO(100) support on adsorptive and absorptive properties of Pd and Pt nanoparticles was shown to be smaller than the effect of nanostructuring itself.

Effect of surface coverage on absorptive properties of supported nanoparticles

Studies described in Section 4.2 provided an important insight into H absorption in nanostructured Pd and Pt; nevertheless, they did not exactly address the experimental situation. Namely, since H absorption in Pd and Pt is less energetically favored than H adsorption, it will take place only when all surface sites are already saturated by H. In Section 3.3, it was shown how subsurface H in Pd and Pt affects binding of surface hydrogen atoms by altering the electronic structure of Pd and Pt nanoparticles or single crystals. Hence, one could expect that the presence of H atoms on the surface may also make H absorption more or less thermodynamically favorable. It seemed necessary to perform a more realistic study, because the results presented in Section 4.2 were not sufficient to explain the facilitated H absorption into Pd NPs compared to bulky Pd samples observed experimentally.[235]

In Section 4.3 absorption of single H atoms in H-covered Pd_{127} and Pt_{127} NPs supported on MgO(100) was analyzed using the same nanoparticle models and the same computational techniques as in Sections 4.1 and 4.2. Since structure of nanoparticles is significantly more complex than the structure of single crystal surfaces, it is much harder to determine the saturation coverage[d] for an adsorbate on a given NP. Often a certain type of surface sites is chosen to be saturated by an adsorbate to simulate the high coverage regime, without claiming that the surface saturation was actually achieved (e.g. see Section 3.3 and Ref. 210). In Section 4.3, a somewhat more sophisticated approach was used. Hydrogen atoms were gradually put on supported nanoparticles until their further adsorption became endothermic. However, to decrease the computational cost of this procedure only highly symmetric configurations of adsorbed hydrogen were considered. In these configurations all or none of the sites of the same type (e.g. terrace fcc sites, edge bridge sites, corner top sites) were occupied. Models of saturated nanoparticles obtained in such a way contained 96 and 116 surface H atoms for the cases of Pd_{127} and Pt_{127}, respectively (Figure 4.4). The resulting saturation coverages, 1.14 and 1.38 ML, respectively, notably exceeded the saturation coverage of 1 ML observed on extended M(111) surfaces. This happened because edge and corner metal atoms belong to two or three facets of a nanoparticle at the same time and, therefore, participate in the formation of a higher number of adsorption sites. The reason why Pt nanoparticles were able to adsorb more hydrogen than similar Pd NPs is the higher propensity of small {100} facets on corners of Pt_{127} for H adsorption.

The effect of high coverage of surface H on hydrogen absorption was found to be rather significant and qualitatively the same on Pd and Pt nanoparticles and single crystals. Namely, on M(111) surfaces adsorbed H destabilized hydrogen absorbed in the subsurface positions by ~0.13 eV, but stabilized hydrogen absorbed deeper in the bulk by ~0.08 eV. On the M_{127} nanoparticles the destabilizing effect of surface H was around 0.06 eV, i.e. somewhat weaker than on extended (111) surfaces, whereas the stabilizing effect was reinforced on the nanoparticles to ~0.19 eV. Both these findings contribute to the higher propensity of Pd and Pt nanoparticles to absorb H compared to the respective single crystals. In the case of Pd nanoparticles the stabilization of deeply absorbed

[d] Here, surface coverage is defined as the ratio between the number of adsorbates and the number of surface metal atoms, which is not equal to the number of available adsorption sites on nanostructured models.

hydrogen by the surface species was sufficient to make H absorption somewhat exothermic, by ~0.11 eV. Together with the decreased surface ↔ subsurface migration barriers at the NP edges documented in Section 4.2, the increased exothermicity of H absorption would allow rapid formation of absorbed H in Pd nanoparticles in typical catalytic conditions. Note that again the nanoparticles were affected by the presence of surface hydrogen in a qualitatively similar but quantitatively different way than the extended surfaces, similarly to the findings in Sections 3.3.

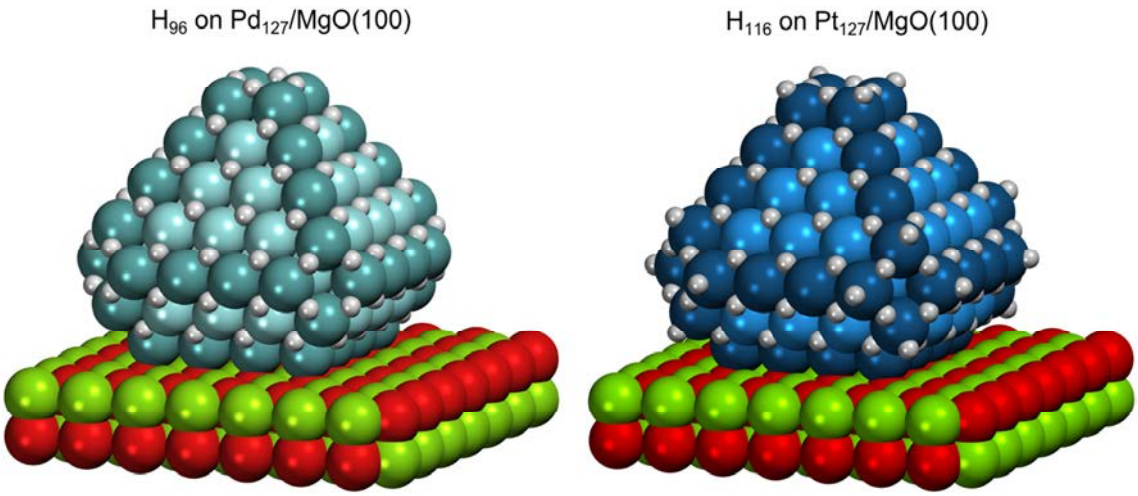

Figure 4.4. Pd and Pt nanoparticles covered by H and supported on MgO(100). The Pt nanoparticle is able to adsorb more hydrogen due to the higher H density at corner {100} facets. Pd atoms are displayed in cyan, Pt – blue, Mg – green, O – red. Darker atoms are located on NP edges.

The effect of highcoverage of surface hydrogen on the distribution of interatomic distances and electronic structure of supported Pd and Pt nanoparticles was also analyzed, in analogy with the considerations in Section 4.1. The average interatomic distances in M_{127} nanoparticles increased by ~2% upon the saturation of surface by H and the densities of states projected on the surface metal atoms shifted to lower energies by few tenth of eV.

Hence, the effects of surface H on both physical and absorptive properties of Pd and Pt nanoparticles was found to clearly exceed those of MgO(100) support. Indeed, the geometric and electronic structure of supported metal nanoparticles were virtually unaffected by the presence of the support (Section 4.1). Moreover, the effect of MgO(100) on the absorption energies of isolated H atoms was within 0.06 eV (Section

4.2), while the effect of surface H reached 0.24 eV. From these findings one can conclude that in computational catalytic studies it is much more important to accurately model the presence of co-adsorbed species on the nanostructured catalyst than the presence of a chemically inert oxide support.[e]

[e] Of course, many supports should not be considered chemically inert for the reasons outlined in the beginning of this Chapter.

Section 4.1

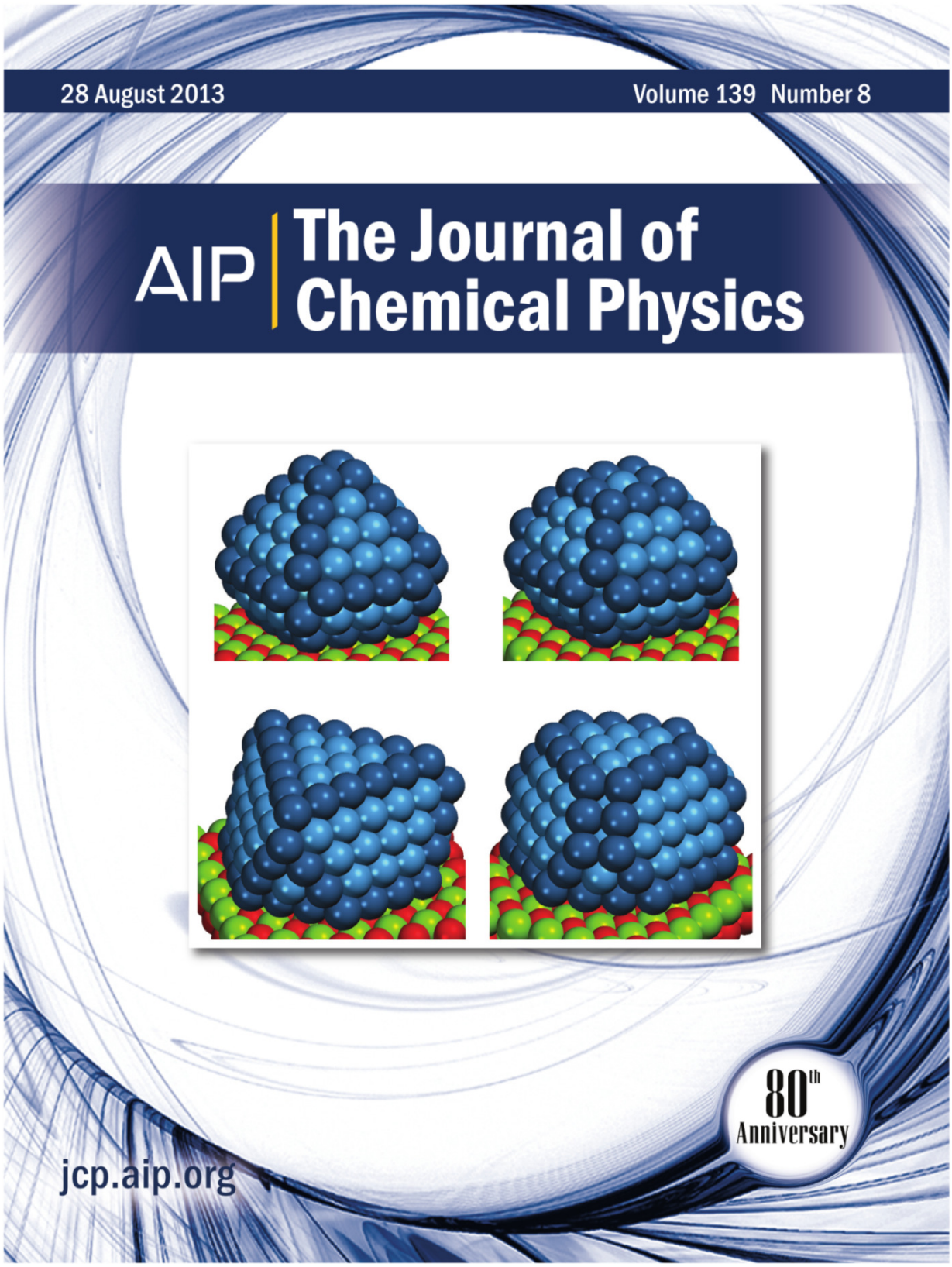
28 August 2013
Volume 139 Number 8
AIP
The Journal of Chemical Physics
80th Anniversary
jcp.aip.org

THE JOURNAL OF CHEMICAL PHYSICS **139**, 084701 (2013)

Effect of MgO(100) support on structure and properties of Pd and Pt nanoparticles with 49-155 atoms

Sergey M. Kozlov,[1] Hristiyan A. Aleksandrov,[1,2] Jacek Goniakowski,[3] and Konstantin M. Neyman[1,4,a)]

[1]*Departament de Química Física and Institut de Química Teòrica i Computacional (IQTCUB), Universitat de Barcelona, C/Martí i Franquès 1, 08028 Barcelona, Spain*
[2]*Faculty of Chemistry and Pharmacy, University of Sofia, Blvd. J. Baucher 1, 1126 Sofia, Bulgaria*
[3]*Institut des Nanosciences de Paris, UMR 7588, CNRS and UMPC-Université Paris 06, 4 place Jussieu, 75252 Paris Cedex 05, France*
[4]*Institució Catalana de Recerca i Estudis Avançats (ICREA), 08010 Barcelona, Spain*

(Received 18 June 2013; accepted 22 July 2013; published online 22 August 2013)

Presently, density functional computational studies of nanostructures in heterogeneous catalysts consider either sufficiently big ("scalable with size") unsupported metal nanoparticles (NPs) or small supported metal clusters. Both models may not be sufficiently representative of a few nm in size supported transition metal NPs dealt with in experiment. As a first step in closing the gap between theoretical models and prepared systems, we investigate the effect of a rather chemically inert oxide support, MgO(100), on relative energies and various properties of Pd and Pt NPs that consist of 49–155 atoms (1.2–1.6 nm in size) and exhibit bulk-like fcc structural arrangements. Shapes and interface configurations of metal NPs on MgO were obtained as a result of thorough optimization within the fcc motif using interatomic potentials. Then the stability and properties of the NPs were studied with a density functional method. We comprehensively characterize interaction between the NPs and MgO(100) support, their interface and effect of the support on NP properties. While the effect of MgO on relative stabilities of NPs with different shapes is found to be significant, other properties of the NPs such as electronic structure and interatomic distances within NP do not notably change upon deposition. This work paves the way to large-scale first-principles computational studies of more realistic models of oxide-supported metal catalysts. © *2013 AIP Publishing LLC*. [http://dx.doi.org/10.1063/1.4817948]

I. INTRODUCTION

Industrially used catalysts commonly exhibit a very complex structure.[1,2] Hence, in-depth laboratory studies are often performed on single crystals[3,4] or so-called model catalysts.[5,6] The latter typically consist of metal nanoparticles (NPs) on an oxide support and may be studied with many surface science techniques. Like industrial catalysts and unlike single crystals, model catalysts feature a variety of (often very active) low-coordinated sites on the surface and also metal–support interactions. Thus, they are thought to be representative for studies relevant to applications.[7,8] In theoretical investigations, single crystal surfaces are modelled by infinite in two dimensions slabs,[9,10] while model catalysts – by supported clusters[11,12] or unsupported *scalable with size* NP models.[7,13–18] The scalability with size, i.e., smooth and monotonous dependency of a property on the NP size, is an indispensable feature that allows one to extrapolate results calculated on computationally tractable NPs of ∼100 atoms (for Pd and Pt) to significantly bigger NPs present in model and real catalysts.[19,20] Clusters of smaller size usually do not feature this behavior, which means that their properties may deviate significantly from the properties of bigger NPs widely used in practice. Note that also the structural motif of a NP may significantly affect its properties. Thus, the scalability with size concept should be applicable only for calculated NP models with the same structural motif as that of bigger experimentally studied species (i.e., the fcc motif in the case of Pd and Pt).

In the approach employing the scalability with size concept, the size of calculated NP models is also assumed to be big enough so that the influence of underlying support on the NP properties can be neglected. Thus, up to now (to the best of our knowledge) an oxide support has not been explicitly included into electronic structure studies of NPs sufficiently big to be in the scalable with size regime. Instead, contemporary studies often consider the influence of the support on shapes and atomic structure motifs of moderately big monometallic (or bimetallic) NPs by performing a global minima search using interatomic-potential (IP) approach.[21–24]

The present study has two main objectives: (1) To examine by means of combined IP and density functional theory (DFT) based calculations relative stabilities of various Pd and Pt NPs supported on MgO(100) surface in order to find highly stable species that would reliably represent bigger experimentally observed supported NPs; (2) to assess the magnitude of changes in NP properties induced by the MgO(100) support. The first objective is achieved via a thorough optimization of the shapes of supported NPs and their interface configurations

a)Author to whom correspondence should be addressed. Electronic mail: konstantin.neyman@icrea.cat.

with interatomic potentials (but keeping the fcc structural motif) and subsequent local optimization of the most stable structures by DFT. To reach the second objective, we investigated in detail the effect of MgO(100) support on interatomic metal–metal distances within Pd and Pt NPs, electronic structure, and charge density. As a result, we obtained well characterized and highly energetically stable models suitable for further studies of adsorptive and reactive properties of Pd and Pt NPs supported on MgO(100) planned in our group.

We have focused our attention on Pd and Pt, because these metals are typical components of catalysts for reactions involving elementary steps of hydrogenation and dehydrogenation of various organic compounds.[25–27] Also these systems are of general importance for hydrogen energy and H storage technologies.[28,29] MgO was chosen as a support for two main reasons. On the one hand, it is often used as a support for Pd and Pt NPs and their interactions have been intensively characterized experimentally.[21,30–37] On the other hand, MgO is an irreducible oxide with only one type of crystal structure. This allows us to exclude from the consideration various complicated phenomena, which could be present on other supports: strong metal–support interaction, support reduction, O vacancy formation, reverse spill-over of O, and transformation of support's crystal structure upon contact with a NP.[38,39]

It is known that under ultra-high vacuum conditions vast majority of Pd NPs on MgO (in line with Wulff-Kaischev construction) have a shape close to a truncated octahedron terminated mostly by {111} and smaller {100} nanofacets.[31,33] The {100} facet that binds to MgO(100) is increased in size and forms a cube on cube epitaxy with the support with Pd atoms located roughly above O atoms.[34,35] Also a fraction of Pd NPs that stick to MgO(100) with {111} facets is observed.[36] The shape of Pt NPs grown on MgO(100) at high temperature appears to be similar to the most common truncated octahedral shape of Pd NPs. At low temperature, the NPs that bind to MgO(100) via {111} facets have been reported.[21,30] Their fraction seems to depend on the preparation conditions, which suggests that this type of NPs is favored kinetically rather than thermodynamically.

II. COMPUTATIONAL DETAILS

A. DFT calculations

Periodic calculations based on DFT were carried out with VASP[40] software package, using generalized gradient approximation in the form of revised Perdew-Burke-Ernzerhof (rPBE) exchange-correlation functional.[41] This particular functional is chosen because in many cases it is shown to yield good description of adsorption processes on transition metal surfaces. Projector augmented wave (PAW) technique was used to model interaction between core and valence electrons, whose eigenstates were calculated using plane-wave basis set with the cut-off energy of 415 eV.[42] First-order Methfessel-Paxton smearing[43] of 0.1 eV was applied to electron density during geometry optimizations; then, all calculated energies were extrapolated to zero smearing. Densities of states (DOS) were calculated using the smearing of 0.3 eV. The calculations involving NPs were done only at Γ point in the reciprocal space, due to significant spatial extent of the systems. 17 × 17 × 17 Monkhorst-Pack k-point mesh[44] was used for calculations of bulk metals. Positions of all transition metal atoms were optimized until forces on relaxed atoms became smaller than 0.2 eV nm^{-1}, positions of Mg and O atoms of the support (if present) were fixed. Tests done with stricter geometry convergence criterion (0.1 eV nm^{-1}) produced only 5 meV changes in total energies.

Excess surface energies[45,46] were calculated from total energies E as $\Delta_{exc}[M_N] = N^{1/3}(E[M_N]/N - E[M_{bulk}])$ for the unsupported NPs of N atoms and $\Delta_{exc}[M_N/MgO] = N^{1/3}((E[M_N/MgO] - E[MgO])/N - E[M_{bulk}])$ for the supported species. One can see that such a definition implies that binding to the substrate lowers the excess surface energies of supported NPs. Binding energies of M_N nanoparticles to the substrate, $E_{bind}[M_N]$, were calculated as $E_{bind}[M_N] = E[MgO] + E[M_N] - E[M_N/MgO]$. With these definitions, smaller Δ_{exc} values indicate higher NP stability and more positive E_{bind} values correspond to stronger chemical binding. In the equations above, $E[M_N]$ and $E[M_N/MgO]$ are the energies of optimized M_N nanoparticles unsupported and supported on MgO(100), respectively. $E[M_{bulk}]$ is the energy of one metal atom in the bulk crystal, E[MgO] – the energy of MgO supercell used as a support.

Charge density differences were obtained by subtracting individually calculated charge densities of NP and the MgO(100) support fixed at the geometry of an optimized NP/MgO structure from the charge density of the whole NP/MgO structure, $\Delta\rho = \rho(NP/MgO) - \rho(NP) - \rho(MgO)$. The visualization was performed by VESTA software.[47]

B. Calculations using interatomic potentials

The first selection of the most stable supported metal particles has been performed with interatomic potentials described in details in Refs. 22 and 46. Briefly, metal–metal interaction was accounted for by the second moment approximation to the tight-binding model,[48–50] with parameterization extended up to the second (Pt) and up to the third (Pd) neighbors.[21,23,46] Metal–MgO interaction has been represented by a many-body potential energy surface (PES), which takes into account main energetic characteristic of the metal–oxide interaction and its behavior as a function of metal coverage, so that, e.g., a metal atom surrounded by other metal atoms interacts weaker with the substrate than an isolated metal adatom does.[21,51] Such PES is system-dependent and has been adjusted to reproduce DFT energetics of various types of Pd[52] or Pt[21] deposits on the MgO(100) surface. This form of the IP has already enabled successful studies on equilibrium[21,23,46,53] and growth shapes[54] of MgO-supported Pd and Pt particles.

Since the present study focuses on metal particles with fcc structural motif, we have generated (in the spirit of Refs. 21, 22, and 46) complete families of closed atomic-shell truncated octahedral metal NPs with different size and symmetry of {111} and {100} truncations. These NPs formed either M{100}‖MgO(100) or M{111}‖MgO(100)

epitaxy relation when put on the MgO substrate. In the latter case, we have additionally considered various orientations of the interfacial M{111} plane with respect to the MgO(100) substrate.[21] For each of such initial particles, quenched molecular dynamics runs were performed under conditions tuned as to preserve the initial form of the metal particles and their initial epitaxy relation with the substrate. This enabled determination of local energy minima, corresponding to the 0 K equilibrium states of fcc moieties of different shape, morphology, and epitaxy. Among thousands of particles generated in this way we have pre-selected the most stable structures (according to their surface excess energies) for each epitaxial family.[55]

C. Models

All Pd and Pt NPs considered in this work are constrained to fcc bulk-like arrangement of atoms (Figure 1). Thus, properties of these NPs may be scalable with size[15,16] but according to previous IP studies the NPs themselves may or may not yet be close to global minima at their respective sizes.[24,56] The NP structures were obtained via optimization and selection procedure described above. Furthermore, we considered only the species that fit into p(7 × 7) supercell of MgO(100), that is, the separation between adjacent supported NPs in this supercell had to be larger than 0.5 nm. The biggest NP considered in this work, Pt_{155}, has the diameter of 1.62 nm, while the smallest, Pd_{49}, is 1.18 nm in size.

The NPs feature extended {100} or {111} facets on the side that will bind to MgO (called the bottom side further in the text). Note that at least in the case of supported Pd NPs the predicted most stable shapes are similar to the shapes of bigger NPs derived from experimental data.[31,33] Interestingly, the type of the bottom nanofacet affects the overall morphology of a NP. Namely, NPs with bottom {100} facets are more spherical, than those with {111} facets. Aspect ratios (lateral diameter to height) of the considered NPs with {100} termination on their bottom side are 1.6 ± 0.6, while for NPs terminated by {111} facets on their bottom these values are 2.2 ± 0.7. Experimentally, aspect ratios from 1.2 to 1.6[32,36,37] were reported for Pd NPs that stick to MgO with {100} facets and 1.4 for both types of supported Pt NPs.[21] Note, however, that in some of these works the aspect ratios might have been calculated as the ratio between the lengths of NP side edges to NP height, which would yield $\sim\sqrt{2}$ times smaller calculated values than those listed above.

In the DFT calculations, separation between unsupported NPs was larger than 0.7 nm. Test calculations done at the 1.0 nm separation between unsupported NPs featured only minor changes (<2 meV per atom) with respect to the presented results. Except for a few test calculations, the support (if present) was modelled by two-layer thick p(7 × 7) MgO(100) slab supercells fixed at experimental bulk-derived positions, which yield O–O distance of 297.8 pm. Separation between adjacent slabs with deposited NPs was larger than 1 nm and lateral separation between supported NPs was larger than 0.5 nm. Accuracy of this modelling approach was assessed for the binding energy of Pd_{74} nanoparticle to a smaller p(6 × 6) MgO supercell. The value of binding energy changed by only 70 meV (3 meV per metal atom on the metal-oxide interface) upon increase of the substrate thickness from 2 to 4 layers. The full relaxation of MgO support during geometry optimization changed the binding energy by 1 meV per metal atom on the interface. Upon the increase of substrate supercell from p(6 × 6) (397 pm separation between adjacent NPs) to p(7 × 7) (the separation of 714 pm), the overall binding energies of Pd_{74} changed by 3 meV. IP calculations for both supported and unsupported particles were performed with no periodic boundary conditions applied.

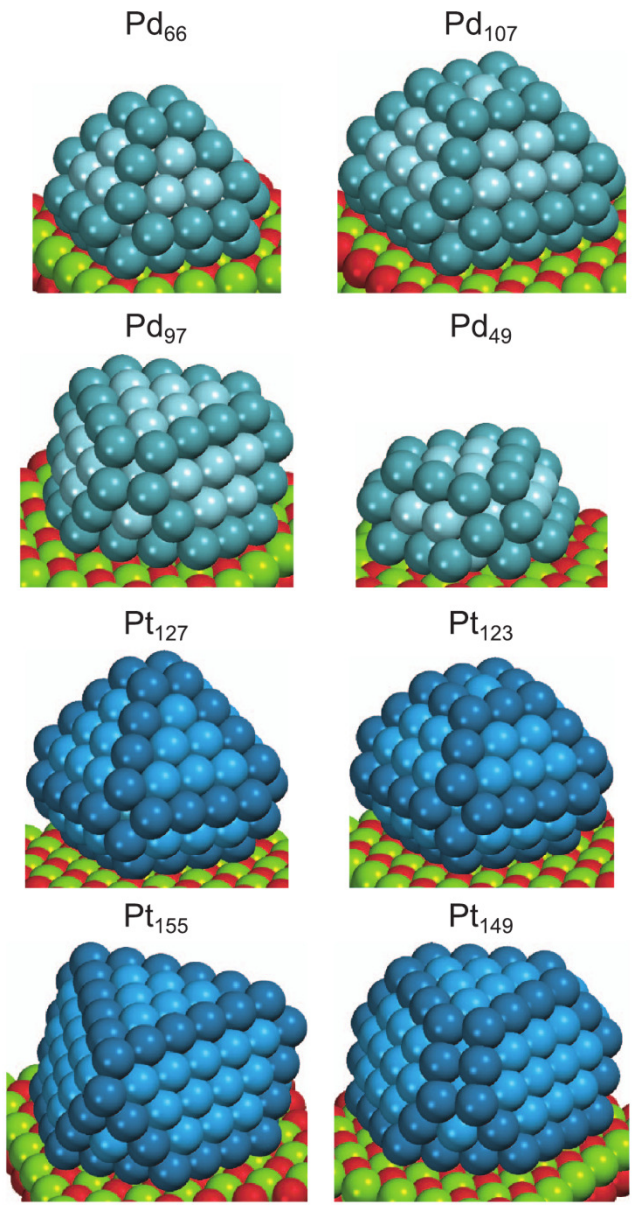

FIG. 1. The most stable (i.e., with the lowest Δ_{exc}) calculated supported NPs of Pd and Pt with {100} or {111} facets in contact with MgO(100). Pd_{127} NP (not shown) with the structure similar to that of Pt_{127} has Δ_{exc} value in between those of Pd_{66} and Pd_{107}. Pd (Pt) atoms on the edges are displayed as turquoise (dark blue) spheres, those on the terraces and in the bulk – by cyan (light blue) spheres; Mg and O atoms are displayed as green and red spheres, respectively.

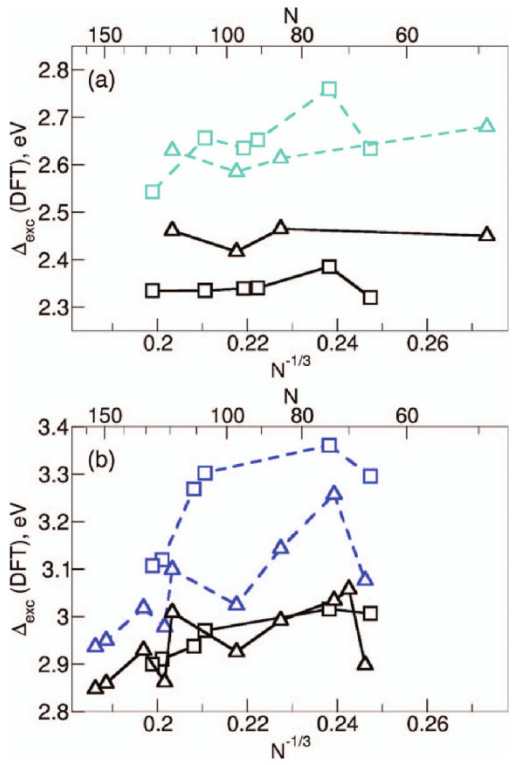

FIG. 2. DFT calculated excess surface energies, Δ_{exc}(DFT), as a function of NP size N, or $N^{-1/3}$ for unsupported (coloured) and supported on MgO(100) (black) (a) Pd and (b) Pt NPs with extended bottom {100} facets (squares) or {111} facets (triangles) on the bottom side (the one in contact with MgO, if present).

III. RESULTS AND DISCUSSION

A. Relative stability of Pd and Pt nanoparticles with different shapes

To analyse relative stabilities of the NPs with different shapes and sizes, we employ excess surface energies, Δ_{exc} (see Sec. II A). This quantity should not depend strongly on NP size and it is expected to converge to a value proportional to the average specific surface energy (Figure 2), reduced by the interaction with the substrate in case of supported NPs. Indeed, the excess surface energies of Pd NPs show no strong dependency on the nanoparticle size N. (Apparent dependency of Δ_{exc} of unsupported Pd NPs with bottom {100} facets on the NP size is due to varying relative area of {100} and {111} facets within the set.) However, one sees that excess surface energies of Pt NPs clearly decrease with size. Actually, the energies show roughly linear dependency on $N^{-1/3}$, a parameter which is proportional to the inverse radius of a NP. This parameter does not only govern average interatomic distances, cohesive energies, and adsorptive properties of metal NPs, but also determines their surface-to-bulk and edge-to-surface ratios.[15,19,20] Thus, the observed linear dependency of Δ_{exc} on $N^{-1/3}$ may indicate that the energy associated with NP edges may significantly contribute to stability of Pt nanoparticles at the considered sizes.

The data (see also Figures S1 and S2 in the supplementary material)[57] show that unsupported Pd NPs with both types of bottom facets have similar stabilities. Deposition on MgO(100) decreases excess surface energies of the Pd NPs with bottom {100} and {111} facets by ∼0.3 and ∼0.15 eV, respectively, making the former significantly more stable. The trends in stability of Pt NPs are somewhat different. The unsupported NPs with bottom {111} facets are clearly more stable than those with {100} facets. Similarly to Pd NPs, upon the interaction with MgO Δ_{exc} of Pt nanoparticles with {100} facets decreases by ∼0.3 eV while for the NPs with bottom {111} facets the decrease is only ∼0.15 eV. Thus, on MgO(100) stabilities of both types of Pt NPs are similar.

Comparison between DFT and IP calculated Δ_{exc} values (Figure 3) reveals that there is a linear dependency between them at least in the case of Pd. This finding makes possible to estimate Δ_{exc}(DFT) from the IP calculated value with inaccuracy $\delta \leq 0.04$ eV for the unsupported species and $\delta \leq 0.10$ eV for the supported Pd NPs. Thus, one can make efficient pre-screening of plausible Pd NP shapes by IP-based optimization and perform DFT calculations only on the lowest-energy structures. The agreement between DFT and IP calculated values is somewhat worse for the Pt NPs with deviations being 0.2 eV for the unsupported particles and 0.11 eV for the supported ones. This is consistent with the fact that the present Pd–Pd interactions have been re-parameterized to improve the energetics of surface atoms,[23] while the standard Pt potential may fail to account for fine variations of Pt excess surface energies with NP size. Nevertheless, even in the case of Pt the interatomic potentials are still able to reproduce

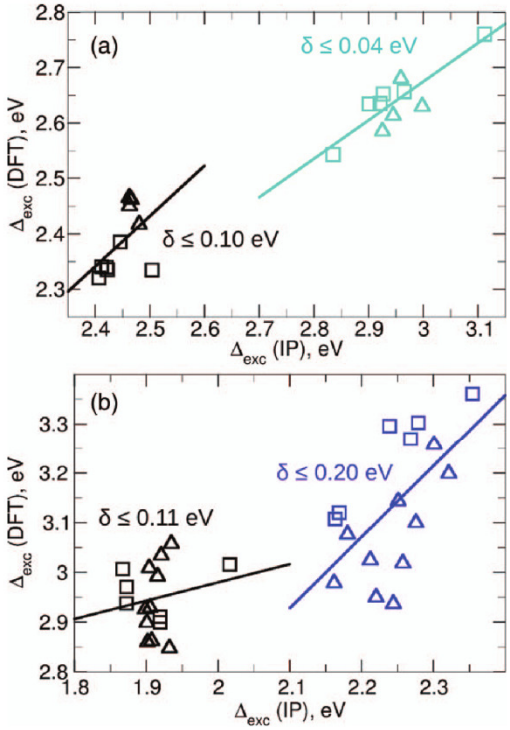

FIG. 3. DFT calculated excess surface energies, Δ_{exc}(DFT), as a function of IP calculated excess surface energies, Δ_{exc}(IP), for unsupported (coloured) and supported on MgO(100) (black) (a) Pd and (b) Pt NPs with extended bottom {100} facets (squares) or {111} facets (triangles) on the bottom side (the one in contact with MgO, if present). Linear regression lines and (maximum) deviations, δ, of Δ_{exc}(DFT) from the linear regression lines are also presented.

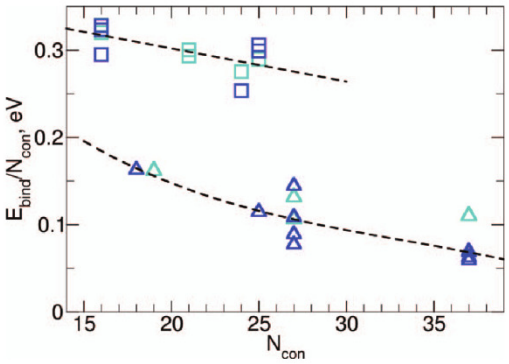

FIG. 4. DFT calculated binding energies to the support, E_{bind}, of Pd (cyan) and Pt (blue) NPs forming M{100}||MgO(100) (squares) and M{111}||MgO(100) (triangles) interfaces per atom on the facet in contact with MgO, N_{con}. The dashed lines are to guide the eye only.

the trend in Δ_{exc}(DFT), and could be used if some caution is applied.

B. Binding energies of metal nanoparticles to MgO(100)

Due to the difference in symmetry, the NPs with bottom {111} facets bind to MgO(100) significantly weaker than NPs with bottom {100} facets (Figure 4). Binding energies per metal atom in contact with MgO, N_{con}, are similar for Pd and Pt NPs and decrease with N_{con} from 0.32 to 0.25 eV for the NPs with bottom {100} facets and from 0.16 to 0.06 eV for the NPs with bottom {111} facets. Interestingly, very similar binding energies of ~0.3 eV per atom were calculated for pseudomorphic Pd_4 clusters adsorbed on MgO(100).[58,59] In principle, one could expect lower binding energies per atom for bigger NPs due to increased mismatch between metal and MgO lattices. Earlier IP studies of Pd and Pt NPs on MgO(100) predicted a similar weakening of binding interaction but only for NPs with bottom {100} facets, which eventually results in the NPs forming M{111}||MgO(100) interface becoming more stable.[21,23,46] The most recent experimental studies of Pd NPs on MgO estimated the binding energy of Pd{100}||MgO(100) interface to be 0.24 eV per atom in contact (0.5 J m^{-2}),[31] while several earlier studies reported higher values in the range of 0.43–0.53 eV per atom in contact (0.9–1.1 J m^{-2}).[36,37,60]

One can notice significant spread of E_{bind}/N_{con} values for Pt NPs that expose {111} facet consisting of 27 atoms on the bottom side. The reason is that some of these NPs (as well as Pt_{122} with 25 atoms on the bottom facet) are found to prefer not to form a full contact with MgO(100) substrate, but to bind to it with only a part of the bottom {111} facet (Figure S3 in the supplementary material).[57] This allows for smaller NP-substrate separation in the areas where metal atoms are located almost above O atoms and bigger separation in the areas where M atoms are closer to Mg than to O atoms. This reduces repulsive interaction between the NPs and Mg atoms of the substrate and, in turn, leads to stronger binding. Note that this feature is present only in DFT calculations, while IP yield full contact between the discussed Pt NPs and MgO(100) substrate.

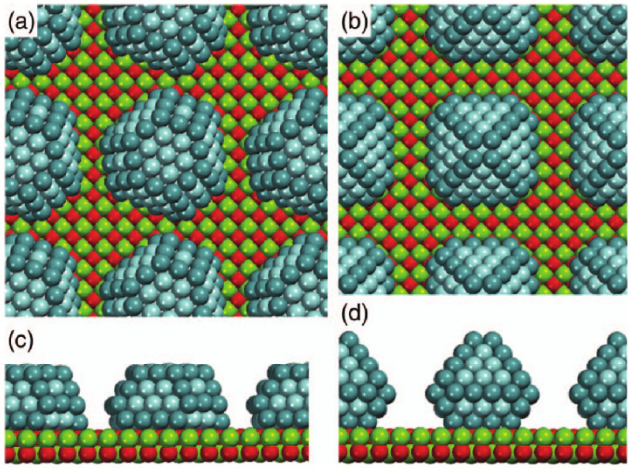

FIG. 5. Pd NPs on MgO support: (a) and (c) top and side views of Pd_{119} forming Pd{111}||MgO(100) interface and (b) and (d) top and side views of Pd_{127} forming Pd{100}||MgO(100) interface. Pd atoms (on the edges) are displayed as cyan (turquoise) spheres; Mg and O atoms are displayed as green and red spheres, respectively. Structures of the respective bare and supported Pt_{119} and Pt_{127} NPs are similar.

Except for one outlier, the agreement between the IP and DFT calculated binding energies is satisfactory for the NPs with bottom {100} facets (Figure S4 in the supplementary material).[57] However, for the NPs forming M{111}||MgO(100) interface the agreement is worse. The reason is that the DFT results show significant variation of the binding energies among these NPs, while the IP calculations tend to yield very similar binding energies for all NPs of this type (in line with Refs. 21 and 23).

C. Structure of the interface between the nanoparticles and MgO(100)

In this and Secs. III D 1–III D 3, we focus on the structure and properties of M_{119} and M_{127} NPs (Figure 5) as typical representatives of the whole set. M_{127} are the biggest considered NPs with bottom {100} facets and are very stable compared to other studied NPs. M_{119} NPs terminated by {111} facets on the bottom side are chosen because of their size similar to M_{127} and good relative energetic stability, at least in the case of Pd.

Experimentally, it was found that when relatively small Pd and Pt NPs stick to MgO with extended {100} facets, metal atoms are located approximately above O atoms with $[001](100)_M||[001](100)_{MgO}$ epitaxy (Figure 6).[21,35,36] This is also in line with preferential adsorption of isolated transition metal atoms[61,62] and transition metal films[63] above O atoms on MgO(100). However, the lateral positions of metal and O atoms are not exactly the same due to the mismatch of Pd or Pt lattice parameters with those of MgO(100). In the present study, the preference for this adsorption configuration is supported by IP optimization of the interface structure. Also we corroborated it by DFT calculations of M_{74} NPs located in various adsorption configurations on p(6 × 6) MgO(100) supercell. Metal atoms tend to bind to O atoms on the surface even when NPs form M{111}||MgO(100) interfaces.

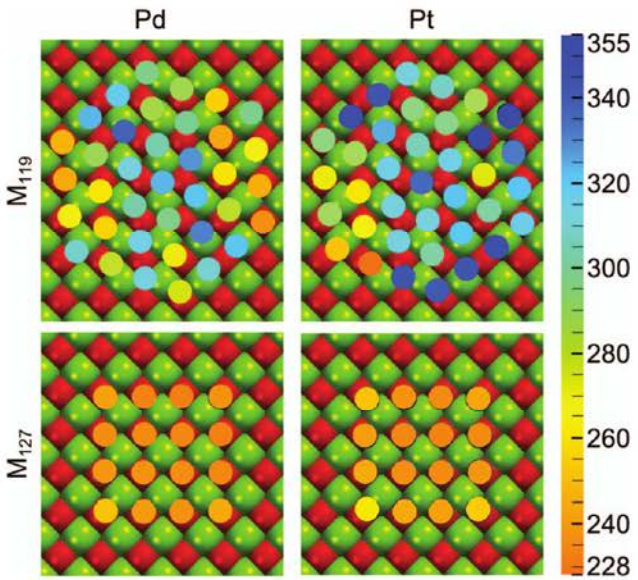

FIG. 6. Colour coded metal–oxygen distances on the interface between M_{119}, M_{127} NPs and MgO(100) substrate calculated by DFT. Mg and O atoms are displayed as green and red spheres.

However, in this case not all metal atoms are located above O atoms due to the distinct symmetries of the two surfaces. Also the NPs with bottom {111} facets are calculated to be always disoriented by a different angle with respect to MgO(100) lattice, which allows for higher number of M–O contacts for each particular NP shape. A fraction of NPs with similar misalignment of up to 5° in magnitude was observed experimentally for bigger Pt NPs, despite that the majority of NPs had $[1\bar{1}0](111)_{Pt}\|[011](100)_{MgO}$ or (less often) $[1\bar{1}0](111)_{Pt}\|[001](100)_{MgO}$ epitaxy.[21]

As one can see in Figure 6, the considered M_{119} NPs exhibit a variety of M–O distances on their interface with MgO, which is a natural consequence of different symmetries of M(111) and MgO(100) surfaces. On the $Pd_{119}\|MgO(100)$ interface, one can notice a Moiré-like pattern with two strongly bound regions with Pd–O distances of 240–260 pm on the edges separated by a loosely bound region with the distances up to 325 pm. One sees only one tightly bound area on the $Pt_{119}\|MgO(100)$ interface. The unusual pattern of Pt–O distances in the case of supported Pt_{119} is due to highly corrugated profile of the bottom {111} facet of unsupported Pt_{119} species caused by internal strain. For both NPs, perturbations of atomic positions induced by the interaction with MgO strongly decrease in magnitude with increasing distance from the substrate. In general, the interatomic potentials reproduce the pattern observed in the DFT calculations; however, they tend to underestimate M–O distances in loosely bound areas (Figure S5 in the supplementary material).[57]

The variation of M–O distances is much smaller on $M_{127}\|MgO(100)$ interface and is caused by the difference between lattice parameters of M(100) surfaces with those of MgO(100). In general, the Pd–O distances are 233–250 pm long and the Pt–O distances are 234–260 pm long. The distances appear not to be distributed in a symmetric fashion across the interface, which indicates that binding energies of the NPs vary only slightly upon a small lateral displacement in the vicinity of the considered epitaxial adsorption mode. This happens because any small displacement will make some M–O bonds longer and weaker, but other bonds shorter and stronger, producing only small overall effect on the binding energy. Experimentally, the Pd–O distances on the Pd{100}‖MgO(100) interface were measured to be 222 ± 3 pm,[34,35] which is somewhat shorter than the values obtained in the present work. This difference can be partially attributed to overestimated size of Pd atoms by the employed rPBE functional. This notion is reflected by the fact that calculated nearest Pd–Pd distances in bulk crystals exceed by ∼6.5 pm the experimental values.[64] Note also that only a minor fraction of pseudomorphic Pd (that resides exactly above O atoms due to adoption of the MgO lattice parameter) is present at the interface, which is in disagreement with some experiments.[34] The latter, however, were performed at room temperature, which might be not enough to reach thermal equilibrium. In fact, IP calculations of bigger supported NPs suggest that the mismatch between M(100) and MgO(100) lattice parameters leads to the formation of Moiré-like patterns of interface misfit dislocations on the M{100}‖MgO(100) interface for Pd NPs bigger than 3.5 nm and Pt NPs bigger than 5 nm.[21,46]

D. Influence of MgO(100) support on properties of Pd and Pt NPs

A common point of criticism of computational studies when they deal with sufficiently big unsupported NPs is that they do not include into consideration effect of support material on NP properties. Thus, the employed unsupported models are thought not to represent experimental systems sufficiently well. This notion is often invoked to rationalize differences between results of the theoretical and experimental investigations without precise understanding of what is the role of support in every particular case. In this section, we assess the influence of relatively chemically inactive MgO(100) support on such NP properties as interatomic distances, their electronic structure, and charge accumulated on metal atoms.

1. *Interatomic distances within the NPs*

A detailed investigation of the nearest neighbor interatomic distances, d(M–M), within unsupported and supported M_{119} and M_{127} NPs reveals that the effect of MgO(100) support on partition of the distances is minor (Figure 7). The induced change of average interatomic distances is calculated to be 1.3 pm for Pt_{119} and less than 1 pm in all other cases. The increased average d(M–M) in supported Pd_{119}, Pd_{127}, and Pt_{127} in comparison with respective unsupported species is probably due to stabilization of the bottom NP facets by MgO and concomitant reduction of internal pressure caused by surface tension. Another rationalization for such an elongation could be strain caused by incommensurability of metal lattice with that of MgO(100) support, which is clearly the

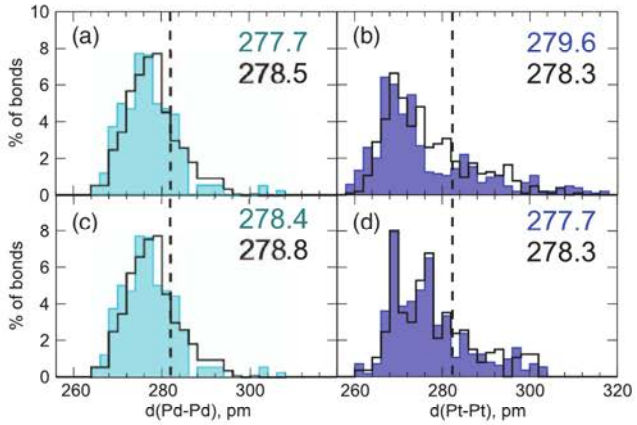

FIG. 7. Partitions of interatomic distances in supported (solid line) and unsupported (filled area) NPs (a) Pd_{119}, (b) Pt_{119}, (c) Pd_{127}, and (d) Pt_{127} calculated by DFT. Average interatomic distances of the unsupported (upper value) and supported NPs (lower value) are also presented in each panel. Dashed lines mark DFT optimized interatomic distances in the bulk crystals, 282 and 282.5 pm for Pd and Pt, respectively.

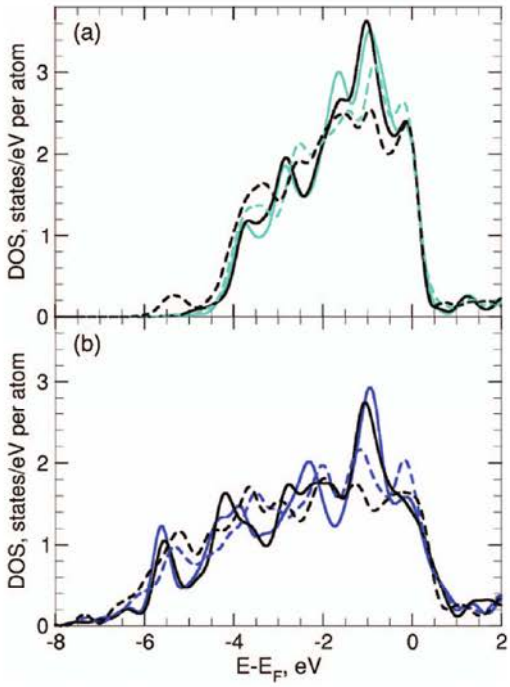

FIG. 8. DOS projected on the metal atoms located on the bottom edges (those in contact with MgO, if present) of unsupported (coloured) and supported (black) M_{119} (solid line) and M_{127} (dashed line), where (a) M = Pd, (b) M = Pt. Electron energies are given with respect to the Fermi level.

case for small supported Pd clusters.[58,65] However, a detailed look on the M–M distances on M_{119}‖MgO and M_{127}‖MgO interfaces shows that they are not significantly longer than the average d(M–M) in the respective NPs. This finding and the relatively small binding energies (per M atom in contact) of NPs to MgO(100) suggest that the change of average interatomic distances is not governed by the incommensurability. Note that for Pt_{119} NPs the average interatomic distances are smaller in the supported species than in the unsupported one. This happens because the support decreases corrugation of the bottom {111} facets caused by the internal strain in the unsupported species. Note that in all the cases average interatomic distances in the supported NPs are still > 3 pm shorter than the bulk-optimized values. However, this difference may become experimentally undetectable already for 2–3 times bigger NPs.[66]

The internal strain in all the considered NPs is reflected by the wide distributions of d(M–M), which show not only the expected presence of very short M–M bonds, but also the existence of unusually long bonds significantly exceeding the bulk-optimized values. Namely, M–M distances of up to 310 and 320 pm are observed in Pd_{119} and Pt_{119} NPs, respectively. Even in more spherical Pd_{127} and Pt_{127} NPs, there are M–M bonds of 294 and 304 pm, respectively. A closer look reveals that the longest bonds are formed between terrace and bulk atoms located close to edges, while the shortest bonds connect edge atoms (Figures S6 and S7 in the supplementary material).[57] This could be rationalized by a significant inward displacement of edge atoms due to their lower coordination, which causes a considerable shortening of M–M bonds between edge atoms and their neighbors. In turn, this induces an important elongation of certain bonds between the terrace and bulk atoms in the direct edge vicinity and pushes the terrace atoms outwards. In this way, the displacement of edge atoms causes curvature of {111} facets on the sides of the considered metal NPs.

2. Effect of MgO on electronic structure of the supported metal NPs

In general, the influence of MgO support on electronic structure of sufficiently big metal NPs is rather limited. Figure 8 displays DOS of M_{119} and M_{127} species projected on metal atoms located on the NP edges in contact with MgO. One can see that the effect of MgO on the electronic structure of these atoms is very moderate despite their immediate vicinity to the substrate. Even smaller changes are revealed by the overall DOS of the NPs (not shown). From this observation, we conclude that, not surprisingly, the effect of certain (chemically inert) supports on the electronic structure of deposited metal NPs of considerable size is negligible and supported NPs can be reliably represented by unsupported species in theoretical studies.

In fact, the electronic structure of the considered atoms seems to depend more on the NP shape, than on the presence of the support. This is due to the fact that bottom edges in M_{119} NPs are intersections of two {111} facets with the angle of $\arccos(1/3) = 71^\circ$, while {100} and {111} facets forming the bottom edge of M_{127} have the angle of $\arccos(\sqrt{3}/3) = 125^\circ$ between them. This difference in the edge structures, in turn, affects coordination numbers of metal atoms on the edges, 6 for M_{119} and 7 for M_{129}, which is very important for the electronic properties of an atom.

3. Charge transfer between the supported NPs and MgO(100)

Analysis of Bader charges[67] in supported M_{119} and M_{127} nanoparticles indicates that there is a transfer of 2.5–3.5

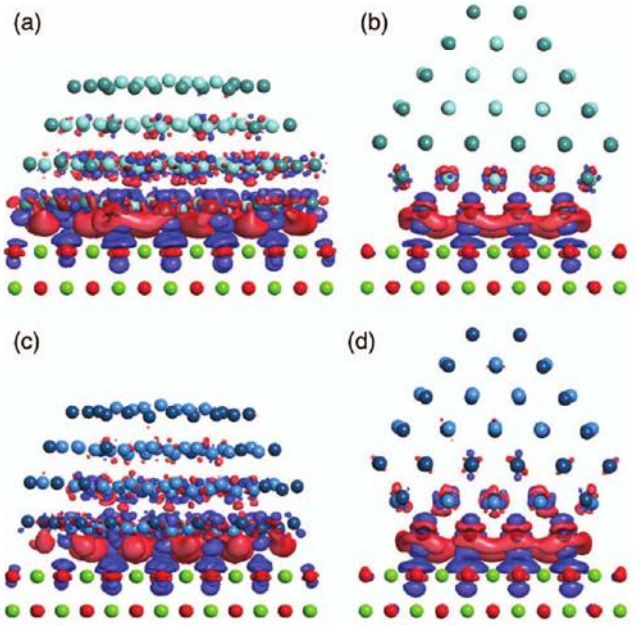

FIG. 9. Charge density difference plots for deposition of (a) Pd_{119}, (b) Pd_{127}, (c) Pt_{119}, and (d) Pt_{127} NPs on MgO(100). Red (blue) areas indicate regions of electron accumulation (depletion). The density difference was calculated as $\Delta\rho = \rho(\text{NP/MgO}) - \rho(\text{NP}) - \rho(\text{MgO})$ with geometries of NP and MgO fixed on those from optimized NP/MgO system. Pd (Pt) atoms on the edges are displayed as turquoise (dark blue) spheres, those on the terraces and in the bulk – by cyan (light blue) spheres; Mg and O atoms are displayed as green and red spheres, respectively.

electrons from MgO to the NPs. However, due to the significant size of the NPs this leads to average charges on Pd and Pt atoms of only −0.02 or −0.03, respectively (here and further in the text, charges are given in elementary charge units). The accumulated charge is mostly located on the metal atoms of bottom facets, which carry 0.09–0.14 excess electrons on average. Notably, due to the significant area of bottom {111} facets in M_{119}, which consist of 37 atoms, the negative charge accumulated on the bottom facets actually somewhat exceeds the overall charge on the NP by −0.2 for Pd_{119} and −0.8 for Pt_{119}. This indicates a significant polarization of the charge density within the NP itself: the bottom part being negatively charged, the middle part – slightly positively charged, and no noticeable charge on the top part.

A more detailed, although not quantitative, insight can be gained from charge density difference plots calculated for deposition of M_{119} and M_{127} on MgO(100) (Figure 9), which show charge redistribution and electron transfer from the substrate to the NPs. In line with Ref. 68, we find that to minimize the Pauli repulsion between the NPs and MgO and to fit to non-uniform electrostatic potential near the substrate the electron density partially shifts from p(z) orbitals of O and $d(z^2)$ orbitals of M atoms on the interface to d(xy) and $d(x^2–y^2)$ orbitals of the metal atoms (z is the direction normal to the substrate). Due to the highly polarizable nature of the NPs, the electron transfer induces charge redistribution in the whole nanoparticle, but it decays rapidly with increasing distance from the substrate. These results are in line with conclusions of previous studies of CO adsorption on small Ni clusters on alumina, which revealed that the substrate-induced change of adsorptive properties is limited basically to the metal atoms in direct contact with the substrate.[69] Another important aspect is that the electron density is drawn from O atoms below the NPs. While it seems to be not so important for MgO substrate, in other oxide materials it could cause significant surface reconstruction.

IV. CONCLUSIONS

Pd and Pt nanoparticles consisting of 49–155 atoms and their deposition onto MgO(100) support were studied by means of interatomic potentials and electronic structure calculations. First, optimization and pre-selection of shapes and interface configurations of the supported NPs was performed with interatomic potentials keeping fcc motif intact. Then the most stable structures at a given NP size were locally re-optimized via DFT calculations. This enabled the considered nanoparticles and their adsorption modes to resemble NP structures observed in experiment.

Pd and Pt NPs stick to MgO(100) via extended {100} or {111} facets with adhesion energies of ∼0.3 and ∼0.1 eV per metal atom in contact, respectively (for both metals). Despite that {100} facets bind much stronger to MgO(100) due to the matching symmetry of the two surfaces, their intrinsic stability is lower than that of {111} facets. This results in Pd nanoparticles forming Pd{100}‖MgO(100) interface to be more stable than those forming Pd{111}‖MgO(100) interface, while the stabilities of both types of supported Pt NPs are similar. However, in the unsupported state Pt NPs with only extended {111} facets are more stable than those with one extended {100} facet, at the same time both types of unsupported Pd nanoparticles have similar stability. Thus, the presence of a support is shown to alter relative stability of different NP shapes for both metals.

Effect of the support on nanoparticle properties other than the shape is found to be minor. Partitions of interatomic distances in Pd and Pt NPs were found to marginally change upon deposition on MgO and small change in average metal–metal distances was calculated. Influence of MgO on the densities of states of the nanoparticles is also minor, even when DOS are projected on edge metal atoms in direct contact with the substrate. In fact, the nanoparticle shape seems to be more important both for interatomic distances within the NP and for its electronic structure. Although calculations reveal that there is charge transfer of 2.5–3.5 electrons from the support to the NPs of ∼120 atoms, the electron transfer is delocalized on many atoms in the vicinity of MgO, but does not involve metal atoms more distant from the substrate. Thus, no significant changes in adsorptive properties and activity of metal NPs upon deposition on MgO(100) should be expected in most cases (at least for adsorption or active sites at some distance from the substrate). However, for more reactive substrates such as reducible oxides or materials with several feasible crystal structures one can expect a bigger electron transfer and more complex metal-oxide interplay. Also, if a deposited material features two phases close in energy, e.g., fcc and hcp motifs in Ni NPs, then even such an inert support as MgO(100) could favor formation of one phase or another

and, thus have a considerable effect on the properties of the system.[70,71]

To conclude, this study shows that chemically inert supports, represented here by MgO(100) surface, do not alter significantly properties of deposited nanoparticles despite a possible modification of their shapes. Nevertheless, it is demonstrated that consideration of a support in electronic structure studies of adsorptive, reactive, and other properties of sizable NPs is already feasible and it should not be neglected in state-of-the-art investigations in pertinent cases. In this work, we performed the first step in such an investigation, i.e., we determined which NP and interface structures have the lowest energies on a given support and also characterized the NP-support interaction.

ACKNOWLEDGMENTS

S.M.K. thanks the Spanish Ministerio de Educación for a pre-doctoral FPU grant AP2009-3379. H.A.A. is grateful for the post-doctoral grant SB2010-0172 (Spain) and the FP7 programme (project Beyond Everest). Financial support has been provided by the European Community (Project ChipCAT, Reference 310191 FP7-NMP.2012.1.1-1) and the Spanish MICINN (CTQ2012-34969 and FIS2008-02238). This work is also a part of COST Actions CM1104 and MP1103. Computer resources, technical expertise and assistance provided by the Red Española de Supercomputación are gratefully acknowledged.

[1]*Handbook of Heterogeneous Catalysis*, edited by G. Ertl, H. Knözinger, F. Schüth, and J. Weitkamp, 2nd ed. (Wiley-VCH, Weinheim, 2008).
[2]K. P. de Jong, L. C. A. van den Oetelaar, E. T. C. Vogt, S. Eijsbouts, A. J. Koster, H. Friedrich, and P. E. de Jongh, J. Phys. Chem. B **110**, 10209 (2006).
[3]G. Ertl, Angew. Chem., Int. Ed. **47**, 3524 (2008).
[4]U. Diebold, Surf. Sci. Rep. **48**, 53 (2003).
[5]M. Bäumer and H.-J. Freund, Prog. Surf. Sci. **61**, 127 (1999).
[6]H.-J. Freund, Chem. Eur. J. **16**, 9384 (2010).
[7]F. Viñes, Y. Lykhach, T. Staudt, M. P. A. Lorenz, C. Papp, H.-P. Steinrück, J. Libuda, K. M. Neyman, and A. Görling, Chem. Eur. J. **16**, 6530 (2010).
[8]S. Schauermann, J. Hoffmann, V. Johánek, J. Hartmann, J. Libuda, and H.-J. Freund, Angew. Chem., Int. Ed. **41**, 2532 (2002).
[9]K. M. Neyman and F. Illas, Catal. Today **105**, 2 (2005).
[10]J. K. Nørskov, T. Bligaard, J. Rossmeisl, and C. H. Christensen, Nat. Chem. **1**, 37 (2009).
[11]I. X. Green, W. Tang, M. Neurock, and J. T. Yates, Science **333**, 736 (2011).
[12]I. X. Green, W. Tang, M. Neurock, and J. T. Yates, Angew. Chem., Int. Ed. **50**, 10186 (2011).
[13]K. M. Neyman and S. Schauermann, Angew. Chem., Int. Ed. **49**, 4743 (2010).
[14]S. M. Kozlov, G. F. Cabeza, and K. M. Neyman, Chem. Phys. Lett. **506**, 92 (2011).
[15]I. V. Yudanov, A. Genest, and N. Rösch, J. Cluster Sci. **22**, 433 (2011).
[16]S. M. Kozlov and K. M. Neyman, Top. Catal. **56**, 867 (2013).
[17]I. V. Yudanov, R. Sahnoun, K. M. Neyman, and N. Rösch, J. Chem. Phys. **117**, 9887 (2002).
[18]H. A. Aleksandrov, F. Viñes, W. Ludwig, S. Schauermann, and K. M. Neyman, Chem.-Eur. J. **19**, 1335 (2013).
[19]A. Roldán, F. Viñes, F. Illas, J. M. Ricart, and K. M. Neyman, Theor. Chem. Acc. **120**, 565 (2008).
[20]F. Viñes, F. Illas, and K. M. Neyman, J. Phys. Chem. A **112**, 8911 (2008).
[21]J. Olander, R. Lazzari, J. Jupille, B. Mangili, and J. Goniakowski, Phys. Rev. B **76**, 075409 (2007).
[22]R. Ferrando, G. Rossi, A. C. Levi, Z. Kuntová, F. Nita, A. Jelea, C. Mottet, G. Barcaro, A. Fortunelli, and J. Goniakowski, J. Chem. Phys. **130**, 174702 (2009).
[23]J. Goniakowski, A. Jelea, C. Mottet, G. Barcaro, and A. Fortunelli, J. Chem. Phys. **130**, 174703 (2009).
[24]G. Rossi, C. Mottet, F. Nita, and R. Ferrando, J. Phys. Chem. B **110**, 7436 (2006).
[25]H.-U. Blaser, A. Indolese, A. Schnyder, H. Steiner, and M. Studer, J. Mol. Catal. A: Chem. **173**, 3 (2001).
[26]N. R. Shiju and V. V. Guliants, Appl. Catal., A **356**, 1 (2009).
[27]S. M. Kozlov, H. A. Aleksandrov, L. V. Moskaleva, M. Bäumer, and K. M. Neyman, in *Comprehensive Inorganic Chemistry II* (Second edition), edited by J. Reedijk and K. Poeppelmeier, Vol. 7, Surface Inorganic Chemistry and Heterogeneous Catalysis, edited by R. Schlögl and J. W. Niemantsverdriet (Elsevier, Oxford, 2013), p. 475.
[28]S. Kishore, J. A. Nelson, J. H. Adair, and P. C. Eklund, J. Alloys Compd. **389**, 234 (2005).
[29]S. K. Mohapatra, M. Misra, V. K. Mahajan, and K. S. Raja, J. Phys. Chem. C **111**, 8677 (2007).
[30]C. Gatel, P. Baules, and E. Snoeck, J. Cryst. Growth **252**, 424 (2003).
[31]P. Nolte, A. Stierle, N. Kasper, N. Y. Jin-Phillipp, N. Jeutter, and H. Dosch, Nano Lett. **11**, 4697 (2011).
[32]P. Nolte, A. Stierle, N. Kasper, N. Y. Jin-Phillipp, H. Reichert, A. Rühm, J. Okasinski, H. Dosch, and S. Schöder, Phys. Rev. B **77**, 115444 (2008).
[33]N. Kasper, A. Stierle, P. Nolte, Y. Jin-Phillipp, T. Wagner, D. G. de Oteyza, and H. Dosch, Surf. Sci. **600**, 2860 (2006).
[34]G. Renaud, A. Barbier, and O. Robach, Phys. Rev. B **60**, 5872 (1999).
[35]G. Renaud and A. Barbier, Surf. Sci. **433–435**, 142 (1999).
[36]C. Revenant, F. Leroy, R. Lazzari, G. Renaud, and C. R. Henry, Phys. Rev. B **69**, 035411 (2004).
[37]G. Renaud, R. Lazzari, C. Revenant, A. Barbier, M. Noblet, O. Ulrich, F. Leroy, J. Jupille, Y. Borensztein, C. R. Henry, J.-P. Deville, F. Scheurer, J. Mane-Mane, and O. Fruchart, Science **300**, 1416 (2003).
[38]A. Bruix, A. Migani, G. N. Vayssilov, K. M. Neyman, J. Libuda, and F. Illas, Phys. Chem. Chem. Phys. **13**, 11384 (2011).
[39]T. Schalow, B. Brandt, D. E. Starr, M. Laurin, S. K. Shaikhutdinov, S. Schauermann, J. Libuda, and H.-J. Freund, Phys. Chem. Chem. Phys. **9**, 1347 (2007).
[40]G. Kresse and J. Furthmuller, Phys. Rev. B **54**, 11169 (1996).
[41]B. Hammer, L. B. Hansen, and J. K. Nørskov, Phys. Rev. B **59**, 7413 (1999).
[42]G. Kresse and D. Joubert, Phys. Rev. B **59**, 1758 (1999).
[43]M. Methfessel and A. T. Paxton, Phys. Rev. B **40**, 3616 (1989).
[44]H. J. Monkhorst and J. D. Pack, Phys. Rev. B **13**, 5188 (1976).
[45]T. Halicioglu, Phys. Status Solidi B **199**, 345 (1997).
[46]W. Vervisch, C. Mottet, and J. Goniakowski, Phys. Rev. B **65**, 245411 (2002).
[47]K. Momma and F. Izumi, J. Appl. Crystallogr. **41**, 653 (2008).
[48]R. P. Gupta, Phys. Rev. B **23**, 6265 (1981).
[49]V. Rosato, M. Guillopé, and B. Legrand, Philos. Mag. A **59**, 321 (1989).
[50]F. Cyrot-Lackmann and F. Ducastelle, Phys. Rev. B **4**, 2406 (1971).
[51]J. Goniakowski, Phys. Rev. B **58**, 1189 (1998).
[52]L. Giordano, J. Goniakowski, and G. Pacchioni, Phys. Rev. B **64**, 075417 (2001).
[53]A. Jelea, C. Mottet, J. Goniakowski, G. Rossi, and R. Ferrando, Phys. Rev. B **79**, 165438 (2009).
[54]J. Goniakowski and C. Mottet, Phys. Rev. B **81**, 155443 (2010).
[55]J. Goniakowski and C. Mottet, J. Cryst. Growth **275**, 29 (2005).
[56]F. Baletto, R. Ferrando, A. Fortunelli, F. Montalenti, and C. Mottet, J. Chem. Phys. **116**, 3856 (2002).
[57]See supplementary material at http://dx.doi.org/10.1063/1.4817948 for additional figures.
[58]I. V. Yudanov, S. Vent, K. Neyman, G. Pacchioni, and N. Rösch, Chem. Phys. Lett. **275**, 245 (1997).
[59]A. V. Matveev, K. M. Neyman, G. Pacchioni, and N. Rösch, Chem. Phys. Lett. **299**, 603 (1999).
[60]H. Graoui, S. Giorgio, and C. R. Henry, Surf. Sci. **417**, 350 (1998).
[61]I. Yudanov, G. Pacchioni, K. Neyman, and N. Rösch, J. Phys. Chem. B **101**, 2786 (1997).
[62]K. M. Neyman, C. Inntam, V. A. Nasluzov, R. Kosarev, and N. Rösch, Appl. Phys. A **78**, 823 (2004).
[63]J. Goniakowski, Phys. Rev. B **59**, 11047 (1999).
[64]P. Janthon, S. M. Kozlov, F. Viñes, J. Limtrakul, and F. Illas, J. Chem. Theory Comput. **9**, 1631 (2013).
[65]K. M. Neyman, N. Rösch, and G. Pacchioni, Appl. Catal., A **191**, 3 (2000).

[66]L. Pasquini, F. Boscherini, E. Callini, C. Maurizio, L. Pasquali, M. Montecchi, and E. Bonetti, Phys. Rev. B **83**, 184111 (2011).
[67]R. F. W. Bader, *Atoms in Molecules: A Quantum Theory* (Oxford Science, Oxford, 1990).
[68]J. Goniakowski, Phys. Rev. B **57**, 1935 (1998).
[69]G. Pacchioni and N. Rösch, Surf. Sci. **306**, 169 (1994).
[70]R. Ferrando, G. Rossi, F. Nita, G. Barcaro, and A. Fortunelli, ACS Nano **2**, 1849 (2008).
[71]G. Rossi, L. Anghinolfi, R. Ferrando, F. Nita, G. Barcaro, and A. Fortunelli, Phys. Chem. Chem. Phys. **12**, 8564 (2010).

Section 4.2

THE JOURNAL OF PHYSICAL CHEMISTRY C

Article

pubs.acs.org/JPCC

Adsorbed and Subsurface Absorbed Hydrogen Atoms on Bare and MgO(100)-Supported Pd and Pt Nanoparticles

Sergey M. Kozlov,[†] Hristiyan A. Aleksandrov,[†,‡] and Konstantin M. Neyman*[,†,§]

[†]Departament de Química Física and Institut de Química Teòrica i Computacional (IQTCUB), Universitat de Barcelona, c/ Martí i Franquès 1, 08028 Barcelona, Spain

[‡]Faculty of Chemistry and Pharmacy, University of Sofia, 1126 Sofia, Bulgaria

[§]Institucio Catalana de Recerca i Estudis Avançats (ICREA), 08010 Barcelona, Spain

Supporting Information

ABSTRACT: Heterogeneous catalysts customarily contain active metal nanoparticles (NPs) deposited on oxides. It is often difficult to understand in detail the influence of supports on NP properties based solely on experimental data. Here, we study by means of electronic structure calculations the effect of a rather chemically inert defect-free support MgO(100) on adsorption and absorption properties of 1.6 nm large Pd_{127} and Pt_{127} NPs representative of bigger species. We show that metal nanostructuring only slightly affects adsorption of single hydrogen atoms on terrace sites. At the same time, structural flexibility of the NPs increases thermodynamic stability of subsurface H in Pt NPs and seems to kinetically assist absorption of H in both Pd and Pt. For H bound to Pd, NPs influence of the support is only noticeable near the metal−oxide interface, while for Pt NPs H atoms more distant from the interface are also affected. Overall, the support is found to change the binding energies of H to Pd_{127} and Pt_{127} NPs by less than 0.1 eV. Quantitative estimates of the differences between adsorption and absorption properties of bare and MgO-supported noble metal NPs are important for modeling of catalytic systems not featuring strong metal−support interactions.

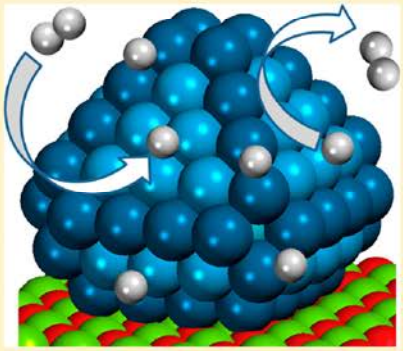

1. INTRODUCTION

Heterogeneous catalysts often consist of metal nanoparticles (NPs) supported on oxide frameworks with complex structure. In many cases, nanostructuring introduces new active sites and significantly affects properties of the metal.[1−3] Probably the most striking example is low-temperature CO oxidation activity of nanoparticulate gold, which is very inactive in the bulk state.[4−6] Moreover, certain (mostly reducible) oxides such as CeO_2 are able to dramatically influence catalytic properties of NPs supported on them,[5,7,8] while effects of other oxides, e.g., SiO_2, Al_2O_3, and MgO, are not so apparent.[9−11] Among the latter, MgO is one of the most inert supports due to its highly ionic and unreactive nature. However, it is still difficult to precisely quantify to what extent MgO changes properties of metal NPs deposited on it in the absence of experiments on unsupported (and unsolvated) NPs.

At the same time, accurate computational density-functional studies of unsupported transition metal NPs for catalytic applications have been performed since 2000s, using "scalability with size" (SwS) concept.[12−15] This concept postulates that properties of NPs with similar structure (e.g., *fcc*) depend smoothly and monotonously on the NP size for sufficiently big species, while they may change abruptly for smaller clusters. For example, Pd and Pt NPs of ∼100 atoms were concluded to be SwS;[1,16,17] that is, results calculated using these models can be reliably extrapolated to bigger NPs often present in experiments and industrial catalysts. Note that this extrapolation may not be valid for the results obtained on high-index Miller surfaces, due to inherent differences between the structures of NP edges and surface steps.[18,19] Because of the considerable size (∼1.5 nm) of the SwS models, until recently it was exceedingly time-consuming to perform first-principles electronic structure calculations of SwS NPs on a support. Therefore, it was not possible to assess the magnitude of a support's influence on properties of sizable NPs from theoretical studies. Nevertheless, some electronic structure studies suggested this influence to be very important, based on the calculated effect of support on properties of rather small metal clusters.[20−22] Such clusters, due to their size, had not only an extreme fraction of atoms on their surface, but also a very high fraction of atoms in contact with the support. One may ask to what extent these strong support effects identified for small clusters would be preserved for bigger metal NPs commonly dealt with in catalytic experiments and applications.

Recently, we have shown that various physical properties of Pd and Pt NPs of >100 atoms with *fcc* structure do not change noticeably upon deposition on MgO(100).[23] The only exception is the thermodynamically prefered shape of the NPs, since the rule governing the NP shape changes from Wulff construction to Wulff−Kaischev construction upon the

Received: March 14, 2014
Revised: June 20, 2014
Published: June 20, 2014

interaction with the support. Other properties, such as distribution of interatomic distances in the NPs, their densities of states (DOS), and charge distribution at some distance from the support, were found to be basically independent of the presence of the support. However, it is not straightforward to conclude from apparently similar geometric and electronic structures of two systems that their chemical activities are also very similar; it is even harder to give any quantitative measure of such similarity. Chemical properties can be very sensitive to relatively small changes in the environment and structure of a nanoparticle.[16,24,25]

Among various chemical properties of nanostructured Pd and Pt, their interaction with H is especially important because Pd is regarded as a material for hydrogen storage[26−28] and because NPs of Pd and Pt are widely used to catalyze reactions involving elementary steps of hydrogenation and dehydrogenation.[29−31] Even though the activity of Pt is only somewhat different from that of Pd in such reactions as methanol[32] and ethanol[33,34] steam reforming as well as water gas shift reaction,[35] Pt seems to be more selective in these processes. To explain the peculiarities in the (un)selectivity of Pd catalysts, the presence of H atoms absorbed in the subsurface region of the catalyst is often invoked, because these species are assumed to be more chemically active and less selective than H atoms on the surface.[36−38] The presence of subsurface H in Pd opens new possibilities to tune activity of Pd-based catalysts, because hydrogen diffusion into the subsurface region of Pd can be promoted[39−41] by nanostucturing[26,36,42] and by subsurface carbon formed under catalyst pretreatment or typical reaction conditions.[43−45]

Weakly bound subsurface H species start to form when Pd samples are exposed to high H_2 pressures and low temperatures, after the surface is saturated with adsorbed H.[31,42,46] Upon further diffusion of H into Pd first α-hydride forms and then β-hydride is formed at higher H content with the exact phase transition conditions depending on the Pd nanostructure.[27,28,47−50] In both hydrides, H atoms occupy octahedral interstitial sites, but in the case of α-hydride there is only negligible lattice expansion, and in the case of β-hydride Pd lattice expands by ∼3%.[49] Bulk Pt is known not to absorb H. However, formation of subsurface H in Pt was suggested in some studies to interpret electrochemical data,[51,52] while in other studies the presence of subsurface H in Pt (albeit at concentration of only 0.29%) was concluded based on the results of nuclear reaction analysis.[53] In contrast with macroscopic Pt samples, absorption of H was found to be feasible in nanoparticulate Pt,[50,54,55] implying intriguing chemical properties of Pt NPs. Investigation of H adsorption on and subsurface absorption in Pd and Pt NPs will enrich the knowledge on the effect of nanostructuring on catalytic action of these metals. In turn, this may eventually help to develop nanostructured catalysts with improved performance.

In the present study, we directly assess the effect of the defect-free MgO(100) support on chemical properties of scalable with size Pd and Pt NPs of >100 atoms probed by adsorption and subsurface absorption of single hydrogen atoms. Herein, we focus on binding of H to {111} nanofacets of 1.6 nm big M_{127} (M = Pd, Pt) species that are energetically stabilized on MgO(100) compared to other considered NPs of similar size.[23] First, we show that these species are indeed SwS with respect to H interaction with {111} facets, and therefore they are suitable to represent {111} facets of bigger NPs common in catalytic experiments. Then, we investigate adsorption and subsurface absorption of H in various positions on M(111), M_{127}, and M_{127}/MgO(100) and quantify differences between results obtained on the different models.

2. COMPUTATIONAL DETAILS

Density-functional calculations were performed using revised Perdew−Burke−Ernzerhof (rPBE) exchange-correlation functional[56] and VASP software package.[57] Projector augmented wave (PAW) technique[58] was employed to describe interactions between core and valence electrons. Electron density was represented using plane-wave basis sets with the cutoff energy of 415 eV and Methfessel-Paxton smearing[59] of 0.1 eV; finally, calculated energies were extrapolated to zero smearing. For $p(3 \times 3)$ metal slabs the reciprocal space was sampled by 5 × 5 × 1 Monkhorst−Pack mesh. Calculations involving NPs were done at Γ point. Geometry optimization with relaxation of H and Pd or Pt atoms was carried out until forces acting on each of the atoms became less than 0.2 eV/nm. Only three top layers of five-layer transition metal slabs were relaxed, while atomic positions in two bottom layers were determined by the respective experimental lattices (r(Pd−Pd) = 275.1 pm, r(Pt−Pt) = 277.2 pm) and kept fixed. When rPBE-optimized lattice parameters for bulk (r(Pd−Pd) = 282.0 pm, r(Pt−Pt) = 282.5 pm) are used for slab construction, binding energies of H to M(111) slabs increase by up to 0.05 and 0.09 eV for adsorption and absorption sites, respectively. Herein we compare calculated data for the NPs to the data for the slabs with the experimental lattice parameters, because on the slabs with the bulk-optimized lattice parameters some absorption sites were found to be locally unstable for H, which hinders the comprehensive comparison in this case. MgO support was modeled by a two-layer thick MgO(100) slab with (7 × 7) surface supercell, where all atoms were fixed at positions corresponding to a cut from bulk with experimental lattice parameter. Note that increasing the thickness of the MgO(100) slab or relaxing its atomic positions was shown to negligibly affect considered metal−support interactions.[23] The distance between the nearest metal slabs was larger than 1.5 nm, while the minimum separation between metal NPs (unsupported and supported) was 0.7 nm. Our benchmark calculations done at 1.0 nm separation between unsupported NPs revealed only minor changes of ∼3 meV in H adsorption energies. For bare M_{127} NPs and M(111) slabs optimized structures were confirmed to be local minima on potential energy surface for H atom by vibrational frequency analysis performed for H atom displaced by ±3 pm in all three Cartesian directions. If not stated otherwise, presented in the following adsorption and absorption energies of H were corrected for zero-point energy (ZPE). Inclusion of the first coordination sphere of H in the vibrational analysis caused changes of ZPE corrections to binding energies of ≤5 meV. When possible, ZPE for H on a given site of a supported NP were assumed to be the same as for H on the corresponding site of the unsupported NP; otherwise they were calculated as described above. Calculations of density of states (DOS) were performed using 9 × 9 × 1 k-point mesh and electron states smearing width of σ = 0.3 eV.

Adsorption and absorption energies of atomic hydrogen on a substrate (in the following referred to as E_H in both cases) were calculated as $E_H = E[\text{substrate}] + {}^1/_2E[H_2] - E[\text{H/substrate}]$. Here, E[H/substrate] is the energy of interacting H and substrate, E[substrate] is the energy of clean substrate (supported or unsupported M_N NP or M(111) slab), and $E[H_2]$ is the energy of H_2 molecule in the gas phase. With this

definition, a positive E_H value indicates an exothermic ad-/absorption. The calculated energy gain due to formation of H_2 molecule from isolated H atoms, 4.57 eV, compares nicely to the experimental value of 4.52 eV.[60]

We considered the following sites for ad-/absorption of H: (1) sites on-*top* of a surface metal atom with tetrahedral *tss'* sites just below these atoms; (2) *bridge* sites above centers of bonds between two surface metal atoms; (3) 3-fold hollow *fcc* and *hcp* surface sites along with octahedral *oss* and tetrahedral *tss* subsurface sites located below these surface sites, respectively. We also considered tetrahedral *t2ss* and octahedral *o2ss* sites between the second and the third surface layers, directly below the just mentioned subsurface sites. Because the *t2ss* and *o2ss* sites are not composed of surface metal atoms, we classify them as bulk sites.

3. COMPARISON BETWEEN EXPERIMENTAL AND CALCULATED BINDING ENERGIES OF H

Binding energies of H to such systems as bulk Pd[47,61] as well as Pd(111)[62] and Pt(111)[63,64] surfaces have been studied experimentally. We use the available experimental data to assess the ability of common exchange-correlation functionals, PW91,[65] rPBE[56] and TPSS,[66] to quantitatively describe interaction of hydrogen with Pd. Unfortunately, the spread of the published experimental values for H adsorption energy on Pt(111) from 0.21 eV in ref 63 to 0.49 eV in ref 64 does not allow us to assess the performance of the functionals for H−Pt interaction. As discussed in section 5.1, our study with rPBE functional showed that for H adsorbed on Pd(111) surfaces *fcc* positions are the most stable, in line with experiment.[67] Therefore, in the case of Pd(111) we compare E_H values calculated at the coverage of 0.11 monolayer (ML) with the experimental value by Conrad et al.[62] concluded to be independent of H coverage up to $\theta = {}^1/_2$ML. Finally, the H:Pd ratio may vary between 0.4 and 0.65 in the β-hydride formed upon absorption,[49,69] but the absorption energy does not seem to depend on H content.[47] We model the absorption by considering a cubic H_2Pd_4 cell with optimized lattice parameters, where H atoms occupy octahedral cavities, in line with experimental results.[70,71]

Data in Table 1 show that calculations with PW91 functional overestimate the strength of H−Pd interaction by ~0.13 eV on average. Functional rPBE, which was designed to provide accurate adsorption energies,[56] underbinds H to Pd by ~0.1 eV and so performs very slightly better than PW91. If the PW91 functional is employed in the present study, the conclusions would stay the same. The only notable difference would be the change of subsurface absorption of H in Pd from slightly endothermic to slightly exothermic. Geometry optimization with TPSS functional was found to be very computationally expensive, so we performed single-point TPSS calculations for geometries optimized with PW91 functional. No ZPE corrections were applied in this case. The strength of H−Pd interactions is underestimated by the TPSS calculations by 0.15 ÷ 0.20 eV, indicating that this functional is not the best choice for the purposes of our study. Therefore, we chose to use rPBE functional in this work. Note, however, inaccuracies of rPBE approach for modeling bulk properties of transition metals.[72]

Table 1. Binding Energies of H Atom, E_H (eV), Calculated in Selected Positions of Pd Using Different Exchange-Correlation Functionals in Comparison with Experiment

H position/substrate	PW91	TPSS[a]	rPBE	experiment
fcc/Pd(111)[b]	0.64	0.25	0.34	0.45[c]
oct/bulk Pd[d]	0.25	0.06	0.10	0.19[e]

[a]TPSS single-point data obtained for PW91 optimized geometry. [b]Calculated at H coverage θ = 0.11 ML. [c]Ref 62. [d]Formation energy of Pd_2H with H in octahedral cavities calculated with k-point mesh 13 × 13 × 13. [e]Refs 47 and 61.

4. SCALABILITY WITH SIZE OF ADSORPTION AND ABSORPTION PROPERTIES OF THE NPS

A recent work employing the same density-functional method and computational parameters as in this study (in combination with an interatomic potentials technique to screen a multitude of plausible structures) addressed adsorption configurations of Pd and Pt NPs of various sizes and shapes on MgO(100).[23] The results obtained in that study were in line with the experimental findings,[73,74] which indicates the suitability of the employed computational approach for studies of the MgO(100)-supported Pd and Pt NPs. From the NPs studied in ref 23, we chose Pd_{127} and Pt_{127} NPs for a detailed investigation, because of their considerable size and high energetic stability compared to analogues under scrutiny.

To determine, whether Pd_{127} and Pt_{127} NPs are in *scalable with size* regime for calculation of H adsorption and absorption energies, we modeled interaction of H with other NPs of similar structure (Figure 1). NPs of 136, 111, and 86 atoms were cut from truncated octahedral M_{140} NPs, by successive removal of atomic layers in [100] direction (later referred to as vertical direction). The M_{127} NPs can also be formed in such a way. We have chosen M_{140} as a basis for other NP models because of its energetic stability in the unsupported form, which was recently corroborated by a theoretical investigation of equilibrium shapes of Pt NPs in different reaction conditions during oxygen reduction.[75] The smallest M_{74} NPs were created by further removing one layer (three atoms) from each of four {100}-type nanofacets located on the sides of M_{86}. NPs

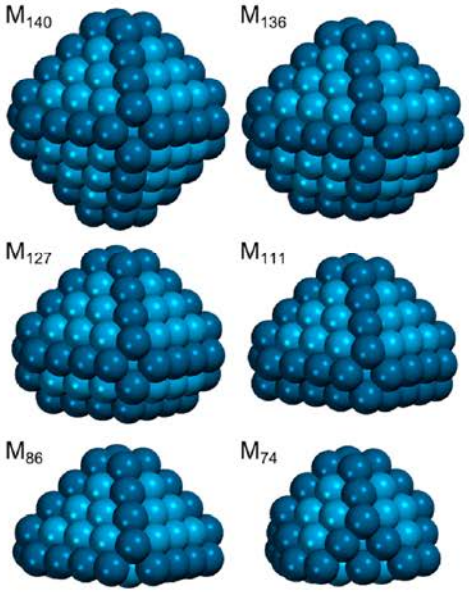

Figure 1. Considered Pd_N and Pt_N NPs. Darker spheres represent edge and corner atoms.

constructed in this way keep C_{4v} symmetry and exhibit bottom {100}-type nanofacets bigger than those predicted by Wulff construction. For comparison with other studies, we also considered truncated octahedral M_{79} models widely used before.[39,40,76−78]

For this set of models, we calculate adsorption of H onto *fcc* sites and subsurface absorption into *oss* sites in the centers of top {111} facets (Figure 2). Note that *oss* sites may not be

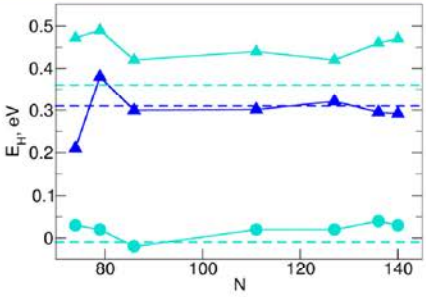

Figure 2. Binding energies E_H of H (not including ZPE) on terrace *fcc* sites (triangles) of Pd and Pt nanoparticles and terrace *oss* sites (circles) of Pd nanoparticles. Pd—cyan, Pt—blue. Energies calculated on (111) slabs are displayed as dashed lines.

locally stable for H in Pt, so they are not discussed. One can see that the binding energies vary insignificantly for Pt_N ($N > 80$) and all considered Pd NPs and, in general, are quite close to the respective values calculated on the slabs. The difference between the values calculated on the slabs and on the NPs may be partially attributed to the different strain on the surface metal atoms in the two models, which affects their adsorptive properties. Therefore, one can conclude that Pd_{127} and Pt_{127} NPs are, indeed, sufficiently big to serve as representative models of nanoparticulate substrate for studies of H adsorption and absorption.

5. ADSORPTION AND ABSORPTION OF H ON BARE AND SUPPORTED ON MgO(100) Pd_{127} AND Pt_{127} NANOPARTICLES

In this section, we discuss H adsorption and absorption on various sites of unsupported and MgO(100)-supported Pd_{127} and Pt_{127} NPs and also compare the results with those calculated on respective M(111) slabs. Due to the abundance of the symmetry inequivalent sites with similar structure on the NPs, our goal was not to study every single one of them but to characterize one site of each type in distinct regions of M_{127}. Namely, we focused on surface and subsurface sites located on terraces and edges of {111} nanofacets in contact and at a distance from the support (Figure 3). Only H species on the former facets are expected to be sensitive to the presence of MgO.

5.1. H on Pd(111) and Pt(111) Surfaces. In agreement with experimental findings for Pd(111),[67,68] H is calculated to be the most stable on 3-fold hollow *fcc* sites. While the other type of 3-fold sites, *hcp*, binds H almost as strongly as the *fcc*, the *top* and *bridge* sites with lower coordination of adsorbed H are not even locally stable (Table 2). We calculate subsurface absorption of hydrogen in Pd(111) to be almost energy-neutral (with respect to $^1/_2H_2$ in gas phase), so it should take place only after all more stable surface sites are populated. Among the subsurface sites, the *oss* is found to be the most stable one. Below the subsurface Pd layer, *o2ss* sites are found to be

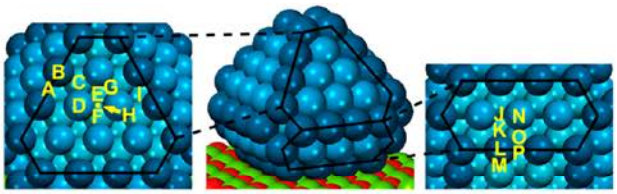

Figure 3. Sketch of a M_{127} nanoparticle supported on MgO(100) with labels of sites on its top and bottom {111} facets considered for H adsorption or subsurface absorption.

significantly more stable for H than tetrahedral *t2ss* sites, in line with preferential occupation of octahedral cavities in Pd hydrides.[70,71] Our results (see Table S1, Supporting Information for values without ZPE corrections) nicely agree with results of previous theoretical studies.[40,47,79−83] Note, however, that the chosen computational technique tends to underestimate energy of H absorption in Pd by almost 0.1 eV (Table 1). Keeping this in mind, one concludes that the presented results corroborate experimental findings[84] that subsurface H can be formed in Pd(111) even after moderate H_2 exposures.

On Pt(111) surface adsorption energy of H on the most stable site, *fcc*, is calculated to be rather close to adsorption energy of H on Pd(111). All the other high-symmetry adsorption sites on Pt(111) are only slightly less stable than the *fcc* sites (Table 3). In fact, *top* sites are calculated to bind H even slightly stronger than *fcc* sites, if ZPE corrections are not taken into account (Table S2, Supporting Information). H absorption in Pt(111) is found to be strongly endothermic, with E_H around −0.45 eV and *tss′* site featuring the highest relative stability. The notably endothermic character of the H absorption may explain minor concentration of subsurface H in Pt(111) measured experimentally.[53] Bulk *o2ss* and *t2ss* sites in Pt(111) are even less stable for H with binding energies of ∼−0.75 eV. In general, our results are in agreement with other computational investigations.[79,81,85−87] However, stronger H−Pt binding was calculated using the same rPBE functional in ref 88. There, E_H values on *tss* and *oss* sites were calculated to be −0.05 and −0.16 eV, respectively.

5.2. H on Pd_{127} and Pt_{127} Nanoparticles. Metal nanostructuring stabilizes H in surface and subsurface sites on terraces of unsupported Pd_{127} by 0.04 ÷ 0.08 eV, whereas H in the second subsurface sites is stabilized by 0.09 in the *o2ss* sites and only 0.02 eV in the *t2ss* sites (Table 2). Previously, the effect of nanostructuring was found to be within 0.08 eV for Pd_{55} and Pd_{79} NPs.[40,79] Note, however, that in ref 40 no systematic investigation of various sites for H adsorption and absorption was performed, and ref 79 dealt with a much smaller Pd NP that did not actually feature terrace adsorption sites for H. *fcc* and *bridge* sites on edges of Pd_{127} are by 0.11 and 0.17 eV more stable than the respective sites on regular Pd(111) surface. Quite substantial stabilization of *bridge* sites on edges of Pd NPs was demonstrated also for other adsorbates, even for those preferring 3-fold sites on the terraces.[76,77,89] The higher flexibility of the NP edges could also stabilize H at adjacent subsurface sites, but instead it seems to lower H subsurface → surface migration barriers to such extent that the subsurface sites become locally unstable. Therefore, the observed[37,84] pivotal role of the low-coordinated sites for surface ↔ subsurface migration of H is not due to more favorable thermodynamic stability of the absorbed species. Instead, higher flexibility of the NP edges is probably responsible for

Table 2. Calculated Binding Energies of *H*, E_H (eV), on Bare and Supported Pd_{127} Nanoparticles and Pd(111) Slabs

site	Pd(111)[a]		Pd_{127}[b]			Pd_{127}/MgO(100)[b]	
fcc	0.34	0.39	0.42	0.33	0.38	0.40	0.40
	(0.39)	E	I	K	E	I	K
hcp	0.30	0.32	0.38	0.36	0.35	0.38	0.31
	(0.35)	C	F	O	C	F	O
bridge	0.22[c]			0.37			
				P			
top	−0.09[c]	−0.01					
	(−0.08)[c]	D					
oss	−0.02	0.02	0.08[c]		0.00	0.07[c]	
		E	I		E	I	
tss	−0.09			−0.04			−0.02
				F			F
tss′	−0.07		−0.01	−0.07		−0.02	−0.02 L
	(0.01)		D	L		D	
o2ss	−0.03	−0.01[c]			−0.02[c]		
	(0.03)						
t2ss	−0.20	−0.18			−0.16		
	(−0.11)						

[a]The values in parentheses are calculated on the slab with the bulk-optimized lattice parameter. [b]Sites are labeled in Figure 3. [c]Unstable sites according to the frequency analysis.

Table 3. Calculated Binding Energies of *H*, E_H (eV), on Bare and Supported Pt_{127} Nanoparticles and Pt(111) Slabs

site	Pt(111)[a]		Pt_{127}[b]			Pt_{127}/MgO(100)[b]	
fcc	0.31	0.32	0.29		0.32	0.28	
	(0.35)	E	I		E	I	
hcp	0.27		0.25[c]				0.11[c]
	(0.31)		F				O
bridge	0.27	0.39	0.28	0.49	0.40	0.32	
	(0.31)	A	H	P	A	H	
		0.33	0.36	0.39		0.41	
		G	J	M		J	
top	0.29	0.32	0.34	0.39	0.30	0.37	
	(0.31)	B	D	L	B	D	
oss	−0.45[c]	−0.47			−0.42		
		E			E		
tss	−0.48		−0.43[d]	−0.46		−0.37[d]	
			F	O		F	
tss′	−0.43		−0.30			−0.25	−0.28
	(−0.41)		D			D	N
o2ss	−0.73	−0.79			−0.76		
	(−0.67)						
t2ss	−0.75	−0.69			−0.66		
	(−0.70)						

[a]The values in parentheses are calculated on the slab with the bulk-optimized lattice parameter. [b]Sites are labeled in Figure 3. [c]Unstable sites according to the frequency analysis. [d]H migrates from the *tss* site F to subsurface site composed of three Pt atoms and located below *bridge* site H.

facilitated kinetics of the H migration, similarly to the subsurface migration of C atoms at the edges of Pd NPs.[90]

Most of the terrace sites on Pt_{127} NP are slightly, by up to 0.06 eV, more stable for H than the respective sites on Pt(111) surface (Table 3). Only terrace *bridge* sites J and subsurface terrace *tss′* sites D are stabilized stronger, by additional ∼0.05 eV. On the one hand, such stabilization is not sufficient to make the subsurface absorption exothermic. On the other hand, it is enough to significantly increase the concentration of subsurface H in Pt NPs compared to Pt(111) single crystals (the respective Boltzmann factor at the room temperature is $\exp(-\Delta E/kT) \approx 10^2$). Note that a new type of subsurface sites was calculated to be available for H absorption in Pt NPs. H put in a terrace *tss* site F in Pt_{127} moves during the geometry optimization to a subsurface position below *bridge* site H and becomes coordinated by three Pt atoms. This type of subsurface sites is not stable in Pt(111). The effect of nanostructuring on the stability of the second subsurface sites is calculated to be ±0.06 eV. As shown in section 5.4, the stabilization of *t2ss* sites is due to the higher flexibility of the NP structure, while the destabilization of *o2ss* sites is a consequence of the lattice contraction in metal NPs. In the case of Pt, the effect of edges on H stability can be as big as 0.22 eV and similarly to Pd it is the strongest for *bridge* sites. Stronger effect of nanostructuring on properties of Pt than of Pd was also calculated for H binding to M_{55} clusters[79] and for ethylene

adsorption on transition metal NPs.[19] This is consistent with the finding that bigger models of Pt NPs are required to work in the SwS regime (see section 4).

Hydrogen adsorption on small {100} facets of the M_{127} NPs was considered only briefly, because these facets consist of only four atoms and may not be representative of {100} facets on bigger NPs. In the case of Pd_{127}, H adsorbs on the {100} facets with binding energies of 0.2 ÷ 0.3 eV, i.e., weaker than on the {111} facets. However, on Pt_{127} NPs edge *bridge* sites on the {100} facets adsorb H as strongly as the *bridge* sites on the edges between the {111} facets with $E_H \approx 0.45$ eV.

5.3. Effect of MgO(100) Support on Binding of H to Pd and Pt NPs. In general, the influence of support on adsorption and absorption properties of the SwS Pd_{127} and Pt_{127} NPs was found to be very moderate, at most 0.07 eV (Figure 4). These

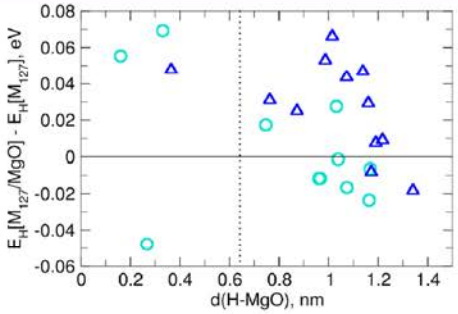

Figure 4. Change in H binding energies, $\Delta E_H = E_H[M_{127}/MgO] - E_H[M_{127}]$, on various sites of Pd_{127} (circles) and Pt_{127} (triangles) NPs caused by the presence of MgO(100) support versus H-support distance, d(H-MgO). Dotted line separates data for the top (right-hand side) and bottom (left-hand side) {111}-type facets.

results are in line with our previous finding that MgO(100) support insignificantly affects the distribution of interatomic distances and DOS of the supported Pd_{127} and Pt_{127} NPs.[23] On average, H binds by 0.03 eV more strongly to the supported Pt_{127} NPs than to the respective unsupported species, while for Pd the average stabilization is less than 0.01 eV. In the latter case, the effect of support on H binding energies decreases rapidly with growing H-support separation, calculated as the distance from the H atom to the plane of the top surface layer of MgO(100). While E_H values are altered by up to 0.07 eV on bottom {111} facets of Pd_{127} (d(H-MgO) < 0.5 nm), on top {111} facets the effect of support is limited to 0.03 eV. This agrees nicely with our finding that the effect of MgO(100) on the distribution of electron density in Pd and Pt NPs decays rapidly with the distance from the support.[23] Also one can see that H atoms on certain sites adjacent to the substrate, such as *hcp* site O on Pd_{127}, may be destabilized by steric repulsion with MgO. On the Pt_{127} NPs noticeable effect of support is observed even for sites at a distance of ∼1 nm from it. Since this observation cannot be explained by the effect of the support on the geometric structure, DOS, or electron density of the supported NPs, we suppose that more subtle changes in the electronic structure are responsible for the changes in E_H on Pt NPs. For example, one of such changes may be the shape of electron states near the Fermi level that often governs chemical properties of materials.[91]

Another important aspect is that the presence of support influences local stability of certain sites for H. For example, on the unsupported Pd and Pt NPs H is very stable on bridge sites P located on the very bottom edges between {111} and extended {100} facets. Naturally, in the presence of MgO these sites (as well as top sites L on the bottom edges of Pt_{127}) become unstable due to the steric repulsion between the substrate and the adsorbed H. Also subsurface *tss* sites O become unstable on supported Pt_{127}, which is probably due to the strain in the region of the NP/substrate interface.

5.4. Structural Data for H on Pd and Pt. In this section we discuss the strain induced by absorbed H on Pd and Pt substrates. On {111} nanofacets of supported Pd_{127} NPs and on Pd(111) absorbed H elongates distances between adjacent Pd atoms by ∼1% in octahedral sites and by 4−5% in tetrahedral sites. The pronounced increase in average Pd−Pd distances in the case of tetrahedral cavities is mostly due to the notable displacement of one of the four Pd atoms composing the site (the one from the second layer for *tss* and *t2ss*, and the one from the first layer for *tss′*). The lattice expansion during the formation of the β-phase of Pd hydride is ∼3%, i.e., of the same magnitude as the presented values.[49] Because H is calculated to be stable only in a few subsurface sites located at the edges of Pd_{127} one can only speculate if the flexibility of Pd atoms at the edges actually allows a better accommodation of subsurface H atoms. Indeed, the 2% increase of average Pd−Pd bonds was calculated upon H absorption in the *oss* site I (which is unstable according to the frequency analysis) and 6% increase was calculated for the *tss′* site L at the interface with MgO. However, while sites I are calculated to be more stable for H than *oss* sites on Pd(111), the stability of *tss′* sites L is decreased compared to the respective sites on the single crystals.

On Pt(111) and on terraces of supported Pt NPs absorbed H increases the interatomic distances between adjacent Pt atoms by 3% when absorbed in *oss* sites and by 6−7% when absorbed in tetrahedral sites. These values exceed by 2% those for Pd, in line with lower stability of absorbed H in Pt. Second subsurface *o2ss* sites are more rigid, and in this case the expansion is only 1%. A similar expansion of the absorption site takes place when H is absorbed in the *t2ss* site in Pt(111), but in Pt_{127}/MgO(100) upon absorption of H *t2ss* site expands by 6%, due to more flexible structure of the NP. The expansion of edge *tss* site O upon H absorption is more pronounced, 8%, and is again related to a significant movement of only one of the Pt atoms forming the site. Like in *tss′* sites on the edges of Pd_{127}, higher flexibility of the edge of Pt NPs does not result in a pronounced stabilization of the subsurface H.

Another way to look into structural properties of systems with absorbed H is to consider deformation energies, i.e., energy gain due to the substrate relaxation when absorbed H is removed (Table S3, Supporting Information). Similarly to the induced strain, on the Pd NPs the deformation energies are of the same order as on the Pd(111) slab. For *oss* and *o2ss* sites in Pd(111) or Pd_{127}/MgO, the deformation energies are 0.03 ÷ 0.07 eV, while for the smaller tetrahedral sites they are 0.10 ÷ 0.16 eV. The deformation energies of Pt substrates are significantly higher, almost by 0.15 eV for the tetrahedral absorption sites. However, this may only partially explain the lower stability of absorbed H in Pt than in Pd. Upon nanostructuring the deformation energies of Pt for H absorption in *tss′* sites decrease by 0.15 eV, which explains the 0.18 eV higher stability of H in these sites in supported Pt_{127} species compared to Pt(111). In contrast, H absorbed in *o2ss* positions deforms the supported Pt NPs by 0.09 eV stronger than Pt(111), because average calculated Pt−Pt distances in the NP are decreased to 278.3 pm from 282.5

pm in Pt bulk,[23] so that the volume of octahedral cavities is reduced.

We also calculated DOS projected on H atoms adsorbed or absorbed on different sites on Pd(111) and Pt(111) surfaces (see Figure S1, Supporting Information). On both surfaces, the peak of H-projected DOS shifts to lower energies when moving from adsorption to subsurface and then to bulk sites, i.e., with destabilization of H atoms. Hence, the DOS of H in the most stable *fcc* position is the closest to the d-band of the metal and has the largest overlap with it. This finding can rationalize the highest stability of H in the *fcc* positions.

Finally, we note that Bader charges on H located on the considered Pd slabs and NPs are −0.17 ÷ −0.14 |e| for the *fcc* sites and −0.07 ÷ −0.06 |e| for the *oss* sites. Hydrogen adsorbed in the *fcc* sites on Pt is characterized by Bader charge around −0.1 |e|, while subsurface H in the *oss* sites carries charge between −0.07 and 0.00 |e|. These data indicate quite small polarity of Pd−H and Pt−H interactions, which may have important implications at higher loadings of hydrogen.

6. CONCLUSIONS

We studied interactions of hydrogen with bare and MgO(100)-supported Pd and Pt NPs shown to be in the "scalable with size" regime, that is, adequate for simulations of H adsorption and absorption on bigger metal NPs typical for catalytic experiments and applications.

As expected for such unreactive support as MgO, it does not strongly influence the properties of the supported NPs, modifying H binding energies with the NPs by up to 0.07 eV. This is one of the first quantifications of the effect of oxide supports on the adsorption properties of sizable metal NPs. While for Pd NPs the effect of the support rapidly decreases with increasing separation between H and MgO, on Pt NPs a notable support effect is identified at a H−MgO distance of ∼1 nm. This indicates that metal−support interaction, irrespective of its strength, may not be limited to the region of NP−support interface. The most prominent effect of the support on H at the metal−oxide interface is the steric repulsion with the adsorbate, which makes certain adsorption sites locally unstable. These findings suggest that unsupported scalable with size transition metal NPs are adequate models of catalytic systems not manifesting strong metal−support interaction. On the other hand, we show that explicit density-functional description of sufficiently big metal NPs together with their supports is feasible, and thus the presence of the supports should not be neglected when important.

We also investigated the difference between adsorption and absorption of single atoms H on Pd and Pt NPs. It is found in agreement with previous studies that the dissociative absorption of H_2 into the subsurface region of Pd is almost energy neutral, while the occupation of subsurface sites is significantly disfavored in Pt. H on Pd NPs was calculated to adsorb and absorb only slightly stronger, by up to 0.08 eV, than on Pd(111). However, on Pt the stabilization of certain sites due to nanostructuring is more pronounced, up to 0.18 eV in the case of tetrahedral subsurface *tss′* sites. Thus, the absorption of hydrogen in the subsurface region of Pt NPs becomes endothermic by only 0.25 eV per atom. This stabilization may considerably increase the concentration of subsurface H in nanostructured Pt in comparison with Pt single crystals. In general, stability of the absorbed H in nanostructured metals can be promoted by higher structural flexibility of metal NPs or hindered by lattice contraction in them, depending on the absorption site. Note that due to the very flexible structure of the edge sites in the majority of cases H escaped during geometry optimization from subsurface sites at NP edges to more stable adsorption sites. Therefore, the role of NP edges appears to be not to stabilize subsurface H but rather to promote formation of subsurface H by decreasing the surface to subsurface migration barrier.

■ ASSOCIATED CONTENT

Supporting Information

E_H values without ZPE corrections, substrate relaxation energies upon H removal from various absorption sites, DOS plots. This material is available free of charge via the Internet at http://pubs.acs.org.

■ AUTHOR INFORMATION

Corresponding Author

*E-mail: konstantin.neyman@icrea.cat. Tel.: (+34) 93 403 7212. Fax: (+34) 93 402 1231.

Notes

The authors declare no competing financial interest.

■ ACKNOWLEDGMENTS

Financial support from the Spanish MEDU is gratefully acknowledged by S.M.K. (FPU Grant AP2009-3379) and H.A.A. (Postdoctoral Grant SB2010-0172). H.A.A. is also grateful to the Bulgarian Science Fund (Grant DCVP 02/1) and the FP7 programme (project Beyond Everest). This study was also supported by the European Commission (FP7-NMP.2012.1.1-1 project ChipCAT, Ref. No. 310191), the Spanish MINECO (CTQ2012-34969), and the Generalitat de Catalunya (2014SGR97, XRQTC). It is a part of COST Actions CM1104 and MP1103. The authors thank Red Española de Supercomputación for provided computer resources and technical assistance.

■ REFERENCES

(1) Viñes, F.; Lykhach, Y.; Staudt, T.; Lorenz, M. P. A.; Papp, C.; Steinrück, H.-P.; Libuda, J.; Neyman, K. M.; Görling, A. Methane Activation by Platinum: Critical Role of Edge and Corner Sites of Metal Nanoparticles. *Chem.—Eur. J.* **2010**, *16*, 6530−6539.

(2) Roldan Cuenya, B. Synthesis and Catalytic Properties of Metal Nanoparticles: Size, Shape, Support, Composition, and Oxidation State Effects. *Thin Solid Films* **2010**, *518*, 3127−3150.

(3) Doyle, A. M.; Shaikhutdinov, S. K.; Freund, H.-J. Surface-Bonded Precursor Determines Particle Size Effects for Alkene Hydrogenation on Palladium. *Angew. Chem., Int. Ed.* **2005**, *44*, 629−631.

(4) Haruta, M.; Yamada, N.; Kobayashi, T.; Iijima, S. Gold Catalysts Prepared by Coprecipitation for Low-Temperature Oxidation of Hydrogen and of Carbon Monoxide. *J. Catal.* **1989**, *115*, 301−309.

(5) Haruta, M. Size- and Support-Dependency in the Catalysis of Gold. *Catal. Today* **1997**, *36*, 153−166.

(6) Valden, M.; Lai, X.; Goodman, D. W. Onset of Catalytic Activity of Gold Clusters on Titania with the Appearance of Nonmetallic Properties. *Science* **1998**, *281*, 1647−1650.

(7) Jin, M.; Park, J.-N.; Kuk Shon, J.; Kim, J. H.; Li, Z.; Park, Y.-K.; Man Kim, J. Low Temperature CO Oxidation over Pd Catalysts Supported on Highly Ordered Mesoporous Metal Oxides. *Catal. Today* **2012**, *185*, 183−190.

(8) Bruix, A.; Rodriguez, J. A.; Ramírez, P. J.; Senanayake, S. D.; Evans, J.; Park, J. B.; Stacchiola, D.; Liu, P.; Hrbek, J.; Illas, F. A New Type of Strong Metal−Support Interaction and the Production of H_2 Through the Transformation of Water on Pt/CeO_2(111) and Pt/CeO_x/TiO_2(110) Catalysts. *J. Am. Chem. Soc.* **2012**, *134*, 8968−8974.

(9) Okumura, K.; Motohiro, T.; Sakamoto, Y.; Shinjoh, H. Effect of Combination of Noble Metals and Metal Oxide Supports on Catalytic Reduction of NO by H_2. *Surf. Sci.* **2009**, *603*, 2544−2550.
(10) Yoshida, H.; Nakajima, T.; Yazawa, Y.; Hattori, T. Support Effect on Methane Combustion over Palladium Catalysts. *Appl. Catal., B* **2007**, *71*, 70−79.
(11) Marginean, P.; Olariu, A. Influence of Metal Oxides on the Catalytic Activity of Nickel. *Appl. Catal., A* **1997**, *165*, 241−248.
(12) Yudanov, I. V.; Sahnoun, R.; Neyman, K. M.; Rösch, N. Metal Nanoparticles as Models of Single Crystal Surfaces and Supported Catalysts: Density Functional Study of Size Effects for CO/Pd(111). *J. Chem. Phys.* **2002**, *117*, 9887−9869.
(13) Kozlov, S. M.; Neyman, K. M. Catalysis From First Principles: Towards Accounting for the Effects of Nanostructuring. *Top. Catal.* **2013**, *56*, 867−873.
(14) Yudanov, I. V.; Genest, A.; Rösch, N. DFT Studies of Palladium Model Catalysts: Structure and Size Effects. *J. Cluster Sci.* **2011**, *22*, 433−448.
(15) Neyman, K. M.; Sahnoun, R.; Inntam, C.; Hengrasmee, S.; Rösch, N. Computational Study of Model Pd-Zn Nanoclusters and Their Adsorption Complexes with CO Molecules. *J. Phys. Chem. B* **2004**, *108*, 5424−5430.
(16) Yudanov, I. V.; Genest, A.; Schauermann, S.; Freund, H.-J.; Rösch, N. Size Dependence of the Adsorption Energy of CO on Metal Nanoparticles: A DFT Search for the Minimum Value. *Nano Lett.* **2012**, *12*, 2134−2139.
(17) Yudanov, I. V.; Metzner, M.; Genest, A.; Rösch, N. Size-Dependence of Adsorption Properties of Metal Nanoparticles: A Density Functional Study on Palladium Nanoclusters. *J. Phys. Chem. C* **2008**, *112*, 20269−20275.
(18) Chang, L. Y.; Barnard, A. S.; Gontard, L. C.; Dunin-Borkowski, R. E. Resolving the Structure of Active Sites on Platinum Catalytic Nanoparticles. *Nano Lett.* **2010**, *10*, 3073−3076.
(19) Pozun, Z. D.; Tran, K.; Shi, A.; Smith, R. H.; Henkelman, G. Why Silver Nanoparticles Are Effective for Olefin/Paraffin Separations. *J. Phys. Chem. C* **2011**, *115*, 1811−1818.
(20) Li, Z.; Li, Y.; Li, J. Support Effects on the Dissociation of Hydrogen over Gold Clusters on ZnO(101) Surface: Theoretical Insights. *J. Chem. Phys.* **2012**, *137*, 234704.
(21) Corral Valero, M.; Raybaud, P.; Sautet, P. Interplay between Molecular Adsorption and Metal−Support Interaction for Small Supported Metal Clusters: CO and C_2H_4 Adsorption on Pd_4/γ-Al_2O_3. *J. Catal.* **2007**, *247*, 339−355.
(22) Eichler, A. Chemical Characterization of a Zirconia-Supported Pt Cluster. *Phys. Rev. B* **2005**, *71*, 125418.
(23) Kozlov, S. M.; Aleksandrov, H. A.; Goniakowski, J.; Neyman, K. M. Effect of MgO(100) Support on Structure and Properties of Pd and Pt Nanoparticles with 49−155 atoms. *J. Chem. Phys.* **2013**, *139*, 084701.
(24) Roldán, A.; Viñes, F.; Illas, F.; Ricart, J. M.; Neyman, K. M. Density Functional Studies of Coinage Metal Nanoparticles: Scalability of Their Properties to Bulk. *Theor. Chem. Acc.* **2008**, *120*, 565−573.
(25) Roldán, A.; Ricart, J. M.; Illas, F. Origin of the Size Dependence of Au Nanoparticles toward Molecular Oxygen Dissociation. *Theor. Chem. Acc.* **2011**, *128*, 675−681.
(26) Kishore, S.; Nelson, J. A.; Adair, J. H.; Eklund, P. C. Hydrogen Storage in Spherical and Platelet Palladium Nanoparticles. *J. Alloys Compd.* **2005**, *389*, 234−242.
(27) Yamauchi, M.; Ikeda, R.; Kitagawa, H.; Takata, M. Nanosize Effects on Hydrogen Storage in Palladium. *J. Phys. Chem. C* **2008**, *112*, 3294−3299.
(28) Langhammer, C.; Zoric, I.; Kasemo, B.; Clemens, B. M. Hydrogen Storage in Pd Nanodisks Characterized with a Novel Nanoplasmonic Sensing Scheme. *Nano Lett.* **2007**, *7*, 3122−3127.
(29) Blaser, H.-U.; Indolese, A.; Schnyder, A.; Steiner, H.; Studer, M. Supported Palladium Catalysts for Fine Chemicals Synthesis. *J. Mol. Catal. A: Chem.* **2001**, *173*, 3−18.
(30) Raveendran Shiju, N.; Guliants, V. V. Recent Developments in Catalysis Using Nanostructured Materials. *Appl. Catal., A* **2009**, *356*, 1−17.
(31) Wilde, M.; Fukutani, K.; Ludwig, W.; Brandt, B.; Fischer, J.-H.; Schauermann, S.; Freund, H.-J. Influence of Carbon Deposition on the Hydrogen Distribution in Pd Nanoparticles and Their Reactivity in Olefin Hydrogenation. *Angew. Chem., Int. Ed.* **2008**, *47*, 9289−9293.
(32) Takezawa, N.; Iwasa, N. Steam Reforming and Dehydrogenation of Methanol: Difference in the Catalytic Functions of Copper and Group VIII Metals. *Catal. Today* **1997**, *36*, 45−56.
(33) Breen, J. P.; Burch, R.; Coleman, H. M. Metal-Catalysed Steam Reforming of Ethanol in the Production of Hydrogen for Fuel Cell Applications. *Appl. Catal., B* **2002**, *39*, 65−74.
(34) Liguras, D. K.; Kondarides, D. I.; Verykios, X. E. Production of Hydrogen for Fuel Cells by Steam Reforming of Ethanol over Supported Noble Metal Catalysts. *Appl. Catal., B* **2003**, *43*, 345−354.
(35) Bunluesin, T.; Gorte, R. J.; Graham, G. W. Studies of the Water-Gas-Shift Reaction on Ceria-Supported Pt, Pd, and Rh: Implications for Oxygen-Storage Properties. *Appl. Catal., B* **1998**, *15*, 107−114.
(36) Doyle, A. M.; Shaikhutdinov, Sh. K.; Freund, H.-J. Alkene Chemistry on the Palladium Surface: Nanoparticles vs Single Crystals. *J. Catal.* **2004**, *223*, 444−453.
(37) Ludwig, W.; Savara, A.; Dostert, K.-H.; Schauermann, S. Olefin Hydrogenation on Pd Model Supported Catalysts: New Mechanistic Insights. *J. Catal.* **2011**, *284*, 148−156.
(38) Kim, S. K.; Kim, C.; Lee, J. H.; Kim, J.; Lee, H.; Moon, S. H. Performance of Shape-Controlled Pd Nanoparticles in the Selective Hydrogenation of Acetylene. *J. Catal.* **2013**, *306*, 146−154.
(39) Aleksandrov, H. A.; Viñes, F.; Ludwig, W.; Schauermann, S.; Neyman, K. M. Tuning the Surface Chemistry of Pd by Atomic C and H: A Microscopic Picture. *Chem.—Eur. J.* **2013**, *19*, 1335−1345.
(40) Neyman, K. M.; Schauermann, S. Hydrogen Diffusion into Palladium Nanoparticles: Pivotal Promotion by Carbon. *Angew. Chem., Int. Ed.* **2010**, *49*, 4743−4746.
(41) Savara, A.; Ludwig, W.; Dostert, K. H.; Schauermann, S. Temperature Dependence of the 2-Butene Hydrogenation over Supported Pd Nanoparticles and Pd(111). *J. Mol. Catal. A - Chem.* **2013**, *377*, 137−142.
(42) Morkel, M.; Rupprechter, G.; Freund, H.-J. Finite Size Effects on Supported Pd Nanoparticles: Interaction of Hydrogen with CO and C_2H_4. *Surf. Sci.* **2005**, *588*, L209−L219.
(43) Kozlov, S. M.; Yudanov, I. V.; Aleksandrov, H. A.; Rösch, N. Theoretical Study of Carbon Species on Pd(111): Competition Between Migration of C Atoms to the Subsurface Interlayer and Formation of C_n Clusters on the Surface. *Phys. Chem. Chem. Phys.* **2009**, *11*, 10955−10963.
(44) Teschner, D.; Vass, E.; Hävecker, M.; Zafeiratos, S.; Schnörch, P.; Sauer, H.; Knop-Gericke, A.; Schlögl, R.; Chamam, M.; Wootsch, A.; et al. Alkyne Hydrogenation over Pd Catalysts: A New Paradigm. *J. Catal.* **2006**, *242*, 26−37.
(45) Bowker, M.; Morgan, C.; Perkins, N.; Holroyd, R.; Fourre, E.; Grillo, F.; Macdowall, A. Ethene Adsorption, Dehydrogenation and Reaction With Pd(110): Pd as a Carbon 'Sponge'. *J. Phys. Chem. B* **2005**, *109*, 2377−2386.
(46) Wilde, M.; Fukutani, K.; Naschitzki, M.; Freund, H.-J. Hydrogen Absorption in Oxide-Supported Palladium Nanocrystals. *Phys. Rev. B* **2008**, *77*, 113412.
(47) Jewell, L. L.; Davis, B. H. Review of Absorption and Adsorption in the Hydrogen−Palladium System. *Appl. Catal., A* **2006**, *310*, 1−15.
(48) Hakamada, M.; Nakano, H.; Furukawa, T.; Takahashi, M.; Mabuchi, M. Hydrogen Storage Properties of Nanoporous Palladium Fabricated by Dealloying. *J. Phys. Chem. C* **2010**, *114*, 868−873.
(49) Eastman, J. A.; Thompson, L. J.; Kestel, B. J. Narrowing of the Palladium-Hydrogen Miscibility Gap in Nanocrystalline Palladium. *Phys. Rev. B* **1993**, *48*, 84−93.
(50) Yamauchi, M.; Kobayashi, H.; Kitagawa, H. Hydrogen Storage Mediated by Pd and Pt Nanoparticles. *ChemPhysChem* **2009**, *10*, 2566−2576.

(51) Marković, N. M.; Grgur, B. N.; Lucas, C. A.; Ross, P. N. Surface Electrochemistry of CO on Pt(110)-(1 × 2) and Pt(110)-(1 × 1) Surfaces. *Surf. Sci.* **1997**, *384*, L805−L814.
(52) Martins, M. E.; Zinola, C. F.; Andreasen, G.; Salvarezza, R. C.; Arvia, A. J. The Possible Existence of Subsurface H-Atom Adsorbates and H_2 Electrochemical Evolution Reaction Intermediates on Platinum in Acid Solutions. *J. Electroanal. Chem.* **1998**, *445*, 135−154.
(53) Fukutani, K.; Itoh, A.; Wilde, M.; Matsumoto, M. Zero-Point Vibration of Hydrogen Adsorbed on Si and Pt Surfaces. *Phys. Rev. Lett.* **2002**, *88*, 116101.
(54) Isobe, Y.; Yamauchi, M.; Ikeda, R.; Kitagawa, H. A Study of Hydrogen Adsorption of Polymer Protected Pt Nanoparticles. *Synth. Met.* **2003**, *135*−*136*, 757−758.
(55) Yamauchi, M.; Kitagawa, H. Hydrogen Absorption in Size-Controlled Pt Nanoparticle. *Chem. Eng. Trans.* **2005**, *8*, 159−163.
(56) Hammer, B.; Hansen, L. B.; Nørskov, J. K. Improved Adsorption Energetics within Density-Functional Theory Using Revised Perdew-Burke-Ernzerhof Functionals. *Phys. Rev. B* **1999**, *59*, 7413.
(57) Kresse, G.; Furthmuller, J. Efficient Iterative Schemes for Ab Initio Total-Energy Calculations Using a Plane-Wave Basis Set. *Phys. Rev. B* **1996**, *54*, 11169−11186.
(58) Kresse, G.; Joubert, D. From Ultrasoft Pseudopotentials to the Projector Augmented-Wave Method. *Phys. Rev. B* **1999**, *59*, 1758.
(59) Methfessel, M.; Paxton, A. T. High-Precision Sampling for Brillouin-Zone Integration in Metals. *Phys. Rev. B* **1989**, *40*, 3616−3621.
(60) Chase, M. W., Jr. NIST-JANAF Themochemical Tables, Fourth Edition. *J. Phys. Chem. Ref. Data, Monograph 9* **1998**, 1−1951.
(61) Gillespie, L. J.; Ambrose, H. A. The Heat of Absorption of Hydrogen by Palladium Black At 0°. *J. Phys. Chem.* **1931**, *35*, 3105−3110.
(62) Conrad, H.; Ertl, G.; Latta, E. E. Adsorption of Hydrogen on Palladium Single Crystal Surfaces. *Surf. Sci.* **1974**, *41*, 435−446.
(63) Christmann, K.; Ertl, G.; Pignet, T. Adsorption of Hydrogen on a Pt(111) Surface. *Surf. Sci.* **1976**, *54*, 365−392.
(64) Xu, L. S.; Ma, Y. S.; Zhang, Y. L.; Teng, B. T.; Jiang, Z. Q.; Huang, W. X. Revisiting H/Pt(111) by a Combined Experimental Study of the H-D Exchange Reaction and First-Principles Calculations. *Sci. China Chem.* **2011**, *54*, 745−755.
(65) Perdew, J. P.; Wang, Y. Accurate and Simple analytic Representation of the Electron-Gas Correlation Energy. *Phys. Rev. B* **1992**, *45*, 13244.
(66) Tao, J.; Perdew, J. P.; Staroverov, V. N.; Scuseria, G. E. Climbing the Density Functional Ladder: Nonempirical Meta-Generalized Gradient Approximation Designed for Molecules and Solids. *Phys. Rev. Lett.* **2003**, *91*, 146401.
(67) Felter, T. E.; Sowa, E. C.; Van Hove, M. A. Location of Hydrogen Adsorbed on Palladium (111) Studied by Low-Energy Electron Diffraction. *Phys. Rev. B* **1989**, *40*, 891−899.
(68) Mitsui, T.; Rose, M. K.; Fomin, E.; Ogletree, D. F.; Salmeron, M. Hydrogen Adsorption and Diffusion on Pd(111). *Surf. Sci.* **2003**, *540*, 5−11.
(69) Lässer, R.; Klatt, K.-H. Solubility of Hydrogen Isotopes in Palladium. *Phys. Rev. B* **1983**, *28*, 748−758.
(70) Nelin, G. A Neutron Diffraction Study of Palladium Hydride. *Phys. Status Solidi B* **1971**, *45*, 527−536.
(71) Mackay, K. M. *Hydrogen Compounds of the Metallic Elements*; Spon Ltd.: London, U.K., 1966; pp 86−90.
(72) Janthon, P.; Kozlov, S. M.; Viñes, F.; Limtrakul, J.; Illas, F. Establishing the Accuracy of Broadly Used Density Functionals in Describing Bulk Properties of Transition Metals. *J. Chem. Theory Comput.* **2013**, *9*, 1631−1640.
(73) Olander, J.; Lazzari, R.; Jupille, J.; Mangili, B.; Goniakowski, J. Size- and Temperature-Dependent Epitaxy for a Strong Film-Substrate Mismatch: The Case of Pt/MgO(001). *Phys. Rev. B* **2007**, *76*, 075409.
(74) Revenant, C.; Leroy, F.; Lazzari, R.; Renaud, G.; Henry, C. R. Quantitative Analysis of Grazing Incidence Small-Angle X-Ray Scattering: Pd/MgO(001) Growth. *Phys. Rev. B* **2004**, *69*, 035411.
(75) Tripkovic, V.; Cerri, I.; Bligaard, T.; Rossmeisl, J. The Influence of Particle Shape and Size on the Activity of Platinum Nanoparticles for Oxygen Reduction Reaction: A Density Functional Theory Study. *Catal. Lett.* **2014**, *144*, 380−388.
(76) Yudanov, I. V.; Matveev, A. V.; Neyman, K. M.; Rösch, N. How the C-O Bond Breaks During Methanol Decomposition on Nanocrystallites of Palladium Catalysts. *J. Am. Chem. Soc.* **2008**, *130*, 9342−9352.
(77) Kozlov, S. M.; Cabeza, G. F.; Neyman, K. M. Bonding and Vibrations of CH_x and CH_xO (x = 1−3) Species on a Pd_{79} Nanoparticle Representing Model Catalysts. *Chem. Phys. Lett.* **2011**, *506*, 92−97.
(78) Yudanov, I. V.; Neyman, K. M.; Rösch, N. Density Functional Study of Pd Nanoparticles with Subsurface Impurities of Light Element Atoms. *Phys. Chem. Chem. Phys.* **2004**, *6*, 116−123.
(79) Tan, T. L.; Wang, L.-L.; Johnson, D. D.; Bai, K. A. Comprehensive Search for Stable Pt−Pd Nanoalloy Configurations and Their Use as Tunable Catalysts. *Nano Lett.* **2012**, *12*, 4875−4880.
(80) Qi, X. Q.; Wei, Z. D.; Li, L.; Ji, M. B.; Li, L. L.; Zhang, Q.; Xia, M. R.; Chen, S. G.; Yang, L. J. DFT Study on Interaction of Hydrogen with Pd(111). *Comp. Theor. Chem.* **2012**, *979*, 96−101.
(81) Greeley, J.; Mavrikakis, M. Surface and Subsurface Hydrogen: Adsorption Properties on Transition Metals and Near-Surface Alloys. *J. Phys. Chem. B* **2005**, *109*, 3460−3471.
(82) González, S.; Neyman, K. M.; Shaikhutdinov, S.; Freund, H.-J.; Illas, F. On the Promoting Role of Ag in Selective Hydrogenation Reactions over Pd-Ag Bimetallic Catalysts: A Theoretical Study. *J. Phys. Chem. C* **2007**, *111*, 6852−6856.
(83) Løvvik, O. M.; Olsen, R. A. Adsorption Energies and Ordered Structures of Hydrogen on Pd(111) from Density-Functional Periodic Calculations. *Phys. Rev. B* **1998**, *58*, 10890−10898.
(84) Ludwig, W.; Savara, A.; Madix, R. J.; Schauermann, S.; Freund, H.-J. Subsurface Hydrogen Diffusion into Pd Nanoparticles: Role of Low-Coordinated Surface Sites and Facilitation by Carbon. *J. Phys. Chem. C* **2012**, *116*, 3539−3544.
(85) Watson, G. W.; Wells, R. P. K.; Willock, D. J.; Hutchings, G. J. A Comparison of the Adsorption and Diffusion of Hydrogen on the {111} Surfaces of Ni, Pd, and Pt from Density Functional Theory Calculations. *J. Phys. Chem. B* **2001**, *105*, 4889−4894.
(86) Ford, D. C.; Xu, Y.; Mavrikakis, M. Atomic and Molecular Adsorption on Pt(111). *Surf. Sci.* **2005**, *587*, 159−174.
(87) Olsen, R. A.; Kroes, G. J.; Baerends, E. J. Atomic and Molecular Hydrogen Interacting with Pt(111). *J. Chem. Phys.* **1999**, *111*, 11155.
(88) Légaré, P. A Theoretical Study of H Surface and Subsurface Species on Pt(111). *Surf. Sci.* **2004**, *559*, 169−178.
(89) Yudanov, I. V.; Sahnoun, R.; Neyman, K. M.; Rösch, N.; Hoffmann, J.; Schauermann, S.; Johanek, V.; Unterhalt, H.; Rupprechter, G.; Libuda, J.; et al. CO Adsorption on Pd Nanoparticles: Density Functional and Vibrational Spectroscopy Studies. *J. Phys. Chem. B* **2003**, *107*, 255−264.
(90) Viñes, F.; Loschen, C.; Illas, F.; Neyman, K. M. Edge Sites as a Gate for Subsurface Carbon in Palladium Nanoparticles. *J. Catal.* **2009**, *266*, 59−63.
(91) Hammer, B.; Nørskov, J. K. Why Gold Is the Noblest of All the Metals. *Nature* **1995**, *376*, 238−240 1995.

Section 4.3

Energetic Stability of Absorbed H in Pd and Pt Nanoparticles in a More Realistic Environment

Sergey M. Kozlov,[1] Hristiyan A. Aleksandrov,[1,2] Konstantin M. Neyman[1,3]*

[1] Departament de Química Física and Institut de Química Teòrica i Computacional (IQTCUB), Universitat de Barcelona, c/ Martí i Franquès 1, 08028 Barcelona, Spain

[2] Faculty of Chemistry and Pharmacy, University of Sofia, 1126 Sofia, Bulgaria

[3] Institucio Catalana de Recerca i Estudis Avançats (ICREA), 08010 Barcelona, Spain

Abstract

Absorbed hydrogen can dramatically increase hydrogenation activity of Pd nanoparticles and was predicted to do so also for Pt. This calls for investigations of the energetic stability of absorbed H in Pd and Pt using nanoparticle models as realistic as possible, i.e. a) sufficiently large, b) supported, and c) pre-covered by hydrogen. Herein, hydrogen absorption is studied in MgO(100)-supported 1.6 nm large Pd and Pt nanoparticles with surfaces saturated by hydrogen. The effect of surface H on the stability of absorbed H is found to be significant and to exceed the effect of the support. H absorption is calculated to be endothermic in Pt, energy neutral in Pd(111) and bare Pd nanoparticles and exothermic in H-covered Pd nanoparticles. Hence, we identify the abundance of surface H and the nanostructuring of Pd as prerequisites for facile H absorption in Pd and for the concomitantly altered catalytic activity.

1. INTRODUCTION

Hydrogen, the element with the smallest atoms, is known to be absorbed by some of transition metals under special conditions after their surface is saturated by H.[1] Interplay between adsorbed hydrogen and hydrogen absorbed near surface reveals intriguing consequences for the surface reactivity of late transition metals.[2-7] For instance, density-functional calculations[7] show that the presence of subsurface H in Pd and Pt substantially weakens the binding of adsorbed H species (H^{ads}), making them much more active in hydrogenation reactions. Notably, absorbed H atoms in metal nanoparticles (NPs) affect the binding and the activity of H^{ads} much stronger than in the corresponding (111) single crystals.[7]

In view of these findings, the pivotal issue of energetic stability of absorbed H in Pd and Pt nanoparticles should be addressed. Experimentally, Pd nanoparticles provided higher quantities of (released) absorbed H compared to Pd(111) single crystals.[8-10] For instance, Wilde et al. measured for Pd NPs the enthalpy of absorption to be 0.28 ± 0.02 eV per H atom at low hydrogen concentration.[11] (Here and in the following positive energy values characterize exothermic processes.) At the same time, the internal energy and the enthalpy of formation of β-phase of Pd hydride in bulk samples were measured to be 0.09 eV lower.[12,13]

There are only few computational studies of H absorption in Pd nanoparticles sufficiently big to be representative of larger experimentally studied species.[14-17] However, these studies 1) either do not explicitly consider stability of H absorbed in Pd nanoparticles compared to gas phase H_2 molecules or to H absorbed in bulk Pd or 2) do not account for a very important fact[7,18,19] that H absorption occurs only in nanoparticles with surface densely covered by H or 3) consider nanoparticles in the unsupported state.

The available literature on H absorption in Pt is less clear. In Pt(111) single crystals absorbed H was found to be present in very small (if any) concentration,[20,21] whereas some studies reported significant H absorption in Pt nanoparticles.[22-24] Computationally H absorption in sufficiently big Pt nanoparticles was addressed without considering surface saturation by adsorbed H atoms.[17]

Herein, we model hydrogen absorption in 1.6 nm large Pd_{127} and Pt_{127} nanoparticles covered by adsorbed H and located on MgO(100) oxide support. In order to disentangle the effect of surface H on the absorption energies from that of metal nanostructuring, the

obtained H absorption energies are analyzed in comparison with those calculated on pristine (clean) nanoparticles and extended (111) surfaces. For both metals H^{ads} is found to destabilize hydrogen absorbed in the subsurface region, but to stabilize hydrogen absorbed deeper in the bulk. This made H absorption in some sites of Pd nanoparticles covered by H^{ads} by 0.08 eV more exothermic than in Pd bulk. The influence of adsorbed H on H absorption is found to be notably stronger than the effect induced by clean (100) surface of a defect-free MgO support.

2. COMPUTATIONAL DETAILS

The VASP software package[25] was used to perform electronic structure calculations with the revised Perdew-Burke-Ernzerhof exchange-correlation functional.[26] This functional was shown to be suitable for treatment of H-Pd and H-Pt interactions, despite that it underestimates the adsorption and absorption energies of H in Pd by 0.09 eV.[17] Calculations were carried out using plane waves with the energy cut-off 415 eV in the spin-unpolarized manner. The latter approximation for paramagnetic conducting materials is justified by the rehybridization of electronic states upon H interaction with transition metals discussed by Newns[27] and by explicit computational tests performed in previous studies.[28] The interaction between core and valence electrons was described using the PAW technique.[29] During the geometry optimization all H atoms were relaxed, while all Mg and O atoms were kept fixed. The relaxation of MgO(100) support was shown to affect the strength of its interaction with Pd NPs by less than 3 meV per metal atom on the interface.[31] All metal atoms composing the NPs were relaxed during the geometry optimization. Out of six layers of the employed p(3×3) M(111) slabs only the top four layers were relaxed, while the two bottom layers were fixed on the cut from bulk geometry with the experimental lattice parameter. More computational details can be found in Ref. 17.

Binding energies of adsorbed and absorbed H were calculated as $E_H = E[H_{N-1}/substrate] + \frac{1}{2}E[H_2] - E[H_N/substrate]$, where $E[H_N/substrate]$ is the total energy of interacting system of N atoms of H and the substrate, $E[H_{N-1}/substrate]$ is the energy of this system after removal of the given H atom and $E[H_2]$ is the energy of the gas phase H_2 molecule. No zero-point energy corrections were applied as justified elsewhere.[17]

The charge density difference was calculated as $\Delta\rho = \rho[H_N/substrate] - \rho[H_N] - \rho[substrate]$ with geometries of hydrogen atoms and *substrate* (MgO supported NPs) fixed on

those from optimized H_N/*substrate* system. The isosurfaces were visualized with VESTA software[30] at the isovalue of ~20 nm^{-3} (3×10^{-3} $bohr^{-3}$ exactly).

3. EMPLOYED MODELS

The models of supported Pd and Pt NPs employed in this study consist of M_{127} species located on two-layer thick MgO(100) slabs with p(7×7) supercells (Figure 1). There, adjacent NPs are separated by more than 0.7 nm. Increased separation between the NPs or thickness of the MgO slabs were shown not to change the NP-oxide interaction in any significant way.[31]

In this work we considered Pd and Pt nanoparticles with fcc lattice structure, because the latter is exhibited by much bigger NPs commonly dealt with in experiment and application. As a consequence the morphologies of the majority of surface and subsurface sites on the employed nanoparticle models are the same as on respective (111) single crystals. The adsorptive and absorptive properties of M_{127} NPs and M(111) surfaces with respect to single H atoms are also very similar.[17] Note that less regular and less symmetric clusters may not feature these properties, despite their possibly higher energetic stability at the considered nanoparticle sizes. Hence, it may impossible to extrapolate results calculated on them to bigger species appearing in the majority of experimental catalytic studies.

The shape of employed Pd_{127} and Pt_{127} nanoparticles was optimized in a previous study through extensive screening of feasible NP structures with interatomic potentials and subsequent evaluation of energetic stability of low-energy species with DFT.[31] The employed shapes are also in line with experimental observations for bigger nanoparticles[32,33] and Wulff-Kaischev construction.

The size of Pd_{127} and Pt_{127} nanoparticles is sufficient to allow *scalability with size* of their adsorptive and absorptive properties.[34] That is, these properties have been shown to vary smoothly and monotonously, when moving from Pd and Pt nanoparticles of >1 nm to bigger species with *fcc* structure.[35,36] Calculations of single H atom on Pd_N and Pt_N (N = 74 – 140) NPs with gradually varying shape and size in Ref. 17 revealed minor dependency of H binding energies on any of these two parameters. This finding suggests that the dependency of the effects described herein on nanoparticle shape and size should not be very strong and that the extrapolation of the obtained results onto reasonably similar Pd and Pt NP is appropriate.

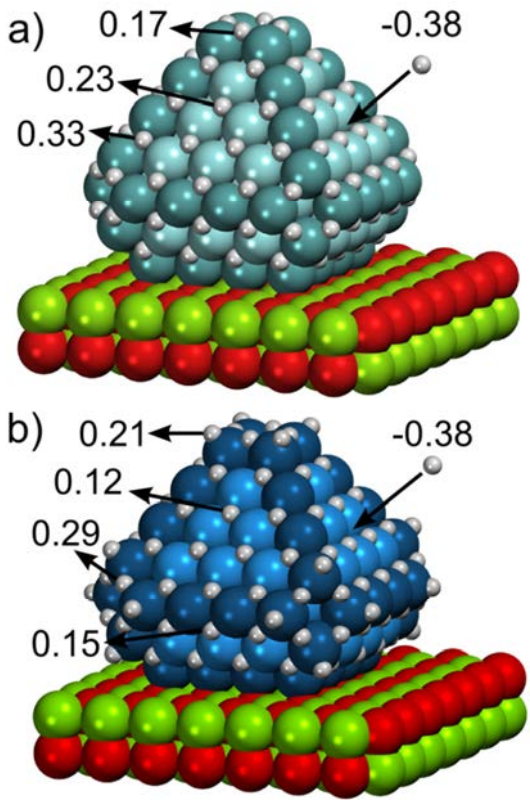

Figure 1. MgO(100)-supported metal nanoparticles saturated by adsorbed H: a) H_{96}/Pd_{127} and b) H_{116}/Pt_{127}. Adsorption energies of the present H atoms in various positions (arrows on the left-hand side) and adsorption energy of an additional H atom (arrows on the right-hand side) are given in eV with respect to gas-phase H_2. Pd and Pt atoms on the edges are displayed as the turquoise and dark blue spheres, those on the terraces – by the cyan and light blue spheres, respectively; Mg atoms – green spheres, O atoms – red spheres.

The covered by H NP models were generated by successively populating adsorption sites with H atoms until further H adsorption became endothermic (with respect to gas-phase H_2). In such a way it was possible to accommodate 96 H atoms on the supported Pd_{127} NP (Figure 1a). There, H atoms occupied both the three-fold hollow *fcc* sites on the {111} facets (in line with experimental results for Pd(111) single crystals)[37] and the bridge sites between a pair of metal atoms on the small {100} facets. The supported, surface-saturated with H Pt_{127} NP differs from the respective Pd_{127} NP by the presence of additional 20 H atoms adsorbed on-top of Pt atoms composing the small {100} facets (Figure 1b). Figure 1 displays the corresponding adsorption energies. Further adsorption of H on $H_{96}Pd_{127}$ and $H_{116}Pt_{127}$ is endothermic by 0.38 eV, justifying that surfaces of these nanoparticles are close to be saturated by H. Note that since the density of gas phase hydrogen at standard conditions is

less than 1 molecule per 30 nm^3, no gas phase H_2 molecules were included in actual calculations.

These models were used to study H absorption in interstitial octahedral subsurface *oss* cavities and tetrahedral subsurface *tss* and *tss`* sites between the first and the second surface metal layers. The two types of tetrahedral sites differ by their location below either three-fold hollow or top surface sites, respectively. For the H absorption between the second and the third surface metal layers we examined tetrahedral *t2ss* and octahedral *o2ss* cavities. Since these sites are not composed by surface metal atoms, we refer to them as bulk sites. We also studied pristine NPs and H-covered and pristine Pd(111) and Pt(111) single crystals.

4. ABSORPTION ENERGIES OF H IN Pd AND Pt

Absorption energies of hydrogen in Pd(111) single crystals and supported Pd_{127} nanoparticles are calculated to be very close to each other. Namely, H absorption is calculated to be almost energy neutral in subsurface sites and ~0.1 eV endothermic in deeper "bulk" sites in line with other studies.[38-40] Surface coverage by H^{ads} changes this picture as follows: 1) it *destabilizes* subsurface H by 0.07 – 0.17 eV on Pd(111) and by 0.02 – 0.06 eV on Pd NPs; 2) it *stabilizes* bulk hydrogen by ~0.05 eV on Pd(111) and by 0.20 – 0.24 eV on Pd NPs. The destabilization of subsurface H is associated with the displacement of the absorbed moieties from the top to the bottom part of the subsurface cavities. For instance, the distance from *oss*-located H in supported Pd_{127} to the nearby surface (subsurface) Pd atoms is around 180 (230) pm when no surface H is present and it changes to 245 (180) pm when the surface is covered by H^{ads}. Note that the destabilizing effect of surface H on absorbed H is smaller on the NPs, whereas the stabilizing effect is larger. It is also worth pointing out that H absorption should be considered feasible in sites with calculated energetic stability around zero, since the employed rPBE exchange-correlation functional somewhat underestimates the strength of H-Pd bonds.[17]

Thus, absorption energy of H in *t2ss* sites of Pd_{127} nanoparticles becomes 0.11 eV upon surface coverage by H^{ads}. At the same time, the formation energy of the hydride Pd_2H is calculated to be only 0.03 eV.[41] Thus, we estimate the combined effect of Pd nanostructuring and surface saturation on the absorption energies of H in Pd to be 0.08 eV, which compares surprisingly well with the stabilization of 0.09 eV derived from measurements by Wilde et al.[11-13]

Table 1. Absorption energies (in eV, with respect to gas-phase H_2) of H in (111) single crystals and MgO-supported nanoparticles of Pd and Pt depending on the absorption site and presence of adsorbed H.

Site	Pd(111)		Pd_{127}/MgO(100)		Pt(111)		Pt_{127}/MgO(100)	
	pristine	H-covered	pristine	H-covered	pristine	H-covered	pristine	H-covered
oss	-0.01	-0.16	0.00	-0.04	-0.43[a]	-0.58	-0.40	-0.45
oss/edge			0.04[a]	-0.26			→*fcc*[b]	-0.54
tss	-0.02	-0.19	-0.01	-0.07	-0.46	-0.56	-0.38[c]	-0.52
tss`	-0.03	-0.10	0.01	-0.01	-0.43	-0.58	-0.26	-0.33
tss/edge[d]			→*hcp*[b]	-0.19			→*bridge*[b]	-0.54
o2ss	-0.12	-0.06	-0.11[a]	0.09	-0.76	-0.69	-0.75	-0.56
t2ss	-0.16	-0.11	-0.13	0.11	-0.73	-0.61	-0.66	-0.55

[a] H in this position was found to be unstable via frequency analysis in Ref. 17; [b] H escapes from this site during the geometry optimization to the site pointed to by arrow; [c] H migrates from the *tss* site to subsurface site below bridge site composed of two surface and one subsurface Pt atom; [d] *tss* and *tss`* sites on the edges are structurally identical.

Hence, the effect of nanostructuring on the surface reactivity of Pd is twofold. On the one hand, nanostructuring (in synergy with surface saturation by H^{ads}) promotes H absorption into Pd. On the other hand, nanostructuring has been recently shown to make hydrogenation activity of transition metal catalysts more sensitive to the presence of adsorbed and absorbed H.[7] Both these effects contribute to experimentally observed increase of hydrogenation activity of Pd upon nanostructuring.[4,9]

Note that H atoms are not stable in the subsurface sites located at the edges of pristine Pd NPs and escape from them to the surface during geometry optimization calculations (Table 1). Nevertheless, it is possible to stabilize H in these sites by occupying all the *fcc*

surface sites on Pd NPs by H atoms. In the latter case, one finds that H in the subsurface sites at the edges is 0.1 – 0.2 eV less stable than in the terrace subsurface sites. The lower energetic stability can be either intrinsic for H at the edge sites or due to the high number of adsorbed H around these sites.

The absorption of H by Pt is significantly energetically unfavorable (Table 1), which agrees with very small concentration of the subsurface H measured in Pt(111).[42] In fact, calculated absorption energies of H in subsurface sites of Pt(111) are in line with the estimated enthalpy of H solution in Pt, -0.48 eV.[1] Similarly to the case of Pd, surface H destabilizes H atoms in subsurface sites of Pt(111) by 0.10 – 0.15 eV and stabilizes H atoms in the bulk sites by ~0.1 eV. In turn, on supported Pt nanoparticles subsurface H is destabilized by 0.07 – 0.14 eV and bulk H is stabilized by 0.11 – 0.19 eV in the presence of adsorbed H. So the changes by the surface H species of the absorption energies are significantly smaller than the intrinsic endothermicity of the H absorption in Pt. Similarly to Pd NPs, we were unable in our calculations to locate H in the subsurface sites at the edges of the pristine Pt NPs. However, the subsurface sites at the edges of Pt NPs covered by adsorbed H are locally stable for H and the absorption energies there are similar to those of the terrace absorption sites in the Pt NPs.

Note that the effect of MgO(100) support on H adsorption and absorption in Pd and Pt nanoparticles was found to be limited to 0.07 eV only.[17] Hence, the surface coverage by H^{ads} is more important for the absorption properties of Pd and Pt nanoparticles, than their interaction with MgO(100).

5. EFFECT OF ADSORBED H ON PROPERTIES OF Pd AND Pt

Adsorbed H has a profound effect not only on the absorption properties of the NPs, but also on the interatomic distances in the NPs and the electronic structure of the NPs. For instance (see Figure 2), the interatomic distances (average ± standard deviation) change in the supported M_{127} NPs, when their surfaces are covered by H, from 278.8 ± 5.3 pm to 284.7 ± 3.2 pm for Pd and from 278.3 ± 9.1 pm to 284.7 ± 6.4 pm for Pt. Thus, H adsorption not only makes average distances in Pd and Pt longer, but also decreases their variation within NPs. A qualitatively similar effect of hydrogen on the structure of Al_2O_3-supported Pt nanoparticles was measured in X-ray absorption experiments.[43] However, both the elongation of Pt-Pt contacts and the decrease in standard deviations were measured to be smaller. This could be

partially due to the significant effect of Al_2O_3 on the structure of supported Pt clusters, whereas the effect of MgO on geometric structure of supported Pd and Pt nanoparticles was shown to be basically negligible.[31] Interestingly, the increase in the average interatomic distances is not due to the appearance of too long metal-metal contacts, but due to the reduced number of short contacts. It can be rationalized by the decreased specific surface energies of the {111} facets upon H adsorption. This reduces the pressure imposed on the NP structures by the facets and consequently leads to the smaller number of short metal-metal distances.

The expansion of NPs upon hydrogen adsorption increases the size of interstitial cavities in Pd and Pt and may contribute to higher propensity of the NPs for H absorption. Notably, changes of distances between surface atoms of some bimetallic core-shell NPs by just a few percent have been recently associated with their modified catalytic activity with respect to the monometallic NPs.[44-46] Accordingly, the presently quantified notable structural effects for Pd and Pt NPs imply important modifications in the surface reactivity.

According to the Bader charge analysis[47] each H atom on the H-covered Pd_{127} NPs accumulates (on average) -0.17 atomic units (a.u.) of charge, which results in the concomitant average charge 0.11 a.u. of Pd atoms. In the H-covered Pt_{127} NPs, the charge on H atoms is around -0.12 a.u., while Pt atoms are slightly positively charged, by 0.07 a.u. on average. The electron accumulation on H atoms can be also seen on charge density difference plots (Figure 3). The charge redistribution affects mostly surface metal atoms and may be related to the destabilization of subsurface H in the presence of H^{ads}. The charges on metal atoms are also affected by the electron transfer between the NPs and the MgO(100) support, in which the latter is calculated to donate in total 2.5÷3.5 electrons to the deposited NPs.[31] Therefore, the metal-support interactions modify the charge distributions in the metal NPs notably less than the interactions with H atoms can do.

There is also a significant effect of the adsorbed H on the electronic structure of the MgO(100)-supported M_{127} NPs (Figure 4), which indicates a dependency of the catalytic properties of Pd and Pt NPs on the amount of H on their surfaces. In the absence of H DOS projected on the metal atoms forming the {111} facets of the NPs are close to the DOS of the metal atoms on the respective (111) surfaces. Upon H adsorption, DOS of the metal atoms shift to lower energies and the shift is more significant for the NPs than for the single crystals. This means that even if surface reactivity of the NPs are very close to that of the

single crystals at low H pressures, the situation may strongly change at higher H pressures and concomitantly higher H surface coverage. In variation, the interaction between supported Pd and Pt NPs and MgO(100) was shown to very slightly modify the electronic structure of the nanoparticles.[31]

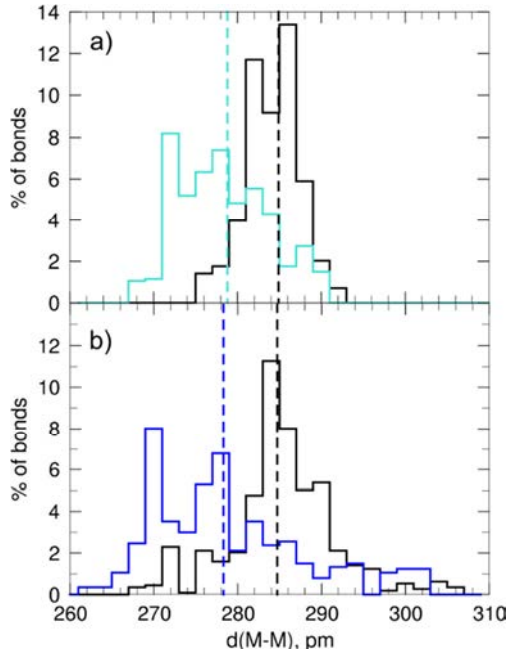

Figure 2. Partition of interatomic distances in pristine (color line) and H-covered (black line) M_{127} NPs supported on MgO: a) M = Pd; b) M = Pt. Vertical dashed lines marc average interatomic distances.

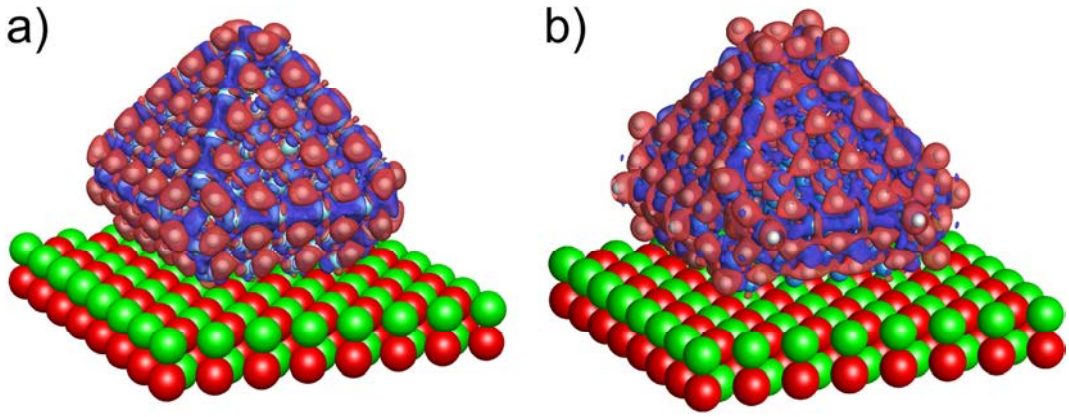

Figure 3. Isosurfaces of charge density difference for adsorption of a) 96 H atoms on Pd_{127} and b) 116 H atoms on Pt_{127} on MgO(100) support. Red and blue areas indicate regions of electron accumulation and depletion, respectively. Atoms are displayed like on Figure 1.

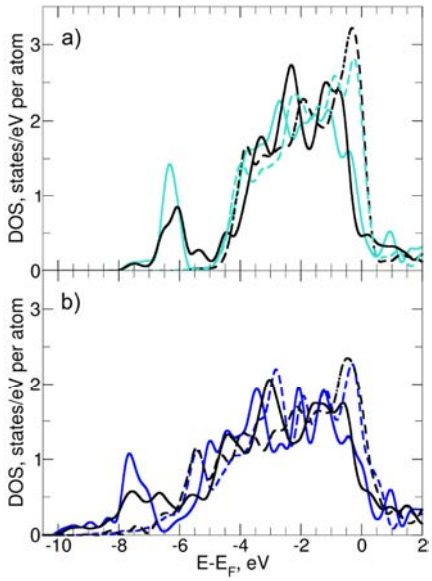

Figure 4. DOS projected on a) Pd and b) Pt atoms on {111} terraces of pristine (dashed lines) and covered by H (solid lines) M(111) single crystals (colored lines) and MgO-supported M_{127} NPs (black lines).

6. CONCLUSIONS

To conclude, we found that surface H significantly affects geometric and electronic structure of 1.6 nm large Pd and Pt nanoparticles supported on MgO(100) as well as their absorption properties with respect to H atoms. Surface H is found to destabilize subsurface H atoms and to stabilize H atoms absorbed deeper in the bulk for both nanoparticles and (111) single crystals of Pd and Pt. This made calculated H absorption exothermic in H-covered Pd nanoparticles, in variation with pristine Pd nanoparticles and H-covered and pristine Pd(111) single crystals. In fact, we calculated the difference between H absorption energies in H-covered Pd nanoparticles and infinite Pd bulk to be 0.08 eV, whereas the value of 0.09 eV was estimated from experimental data. Thus, both the nanostructuring and the effect of surface H on nanoparticle properties appear to be required for facile H absorption in Pd. Since absorbed H atoms are known to be essential for certain reactions, this finding helps to explain the effect of nanostructuring on hydrogenation activity of Pd catalysts. In Pt we quantified the absorption of H to be endothermic by at least ~0.45 eV in (111) single crystals and by at least ~0.3 eV in nanoparticles. Thus, our density-functional calculations predict concentration of absorbed H in Pt nanoparticles to be higher than in Pt single crystals, but less than evaluated in experimental studies. Finally, this study demonstrates that the effect of surface coverage and nanostructuring on properties of transition metals is notably stronger

than the effect of a rather inert MgO support. This finding is fundamental for the elaboration of realistic, trustworthy and computationally efficient modelling schemes in a wide range of studies concerning heterogeneous catalysis.

AUTHOR INFORMATION

Corresponding Author. *E-mail: konstantin.neyman@icrea.cat.
Tel.: (+34) 93 403 7212. Fax: (+34) 93 402 1231.

Notes. The authors declare no competing financial interest.

ACKNOWLEDGMENTS Financial support from the Spanish MEDU is gratefully acknowledged (FPU grant AP2009-3379 to SMK and post-doctoral grant SB2010-0172 to HAA). This study was also supported by the European Commission (FP7-NMP.2012.1.1-1 project ChipCAT, Ref. Nº310191), the Spanish MINECO (CTQ2012-34969) and the Generalitat de Catalunya (2014SGR97, XRQTC). It is a part of COST Actions CM1104 and MP1103. HAA is grateful to the FP7 programme (project Beyond Everest). The authors thank Red Española de Supercomputación for provided computer resources and technical assistance.

REFERENCES

(1) Wilde, M.; Fukutani, K. Hydrogen Detection near Surfaces and Shallow Interfaces with Resonant Nuclear Reaction Analysis. *Surf. Sci. Reports* **2014**, *69*, 196–295.

(2) Johnson, A. D.; Daley, S. P.; Utz, A. L.; Ceyer, S. T. The Chemistry of Bulk Hydrogen: Reaction of Hydrogen Embedded in Nickel with Adsorbed CH_3. *Science* **1992**, *257*, 223–225.

(3) Brandt, B.; Fischer, J.-H.; Ludwig, W.; Libuda, J.; Zaera, F.; Schauermann, S.; Freund, H.-J. Isomerization and Hydrogenation of cis-2-Butene on Pd Model Catalyst. *J. Phys. Chem. C* **2008**, *112*, 11408–11420.

(4) Doyle, A. M.; Shaikhutdinov, S. K.; Jackson, S. D.; Freund, H.-J. Hydrogenation on Metal Surfaces: Why Are Nanoparticles More Active Than Single Crystals? *Angew. Chem. Int. Ed*. **2003**, *42*, 5240–5243.

(5) Teschner, D.; Borsodi, J.; Wootsch, A.; Révay, Z.; Hävecker, M.; Knop-Gericke, A.; Jackson, S. D.; Schlögl, R. The Roles of Surface Carbon and Hydrogen in Palladium-Catalyzed Alkyne Hydrogenation. *Science* **2008**, 320, 86–89.

(6) Wilde, M.; Fukutani, K.; Ludwig, W.; Brandt, B.; Fischer, J.-H.; Schauermann, S.; Freund, H.-J. Influence of Carbon Deposition on the Hydrogen Distribution in Pd Nanoparticles and their Reactivity in Olefin Hydrogenation. *Angew. Chem. Int. Ed*. **2008**, *47*, 9289–9293.

(7) Aleksandrov, H. A.; Kozlov, S. M.; Schauermann, S.; Vayssilov, G. N.; Neyman, K. M. How Absorbed Hydrogen Affects Catalytic Activity of Transition Metals. *Angew. Chem. Int. Ed*. **2014**, *53*, doi: 10.1002/anie.201405738.

(8) Savara, A.; Ludwig, W.; Schauermann, S. Kinetic Evidence for a Non-Langmuir-Hinshelwood Surface Reaction: H/D Exchange over Pd Nanoparticles and Pd(111). *Chem. Phys. Chem.* **2013**, *14*, 1686-1695.

(9) Doyle, A. M.; Shaikhutdinov, Sh. K.; Freund , H.-J. Alkene Chemistry on the Palladium Surface: Nanoparticles vs Single Crystals. *J. Catal.* **2004**, *223*, 444–453.

(10) Ludwig, W.; Savara, A.; Madix, R. J.; Schauermann, S.; Freund, H.-J. Subsurface Hydrogen Diffusion into Pd Nanoparticles: Role of Low- Coordinated Surface Sites and Facilitation by Carbon. *J. Phys. Chem. C* **2012**, *116*, 3539−3544.

(11) Wilde, M.; Fukutani, K.; Naschitzki, M; Freund, H.-J. Hydrogen Absorption in Oxide-Supported Palladium Nanocrystals. *Phys. Rev. B* **2008**, *77*, 113412.

(12) Jewell, L. L.; Davis, B. H. Review of Absorption and Adsorption in the Hydrogen−Palladium System. *Appl. Catal. A* **2006**, *310*, 1−15.

(13) Gillespie, L. J.; Ambrose, H. A. The Heat of Absorption of Hydrogen by Palladium Black at 0°. *J. Phys. Chem.* **1931**, *35*, 3105−3110.

(14) Yudanov, I. V.; Neyman, K. M.; Rösch, N. Density Functional Study of Pd Nanoparticles with Subsurface Impurities of Light Element Atoms. *Phys. Chem. Chem. Phys*. **2004**, *6*, 116–123.

(15) Neyman, K. M.; Schauermann, S. Hydrogen Diffusion into Palladium Nanoparticles: Pivotal Promotion by Carbon. *Angew. Chem. Int. Ed.* **2010**, *49*, 4743–4746.

(16) Aleksandrov, H. A.; Viñes, F.; Ludwig, W.; Schauermann, S.; Neyman, K. M. Tuning the Surface Chemistry of Pd by Atomic C and H: A Microscopic Picture. *Chem. Eur. J.* **2013**, *19*, 1335–1345.

(17) Kozlov, S. M.; Aleksandrov, H. A.; Neyman, K. M. Adsorbed and Subsurface Absorbed Hydrogen Atoms on Bare and MgO(100)-Supported Pd and Pt Nanoparticles. *J. Phys. Chem. C* **2014**, *118*, 15242–15250.

(18) Tao, F.; Salmeron, M. In Situ Studies of Chemistry and Structure of Materials in Reactive Environments. *Science,* **2011***, 331*, 171–174.

(19) Lopez, N.; Łodziana, Z.; Illas, F.; Salmeron, M. When Langmuir Is Too Simple: H_2 Dissociation on Pd(111) at High Coverage. *Phys. Rev. Lett.* **2004**, *93*, 146103.

(20) Fukutani, K.; Itoh, A.; Wilde, M.; Matsumoto, M. Zero-Point Vibration of Hydrogen Adsorbed on Si and Pt Surfaces. *Phys. Rev. Lett.* **2002**, *88*, 116101.

(21) Zaera, F. Key Unanswered Questions about the Mechanism of Olefin Hydrogenation Catalysis by Transition-Metal Surfaces: A Surface-Science Perspective. *Phys. Chem. Chem. Phys*. **2013**, *15*, 11988–12003.

(22) Yamauchi, M.; Kobayashi, H.; Kitagawa, H. Hydrogen Storage Mediated by Pd and Pt Nanoparticles. *Chem. Phys. Chem*. **2009**, *10*, 2566−2576.

(23) Isobe, Y.; Yamauchi, M.; Ikeda, R.; Kitagawa, H. A Study of Hydrogen Adsorption of Polymer Protected Pt Nanoparticles. *Synth. Met.* **2003**, *135−136*; 757−758.

(24) Yamauchi, M.; Kitagawa, H. Hydrogen Absorption in Size- Controlled Pt Nanoparticle. *Chem. Eng. Trans.* **2005**, *8*, 159−163.

(25) Kresse, G.; Furthmuller, J. Efficient Iterative Schemes for ab initio Total-Energy Calculations Using a Plane-Wave Basis Set. *Phys. Rev. B* **1996**, *54*, 11169–11186.

(26) Hammer, B.; Hansen, L. B.; Nørskov, J. K. Improved Adsorption Energetics within Density-Functional Theory Using Revised Perdew-Burke-Ernzerhof Functionals. *Phys. Rev. B* **1999**, *59*, 7413.

(27) Newns, D. M. Self-Consistent Model of Hydrogen Chemisorption. Phys. Rev. **1969**, *178*, 1123-1135.

(28) Fajín, J. L. C; Cordeiro, M. N. D. S.; Gomes, J. R. B.; Illas, F. On the Need for Spin Polarization in Heterogeneously Catalyzed Reactions on Nonmagnetic Metallic Surfaces. *J. Chem. Theory Comput.*, **2012**, *8*, 1737–1743.

(29) Kresse, G.; Joubert, D. From Ultrasoft Pseudopotentials to the Projector Augmented-Wave Method. *Phys. Rev. B* **1999**, *59*, 1758-1775.

(30) Momma, K.; Izumi, F.VESTA 3 for three-dimensional visualization of crystal, volumetric and morphology data. *J. Appl. Crystallogr.* **2011**, *44*, 1272-1276.

(31) Kozlov, S. M.; Aleksandrov, H. A.; Goniakowski, J.; Neyman, K. M. Effect of MgO(100) Support on Structure and Properties of Pd and Pt Nanoparticles with 49-155 Atoms. *J. Chem. Phys.* **2013**, *139*, 084701.

(32) Olander, J.; Lazzari, R.; Jupille, J.; Mangili, B.; Goniakowski, J. Size- and Temperature-Dependent Epitaxy for a Strong Film-Substrate Mismatch: The Case of Pt/MgO(001). *Phys. Rev. B* **2007**, *76*, 075409.

(33) Revenant, C.; Leroy, F.; Lazzari, R.; Renaud, G.; Henry, C. R. Quantitative Analysis of Grazing Incidence Small-Angle X-Ray Scattering: Pd/MgO(001) Growth. *Phys. Rev. B* **2004**, *69*, 035411.

(34) Kozlov, S. M.; Neyman, K. M. Catalysis from First Principles: Towards Accounting for the Effects of Nanostructuring. *Top. Catal.* **2013**, *56*, 867-873.

(35) Yudanov, I. V.; Genest, A.; Schauermann, S.; Freund, H.-J.; Rösch, N. Size Dependence of the Adsorption Energy of CO on Metal Nanoparticles: A DFT Search for the Minimum Value. *Nano Lett.* **2012**, *12*, 2134−2139.

(36) Li, L.; Larsen, A. H.; Romero, N. A.; Morozov, V. A.; Glinsvad, C.; Abild-Pedersen, F.; Greeley, J.; Jacobsen, K. W.; Nørskov, J. K. Investigation of Catalytic Finite-Size-Effects of Platinum Metal Clusters. *J. Phys. Chem. Lett.* **2013**, *4*, 222−226.

(37) Mitsui, T.; Rose, M. K.; Fomin, E.; Ogletree, D. F.; Salmeron, M. Hydrogen Adsorption and Diffusion on Pd(111). *Surf. Sci.* **2003**, *540*, 5–11.

(38) Qi, X. Q.; Wei, Z. D.; Li, L.; Ji, M. B.; Li, L. L.; Zhang, Q.; Xia, M. R.; Chen, S. G.; Yang, L. J. DFT Study on Interaction of Hydrogen with Pd(111). *Comp. Theor. Chem.* **2012**, *979*, 96–101.

(39) Greeley, J.; Mavrikakis, M. Surface and Subsurface Hydrogen: Adsorption Properties on Transition Metals and Near-Surface Alloys. *J. Phys. Chem. B* **2005**, *109*, 3460–3471.

(40) Løvvik, O. M.; Olsen, R. A. Adsorption Energies and Ordered Structures of Hydrogen on Pd(111) from Density-Functional Periodic Calculations. *Phys. Rev. B* **1998**, *58*, 10890–10898.

(41) The internal energy of Pd_2H formation moves 0.07 eV closer to the experimental value of 0.19 eV when zero-point energy corrections are taken into account.

(42) Fukutani, K.; Itoh, A.; Wilde, M.; Matsumoto, M. Zero-Point Vibration of Hydrogen Adsorbed on Si and Pt Surfaces. *Phys. Rev. Lett.* **2002**, *88*, 116101.

(43) Sanchez, S. I.; Menard, L. D; Bram, A; Kang, J. H.; Small, M. W.; Nuzzo, R. G.; Frenkel, A. I. The Emergence of Nonbulk Properties in Supported Metal Clusters: Negative Thermal Expansion and Atomic Disorder in Pt Nanoclusters Supported on γ-Al_2O_3. *J. Am. Chem. Soc.,* **2009**, *131*, 7040–7054.

(44) Strasser, P.; Koh, S.; Anniyev, T.; Greeley, J.; More, K.; Yu, C.; Liu, Z.; Kaya, S.; Nordlund, D.; Ogasawara, H.; Toney, M. F.; Nilsson, A. Lattice-Strain Control of the Activity in Dealloyed Core-Shell Fuel Cell Catalysts. *Nature Chem*. **2010**, *2*, 454–460.

(45) Shao, M.; Odell, J. H.; Peles, A.; Su, D. The Role of Transition Metals in the Catalytic Activity of Pt Alloys: Quantification of Strain and Ligand Effects. *Chem. Commun*. **2014**, *50*, 2173–2176.

(46) Prabhudev, S.; Bugnet, M.; Bock, C.; Botton, G. A. Strained Lattice with Persistent Atomic Order in Pt_3Fe_2 Intermetallic Core-Shell Nanocatalysts. *ACS Nano* **2013**, 7, 6103–6110.

(47) Bader, R. F. W. *Atoms in Molecules: A Quantum Theory*; Oxford Science: Oxford, 1990.

Chapter 5

Steps on Surfaces

In practice, atomically flat extended surfaces of any material can be produced only in exceptional cases, due to their extremely low entropy. On the subnanometer scale surface's roughness is manifested as the presence of atomic steps between more or less extended terraces (Figure 5.1). Similarly to nanoparticle edges,[1] these steps contain some undercoordinated atoms and so they represent another very important form of nanostructuring intrinsically present in most of the samples. Moreover, the abundance of steps may be further controlled by high-temperature annealing or ion sputtering. Also vicinal surfaces with high Miller indexes expose steps arranged in regular pattern. All this makes stepped surfaces important model systems to study properties of low-coordinated atoms, since their atomic structure is generally easier to resolve than the atomic arrangement in nanoparticles. Experimentally steps on surfaces are often studied with scanning tunneling microscopy or spectroscopy as well as atomic force microscopy.[35,289,290] Theoretical studies of stepped surfaces are also rather common, since they are only somewhat more computationally expensive than studies of extended flat surfaces.[26,291,292]

In heterogeneous catalysis atomic steps are very ubiquitous features. One may expect them to be present both on nanoparticulate catalysts[26,293,294] and on their supports.[295,296] In some cases steps may have altered electronic structure,[289,297] due to the presence of low-coordinated atoms. As a consequence, steps commonly bind various species stronger than respective terraces.[295,298] In some cases the stronger adsorption is just due to the possibility for an adsorbate to form more bonds with the substrate when the adsorption happens at the bottom of the step.[299,300] In turn, on catalytic materials many reactions happen preferentially on steps. [25,26,301] On the other hand, steps on supports may serve as nucleation centers for catalytically active nanoparticles and, thus, also affect the reaction.[296,302]

Cerium dioxide in heterogeneous catalysis

In order to achieve a better consistency of the thesis, steps on only one exemplary, but very important material, CeO_2, were investigated from various points of view. Ceria was chosen for a detailed investigation since it is relatively abundant on

[1] The actual degree of similarity between steps on surfaces and respective nanoparticle edges is still controversially discussed in the literature.[293]

Earth and has many diverse applications,[303–305] in particular, it is commonly used as an *active* support for heterogeneous catalysts.[168,218,253] For instance, one of the most prominent applications of ceria is as support in three-way catalysts to abate hydrocarbon, CO and NO emissions from vehicles.[306–308] The ability of cerium oxide support to affect catalytic reactions is often linked to its reducibility, i.e. the ability of cerium to form Ce^{3+} and Ce^{4+} oxidation states in CeO_x oxides of varying stoichiometry.[59,309,310] This allows cerium oxides to serve as an O buffer[12,311,312] or to participate in charge transfer with supported metal clusters.[261,313,314] Nanostructuring of ceria is known to be particularly important for its properties[55,315] and often leads to improved activity of ceria-containing catalysts.[20,316,317] Some studies relate the higher activity of nanostructured ceria to its higher reducibility manifested as lower formation energies of O vacancies, $E_f(O_{vac})$.[55,318,319]

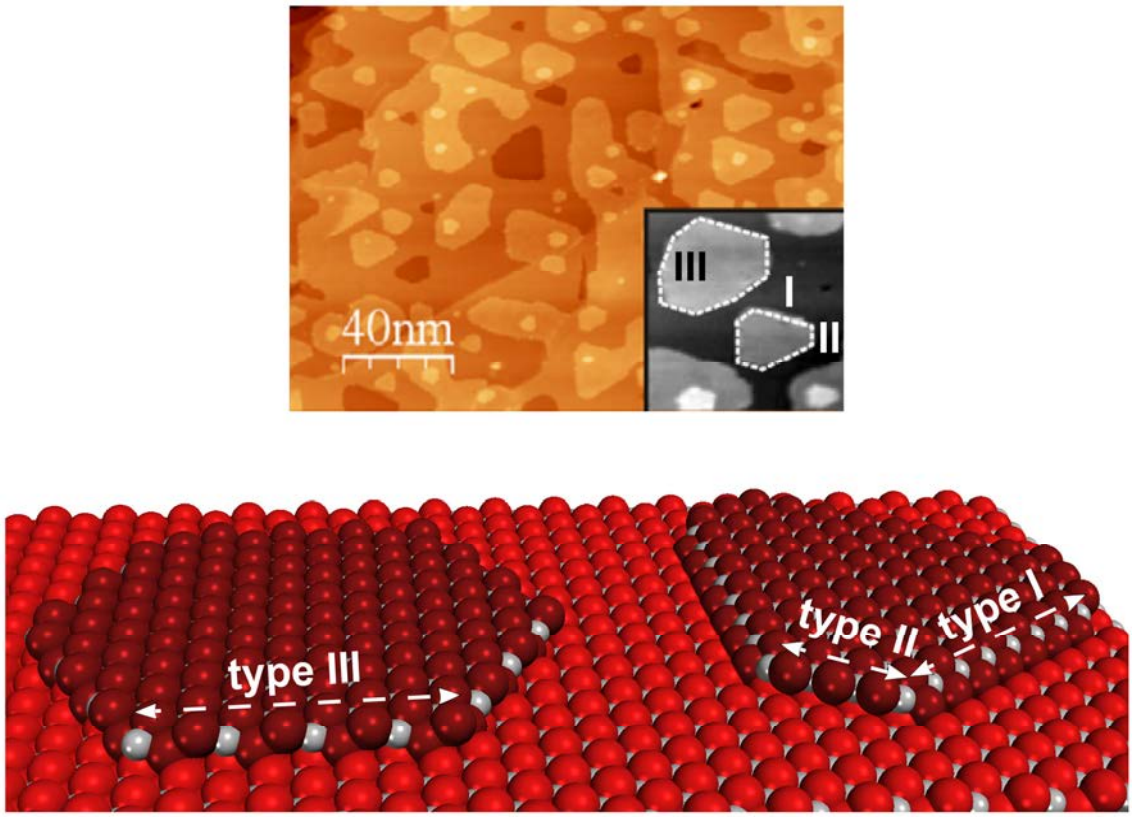

Figure 5.1. STM image and atomic model of rough $CeO_2(111)$ films produced in a controllable way through high-temperature annealing. Nanoislands on the surface expose three different step types. The inset displays area of 30×30 nm. O atoms are displayed in red and Ce ions in grey.

Since steps on surfaces are also a form of nanostructuring, one could expect steps on the most stable surface of ceria, $CeO_2(111)$,[320,321] to be very important for catalysis. Systematic studies of these steps have started only recently and not much is known about their particular role in catalytic processes. However, it is already clear that they are very important for Au/ceria catalysts,[20,271] because they serve as nucleation centers for Au nanoparticles[169,296] and may[299] or may not[47] be preferential adsorption sites for Au atoms. Also Rh and Pd nanoparticles are known to nucleate preferentially at the ceria steps.[322] Also steps on $CeO_2(111)$ appear to adsorb CO somewhat stronger than the regular (111) terraces, but still much weaker than most transition metals.[323]

Unfortunately, in many cases cerium oxides are not adequately described by most LDA and GGA exchange-correlation functionals. Namely, these functionals predict delocalized character of electronic states composing 4f-band of ceria (unoccupied in CeO_2). However, localized f-electrons on Ce cations are observed experimentally, which is manifested as a clear distinction between Ce^{4+} and Ce^{3+} cations in partially reduced ceria and energetic separation between DOS of occupied and unoccupied f-states.[251,324,325] The erroneous description of CeO_x by LDA and GGA may be seamlessly corrected by reducing the self-interaction error[2] via introduction of Hartree-Fock exchange in hybrid functionals.[318,326,327] However, the computational cost of hybrid functionals makes prohibitive simulations of many models sufficiently big to be realistic or representative. A more practical and less computationally expensive way to "fix" LDA and GGA functionals is to introduce Hubbard U corrections for f-states of Ce (see Section 2.2 and Figure 5.2).[324,328,329] These corrections directly apply energetic penalty to solutions with delocalized electrons, and so they favor the formation of individual Ce^{3+} cations. The disadvantage of the simpler DFT+U approach is the absence of a clear procedure to choose the U parameter, which may affect certain results. [261,330] In particular, the value of U seems to shift relative stability of Ce^{3+} and Ce^{4+} cations, which affects the evaluation of reducibility of cerium oxides. Unfortunately, various groups have independently chosen different U parameters in the range of 3 – 7 eV for f-

[2] Since the decay of electron's wavefunction far from atomic nuclei is $\sim e^{-r}$ in calculations without the self-interaction and only $\sim 1/r$ in calculations with the self-interaction error,[399] the latter strongly contributes to the prevalence of delocalized solutions.

states of cerium using different reasonings.[321,331,332] Hence, often no quantitative comparison between different computational studies is possible.

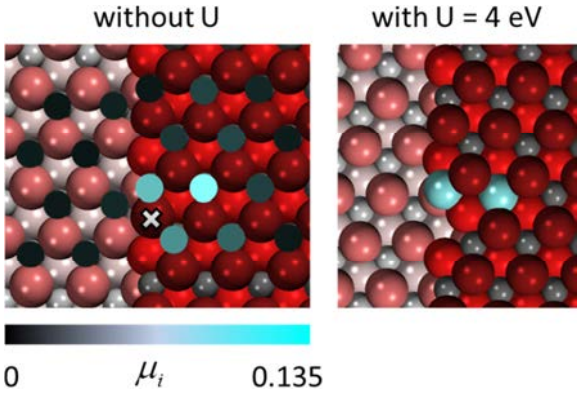

Figure 5.2. Distribution of two excess electrons (i.e. magnetization on Ce cations, μ in Bohr magnetons) formed upon removal of O atom from CeO_2 surface in a GGA calculation with and without U corrections. In the latter case the electrons are localized on two particular Ce cations. O anions are displayed in red and Ce^{4+} ions in grey, Ce^{3+} – cyan. Atoms with darker colors are located in higher layers.

Objectives of this Chapter

Studies discussed in this section aim at versatile characterization of various intrinsic properties of steps on CeO_2(111), that is, properties that are equally important for almost any process happening on them. First of all, this includes unequivocal determination of atomic structures of various step types observed on CeO_2(111), which is an essential prerequisite for subsequent studies. Then, such basic properties as the electronic structure and energetic stability of the steps were considered. The former is particularly interesting in view of ionic character of cerium dioxide, which should result in uncompensated polarity of the steps. Finally, since many advantageous properties of ceria are related to its reducibility, also the ability of steps to form O vacancies, O_{vac}, was simulated.

Because of the size of considered supercells with steps on CeO_2(111), most of the studies were performed using GGA+U approach. In particular, PW91[333] functional augmented by U = 4 eV was chosen based on the analysis[114] of suitability of various U values for description of bulk CeO_2 and Ce_2O_3 and in line with recent works by Neyman et. al.[318,261,334] In Section 5.3 screened hybrid HSE06[94,95] exchange-correlation functional was also used for test purposes. Note that this functional was not fitted to reproduce any data set. It was found that for steps on CeO_2(111) results yielded by

HSE06 are very close to those obtained by the employed PW91+4 approach, which corroborates the suitability of the latter for the purposes of the discussed studies.

Atomic and electronic structure of steps on CeO_2(111)

Naturally, atomic structure of steps on any surface is governed by the crystal structure of the material and the orientation of steps. Cerium dioxide has the fluorite, CaF_2, crystal structure with fcc lattice and similarly to fluorite it is a rather ionic material. Thus, one could expect structures of steps on CeO_2(111) surface to resemble those on CaF_2(111).[24,37,335] Experimentally it was found that steps on CaF_2(111) surface form preferentially parallel to <110>, <211> and <321> directions, however, their atomic structure was not identified.[24] Various steps on CaF_2(111) were also investigated computationally.[335] Depending on the direction of descent from the higher {111} terrace to the lower {111} terrace the following four structures were proposed: type I steps for descent in $[2\bar{1}\bar{1}]$, type II and type II* for descent in $[\bar{2}11]$, and type III steps for descent in $[1\bar{1}0]$ (Figure 5.3). First thing one notes is that two step structures, type II and type II*, are proposed for the descent in $[\bar{2}11]$ direction. The reason is that type II steps have concave structure with some anions "hanging" on the edge above the terrace. Intuitively, one would think that these steps are less energetically stable than type II* steps with the "hanging" anions put down to the lower terrace; however, Hartree-Fock calculations of stepped CaF_2(111) yielded the opposite result. Second, it is important to realize that type I and type II or II* steps correspond to *exactly opposite* descent directions. The reason is the structure of CaF_2(111) and CeO_2(111) surfaces, in which $[2\bar{1}\bar{1}]$ and $[\bar{2}11]$ are not symmetry equivalent. In variations, $[1\bar{1}0]$ and $[\bar{1}10]$ directions are equivalent on CaF_2(111), so there is only one step structure for both of these descent directions.

Steps on CeO_2(111) films on Ru(0001) addressed in Section 5.1 were prepared via high-temperature annealing. When the annealing temperature was below 1000 K distorted hexagonal nanoislands bordered by steps perpendicular to <211> directions[3] appeared on the surface. If the annealing temperature was set above 1000 K nanoislands with regular hexagonal shape and steps perpendicular to <110> directions evolved.

[3] The crystallographic directions were determined by LEED.

Previously it was impossible to conclude on the arrangement of atoms on the steps based solely on results of STM studies despite the achieved atomic resolution.[336,337]

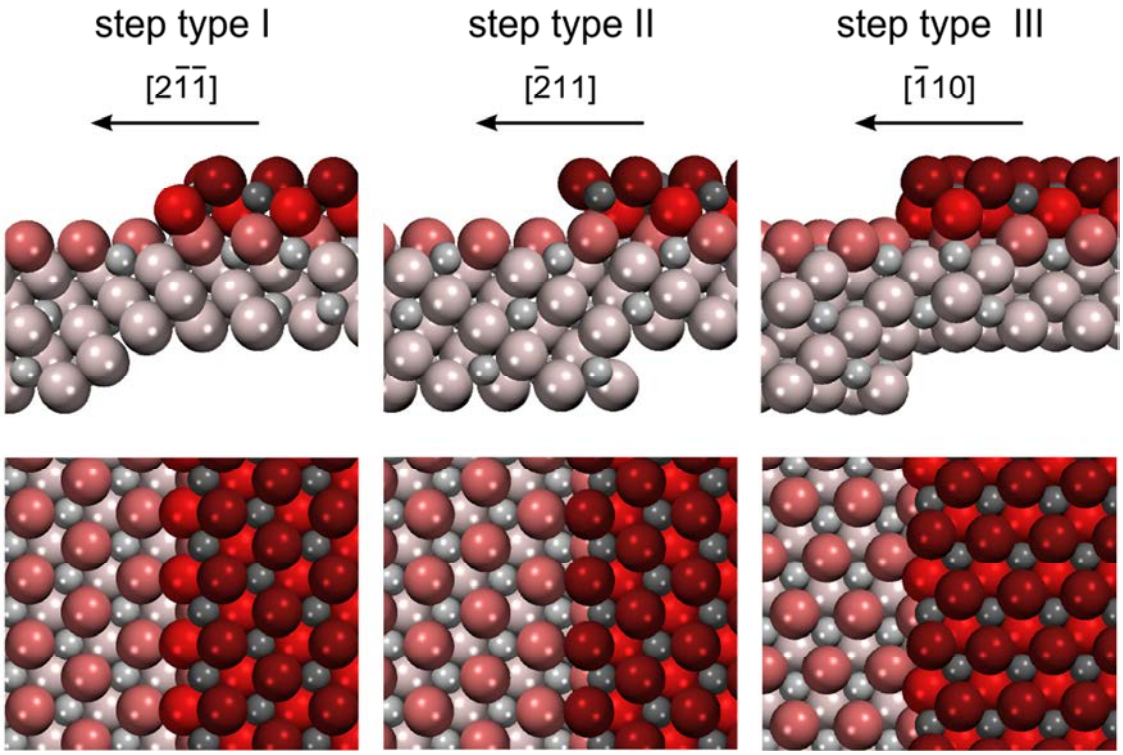

Figure 5.3. Identified stable step structures on CeO_2(111). O anions are displayed in red and Ce ions in grey. Atoms with darker colors are located in surface layers.

To determine the atomic structures of steps on CeO_2(111) STM images were modelled with the Tersoff-Hamann approach at different tunneling voltages and compared to the experimental data.[338] Only similar variation of simulated and measured STM images with the voltage allowed determining the structures unequivocally. Namely, type I steps were calculated to be very bright at lower tunneling voltages, similarly to long edges of nanoislands produced at T < 1000 K. According to simulations, type II steps should not be bright at any voltage like short edges of these nanoislands. Steps perpendicular to <110> directions were predicted to gain brightness only at higher tunneling voltages in full agreement with differential conductance images of nanoislands obtained at T > 1000 K. Finally, type II* steps would appear extremely bright in experiment even at quite low voltages, but such bright steps were never observed. Note that facets of all observed step types are parallel to various surfaces of (110) type.

The reason for the bright appearance of steps in experimental and simulated STM images was their particular electronic structure. Steps of types I, III and especially II* developed step-specific split-off states in the unoccupied 5d-band of Ce. Unlike the rest of the 5d-band the split-off states had significant contributions from s- and p-orbitals in order to accommodate better to the asymmetric electrostatic Madelung potential at the steps.[4] Since s- and p- orbitals extend much further from the nuclei than d-orbitals, the former were much more accessible to the tunneling current, which rendered them very bright in STM.

The energy of the split-off states was governed by the dipole moment on the edges, which was estimated using Bader charge analysis. The dipole moments on type I and II* steps were bigger than 1 Debye per CeO_2 unit and pointed towards vacuum, which lowered the energy of the state-specific states. In variation, the dipole moment on type II steps was pointing towards the support, which moved the split-off states to higher energies and made them undistinguishable from the main band. Finally, type III steps featured rather small dipole moment pointing along the surface, so the position of the split-off states in the density of states was just below the main 5d-band. The effect of dipole moments on the electronic structure of the steps was confirmed by scanning tunneling spectroscopy experiments.

Specific energies of steps on CeO_2(111)

One of the most important characteristic of any object is its (specific) energy, because it determines the abundance of this object in thermodynamic equilibrium. Whereas energies of material objects are often straightforward to derive, there was no good and reliable method to calculate specific energy of such topological feature as a step on a surface. In some studies step energies were derived from specific surface energies of a vicinal surface.[292,339,340] When the latter are calculated using broken bonds approximation the step energy appears as one of the coefficients.[5] At the same time, in

[4] The Madelung potential at steps does not have inverse symmetry because of some missing O anions. However, all atomic orbitals with a defined orbital quantum number possess the inverse symmetry and so cannot fit fully to the potential. The inverse symmetry can be broken only by (partial) hybridization of electronic states.

[5] The specific energy of a vicinal surface, $\gamma_{vicinal}$, may be approximately expressed through the surface energy of the terraces, $\gamma_{terrace}$, and the step energy, β, as $\gamma_{vicinal}$ =

other works various alternative formulas based on decomposition of total energy of the considered slab were proposed without any rigorous justification.[341–343] The latter formulas probably led to qualitatively correct results, but were loosely connected to the actual thermodynamics of the system and so they were not considered very reliable by the theoretical community. Another complication came from the fact that in some practically important cases it remains not straightforward to assess the accuracy of all these theoretical approaches based on the experimental data.[344] The reason is that the determination of absolute specific step energies from STM data requires a very complex analysis of step fluctuations.[345–347]

Three different methods were used to evaluate absolute specific energies of steps on CeO_2(111) in Section 5.2. In the first method, vicinal-γ, step energies were derived bases on the analysis of surface energies of vicinal surfaces. This is the same way that was used in some previous studies.[292,340,348] Other two methods were proposed for the first time and were based on the decomposition of the total energy of slabs with vicinal surfaces in the vicinal-*E* method or slabs with stripes on them in the stripe-*E* method. Importantly, all the involved formulas were derived within the same theoretical framework, which guaranteed the consistency between different methods. In turn, energies of steps on CeO_2(111) calculated with all three methods nicely agreed with each other.

In all these three methods step energies are obtained through linear regression of a set of total or surface energies of pertinent structures. This way of analysis is necessary to avoid high sensitivity of the obtained values to certain computational parameters, known also for calculations of surface energies.[349,350] Since step energies were calculated using a statistical procedure, it became possible to estimate their *statistical* accuracy, which reflects deviations of DFT-calculated values from theoretically derived trends.[6] In line with the central limit theorem, the accuracy of the energies (slowly) improves with the growing number of data points used in the regression. At the same time, since a rather demanding electronic structure calculation

---

$\gamma_{terrace}*cos(\theta) + \beta/L$, where L is the distance between adjacent steps and θ is the misalignment angle between the two surfaces. Possible deviations from this relation are usually *defined* as step-step interactions.

[6] Some authors attribute these deviations to step-step interactions.[292,348]

of a stepped surface is required for each data point, one would want to keep the number of data points at minimum. Thus, it is could be helpful to devise a method that yields the most accurate step energies with the lowest number of calculations involved.

The well-known vicinal-γ method led to a rather poor statistical accuracy (up to 20%) in the derived step energies of steps on $CeO_2(111)$. This degree of accuracy may render this method barely applicable in some cases, e.g. for steps on $TiO_2(101)$.[292] The accuracy of the newly proposed vicinal-*E* method was 50% higher. Moreover, this method required four times less calculations than the vicinal-γ method, because it deals with total energies of slabs of vicinal surfaces instead of respective specific surface energies.[7] The third method, stripe-*E*, was even more accurate than the vicinal-*E* method, despite that it required the same number of calculations. The disadvantage of this method, however, is that it does not yield specific energy of single step, but rather a sum of specific energies for steps located on both sides of the considered stripe. Whereas stripes with type III steps have the same type of steps on each side, stripes with type I steps on one side have to have type II or II* steps on the opposite side due to the symmetry considerations. Thus, only sums $\beta(I) + \beta(II)$ and $\beta(I) + \beta(II^*)$ were possible to obtain with the stripe-*E* method.

The calculated specific energies of steps on $CeO_2(111)$ were in line with the results of STM experiments. Namely, steps of type I had the lowest calculated energy and was the most abundant on the surface, when annealing was performed at $T < 1000$ K. Type II steps were estimated to have ~30% higher energy at this temperature, which was in good agreement with 25% energy difference obtained from experimental data via the reverse Wulff construction of the shape of observed nanoislands. Specific energy of type III steps was calculated to be very similar to the energy of type II steps, which explains their appearance in experiment at higher annealing temperatures. In turn, the specific energy of type II* steps was calculated to be roughly twice higher than energies of other step types. So it is not surprising that the presence of type II* steps were not detected in experiment.

[7] Surface energies are also calculated via the linear regression of several data points, which increases the total number of considered structures few times.

Formation of oxygen vacancies on steps on $CeO_2(111)$

As was commented before, many advantageous properties of cerium oxide are thought to be due to its reducibility, which may be described by the formation energy of O vacancies, $E_f(O_{vac})$, in CeO_2.[319] So the formation of O vacancies has been addressed computationally for many systems based on ceria.[59,315,319,332] Interestingly, $E_f(O_{vac})$ was calculated to dramatically decrease from 2.60 eV on extended $CeO_2(111)$ surface to 0.46 eV on $Ce_{80}O_{160}$,[315] which indicates much higher reducibility of nanostructured ceria compared to more regular samples. Hence, one could expect also a higher reducibility of stepped ceria surfaces compared to pristine $CeO_2(111)$.

Computational studies of ceria with oxygen vacancies (and partially reduced cerium oxide,[313,328,351] in general) are complicated by the presence of both Ce^{3+} and Ce^{4+} cations in the same system. With each oxygen vacancy formed through the removal of a neutral O atom (instead of O^{2-}) two Ce^{4+} ions are reduced to Ce^{3+}. According to the Boltzmann distribution in experiment at moderate[8] temperatures O vacancies and Ce^{3+} cations will adopt the most thermodynamically stable configuration. However, in computational studies almost all possible configurations with varying positions of O_{vac} and Ce^{3+} may be calculated, not only those corresponding to the lowest possible energy. Thus, in order for computational studies to represent the experimental situation the most energetically stable $O_{vac} + 2Ce^{3+}$ configuration should be identified among a multitude of possibilities. This is not a doable task in simplest cases, e.g. O_{vac} formation on ideal $CeO_2(111)$ surface, where many different sites are equivalent by symmetry.[261,324,327] However, systems with more complex morphologies, such as ceria nanoparticles[315,318,328] or stepped ceria surfaces, typically expose a significant number of inequivalent sites. For these systems the location of the most stable configuration cannot be achieved just by the "brute-force" approach and more sophisticated methods are required. One such method is to perform a prescreening of various structures with interatomic potentials and then to reoptimize a limited set of low-energy structures with DFT.[328] However, this method may not be applicable for systems containing not only Ce and O ions but also other elements, for which good interatomic potentials do not yet exist.

[8] That is temperatures sufficient to overcome existing kinetic barriers, but not high enough to make probable the presence of high-energy structures.

Despite that the location of the lowest energy O_{vac} + $2Ce^{3+}$ configuration may be require some effort, in many cases it must be done to correctly predict the energetics of the system or process. Indeed, the energy of the system may vary by ~0.5 eV depending on the position of O_{vac} and by additional ~0.5 eV depending on positions of Ce^{3+} cations as computed for CeO_2(111).[261,324,327] In the lowest-energy configuration on CeO_2(111) oxygen vacancy is formed in the subsurface (third atomic) layer and Ce^{3+} ions settle within the top surface Ce layer in the second cerium coordination sphere of the vacancy. In variation, in ceria nanoparticles O vacancies form preferentially at the edges between {100} and {111} facets and Ce^{3+} ions are located on the nanoparticle corners or edges in the most energetically stable configurations.[315,318] Energies of various structures are found to vary by up to 1.1 eV depending on sites occupied by Ce^{3+} cations and by more than 1.5 eV depending on the location of O_{vac}. The relative stability of various O_{vac} + $2Ce^{3+}$ configurations appears to be governed by the electrostatic potential at O_{vac} and Ce^{3+}, instead of their position with respect to each other. Since ceria is an ionic material, there is a significant variation of the electrostatic potential within nanoparticles, which explains strong dependency of relative energies of Ce_NO_{2N-1} NPs on positions of O_{vac} and Ce^{3+}. However, on stepped surfaces the variation of electrostatic potential between different sites was found to be not so strong in Section 5.3 and other effects become important for relative stability of different O_{vac} + $2Ce^{3+}$ configurations. Hence, electrostatic potential at different sites could not be used as a guideline to predict the relative energies. Moreover, a more detailed analysis of the calculated results reveals that the correlation between relative energies and coordination numbers of the vacancies is very weak.[315] In view of the calculated spread of relative energies depending on O_{vac} + $2Ce^{3+}$ configurations, it becomes extremely important to identify the configuration with the lowest energy correctly. Indeed, the formation of O vacancies and/or reduction of Ce^{4+} to Ce^{3+} happens also in the course of various reactions on ceria and deviations of ~0.5 eV for CeO_2(111) or even ~1.5 eV for ceria NPs would lead to *qualitatively* different results.

In Section 5.3 the formation of O vacancies and concomitant Ce^{3+} cations on the experimentally identified step types on CeO_2(111) is considered and a novel procedure to search for the lowest-energy configuration of Ce^{3+} is presented. Using this procedure it was possible to obtain the lowest possible O vacancy formation energies, $E_f(O_{vac})$, with the probability of more than 97% for each step type. In order to achieve the

convergence of $E_f(O_{vac})$ with respect to the size of employed slab supercells, rather big cells with the area of around 2 nm^2 were employed. These cells contained ~150 atoms, which resulted in 2610 – 3780 feasible $O_{vac} + 2Ce^{3+}$ configurations to be considered for each step type. The proposed prescreening procedure, however, allowed performing only 25 – 31 DFT calculations per step type to identify the lowest-energy structure with > 97% probability. That is, the proposed prescreening procedure decreased the computational cost of the study roughly hundred times.

The prescreening procedure is based on a certain correlation between relative energies obtained in GGA+U calculations with magnetization on Ce ions in respective calculations without Hubbard U corrections (Figure 5.2). In the latter calculations, excess electrons formed with the O_{vac} become (incorrectly) delocalized among many Ce cations, partially reducing them from Ce^{4+} to $Ce^{(4-\delta)+}$. The degree of reduction can be monitored by the magnetization on involved atoms. It turns out Ce ions that are more (partially) reduced in a calculation without Hubbard corrections are the same ions that are easier to reduce in a GGA+U calculation. Thus, having performed a single calculation of defective ceria without U corrections, one can prepare a list of structures that are likely to yield low-energies in GGA+U calculations with localized excess electrons. Unfortunately, on $CeO_2(111)$ with steps the numerical correlation between relative $E_f(O_{vac})$ and relative magnetizations calculated by pristine DFT is not so strong.[9] So only via quantile regression analysis it was possible to establish a reliable criterion used in the prescreening procedure.

With the help of this procedure it was found that steps on $CeO_2(111)$ are indeed more reducible than pristine $CeO_2(111)$. Namely, the formation energy of O vacancies on type I, II, and III steps were calculated to be 0.53 – 0.70 eV lower than on the regular (111) surface. This decrease in $E_f(O_{vac})$ will, of course, manifest itself in many reactions taking place on the steps. Similar decrease of $E_f(O_{vac})$ with respect to $CeO_2(111)$ was calculated on $CeO_2(110)$.[329,331] In all most energetically stable configurations two or three-coordinated O was removed from the upper or the lower part of the step. Concomitant Ce^{3+} cations were located either on the upper terrace of the step in the second cerium coordination sphere of the vacancy (like on regular $CeO_2(111)$ surface)

[9] One could expect the correlation to be stronger on e.g. nanoparticulate ceria, where there is more variation between properties of different sites.

or on the step itself in the first coordination sphere of the vacancy. The only exception was type II step with O_{vac}, where one of Ce^{3+} cations locates in the *subsurface* (fifth atomic) layer. This illustrates that the formation of subsurface Ce^{3+} cations is energetically feasible and may happen in certain situations. In fact, by analyzing all calculated O_{vac} + $2Ce^{3+}$ configurations it was found that on average systems with subsurface Ce^{3+} are only ~0.1 eV less energetically stable than those with only surface Ce^{3+} cations. The possible presence of subsurface Ce^{3+} cations is rarely ever considered in many computational studies in order to decrease astonishing number of possible O_{vac} + $2Ce^{3+}$ configurations. However, they can be accounted for using the developed prescreening procedure.

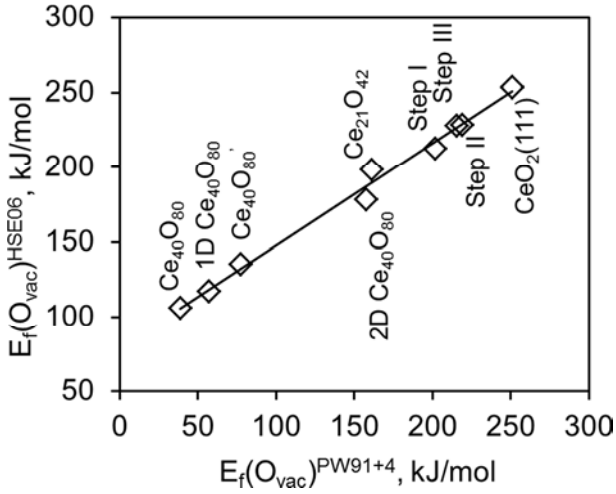

Figure 5.4. The correlation between formation energies of O vacancies on various forms of nanostructured ceria (including those from Section 11.7) calculated with PW91 functional with U = 4 eV corrections and much more computationally expensive hybrid HSE06 functional.

To assess the accuracy of the employed GGA+U scheme formation energies of O vacancies on stepped ceria surfaces were calculated also by supposedly more reliable hybrid HSE06 functional (Figure 5.4). These energies were compared to those obtained using the employed GGA+U method, PW91 functional with U = 4 eV, and two other common variations, PW91 or PBE[81] functional with U = 5 eV. Among those three methods the employed approach yielded values that were the closest to HSE06 values with deviations inferior to 0.2 eV. This suggests that the employed computational scheme was as reliable as more time-consuming hybrid calculations for the purposes of the discussed studies.

Section 5.1

Formation of One-Dimensional Electronic States along the Step Edges of $CeO_2(111)$

Niklas Nilius,[†,*] Sergey M. Kozlov,[‡] Jan-Frederick Jerratsch,[†] Martin Baron,[†] Xiang Shao,[†] Francesc Viñes,[‡] Shamil Shaikhutdinov,[†,*] Konstantin M. Neyman,[‡,§,*] and Hans-Joachim Freund[†]

[†]Fritz-Haber-Institut der Max-Planck-Gesellschaft, Faradayweg 4-6, 14195 Berlin, Germany, [‡]Departament de Química Física, Universitat de Barcelona, C/Martí i Franquès 1, 08028 Barcelona, Spain, and [§]Institució Catalana de Recerca i Estudis Avançats (ICREA), 08010 Barcelona, Spain

ABSTRACT

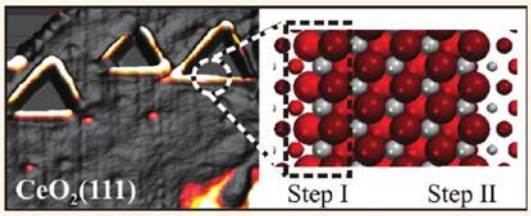

Scanning tunneling microscopy (STM) combined with density functional theory (DFT) are used to analyze the structural and electronic properties of step edges on the surface of $CeO_2(111)$ films grown on Ru(0001). Depending on the preparation conditions, ⟨211⟩ or ⟨110⟩-oriented steps develop on the surface, which results in the formation of ceria ad-islands with hexagonal or triangular shapes. STM conductance spectroscopy reveals pronounced differences in the electronic properties of the step edges, as reflected in different onset positions of the ceria conduction band. The band shifts are related to the development of distinct edge electronic states that split-off from the ceria conduction band, as shown with DFT calculations. The separation of the edge states from the main band is governed by the atom-coordination and local charge-distribution along the edge, the latter giving rise to the development of electrostatic dipoles. We expect that the observed edge morphologies determine not only the electronic properties but also the adsorption behavior of step edges on the $CeO_2(111)$ surface.

KEYWORDS: ceria · step edges · electronic properties · edge polarity · STM · DFT

Cerium dioxide plays an important role in heterogeneous catalysis, both as active material and support.[1−4] Its outstanding redox properties rely on two closely related aspects. First, ceria exhibits a particularly low formation energy for oxygen vacancies, which renders lattice oxygen available in chemical reactions.[5−7] Second, ceria is a good electron acceptor, as the initially empty Ce 4f states can be filled up with electrons, thereby reducing the charge state of respective Ce ions from +4 to +3.[8] The latter effect facilitates electron transfer from suitable adspecies into the oxide surface, promoting the chemical activity of the material.[4,9]

Naturally, defects and low-coordinated sites in the ceria surface are most susceptible to reduction processes and therefore strongly involved in the oxide chemistry. This has been demonstrated in a number of recent experiments that revealed a higher catalytic activity for defect-rich ceria nanoparticles with respect to the extended surface.[10−13] Moreover, one-dimensional (1D) defects, that is, step edges and dislocation lines, have been identified as preferred nucleation sites for metal particles.[14] The specific properties of such defects have several reasons. Naturally, atoms along step edges and grain boundaries are characterized by a reduced number of nearest neighbors, which renders them susceptible to desorption[15] and explains the small vacancy-formation energies.[16] A reduced atom-coordination also alters the electronic structure of line defects, being characterized by split-off and 1D electronic states that are not present in the bulk.[17−20] In addition, the geometric distortions that are exerted in the ceria lattice by converting Ce^{4+} into more spacious Ce^{3+} ions are better accommodated at step edges than in the ideal surface.[6,21,22] Another, widely disregarded point concerns the charge imbalance that is produced in an ionic crystal by certain defects. The (111) surface of ceria comprises alternating layers of cations and anions and belongs to type II polar terminations according to Tasker's scheme.[23,24] Whereas O^{2-}−Ce^{4+}−O^{2-} trilayers, being the regular (111) building blocks, are fully charge compensated, any perturbation of this configuration may induce a dipole moment. Given the large energies associated with polar structures, the contribution of such defects to the surface free-energy and hence the chemical properties of ceria might be substantial.[23]

* Address correspondence to nilius@fhi-berlin.mpg.de, shaikhutdinov@fhi-berlin.mpg.de, konstantin.neyman@icrea.es.

Received for review September 22, 2011 and accepted December 29, 2011.

Published online December 29, 2011
10.1021/nn2036472

In this work, we have analyzed the topographic and electronic structure of step edges on the CeO_2(111) surface, using a combined scanning tunneling microscopy (STM) and density functional theory (DFT) approach. Whereas a detailed geometric characterization of the ceria steps has been reported in a recent atomic-force microscopy study,[25] no information on their electronic structure has been provided so far. Here, we demonstrate that step edges on the CeO_2(111) surface have unusual electronic and electrostatic properties that might be decisive for the adsorption and reaction behavior of this particular oxide.

RESULTS AND DISCUSSION

Step Morphologies. Large-scale STM images of crystalline CeO_2(111) films exhibit two kinds of step edges (Figure 1a). The first one delimits wide, atomically flat terraces and originates from steps in the underlying Ru(0001) support. The second type borders hexagonal ad-islands and pits that develop during oxide growth. We will focus our discussion to the latter type that is intrinsic to the ceria lattice. Step edges surrounding the ceria ad-islands have the typical height of one O−Ce−O trilayer (0.31 nm), indicating that the (111) surface develops a sole termination. Depending on the preparation conditions, two prevalent step orientations are observed:

(i) Low temperature films (T_{anneal} < 1000 K) develop two ⟨110⟩-oriented edge types that run along the high-symmetry axes of the ceria lattice and have opposite descents (Figure 1b). In both cases, the spacing between the edge atoms amounts to 0.382 nm, which matches the bulk lattice constant of ceria.[26] The length ratio between the two step types was found to vary with annealing temperature of the film. Whereas at 1000 K, one step type is roughly two times longer than the other, producing islands with truncated triangular shape (Figure 1b), the two edges are equally long at 900 K and the islands become hexagonal.[25] The orientation of the triangular islands inverts when crossing a step edge or domain boundary in the film, suggesting that the respective step type changes position within the island (Figure 1a).

(ii) The second step type runs along ⟨211⟩ directions of the oxide lattice and preferentially develops at annealing temperatures above 1000 K (Figure 1c). In accordance with the 30° rotation with respect to the ⟨110⟩ edges, the spacing of the edge atoms is larger by a factor of $\sqrt{3}$ (0.67 nm). Only one step configuration is observed in this case and all ad-islands are therefore of hexagonal shape.

On the basis of the orientation and topographic appearance of step edges in the experiment, we have searched for corresponding structure models by means of total energy calculations. Out of various considered configurations, we have concentrated on those that are characterized by low formation energies and have the stoichiometry of bulk ceria.[16] Optimized ⟨110⟩-oriented steps either comprise down-sloping O−O units perpendicular to the edge direction (Figure 2a, left) or display a concave shape with the outermost atom row being an O-row in the topmost atomic plane (Figure 2a, center). Following the established notation for step edges on the iso-structural CaF_2(111) surface,[27−29] we refer to the two step configurations as type I (positive descent) and type II (negative descent) in the following. While the positive descent of the type I edge corresponds to a (110) nanofacet, the type II descent resembles a (111) plane. The two step types can also be distinguished *via* their normal-vectors within the surface, which run along

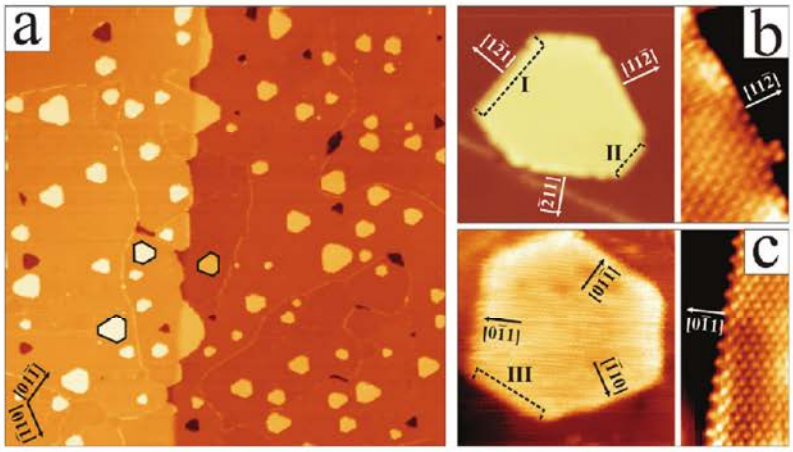

Figure 1. (a) STM image showing the CeO_2/Ru(0001) film-morphology after annealing to a maximum temperature of 1000 K (U_S = 3.0 V, 280 × 280 nm^2). All islands are delimited by type I and II steps and invert their shape when crossing a domain boundary or step edge. (b) Close-up images of a truncated triangular I/II island (20 × 20 nm^2) and a type I step shown with atomic resolution (6 × 3 nm^2). (c) STM images of a hexagonal island bordered by type III steps (20 × 20 nm^2) and the same step type shown with atomic resolution (10 × 5 nm^2). The corresponding normal-vectors are indicated in the figures.

[11$\bar{2}$], [1$\bar{2}$1], or [$\bar{2}$11] directions for type I edges and along [$\bar{1}\bar{1}$2], [$\bar{1}$2$\bar{1}$], or [2$\bar{1}\bar{1}$] for type II.

The crystallographic reason for the occurrence of two inequivalent ⟨110⟩ steps is that the corresponding plane perpendicular to the surface is not a symmetry plane of the fluorite lattice. This also explains why the relative step positions within a given island change when going from one trilayer to the next (Figure 1a). The fact that the island shape inverts also when crossing a domain boundary suggests that two stacking-domains with a reversed sequence of the oxygen planes (ABC and CBA) are present in our films. The observed temperature-driven changes from triangular to hexagonal island shapes, on the other hand, reflect the different thermodynamic stabilities of type I and II steps, which will be discussed in a forthcoming paper.

As the ⟨211⟩-oriented steps follow a symmetry plane of the fluorite lattice, only one step type is revealed in this case (Figure 2b). The energetically favored structure has a vertical descent and all planes of the O−Ce−O trilayer terminate at the same position. The normal vector of ⟨211⟩ steps points to one of the equivalent ⟨$\bar{1}$10⟩ directions and the respective nanofacet is a ($\bar{1}$10)-type of plane. We will refer to these steps as type III in the following. We note again that only stoichiometric step configurations have been considered here due to computational limitations. Potential nonstoichiometric models can be found in the literature.[16,25]

Electronic Properties of Step Edges: Experimental Results. The easiest way to explore the electronic structure of the ceria step edges is the acquisition of bias-dependent STM images, as shown for type I and II steps in Figure 3. None of the exposed edges feature a particular contrast at small positive bias, when electrons tunnel from the tip into the empty f-states of ceria.[30,31] This situation changes above 4.0 V when the longer steps of the quasi hexagonal islands (assigned to type I) and sections of the domain boundaries start to appear bright. This contrast enhancement gives a first hint on the different electronic nature of line defects with respect to the flat CeO_2 surface. Differential conductance (d*I*/d*V*) maps that directly probe the availability of electronic states at a given bias provide deeper insight into the state-density along the step edges. A corresponding image series is shown in Figure 4a for quasi-hexagonal islands bordered by longer type I and shorter type II steps. Below 4.0 V, no topographic contrast is revealed for the island edges as compared to the interior, whereas the simultaneously taken d*I*/d*V* map already features an enhanced edge-signal due to a new, yet weak conductance channel. Above 4.0 V, the type I steps exhibit a sharp increase of their apparent height that is absent for type II steps and imprints a distinct 3-fold symmetry onto the actually hexagonal islands. In the d*I*/d*V* maps, the contrast maximum shifts from the step edges to the flat surface, suggesting that the new transport channel becomes available there as well. At even higher bias (4.4 V), the contrast enhancement of type I steps diminishes again in the topographic channel and the d*I*/d*V* maximum shifts from the flat surface to the interior of the spatially confined islands. The described contrast evolution is

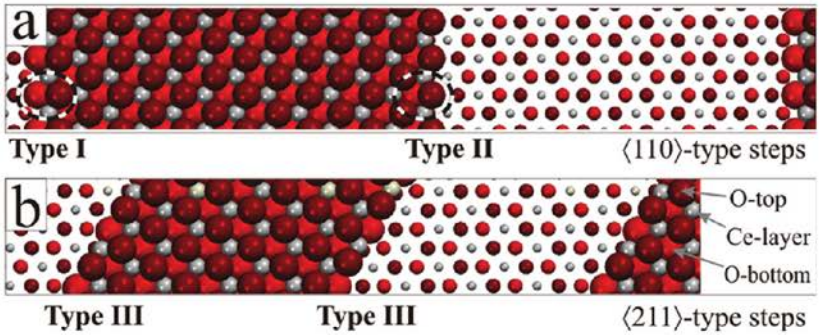

Figure 2. (a) DFT structure model of a CeO_2(111) trilayer stripe exposing type I (left) and type II steps (center). Typical building blocks of the steps are marked by dashed ovals. (b) Structure model of a trilayer stripe delimited by type III steps.

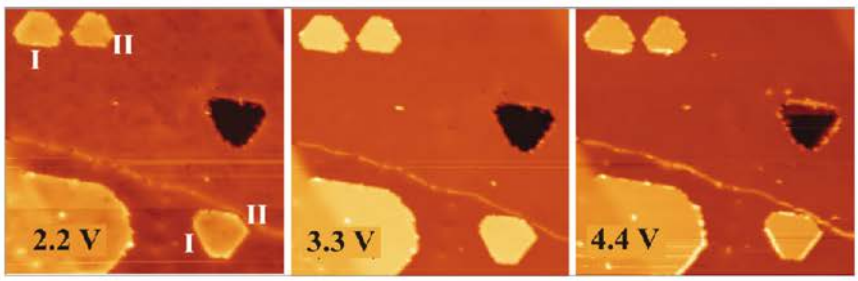

Figure 3. STM topographic images of the ceria surface exposing type I and II steps at three different bias voltages (65 × 65 nm^2). Note the bright appearance of type I steps and lines defects at 4.4 V sample bias.

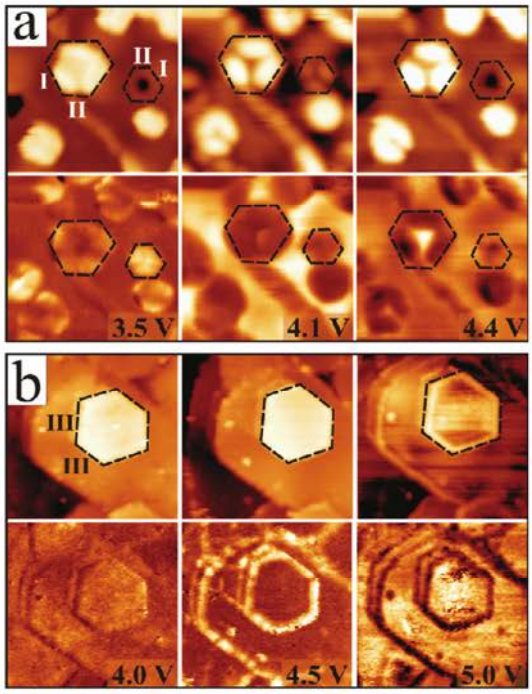

Figure 4. Topographic (upper row) and conductance images (lower row) of ceria ad-islands and holes exposing (a) type I/II and (b) type III steps. The images are 25 × 25 nm^2 in panel a and 45 × 45 nm^2 in panel b and have been taken at the indicated bias voltages.

not specific to the edges of ceria ad-islands, but occurs in a similar fashion for trilayer-deep holes and grain boundaries (Figure 4a). Also there, certain fractions of the line defects turn bright at relatively low bias, indicating a similar electronic structure.

Ceria islands terminated by type III steps show a comparable behavior, only that the threshold bias at which the contrast change occurs is higher. Below 4.5 V, the inner part of the ad-islands and surrounding step edges appear with the same topographic height, while a characteristic brim becomes visible in the accompanying d*I*/d*V* maps (Figure 4b). Again, the signal enhancement at the edges emerges first in the conductance channel, while the topographic signature only follows at 0.5 V higher bias. This offset reflects the integrating nature of STM images, where all electronic states between a preset sample bias and the Fermi level contribute to the detected contrast.

The presence of distinct electronic states along type I ceria step edges is confirmed with d*I*/d*V* spectra taken in the region of the conduction band (Figure 5). Apart from a small peak at 2.3 V that marks the empty Ce 4f states,[30] no conductance signal is detected below 3.5 V in agreement with the large oxide band gap. Surprisingly, the conduction-band onset that shows up as pronounced maximum is reached at different energies depending on the surface position selected for spectroscopy. The lowest onset is detected for type I step edges (3.6 V), in correspondence with their bright

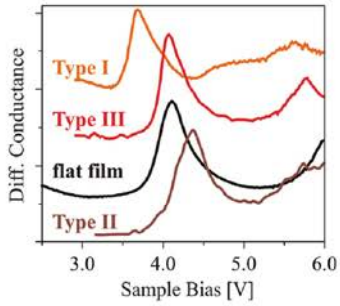

Figure 5. Differential conductance spectra taken at different step edges and the flat CeO_2(111) surface with enabled feedback loop.

appearance in topographic images taken in this bias range. The flat surface and type III edges follow at around 4.1 V and the highest onset position (4.4 V) is found for type II steps that indeed remain featureless in the topographic images. It is this spatial variation in the conduction-band onset that is responsible for the distinct bias-dependent contrast of ceria step edges in the STM. We note that d*I*/d*V* spectroscopy can only provide an approximate value of the band onset, as the oxide states experience a slight upshift in the tip-induced electric field. However, relative changes in the band positions are reliably determined in the experiment.

Electronic Properties of Step Edges: Results of the DFT Calculations. To analyze the nature of electronic states emerging on the ceria step edges, we have calculated their LDOS using the structure models shown in Figure 2. The lowest unoccupied states are the Ce 4f orbitals at 2.5 eV above the valence-band edge, that is, inside the fundamental gap. The conduction band is reached at around 5.0 eV (Figure 6), a value that slightly depends on the size of the considered system and the proximity to adjacent step edges. On the regular (111) surface, the states at the band onset have Ce 5d character with a small 6sp contribution; however this picture changes at the step edges. Along type I steps, new states with notable sp contribution occur at 0.6 eV below the conduction-band onset. Similar states are found along type III steps, only their energy splitting from the main band is just 0.15 eV. A significant sp contribution and energy position below the main band renders these split-off states particularly important for electron tunneling into the step edges. This relevance becomes immediately clear from the simulated STM images, as shown for the different edge types in Figure 7. Below the conduction band onset, that is, inside the gap, the topographic contrast is entirely governed by the true height difference between the ad-island and the oxide surface and the step edges remain featureless. At 4.5 V, the type I step appears bright because its split-off band becomes available for tunneling. The contrast enhancement vanishes above 5.0 V, when the regular conduction band is reached on type II steps and the flat surface as well. A similar behavior is revealed for

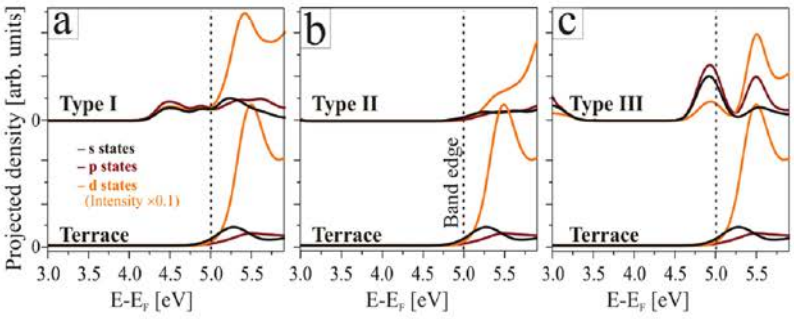

Figure 6. Calculated density of *s*, *p*, and *d*-states along the different step edges and the flat ceria surface. The split-off states below the conduction band onset are clearly visible for type I and III steps.

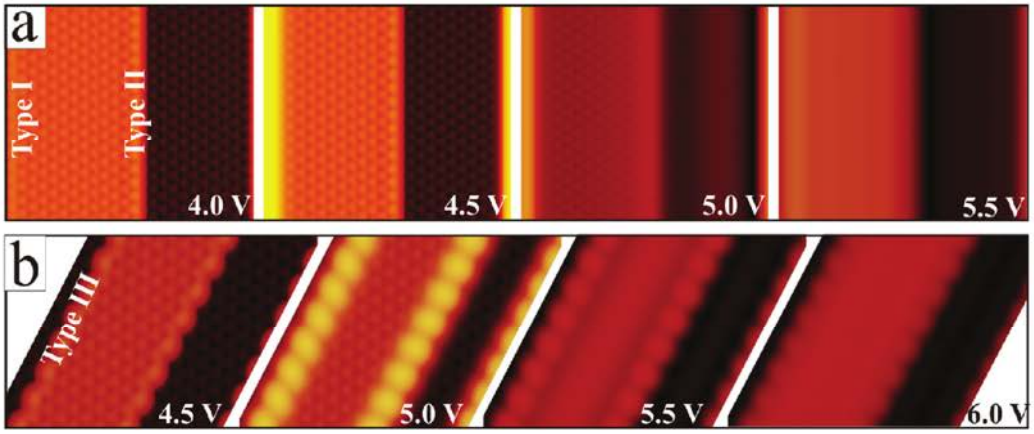

Figure 7. Simulated STM images for (a) type I/II and (b) type III step edges. Depending on the bias voltage, the type I and III step edges appear bright with respect to the flat surface.

type III steps, which also appear with their true topographic height for bias values inside the gap, but turn bright once the edge states are reached at 5.0 V. The split-off states identified in the DFT calculations thus provide a plausible explanation for the distinct edge contrast observed in the STM. Their presence is also compatible with the lower conductance onset revealed for type I steps in the d*I*/d*V* spectra shown in Figure 5.

Discussion. In this section, we will address the structural and electrostatic peculiarities of the ceria step edges that are responsible for the development of the split-off states. The most obvious deviation from he flat surface is the lower coordination number of the step atoms. Whereas Ce ions along type I and II steps are six-fold coordinated (compared to seven-fold in the flat surface), this number reduces to five at type III edges. A smaller coordination number weakens the Madelung potential and lowers its symmetry at the edge, which in turn affects the local gap size. This influence has been explored for the Ce d states that experience a symmetry-dependent energy shift. On type I steps, mainly the d(xz) and d(z^2) orbitals are stabilized, whereas on type III steps the d(xy), d(xz), and d(x^2-y^2) states appear at reduced energy. Furthermore, an asymmetric Madelung potential is incompatible with the intrinsic inversion symmetry of d levels, which explains why the split-off states have a pronounced sp character. The role of the Madelung potential on the local gap-size has been previously discussed for step edges in the MgO(001) surface.[32,33]

A reduced coordination number at the edge also induces qualitative changes in the chemical bonding between cations and anions. Whereas ionic contributions are strengthened in a dense-packed lattice, covalent interactions gain importance among undercoordinated atoms and ions. Such modifications in the binding character can be probed by the Bader charges calculated for the different step configurations.[34] Indeed, the absolute charges of Ce and O ions are slightly reduced by up to 0.1e at the step with respect to the ideal surface (Ce: +2.35e, O: −1.2e), indicating a larger covalent contribution. The more covalent character of the bonds results in the formation of mixed Ce−O states that may be displaced from the main bands. Such a splitting of discrete states from a bulk continuum is a common phenomenon and has been observed for surfaces and step edges of various metallic, semiconducting, and insulating materials.[17,20,35,36] The split-off states revealed here are therefore fully compatible with the concept of 1D edge states.

Although the occurrence of distinct edge states may be rationalized by the deviating binding properties

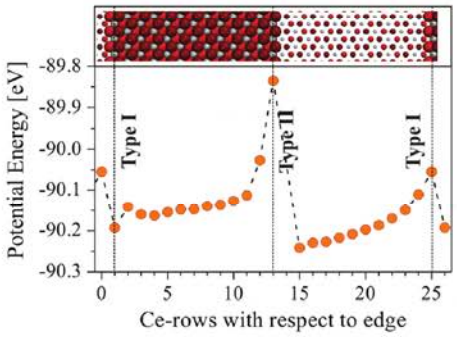

Figure 8. Electrostatic potential energy of a probe electron in a Ce ion at different distances from type I/II step edges. The potential course reflects the repulsive/attractive forces induced by negative/positive excess charges at different positions of the step edge. A corresponding structure model is shown in the top panel.

along the ceria steps, their energy positions is governed by another parameter that is the local charge distribution. CeO_2(111), as a layered ionic material, is particularly susceptible to polarity effects, as defects often break the charge balance within the surface O−Ce−O trilayer.[23] In general, an accumulation of positive charges leads to a stabilization of the oxide electronic states and lowers their energy, while extra electrons push the oxide bands upward. The largest perturbation in the charge balance occurs on type I steps, which feature a positive descent with the O-top plane terminating earlier than the O-bottom plane (Figure 2a). This gives rise to a lack of negative charges at the top of the edge and an electron accumulation at its bottom, producing a positive electrostatic dipole pointing toward the vacuum. As sketched above, such a charge distribution stabilizes the electrons and leads to a rigid shift of the edge electronic states to lower energies. The magnitude of this effect is derived from the calculated potential energy experienced by an electron in a Ce ion at different distances from the edge (Figure 8). When approaching a type I edge from the upper terrace, the potential energy first decreases before it jumps to higher values once the step is passed. This potential switch reflects the stabilizing effect of the positive charges at the top of step I followed by a destabilization due to the excess electrons at its bottom. The strength of the associated dipole moment projected onto the surface normal μ_z can be estimated with: $\mu_z = \Sigma q_i z_i$. Using the computed ion charges and vertical positions, q_i and z_i, the dipole moment at the type I step is determined to be +1.2 D per CeO_2 unit. This edge dipole is the main reason for the down-shift of the type I split-off states.

The type II steps with their negative decent exhibit the opposite trend, as extra charges accumulate in the top plane and the resulting dipole points away from the vacuum ($\mu_z = -1.1$D). As a result, the edge states move toward higher energy, merging with the main conduction band, and the electrostatic energy rises when approaching the step from the upper terrace. The absence of low-lying split-off states in this case is reflected in the dark appearance of type II steps, both in topographic and conductance images. Finally, the type III steps have the most compact configuration and are nearly dipole compensated ($\mu_z = +0.04$ D). The energy position of the split-off states is therefore mainly determined by the low coordination number of the edge ions, while electrostatic contributions play a negligible role. In fact, the good polarity compensation of type III steps might be responsible for a preferred development at high temperature, where low-energy and nonpolar configurations become favored.

CONCLUSIONS

STM imaging and spectroscopy revealed distinct differences in the electronic structure of ceria step edges with respect to the perfect (111) surface. Three kinds of trilayer steps have been identified, which differ in their orientation, in the inclination of the associated nanofacet and the local charge distribution. One of them, the type I step, stands out as it appears bright in low-bias STM images and has a downshifted conduction band onset in d*I*/d*V* spectra. Density functional GGA+U calculations ascribed this experimental finding to the formation of edge-electronic states that are displaced from the main conduction band of ceria. The split-off states have significant sp contribution and therefore dominate the tunneling into the step edges at low sample bias. The edge electronic states develop due to a lower atom-coordination number and a more covalent nature of bonds along the step edges. A sizable electrostatic dipole at type I steps further promotes the splitting of the respective states from the main band.

The peculiar electronic structure in combination with an uncompensated edge-dipole will largely affect the adsorption behavior of ceria step edges and might provide an explanation for the high chemical activity of ceria nanoislands.[3,4] We will explore this issue in future studies that address the interaction of adsorbates with the different step types. Also, the dominance of specific step edges at certain preparation conditions calls for additional experiments, as this might open an interesting route to alter the chemical properties of CeO_2-(111) by tuning the step morphology.

METHODS

The experiments were performed in an ultrahigh vacuum chamber equipped with a custom-built Beetle-type STM operated at 10 K. While imaging was accomplished in the constant current mode ($I = 5$ pA), the electronic properties were deduced from differential conductance (d*I*/d*V*) measurements

performed with a lock in amplifier. The ceria film was prepared by depositing a Ce wetting layer in 10^{-6} mbar O_2 onto the O(2 × 1) Ru(0001) surface at 100 K.[37,38] After an increase in the temperature to 700 K, additional Ce was dosed at constant O_2 pressure, and the sample was finally annealed to temperatures between 900 and 1100 K for 10 min. The procedure resulted in the formation of crystalline and atomically flat CeO_2(111) films, as concluded from STM images and low-energy-electron-diffraction data displaying a sharp (1.4 × 1.4) pattern with respect to the substrate spots. The average film thickness was determined to be six O−Ce−O trilayers (1.8 nm), using the attenuation of the Ru 3d signal in X-ray photoelectron spectroscopy.

To gain theoretical insight into the properties of ceria step edges, spin-restricted DFT calculations were performed with the VASP code,[39,40] using the generalized gradient approximation and the PW91 exchange-correlation functional.[41] Test calculations including spin-degrees of freedom gave similar results. In accordance with earlier studies, the Hubbard correction scheme[42] with U_{eff} = 4 eV was applied to reinforce the localization of the Ce 4f orbitals.[43,44] The core−valence interaction was treated with the projector augmented wave method,[45] setting the energy cutoff to 415 eV. The local density of states (LDOS) was computed with dense (1 × 11 × 1) and (1 × 7 × 1) Monkhorst grids, while structural optimization was performed with a (1 × 3 × 1) grid. As the Fermi level in an insulating system depends on both defect structure and temperature, all energies are given with respect to the valence band edge, that is, the highest occupied state of the system. The STM images were simulated with the Tersoff−Hamann approach.[46] The different step edges were modeled with stoichiometric O−Ce−O stripes located on top of a double-trilayer thick CeO_2(111) slab. To minimize mutual interactions between the steps, relatively large unit cells were used that consist of 61 Ce and 122 O atoms (top layer, $Ce_{13}O_{26}$; second and third trilayer, $Ce_{24}O_{48}$ each). The ⟨110⟩-oriented steps were modeled with a rectangular 7.935 × 0.382 nm^2 supercell, while ⟨211⟩ steps were described with a rhombic 5.291 × 0.661 nm^2 cell. The slabs were separated by 1.7 nm of vacuum from their nearest periodic image. The topmost trilayers were relaxed during geometry optimization until atomic forces decreased to 0.15 eV/nm, whereas the bottom trilayer was kept at its bulk position. The potential energy of a trial electron was calculated by using spatial charge-density distributions without assigning the electron density to specific atoms.

Acknowledgment. The authors acknowledge financial support from the Cluster of Excellence `UNICAT' through the German Science Foundation, the Spanish MICINN (grant FIS2008-02238), and the Generalitat de Catalunya (Grants 2009SGR1041 and XRQTC). S. Kozlov is grateful to the Spanish Ministerio de Educación for a predoctoral FPU research fellowship AP2009-3379. F. Viñes thanks the MICINN for a postdoctoral *Juan de la Cierva* grant (JCI-2010-06372).

Supporting Information Available: Discussion of the atom relaxation along different step edges; introduction of alternative step configurations. This material is available free of charge *via* the Internet at http://pubs.acs.org.

REFERENCES AND NOTES

1. Trovarelli, A. *Catalysis by Ceria and Related Materials*; Imperial College Press: London, 2002.
2. Fu, Q.; Saltsburg, H.; Flytzani-Stephanopoulos, M. Active Nonmetallic Au and Pt Species on Ceria-Based Water−Gas Shift Catalysts. *Science* **2003**, *301*, 935.
3. Yang, F.; Graciani, J.; Evans, J.; Liu, P.; Hrbek, J.; Fdez. Sanz, J.; Rodriguez, J. A. CO Oxidation on Inverse CeO(*x*)/Cu(111) Catalysts: High Catalytic Activity and Ceria-Promoted Dissociation of O_2. *J. Am. Chem. Soc.* **2011**, *133*, 3444–3451.
4. Vayssilov, G. N.; Lykhach, Y.; Migani, A.; Staudt, T.; Petrova, G. P.; Tsud, N.; Skála, T.; Bruix, A.; Illas, F.; Prince, K. C.; *et al.* Support Nanostructure Boosts Oxygen Transfer to Catalytically Active Platinum Nanoparticles. *Nat. Mater.* **2011**, *10*, 310.
5. Nolan, M.; Parker, S. C.; Watson, G. W. The Electronic Structure of Oxygen Vacancy Defects at the Low Index Surfaces of Ceria. *Suf. Sci.* **2005**, *595*, 223.
6. Ganduglia-Pirovano, M. V.; Da Silva, J. L.; Sauer, J. Density-Functional Calculations of the Structure of Near-Surface Oxygen Vacancies and Electron Localization on CeO_2(111). *Phys. Rev. Lett.* **2009**, *102*, 026101.
7. Migani, A.; Vayssilov, G. N.; Bromley, S. T.; Illas, F.; Neyman, K. M. Greatly Facilitated Oxygen Vacancy Formation in Ceria Nanocrystallites. *Chem. Commun.* **2010**, *46*, 5936–5938.
8. Skorodumova, N. V.; Simak, S. I.; Lundqvist, B. I.; Abrikosov, I. A.; Johansson, B. Quantum Origin of the Oxygen Storage Capability of Ceria. *Phys. Rev. Lett.* **2002**, *89*, 166601.
9. Baron, M.; Abbott, H.; Bondarchuk, O.; Stacchiola, D.; Uhl, A.; Shaikhutdinov, S.; Freund, H. J.; Popa, C.; Ganduglia-Pirovano, M. V.; Sauer, J. Resolving the Atomic Structure of Vanadia Monolayer Catalysts: Monomers, Trimers, and Oligomers on Ceria. *Angew. Chem., Int. Ed.* **2009**, *48*, 8006.
10. Carrettin, S.; Concepcion, P.; Corma, A.; Nieto, J. M. L.; Puntes, V. F. Nanocrystalline CeO_2 Increases the Activity of Au for CO Oxidation by Two Orders of Magnitude. *Angew. Chem., Int. Ed.* **2004**, *43*, 2538–2540.
11. Guzman, J.; Carrettin, S.; Corma, A. Spectroscopic Evidence for the Supply of Reactive Oxygen during CO Oxidation Catalyzed by Gold Supported on Nanocrystalline CeO_2. *J. Am. Chem. Soc.* **2005**, *127*, 3286–3287.
12. Murugan, B.; Ramaswamy, A. V. Defect-Site Promoted Surface Reorganization in Nanocrystalline Ceria for the Low-Temperature Activation of Ethylbenzene. *J. Am. Chem. Soc.* **2007**, *129*, 3062–3063.
13. Hsiao, W. I.; Lin, Y.-S.; Chen, Y.-C.; Lee, C.-S. The Effect of the Morphology of Nanocrystalline CeO_2 on Ethanol Reforming. *Chem. Phys. Lett.* **2007**, *441*, 294–299.
14. Lu, J.-L.; Gao, H.-J.; Shaikhutdinov, S.; Freund, H.-J. Morphology and Defect Structure of the CeO_2(111) Films Grown on Ru(0001) as Studied by Scanning Tunneling Microscopy. *Surf. Sci.* **2006**, *600*, 5004–5010.
15. Knudsen, J.; Merte, L. R.; Grabow, L. C.; Eichhorn, F. M.; Porsgaard, S.; Zeuthen, H.; Vang, R. T.; Lægsgaard, E.; Mavrikakis, M.; Besenbacher, F. Reduction of FeO/Pt(111) Thin Films by Exposure to Atomic Hydrogen. *Surf. Sci.* **2010**, *604*, 11–20.
16. Branda, M. M.; Loschen, C.; Neyman, K. M.; Illas, F. Atomic and Electronic Structure of Cerium Oxide Stepped Model Surfaces. *J. Phys. Chem. C* **2008**, *112*, 17643–17651.
17. Bollinger, M. V.; Lauritsen, J. V.; Jacobsen, K. W.; Nørskov, J. K.; Helveg, S.; Besenbacher, F. One-Dimensional Metallic Edge States in MoS_2. *Phys. Rev. Lett.* **2001**, *87*, 196803.
18. McKenna, K. P.; Shluger, A. L. Electron-Trapping Polycrystalline Materials with Negative Electron Affinity. *Nat. Mater.* **2008**, *7*, 859.
19. Benia, H. M.; Myrach, P.; Gonchar, A.; Risse, T.; Nilius, N.; Freund, H.-J. Electron Trapping in Misfit Dislocations of MgO Thin Films. *Phys. Rev. B* **2010**, *81*, 241415.
20. Freitag, A.; Staemmler, V.; Cappus, D.; Ventrice, C. A.; Al-Shamery, K. A.; Kuhlenbeck, H.; Freund, H. J. Electronic Surface State of NiO(100). *Chem. Phys. Lett.* **1993**, *210*, 10–14.
21. Esch, F.; Fabris, S.; Zhou, L.; Montini, T.; Africh, C.; Fornasiero, P.; Comelli, G.; Rosei, R. Electron Localization Determines Defect Formation on Ceria Substrates. *Science* **2005**, *309*, 752.
22. Fabris, S.; Vicario, G.; Balducci, G.; de Gironcoli, S.; Baroni, S. Electronic and Atomistic Structures of Clean and Reduced Ceria Surfaces. *J. Phys. Chem. B* **2005**, *109*, 22860.
23. Goniakowski, J.; Finocchi, F.; Noguera, C. Polarity of Oxide Surfaces and Nanostructures. *Rep. Prog. Phys.* **2008**, *71*, 016501.
24. Goniakowski, J.; Noguera, C. Polarity at the Nanoscale. *Phys. Rev. B* **2011**, *83*, 115413.
25. Torbrügge, S.; Cranney, M.; Reichling, M. Morphology of Step Structures on CeO_2(111). *Appl. Phys. Lett.* **2008**, *93*, 073112.
26. Duclos, S. J.; Vohra, Y. K.; Ruoff, A. L.; Jayaraman, A.; Espinosa, G. P. High-Pressure X-ray Diffraction Study of

CeO_2 to 70 GPa and Pressure Induced Phase Transformation from the Fluorite Structure. *Phys. Rev. B* **1998**, *38*, 7755.
27. Engelhardt, J. B.; Dabringhaus, H.; Wandelt, K. Atomic Force Microscopy Study of the CaF_2(111) Surface: from Cleavage *via* Island to Evaporation Topographies. *Surf. Sci.* **2000**, *448*, 187–200.
28. Dabringhaus, H.; Wandelt, K. Theoretical Study of the Adsorption of a CaF_2 Molecule at the (111) Surface of CaF_2 I. Equilibrium Adsorption Positions. *Surf. Sci.* **2003**, *526*, 257–272.
29. Puchin, V. E.; Puchina, A. V.; Huisinga, M.; Reichling, M. Theoretical Modelling of Steps on the CaF_2(111) Surface. *J. Phys.: Condens. Matter* **2001**, *13*, 2081–2094.
30. Jerratsch, J. F.; Shao, X.; Nilius, N.; Freund, H.-J.; Popa, C.; Ganduglia-Pirovano, M. V.; Burow, A. M.; Sauer, J. Electron Localization in Defective Ceria Films: A Study with Scanning-Tunneling Microscopy and Density-Functional Theory. *Phys. Rev. Lett.* **2011**, *106*, 246801.
31. Shao, X.; Jerratsch, J.-F; Nilius, N.; Freund, H.-J. Probing the f States of Ceria by Tunneling Spectroscopy. *Phys. Chem. Chem. Phys.* **2011**, *13*, 12646–12651.
32. Shluger, A. L.; Sushko, P. V.; Kantorovich, L. N. Spectroscopy of Low-Coordinated Surface Sites: Theoretical Study of MgO. *Phys. Rev. B* **1999**, *59*, 2417.
33. Sushko, P. V.; Shluger, A. L.; Catlow, C. R. A. Relative Energies of Surface and Defect States: *Ab Initio* Calculations for the MgO (001) Surface. *Surf. Sci.* **2000**, *450*, 153–170.
34. Bader, R. F. W. *Atoms in molecules: A quantum theory*; Oxford Science: United Kingdom, 1990.
35. Mugarza, A.; Mascaraque, A.; Perez-Dieste, V.; Repain, V.; Rousset, S.; Garcia de Abajo, F. J.; Ortega, J. E. Electron Confinement in Surface States on a Stepped Gold Surface Revealed by Angle-Resolved Photoemission. *Phys. Rev. Lett.* **2001**, *87*, 107601.
36. Schmid, M.; Shishkin, M.; Kresse, G.; Napetschnig, E.; Varga, P.; Kulawik, M.; Nilius, N.; Rust, H.-P.; Freund, H.-J. Oxygen-Deficient Line Defects in an Ultrathin Aluminum Oxide Film. *Phys. Rev. Lett.* **2006**, *97*, 046101.
37. Baron, M.; Bondarchuk, O.; Stacchiola, D.; Shaikhutdinov, S.; Freund, H.-J. Interaction of Gold with Cerium Oxide Supports: CeO_2(111) Thin Films *vs* CeO_x Nanoparticles. *J. Phys. Chem. C* **2009**, *113*, 6042.
38. Mullins, D. R.; Radulovic, P. V.; Overbury, S. H. Ordered Cerium Oxide Thin Films Grown on Ru(0001) and Ni(111). *Surf. Sci.* **1999**, *429*, 186.
39. Kresse, G.; Furthmüller, J. Efficient Iterative Schemes for *Ab Initio* Total-Energy Calculations Using a Plane-Wave Basis Set. *Phys. Rev. B* **1996**, *54*, 11169.
40. Kresse, G.; Hafner, J. *Ab initio* Molecular Dynamics for Liquid Metals. *Phys. Rev. B* **1993**, *47*, 558.
41. Perdew, J. P.; Wang, Y. Accurate and Simple Analytic Representation of the Electron-Gas Correlation Energy. *Phys. Rev. B* **1992**, *45*, 13244.
42. Dudarev, S. L.; Botton, G. A.; Savrasov, S. Y.; Humphreys, C. J.; Sutton, A. P. Electron-Energy-Loss Spectra and the Structural Stability of Nickel Oxide: An LSDA+U Study. *Phys. Rev. B* **1998**, *57*, 1505.
43. Loschen, C.; Carrasco, J.; Neyman, K. M.; Illas, F. First-Principles LDA+U and GGA+U Study of Cerium Oxides: Dependence on the Effective U Parameter. *Phys. Rev. B* **2007**, *75*, 035115.
44. Da Silva, J. L. F.; Ganduglia-Pirovano, M. V.; Sauer, J.; Bayer, V.; Kresse, G. Publisher's Note: Hybrid Functionals Applied to Rare-Earth Oxides: The Example of Ceria. *Phys. Rev. B* **2007**, *75*, 089901.
45. Blöchl, P. E. Projector Augmented-Wave Method. *Phys. Rev. B* **1994**, *50*, 17953.
46. Tersoff, J.; Hamann, D. Theory of the Scanning Tunneling Microscope. *Phys. Rev. B* **1985**, *31*, 805.

Section 5.2

THE JOURNAL OF PHYSICAL CHEMISTRY Letters

Letter

pubs.acs.org/JPCL

Absolute Surface Step Energies: Accurate Theoretical Methods Applied to Ceria Nanoislands

Sergey M. Kozlov,[†] Francesc Viñes,[†] Niklas Nilius,[‡] Shamil Shaikhutdinov,[‡] and Konstantin M. Neyman*[,†,§]

[†]Departament de Química Física and Institut de Química Teòrica i Computacional (IQTCUB), Universitat de Barcelona, C/Martí i Franquès 1, 08028, Barcelona, Spain

[‡]Fritz-Haber-Institut der Max-Planck-Gesellschaft, Faradayweg 4-6, 14195 Berlin, Germany

[§]Institució Catalana de Recerca i Estudis Avançats (ICREA), 08010 Barcelona, Spain

ABSTRACT: Steps are ubiquitous structural features present on surfaces. They often exhibit unique physical and chemical properties, which in many cases are of even greater practical importance than the respective properties of surface terraces. Herein, we present two new methods to derive absolute values of surface step energies from electronic structure calculations, the efficiency and accuracy of which are superior to the methods previously employed. Application of these advanced methods allowed us to successfully explain the multitude of nanoisland shapes and orientations observed to form on $CeO_2(111)$ films via scanning tunneling microscopy studies. These methods are readily applicable to various systems and provide insights into the abundance and form of two-dimensional nanostructures, which are controlled by step energies.

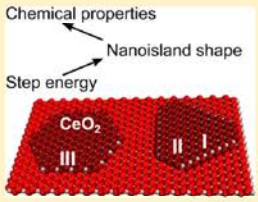

SECTION: Surfaces, Interfaces, Porous Materials, and Catalysis

Nanoislands are commonly observed nanostructures.[1−5] Their shape, orientation,[6−8] and thereby governed properties[4] are determined by step energies, similar to nanoparticles, whose shape[9] and other properties[10−13] are often controlled by the surface energies of the exposed nanofacets. Specifically, steps, which limit the growth of nanoislands, are known to have different electronic features,[4,14] adsorptive properties,[15] and chemical activity[16−18] compared to surface terraces. They also serve as nucleation centers[19] and, thus, play a crucial role in catalysis,[20] semiconductor technologies,[3] and nanotechnology.[14] Notably, structural and other properties of steps observed on vicinal or rough surfaces may be very similar to those present at the perimeters of nanoislands.

Properties of steps have been intensely studied. Nevertheless, the pivotal issues of step energy and stability have been scarcely addressed theoretically (with the pertinent studies basically limited to refs 6, 21−26) or experimentally.[7,8,27] This is partially due to the lack of accurate, reliable, and, at the same time, efficient methods to derive step energies from electronic structure calculations. The existing methods either provide step energies in a rather frugal way,[23−25] which may produce inaccurate results in practice, or derive them from surface energies of vicinal surfaces,[25,26] which requires numerous calculations. Here, we propose two novel methods of step energy calculation (applicable, in principle, to any material), hitherto never communicated, which are not only much less computationally demanding but also more accurate than the existing approaches.

We have applied these methods to rationalize, in terms of step energies derived from density functional (DFT) calculations, various shapes and orientations of nanoislands formed on $CeO_2(111)$ films, as observed in our scanning tunneling microscopy (STM) studies. Ceria surfaces have been extensively characterized[1,4,5] due to the importance of ceria in catalysis[28−30] and energy-related technologies.[31−33] Atomic resolution studies have shown that steps on the $CeO_2(111)$ surface are, in general, stoichiometric and have the arrangements of atoms similar to that of the bulk.[1,4,5] As mentioned above, ceria steps have different electronic[4] and chemical properties[17,18] compared to $CeO_2(111)$ terraces and serve as nucleation centers for metal atoms[34] and nanoparticles.[20] The methods that we have developed pave the way toward the understanding and subsequent control of the abundance, shape, and other related properties of nanoislands on various materials, eventually enabling their potential use in nanotechnology applications. Indeed, these methods enable calculations of step energies in a variety of experimental conditions, which will help to tune the preparation procedures to preferentially form a certain step type.

In the absence of steps, the total energy, E, of a perfectly flat slab, an infinite 2D crystal limited in the third dimension by two planes, is usually expressed as[35−37]

$$E = \varepsilon N + 2\gamma A \quad (1)$$

Here, the first term corresponds to the bulk energy produced by the overall number N of (smallest) stoichiometric units forming the slab with energy ε per unit. The second one represents the destabilizing contribution from the two surfaces of the slab, which are assumed to have the same atomic arrangement, each with area A and specific surface energy γ. If steps (line defects) and point defects are present on the surface (Figure 1), the total energy includes two more terms

$$E = \varepsilon N + 2\gamma_0 A_0 + \sum (\beta_i + \gamma_0 \Delta_i) L_i + \sum \xi_j \quad (2)$$

Received: May 29, 2012
Accepted: July 6, 2012

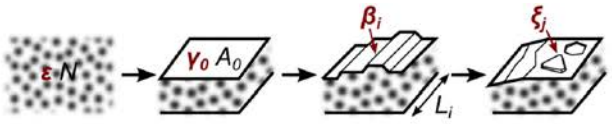

Figure 1. Illustration of terms in eq 2.

where the second term is the contribution from two terraces of a low-index surface, each with area A_0 and specific surface energy γ_0. The third term is the sum over all steps with length L_i, width projected on the terrace plane Δ_i (if a step is normal to the surface, $\Delta_i = 0$), and step energy β_i per unit length. The last term represents the energy contributions from corners between steps and other point defects, which will not be discussed further due to the absence of these features in the models addressed in this work. Equation 2 assumes that (i) steps and the two slab surfaces are well separated and do not interact with each other and (ii) the arrangement of atoms on the surface is not changed upon crossing the step.

Equation 2, however, is seldom used[22,24] because it yields limited accuracy in practical calculations. Such inaccuracies emerge if one derives ε and γ_0 values from calculations of systems different from a rough slab (i.e., containing terraces and steps) and then applies eq 2.[36,37] For example, let us consider a case where the calculated energy of the smallest stoichiometric unit in the bulk, ε_b, is different from the actual ε in the rough slab by only 0.007 eV (this value and those presented further in this paragraph are based on the typical calculations performed in the present work). A variety of technical reasons, such as different k-points sets, the number of plane waves in the basis sets, and the geometry optimization details in the calculations of the two systems, may produce this subtle energy difference. If one now uses ε_b instead of ε in eq 2, this difference is multiplied by $N = 50$ for the 0.382 nm wide cell with two steps typically used in the present work, thus introducing a 0.46 eV/nm error in the derived step energy. Due to similar reasons, the difference between terrace surface energies calculated in a rough slab supercell and the smallest terrace (1×1) unit cell may be up to 0.15 eV/nm^2. This value multiplied by a surface area of 1.22 nm^2 (on each side of the slab for the typical 0.382 nm wide unit cells) introduces an additional error of 0.48 eV/nm to the step energy. Thus, the overall uncertainty is ~1 eV/nm, which makes the direct approach inapplicable to many practical problems. A way to circumvent this drawback, and decisively reduce the related inaccuracy, is to perform only calculations of rough slabs with the slightly varying structure and dimensions of the unit cells.

To do so, let us consider a periodic slab exposing only one type of steps, repeated with periodicity L (Figure 2a). Following eq 2, the energy per primitive unit cell of the slab is

$$E = (\varepsilon t + 2\gamma_0 wl)L_0/l + 2(\beta + \gamma_0\Delta)w \quad (3)$$

Here, t is the number of stoichiometric layers composing the slab (i.e., its thickness), w is the width of the primitive unit cell (one stoichiometric unit) in the direction along the step, L_0 is the length of the low-index surface terrace, and l is the distance between adjacent rows of stoichiometric units in the direction normal to the step. Thus, L_0/l is the number of stoichiometric units composing the surface of the low-index terrace.

Calculating the surface energy defined in eq 1 as the intercept of the linear regression of E as a function of t in eq 3,[35−37] one gets

$$\gamma A = \gamma_0 wL_0 + (\beta + \gamma_0\Delta)w$$

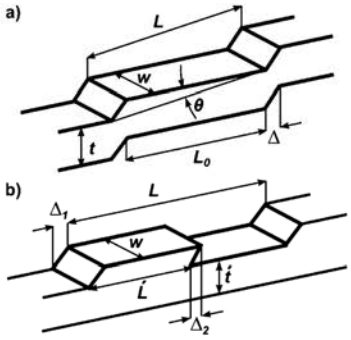

Figure 2. The geometric parameters used in eqs 3−5 for (a) a slab terminated with vicinal surfaces and (b) a stripe on a substrate.

which is equivalent to the known formula[22,25,26] for the energy of a vicinal surface

$$\gamma = [\gamma_0(L_0 + \Delta) + \beta]/L = \gamma_0 \cos\theta + \beta/L \quad (4)$$

where θ is the misalignment angle between the vicinal and low-index surfaces. Using this formula, one can derive β as the slope of the linear regression of $\gamma/\cos\theta$ as a function of $(L \cos\theta)^{-1}$. In the following, this method will be referred to as vicinal-γ. In practice, however, derivation of the slope energy from ab initio calculations using this approach requires linear regression of $\gamma/\cos\theta$ versus $(L \cos\theta)^{-1}$, with each point of the data set calculated, in turn, by linear regression of E versus t. This makes the established approach computationally expensive or even prohibitive for accurate calculations. By accuracy, we mean 95% confidence intervals for coefficients obtained in linear regression, and thus, the term accuracy used here is unrelated to the intrinsic accuracy of the electronic structure calculation.

To advance this approach, we pose an alternative, the so-called vicinal-E method, where one can directly calculate the value of $\beta + \gamma_0\Delta$ as the intercept of the linear regression of $E(2w)^{-1}$ as a function of L_0/l via eq 3. In this way, the method avoids calculation of the surface energy of a vicinal surface and solves the issue of computational efficiency. Note, that $\gamma_0\Delta$ has to be subtracted from the obtained value for the steps with nonzero width. Because the monolayer step width is typically ~0.1 nm, the uncertainty introduced by this correction is only ~0.01 eV/nm due to the ~0.1 eV/nm^2 accuracy of independent calculations of the terrace surface energy.

To cross-check the validity of the approaches employing vicinal surfaces, we also consider rough slab models in the form of periodic, one-layer high, linear stripes on a flat substrate (Figure 2b). Using eq 2, the energy of the slab's primitive unit cell containing two slopes can be expressed as

$$E = \varepsilon\acute{t}L/l + \varepsilon\acute{L}/l + 2\gamma_0 wL + w\sum\beta_i \quad (5)$$

Here, $\acute{t}$ is the thickness of the substrate in stoichiometric layers, L ($\acute{L}$) is the length of the unit cell (stripe) in the direction perpendicular to the step. From this expression, one can derive the sum of the step energies, $\sum\beta_i$, as the intercept of a linear regression of $E - E_{sub}$ as a function of $\acute{L}$, where E_{sub} is the energy of the unit cell of the substrate without the stripe. This method, further referred to as stripe-E, does not require calculation of any surface energy, but only provides $\sum\beta_i$, not each β_i separately. Note that this method can be generalized to the case where different terraces have different terminations or even when the stripe and the substrate have distinct nature, that is, composed of different materials.

dx.doi.org/10.1021/jz3006942 | J. Phys. Chem. Lett. 2012, 3, 1956−1961

In our calculations of the energies of steps on ceria we used slabs featuring vicinal surfaces with steps like those sketched in Figure 3 (more details on the step structures can be found in refs 4 and 38). The slabs consisted of t = 3, 4, and 5 O−Ce−O trilayers and were completely relaxed during geometry optimization. Terrace length, L_0, ranged from $7l$ to $10l$ for slabs with type I, II, and II* steps and $9l$ and $12l$ for slabs with type III steps. This yielded a distance between steps of L > 2.2 nm in the first case and L > 1.7 nm in the second case. Stoichiometric CeO_2 stripes on the $CeO_2(111)$ substrate had a height of one O−Ce−O trilayer and width, $\acute{L}$, of up to $13l$. The substrate was modeled by a two-trilayers-thick slab. A rectangular $24l \times w$ (7.935 × 0.382 nm^2) supercell was used for calculations of ⟨110⟩ stripes, while ⟨211⟩ stripes were modeled in a $24l \times w$ supercell with lattice vectors of 5.291 and 0.661 nm along the $[2\bar{1}\bar{1}]$ and $[11\bar{2}]$ directions, respectively. Cell dimensions did not vary with the stripe width. During geometry optimization, the stripe and the topmost trilayer of the substrate were relaxed, while the bottom O−Ce−O trilayer was fixed. The surface energy of $CeO_2(111)$ was calculated to be γ_0 = 4.00 ± 0.11 eV/nm^2. Step widths, Δ, were 0.11 nm for type I steps, −0.11 nm for type II and type II* steps, and 0 for type III steps.

Step energies on the aforementioned models were calculated using all three methods. First, we discuss results from the vicinal-γ and vicinal-E methods, both of which derive step energies from the energies of slabs terminated by vicinal surfaces (Table 1).

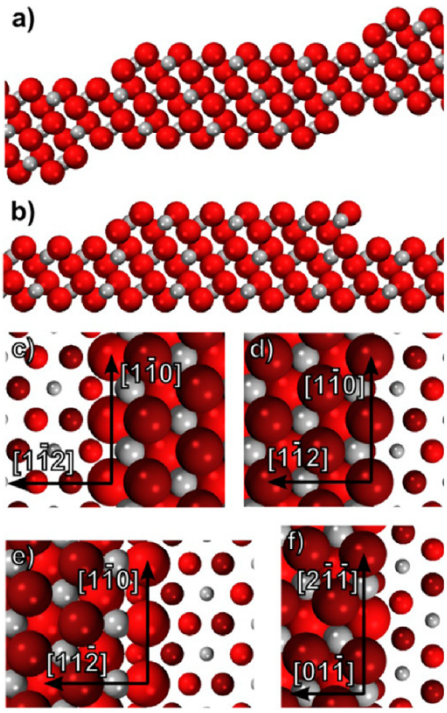

Figure 3. Atomic structures of considered models of ceria. Side views of (a) the CeO_2 slab terminated by a vicinal surface, featuring type I steps and (b) the CeO_2 stripe with type I and II steps. Ce atoms are displayed as gray spheres and O atoms are shown as red spheres. Top views of stoichiometric (c) type I, (d) type II, (e) type II*, and (f) type III steps with the height of one O−Ce−O trilayer on $CeO_2(111)$ terraces. O atoms located in the first, third, fourth, and sixth atomic layers are displayed as big dark, big bright, small dark, and small bright red spheres, respectively. Ce atoms in the second and fifth atomic layers are displayed as big and small gray spheres, respectively. Crystal directions on the surface are also shown.

Table 1. Step Energies β, in eV/nm, Calculated with the Vicinal-γ and Vicinal-E Methods[a]

step type	vicinal-γ	vicinal-E
type I	1.39 ± 0.27	1.50 ± 0.08 (1.30)
type II	2.12 ± 0.11	2.06 ± 0.06 (1.72)
type II*	4.03 ± 0.15	4.20 ± 0.09 (4.04)
type III	2.01 ± 0.12	2.04 ± 0.20 (1.97)

[a]Estimated step energies at a temperature of 1000 K are given in parentheses.

The vicinal-γ method operates with surface energies and thus requires calculations of slabs with varying thicknesses. In the present work, slabs of 3, 4, and 5 O−Ce−O trilayers were considered, which are sufficiently thick for reliable calculations of surface energies.[21,39] The latter were calculated for four vicinal surfaces with different terrace lengths. Thus, each step energy obtained by the vicinal-γ method required 12 electronic structure calculations.

To use the vicinal-E method, the calculation of slabs with the same thickness is sufficient. Thus, only four electronic structure calculations were performed to obtain each step energy value. The difference between step energies calculated for three-, four-, and five-layer slabs is less than 0.07 eV/nm, and only the values for the latter slabs are presented in Table 1. In this case, the uncertainties are estimated as a sum of 95% confidence intervals for $\beta + \gamma_0\Delta$, with uncertainty introduced by subtracting the $\gamma_0\Delta$ term (∼0.01 eV/nm).

The comparison of step energies calculated by the conventional, vicinal-γ method and those obtained with our vicinal-E method shows that the difference between them is within the estimated error. However, the accuracy is higher for the vicinal-E method (0.1 eV/nm on average) than that for the vicinal-γ method (0.16 eV/nm on average), despite the three times fewer calculations required for the former. This ratio would grow if a higher accuracy was required because using the vicinal-γ method one would need to consider slabs with a broader range of thicknesses to calculate more accurate surface energies.

When step energies are calculated with the stripe-E method, only the sum of the energies of steps on both sides of the stripe is gained. Thus, sums of step energies calculated with the different methods are provided in Table 2. Stripe-E step energies are, in general, somewhat larger than the vicinal-γ and vicinal-E values, but only in the type I + II* case does the difference somewhat exceed the estimated accuracy of the former methods. The stripe-E method also yields tighter confidence intervals than the other methods when a comparable number of calculations is used in the linear interpolation. Stripes of various thickness were calculated in each case, but total energies of only four systems were used in every case. The reason for this is that inclusion of stripes with widths less than 1.5 nm made confidence intervals broader. Note that inclusion of a few more structures easily improves the accuracy of the calculations by an order of magnitude, for example, the step energy of I + II is calculated to be 3.71 ± 0.05 using six systems. The employed

Table 2. Energies β, in eV/nm, of Step Pairs Appearing on Stripes on the $CeO_2(111)$ Surface

step types	stripe-E	vicinal-γ	vicinal-E
I + II	3.65 ± 0.20	3.51 ± 0.38	3.56 ± 0.15
I + II*	6.01 ± 0.04	5.42 ± 0.42	5.70 ± 0.17
III + III	4.28 ± 0.07	4.03 ± 0.24	4.08 ± 0.39

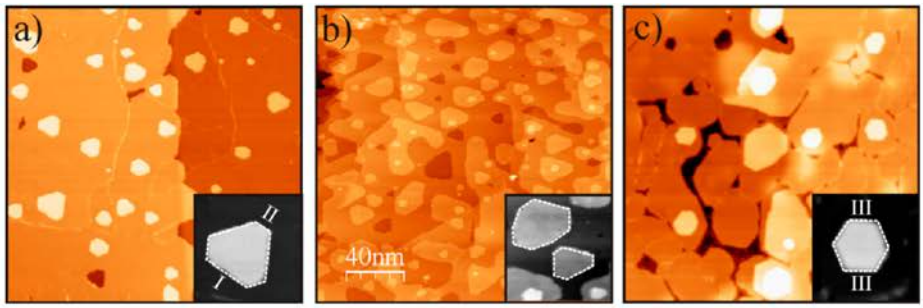

Figure 4. STM images (200 nm × 200 nm) of thin $CeO_2(111)$ films grown on Ru(0001) and annealed in 10^{-6} mbar of O_2 at 980 (a,b) and ~1100 K (c). The films expose atomically flat terraces and single-layer islands and pits. The characteristic island shapes are detailed in the insets (30 nm × 30 nm). While the steps of type I and II dominate film (a), the steps are preferentially of type III in image (c). Image (b) illustrates the intermediate state with several step orientations. More roundish islands, observed in (b), are indicative for a gradual transition of the preferred step orientation.

eqs 2−5 assume that adjacent steps do not interact with each other, which holds only at sufficiently large (1.5 nm) step separation. For slabs terminated by vicinal surfaces, the distances between adjacent steps exceed 1.7 nm, thereby fulfilling this condition.

The differences in the step energies manifest themselves via the preferential formation of step edges with a certain orientation. This is illustrated by STM images (Figure 4) of the $CeO_2(111)$ thin films grown on Ru(0001), which expose atomically flat nanoislands (and pits), measuring a single O−Ce−O trilayer in height (depth). Atomically resolved STM images, in combination with tunneling conductance spectroscopy, have identified type I, II, and III steps[4] but no type II* steps, in agreement with the high calculated formation energy of the latter.

Figure 4a shows a film with an abundance of nanoislands in truncated triangular shapes. The islands are bordered by three long, type I steps and three short, type II steps (see inset in Figure 4a). The ratio between the lengths of type I and type II steps $L_I/L_{II} = 2 \pm 0.3$ was measured on a sample prepared by oxidation at ~1000 K, which clearly indicates that the type I steps are thermodynamically more stable than type II steps, in agreement with the calculated data presented above.

Applying the Wulff construction scheme[9] to the nanoisland shapes,[7,8] one will get $\beta_i/\beta_j = R_i/R_j$, where R is the (shortest) distance from the nanoisland's center of mass to the step. For an island of truncated hexagonal shape bordered by type I and type II steps, this ratio transforms to

$$\frac{\beta_1}{\beta_2} = \frac{2 + L_1/L_2}{1 + 2L_1/L_2} = 0.8$$

which is in excellent agreement with the ratio of 0.76 estimated at 1000 K (see Table 1).

Analysis of numerous films prepared in our laboratories suggests that higher oxidation temperatures are necessary to produce type III structures, which is in good agreement with the higher formation energy of type III + III step pairs, as compared to type I + II pairs (see Table 2). Also, the precise experimental conditions (e.g., oxidation temperature and oxygen pressure, presence of adsorbates, the metal support in the case of the thin films, etc.) may affect the size, orientation, and shape distribution of nanoislands.[4,15,40−42] Good agreement between our experimental and theoretical results suggests that the step structures observed here are thermodynamically stable and not significantly affected by kinetic limitations.

In summary, we critically compared the conventional method of calculating step energies through surface energies of slabs terminated by vicinal surfaces with two alternative methods, which have been described for the first time within this work. All three methods were found to yield similar values of step energies, but the new methods require significantly fewer calculations to produce results with even higher accuracy. We have applied the three methods to the analysis of monolayer step energies on $CeO_2(111)$ films, which determine the shape and orientation of nanoislands detected and characterized by STM. The computationally derived stabilities for various conceivable steps are in very good agreement with STM data. As such, we have acquired in-depth knowledge of the structure−stability relations for islands abundantly formed on the $CeO_2(111)$ surface, nanoobjects highly important for understanding ceria reactivity at the nanoscale. This study paves the way for investigations of step stabilities on various surfaces with different compositions. Such studies are presently scarce due to the high cost of sufficiently accurate step energy calculations when using conventional methodologies.

■ EXPERIMENTAL AND COMPUTATIONAL DETAILS

Periodic DFT calculations were carried out using the VASP package[43] and employing the Perdew−Wang (PW91)[44] exchange−correlation functional of generalized gradient approximation type, augmented with the Hubbard self-interaction correction[45] (GGA+U) scheme, with $U_{eff} = 4$ eV.[46] Other computational parameters can be found elsewhere.[4] Test calculations done without the self-interaction correction yielded step energies ~0.2 eV/nm different from those obtained with it. To estimate the contribution of harmonic vibrations to the Gibbs energy, ΔG, at finite temperature, the vibrational frequencies of CeO_2 units located on the steps and on the terrace were calculated with a finite differences technique. The ΔG of the step energy was then calculated as the difference between ΔG of the CeO_2 unit on the step and that on the terrace. Thin ceria films of ~3 nm thickness were prepared in two different experimental setups using virtually identical preparation protocols,[42] albeit the precise recipe had to be adapted for each setup.[4] Briefly, the clean Ru(0001) surface was oxidized in 10^{-6} mbar of O_2 at 600 K. Then Ce was deposited in 10^{-6} mbar of O_2 at ~100 K in amounts approximately equivalent to form one monolayer of $CeO_2(111)$ on Ru(0001). Subsequently, the temperature was slowly increased and kept at 700 K during deposition of the next several layers. After the deposition, the sample was annealed at ~1000 K at the same oxygen pressure.

■ AUTHOR INFORMATION

Corresponding Author

*E-mail: konstantin.neyman@icrea.cat.

Notes

The authors declare no competing financial interest.

■ ACKNOWLEDGMENTS

The authors gratefully acknowledge the financial support by the Spanish MICINN (FIS2008-02238) and the Generalitat de Catalunya (2009SGR1041) and the access to computational resources of the Red Española de Supercomputación. S.M.K is also grateful to the Spanish Ministerio de Economia y Competitividad for the predoctoral FPU Grant AP2009-3379. F.V. thanks the Spanish MICINN for the postdoctoral grant under the program *Juan de la Cierva* JCI-2010-06372. We thank M. Baron, J.-F. Jerratsch, and X. Shao for STM data, as well as W. Kaden for his comments to the text. This work is part of the COST Action CM1104 "Reducible oxide chemistry, structure and functions".

■ REFERENCES

(1) Torbrügge, S.; Cranney, M.; Reichling, M. Morphology of Step Structures on CeO_2(111). *Appl. Phys. Lett.* **2008**, *93*, 073112.
(2) Layson, A. R.; Evans, J. W.; Fournée, V.; Thiel, P. A. The Effect of Common Gases on Nucleation of Metal Islands: The Role of Oxygen in Ag(100) Homoepitaxy. *J. Chem. Phys.* **2003**, *118*, 6467−6472.
(3) Voigtländer, B. Fundamental Processes in Si/Si and Ge/Si Epitaxy Studied by Scanning Tunneling Microscopy during Growth. *Surf. Sci. Rep.* **2001**, *43*, 127−254.
(4) Nilius, N.; Kozlov, S. M.; Jerratsch, J.-F.; Baron, M.; Shao, X.; Viñes, F.; Shaikhutdinov, S.; Neyman, K. M.; Freund, H.-J. Formation of One-Dimensional Electronic States along the Step Edges of CeO_2(111). *ACS Nano* **2012**, *6*, 1126−1133.
(5) Shahed, S. M. F.; Sainoo, Y.; Komeda, T. Scanning Tunneling Microscope Study of Surface Morphology Variation of CeO_2 (111) with Changing Annealing Condition. *Jpn. J. Appl. Phys.* **2011**, *50*, 08LB05.
(6) Gong, X.-Q.; Selloni, A.; Batzill, M.; Diebold, U. Steps on Anatase TiO_2(101). *Nat. Mater.* **2006**, *5*, 665−670.
(7) Kodambaka, S.; Petrova, V.; Khare, S. V.; Johnson, D. D.; Petrov, I.; Greene, J. E. Absolute TiN(111) Step Energies from Analysis of Anisotropic Island Shape Fluctuations. *Phys. Rev. Lett.* **2002**, *88*, 146101.
(8) Ikonomov, J.; Starbova, K.; Ibach, H.; Giesen, M. Measurement of Step and Kink Energies and of the Step-Edge Stiffness from Island Studies on Pt(111). *Phys. Rev. B* **2007**, *75*, 245411.
(9) Wulff, G. Z. Zur Frage der Geschwindigkeit des Wachstums und die Auflosung der Kristallfachen. *Kristallogr. Mineral.* **1901**, *34*, 449−530.
(10) Jin, R.; Cao, Y. C.; Hao, E.; Métraux, G. S.; Schatz, G. C.; Mirkin, C. A. Controlling Anisotropic Nanoparticle Growth through Plasmon Excitation. *Nature* **2003**, *425*, 487−490.
(11) Pal, S.; Tak, Y. K.; Song, J. M. Does the Antibacterial Activity of Silver Nanoparticles Depend on the Shape of the Nanoparticle? A Study of the Gram-Negative Bacterium Escherichia Coli. *Appl. Environ. Microb.* **2007**, *73*, 1712−1720.
(12) McLaren, A.; Valdes-Solis, T.; Li, G.; Tsang, S. C. Shape and Size Effects of ZnO Nanocrystals on Photocatalytic Activity. *J. Am. Chem. Soc.* **2009**, *131*, 12540−12541.
(13) Viñes, F.; Görling, A. Template-Assisted Formation of Fullerenes from Short-Chain Hydrocarbons by Supported Platinum Nanoparticles. *Angew. Chem., Int. Ed.* **2011**, *50*, 4611−4614.
(14) Rusponi, S.; Cren, T.; Weiss, N.; Epple, M.; Buluschek, P.; Claude, L.; Brune, H. The Remarkable Difference between Surface and Step Atoms in the Magnetic Anisotropy of Two-Dimensional Nanostructures. *Nat. Mater.* **2003**, *2*, 546−551.
(15) Kalff, M.; Comsa, G.; Michely, T. How Sensitive is Epitaxial Growth to Adsorbates? *Phys. Rev. Lett.* **1998**, *81*, 1255−1258.
(16) Vook, R. W.; Oral, B. Weakly Bound Carbon Monoxide at Catalytically Active Sites on Cu(111)/Pd(111) Thin Films. *Appl. Surf. Sci.* **1992**, *60*, 681−687.
(17) Fuente, S.; Branda, M. M.; Illas, F. Role of Step Sites on Water Dissociation on Stoichiometric Ceria Surfaces. *Theor. Chem. Acc.* **2012**, *131*, 1190.
(18) Lykhach, Y.; Johánek, V.; Aleksandrov, H. A.; Kozlov, S. M.; Happel, M.; Skála, T.; Petkov, P. S.; Tsud, N.; Vayssilov, G. N.; Prince, K. C.; Neyman, K. M.; Matolín, V.; Libuda, J. Water Chemistry on Model Ceria and Pt/Ceria Catalysts. *J. Phys. Chem. C* **2012**, *116*, 12103−12113.
(19) Diebold, U. The Surface Science of Titanium Dioxide. *Surf. Sci. Rep.* **2003**, *48*, 53−229.
(20) Lu, J.-L.; Gao, H.-J.; Shaikhutdinov, S.; Freund, H.-J. Gold Supported on Well-Ordered Ceria Films: Nucleation, Growth and Morphology in CO Oxidation Reaction. *Catal. Lett.* **2007**, *114*, 8−16.
(21) Branda, M. M.; Loschen, C.; Neyman, K. M.; Illas, F. Atomic and Electronic Structure of Cerium Oxide Stepped Model Surfaces. *J. Phys. Chem. C* **2008**, *112*, 17643−17651.
(22) Jeong, H. C.; Williams, E. D. Steps on Surfaces: Experiment and Theory. *Surf. Sci. Rep.* **1999**, *34*, 171−294.
(23) Kern, G.; Hafner, J. *Ab Initio* Calculations of the Atomic and Electronic Structure of Diamond (111) Surfaces With Steps. *Phys. Rev. B* **1998**, *58*, 2161−2169.
(24) Yu, B. D.; Scheffler, M. *Ab Initio* Study of Step Formation and Self-Diffusion on Ag(100). *Phys. Rev. B* **1997**, *55*, 13916−13924.
(25) Barreteau, C.; Raouafi, F.; Desjonquères, M. C.; Spanjaard, D. Modelling of Transition and Noble Metal Vicinal Surfaces: Energetics, Vibrations and Stability. *J. Phys.: Condens. Matter* **2003**, *15*, S3171−S3196.
(26) Frenken, J. W. M.; Stoltze, P. Are Vicinal Metal Surfaces Stable? *Phys. Rev. Lett.* **1999**, *82*, 3500−3503.
(27) Giesen, M. Step and Island Dynamics at Solid/Vacuum and Solid/Liquid Interfaces. *Prog. Surf. Sci.* **2001**, *68*, 1−154.
(28) Trovarelli, A.; de Letenburg, C.; Boaro, M.; Dolcetti, G. The Utilization of Ceria in Industrial Catalysis. *Catal. Today* **1999**, *50*, 353−367.
(29) Fu, Q.; Saltsburg, H.; Flytzani-Stephanopoulos, M. Active Nonmetallic Au and Pt Species on Ceria-Based Water−Gas Shift Catalysts. *Science* **2003**, *301*, 935−938.
(30) Vayssilov, G. N.; Lykhach, Y.; Migani, A.; Staudt, T.; Petrova, G. P.; Tsud, N.; Skála, T.; Bruix, A.; Illas, F.; Prince, K. C.; Matolin, V.; Neyman, K. M.; Libuda, J. Support Nanostructure Boosts Oxygen Transfer to Catalytically Active Platinum Nanoparticles. *Nat. Mater.* **2011**, *10*, 310−315.
(31) Hibino, T.; Hashimoto, A.; Inoue, T.; Tokuno, J.; Yoshida, S.; Sano, M. A Low-Operating-Temperature Solid Oxide Fuel Cell in Hydrocarbon−Air Mixtures. *Science* **2000**, *288*, 2031−2033.
(32) Steele, B. C. H. Appraisal of $Ce_{1-y}Gd_yO_{2-y/2}$ Electrolytes for IT-SOFC Operation at 500°C. *Solid State Ionics* **2000**, *129*, 95−110.
(33) Chueh, W. C.; Falter, C.; Abbott, M.; Scipio, D.; Furler, P.; Haile, S. M.; Steinfeld, A. Thermochemical Dissociation of CO_2 and H_2O Using Nonstoichiometric Ceria. *Science* **2010**, *330*, 1797−1801.
(34) Castellani, N. J.; Branda, M. M.; Neyman, K. M.; Illas, F. Density Functional Theory Study of the Adsorption of Au Atom on Cerium Oxide: Effect of Low-Coordinated Surface Sites. *J. Phys. Chem. C* **2009**, *113*, 4948−4954.
(35) Chen, Z.-X.; Neyman, K. M.; Gordienko, A. B.; Rösch, N. Surface Structure and Stability of PdZn and PtZn Alloys: Density Functional Slab Model Studies. *Phys. Rev. B* **2003**, *68*, 075417.
(36) Boettger, J. C. Nonconvergence of Surface Energies Obtained from Thin-Film Calculations. *Phys. Rev. B* **1994**, *49*, 16798−16800.
(37) Fiorentini, V.; Methfessel, M. Extracting Convergent Surface Energies from Slab Calculations. *J. Phys.: Condens. Matter* **1996**, *8*, 6525−6529.
(38) Puchin, V. E.; Puchina, A. V.; Huisinga, M.; Reichling, M. Theoretical Modelling of Steps on the CaF_2(111) Surface. *J. Phys.: Condens. Matter* **2001**, *13*, 2081−2094.

(39) Skorodumova, N. V.; Baudin, M.; Hermansson, K. Surface Properties of CeO_2 from First Principles. *Phys. Rev. B* **2004**, *69*, 075401.
(40) Zhou, Y.; Zhou, J. Ti/CeO_x(111) Interfaces Studied by XPS and STM. *Surf. Sci.* **2012**, *606*, 749−753.
(41) Dvořák, F.; Stetsovych, O.; Steger, M.; Cherradi, E.; Matolínová, I.; Tsud, N.; Škoda, M.; Skála, T.; Mysliveček, J.; Matolín, V. Adjusting Morphology and Surface Reduction of CeO_2(111) Thin Films on Cu(111). *J. Phys. Chem. C* **2011**, *115*, 7496−7503.
(42) Baron, M.; Bondarchuk, O.; Stacchiola, D.; Shaikhutdinov, S.; Freund, H.-J. Interaction of Gold with Cerium Oxide Supports: CeO_2(111) Thin Films vs CeO_x Nanoparticles. *J. Phys. Chem. C* **2009**, *113*, 6042−6049.
(43) Kresse, G.; Furthmüller, J. Efficient Iterative Schemes for *Ab Initio* Total-Energy Calculations Using a Plane-Wave Basis Set. *Phys. Rev. B* **1996**, *54*, 11169.
(44) Perdew, J. P.; Wang, Y. Accurate and Simple Analytic Representation of the Electron−Gas Correlation Energy. *Phys. Rev. B* **1992**, *45*, 13244.
(45) Dudarev, S. L.; Botton, G. A.; Savrasov, S. Y.; Humphreys, C. J.; Sutton, A. P. Electron-Energy-Loss Spectra and the Structural Stability of Nickel Oxide: An LSDA+U Study. *Phys. Rev. B* **1998**, *57*, 1505.
(46) Loschen, C.; Carrasco, J.; Neyman, K. M.; Illas, F. First Principles LDA+U and GGA+U Study of Cerium Oxides: Dependence on the Effective U-Parameter. *Phys. Rev. B* **2007**, *75*, 035115.

Section 5.3

PCCP

PAPER

O vacancies on steps on the CeO_2(111) surface

Sergey M. Kozlov[a] and Konstantin M. Neyman*[ab]

Cite this: *Phys. Chem. Chem. Phys.*, 2014, **16**, 7823

Received 10th January 2014,
Accepted 21st February 2014

DOI: 10.1039/c4cp00136b

www.rsc.org/pccp

Cerium dioxide is a compound important for heterogeneous catalysis, energy technologies, biomedical applications, *etc.* One of its most remarkable properties is low O vacancy (O_{vac}) formation energy E_f. Nanostructuring of ceria was shown to decrease E_f and to make the oxide material more active in oxidative reactions. Here we investigate computationally formation of O_{vac} on CeO_2(111) surfaces nanostructured by steps with experimentally observed structures. To facilitate the search for O_{vac} + $2Ce^{3+}$ configurations that yield the lowest E_f values we proposed and employed an efficient computational scheme where DFT + U calculations were preceded by a pre-screening procedure based on the results of plain DFT calculations. E_f values on the steps were calculated to be up to 0.7 eV lower than on a regular CeO_2(111) surface. Some energetically stable O_{vac} + $2Ce^{3+}$ configurations were found to include subsurface Ce^{3+} ions. The present results quantify to what extent the roughness of the CeO_2(111) surface affects its reducibility.

1 Introduction

Many physical and chemical properties of ceria (CeO_2) are determined by its striking ability to release/store oxygen,[1] which is crucial for a great variety of current and prospective applications. Pertinent examples include usage of ceria-based materials as ionic conductors[2,3] and antioxidants in living systems,[4,5] for green production of fuels[6] and as indispensable components of automotive and other catalysts.[7–9] The process of oxygen release is commonly related to the creation of oxygen vacancies, O_{vac}, and triggered by the reducible character of the oxide. Surface O_{vac} formation on various single-crystal planes of CeO_2 has been comprehensively addressed during the past few years using theoretical modeling methods based on density functional theory (DFT).[10–13] These and other computational studies documented that the energy cost E_f required to create a surface O_{vac} is notably lower than to make it in bulk ceria. Also, electronic structure calculations of nanoparticulate ceria lately have become a hot topic.[14–21] For instance, modelling predicted remarkably low E_f values of nanocrystallites $(CeO_2)_n$, $n \leq 80$.[15,16] This lowering makes oxygen transfer from the oxide nanostructures to Pt species deposited on them energetically viable and allows one to rationalize experimental observations for this very important catalytic system.[18]

Detailed geometric structures of the above mentioned ceria nanoparticles are still awaiting their unequivocal experimental verification. At variance, such form of ceria nanostructuring as steps on the CeO_2(111) surface has been recently meticulously characterized structurally by combination of spectroscopic experiments and so-called DFT + U calculations.[22,23] The steps, which can be produced in a controllable way *via* high-temperature annealing, appear to be excellent model systems for comprehensive studies of nano-effects in ceria. It is particularly interesting to evaluate how much O vacancy formation energies on the steps differ from those on a regular (111) surface and small ceria nanoparticles. The first DFT + U study of steps with O_{vac} defects on the CeO_2(111) surface[24] had to rely on *ad hoc* structures and it left aside the energetic aspect of the vacancy formation. Very recently, the structures of ceria steps[22,23] have been employed to explore the Mars–van Krevelen mechanism of CO oxidation at the interface of Au clusters with the steps on CeO_2(111).[25] In other studies, the steps were shown to have interesting features in their electronic structure,[22] to be able to dissociate adsorbed water[26,27] and to serve as preferential adsorption sites for gold atoms[28] as well as nucleation centers for Au nanoparticles.[25,29] Also, undercoordinated Ce atom bordering pits on very thin CeO_2(110) films were recently shown to be highly active in CO oxidation.[30] Unfortunately, linear defects on ceria surfaces other than CeO_2(111) are yet to be characterized, which makes their computational investigation difficult. However, since lower stability is often associated with higher chemical activity,[12,13,31] it would be very interesting to study the properties of other ceria surfaces and steps on them.

The present work aims at comprehensive structural and energetic characterization of O_{vac} formation on various experimentally observed steps on CeO_2(111) by means of DFT + U and hybrid-functional calculations. Removal of an atomic O from

[a] *Departament de Química Física and Institut de Quimica Teòrica i Computacional (IQTCUB), Universitat de Barcelona, C/Marti i Franques 1, 08028 Barcelona, Spain*

[b] *Institucio Catalana de Recerca i Estudis Avançats (ICREA), 08010 Barcelona, Spain. E-mail: konstantin.neyman@icrea.cat*

CeO_2, which consists of ions in the formal charge states Ce^{4+} and O^{2-}, leaves two electrons on two Ce^{4+} cations, reducing them to Ce^{3+}. To explore a multitude of conceivable $O_{vac} + 2Ce^{3+}$ configurations, an efficient pre-screening procedure has been developed and implemented, allowing reliable determination of the lowest E_f values by performing only a limited number of calculations for each type of steps. Notably, E_f values are calculated to vary by up to 1 eV depending on the O_{vac} position; furthermore, depending on the location of Ce^{3+} ions E_f changes by up to 0.4 eV. We show that the most facile O_{vac} formation on stepped surfaces requires substantially, by 0.53–0.70 eV, less energy than on regular $CeO_2(111)$ terraces. This implies a strong change of reaction and activation energies of processes involving O vacancies on the steps.

2 Computational details

VASP software[32] was employed to perform density functional calculations using the Perdew–Wang 91 exchange–correlation functional[33] and self-interaction (U) corrections.[34] The value U = 4 eV was chosen for consistency with our previous studies;[15–23,35] this approach is hereafter referred to as PW91 + 4. Calculations using the hybrid HSE06 exchange–correlation functional[36,37] were performed in a single-point fashion on PW91 + 4 optimized geometries. Spin-polarized calculations were carried out for Ce_xO_{2x-1} systems; no spin-polarization was considered for stoichiometric Ce_xO_{2x} systems. The plane-wave basis set with the 415 eV cutoff described states of valence electrons, while core electrons were accounted for using the projector augmented wave (PAW) technique.[38] Note that the presented values of E_f were corrected for the aspherical gradient contributions inside PAW spheres after geometry optimization. Inclusion of these corrections in the geometry optimization procedure is time consuming and changes the resulting values merely by $\leq$0.04 eV. All calculations were performed at the Γ-point in the reciprocal space; tests performed using denser k-point meshes yielded E_f by $\leq$0.07 eV different from the E_f values presented in the following. The latter were calculated with respect to the half of the energy of (triplet) the O_2 molecule in the gas phase. Statistical analysis was performed using free R environment[39] and quantreg library.[40]

Main results were calculated for regular $CeO_2(111)$ and vicinal surfaces with type I, II, and III steps (Fig. 1) modeled by three (tri-)layer thick slabs. This thickness was shown to be sufficient to calculate properties of the steps.[23] All atoms in the supercells were relaxed during geometry optimization, while the lateral dimensions of the cells were fixed on parameters derived from experimental bulk geometry (a = 540 pm). If bulk optimized lattice parameter a = 549 pm was used E_f would decrease by 0.2–0.4 eV, due to more space to accommodate bigger Ce^{3+} ions.[41] Since E_f depends only moderately on the lattice parameter value, the choice of the latter does not affect conclusions of our study, which may not be the case for studies of other properties of ceria-based systems.[42] A hexagonal $p(3 \times 3)$ supercell of 1.15 × 1.15 nm size was employed to model the $CeO_2(111)$ surface. Rectangular $3 \times Ce_{15}O_{30}$ ($+O_{vac}$ if present) supercells of vicinal surfaces with dimensions of 1.15 × 1.76 nm and 1.15 × 1.54 nm were used for steps of types I and II, respectively. Type III steps were modeled in a

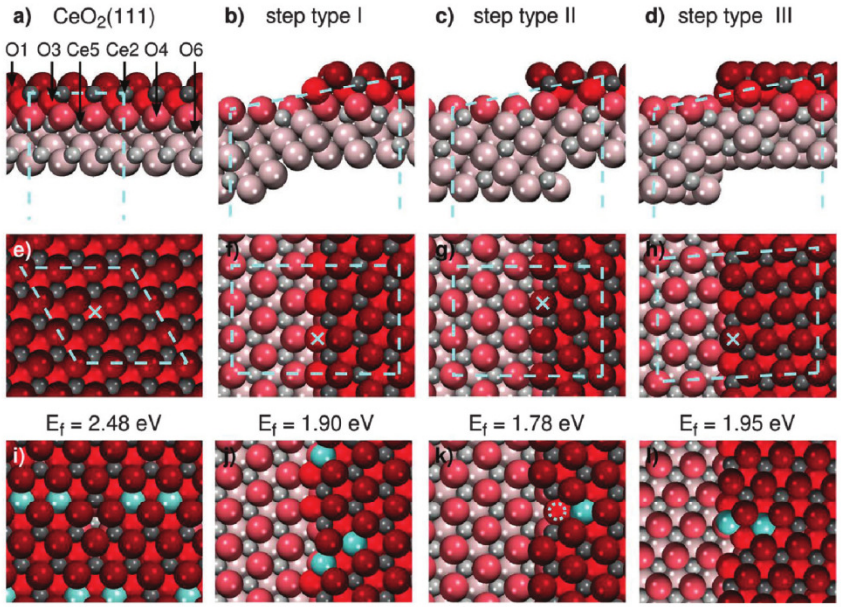

Fig. 1 (a)–(d) Side and (e)–(h) top views on stoichiometric surfaces as well as (i)–(l) top views on the respective surfaces with O_{vac} for the following systems: (a), (e), (i) – pristine $CeO_2(111)$; (b), (f), (j) – vicinal surface with steps of type I; (c), (g), (k) – vicinal surface with steps of type II; (d), (h), (l) – vicinal surface with steps of type III. O atoms are displayed as big reddish spheres, Ce^{4+} ions as small grayish spheres, and Ce^{3+} ions as big cyan spheres. Atoms with darker colors are located in upper atomic layers (see numbering of the latter on panel (a)). The location of subsurface Ce^{3+} ions is marked by a dotted circle; the easiest to remove O atom for each stoichiometric model is marked by a cross.

1.32 × 1.83 nm cell composed of 3 × $Ce_{18}O_{36}$ (+O_{vac} if present); the angle between the lateral lattice vectors was arccos(0.301) = 72.5°. The separation between adjacent periodically repeated slabs was ~1 nm.

In line with previous studies,[13,41,43] we have calculated that on pristine CeO_2(111) the most stable O_{vac} + 2Ce^{3+} configuration (E_f = 2.48 eV) is that where an O atom is removed from the subsurface (third atomic) layer and Ce^{3+} ions are next nearest neighbors of the vacancy. For test purposes, we calculated a similar configuration in the employed supercells of vicinal surfaces as far as possible from the steps. E_f values obtained in such a way differ by less than 0.04 eV from the value we calculated for the pristine surface.

In order to compare the performance of DFT + U methods to that of a more computationally expensive HSE06 hybrid functional method the following smaller supercells were considered: for steps of types I and II we calculated rectangular 3 × Ce_8O_{16} (+O_{vac} if present) cells of 0.76 × 1.45 nm and 0.76 × 1.23 nm, respectively; a 0.66 × 1.34 nm cell with the angle of arccos(0.082) = 85.3° between the lattice vectors and stoichiometry 3 × Ce_7O_{14} (+O_{vac} if present) was used to model type III steps. The 1.15 × 1.15 nm hexagonal p(3 × 3) supercell was used to model the flat CeO_2(111) surface.

3 Results and discussion

Calculation of E_f in a given system involves searching for the most energetically stable O_{vac} + 2Ce^{3+} configuration among many conceivable ones. We perform this search *via* a pre-screening procedure described in the Appendix, which allows us to determine the most stable O_{vac} + 2Ce^{3+} configuration and the lowest E_f with >97% probability for each type of steps (see Fig. 1).

The lowest E_f value, 1.78 eV, is calculated for type II steps. The latter, despite being the least stable among the considered step types,[23] were found to be ubiquitously exposed after annealing at 1000 K.[22] In this case a two-coordinated O atom is removed from the top part of the step and both Ce^{3+} cations are created in the second coordination sphere of the O_{vac}. Interestingly, while one of the Ce^{3+} cations is located on the upper terrace close to the edge, the other is located in the subsurface (fifth atomic) layer right below the step. E_f is slightly higher, 1.90 eV, on steps I, which were calculated to be the most stable step type.[23] In the most stable configuration on steps I, a three-coordinated O is removed from the bottom of the step; one of the Ce^{3+} ions is directly located on the step and the other is located on the upper terrace, in the second coordination sphere of the O_{vac}. Steps of type III, abundant after annealing at T > 1000 K, feature the highest E_f value, 1.95 eV, for the considered steps.[22,23] In this case, the O_{vac} is formed on a two-coordinated site on the top part of the step. One Ce^{3+} is located on the step next to the vacancy and another Ce^{3+} is close to the step in the second coordination sphere of the O_{vac}. Note that on the CeO_2(110) surface, which is parallel to the slopes of steps I, II, and III, E_f is ~0.6 eV lower than that on the most stable CeO_2(111) surface according to other DFT + U calculations.[44,45] Concomitantly, on a less stable CeO_2(100) surface O_{vac} formation energy was calculated to be only by 0.3 eV lower than that on CeO_2(111).[45]

Data calculated for other positions of O_{vac} on stepped and regular CeO_2(111) surfaces are summarized in Table 1. In general, E_f changes by up to 1 eV depending on the location of O_{vac} and by up to 0.4 eV depending on the location of two Ce^{3+} ions. O_{vac} formation is facilitated directly at the steps and also on the lower terrace in the vicinity of steps I and III. In all other configurations E_f values are quite close to the values calculated on a regular CeO_2(111) surface. Note that O vacancies are calculated to be locally unstable in certain positions. For example, when O is removed from the top part of step I, the vacancy migrates to the bottom part of the step during geometry optimization. A similar situation occurs on steps III, where O vacancies spontaneously migrate to the step from adjacent sites on the upper terrace. This indicates that the steps may have a rather flexible structure, which can decrease activation energies of certain processes, such as O_{vac} diffusion.

An insight into the relative stability of surface and subsurface Ce^{3+} cations can be obtained from a statistical analysis of the calculated configurations (Fig. 2). The configurations that involve subsurface Ce^{3+} ions yield an average E_f of only 0.1 eV higher than the configurations with solely surface Ce^{3+} ions. At the same time, standard deviations of the respective distributions are around 0.3 eV, *i.e.* higher than the difference between the average E_f values. Thus, there is no reason to *a priori* assume subsurface Ce^{3+} ions to be less stable than the surface ions. This notion is also supported by the presence of subsurface Ce^{3+} in the most stable O_{vac} + 2Ce^{3+} configuration on type II steps.

Table 1 Ranges of calculated O vacancy formation energies (E_f, eV), on steps of types I, II, and III and on a regular CeO_2(111) surface (see Fig. 1) as well as numbers of considered configurations of Ce^{3+} ions in each case (in parentheses)

Position of O_{vac}[a]	Step type I	Step type II	Step type III	CeO_2(111)
On step	Unstable[b]	1.78–2.09 (9)	1.95–2.37 (6)	
Sub step	1.90–2.21 (14)	2.06–2.31 (6)	2.01–2.27 (16)	
On upper	2.67–3.07 (3)	2.75–3.09 (2)	Unstable[b]	2.72–3.04 (6)
Sub upper	2.54–2.63 (2)	2.63–2.74 (4)	Unstable[b]	2.48–2.74 (6)
On lower	2.15–2.33 (7)	2.81–2.90 (2)	2.72–2.75 (2)	
Sub lower	2.14–2.30 (5)	2.77–2.80 (2)	2.32–2.43 (3)	

[a] "On" and "sub" denote O vacancies located in the topmost (first atomic) and subsurface (third atomic) layers, respectively. "Step", "upper", and "lower" mean that the O vacancy is located on the step edge or adjacent sites on upper or lower terraces, respectively. [b] O_{vac} position locally unstable during geometry optimization.

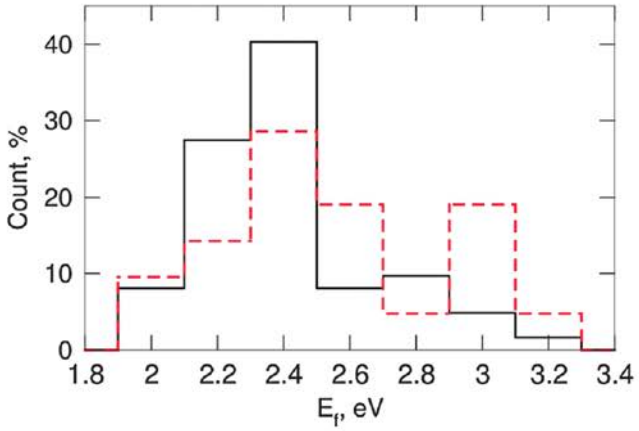

Fig. 2 Partitions of O vacancy formation energies, E_f, on the stepped surfaces for 62 configurations without subsurface Ce^{3+} cations (solid line) and 21 configurations with subsurface Ce^{3+} (dashed line). At variance with values in Fig. 1 and Table 1, the energies were calculated without the gradient corrections inside the PAW spheres.

To evaluate the dependence of calculated E_f values on the computational method used we compare results of various DFT + U approaches – PW91 with U = 4 or 5 eV and PBE with U = 5 eV, later referred to as PW91 + 4, PW91 + 5 and PBE + 5, respectively – and those obtained using the HSE06 hybrid functional. HSE06 is presently often considered to be one of the most reliable computational techniques to treat ceria due to the following reasons: (i) it is a screened hybrid functional particularly suited for solid state systems; (ii) it is not based on any empirical fitting; (iii) it seamlessly predicts localized f-states in reduced ceria. However, all this comes at the expense of high computational cost, which forced us to use smaller supercells for the assessment. Note that in this case for each step type we calculated the O_{vac} + $2Ce^{3+}$ configurations that are depicted in Fig. 1.

The method employed in the present work, PW91 + 4, shows the best agreement with the hybrid HSE06 functional (Table 2). The biggest difference between E_f values calculated using the two methods is 0.19 eV for type III steps. Mind, however, that the good agreement is probably due to a fortuitous cancellation of errors. Indeed, binding energies of the O_2 molecule were calculated to be 6.14 eV using the PW91 method and 5.19 eV using the HSE06 functional, compared to the experimental value of 5.17 eV.[46] Thus, one could expect a ~0.5 eV difference between O_{vac} formation energies calculated using the two functionals with respect to $1/2E(O_2)$. Also previous studies of ceria nanoparticles[15] revealed a correlation but no quantitative agreement between PW91 + 4 and HSE06 E_f values. Other functionals, PW91 + 5 or PBE + 5, yield E_f values 0.3–0.5 eV lower than those of PW91 + 4 and, therefore, deviate more from the HSE06 values.

Comparison of PW91 + 4 data for supercells of different sizes (Fig. 1 and Table 2) shows that the effect of the supercell size on E_f may be up to 0.35 eV. Since the variation of E_f among different step types is within 0.2 eV, this change is enough to alter relative reducibility of different steps. For example, when

Table 2 O vacancy formation energies (E_f, eV) calculated by various DFT + U approaches and the HSE06 hybrid functional method in smaller cells for test purposes

	PW91 + 4	PW91 + 5	PBE + 5	HSE06
CeO_2(111)	2.48	2.07	2.11	2.44
Step type I	1.94	1.63	1.50	2.10
Step type II	2.13	1.68	1.66[a]	2.19
Step type III	2.11	1.64	1.70	2.30

[a] A reconstruction of the step structure occurs in this case due to the limited cell size. This reconstruction becomes endothermic in the bigger supercell.

E_f values are calculated in the bigger supercells, steps II are found to be the easiest to reduce, but when smaller supercells are used, steps II are the hardest to reduce. A recent PBE + 5 investigation[25] by Kim and Henkelman also touched the issue of O_{vac} formation on stepped ceria surfaces using another set of models with a smaller step–step separation than in the present work. The values calculated in ref. 25 agree well with the PBE + 5 values in Table 2, with the maximum deviation of 0.18 eV. However, while in the present work O vacancies were calculated to form easier on steps I than on steps III, in ref. 25 steps III were concluded to be easier to reduce than steps I, which can be explained by the difference between the used supercells.

4 Conclusion

In summary, we have investigated by means of PW91 + 4 calculations O vacancy formation energies on three types of steps experimentally observed on the CeO_2(111) surface. The energies were found to change by up to 0.4 eV depending on the location of Ce^{3+} ions and by up to 1 eV depending on the position of the O vacancy. To find the most energetically stable position of created Ce^{3+} ions we proposed the pre-screening procedure based on results of DFT calculations without U corrections. This allowed us to locate the O_{vac} + $2Ce^{3+}$ configurations that yield the lowest O_{vac} formation energies with >97% probability. Our results show that O vacancy formation energies are by 0.58, 0.70, and 0.53 eV lower on steps of type I, type II, and type III, respectively, than on a regular CeO_2(111) surface. This will significantly change reaction and activation energies of processes involving O vacancies on the steps, such as oxidative reactions. Also, the lower O vacancy formation energies on the steps may affect reverse O spillover processes from ceria to supported nanoparticles[18] and, therefore, change properties of ceria as an active support. For example, according to calculations of O binding energies to various substrates,[47] certain deposited alloys containing Fe, Co, Ni, Ru and Rh may be sensitive to the presence of weaker bound oxygen on the steps and thus become partially oxidized on stepped surfaces.

Ce^{3+} ions in the most stable configurations were found to be in the first and the second coordination spheres of the O vacancies. In the case of steps II the O_{vac} + $2Ce^{3+}$ configuration with the lowest energy also involves Ce^{3+} ions located in the subsurface (fifth atomic) layer just below the step. This finding illustrates the often disregarded necessity to systematically

inspect all conceivable configurations of Ce^{3+} ions (including those with subsurface Ce ions) to determine the most stable structure. This task can be accomplished in a reasonable time with the help of the proposed pre-screening procedure.

Appendix: the pre-screening procedure

The formation of the O vacancy on a regular $CeO_2(111)$ surface is commonly assumed to take place either in the top or in the subsurface (third atomic) O layer.[10,13] When steps are present on the surface, there is no known rule that defines thermodynamic stability of O_{vac} depending on their position with respect to these irregularities. In this work we investigate formation of the surface and the subsurface O_{vac} on the steps and on CeO_2 rows on upper and lower terraces in the immediate vicinity of the steps. Since reduced Ce ions may be located not only on the $CeO_2(111)$ surface (second atomic layer) but also on the subsurface (fifth atomic layer),[11] here we consider possible reduction of all surface and subsurface Ce ions. Thus, we investigate $N(O_{vac}) = 6$ possible O_{vac} locations for each step type and $N(Ce^{3+}) = 2 \times 15$ possible Ce^{3+} sites for the cells of type I and II steps and $N(Ce^{3+}) = 2 \times 18$ for the cells of type III steps. The overall number of $O_{vac} + 2Ce^{3+}$ configurations is $N(O_{vac}) \times N(Ce^{3+}) \times [N(Ce^{3+}) - 1]/2 = 2610$ for steps of types I and II and 3780 for steps of type III. Note that up to a half of the configurations for steps of types I and II may be equivalent to each other due to the presence of a vertical symmetry plane.

To efficiently search for the $O_{vac} + 2Ce^{3+}$ configuration yielding the lowest O_{vac} formation energy E_f we employ a novel pre-screening procedure based on results of DFT calculations obtained without U corrections. A correlation between relative E_f values of various $O_{vac} + 2Ce^{3+}$ configurations and electrostatic potential on the involved O and Ce ions was found before for ceria nanoparticles.[16] However, this correlation is much weaker in the present case due to a smaller variation of electrostatic potential among Ce or O atoms on stepped surfaces compared with CeO_2 nanoparticles. Therefore, we had to resort to a more complicated analysis detailed below.

In a DFT calculation of partially reduced ceria without U corrections some Ce ions accumulate more excess electrons than others, which is reflected by their higher absolute magnetization $|\mu_i|$. The uneven distribution of excess electrons is due to more positive electrostatic potential on some Ce ions and/or higher flexibility of their local environment necessary to accommodate somewhat bigger (partially) reduced Ce ions. The same factors govern relative stability of Ce^{3+} ions in DFT + U calculations. Therefore, one can expect DFT + U calculated E_f to correlate with absolute magnetization on the reduced Ce ions, $M = |\mu_1| + |\mu_2|$, in the respective U-uncorrected DFT calculation.

Suppose a given pair of Ce ions in ceria with O_{vac} acquires absolute magnetization M in a calculation without U corrections, and yields O_{vac} formation energy $E_f|_M$ in the calculation with U. Let M^{max} denote the highest M for a given system, *e.g.* a stepped surface with O_{vac} on a certain site. Then relative magnetization $M^{max} - M$ values correlate with relative O_{vac} formation energies $E_f|_M - E_f|_{M^{max}}$ across different $O_{vac} + 2Ce^{3+}$ configurations in different systems (Fig. 3). Note that the configurations with subsurface Ce^{3+} ions tend to have rather high M, but only moderate E_f. To account for this observation, we split the configurations with and without subsurface Ce^{3+} ions into different subgroups, which are then treated separately with individual M^{max} and $E_f|_{M^{max}}$ for each subgroup. Note also that configurations with the highest spin polarization, *i.e.* with $E_f|_M - E_f|_{M^{max}} = 0$ and $M^{max} - M = 0$, are not plotted in Fig. 3 and not included in the statistical analysis. This is because these data points do not convey any information about peculiarities of the considered system.

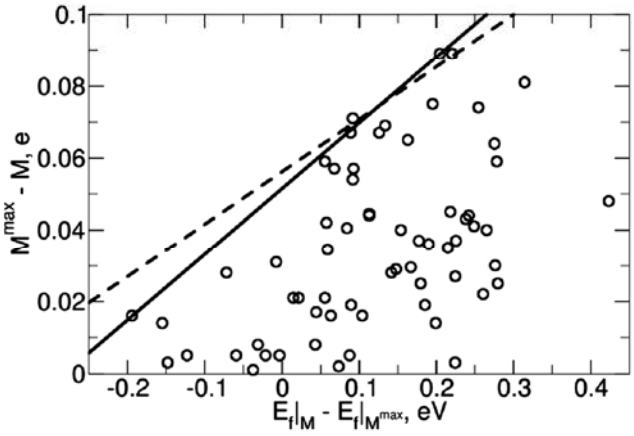

Fig. 3 Correlation between relative magnetization of Ce ions in a PW91 calculation, $M^{max} - M$, and relative O vacancy formation energy, $E_f|_M - E_f|_{M^{max}}$, in the respective PW91 + 4 calculation. Linear quantile regression $y = \alpha + \beta^*x$ for quantile $\tau = 0.97$ used in (1) is displayed as a solid line, $y = \alpha + \sigma_\alpha + (\beta - \sigma_\beta)^*x$ used in (2) as a dashed line.

If linear quantile regression of this correlation for $\tau = 0.97$ (used in this work) results in a dependency $y = \alpha + \beta^*x$, then by construction $M^{max} - M < \alpha + \beta(E_f|_M - E_f|_{M^{max}})$ or $M > M^{max} - \alpha + \beta(E_f|_{M^{max}} - E_f|_M)$ with a probability of 97%. Suppose E_f^{step} is the lowest O_{vac} formation energy found for a given step type after a set of calculations. Then with 97% probability a configuration with $E_f < E_f^{step}$ (if exists) should have

$$M > M^{max} - \alpha + \beta(E_f|_{M^{max}} - E_f^{step}). \quad (1)$$

The $O_{vac} + 2Ce^{3+}$ configurations that do not satisfy criterion (1) with 97% probability are not the most stable configurations for a given step type, therefore, they ought to be discarded during the pre-screening.

Coefficients α and β in (1) derived from a statistical analysis have statistical inaccuracies or dispersions σ_α and σ_β, respectively, associated with them. These inaccuracies are caused by a finite number of data points used in the quantile regression procedure and they will decrease to zero with increasing data set size. In fact, to strengthen criterion (1) against the possibility that the amount of data used in the statistical analysis is insufficient, we used an even more conservative criterion.

Namely, we performed PW91 + 4 calculations for all $O_{vac} + 2Ce^{3+}$ configurations, for which

$$M > M^{max} - \alpha - \sigma_a + (\beta - \sigma_\beta)(E_f|_{M^{max}} - E_f^{step}). \quad (2)$$

Accounting for the statistical inaccuracies will require a much more complicated analysis if one performs a quantile regression of $E_f|_M - E_f|_{M^{max}}$ as a function of $M^{max} - M$. However, the two ways of statistical analysis yield almost identical results if this step is omitted.

In practice, both criteria often reduce to $M > M^{max}$, which is never satisfied and allows to discard $\sim$99% of the possible configurations. For such cases it is sufficient to calculate only two $E_f|_{M^{max}}$, one for the subgroup with only surface Ce^{3+} ions and another for the subgroup with subsurface Ce^{3+}.

The quantile regression obtained in this work (α = 0.0515, β = 0.183, σ_α = 0.0046, σ_β = 0.037 for τ = 0.97) is based on 63 data points, 53 of which were calculated on stepped surfaces and 10 on regular CeO_2(111). Also, as was mentioned above 30 calculated points for steps and 2 points for CeO_2(111) with $M = M^{max}$ and $E_f|_M = E_f|_{M^{max}}$ were not considered in the statistical analysis. If the pre-screening procedure was known beforehand, we would have to perform $\sim$50 calculations using criterion (1) or $\sim$60 calculations using stricter criterion (2) to determine E_f on the steps. This amounts to 3.3 and 4 configurations of $2Ce^{3+}$ per each of 15 locally stable O_{vac} positions on the steps, respectively.

One could also expect that E_f is influenced by the stability of electrons on O atoms subject to removal, which can be monitored by potential energy of trial electrons on the respective O nuclei. Among considered O_{vac} locations on steps II and III the e^- potential energy is, indeed, the highest on the easiest to remove O anions. However, on steps I the easiest to remove "sub-step" O has the highest e^- potential energy only among subsurface O anions, while some surface O atoms feature even higher e^- potential. Despite these findings, if one considers O_{vac} formation on all sites (not only the most stable configurations) it does not seem to be possible to establish a clear correlation between the e^- potential on O atoms and E_f (data not presented). Therefore, we could not establish a reliable pre-screening procedure to help the search for the most stable O_{vac} location.

Acknowledgements

This work was financially supported by the European Community (FP7-NMP.2012.1.1-1 project ChipCAT, Reference No. 310191) and the Spanish MINECO (CTQ2012-34969); it is also a part of the COST Action CM1104 "Reducible oxide chemistry, structure and functions". Computer resources, technical expertise and assistance provided by the Red Española de Supercomputación are gratefully acknowledged. Finally, S.M.K. thanks Spanish Ministerio de Educación for a pre-doctoral FPU grant AP2009-3379.

References

1 M. Mogensen, N. M. Sammes and G. A. Tompsett, *Solid State Ionics*, 2000, **129**, 63.
2 D. A. Andersson, S. I. Simak, N. V. Skorodumova, I. A. Abrikosov and B. Johansson, *Proc. Natl. Acad. Sci. U. S. A.*, 2006, **103**, 3518.
3 J. W. Fergus, *J. Power Sources*, 2006, **8**, 30.
4 R. W. Tarnuzzer, J. Colon, S. Patil and S. Seal, *Nano Lett.*, 2005, **5**, 2573.
5 F. Pagliari, C. Mandoli, G. Forte, E. Magnani, S. Pagliari, G. Nardone, S. Licoccia, M. Minieri, P. Di Nardo and E. Traversa, *ACS Nano*, 2012, **6**, 3767.
6 W. C. Chueh, C. Falter, M. Abbott, D. Scipio, P. Furler, S. M. Haile and A. Steinfeld, *Science*, 2010, **330**, 1797.
7 Q. Fu, H. Saltsburg and M. Flytzani-Stephanopoulos, *Science*, 2003, **301**, 935.
8 C. T. Campbell and C. H. F. Peden, *Science*, 2005, **309**, 713.
9 *Catalysis by Ceria and Related Materials*, ed. A. Trovarelli and P. Fornasiero, Imperial College Press, London, 2nd edn, 2013.
10 F. Esch, S. Fabris, L. Zhou, T. Montini, C. Africh, P. Fornasiero, G. Comelli and R. Rosei, *Science*, 2005, **309**, 752.
11 M. V. Ganduglia-Pirovano, J. L. F. Da Silva and J. Sauer, *Phys. Rev. Lett.*, 2009, **102**, 026101.
12 M. Nolan, *Chem. Phys. Lett.*, 2010, **499**, 126.
13 J. Paier, C. Penschke and J. Sauer, *Chem. Rev.*, 2013, **113**, 3949.
14 S. T. Bromley, I. de P. R. Moreira, K. M. Neyman and F. Illas, *Chem. Soc. Rev.*, 2009, **38**, 2657.
15 A. Migani, G. N. Vayssilov, S. T. Bromley, F. Illas and K. M. Neyman, *Chem. Commun.*, 2010, **46**, 5936.
16 A. Migani, G. N. Vayssilov, S. T. Bromley, F. Illas and K. M. Neyman, *J. Mater. Chem.*, 2010, **20**, 10535.
17 A. Migani, K. M. Neyman and S. T. Bromley, *Chem. Commun.*, 2012, **48**, 4199.
18 G. N. Vayssilov, Y. Lykhach, A. Migani, T. Staudt, G. P. Petrova, N. Tsud, T. Skála, A. Bruix, F. Illas, K. C. Prince, V. Matolín, K. M. Neyman and J. Libuda, *Nat. Mater.*, 2011, **10**, 310.
19 G. N. Vayssilov, M. Mihaylov, P. S. Petkov, K. I. Hadjiivanov and K. M. Neyman, *J. Phys. Chem. C*, 2011, **115**, 23435.
20 G. N. Vayssilov, A. Migani and K. Neyman, *J. Phys. Chem. C*, 2011, **115**, 16081.
21 G. Preda, A. Migani, K. M. Neyman, S. T. Bromley, F. Illas and G. Pacchioni, *J. Phys. Chem. C*, 2011, **115**, 5817.
22 N. Nilius, S. M. Kozlov, J.-F. Jerratsch, M. Baron, X. Shao, F. Viñes, S. Shaikhutdinov, K. M. Neyman and H.-J. Freund, *ACS Nano*, 2012, **6**, 1126.
23 S. M. Kozlov, F. Viñes, N. Nilius, S. Shaikhutdinov and K. M. Neyman, *J. Phys. Chem. Lett.*, 2012, **3**, 1956.
24 M. M. Branda, C. Loschen, K. M. Neyman and F. Illas, *J. Phys. Chem. C*, 2008, **112**, 17643.
25 H. Y. Kim and G. Henkelman, *J. Phys. Chem. Lett.*, 2013, **4**, 216.

26 Y. Lykhach, V. Johánek, H. A. Aleksandrov, S. M. Kozlov, M. Happel, T. Skála, P. St. Petkov, N. Tsud, G. N. Vayssilov, K. C. Prince, K. M. Neyman, V. Matolín and J. Libuda, *J. Phys. Chem. C*, 2012, **116**, 12103.

27 S. Fuente, M. M. Branda and F. Illas, *Theor. Chem. Acc.*, 2012, **131**, 1190.

28 N. J. Castellani, M. M. Branda, K. M. Neyman and F. Illas, *J. Phys. Chem. C*, 2009, **113**, 4948.

29 J.-L. Lu, H.-J. Gao, S. Shaikhutdinov and H.-J. Freund, *Catal. Lett.*, 2007, **114**, 8.

30 Y. Sun, Q. Liu, S. Gao, H. Cheng, F. Lei, Z. Sun, Y. Jiang, H. Su, S. Wei and Y. Xie, *Nat. Commun.*, 2013, **4**, 2899.

31 D. R. Mullins, P. M. Albrecht and F. Calaza, *Top. Catal.*, 2013, **56**, 1345.

32 G. Kresse and J. Furthmuller, *Phys. Rev. B: Condens. Matter Mater. Phys.*, 1996, **54**, 11169.

33 J. P. Perdew and Y. Wang, *Phys. Rev. B: Condens. Matter Mater. Phys.*, 1992, **45**, 13244.

34 S. L. Dudarev, G. A. Botton, S. Y. Savrasov, C. J. Humphreys and A. P. Sutton, *Phys. Rev. B: Condens. Matter Mater. Phys.*, 1998, **57**, 1505.

35 C. Loschen, J. Carrasco, K. M. Neyman and F. Illas, *Phys. Rev. B: Condens. Matter Mater. Phys.*, 2007, **75**, 035115.

36 J. Heyd, G. E. Scuseria and M. Ernzerhof, *J. Chem. Phys.*, 2003, **118**, 8207.

37 J. Heyd, G. E. Scuseria and M. Ernzerhof, *J. Chem. Phys.*, 2006, **124**, 219906.

38 P. E. Blöchl, *Phys. Rev. B: Condens. Matter Mater. Phys.*, 1994, **50**, 17953.

39 R Core Team, *R: A Language and Environment for Statistical Computing*, R Foundation for Statistical Computing, Vienna, Austria, 2013.

40 R. Koenker, quantreg: Quantile Regression, R package 4.98. http://CRAN.R-project.org/package=quantreg, 2013.

41 A. Bruix, A. Migani, G. N. Vayssilov, K. M. Neyman, J. Libuda and F. Illas, *Phys. Chem. Chem. Phys.*, 2011, **13**, 11384.

42 M. M. Branda, N. J. Castellani, R. Grau-Crespo, N. H. de Leeuw, N. C. Hernandez, J. F. Sanz, K. M. Neyman and F. Illas, *J. Chem. Phys.*, 2009, **131**, 094702.

43 H.-Y. Li, H.-F. Wang, X.-Q. Gong, Y.-L. Guo, Y. Guo, G. Lu and P. Hu, *Phys. Rev. B: Condens. Matter Mater. Phys.*, 2009, **79**, 193401.

44 S. Fabris, G. Vicario, G. Balducci, S. de Gironcoli and S. Baroni, *J. Phys. Chem. B*, 2005, **109**, 22860.

45 M. Nolan, S. C. Parker and G. W. Watson, *Surf. Sci.*, 2005, **595**, 223.

46 J. D. Cox, D. D. Wagman and V. A. Medvedev, *CODATA Key Values for Thermodynamics*, Hemisphere Publishing Corp., New York, 1984.

47 J. Greeley and J. K. Nørskov, *Surf. Sci.*, 2005, **592**, 104.

5.4. Water on Steps on CeO_2(111) (Outlook)

Particular electronic structure of steps on CeO_2(111) and their higher reducibility should affect chemical reactions taking place on the steps. One of such reactions is water dissociation, which is a very important step in water gas shift[214,252,352] and various steam reforming reactions.[272,353]

In Section 11.6 water dissociation on pristine CeO_2(111) surface and the same surface with type III steps was investigated. It was found that water adsorbs significantly stronger on type III sites than on (111) terraces. Moreover, whereas on CeO_2(111) water dissociation was found to be endothermic by ~0.2 eV on the steps this process was calculated to be exothermic by ~0.3 eV creating a significant driving force for the dissociation (Figure 5.5). Also water is known to dissociate on O vacancies in ceria.[354] The ability of steps to form O vacancies more easily (Section 5.3) may further facilitate water dissociation on step sites. Note that some other ceria surfaces, in particular CeO_2(110) parallel to the steps facets, were also predicted to be able to dissociate water.[355]

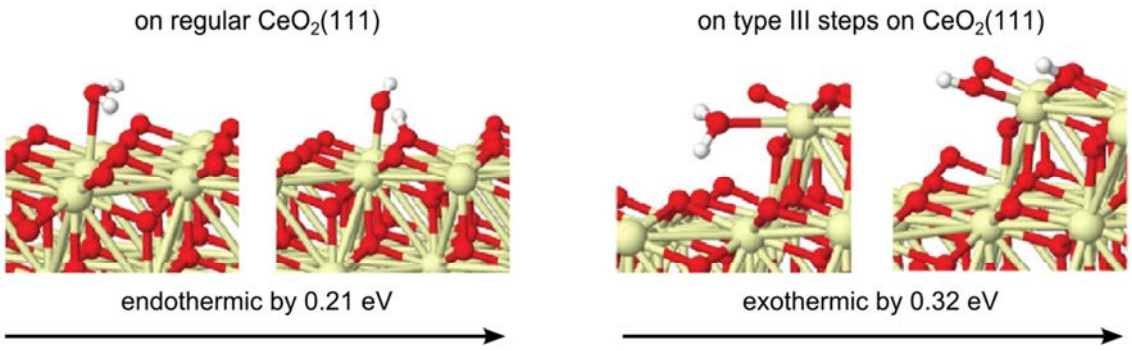

Figure 5.5. Calculated structures involved in water dissociation on regular and stepped CeO_2(111). Ce is displayed in ivory, O – red, H – white.

The computational findings were confirmed experimentally by a combination of various techniques. Namely, OH species formed via water dissociation were detected by photoelectron spectroscopy on rough ceria surface (modelled by type III steps), whereas only intact water molecules were observed on regular CeO_2(111). Interestingly, OH species could not be detected by infrared spectroscopy, which is in line with very small IR intensity of O-H vibrations calculated by DFT.

In addition to these studies also H adsorption on type III steps on $CeO_2(111)$ was studied, because it is reminiscent of water adsorption on ceria containing O vacancies.[356] It was found that on the steps hydrogen atom adsorbs 0.45 eV stronger than on regular $CeO_2(111)$, leading to reduction of one Ce^{4+} to Ce^{3+}.

Thus, the study presented in Section 11.6 confirmed the hypothesis of altered adsorptive properties and reactivity of steps on $CeO_2(111)$ using water and hydrogen species as examples. These findings illustrate the importance of such form of nanostructuring as steps on surfaces for properties of catalytic systems.

5.5. Ceria Nanowires (Outlook)

Similarly to steps on surfaces, nanowires are systems extended in one direction and confined in two other directions. Currently, application of nanowires in heterogeneous catalysis is intensively studied because of their intrinsically high surface area per gram of active material and not too complicated synthesis protocols.[22,23] In particular, nanowires of cerium dioxide have been characterized experimentally[357–359] and found to have higher oxygen storage capacity[360] and to be more active in CO oxidation.[21,316,361] Despite certain experimental interest in this system, until recently properties of ceria nanowires have been simulated only using interatomic potentials.[362]

In Section 11.7 a DFT study of ceria nanowires composed of $Ce_{38}O_{76}$, $Ce_{40}O_{80}$ and $Ce_{80}O_{160}$ nanoparticles is presented. In $Ce_{40}O_{80}$ and $Ce_{80}O_{160}$ nanoparticles the binding between the adjacent building blocks took place through contact of corner Ce atom to four O atoms on the opposite side of the nanoparticles. As a result, binding energies between these two kinds of building blocks were calculated to be very similar. Due to the presence of two corner Ce atoms in $Ce_{40}O_{80}$ it was possible to form also a two-dimensional nanogrid composed of these NPs with the same type of contact between one Ce and four O atoms. The self-assembly energy in this case was almost twice bigger compared to the case of one-dimensional nanowire. This suggests that the energy gained due to the formation of Ce-O_4 contact is insensitive to the nanoparticle size. In variation, in nanowires composed of $Ce_{38}O_{76}$ four Ce atoms from one building block formed bonds with four O atoms from an adjacent building block. Despite the higher number of Ce-O bonds formed in this case, this type of interface actually led to *weaker* binding than the Ce-O_4 contact, indicating that the latter is not improbable.

Since the reducibility of ceria is considered one of its key properties, the formation of O_{vac} in these nanowires and the respective building blocks was investigated and compared to that of steps on CeO_2(111). Through analysis of O vacancies in a multitude of structures[a] it was found that the presence of four-coordinated Ce cations located on corners of some nanoparticles correlated with their $E_f(O_{vac})$ values. In structures containing such cations $E_f(O_{vac})$ were almost always lower than 0.6 eV,

[a] Namely, Ce_XO_{2X} (X = 38, 40, 80, 140) nanoparticles, Ce_XO_{2X} (X = 38, 40, 80) nanowires and $Ce_{40}O_{80}$ nanogrids were considered.

whereas in structures without them O vacancy formation energies exceeded 1 eV. Since the considered self-assembly processes took place through nanoparticle corners, the coordination of Ce atoms on them increased from four to eight O atoms (or to six in the case of $Ce_{38}O_{76}$) upon the agglomeration. As a consequence, the reducibility of the material decreased substantially. Nevertheless, $E_f(O_{vac})$ in all the considered ceria nanostructures were significantly lower than those calculated on steps on $CeO_2(111)$.

The effect of the presence of four-coordinated ceria atoms on $E_f(O_{vac})$ was rationalized via analysis of DOS projected on cerium and oxygen atoms (Figure 5.6). It was found that structures with four-coordinated Ce cations have rather wide unoccupied 4f-bands and consequently lower O_{2p}-Ce_{4f} band gaps. Since these band gaps govern the stability of excess electrons left in the nanoparticle upon removal of an O atom, their values strongly correlate with $E_f(O_{vac})$.

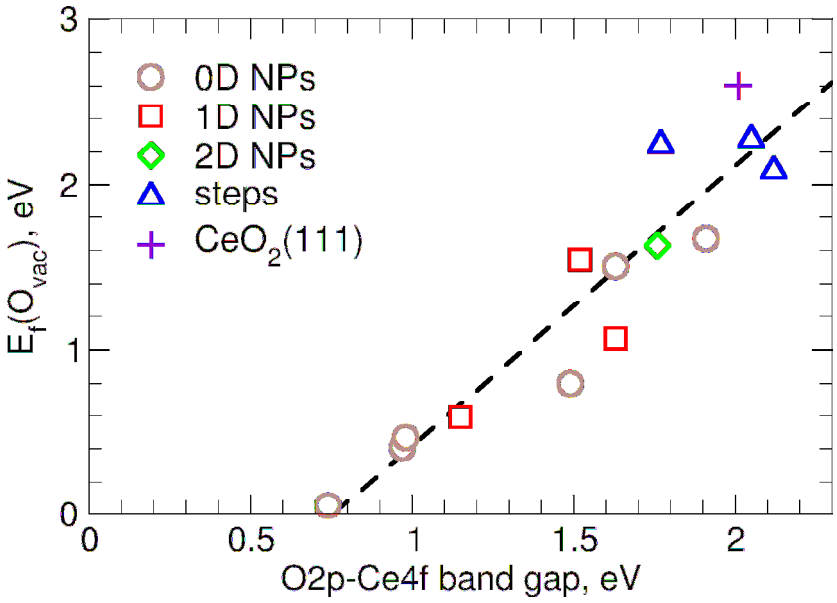

Figure 5.6. The relation between O vacancy formation energy $E_f(O_{vac})$ and the O2p-Ce4f band gap in various forms of nanostructured ceria.

Similarly to the study of steps on $CeO_2(111)$ discussed in Section 5.3 some test calculations with hybrid HSE06 functional were performed in order to assess the reliability of the employed PW91 with U = 4 eV approach. Again a strong linear correlation between $E_f(O_{vac})$ values calculated by the two functionals was found, validating the suitability of the GGA+U method for the purposes of this study.

Chapter 6

Nanometer Thick Films

Thin films (or nanofilms) are structures extended in two (lateral) dimensions and confined in the third (vertical) direction to less than 100 nm. Investigations of various films started a very long time ago (Faraday[363] was one of the pioneers) and intensified in the beginning of XX-th century with the birth of many surface science techniques.[364,365] Rich variety of the latter allows to study surfaces from almost any point of view,[46,290,366] which usually results in their precise characterization. Another important advantage of studies dealing with films is that the latter can often be prepared as single crystals with a minor concentration of defects and regular surface.[365,367]

This structural simplicity could make thin films also perfect model systems for studies of e.g. heterogeneous catalysts; however, it has its own weak sides. First, unlike defectless regular surfaces, industrially applied catalysts have a very complex nanostructure exposing a much higher number of low-coordinated atoms. So the activity of films may not exactly represent the catalytic activity of real catalysts.[368] Second, due to the nanostructuring limited only to one dimension, films have relatively small surface area dictated by the spatial extent of the sample, in contrast to powders with surface areas in the order of m^2. Hence, in some reactions it is very hard to detect chemical activity of films at all. Moreover, the structure and activity of films may change upon exposure to the reactants,[369,370] whereas many surface science techniques operate only in ultra-high vacuum conditions or under relatively low pressures.

Objectives of this Chapter

Despite that there has been a lot of progress in studies of films and structures of some of them have been successfully determined, emergence of more and more materials requires additional investigations. Since often a single surface science technique is insufficient to determine detailed structure of a film,[309,370,371] complementary computational studies have a great potential to clarify the experimental situation. Also theoretical methods are a very powerful tool to provide basic explanation why one or the other film structure appears in experiment.

Studies discussed in this Chapter are devoted to two systems of considerable interest for catalytic community and related to those discussed in Sections 3.4 and Chapter 5. The first study (Section 6.1) focuses on films of cerium sesquioxide, Ce_2O_3, that are currently being studied as model systems for cerium oxide under reducing

conditions found in many applications.[312,325,372] Then in Section 6.2 thin films of PdZn grown on Pd(111) in ultra-high vacuum and under CO atmosphere are examined, since these films were proven to be useful for understanding catalytic performance of real PdZn-based catalysts.[42,58,373] In both studies the goal was to explain why the observed structures of films may differ from known structures of the respective materials in the bulk phase.

Feasible structures of Ce_2O_3 films

The role of cerium oxide in heterogeneous catalysis and other applications was outlined in Chapter 5. Due to its facile reducibility, in applications under sufficiently reducing conditions[374] or at sufficiently high temperatures[312] cerium oxide is present in partially reduced CeO_{2-x} form. The latter is expected to have rather inhomogeneous and hard to investigate structure.[309,310] To reduce the complexity of this system, regular films of fully reduced cerium oxide, Ce_2O_3, were prepared on various substrates for model investigations. The structure of the prepared films, however, differed depending on the substrate or preparation conditions. In some cases films with the hexagonal A-type lattice (like in bulk Ce_2O_3) were prepared,[375,376] whereas in other cases films of the cubic bixbyite phase were obtained,[377,378] despite that the latter could not be stabilized in bulk Ce_2O_3 samples (Figure 6.1). Moreover, when Ce_2O_3 films were grown on Pt(111), a new poorly understood structure emerged.[379,380]

This suggests that the substrate plays an important role in determination of the film structure. This could be either through direct chemical interactions between the substrate and the film through strong interfacial bonds or through the imposed epitaxy. In the latter case the substrate imposes a certain strain or compression on the supported film in order to achieve better matching between the lattice parameters of the film and the substrate. Note that this matching should not be always 1:1; other matching such as 4:3[381] or 12:11[382] were also observed.

To investigate various structures of Ce_2O_3 films a study employing both interatomic potentials and density functional theory methods was performed (Section 6.1). Interatomic potentials were used to screen the configurational space of ~1 nm thick Ce_2O_3 films via the simulated mechanical annealing technique.[383] In this method films are gradually stretched and compressed by up to 30% with the relaxation of atomic

positions at each step. At certain points, the geometry of the film qualitatively changes and converges to some new structure. Then the simulated mechanical annealing technique is repeated for the newly obtained structure, which often results in even more structures being found. Having explored the configurational space of Ce_2O_3 films with interatomic potentials, DFT was used to estimate relative stability of low-energy films in a more accurate way.[2]

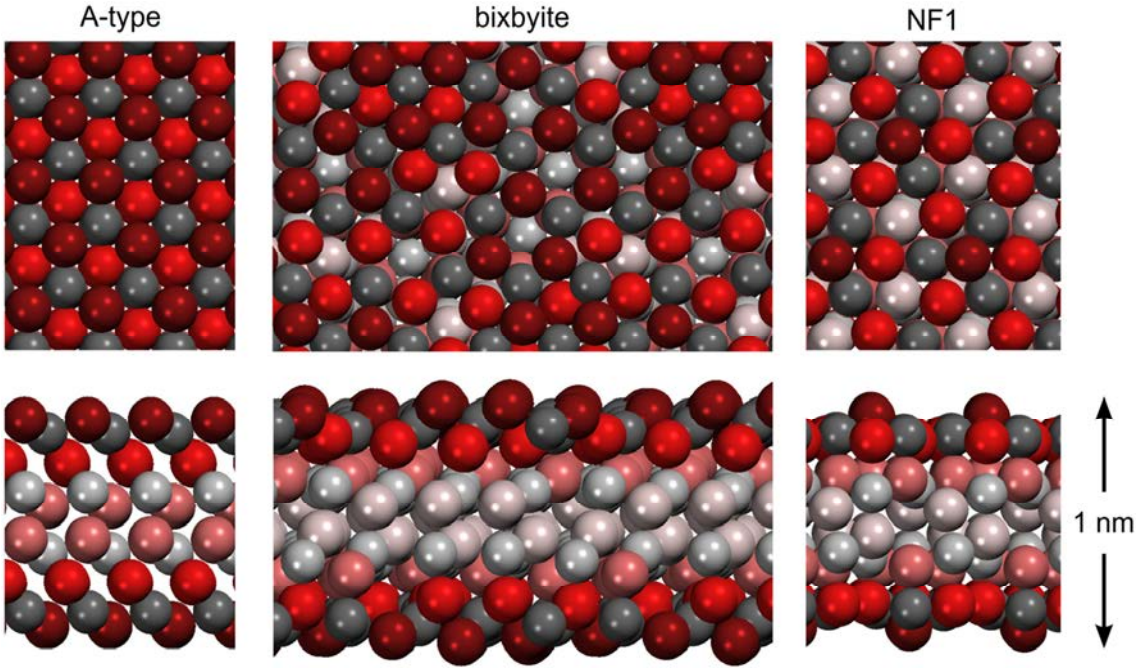

Figure 6.1. Structures of the considered A-type, bixbyite and NF1 Ce_2O_3 films. O atoms are displayed in red and Ce ions in grey. Atoms with darker colors are located in surface layers.

This study showed that on substrates that favor smaller lattice parameters (< 386 pm) of supported Ce_2O_3 films would favor the A-type structure of Ce_2O_3 films. The substrates that impose intermediate lattice parameters (between 390 and 406 pm) would favor the bixbyite structure. Finally, a new NF1 structure was predicted to appear on substrates that favor lattice parameters over 410 pm. The new structure is not similar to any bulk structure of any A_2B_3 material and has well separated protruding O anions on its surface. Also it has fewer bonds per atom than A-type and bixbyite films and exhibit

[2] The comparison of DFT and IP results showed a remarkably good agreement, also observed in other papers on partially reduced ceria.[192,328] This strengthens the confidence in the power of IP to predict new polymorphs of Ce_2O_3 films.

reduced band gaps in its electronic structure. All this may result in altered chemical properties and reactivity.

The preference for one or the other film structure depending on the substrate was, in general, in good agreement with available experimental literature. Only in a couple of cases, on Si(111) and CeO_2(111) substrates, the bixbyite phase was prepared experimentally, despite that the calculations predicted higher thermodynamic stability of the A-type phase. However, this could happen due to the *metastability* of bixbyite, that is, due to a very long time required to overcome the kinetic barrier of transition to a more stable phase. In fact, according to calculations, A-type should be up to 0.06 eV per Ce_2O_3 more stable in these cases, whereas the metastability is observed even when energy differences between the two phases reach 0.15 eV per unit. Moreover, Pt(111) seems to be one of the substrates imposing larger lattice parameters on Ce_2O_3 films. For this substrate, the emergence of the new NF1 structure is predicted and some exotic films structures are also observed experimentally.[379,380]

This study was the first to employ simulated mechanical annealing method for global optimization of film structures. It shows the potential of this method for investigations of intrinsic stability of plausible film structures and prediction of new polymorphs. It also serves as guidance to experimentalists in choosing appropriate substrates for discovery of new film structures.

The effect of adsorbed CO on structure of PdZn/Pd(111) films

PdZn is an intermetallic compound made of a d-metal Pd and an sp-element Zn, which results in very strong heteroatomic bonds (Ref. 384 and Section 3.4) and charge redistribution between the elements. Namely, Bader charges on Pd and Zn atoms in bulk PdZn were calculated to be -0.4 and +0.4 atomic units, respectively.[385] Consequently, some authors propose the notation ZnPd to be more consistent with the IUPAC nomenclature than PdZn, since the positively charged species should come first.

Due to the notably exothermic bonding between Pd and Zn atoms, the most thermodynamically stable structure of PdZn single crystals or NPs (see Section 3.4) is the one that allows the formation of the maximum possible number of heteroatomic Pd-Zn bonds. Namely, it is the regular $L1_0$ alloy structure, which follows fcc lattice with Pd and Zn atoms arranged in layers perpendicular to [001] direction.[386] Consequently, the

most stable (111) surfaces of PdZn expose Pd and Zn atoms arranged in alternating rows. In turn, this results in the absence of three-fold hollow surface sites composed entirely of Pd or Zn on PdZn(111), which may facilitate certain desirable or undesirable reactions. Moreover, the structure of bulk PdZn features the tetragonal distortion,[385] that is Pd-Pd and Zn-Zn bonds are significantly longer than Pd-Zn bonds.[3] Hence, the interatomic distance between Pd atoms on PdZn(111) exceeds that on Pd(111), which again contributes to the catalytic activity of the surface.

Naturally, such drastic (for an alloy) charges on atoms strongly affect the electronic structure of the material. Density of states projected on surface Pd atoms in PdZn was found to be closer to DOS of Cu than that of pure Pd.[58] Thus, there is no surprise that the activity and the selectivity of PdZn-based catalysts in such reaction as methanol steam reforming (MSR) are very close to the industrially employed Cu-based catalysts.[58,258] Unlike pure Pd that tends to decompose methanol to hydrogen and CO, copper (similarly to PdZn) is both active and selective to CO_2 in MSR (see Section 11.4). The latter is very important, because CO is a strong poison for Pt-catalysts often encountered in fuel cells.[6] The critical advantage of PdZn catalysts compared to Cu-based catalysts for MSR is that the former[386–388] are more stable, less prone to sintering and are not pyrophoric unlike the latter.[26,389,390] At the same time, selectivity of PdZn is known to critically depend on the alloy composition in general and that of subsurface layers in particular, which may be detrimental for their performance.[373,391] Note that despite most of attention being devoted to the application of PdZn alloys as MSR catalysts, they also catalyze water-gas shift[387,392,393] and hydrogenation reactions.[394]

In Section 6.2 films of PdZn on Pd(111) single crystals were investigated both theoretically and experimentally in the presence and in the absence of CO. Some scientists consider it as a "probe" molecule suitable to investigate the intrinsic properties of surfaces. Nevertheless, in Section 6.2 it is shown how adsorbed CO may lead to reconstruction of the surface under investigation and in this way to considerably affect its properties. Density functional calculations were performed on one, two and four monolayer thick PdZn films on Pd(111) substrate with the bulk-like arrangement of atoms in alternating rows of Pd and Zn as well as with an alternative arrangement in zigzags (Figure 6.2). Adsorption of carbon monoxide on each of these structures was

[3] This is in line with charges accumulated on atoms.

simulated at low and high coverage. Also polarization-modulated infrared spectroscopy experiments as well as temperature programmed desorption studies of CO molecules on two and four monolayer thick PdZn films on Pd(111) were performed.

The alternative zigzag arrangement of atoms was calculated to be more energetically stable than the conventional row structure for monolayer thick PdZn surface alloys. The reason for the higher stability is a surface relaxation in the less symmetric zigzag structure, which does not lead to a decreased number of heteroatomic Pd-Zn bonds in the case of monolayer films. In the case of surface saturation by CO molecules the zigzag arrangement of surface atoms becomes more stable than the row arrangement for alloys of any considered thickness. This is because the zigzag structure allows for longer distances between adjacent CO molecules on the surfaces. In turn, the repulsion between adjacent CO molecules at high coverage is reduced.

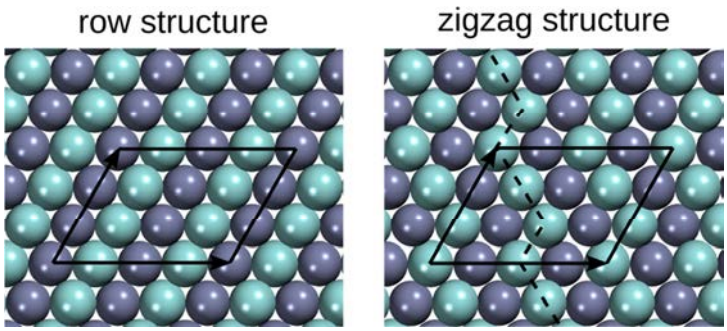

Figure 6.2. Row and zigzag structures of PdZn surface alloy films on Pd(111). Pd is displayed in cyan, zinc – slate blue.

The predicted reconstruction of the surface of PdZn/Pd(111) was corroborated by experimental findings. First, CO was predicted to adsorb on top of Pd atoms exposed by PdZn with zigzag arrangement of surface atoms, whereas bridge sites were preferred for adsorption on the row structure. In turn, the vibrational frequency characteristic for on-top adsorbed CO was detected via IR spectroscopy. Also, due to the decreased repulsion between adjacent CO molecules on the zigzag structure, the saturation coverage on the latter was calculated to be one CO per Pd atom on the surface. In variation, the conventional row structure was saturated when two CO molecules were adsorbed per each three Pd atoms on the surface. In temperature programmed desorption experiments the saturation coverage of one CO per one Pd was measured, again in line with the existence of the reconstructed surface structure.

Thus this study documented a very interesting type of surface reconstruction of PdZn films on Pd(111) induced by the adsorption of CO molecules. In this reconstruction the composition and the geometric structure of the surface remains almost the same. It was the relative order of Pd and Zn atoms that changed from rows to zigzags. Since in fact this reconstruction may be aperiodic, its detection via certain surface science techniques may be very elusive.

Section 6.1

Structure Prediction for Ceria Nanofilms

Sergey M. Kozlov,[#] Ilker Demiroglu,[#] Konstantin M. Neyman,*[#,¶] Stefan T. Bromley*[#,¶]

[#] *Departament de Química Física and Institut de Química Teòrica i Computacional (IQTCUB), Universitat de Barcelona, 08028 Barcelona, Spain*

[¶] *Institució Catalana de Recerca i Estudis Avançats (ICREA), 08010 Barcelona, Spain*

Experimentally, Ce_2O_3 films are used to study cerium oxide in its fully or partially reduced state, as present in many applications. We have employed structure searching and *ab initio* density functional calculations to explore the low energy structures of Ce_2O_3 nanofilms. Our results firstly help to rationalize observations of nanofilms with different bulk crystalline structures (e.g. A-type or bixbyite) depending on the support used. We further predict a novel, as yet experimentally unresolved, nanofilm which has a structure that does not correspond to any previously reported bulk A_2B_3 phase and an energetic stability between that of A-type and bixbyite. To assist identification and fabrication of this new nanofilm we calculate some observable properties and propose supports for its epitaxial growth.

Keywords: Ce_2O_3 nanofilms; epitaxial growth; structure prediction; simulated mechanical annealing; DFT calculations

Cerium oxide (ceria) may gradually change its stoichiometry between CeO_2 and Ce_2O_3 depending on the environment. This makes it a key reducible oxide in numerous technological applications (e.g. gas sensors, fuel cells, catalysis).[1-3] Nanostructuring dramatically affects reducibility of CeO_2, facilitating the formation of O vacancies.[4-6] The latter results in the increased catalytic activity of noble metals supported on CeO_2 and, in particular, on nanostructured CeO_2.1,[7] Since stoichiometric cerium dioxide is present only at oxidizing conditions and/or moderate temperatures, there is a growing interest in (partially) reduced forms of ceria. Recently, ultrathin supported nanoscale films of crystalline stoichiometric cerium sesquioxide Ce_2O_3 have been prepared on various substrates.[8,9] Such nanofilms provide well-defined model systems for studying the reactivity of ceria in extremely reducing conditions8 and have potential applications as high-k transistor gate dielectrics.[9] Curiously, many of these nanofilms do not possess the hexagonal A-type structure, which is generally thought to be the thermodynamically stable bulk Ce_2O_3 polymorph.

Generally, for many oxide materials reduction of their thickness to only a few monolayers has opened up a wealth of new technological opportunities in diverse application areas.[10] In only a few cases, however, are supported oxide nanofilms found to possess well-ordered atomic structures unlike that of the corresponding most stable bulk crystalline phase (e.g. Al_2O_3,[11] SiO_2,[12,13] MgO,[14] ZnO[15]). These nanofilms can be divided into two types: (*i*) non-stoichiometric films (e.g. oxides of Al,[11] Si[12]), where chemical bonds of a noticeable strength form with a strongly interacting support, or (*ii*) stoichiometric films, essentially without chemical bonds with the support (e.g. MgO,[14] ZnO,[15] SiO_2[13]). In all these cases *ab initio* calculations have been indispensable in confirming,[11,12,16] and even predicting[17] the atomic structure of the nanofilms. Although, in a real experimental set-up, oxide nanofilms are almost always grown on a support, computationally, via modelling free-standing sheets, one can enquire into the *inherent* stability of different nanofilm structures independently of a specific support. For known stoichiometric oxide nanofilms, the interactions with the support tend to be weak and the nanofilm structures can be well-described by free-standing sheet models.[16-18] Note that even for nanofilms that weakly interact with the support epitaxial matching between the nanofilm and the support is generally observed. Comparison of free-standing models with experimental data can help to determine to what extent the observed polymorph is the result of: (*i*) intrinsic nanoscale structural/energetic tendencies of the

material or (*ii*) experimental conditions (e.g. epitaxy with a specific support, metastability of obtained structures, etc.).

Herein we use a powerful structure search method and accurate electronic structure calculations to systematically explore the stabilities and structures of a range of free-standing stoichiometric Ce_2O_3 nanofilms in order to understand the experimental observations. Specifically, we address the issue of thermodynamic versus kinetic stability in experimentally prepared Ce_2O_3 nanofilms. Moreover, we predict new low energy Ce_2O_3 nanofilms that may be prepared in the future.

Diminution of inorganic materials to the nanoscale often induces one or more alternative atomic orderings relative to the most stable bulk crystal.[19] In order to test this possibility for reduced ceria we explored the space of stable Ce_2O_3 nanofilm structures with ~1 nm thickness, i.e. containing four monolayers (MLs). Here, we define monolayers based on the number of cerium atoms, i.e. the O-Ce-O-Ce-O unit found in the vertical stacking of atomic layers in A-type Ce_2O_3(001) is counted as 2 ML. We employed the simulated mechanical annealing (SMA) technique[20-22] for searching the space of low energy film structures. Following the experimental observation of structural relaxation via application of mechanical stress (termed mechanical annealing[23]) in submicrometre atomic systems, the SMA method consists of cyclically gradually compressing and stretching the simulated Ce_2O_3 nanofilms laterally (by up to ±30%) in a step-wise fashion. After each application of stress/strain to the nanofilm structure (achieved through systematically varying the cell parameters) all atomic positions are optimised. Upon these optimisations the atomic positions sometimes relaxed to give a new polymorph. We repeatedly applied the SMA stretching and compressing procedure to the Ce_2O_3 nanofilms for every new polymorphic structure found until no further structural changes occurred. To reduce the bias on the choice of initial nanofilm structure, we repeated the above process starting from three distinct archetypal A_2O_3 sesquioxide polymorphs: corundum, A-type, and bixbyite. Due to high computational cost of following this protocol directly with *ab initio* methods we initially performed the SMA search with suitable classical interatomic potentials (IPs)[24-26] using the GULP[27] code. From this search, ten of the resulting lowest energy nanofilm structures were then optimised using density functional theory (DFT) calculations. As detailed below (see also Supporting Information, Figures S1, S2) both the lattice parameters and the relative energies calculated using IPs and DFT schemes correlate with one another very well. This excellent correspondence is in line

with our previous experience in modelling stoichiometric[4,28] and reduced ceria nanoparticles,[26] giving us confidence in using the IPs for our SMA searches.

In all reported periodic DFT calculations for both nanofilm and bulk structures, the unit cell parameters and all atomic positions were locally optimized (forces <0.2 eV nm^{-1}) with the PW91[29] form of the generalized gradient approximation (GGA) functional using the VASP code.[30] An onsite Coulombic correction (U_{eff} = U – J)[31,32] was applied to obtain a localized description of Ce 4f-electrons, resulting in a GGA+U corrected functional. Following previous studies,[4,5] a U_{eff} value of 4 eV was used. The suggestion that a LDA+U description of the relative stabilities of Ce_2O_3 polymorphs may provide a better match to experiment than a GGA+U approach[33] is briefly discussed below. The projector augmented wave approach[34,35] was used to describe the effect of core electrons on valence states, with the latter represented by a plane wave basis with a 600 eV cut-off. Nanofilms were separated by over 1 nm in the *c*-stacking direction to avoid spurious periodic interactions. Reciprocal space *k*-point sampling was achieved through appropriate Monkhorst-Pack grids[36] (see Table 1). Tests showed that all nanofilm energies were converged to <0.5 kJ mol^{-1} per Ce_2O_3 with respect to *k*-point sets and completeness of the plane wave basis.

Bulk calculations. The hexagonal A-type phase is generally thought to be the most thermodynamically stable bulk phase of Ce_2O_3.[37] Our GGA+U calculations, however, predict the A-type structure to be higher in energy than the cubic bixbyite structure (E_{rel} = 19.9 kJ mol^{-1} per Ce_2O_3, see Table 1). Using a similar calculation set-up, an apparent improvement in the treatment of reduced ceria via the use of an LDA+U approach with respect to GGA+U one has been noted previously.[33] Our DFT calculations using the Local Density Approximation with a Hubbard U correction (LDA+U, with U = 6 eV) bring the energies of the two phases closer whereby the A-type phase becomes only 0.5 kJ mol^{-1} per Ce_2O_3 less stable than bixbyite. We note that the lower relative energetic stability of bixbyite in ref 33 can be probably ascribed to the known problem of the presence of many meta-stable self-consistent electronic solutions to Kohn-Sham equations for reduced cerium oxide. These solutions differ by the shape and symmetry of occupied *f*-orbitals of Ce^{3+} cations, which may be sub-optimal in the electrostatic Madelung potential of the crystal.[38] We found that, for bixbyite especially, occupied *f*-orbitals would often converge to be f_{z^3}-like, instead of more stable f_{xyz}-like ones, significantly affecting the calculated total energy of the system.[39] In general, due to their more refined account of electron density variations, GGA functionals

have proven to be superior to LDA functionals for calculating the relative stability of different oxide polymorphs when the coordination environment of the constituent atoms varies (e.g. SiO_2,[40] HfO_2[41]). Specifically, GGA functionals help to correct the tendency of LDA functionals to overstabilise polymorphic structures that have more bonds per atom. In the present study when going from bixbyite to A-type, the average bonding coordination environment of Ce increases from six to seven; this may rationalize the increased relative stabilization of A-type in LDA+U calculations with respect to GGA+U treatments. The advantage of a GGA-based approach over LDA is expected to be more pronounced for structures with less homogeneous electron densities, in situations where bonds are being stretched, or for terminated structures.

Table 1. In-plane film lattice parameter (a_0 in pm), relative energies (E_{rel}, with respect to bixbyite, per Ce_2O_3 unit, in kJ mol^{-1}), Monkhorst-Pack *k*-point mesh, and thicknesses (in pm) of optimised Ce_2O_3 bulk polymorphs and nanofilms from GGA+U calculations.

System	a_0	a_0 per unit	E_{rel}	*k*-points	Thickness
Bulk					
A type	391[a]	391	19.9	5×5×5	∞
bixbyite	1130	399	0	3×3×3	∞
Film					
A type	384	384	11.1	3×3×1	1081
bixbyite	1587	397	0	1×1×1	1186
NF1	713×707[b]	~410	5.5	5×5×1	1129
NF2	1364	394	20.8	3×3×1	1147
NF3	1383×1379[b]	~399	26.2	3×3×1	1150
NF4	1407	406	22.2	3×3×1	1118

[a] The experimental value is 389 pm.[37]

[b] Two lattice parameters are given for films with distorted hexagonal structure.

Although in the case of the relative bulk energetics of bixbyite versus A-type polymorphs, GGA+U appears to overcompensate the failings of LDA+U, in principle GGA+U should provide an improved description of Ce_2O_3 systems. One way to assess this assertion is to compare the GGA+U results with those from computationally intensive calculations employing hybrid functionals; the current DFT benchmark standard for periodic systems like ceria.3 Using the hybrid HSE06 functional[42] we find bixbyite to be more stable

than A-type by 25 kJ mol^{-1} per Ce_2O_3 unit, confirming the energetic ordering calculated using GGA+U approach.

Considering the above mentioned arguments, in this work where we report the calculated properties of strained surface-terminated nanostructures, which possess novel polymorphic structures with variable bonding coordination, we preferred GGA+U over LDA+U.

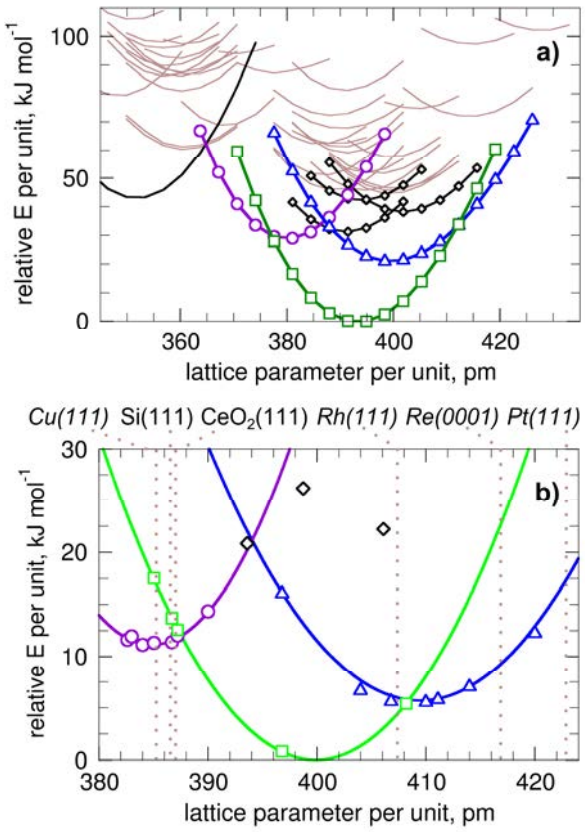

Figure 1. Results of a) the IP-based SMA search, and b) GGA+U calculations for films with: A-type (circles), bixbyite (squares) and NF1 (triangles), NF2-4 (diamonds), corundum (black, no symbol) and other structures (brown, no symbol). Energies (relative to that of the optimized bixbyite nanofilm) and lattice parameters are given per Ce_2O_3 unit. Solid lines in b) are parabolic fits to the data points to guide the eye. Vertical dotted lines in b) indicate GGA-calculated lattice parameters of possible supports for nanofilm growth (multiplied by 3/2 for transition metals).

Nanofilm calculations. The strain versus total energy curves resulting from the SMA searches for low energy Ce_2O_3 four ML nanofilms using IPs are shown in Fig. 1a. These searches revealed more than 30 distinct nanofilm structures of which ten with the lowest

energy were further optimized using DFT calculations. Results for six of them, A-type, bixbyite and nanofilms 1 to 4 (NF1-NF4), as well as for A-type and bixbyite bulks are presented in Table 1. Bixbyite, as a four ML nanofilm, is still predicted by our GGA+U calculation to be more stable than the corresponding A-type nanofilm. However, its stability with respect to A-type decreases to 11.1 kJ mol^{-1} from 19.9 kJ mol^{-1} per Ce_2O_3 in the bulk. This reduction in polymorphic energy differences when going from bulk to nanofilm appears to be a general phenomenon that has been predicted to occur for a number of materials.[43] The new nanofilms NF1-NF4 found in our SMA searches all have energies slightly higher than the bixbyite nanofilm by 5.5 – 26.2 kJ mol^{-1} per Ce_2O_3. It is of note that the four nanofilms, NF1-NF4, have structures which do not correspond to any known bulk crystalline A_2O_3 polymorph. The 4 ML NF1 nanofilm is particularly interesting as it is the only new film that is predicted to be more energetically stable than the A-type 4 ML nanofilm. We note that this prediction in also confirmed by our calculations using the hybrid HSE06 functional. In Figure 2 we show the structures of the NF1, bixbyite and A-type 4 ML nanofilms. For these three nanofilms we have performed GGA+U calculations under externally applied stress or strain (within the plane of each nanofilm) and generated three characteristic curves of relative energy *versus* the in-plane *a* lattice parameter per Ce_2O_3 unit (see Figure 1b). The shapes and relative positions of the three curves in Figure 1b match quite well with the corresponding IP-based curves (see highlighted curves in Figure 1a). Although the DFT-calculated energetic ordering of the nanofilms is generally well reproduced by the IP calculations, the latter results span a twice larger energy range. This finding is fully in line with a combined IP and GGA+U study of partially reduced ceria nanoclusters.[26] We note that according to the IP data bixbyite films are more stable than A-type and NF1 films even at their points of minimum energy. For the DFT calculations, however, the NF1 and A-type energy minima lay outside of the energy *versus* strain curve of bixbyite. This finding suggests that by using substrates with different lattice parameters one could favour the epitaxial growth of a particular nanofilm structure.

Experimentally, a few Ce_2O_3 nanofilm structures have already been produced on different substrates. In Figure 1b we include the in-plane lattice parameters of a selection of surfaces that have been employed to grow supported Ce_2O_3 nanofilms, as calculated using GGA-based DFT. For the Cu(111) surface, 2.5 ML fluorite CeO_2(111) nanofilms were grown with a 2:3 epitaxy. Upon heating to 1070 K these nanofilms could be transformed into Ce_2O_3 nanofilms with the A-type structure while retaining a very similar epitaxial matching.[44] From

a thermodynamical perspective, such a transition is in agreement with our calculations (Figure 1b) where the Cu(111) surface and A-type films have closely matching lattice parameters (after multiplying the lattice parameter of the A-type film by 3/2). Using metallic Ce as a reducing agent, and annealing under slightly milder thermal conditions (900 K), similar Cu(111)-supported 4 ML CeO_2 films could be reduced to Ce_2O_3 nanofilms exhibiting the bixbyite structure.[9] Here, assuming no structural relaxation of the Cu(111) surface and perfect 3:2 epitaxy, we predict that a suitably contracted free-standing 4 ML bixbyite nanofilm would be moderately metastable (+6 kJ mol^{-1} per Ce_2O_3) relative to an A-type nanofilm with the same lattice parameter (see Figure 1b). We thus suggest that the observation of bixbyite films grown at relatively moderate temperature on Cu(111) does not necessarily require their preferential energetic stability on the support. Rather, it can be due to kinetics whereby the preparation retains much of the original fluorite structure of the CeO_2 precursor. Bixbyite Ce_2O_3 nanofilms of 2-5 ML have also been grown on Cl-passivated Si(111) surfaces by Flege et al.[8] For such a situation we predict an even smaller metastability of 4 ML bixbyite films (+2 kJ mol^{-1} per Ce_2O_3) with respect to A-type. This very small calculated energy difference points again to kinetic stabilization of these experimentally observed bixbyite nanofilms. For the significantly larger lattice parameter of Rh(111), supported CeO_2 nanofilms with 1-6 ML thicknesses have been shown to decompose at temperatures 700-800 °C to give a reduced ceria islands and a (4×4) Low-Energy Electron Diffraction (LEED) pattern.[45] Although in ref 45 this LEED pattern is ascribed to Ce-Rh alloy formation, with hindsight, another interpretation of such a measurement may be the emergence of the bixbyite structure. In Figure 1b we see that such an interpretation is consistent with the calculated small energetic preference for 3:2 epitaxial 4 ML bixbyite nanofilms on Rh(111).

Although we are aware of no reports directly identifying our predicted NF1 nanofilm we can see from Figure 1b that supports with a larger lattice parameter than those cited above for ultrathin films would be required to produce NF1. For instance, Re(0001) or Pt(111) with calculated a_0 of 278 and 282 pm, respectively. In fact, reduced ceria films have been prepared on Re(0001),[46] but, as far as we are aware, only with relatively large thicknesses (>20 ML) of limited relevance to the present study. On the Pt(111) surface, reduction of 1-2 ML CeO_2 nanofilms with 4:3 epitaxy has led to novel nanofilms with, as yet, undetermined structures.[47,48] Assuming a 3:2 epitaxy, our calculations indicate that the Pt(111) surface should thermodynamically favour the formation of the 4 ML NF1 nanofilm relative to

bixbyite and A-type. In ref. 47 a strongly reduced 2 ML CeO_2 nanofilm is found to exhibit an unresolved structure with a 9/4($\sqrt{3}\times\sqrt{3}$)R30° periodicity (with respect to Pt) which is consistent with that of NF1 (see Figure 2). Similarly to the structure of NF1, the 1 ML Ce_2O_3 nanofilm reported in ref. 48 has a hexagonal unit cell with a lattice constant that is approximately twice that of A-type (see Table 1). Additionally, scanning tunneling microscopy of this latter nanofilm shows protruding add-atoms at three-fold coordinated sites covering. This observation is in line with the curious structure of NF1, which displays protruding oxygen atoms at three-fold coordinated sites, albeit with a higher density than that observed in experiment. The finding that the adatoms in the experimentally prepared 1 ML nanofilm are disordered whereas those in NF1 are ordered may be a reflection of experimental conditions (e.g. finite temperatures, 1 ML versus 4ML) or again kinetic limitations.

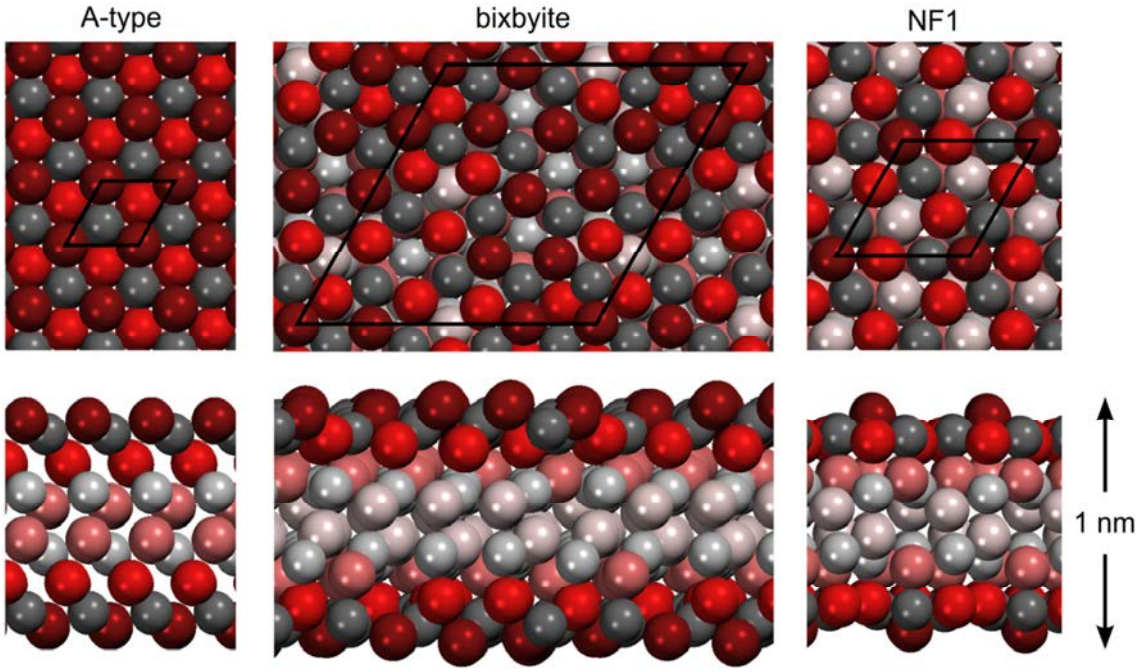

Figure 2. Top and side views of A-type, bixbyite and NF1 Ce_2O_3 nanofilms of 4 ML thickness. O atoms are displayed as red spheres and Ce^{3+} ions as grey spheres. Atoms with darker colors are located in surface layers. Employed unit cells are denoted by black lines.

In order to encourage further experimental work to better characterize such reduced ceria nanofilms, in Table 2 we present some calculated properties of NF1 to help distinguish it from A-type and bixbyite nanofilms. Firstly, in line with its relatively larger in-plane lattice parameter, both the Ce and O atoms in the NF1 nanofilm have lower average coordination

numbers than in A-type and bixbyite nanofilms. With respect to conductivity, GGA+U band gaps (O2p – Ce4f+5d) are rather similar, ~3.9 eV, in the considered bulk structures and A-type film. However, in bixbyite and NF1 films these band gaps are reduced to ~2.7 eV, which could be explained by the presence of five-coordinated Ce ions. In fact, under-coordinated Ce ions were already shown to reduce the band gap in CeO_2 nanoparticles and concomitantly greatly increase their reducibility.[49] As these properties are amenable to measurement (e.g. via EXAFS, PES), we hope that our predicted new NF1 nanofilm will be indentified in future experimental studies.

Table 2. Calculated GGA+U energy gap values Δε (in eV) between the highest occupied (HO) and the lowest unoccupied (LU) states of Ce and O and average coordination numbers of Ce, N(Ce), in bulk and 4 ML nanofilm structures.[a]

System	$\Delta\varepsilon(HO_{Ce}\text{-}HO_O)$	$\Delta\varepsilon(HO_{Ce}\text{-}LU_O)$	$\Delta\varepsilon(HO_O\text{-}LU_{Ce})$	N(Ce)[b]
A-type bulk	1.4	2.0	3.9	7.00
bixbyite bulk	1.8	1.7	3.8	6.00
A-type film	1.4	2.3	4.1	6.50
bixbyite film	1.1	0.8	2.7	5.63
NF1 film	1.4	1.0	2.7	5.50

[a] Note that the presented GGA+U absolute band gap values $\Delta\varepsilon(HO_O\text{-}LU_{Ce})$ are expected to be notably underestimated with respect to both those from hybrid-functional DFT calculations and experimental data.3

[b] Average coordination numbers of O are 1.5 times smaller than N(Ce).

To summarise, using simulated mechanical annealing searches and density functional calculations we identify a range of new low energy 4 ML Ce_2O_3 nanofilm structures. We find that our calculations of energetic stability versus in-plane lattice parameter are consistent with stability of experimentally observed nanofilm phases depending on the substrates used to prepare them. Further, we propose a new energetically stable NF1 film structure and suggest suitable substrates that would favor its growth. Note that there are indications that an NF1-like reduced ceria film may have been observed on Pt(111) surfaces. Finally, we present specific calculated properties of the NF1 nanofilm that should assist in its experimental identification.

ACKNOWLEDGMENTS

SMK thanks the Spanish MEDU for FPU grant AP2009-3379. This study has been supported by grants of the Spanish Ministry of Economy and Competitiveness (CTQ2012-34969; MAT2012-30924), the European Union FP7 Program under grant agreement number 310191, the Generalitat de Catalunya (2014SGR97; XRQTC) and by the COST Action CM1104. We also acknowledge use of supercomputing resources provided by the Red Española de Supercomputación.

References

(1) Sun, C; Li, H.; Chen, A. *Energy Environ. Sci*. **2012**, *5*, 8475–8505.

(2) Catalysis by Ceria and Related Materials. Trovarelli, A.; Fornasiero, P. (Eds.), 2nd Ed., Imperial College Press, London, 2013.

(3) Paier, J.; Penschke, C.; Sauer, J. *Chem. Rev*. **2013**, *113*, 3949–3985.

(4) Migani, A.; Vayssilov, G. N.; Bromley, S. T.; Illas, F.; Neyman, K. M. *Chem. Commun*. **2010**, *46*, 5936–5938.

(5) Migani, A.; Vayssilov, G. N.; Bromley, S. T.; Illas, F.; Neyman, K. M. *J. Mater. Chem*. **2010**, *20*, 10535–10546.

(6) Kozlov, S. M.; Neyman, K. M. *Phys. Chem. Chem. Phys*. **2014**, *16*, 7823–7829.

(7) Carrettin, S.; Concepción, P.; Corma, A.; López Nieto, J. M.; Puntes, V. F. *Angew. Chem. Int. Ed*. **2004**, *43*, 2538–2540.

(8) Flege, J. I.; Kaemena, B.; Gevers, S.; Bertram, F.; Wilkens, T.; Bruns, D.; Bätjer, J.; Schmidt, T.; Wollschläger, J.; Falta, J. *Phys. Rev. B* **2011**, *84*, 235418.

(9) Stetsovych, V.; Pagliuca, F.; Dvořák, F.; Duchoň, T.; Vorokhta, M.; Aulická, M.; Lachnitt, J.; Schernich, S.; Matolínová, I.; Veltruská, K.; Skála, T.; Mazur, D.; Mysliveček, J.; Libuda, J.; Matolín, V. *J. Phys. Chem. Lett*. **2013**, *4*, 866–871.

(10) Oxide Ultrathin Films: Science and Technology, Pacchioni, G.; Valeri, S. (Eds.), Wiley-VCH, Weinheim, 2011.

(11) Kresse, G.; Schmid, M.; Napetschnig, E.; Shishkin, M.; Köhler, L.; Varga, P. *Science* **2005**, 308, 1440–1442.

(12) Weissenrieder, J.; Kaya, S.; Lu, J.-L.; Gao, H.-J.; Shaikhutdinov, S.; Freund, H.-J.; Sierka, M.; Todorova, T. K.; Sauer, J. *Phys. Rev. Lett*. **2005**, *95*, 076103.

(13) Löffler, D.; Uhlrich, J. J.; Baron, M.; Yang, B.; Yu, X.; Lichtenstein, L.; Heinke, L.; Büchner, C.; Heyde, M.; Shaikhutdinov, S.; Freund, H.-J.; Włodarczyk, R.; Sierka, M.; Sauer, J. *Phys. Rev. Lett*. **2010**, *105*, 146104.

(14) Kiguchi, M.; Entani, S.; Saiki, K.; Goto, T.; Koma, A. *Phys. Rev. B* **2003**, *68*, 115402.

(15) Tusche, C.; Mayerheim, H. L.; Kirschner, J. *Phys. Rev. Lett*. **2007**, *99*, 026102.

(16) Goniakowski, J.; Noguera, C.; Giordano, L. *Phys. Rev. Lett*. **2004**, *93*, 215702.

(17) Freeman, C. L.; Claeyssens, F.; Allan, N. L.; Harding, J. H. *Phys. Rev. Lett*. **2006**, *96*, 066102.

(18) Tosoni, S.; Civalleri, B.; Ugliengo, P. *J. Phys. Chem. C* **2010**, *114*, 19984–19992.

(19) Navrotsky, A. *Proc. Nat. Acad. Sci*. **2004**, *101*, 12096–12101.

(20) Sangthong, W.; Limtrakul, J.; Illas, F.; Bromley, S. T. *Nanoscale* **2010**, *2*, 72–77.
(21) Krainara, N.; Limtrakul, J.; Illas, F.; Bromley, S. T. *Phys. Rev. B* **2011**, *83*, 233305.
(22) Krainara, N.; Limtrakul, J.; Illas, F.; Bromley, S. T. *J. Phys. Chem. C* **2013**, *117*, 22908–22914.
(23) Shan, Z. W.; Mishra, R. K.; Syed Asif, S. A.; Warren, O. L.; Minor, A. M. *Nature Mater*. **2007**, *7*, 115–119.
(24) Sayle, T. X. T.; Parker, S. C.; Catlow, C. R. A. *J. Chem. Soc., Chem. Commun*. **1992**, 977–978.
(25) Conesa, J. C. *Surf. Sci*. **1995**, *339*, 337–352.
(26) Migani, A.; Neyman, K. M.; Illas, F.; Bromley, S. T. *J. Chem. Phys*. **2009**, *131*, 064701.
(27) Gale, J. D. *Z. Krist.* **2005**, *220*, 552–554.
(28) Migani, A.; Neyman, K. M.; Bromley, S. T. *Chem. Commun*. **2012**, *48*, 4199–4201.
(29) Perdew, J. P.; Wang, Y. *Phys. Rev. B* **1992**, *45*, 13244–13249.
(30) Kresse, G.; Hafner, J. *Phys. Rev. B* **1993**, *47*, 558–561.
(31) Anisimov, V. I.; Aryasetiawan, F.; Lichtenstein, A. I. *J. Phys.: Condens. Matter* **1997**, *9*, 767–808.
(32) Dudarev, S. L.; Botton, G. A.; Savrasov, S. Y.; Humphreys, C. J.; Sutton, A. P. *Phys. Rev. B* **1998**, *57*, 1505–1509.
(33) Da Silva, J. L. F. *Phys. Rev. B* **2007**, *76*, 193108.
(34) Blöchl, P. E. *Phys. Rev. B* **1994**, 50, 17953–17979.
(35) Kresse, G.; Joubert, D. *Phys. Rev. B* **1999**, *59*, 1758–1775.
(36) Monkhorst, H. J.; Pack, J. D. *Phys. Rev. B* **1976**, *13*, 5188–5192.
(37) Bärnighausen, H.; Schiller, G. *J. Less-Common Met*. 1985, 110, 385–390.
(38) Jiang, H.; Rinke, P.; Scheffler, M. *Phys. Rev. B* **2012**, *86*, 125115.
(39) As an example, we note that the energy associated with improper *f*-orbital symmetry can be up to ~0.5 eV per Ce_2O_3, when the symmetry of all orbitals in the cell are erroneous.
(40) Hamann, D. R. *Phys. Rev. B* **1996**, *76*, 660–663.
(41) Kang, J.; Lee, E.-C.; Chang, K. J. *Phys. Rev. B* **2003**, *68*, 054106.
(42) Heyd, J.; Scuseria, G. E.; Ernzerhof, M. *J. Chem. Phys*. **2003**, *118*, 8207–8215.
(43) Demiroglu, I.; Bromley, S. T. *Phys. Rev. Lett*. **2013**, *110*, 245501.
(44) Matolín, V.; Libra, J.; Matolínová, I.; Nehasil, V.; Sedláček, L.; Šutara, F. *Appl. Surf. Sci.* **2007**, *254*, 153–155.

(45) Eck, S.; Castellarin, C.; Surnev, S.; Ramsey, M. G.; Netzer, F. P. *Surf. Sci*. **2002**, *520*, 173–185.

(46) Xiao, W.; Guo, Q.; Wang, E. G. *Chem. Phys. Lett*. **2003**, *368*, 527–531.

(47) Luches, P.; Pagliuca, F.; Valeri, S. *Phys. Chem. Chem. Phys*. **2014**, *16*, 18848–18857.

(48) Berner, U.; Schierbaum, K.-D. *Phys. Rev. B* **2002**, *65*, 235404.

(49) Sk, M. A.; Kozlov, S. M.; Lim, K. H.; Migani, A.; Neyman, K. M. *J. Mater. Chem. A* **2014**, *2*, 18329–18338.

Section 6.2

THE JOURNAL OF PHYSICAL CHEMISTRY C

Article

pubs.acs.org/JPCC

Geometric Arrangement of Components in Bimetallic PdZn/Pd(111) Surfaces Modified by CO Adsorption: A Combined Study by Density Functional Calculations, Polarization-Modulated Infrared Reflection Absorption Spectroscopy, and Temperature-Programmed Desorption

Christian Weilach,*[,†] Sergey M. Kozlov,[‡] Harald H. Holzapfel,[†] Karin Föttinger,[†] Konstantin M. Neyman,*[,‡,§] and Günther Rupprechter[†]

[†]Institute of Materials Chemistry, Vienna University of Technology, Getreidemarkt 9/BC, 1060 Vienna, Austria

[‡]Departament de Química Física and Institut de Química Teòrica i Computacional, Universitat de Barcelona, Martí i Franquès, 1, 08028 Barcelona, Spain

[§]Institució Catalana de Recerca i Estudis Avançats, 08010 Barcelona, Spain

ABSTRACT: Combining density functional theory (DFT) calculations with experimental data from temperature-programmed desorption (TPD) and polarization-modulated infrared reflection absorption spectroscopy (PM-IRAS), we have provided evidence for the rearrangement of Pd and Zn atoms in PdZn surface alloys on Pd(111) in the presence of CO. Such systems represent valuable models for novel methanol steam reforming catalysts, with CO being an undesired byproduct of this reaction. The reconstructed surface was calculated to be more stable in the presence of CO and capable of adsorbing CO on top of Pd atoms up to a saturation coverage of $^1/_2$ monolayer (ML). To the contrary, on a surface with conventional, bulklike geometric arrangement of Pd and Zn atoms in rows, CO adsorption on bridge sites with a saturation coverage of $\sim^1/_3$ ML was predicted. Adsorption of CO on top sites was confirmed with PM-IRAS and the saturation coverage of $^1/_2$ ML was derived from TPD experiments, supporting the suggested reconstruction of PdZn/Pd(111). The rearrangement of the atomic components on the surface was calculated to affect structural and adsorptive properties but kept essentially unchanged the electronic structure, reflecting the intermetallic character of PdZn on Pd(111). This study sheds light on a new degree of complexity of bimetallic systems, that is, changes of component arrangement on the surface in the presence of certain adsorbates, which is not accompanied by surface segregation. Such rearrangement is expected to notably affect the properties of a bimetallic catalyst.

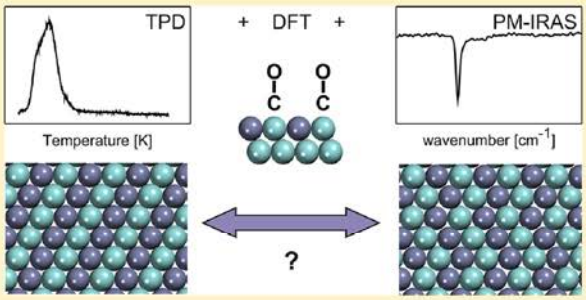

1. INTRODUCTION

Structure and reactivity of a catalyst are well-known to change in the presence of certain adsorbates.[1−4] However, this phenomenon seldom becomes a subject of thorough investigation,[5,6] and often even very chemically potent adsorbates are regarded just as spectator species.[7,8] Nevertheless, experiments suggest that reconstruction of bimetallic Co/Re/γAl_2O_3[9] and LaNi[10] catalysts may occur even in the presence of CO, a common probe molecule, which should not modify the properties of the investigated surface. Thus, especially on bi- or multimetallic alloys, the validity of the spectator species "approximation" should be reassessed.

The reason for these complications is the structural complexity of the alloys, which yields additional degrees of freedom sensitive to the environment, such as surface segregation and geometric arrangement of metal components on the surface. The former process, segregation, is related to changes in the amount of one or the other component on the surface. It recently attracted a lot of attention[11−18] and in certain cases was shown to be promoted or hindered by certain adsorbates.[4,6,19−21] At the same time, component or elemental arrangement, which is related to the change in relative order of components without changing the relative amount of each element on the surface, was neither sufficiently studied experimentally[22,23] nor theoretically.[24−26] However, it will be illustrated in this work that elemental arrangement is as important for catalytic properties of a surface as segregation.[23] Indeed, the arrangement affects (1) elemental composition of adsorption sites present on the surface, (2) distances between atoms in the surface, (3) surface corrugation, and (4) relative stability of an adsorbate on various sites and its saturation coverage. It is shown in the present study that the magnitude

Received: May 10, 2012
Revised: July 17, 2012
Published: August 28, 2012

and importance of the induced changes are significantly amplified by high coverage of an adsorbate. The scarcity of the available studies on the arrangement of elements on a bimetallic surface may be partially attributed to its possible aperiodicity, which makes very difficult to draw definitive conclusions from studies by certain surface science and high-level theoretical techniques essentially limited to periodic systems. However, the combination of experimental and theoretical efforts has proven to be useful to treat this problem.[25]

In the present work, we study the surface reconstruction in the form of elemental rearrangement in thin films of PdZn alloys grown on Pd(111), induced by CO adsorption. Modification of the elemental arrangement and resulting surface reconstruction are suggested by density functional theory (DFT) calculations and corroborated by temperature-programmed desorption (TPD) and polarization-modulated infrared reflection absorption spectroscopy (PM-IRAS) experiments on well-defined model 1:1 PdZn/Pd(111) surface alloys. To the best of our knowledge, modification of elemental arrangement in the presence of adsorbates and its influence on adsorptive properties have not been reported before.

The considered system, PdZn surface alloys grown on Pd(111), has been recently intensively studied,[27−35] because it is envisaged as a possible replacement for presently industrially used pyrophoric[36] and prone to sintering[37] Cu/ZnO catalysts[38] for methanol steam reforming (MSR), $CH_3OH + H_2O \rightarrow CO_2 + 3H_2$.[39,40] This reaction is crucial for future environmentally friendly hydrogen-based energy technologies, because it allows on-board generation of hydrogen from a (bio)renewable source. However, to be used in energy production, MSR has to be performed with high selectivity to avoid CO formation, which is a poison for Pt electrodes in polymer electrolyte membrane fuel cells.[41] In contrast to presently used Cu/ZnO, PdZn-based MSR catalysts are stable at elevated operation temperatures, and unlike pure Pd they exhibit good conversion and high selectivity toward CO_2 and hydrogen in MSR.[42−46] However, after detailed analysis of model studies using PdZn surface alloys, the selectivity was found to depend critically on preparation conditions and, in particular, on elemental composition of subsurface layers and alloy thickness.[31] Thus, we focused our attention only on the stoichiometric PdZn alloys, which are known to have good catalytic properties. Moreover, PdZn-based catalysts prepared by Pd deposition on ZnO were recently shown to be very selective in semi-hydrogenation of alkynes.[47]

In ultrahigh vacuum (UHV) conditions, surface alloys of PdZn have been produced either by evaporation of both Pd and Zn onto a Ru(001) single crystal[48] or by Zn deposition on a Pd(111) substrate. The latter approach is more commonly used, and surface alloys prepared by this method were characterized by means of ultraviolet photoelectron spectroscopy (UPS),[27] low-energy electron diffraction (LEED),[27,49] scanning tunneling microscopy (STM)[34,50] and low-energy ion scattering (LEIS).[33,51,52] The active phase of the catalyst was found to be PdZn surface alloy of 1:1 stoichiometry with a p(2 × 1) surface periodicity,[27,34,49] that is, Pd and Zn atoms aligned in rows. However, a bigger surface cell of 16.52 Å × 6.35 Å was suggested in some LEED experiments and was attributed to surface reconstruction at high temperature and specific preparation conditions.[49] LEIS studies showed that a surface of multilayer PdZn is buckled with Zn atoms on the surface being located approximately 25 pm above surface Pd atoms, while PdZn monolayers on Pd(111) are suggested to be flat or with opposite Pd-out/Zn-in corrugation.[33,34,51,53] The density of states (DOS) of PdZn surface alloys near Fermi level was found to be closer to DOS of Cu(111) than to that of Pd(111) surface[27,53] (in agreement with the PdZn catalytic activity reminiscent of that of Cu).

Studies of PdZn surface alloys with DFT methods corroborated the geometrical and electronic structure of PdZn surface[34,53] and its stability with respect to possible segregation of Zn or Pd.[54] Detailed theoretical investigations of various adsorbed molecules[55] and intermediates[56] relevant to MSR as well as relevant elementary steps[57−64] have been undertaken at low or moderate coverage of the adsorbates on PdZn/Pd(111) with various content of Zn. In addition, recent studies of bulk PdZn suggest that it has intermetallic nature with significant calculated charges on atoms ($Pd^{-0.4}Zn^{+0.4}$).[65]

The issue of atomic arrangement on the surface of PdZn/Pd(111) in the absence of adsorbates has been recently studied with the help of finite temperature Monte Carlo simulations, based on DFT-derived nearest-neighbor interaction energy.[26] These studies suggested that surface reconstruction occurs already at 400 K due to an entropic factor, even if multibody interactions and pair interactions with atoms from farther coordination spheres are not included into the simulation. In the present study, however, we perform DFT calculations at 0 K and the modified elemental arrangement is suggested on the basis of its energetic stability and comparison with experimental results.

The structure of the PdZn/Pd(111) alloy in the presence of CO and other gases has not been extensively studied. However, recent studies[31−33] reveal that the presence of CO shifts the onset of the alloy formation temperature by 75 K to higher T, suggesting a complex nature of the interaction between CO and the substrate.

2. EXPERIMENTAL DETAILS

All experiments described below were carried out in an UHV chamber with a base pressure of 5×10^{-10} mbar. The system is equipped with a Specs ERLEED 150 and a Specs X-ray photoelectron spectroscopy (XPS) system consisting of a nonmonochromatic Al/Mg dual anode and a Phoibos EA 150 hemispherical analyzer. TPD spectra were collected by a differentially pumped MKS eVision+ quadrupole mass spectrometer, and temperature ramping was performed by a Eurotherm 3208 PID controller. Unwanted contributions of residual gases and molecules desorbing from the sample holder were minimized by placing a nozzle in front of the single crystal (~1 mm distance).

For PM-IRAS, a UHV-compatible high-pressure cell coupled to the UHV system has been used.[66] The IR spectra were acquired on a Bruker IFS66v/S spectrometer, and polarization modulation was performed by a Hinds-PEM-90 ZnSe photoelastic modulator. Based on the accurate subtraction of gas-phase contributions, PM-IRAS provides surface vibrational spectra of adsorbed species and can be applied from UHV to ambient pressure.[66−72]

To clean the Pd(111) substrate, the Pd single crystal was sputtered in 5×10^{-6} mbar Ar at 1 kV for 45 min at 300 K, followed by annealing for 15 min at 1200 K. The sample was then cooled in 5×10^{-7} mbar O_2 to 650 K to remove residual carbon. Finally, the single crystal was flashed to 1200 K in UHV. Sample cleanliness was checked by XPS and LEED.

PdZn surface alloys were prepared by physical vapor deposition of Zn (high-purity Zn wire, 99.98%, GoodFellow) out of a Ta crucible mounted in an Omicron ebeam evaporator. The deposited amount of Zn was calibrated by use of a quartz microbalance with the Zn flux during evaporation being additionally controlled via an internal flux monitor. In this respect, one monolayer (ML) is always referred to 1.53×10^{15} atoms/cm^2, that is, the value of a close-packed (111) crystal plane in bulk Pd. It has been shown by Kratzer et al.[35] that when a quartz microbalance is used to calibrate the amount of Zn deposited, great care has to be taken due to the lowered sticking coefficient of Zn on the contaminated surface of the quartz crystal. To overcome this problem we have deposited several ML of Zn on the quartz surface immediately before actual flux calibration.

Upon annealing of the deposited Zn layers, a well-ordered LEED pattern was obtained under UHV, suggesting the coexistence of three rotational domains of a (2×1) structure consisting of alternating rows of Pd and Zn atoms, in agreement with recent STM studies.[34,35] In general, deposition of 1 ML Zn results in the formation of two layers of a PdZn 1:1 surface alloy. However, for submonolayer amounts of Zn, bilayer growth of the surface alloy was observed by STM[34] in agreement with simulations.[26] Thus, 0.5 ML Zn deposition resulted in the formation of two-monolayer-high islands of PdZn layers, rather than one complete PdZn layer covering the whole Pd substrate. To ensure the formation of complete alloy surface layers, we have experimentally studied model systems after deposition of 1 ML Zn (=2 ML PdZn) and 3 ML Zn (>4 ML PdZn).

3. COMPUTATIONAL DETAILS

Spin-restricted periodic DFT calculations were performed with the VASP[73] package with a revised Perdew–Burke–Ernzerhof (RPBE)[74] exchange–correlation functional, which yields adsorption energies for CO on Pd[75−77] close to the experimental values.[78] Plane-wave basis set with cutoff energy of 415 eV was used to calculate eigenstates of valence electrons; core electrons were modeled with projector augmented wave (PAW) technique.[79] The first Brillouin zone was sampled by Monkhorst–Pack $3 \times 3 \times 1$ mesh of k-points,[80] and the Methfessel–Paxton smearing[81] of 0.1 eV was applied to Kohn–Sham eigenstates during geometry optimization. The total energies, however, were extrapolated to 0 smearing. DOS were calculated by use of a denser $5 \times 7 \times 1$ k-points mesh and the smearing of 0.3 eV.

PdZn surface alloys on Pd(111) were modeled by a six-layer-thick p(4×3) supercell, which allowed us to consider CO coverage as low as $^1/_{12}$ ML. Depending on the thickness of surface alloy under consideration, the top four layers of the slab consisted of either stoichiometric PdZn alloy or pure Pd and were relaxed (together with adsorbed CO molecules). The two bottom layers of the slab consisted only of Pd atoms and were fixed at bulk-derived positions with the experimental interatomic Pd–Pd distance of 275 pm. Geometry optimization was performed until all forces acting on atoms became less than 0.1 eV·nm^{-1}.

Average adsorption energies of CO at the coverage $\theta = N/12$ ML, where N is the number of CO molecules present in the supercell, were calculated from the total energies E of systems X, E[X], in the following way:

$$E_{ads}(\theta) = \{E[\mathrm{PdZn/Pd}] + NE[\mathrm{CO_{gas}}] - E[(\mathrm{CO})_N/\mathrm{PdZn/Pd}]\}/N$$

according to which positive values of E_{ads} mean stabilization. Harmonic vibrational frequencies were calculated by displacing C and O atoms by 2 pm in all three Cartesian directions. Estimated contributions of harmonic vibrations to adsorption energy are 0.06 eV per CO molecule at 0 K (zero point energy corrections) and only 0.014 eV per CO molecule at 200 K. Because of their rather small magnitude, these corrections are not included into consideration. The calculated harmonic vibrational frequency of a gas-phase CO molecule, 2120 cm^{-1}, underestimates experimental harmonic frequency of CO stretching by 50 cm^{-1} and is by 23 cm^{-1} lower than experimental anharmonic frequency.[82] Thus, for better comparison of (anharmonic) frequencies yielded by PM-IRAS experiments with calculated frequencies, the latter are shifted by 23 cm^{-1} to higher values.

We have performed test calculations employing (1) PBE exchange–correlation functional,[74] (2) denser k-point grid of $5 \times 5 \times 1$, and (3) supercell constructed with bulk-optimized Pd–Pd distance of 282 pm. Adsorption energies of CO and relative stabilities of the surface alloys obtained in these tests were by less than 0.1 eV different from those discussed in the following.

4. RESULTS AND DISCUSSION

We have found that the results of TPD and PM-IRAS experiments performed in the present study are not compatible with the CO adsorption calculated on conventional structure of PdZn/Pd(111). To resolve this discrepancy between experimental and theoretical results, we propose a revised surface structure with Pd and Zn atoms arranged in zigzags. In this section we first describe the model of PdZn/Pd(111) surface with modified elemental arrangement and discuss the properties of reconstructed surface in the absence and in the presence of CO. Then we compare PM-IRAS and TPD experimental results with observables calculated for the conventional and reconstructed surface structures.

4.1. Stability of Modified Component Arrangement on the Surface of PdZn. Under UHV conditions (in the absence of CO), the elemental arrangement on the surface of PdZn/Pd(111) was determined to be alternating rows of Pd and Zn atoms (Figure 1, left panel)[27,49] and was even visualized by STM.[34] Here and further on in the text we refer to this structure as "row" structure. The modified elemental arrange-

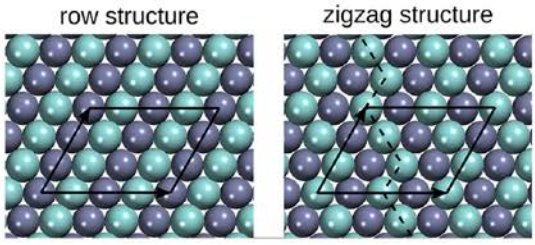

Figure 1. PdZn surface alloy on Pd(111) with bulk terminated row structure and reconstructed zigzag structure. Pd atoms are displayed in cyan, and Zn atoms are displayed in blue. Lateral dimensions of calculated supercells are marked with solid lines; the zigzag arrangement formed by Pd atoms is marked with a dashed line.

ment on the surface was modeled by "zigzag" structure (Figure 1, right panel), which is constructed from the row structure by interchanging Pd and Zn atoms in one horizontal line, thus, transforming rows of Pd and Zn atoms into zigzags. This model may not match exactly the actual elemental arrangement, which may have an intractably big periodically repeated cell or even be aperiodic. Nevertheless, in this study we refrain from considering other plausible arrangements for two main reasons. First, in the absence of experimental input (i.e., supercell size) it is impossible to reliably predict the exact arrangement of atoms by periodic DFT methods. Second (unlike the conventional row structure), the present model is sufficient to reconcile results of PM-IRAS and TPD experiments with those obtained by DFT.

Before discussing other properties of the reconstructed surface with the zigzag arrangement of components, we will address the principal issue of its stability in the absence of adsorbates and in the presence of CO adsorbed on the most stable adsorption sites. Relative stability of the PdZn/Pd(111) surface alloys of various thickness, which have one or more layers arranged in zigzags, with respect to the alloy of the same thickness but structured in rows is displayed in Figure 2. One

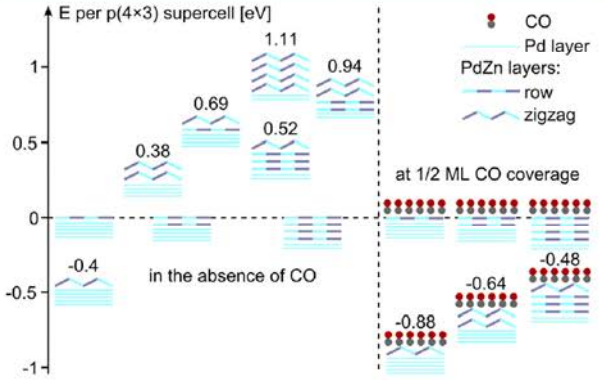

Figure 2. Calculated relative stability of various structures of PdZn/Pd(111) surface alloys with respect to the conventional structure (all layers arranged in rows), depending on the number of layers arranged in zigzags and on the CO coverage. Values are given per p(4 × 3) supercell, which has 12 metal atoms in each layer.

can see that, in the absence of adsorbates, a monolayer PdZn surface alloy is by 0.4 eV per p(4 × 3) supercell more stable with the zigzag structure. However, for multilayer surface alloys the row structure is the most stable one. The second most stable structure is that with two top layers arranged in zigzags in the case of bilayer alloy, and only one zigzag layer in the case of four-layer alloy. Later in the text we discuss only the most stable configurations of zigzag structures, that is, structures with only the top layer arranged in zigzags for the monolayer and four-layer-thick alloy and a structure with two PdZn layers arranged in zigzags for bilayer alloy.

Adsorption of CO at experimentally observed (see section 4.5) surface coverage of $^1/_2$ ML (one CO molecule per Pd atom on the surface), however, stabilizes zigzag structures of multilayer alloys by ~1 eV, turning them into the most stable configuration. The relative stability of monolayer PdZn surface alloy with zigzag structure is further increased by ~0.5 eV.

One should recall here that the suggested zigzag structure is only a model for the most thermodynamically stable elemental arrangement present in the experiment. Thus, the relative energy of the actual arrangement should be even lower than that calculated for zigzag structure.

4.2. Geometric Structure of the Surface Alloys. Structural parameters of PdZn arranged in zigzags are markedly different from those of PdZn with row structure (Figure 3).

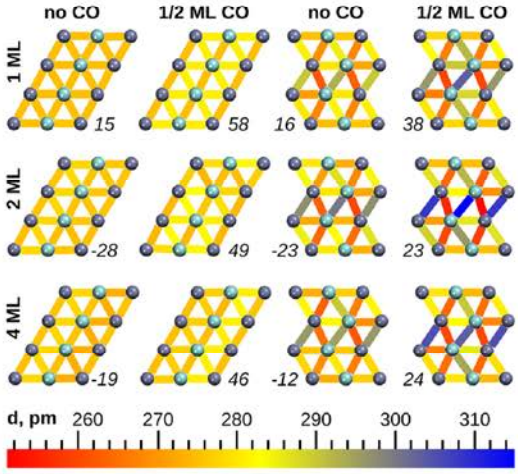

Figure 3. Color-coded interatomic distances, *d*, between atoms in the surface of one-, two-, and four-layer-thick PdZn surface alloys on Pd(111) with row and zigzag structure, in the absence of CO and at θ(CO) = $^1/_2$ ML. Numbers shown in italic type indicate surface corrugation in picometers; positive values correspond to Pd-out/Zn-in type corrugation.

Interatomic distances in the alloy with row structure are within 273–278 pm in the absence of CO and in the range of 274–283 pm at θ(CO) = $^1/_2$ ML. The longest distances are calculated between Pd and Zn atoms, while interatomic Pd–Pd and Zn–Zn distance stay close to 275 pm, the value for Pd(111). The slight elongation of the average bond length at high CO coverage accompanied with negligible lateral displacements is due to substantial increase of surface corrugation. The latter is measured as average difference between vertical coordinates of Pd and Zn atoms located on the surface, $\langle z(\mathrm{Pd})\rangle - \langle z(\mathrm{Zn})\rangle$. In line with previous DFT and LEIS studies,[33,34,51,53] in the present work surface corrugation of PdZn/Pd(111) is calculated to be 15, −28, and −19 pm for monolayer, bilayer, and multilayer surface alloys, respectively. Upon CO adsorption, corrugation increases to 58, 49, and 46 pm on one-, two-, and four-layer-thick alloys, respectively, and becomes of Pd-out/Zn-in type for any alloy thickness.

The distribution of bond lengths is much wider in PdZn surface alloys with the zigzag structure. The lateral reconstruction makes possible elongation of Pd–Pd (284–300 pm) and Zn–Zn (281–297 pm) distances and simultaneous contraction of the majority of Pd–Zn bonds (262–282 pm). These changes in bond lengths, not possible in the highly symmetric row structure, are in line with elongation of Pd–Pd and Zn–Zn bonds (289 pm) and contraction of Pd–Zn bonds (264 pm) measured in PdZn bulk[65] in comparison with interatomic distance in Pd bulk (275 pm). Adsorption of mutually repulsing CO molecules at high coverage drives Pd atoms apart from each other and results in increased Pd–Pd distances of 290–315 pm. This in turn increases distances between adjacent Zn atoms (280–308 pm) and contracts or expands Pd–Zn bonds (259–290 pm). In the absence of CO, the corrugation of PdZn with zigzag structure is not much

different from corrugation of respective alloys arranged in rows, with deviations up to 7 pm. However, the corrugation of PdZn with zigzag structure in the presence of CO is ~40 pm for monolayer and ~25 pm for multilayer alloy. As in the case of PdZn/Pd(111) arranged in rows, Pd-out/Zn-in type corrugation takes place in all cases, but the amplitude of corrugation is ~20 pm smaller in the case of laterally reconstructed surface.

Significant differences between interatomic distances on the surface and surface corrugation of the PdZn alloys arranged in rows and zigzags will affect adsorptive properties of the system. In the present study, this statement is exemplified by considering adsorption of CO, a ubiquitous probe molecule. However, one should note here that on metal surfaces CO usually adsorbs on top, bridge, or 3-fold hollow sites. These sites may be sensitive only to very short-range structural changes and largely insensitive to changes in second and farther coordination spheres of adjacent metal atoms. Also, the considered modification of component arrangement does not introduce new types of the mentioned sites, that is, 3-fold hollow sites made exclusively of Pd or Zn atoms. Thus, one can speculate that adsorption of bigger molecules that interact with higher number of metal atoms on the surface will be much more strongly affected by structural changes induced by the rearrangement of components.

4.3. Electronic Structure of the Alloys. Despite significant structural changes of the surface, the electronic structure of PdZn/Pd(111) with zigzag arrangement is very similar to that of the alloy arranged in rows (Figure 4). Notably, DOS of the monolayer alloys is markedly different from that of the multilayer alloys, being closer to DOS of Pd(111).

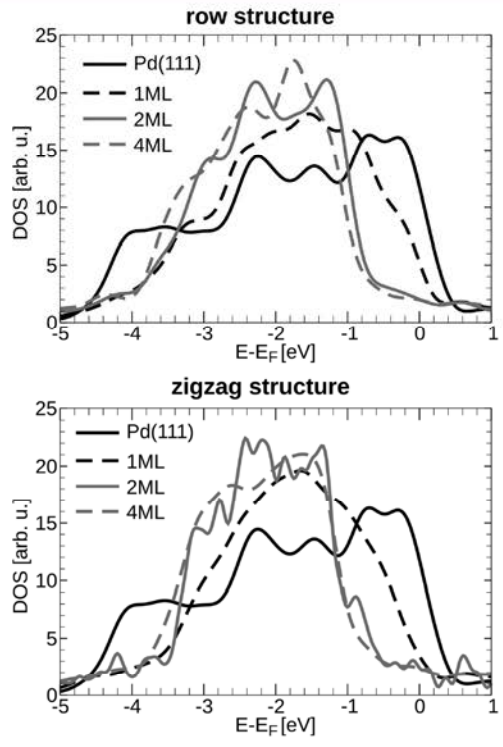

Figure 4. Calculated DOS of one-, two-, and four-layer-thick PdZn surface alloys on Pd(111) in the absence of CO projected on Pd atoms located on the surface. Energies of electronic Kohn–Sham states are given with respect to the Fermi energy, E_F.

Calculated Bader charges[83] reveal that, irrespective of the elemental arrangement, the PdZn surface alloys on Pd(111) have peculiar intermetallic nature in agreement with results calculated for bulk ($Pd^{-0.4}Zn^{+0.4}$).[65] That is, charges of (+0.34) – (+0.43) (herein charges are given in electron units) are induced on the majority of Zn atoms; atoms on the interface of multilayer PdZn and Pd(111) bear charges of (+0.46) – (+0.5). In turn, the charges on most Pd atoms are (−0.4) – (−0.37), and on those located on the interface with Pd substrate, (−0.29) – (−0.21) Thus, calculated charges on Pd atoms located on the surface of monolayer PdZn/Pd(111) are almost 2 times smaller in magnitude than those located on the multilayer alloys, which is again in line with their different catalytic properties.[31]

The difference between electronic properties of surface Pd atoms in monolayer and in multilayer alloys may be rationalized by different numbers of adjacent Zn atoms (4 and 6, respectively). The fewer number of Zn neighbors and higher number of Pd neighbors renders Pd atoms in the monolayer PdZn/Pd with DOS and Bader charges closer to those of pristine Pd(111). This explains the phenomenon of subsurface-controlled selectivity, that is, reported dependency of PdZn/Pd(111) catalyst properties on the surface alloy thickness.[31]

4.4. Adsorption of CO on Different Sites and PM-IRAS Studies. As mentioned above, the modification of elemental arrangement may change the relative stability of different adsorption sites. Because CO was shown not to adsorb on sites including Zn atoms (at temperatures ≥200 K),[31−33] there are only two types of adsorption sites available for it on the surface: on top of Pd atoms and on Pd–Pd bridge sites. In general, three conclusions can be drawn from calculated adsorption energies of CO on PdZn/Pd(111) summarized in Table 1: (i) On the four-layer-thick surface alloy, CO adsorbs by 0.2–0.4 eV more weakly than on the monolayer alloy, illustrating the

Table 1. Adsorption Energies and Vibrational Frequencies of the CO Stretching Mode for CO Adsorbed on PdZn Surface Alloys of Various Thickness and Structure on Pd(111) at θ(CO) = $^1/_{12}$ and $^1/_2$ ML

	top		bridge	
	$^1/_{12}$ ML	$^1/_2$ ML	$^1/_{12}$ ML	$^1/_2$ ML
Rows, One-Layer-Thick PdZn				
adsorption energies (eV)	1.11	0.71	1.25	0.87
vibrational frequencies (cm^{-1})	2035	2083	1893	1995
Rows, Two-Layer-Thick PdZn				
adsorption energies (eV)	0.81	0.36	0.95	0.47
vibrational frequencies (cm^{-1})	2027	2068	1884	1970
Rows, Four-Layer-Thick PdZn				
adsorption energies (eV)	0.81	0.48	0.88	0.5
vibrational frequencies (cm^{-1})	2024	2059	1894	1971
Zigzags, One-Layer-Thick PdZn				
adsorption energies (eV)	1.11	0.95	1.13	0.73
vibrational frequencies (cm^{-1})	2035	2072	1883	1966
Zigzags, Two-Layer-Thick PdZn				
adsorption energies (eV)	0.94	0.64	*a*	*a*
vibrational frequencies (cm^{-1})	2031	2066		
Zigzags, Four-Layer-Thick PdZn				
adsorption energies (eV)	0.91	0.67	0.89	0.44
vibrational frequencies (cm^{-1})	2034	2067	1889	1967

[a]Bridge sites are not stable for these structures; CO moves from bridge to top sites during geometry optimization.

importance of subsurface layers composition on properties of PdZn catalysts. (ii) The adsorption energies of CO on top and on bridge sites are different by up to 0.14 eV at low CO coverage and by up to 0.23 eV at high coverage. (iii) Most importantly, data in Table 1 show that on monolayer and bilayer PdZn arranged in rows, CO adsorption on bridge sites is preferred, whereas on PdZn arranged in zigzags, on-top sites are clearly preferred at high CO coverage. Indeed, on the alloy arranged in rows, bridge sites are more stable than on-top sites by 0.11−0.16 eV for monolayer and bilayer structures but only by 0.02−0.07 eV for a four-layer-thick alloy. On the contrary, on the reconstructed alloys with zigzag structure, on-top sites are more stable than bridge sites by ∼0.2 eV at high CO coverage, while at the low coverage of $^1/_{12}$ ML the adsorption sites have essentially the same stability. Also, on the bilayer alloys with zigzag structure, bridge sites are not stable at all, because the energy difference between adjacent top and bridge sites is sufficient to overcome the diffusion barrier between them. One can also note that at high CO coverage the adsorption is always stronger on the reconstructed surface.

Preference of bridge sites for CO adsorption on unreconstructed surface can be understood in analogy with CO adsorption on pristine Pd(111). Indeed, at low coverage CO is known to adsorb on 3-fold hollow sites on Pd(111)[84] and shows a clear preference for sites with higher coordination by Pd atoms.[85] On the defect-free PdZn surface alloys, 3-fold hollow sites entirely made of Pd atoms are not present; thus the sites with the highest possible coordination are Pd−Pd bridge sites, and CO prefers to adsorb on them. At high coverage a similar reasoning would apply to CO adsorption on the alloy with row structure, because in this case distance between CO molecules does not depend on the type of occupied adsorption sites. However, on the reconstructed zigzag alloy the distance between coadsobates at high coverage depends on where they adsorb, being 317−327 pm for on-top sites and only 279−294 pm for bridge sites on a four-layer-thick alloy. Thus, it is not surprising that on-top sites are most stable in this case at high coverage, allowing reduction of the lateral repulsion between CO adsorbates, while at low coverage the stability of the sites is similar.

By use of PM-IRAS, it could be shown[31−33] that on well-defined PdZn/Pd(111) surface alloys exclusively on-top sites were occupied by adsorbed CO molecules, irrespective of alloy thickness (2−6 PdZn layers). PdZn surface alloys could be characterized by a sharp, characteristic band for on-top CO at ≈2070 cm^{-1} in IR experiments performed in a CO background pressure, that is, at high CO coverage. Similar spectra are obtained on oxide-supported PdZn nanoparticles.[45,86] Only upon annealing of such alloys to temperatures above 623 K, when partial alloy decomposition started, were multiple bound CO species observed by PM-IRAS. DFT-calculated stretching frequencies of CO on top of Pd atoms are 2024−2035 cm^{-1} at θ(CO) = $^1/_{12}$ ML and 2059−2083 cm^{-1} at θ(CO) = $^1/_2$ ML (cf. Table 1) and support the assignment of experimentally observed ≈2070 cm^{-1} peak. In contrast, CO adsorbed on bridge sites was calculated to vibrate with frequencies of 1883−1894 cm^{-1} at low coverage and 1966−1995 cm^{-1} at high CO coverage and was experimentally observed only at high temperatures, when decomposition of the alloy took place. Notably, calculated CO stretching frequencies do not significantly depend on the alloy thickness. Taking into account that some bridge-adsorbed species should be observed on unreconstructed surface, because of their calculated higher stability, one can conclude that PM-IRAS studies provide evidence for the suggested surface reconstruction.

We have also acquired coverage-dependent IR spectra, like those presented in Figure 5 for the system with four PdZn layers. Upon a CO dose of 0.1 Langmuir, a broad band at 2048 cm^{-1} and a sharper, less intense band at 2068 cm^{-1} could be distinguished in the spectrum. Subsequently increasing the CO dose resulted in an intensity increase of the band at 2068 cm^{-1} accompanied by a decrease of the 2048 cm^{-1} band until the latter finally vanished from the spectrum after a CO dose of 10 Langmuir.

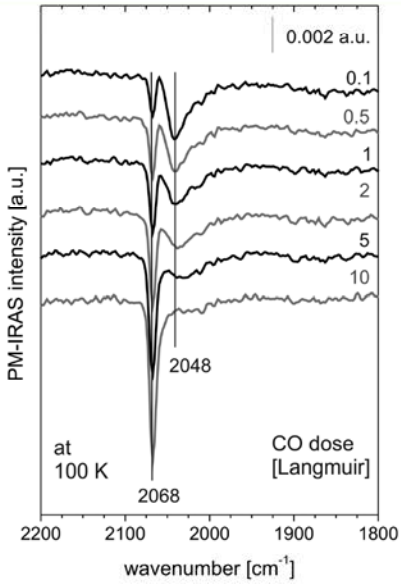

Figure 5. Coverage-dependent IR spectra of CO adsorption on >4 ML PdZn/Pd(111) at 100 K.

Of course, the appearance of two IR bands corresponds to two different CO species on the surface. In our opinion, we can differentiate between CO that does not have other CO molecules at adjacent adsorption sites (dominates at low θ) and those that have (dominates at high θ). Their frequencies are different because increasing dipole−dipole interactions and reduced back bonding from the metal at higher coverage result in a spectral blue shift of the C−O stretching vibration. Positions of experimental bands, 2048 and 2068 cm^{-1}, are in agreement with calculated frequencies of CO adsorbed on the four-layer-thick alloy with zigzag structure at θ(CO) = $^1/_{12}$ and $^1/_2$ ML, 2034 and 2067 cm^{-1}, respectively. Vibrational frequencies of CO adsorbed on top sites of the unreconstructed PdZn with four-layer thickness (2024 and 2059 cm^{-1}, respectively) were somewhat further away from the experimental band positions.

4.5. Adsorption of CO at Intermediate Coverage and TPD Studies. To model TPD spectra, we have calculated differential adsorption energies of CO, that is, energies required for only one CO molecule to desorb at a given coverage, θ = N/12, where N is the number of CO molecules in the supercell, using the following definition:

$$E_{\mathrm{diff}}(\theta) = E[(\mathrm{CO})_{N-1}/\mathrm{PdZn/Pd}] + E[\mathrm{CO_{gas}}] - E[(\mathrm{CO})_N/\mathrm{PdZn/Pd}]$$

We have calculated E_{diff} for CO adsorbed on the on-top sites of the alloys with zigzag structure and both on-top and bridge sites on the alloys with row structure at $\theta = {}^1/_2$ ML ($N = 6$). In some cases calculations were also done at an intermediate coverage (Figure 6).

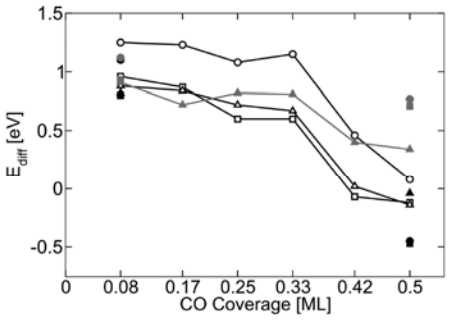

Figure 6. Dependence of differential adsorption energy, E_{diff}, of CO on its coverage on various PdZn/Pd(111) surface alloys. Solid symbols, adsorption on top; open symbols, adsorption on bridge site. Adsorption on the alloys with row structures is presented in black and on those with zigzag structure in gray. Circles, squares, and triangles label the one-, two-, and four-layer-thick alloys, respectively.

It turned out that, on nonreconstructed surfaces arranged in rows, CO is noticeably stable only up to coverage of $\theta \leq 0.33$ ML, with a sharp decrease of stability at higher coverage. This makes full coverage of the surface Pd atoms by CO molecules strongly unfavorable at room temperature for the row structure. At the same time, differential adsorption energies of CO on the reconstructed surface alloy were positive and higher than 0.34 eV even at $\theta(\mathrm{CO}) = {}^1/_2$ ML.

In order to determine experimentally the saturation CO coverage on PdZn/Pd(111) and investigate alloy formation and decomposition in more detail, we have performed TPD measurements monitoring CO adsorption and desorption, depending on the PdZn surface alloy thickness, annealing temperature, and CO dose (Figure 7). In these experiments we have started from unalloyed Zn layers on the Pd substrate (1 and 3 ML Zn deposited at liquid N_2 temperature), with the sample first heated to 273 K and cooled down in 1×10^{-6} mbar CO to 90 K to saturate the surface with CO. After that, repeated TPD runs were performed to consecutively higher end temperatures (each of which was kept for 5 min to anneal the layers at this temperature). The values given in Figure 7 indicate the annealing temperature before the TPD run. After one run was finished, the sample was saturated again with CO during cooling before the next TPD spectrum was acquired.

Mainly three regimes can be differentiated in Figure 7: (i) Up to the annealing temperature of 373 K, basically no CO desorption was observed, in good agreement with the previously reported absence of CO adsorption in PM-IRAS.[33] In this regime, the deposited Zn layers are not yet alloyed with the Pd substrate. Only trace amounts of CO were detected by mass spectrometry, most probably due to CO desorbing from the heating wires holding the crystal or from the crystal edges. (ii) Alloy formation and stability regime: after heating to 473 K, a clear CO desorption peak could be observed, which we attribute to CO desorbing from alloyed PdZn layers. After annealing to 573 K, this peak reached its maximum intensity ("ideal" PdZn alloy) and was made up from two desorption

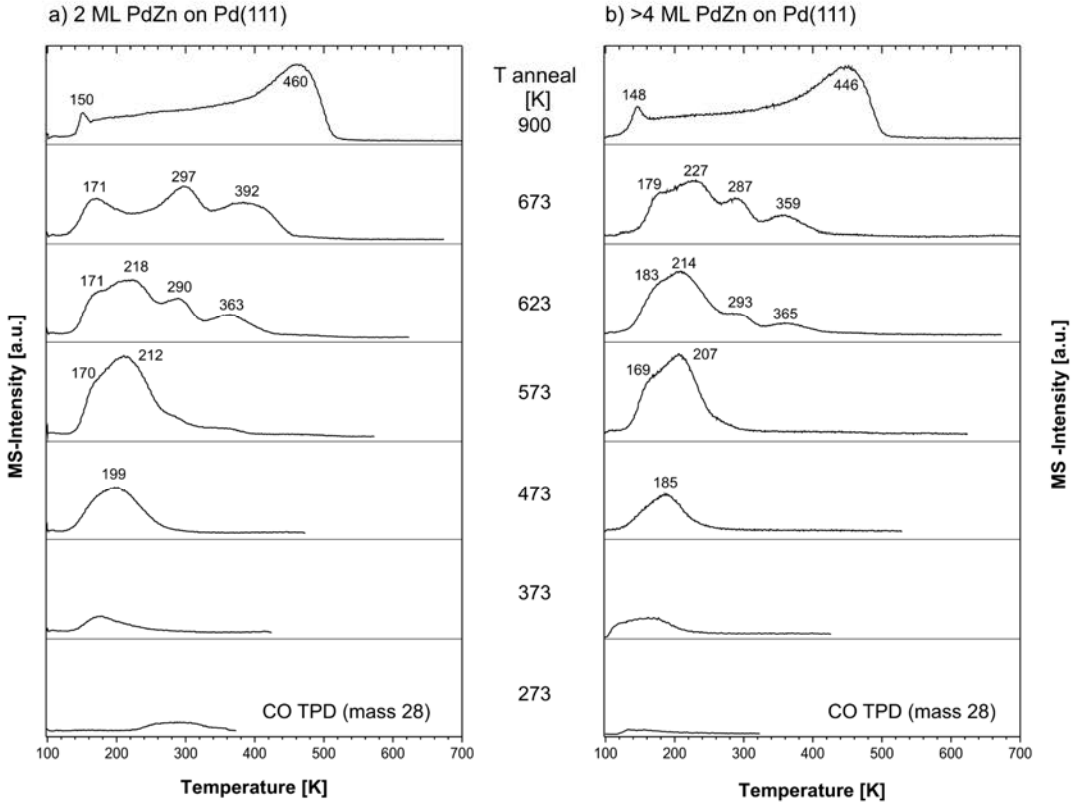

Figure 7. CO TPD spectra from (a) 2 ML and (b) >4 ML PdZn/Pd(111) depending on annealing temperature T_{anneal}.

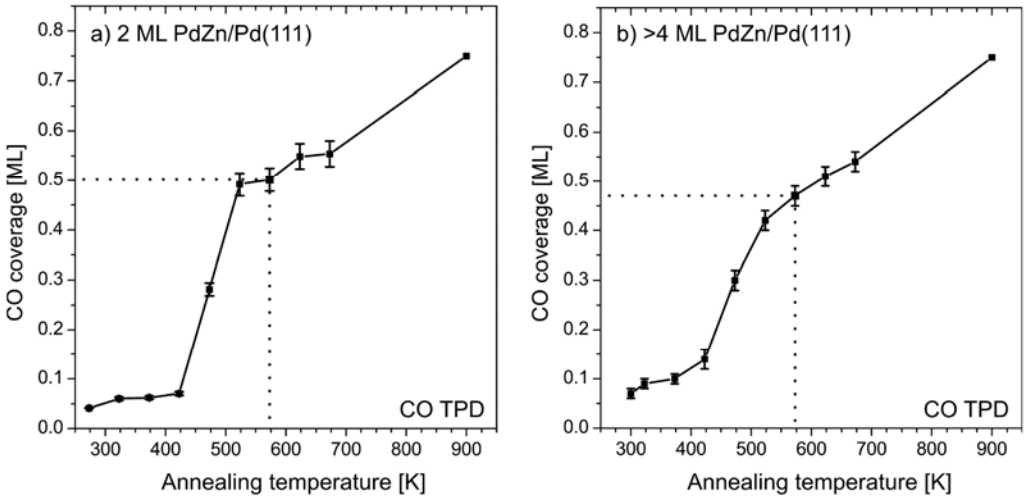

Figure 8. CO coverage as deduced from the TPD spectra in Figure 7 versus annealing temperature. The dashed line indicates saturation coverage on the "perfect" alloy.

features: a shoulder at around 170 K and the peak maximum at 210 K. (iii) Further annealing above 623 K resulted in the appearance of additional desorption features at higher desorption temperature, indicating the onset of alloy degradation via Zn dissolution in the bulk and the reappearance of Pd patches at the surface. Finally, after annealing to 900 K, the PdZn alloy was completely decomposed and the surface had transformed back to clean Pd(111). The acquired TPD (and PM-IRAS) spectra closely resemble the spectra obtained upon CO desorption from Pd(111).[87]

In the TPD spectra shown in Figure 7, no major difference was seen between 2 ML and >4 ML PdZn/Pd(111) (at temperatures when alloys are stable), indicating that CO desorption was not really affected by the thickness of the underlying PdZn layer. When the small differences in calculated CO adsorption energies on bilayer and multilayer alloys are considered (cf. Table 1), this observation seems reasonable. For the "ideal" PdZn alloys (annealing to 573 K), we have estimated the adsorption energy by applying the Redhead equation.[88] A pre-exponential factor for desorption of $10^{15.3}$ s^{-1} was used, which is in good agreement with available data for desorption energies reported for CO on pristine Pd(111).[78]

When CO desorption from the 2 ML PdZn system is considered, the maximum of 212 K corresponds to a desorption energy of E_{TPD} = 0.66 eV per molecule, which is in remarkable agreement with the calculated value of CO adsorption energy E_{ads} = 0.64 eV at high coverage on PdZn with zigzag structure. Also, for the desorption maximum of the 4 ML system at 207 K, the experimentally estimated value of E_{TPD} = 0.64 eV/molecule matches nicely the calculated E_{ads} = 0.67 eV for CO adsorption on the reconstructed surface. This may also be taken as a hint toward CO-induced surface reconstruction, although one has to keep in mind that the experimental numbers change if another pre-exponential factor is chosen.

While the general trend was the same for both PdZn systems investigated, there were some subtle differences in the TPD spectra of Figure 7, especially in the "transformation regime", that is, above 573 K. The experimental results suggest that the transformation back to Pd(111) proceeded faster and more easily on the thinner alloy. For example, the 623 K spectrum from the 2 ML PdZn system (Figure 7 a) closely resembles the 673 K spectrum of the >4 ML PdZn system (Figure 7 b), meaning that lower temperatures were required for the thinner alloy to reach the same surface state. Additionally, there seemed to be some effect of subsurface Zn on the CO adsorption on Pd, because when the TPD spectra acquired after annealing to 900 K are compared, the CO desorption maximum was shifted by about 15 K to lower temperatures for the system with higher Zn content. This finding is in agreement with results of recent DFT studies that showed lowering of CO adsorption energies on Pd(111) if Zn atoms are present in the subsurface region.[55]

By integrating the peak areas and taking the well-known 0.75 ML coverage of the (2 × 2) CO saturation structure on Pd(111) as a reference (see ref 87 and references therein), we have calculated the CO coverage for each TPD spectrum. The obtained data are plotted in Figure 8; error bars were derived from three repeated measurements. After annealing of both systems to 573 K, that is, when the alloy-related TPD and PM-IRAS features were most pronounced (dashed lines in Figure 8), the CO coverage was 0.50 ± 0.02 ML for the 2 ML PdZn/Pd(111) system and only slightly lower, 0.47 ± 0.02 ML, for the >4 ML PdZn system, in good agreement with similarly prepared systems.[89] When it is kept in mind that the Pd:Zn ratio is 1:1 in a PdZn alloy surface layer, these values indicate that every surface Pd atom is occupied by a CO molecule. Along the Pd rows/zigzags the CO molecules are even more densely packed than in the (2 × 2) CO super structure on Pd(111), which could represent a possible driving force for rearrangement of the surface. Altogether, the experimentally determined saturation coverage of 0.5 ML CO, which was computed to be achievable only for the alloy with zigzag structure, gives another strong indication for a surface reconstruction.

To investigate this in more detail, a number of TPD spectra were acquired upon increasing the initial CO dose from 0.5 L to saturation coverage, similar to the PM-IRAS spectra of Figure 5. The TPD spectra obtained after low dosage should be comparable with the calculations at $^1/_{12}$ coverage, whereas the spectra upon higher doses and cooling in CO (i.e., surface saturated with CO) correspond to the calculations at high ($^1/_2$ ML) coverage.

The obtained spectra are plotted in Figure 9, again for the systems of 2 ML and >4 ML PdZn/Pd(111) (panels a and b, respectively). Two desorption regimes can be distinguished in

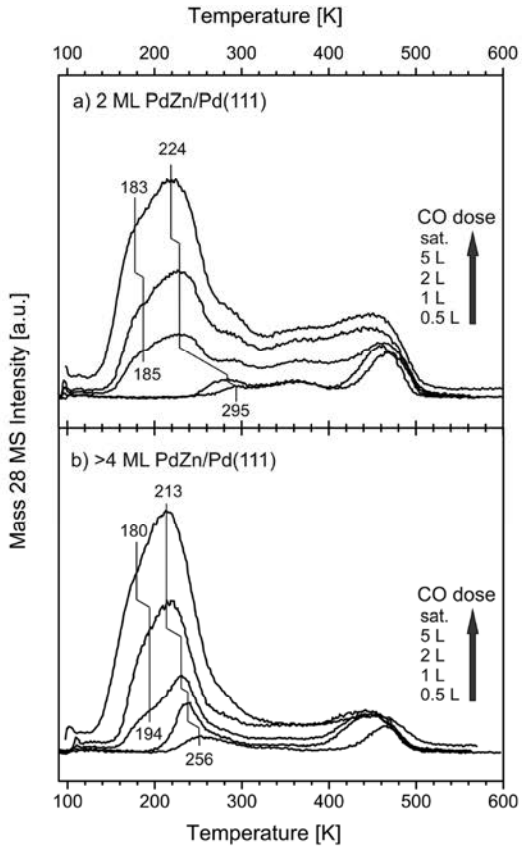

Figure 9. Coverage-dependent CO TPD spectra for (a) 2 ML and (b) >4 ML PdZn/Pd(111). For each series the CO dose was subsequently increased from 0.5 to 5 Langmuir. Saturation coverage (sat.) was achieved by cooling the system in 1×10^{-6} mbar CO to 90 K.

the spectra: CO desorbing from the PdZn surface alloy below 300 K, and CO desorption from remaining Pd(111) areas above 400 K (cf. Figure 7). For interpreting the coverage-dependent adsorption properties of CO on PdZn, we may disregard the latter here and focus on the low temperature desorption features.

After the smallest dosage of 0.5 L CO onto the 2 ML PdZn system, a small desorption feature was observed with a maximum at 295 K, attributed to desorption from the alloy. Increasing the dose gradually shifted the desorption maximum to lower temperature, and it reached a value of 227 K after dosing of 2 L CO. Upon this dose, another desorption feature appeared as a low-temperature shoulder near 183 K. Further CO dosing then increased the signal intensity but basically did not alter the position of the desorption maximum. The third feature around 295 K was also detected in the spectra after elevated doses, which might tentatively be attributed to CO desorbing from imperfect areas of the surface.

The general trend was similar for the thicker PdZn system (Figure 9 b); however, the alloy-related features were more pronounced. CO desorption from PdZn led to a small peak at 256 K, which also subsequently increased in intensity and shifted to lower temperature with increasing CO dose, reaching a maximum at 213 K upon desorption from the saturated surface. Analogous to the thinner PdZn system, after a CO dose of 2 L a low-temperature shoulder appeared at 195 K, which in this case was finally shifted to 180 K.

As for the TPD spectra presented in Figure 7, we have again estimated the desorption energy from the temperature of the peak maximum by applying the Redhead equation. The numbers obtained are summarized in Table 2.

Table 2. CO Desorption Maxima and Respective Desorption Energies for 2 and >4 ML PdZn Surface Alloys[a]

	2 ML PdZn/Pd(111)		>4 ML PdZn/Pd(111)	
CO dose (L)	T_{des} (K)	E_{TPD} (eV)	T_{des} (K)	E_{TPD} (eV)]
0.5	295	0.92	256	0.80
1	285	0.89	236	0.74
2	185/227	0.58/0.70	194/231	0.60/0.72
5	183/226	0.57/0.70	193/218	0.60/0.68
sat.	183/224	0.57/0.69	180/213	0.56/0.67

[a]According to the TPD spectra in Figure 9.

The experimentally measured values of desorption energy E_{TPD} obtained after low dose fit quite well the DFT numbers (compare Table 1). However, because calculated CO adsorption energies on PdZn with row and zigzag structures are very similar at low coverage, it is not possible to differentiate the two structures on the basis of the experimental results.

At higher CO dosage, the main peaks at 210–230 K seem to be reproduced well by average adsorption energy of CO on top sites of the respective alloys with zigzag structure (cf. Table 1). At low CO coverage, the calculated differential adsorption energies of the reconstructed structure are also in line with experimental values. The agreement is worse if one compares experimental values to the E_{diff} values at $\theta(CO) = {}^1/_2$ ML, calculated to be 0.71 and 0.34 eV for two- and four-layer-thick alloys, respectively. At the same time, average adsorption energies for on-top sites in the alloys with row structure are less than 0.5 eV at high coverage and differential adsorption energies are even negative in this case, contradicting the experimental observations. Adsorption of CO on bridge site of the unreconstructed alloys yields somewhat higher adsorption energies. Nevertheless, it does not affect significantly the results at high CO coverage, with E_{ads} still being less than 0.5 eV and E_{diff} still being negative. Thus, the adsorption energies derived from TPD experiments definitely favor the modification of elemental arrangement in the surface layer.

5. CONCLUSION

In the present study we have investigated in detail the interaction between adsorbed CO molecules and a few layers thick PdZn surface alloys on Pd(111) by means of TPD and PM-IRAS spectroscopies and DFT modeling. We have addressed the issue of possible modification of elemental arrangement on the surface by considering alloys of PdZn/Pd(111) with model "zigzag" structure on the surface.

PdZn alloys with the zigzag arrangement on the surface are found to be energetically more stable in the cases of high CO coverage and one-monolayer alloy thickness. The reconstructed surface exhibits markedly different adsorptive properties, adsorbing CO on top of Pd atoms, while adsorption is predicted to preferentially occur on bridge sites on alloys with the conventional "row" structure. CO adsorbed on bridge sites, however, is never observed in PM-IRAS experiments (at moderate annealing temperature), providing evidence for similar surface reconstruction in the experiment. Another line of evidence comes from TPD experiments, where ${}^1/_2$ ML

saturation coverage of CO (one molecule per Pd atom on the surface) on PdZn/Pd(111) was measured. At the same time, calculations of differential adsorption energy of CO molecules suggest that, at $\theta = {}^1/_2$ ML, CO is stable only on alloys with zigzag structure. On multilayer unreconstructed PdZn, the saturation coverage is calculated to be around ${}^1/_3$ ML.

A closer look at the calculated properties of PdZn/Pd(111) alloys with modified elemental arrangement reveals that they feature longer Pd−Pd and Zn−Zn interatomic distances with Pd−Zn bonds being, in general, somewhat shorter. Also the row to zigzag rearrangement significantly affects surface corrugation of the alloy at high CO coverage. However, the electronic structure of the alloys seems to be rather insensitive to the elemental arrangement of the surface. Indeed, calculated DOS projected on the Pd atoms on alloy surface depend mainly on the alloy thickness, explaining different reactivity of monolayer PdZn surface alloys, compared to thicker alloys. Notably, the PdZn surface alloys were found to have intermetallic nature and feature significant polarization of atoms, being roughly $Pd^{-0.4}Zn^{+0.4}$.

In summary, these studies for the first time addressed the issue of elemental rearrangement on the surface of a bimetallic system in the presence of an adsorbate. Experimental evidence of the elemental rearrangement were collected and the influence of the rearrangement on the surface properties was analyzed. This study reveals a new degree of complexity in bimetallic systems under reaction conditions and calls for additional studies of elemental arrangement on the surface of PdZn/Pd(111) and other bimetallic systems.

AUTHOR INFORMATION

Corresponding Author

*(C.W.) E-mail cweilach@imc.tuwien.ac.at, tel +43 1 58801 165 115, fax +43 1 58801 16599. (K.M.N.) E-mail konstantin.neyman@icrea.cat, tel +34 93 40 37 212, fax +34 93 40 21 231.

Notes

The authors declare no competing financial interest.

ACKNOWLEDGMENTS

This work has been performed within activities of the COST Actions MP0903 and CM0904 and was in part supported by the Austrian Science Fund (FWF) [SFB-F4502-N16 FOXSI]. Financial support from the Spanish MICINN (Grant FIS2008-02238), the Generalitat de Catalunya (Grant 2009SGR1041), and XRQTC is gratefully acknowledged. S.M.K. is grateful to the Spanish Ministerio de Eucación, Cultura y Deporte for predoctoral FPU Grant AP2009-3379. S.M.K. also acknowledges support by COST action MP0903 by granting a short-term scientific mission and by HPC-Europa2 by financing his visit and providing computer time in Barcelona Supercomputer Center. We thank C. Rameshan, W. Stadlmayer, N. Memmel, and B. Klötzer for valuable discussions.

REFERENCES

(1) Lambert, R. M.; Williams, F. J.; Cropley, R. L.; Palermo, A. *J. Mol. Catal. A: Chem.* **2005**, *228*, 27−33.
(2) Somorjai, G. A. *Catal. Lett.* **1992**, *12*, 17−34.
(3) Maetz, P.; Touroude, R. *Appl. Catal., A* **1997**, *149*, 189−206.
(4) Dupont, C.; Delbecq, F.; Loffreda, D.; Jugnet, Y. *J. Catal.* **2011**, *278*, 239−245.
(5) Grabow, L. C.; Gokhale, A. A.; Evans, S. T.; Dumesic, J. A.; Mavrikakis, M. *J. Phys. Chem. C* **2008**, *112*, 4608−4617.
(6) Gonzalez, S.; Neyman, K. M.; Shaikhutdinov, S.; Freund, H.-J.; Illas, F. *J. Phys. Chem. C* **2007**, *111*, 6852−6856.
(7) Stamenkovic, V. R.; Mun, B. S.; Arenz, M.; Mayrhofer, K. J. J.; Lucas, C. A.; Wang, G. F.; Ross, P. N.; Markovic, N. M. *Nat. Mater.* **2007**, *6*, 241−247.
(8) Gokhale, A. A.; Dumesic, J. A.; Mavrikakis, M. *J. Am. Chem. Soc.* **2008**, *130*, 1402−1414.
(9) Rygh, L. E. S.; Nielsen, C. J. *J. Catal.* **2000**, *194*, 401−409.
(10) Damyanova, S.; Daza, L.; Fierro, J. L. G. *J. Catal.* **1996**, *159*, 150−161.
(11) Cheng, D.; Atanasov, I. S.; Hou, M. *Eur. Phys. J. D* **2011**, *64*, 37−44.
(12) Demirci, U. B. *J. Power Sources* **2007**, *173*, 11−18.
(13) Chen, S.; Sheng, W. C.; Yabuuchi, N.; Ferreira, P. J.; Allard, L. F.; Shao-Horn, Y. *J. Phys. Chem. C* **2009**, *113*, 1109−1125.
(14) Dai, Y.; Ou, L. H.; Liang, W.; Yang, F.; Liu, Y. W.; Chen, S. L. *J. Phys. Chem. C* **2011**, *115*, 2162−2168.
(15) Wei, Y. C.; Liu, C. W.; Chang, W. J.; Wang, K. W. *J. Alloys Compd.* **2011**, *509*, 535−541.
(16) Wanjala, B. N.; Luo, J.; Fang, B.; Mott, D.; Zhong, C. J. *J. Mater. Chem.* **2011**, *21*, 4012−4020.
(17) Ferrando, R.; Jellinek, J.; Johnston, R. L. *Chem. Rev.* **2008**, *108*, 845−910.
(18) Yudanov, I. V.; Neyman, K. M. *Phys. Chem. Chem. Phys.* **2010**, *12*, 5094−5100.
(19) Baddeley, C. J.; Bloxham, L. H.; Laroze, S. C.; Raval, R.; Noakes, T. C. Q.; Bailey, P. *Surf. Sci.* **1999**, *433*, 827−832.
(20) Owens, T. G.; Jones, T. E.; Noakes, T. C. Q.; Bailey, P.; Baddeley, C. J. *J. Phys. Chem. B* **2006**, *110*, 21152−21160.
(21) van den Oetelaar, L. C. A.; Nooij, O. W.; Oerlemans, S.; van der Gon, A. W. D.; Brongersma, H. H.; Lefferts, L.; Roosenbrand, A. G.; van Veen, J. A. R. *J. Phys. Chem. B* **1998**, *102*, 3445−3455.
(22) Yuhara, J.; Schmid, M.; Varga, P. *Phys. Rev. B* **2003**, *67*, No. 195407.
(23) Maroun, F.; Ozanam, F.; Magnussen, O. M.; Behm, R. J. *Science* **2001**, *293*, 1811−1814.
(24) Stephens, J. A.; Ham, H. C.; Hwang, G. S. *J. Phys. Chem. C* **2010**, *114*, 21516−21523.
(25) Demirci, E.; Carbogno, C.; Gross, A.; Winkler, A. *Phys. Rev. B* **2009**, *80*, No. 085421.
(26) He, X. A.; Huang, Y. C.; Chen, Z. X. *Phys. Chem. Chem. Phys.* **2011**, *13*, 107−109.
(27) Bayer, A.; Flechtner, K.; Denecke, R.; Steinrück, H.-P.; Neyman, K. M.; Rösch, N. *Surf. Sci.* **2006**, *600*, 78−94.
(28) Neyman, K. M.; Lim, K. H.; Chen, Z. X.; Moskaleva, L. V.; Bayer, A.; Reindl, A.; Borgmann, D.; Denecke, R.; Steinrück, H.-P.; Rösch, N. *Phys. Chem. Chem. Phys.* **2007**, *9*, 3470−3482.
(29) Jeroro, E.; Lebarbier, V.; Datye, A.; Wang, Y.; Vohs, J. M. *Surf. Sci.* **2007**, *601*, 5546−5554.
(30) Jeroro, E.; Vohs, J. M. *J. Am. Chem. Soc.* **2008**, *130*, 10199−10207.
(31) Rameshan, C.; Stadlmayr, W.; Weilach, C.; Penner, S.; Lorenz, H.; Hävecker, M.; Blume, R.; Rocha, T.; Teschner, D.; Knop-Gericke, A.; Schlögl, R.; Memmel, N.; Zemlyanov, D.; Rupprechter, G.; Klötzer, B. *Angew. Chem., Int. Ed.* **2010**, *49*, 3224−3227.
(32) Rameshan, C.; Weilach, C.; Stadlmayr, W.; Penner, S.; Lorenz, H.; Hävecker, M.; Blume, R.; Rocha, T.; Teschner, D.; Knop-Gericke, A.; Schlögl, R.; Zemlyanov, D.; Memmel, N.; Rupprechter, G.; Klötzer, B. *J. Catal.* **2010**, *276*, 101−113.
(33) Stadlmayr, W.; Rameshan, C.; Weilach, C.; Lorenz, H.; Hävecker, M.; Blume, R.; Rocha, T.; Teschner, D.; Knop-Gericke, A.; Zemlyanov, D.; Penner, S.; Schlögl, R.; Rupprechter, G.; Klötzer, B.; Memmel, N. *J. Phys. Chem. C* **2010**, *114*, 10850−10856.
(34) Weirum, G.; Kratzer, M.; Koch, H. P.; Tamtögl, A.; Killmann, J.; Bako, I.; Winkler, A.; Surnev, S.; Netzer, F. P.; Schennach, R. *J. Phys. Chem. C* **2009**, *113*, 9788−9796.
(35) Kratzer, M.; Tamtögl, A.; Killmann, J.; Schennach, R.; Winkler, A. *Appl. Surf. Sci.* **2009**, *255*, 5755−5759.

(36) Schuyten, S.; Guerrero, S.; Miller, J. T.; Shibata, T.; Wolf, E. E. *Appl. Catal., A* **2009**, *352*, 133−144.
(37) Kurtz, M.; Wilmer, H.; Genger, T.; Hinrichsen, O.; Muhler, M. *Catal. Lett.* **2003**, *86*, 77−80.
(38) Gunter, M. M.; Ressler, T.; Jentoft, R. E.; Bems, B. *J. Catal.* **2001**, *203*, 133−149.
(39) Sa, S.; Silva, H.; Brandao, L.; Sousa, J. M.; Mendes, A. *Appl. Catal., B* **2010**, *99*, 43−57.
(40) Palo, D. R.; Dagle, R. A.; Holladay, J. D. *Chem. Rev.* **2007**, *107*, 3992−4021.
(41) Song, C. S. *Catal. Today* **2002**, *77*, 17−49.
(42) Iwasa, N.; Mayanagi, T.; Ogawa, N.; Sakata, K.; Takezawa, N. *Catal. Lett.* **1998**, *54*, 119−123.
(43) Iwasa, N.; Takezawa, N. *Top. Catal.* **2003**, *22*, 215−224.
(44) Conant, T.; Karim, A. M.; Lebarbier, V.; Wang, Y.; Girgsdies, F.; Schlögl, R.; Datye, A. *J. Catal.* **2008**, *257*, 64−70.
(45) Föttinger, K.; van Bokhoven, J. A.; Nachtegaal, M.; Rupprechter, G. *J. Phys. Chem. Lett.* **2011**, *2*, 428−433.
(46) Zhang, Q. L.; Farrauto, R. J. *Appl. Catal., A* **2011**, *395*, 64−70.
(47) Tew, M. W.; Emerich, H.; van Bokhoven, J. A. *J. Phys. Chem. C* **2011**, *115*, 8457−8465.
(48) Rodriguez, J. A. *J. Phys. Chem.* **1994**, *98*, 5758−5764.
(49) Gabasch, H.; Knop-Gericke, A.; Schlögl, R.; Penner, S.; Jenewein, B.; Hayek, K.; Klötzer, B. *J. Phys. Chem. B* **2006**, *110*, 11391−11398.
(50) Weirum, G.; Barcaro, G.; Fortunelli, A.; Weber, F.; Schennach, R.; Surnev, S.; Netzer, F. P. *J. Phys. Chem. C* **2010**, *114*, 15432−15439.
(51) Stadlmayr, W.; Penner, S.; Klötzer, B.; Memmel, N. *Surf. Sci.* **2009**, *603*, 251−255.
(52) Stadlmayr, W.; Klötzer, B.; Penner, S.; Memmel, N. *J. Phys. Chem. C* **2012**, *116*, 3635−3644.
(53) Chen, Z. X.; Neyman, K. M.; Gordienko, A. B.; Rösch, N. *Phys. Rev. B* **2003**, *68*, No. 075417.
(54) Chen, Z. X.; Neyman, K. M.; Rösch, N. *Surf. Sci.* **2004**, *548*, 291−300.
(55) Huang, Y. C.; Ding, W. P.; Chen, Z. X. *J. Chem. Phys.* **2010**, *133*, No. 214702.
(56) Koch, H. P.; Bako, I.; Schennach, R. *Surf. Sci.* **2010**, *604*, 596−608.
(57) Huang, Y. C.; He, X.; Chen, Z. X. *J. Chem. Phys.* **2011**, *134*, No. 184702.
(58) Huang, Y. C.; Chen, Z. X. *J. Phys. Chem. C* **2011**, *115*, 18752−18760.
(59) Lin, S.; Xie, D. Q.; Guo, H. *J. Phys. Chem. C* **2011**, *115*, 20583−20589.
(60) Smith, G. K.; Lin, S.; Lai, W. Z.; Datye, A.; Xie, D. Q.; Guo, H. *Surf. Sci.* **2011**, *605*, 750−759.
(61) Lim, K. H.; Chen, Z. X.; Neyman, K. M.; Rösch, N. *J. Phys. Chem. B* **2006**, *110*, 14890−14897.
(62) Chen, Z. X.; Lim, K. H.; Neyman, K. M.; Rösch, N. *J. Phys. Chem. B* **2005**, *109*, 4568−4574.
(63) Chen, Z. X.; Neyman, K. M.; Lim, K. H.; Rösch, N. *Langmuir* **2004**, *20*, 8068−8077.
(64) Chen, Z. X.; Lim, K. H.; Neyman, K. M.; Rösch, N. *Phys. Chem. Chem. Phys.* **2004**, *6*, 4499−4504.
(65) Friedrich, M.; Ormeci, A.; Grin, Y.; Armbrüster, M. *Z. Anorg. Allg. Chem.* **2010**, *636*, 1735−1739.
(66) Rupprechter, G. *Adv. Catal.* **2007**, *51*, 133−263. Rupprechter, G. *Catal. Today* **2007**, *126*, 2−17.
(67) Rupprechter, G.; Weilach, C. *Nano Today* **2007**, *2*, 20−29.
(68) Borasio, M.; de la Fuente, O. R.; Rupprechter, G.; Freund, H.-J. *J. Phys. Chem. B* **2005**, *109*, 17791−17794.
(69) Ozensoy, E.; Meier, D. C.; Goodman, D. W. *J. Phys. Chem. B* **2002**, *106*, 9367−9371.
(70) Gao, F.; McClure, S. M.; Cai, Y.; Gath, K. K.; Wang, Y.; Chen, M. S.; Guo, Q. L.; Goodman, D. W. *Surf. Sci.* **2009**, *603*, 65−70.
(71) Diemant, T.; Zhao, Z.; Rauscher, H.; Bansmann, J.; Behm, R. J. *Surf. Sci.* **2007**, *601*, 3801−3804.
(72) Artiglia, L.; Diemant, T.; Hartmann, H.; Bansmann, J.; Behm, R. J.; Gavioli, L.; Cavaliere, E.; Granozzi, G. *Phys. Chem. Chem. Phys.* **2010**, *12*, 6864−6874.
(73) Kresse, G.; Furthmuller, J. *Phys. Rev. B* **1996**, *54*, 11169−11186.
(74) Perdew, J. P.; Burke, K.; Ernzerhof, M. *Phys. Rev. Lett.* **1996**, *77*, 3865−3868.
(75) Hammer, B.; Hansen, L. B.; Nørskov, J. K. *Phys. Rev. B* **1999**, *59*, 7413−7421.
(76) Lopez, N.; Nørskov, J. K. *Surf. Sci.* **2001**, *477*, 59−75.
(77) Yudanov, I. V.; Sahnoun, R.; Neyman, K. M.; Rösch, N. *J. Chem. Phys.* **2002**, *117*, 9887−9896.
(78) Guo, X. C.; Yates, J. T. *J. Chem. Phys.* **1989**, *90*, 6761−6766.
(79) Kresse, G.; Joubert, D. *Phys. Rev. B* **1999**, *59*, 1758−1775.
(80) Monkhorst, H. J.; Pack, J. D. *Phys. Rev. B* **1976**, *13*, 5188−5192.
(81) Methfessel, M.; Paxton, A. T. *Phys. Rev. B* **1989**, *40*, 3616−3621.
(82) Huber, K.-P.; Herzberg, G. *Molecular Spectra and Molecular Structure, Vol 4: Constants of diatomic molecules*; Van Nostrand: New York, 1979.
(83) Bader, R. F. W. *Atoms in Molecules*; Clarendon Press: Oxford, U.K., 1990.
(84) Rose, M. K.; Mitsui, T.; Dunphy, J.; Borg, A.; Ogletree, D. F.; Salmeron, M.; Sautet, P. *Surf. Sci.* **2002**, *512*, 48−60.
(85) Loffreda, D.; Simon, D.; Sautet, P. *Surf. Sci.* **1999**, *425*, 68−80.
(86) Lebarbier, V.; Dagle, R.; Conant, T.; Vohs, J. M.; Datye, A. K.; Wang, Y. *Catal. Lett.* **2008**, *122*, 223−227.
(87) Morkel, M.; Rupprechter, G.; Freund, H.-J. *J. Chem. Phys.* **2003**, *119*, 10853−10866.
(88) Redhead, P. A. *Vacuum* **1962**, *12*, 203−211.
(89) Tamtögl, A.; Kratzer, M.; Killman, J.; Winkler, A. *J. Chem. Phys.* **2008**, *129*, No. 224706.

Chapter 7

Conclusions

From the results presented in Chapters 3–6 one can draw the following conclusions about considered nanostructuring effects on properties of materials interesting from heterogeneous catalysis perspective:

- Adsorptive and catalytic properties of scalable with size transition metal nanoparticles can differ substantially from those of respective single crystal surfaces. First, edges of Pd nanoparticles are shown to adsorb certain CH_xO_y species significantly stronger than respective {111} facets. Also, these edges are calculated to be more active in methane decomposition than extended Pd(111) surface. In the presence of absorbed hydrogen even {111} terraces of Pd nanoparticles are shown to be more catalytically active in some hydrogenation reactions than Pd(111) single crystals.

- The most energetically stable ordering of components and, in particular, surface composition of bimetallic nanoparticles can be efficiently determined based on the results of electronic structure calculations. This is achieved with the help of proposed topological Hamiltonians fitted to DFT-calculated total energies. For studied nanoalloys, the precision of this method is found to be of the same order as the thermal energy of a considered nanoparticle at room temperature, which is sufficient for practical purposes. The obtained parameters in the Hamiltonians have clear physical interpretations and provide important insights into the nature of binding within bimetallic nanoparticles.

- The effect of chemically rather inert oxide supports (without defects) on physical and adsorptive properties of sizeable metal nanoparticles can be insignificant. This is explicitly shown for 1.6 nm big Pd_{127} and Pt_{127} nanoparticles on MgO(100) surface. The effect of the oxide on geometric and electronic structure of the supported nanoparticles is found to be minor. Moreover, its effect on adsorption and absorption energies of H atoms in Pd and Pt nanoparticle is limited to 0.07 eV only.

- Surface coverage can change properties of transition metal nanoparticles more significantly than a chemically inert oxide support. Indeed, the saturation of the surface of Pd_{127} and Pt_{127} nanoparticles by adsorbed H affects their geometric

and electronic structure much more than the presence of MgO(100) support. The same can be concluded about H absorption in nanostructured Pd and Pt.

- Nanoislands formed on CeO_2(111) surface expose steps with particular electronic structure and increased reducibility. The asymmetric electrostatic potential at the steps results in the formation of edge-specific electronic states, which are identified in DFT calculations as well as in scanning tunneling microscopy and spectroscopy experiments. Also, with the help of a novel procedure implemented to prescreen possible O_{vac} + $2Ce^{3+}$ configurations formation energies of O vacancies on the steps are calculated to be up to 0.7 eV lower than on the pristine CeO_2(111) surface. This indicates the significantly increased reducibility of the steps compared to the regular surface.

- Absolute energies of steps delimiting nanoislands can be efficiently calculated using DFT methods. Two new methods of computation are proposed, which require less electronic structure calculations and yield higher statistical accuracy than the previously available method. Application of these methods to steps on CeO_2(111) surface yield results in good agreement with the experiment.

- Materials with one dimension reduced to a nanometer size (thin films) may have atomic structure drastically different from that of the corresponding bulk. As shown for Ce_2O_3 and PdZn films, this can happen for various reasons. The structure of Ce_2O_3 films is shown to depend on the substrate used for their growth. Namely, films with A-type, bixbyite and new NF1 structures are predicted to be formed on substrates favoring short, moderate and long lattice parameters, respectively. As for PdZn films on Pd(111), the reason for the higher energetic stability of altered "zigzag" structure is longer Pd-Pd distances than in the conventional "row" structure. This makes the "zigzag" structure more stable for monolayer thick PdZn films and for thicker films, when they are covered by CO molecules.

Hence, this work resulted in a new basic knowledge about differences between physics and chemistry of regular extended materials on one side and nanoparticles, nanoislands and nanometer thin films on the other side. New methods how to optimize chemical ordering in bimetallic nanoparticles, how to calculate energies of steps on

surfaces and how to search for the lowest-energy O_{vac} + $2Ce^{3+}$ configuration were proposed. Also the "simulated mechanical annealing" technique was applied to the global optimization of films for the first time. The performed studies of MgO-supported Pd and Pt nanoparticles will serve as a valuable reference point for further exploration of metal-support interactions. Finally, higher sensitivity of properties of transition metal nanoparticles to the presence of adsorbates (e.g. atomic H) was documented for the first time. All these *one-of-a-kind* studies have far-reaching implications for computational and experimental nanoscience and pave the way for further investigations.

8 Resumen en Español

Summary in Spanish

8.1 Introducción

Un catalizador es una sustancia que acelera la velocidad, k, de una determinada reacción química.[1] Energéticamente implica que la energía de activación de la reacción, E^a, disminuye por el catalizador hasta varios órdenes de magnitud (Figura 8.1). Como la velocidad de reacción depende exponencialmente de la energía de activación, $k \sim e^{-E^a/k_{Boltzmann}T}$, la presencia de un catalizador implica una inmensa aceleración de la reacción. En catálisis heterogénea esta reacción ocurre en la superficie entre dos fases distintas, normalmente entre unos reactivos líquidos o gaseosos y un catalizador sólido.

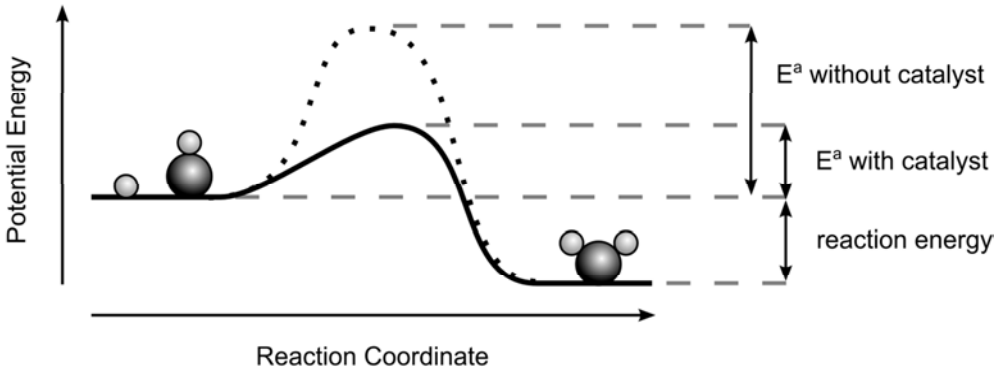

Figura 8.1. Perfil energético de una reacción química. El catalizador disminuye la energía de activación pero al mismo tiempo mantiene la energía de reacción.

La catálisis heterogénea juega un gran papel en el mundo. Muchos materiales de uso común no pueden ser producidos a escala industrial sin catalizadores heterogéneos, y su empleo mejora las eficiencias energética y de costes de la reacción, decisivas para valorar la viabilidad económica del proceso. Probablemente las reacciones catalizadas más importantes del siglo XX han sido el proceso Haber-Bosch[1] (Premios Nobel de Química[2,3] en 1918 y 1931) y los procesos petroquímicos.[4] El primero permitió la producción masiva de fertilizantes de amoníaco, solucionando los problemas de escasez de alimentos a principios del siglo XX, y permitiendo cuadruplicar la población mundial en el último siglo. Los segundos son responsables de la omnipresente del petróleo en nuestras vidas, especialmente en el ámbito de combustibles para vehículos.

[1] La IUPAC define[395] un catalizador como: "Una sustancia que incrementa la velocidad de una reacción sin cambiar la variación de energía estándar de Gibbs de la reacción. El catalizador es a la vez un reactivo y un producto de la reacción."

El siglo XXI plantea nuevos retos en la ciencia, en general, y para la catálisis heterogénea, en particular.[5] Actualmente gran parte del interés científico se centra en desarrollar nuevos catalizadores heterogéneos para resolver problemas energéticos y ambientales venideros. Primero, se requieren catalizadores heterogéneos para celdas de combustible con una menor cantidad de metales preciosos y que a la par permitan extraer energía de una manera más eficiente de los combustibles fósiles.[6] Por ejemplo, el uso del gas natural, que es más respetuoso con el medio ambiente, se ve limitado por la falta de catalizadores heterogéneos para oxidarlo[7,8] o bien convertirlo en combustible líquido.[9,10] La implementación a larga escala de biocombustibles también requiere del desarrollo de nuevos catalizadores.[11] Finalmente, la purificación de los gases de combustión de carburantes fósiles en vehículos u otros aparatos también necesita de catalizadores heterogéneos.[12] Por ejemplo, la falta de catalizadores económicamente asequibles para tratar dichos gases de combustión limita la utilización de motores diésel, dentro de un marco de criterios de emisión de gases cada vez más estrictos.

El uso de catalizadores heterogéneos se ve frecuentemente limitado por su elevado coste, especialmente si contienen metales nobles. Así pues, un factor crítico es la eficiencia catalítica por gramo de material activo. La manera más directa de aumentar ésta eficiencia es incrementar su área superficial, ya que sólo los átomos localizados en la superficie son accesibles para los reactivos. Industrialmente esto se puede conseguir mediante estructuras jerárquicas (Figura 8.2).

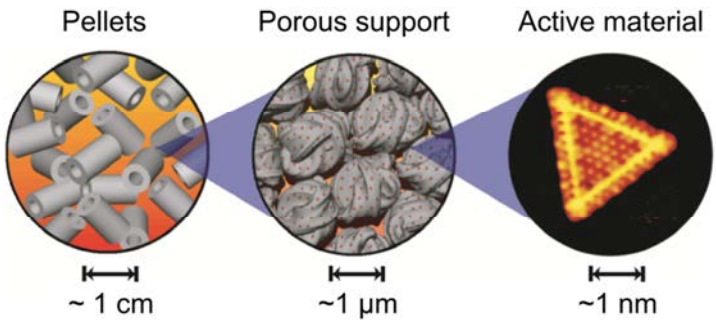

Figura 8.2. Estructura jerárquica de un catalizador heterogéneo. El catalizador se introduce en el reactor en forma de partículas huecas, que contienen el material activo nanoestructurado, depositado en una microestructura (o nanoestructura) de óxido poroso que actúa como soporte. La figura ha sido adaptada de la Ref. 15.

El material activo normalmente se dispersa en forma de pequeñas nanopartículas de manera que tengan la mayoría de sus átomos en la superficie. Para prevenir la aglomeración en partículas de mayor tamaño, de manera que se perdiese área específica y actividad catalítica, la especie activa se soporta sobre un material de gran área superficial. Para permitir la rápida difusión de los reactivos desde el medio hacia el catalizador (y de los productos desde el catalizador al medio) el soporte debe de estar como mínimo microestructurado. Finalmente, porciones del material poroso ya con el material activo soportado se comprimen en forma de pastillas (a veces ayudándose de un material aglomerante) con propiedades mecánicas definidas y adecuadas, y éstas pastillas se introducen en el reactor químico.

En principio todos los niveles de la estructura del catalizador son igualmente importantes para su rendimiento. Sin embargo, el trabajo en esta tesis se centra sólo en la estructura de los catalizadores a la nanoescala. La razón es que en ciertos casos se ha demostrado que la nanoestructura *altera completamente* las propiedades catalíticas del material. Este cambio está íntimamente relacionado con los cambios en la estructura electrónica del catalizador, que se rigen por las interacciones entre electrones tipo onda cuántica. De esta manera, el rendimiento catalítico de un material nanoestructurado se vuelve dependiente de una rica variedad de fenómenos cuánticos.

Hay muchas formas de nanoestructurar un catalizador. La forma de nanopartícula (NP), es decir, diminutos trozos de material bien disgregados y separados, se utiliza ampliamente y activamente en catálisis heterogénea, ya que combina una muy elevada proporción de superficie de trabajo con una relativamente alta estabilidad termodinámica. Es muy común que las propiedades catalíticas se vean afectadas por esta forma de nanoestructuración, como se encuentra en la dependencia de las propiedades catalíticas con el tamaño de nanopartícula.[16,17] Uno de los ejemplos más conocidos es la pronunciada actividad catalítica del oro nanoestructurado para la oxidación de CO, que contrasta con la notable falta de actividad del Au en muchos procesos químicos.[18,19] Un catalizador también puede llegar a ser mucho más activo cuando se usan nanopartículas de un óxido reducible (por ejemplo, CeO_2) como soporte para partículas de metales de transición, siendo estas últimas la fase activa del catalizador heterogéneo.[20]

Los defectos en las superficies son otra forma de nanoestructuración, ya que éstos se presentan de manera natural en cualquier superficie, por más idealmente que se prepare. Normalmente los escalones exponen átomos de baja coordinación con una actividad química modificada.[24] Por ejemplo, se ha demostrado que los escalones en la superficie de Ru(0001) son los responsables de su actividad catalítica en la reducción del nitrógeno molecular a amoniaco.[25] Recientemente también se ha hallado que la actividad de catalizadores comerciales de Cu/ZnO es debida a impurezas de Zn incorporadas a escalones de las superficies de Cu.[26] Por último, la actividad de nanopartículas de Ru en la síntesis de Fischer-Tropsch se atribuye a defectos en su superficie.[27]

Algunos materiales desarrollan nuevas propiedades cuando se reducen a la nanoescala sólo en una dimensión, es decir, cuando se forman nanopelículas. Por ejemplo, esto puede suceder en nanopartículas bimetálicas de núcleo recubierto, donde un metal forma una fina capa que cubre el núcleo de una nanopartícula compuesta de otro metal. Estas nanopelículas pueden tener propiedades diferentes ya sea debido a la interacción electrónica con el núcleo subyacente o simplemente debido a la tensión mecánica inducida. Por ejemplo, se cree que este último factor es el responsable de la actividad catalítica de las nanopartículas de Pt-película/Co-núcleo en la reacción de reducción del oxígeno, con una actividad catalítica superior al Pt puro.[28,29]

Debido a las extremadamente complejas estructuras de los catalizadores comerciales descritas en la Figura 8.2, los estudios experimentales sobre el efecto de la nanoestructuración en su actividad se complican en gran medida por una multitud de fenómenos que tienen lugar al mismo tiempo. Para abordar este problema se han desarrollado catalizadores modelo.[30-32] Estos sistemas presentan un grado de nanoestructuración similar al de los catalizadores comerciales, pero carecen de cualquier complejidad a escala milimétrica y micrométrica. Esto se logra mediante el uso en experimentos de superficies de monocristales como soportes para materiales activos nanoestructurados, en vez de los sofisticados soportes porosos. Para explorar las diferentes formas de nanoestructuración se pueden depositar nanopartículas o delgadas películas sobre un soporte de monocristal, o se pueden estudiar los defectos de sus superficies (Figura 8.3). La ventaja fundamental de la aproximación del catalizador modelo es la capacidad de controlar con precisión la nanoestructuración del material activo, cosa que rara vez se consigue en los catalizadores comerciales.

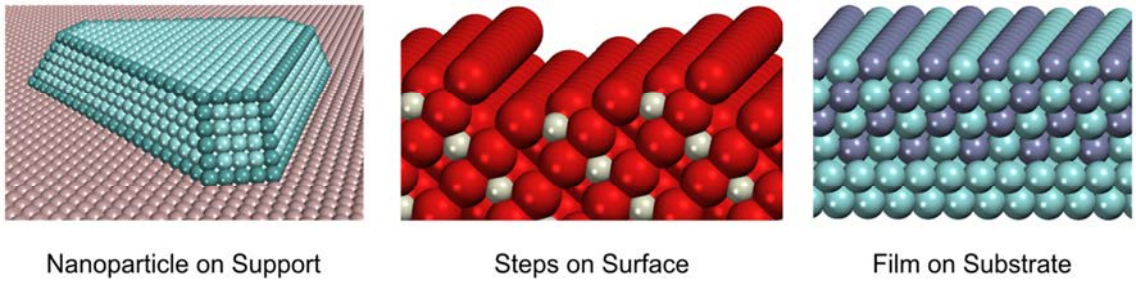

Figura 8.3. Varias formas de catalizadores modelo.

Los estudios computacionales sobre catalizadores heterogéneos suelen considerar superficies monocristalinas perfectas que carecen de cualquier nanoestructuración. En estos casos los catalizadores heterogéneos se pueden modelar como clústeres tratados a nivel cuántico, pero integrados en un entorno tratado clásicamente, o bien como cortes (*slabs*) de la superficie. Estos últimos modelos son películas suficientemente gruesas del material construidas repitiendo de manera periódica el material sólo a lo largo de dos dimensiones de una determinada celda cristalina. Estos modelos se han convertido en la locomotora de los estudios computacionales concernientes a la catálisis heterogénea.[57-59] Algunos ejemplos de estos estudios se comentan en la Sección 11.4. De hecho, este modelo resulta no ser tan preciso, pero todavía muy útil en muchos casos.

La mayoría de los estudios académicos tratan de mejorar la precisión de estos modelos convencionales, haciéndolos más realistas a pesar del aumento considerable en el coste computacional. Esto se puede lograr: a) teniendo en cuenta las reacciones en superficies cubiertas por los reactivos, intermedios, productos y especies *espectadoras* y b) teniendo en cuenta defectos puntuales y escalones presentes en las superficies.

Sin embargo, en muchos casos, es la nanoestructuración la que determina la actividad del catalizador. El modelo de corte o *slab* sólo permite simular formas de nanoestructuración como escalones en superficies y nanopelículas. Para modelar catalizadores en forma de nanopartículas es obligatorio ir más allá de los modelos de capas, en particular cuando la dependencia de las propiedades del catalizador con el tamaño de las nanopartículas es evidente. De hecho, debido a la actual hegemonía de los modelos de capas en los estudios de catálisis computacional, muchos efectos básicos relacionados con la nanoestructuración de los materiales catalíticamente activos o sus soportes permanecen insuficientemente estudiados a nivel teórico.

8.2 Objetivos

La misión principal de esta tesis es investigar cómo varias formas de nanoestructuración pueden alterar las propiedades de diversos materiales usados en catálisis heterogénea, a través de cálculos DFT llevados a cabo tanto en sistemas regularmente extendidos como en sistemas nanoestructurados. Se pueden clasificar varias características estructurales según el número de dimensiones en los que el material se extiende o se confina en la nanoescala. Así pues, se han considerado los siguientes tipos de nanoestructuras en esta tesis

- 0D[2] – nanopartículas, soportadas y sin soportar;
- 1D – escalones en una superficie;
- 2D – capas finas.[3]

El objetivo de esta tesis no era llevar a cabo una serie de estudios sistemáticos de un material en particular o una u otra forma de nanoestructuración. Más bien este trabajo representa una *prueba conceptual* dirigida a explorar las varias maneras en que la nanoestructuración puede afectar a la catálisis. En particular, se plantearon los siguientes objetivos:

- Cuantificar las diferencias entre las propiedades físicas, adsorbentes y catalíticas de aristas y caras de nanopartículas, y los respectivos sitios en superficies de monocristales, para determinados catalizadores metálicos representativos del resto, a diferentes condiciones de reacción.
- Racionalizar la relación entre el enlace en nanopartículas de aleaciones metálicas y las estructuras energéticamente más estables de nanopartículas bimetálicas.
- Estimar la magnitud de los cambios en las propiedades de nanopartículas metálicas inducidas por su interacción con un soporte de óxido inerte.

---

[2] "X" en "XD" se refiere al número de dimensiones extendidas.

[3] Esta clasificación no cubre todos los tipos de nanoestructuración. Por ejemplo, no incluye nanocables 1D y nanomallas 2D compuestas de nanopartículas 0D de ceria, también consideradas en esta tesis.

- Investigar cómo la presencia de escalones en una superficie afecta propiedades tales como la estructura electrónica y la energía requerida para formar vacantes de O en un óxido reducible.

- Entender las razones de cómo y porqué las estructuras observadas de ciertas capas finas difieren de las respectivas estructuras de monocristales para determinados materiales.

La consecución de estos objetivos ampliará el entendimiento de cómo los mecanismos atomísticos de la nanoestructuración pueden afectar a los procesos catalíticos. Ésta será una valiosa contribución al campo de la nanociencia computacional, donde hay aún muchos conceptos básicos a ser descubiertos y explorados.

8.3 Trasfondo Metodológico

Teoría del funcional de la densidad

Hohenberg y Kohn (Premio Nobel de Química en 1998) propusieron una alternativa[76] a los métodos basados en la función de onda demostrando que la energía (al igual que muchos otros observables) del estado fundamental no degenerado de un sistema es, de manera universal, un funcional de la función densidad electrónica.

$$E_0 = F_{HK}[\rho] + \int V(r)\rho(r)dr \qquad (1).$$

Como solución práctica Kohn y Sham propusieron a) separar las contribuciones conocidas y desconocidas en F_{HK} y b) considerar un sistema auxiliar de electrones no interactuantes dentro de un potencial efectivo, V_{KS}, determinado por F_{HK}.[78] Específicamente, el sistema de *N* electrones interactuantes puede ser representado por un sistema de *N* electrones que no interactúan[4] con una dinámica gobernada por

$$\widehat{H}_{KS} = -\frac{\hbar^2}{2m}\nabla^2 + V_{KS}(r) \qquad (2),$$

donde el potencial efectivo contiene el potencial externo y las interacciones coulombicas clásicas entre electrones,[5]

$$V_{KS}(r) = V(r) + \int \frac{e^2\rho(r_2)}{|r-r_2|}dr_2 + V_{XC}(r) \qquad (3).$$

El término restante $V_{XC}(r)$ es denominado *potencial de correlación e intercambio*, el cual está relacionado con F_{HK} mediante un conjunto de ecuaciones:

$$F_{HK}[\rho] = T_s[\rho] + \int \frac{e^2\rho(r_1)\rho(r_2)}{|r_1-r_2|}dr_1dr_2 + E_{XC}[\rho] \qquad (4),$$

donde T_s es la energía cinetica del sistema de electrones no interactuantes tenido en cuenta explícitamente la ecuación (4) y E_{XC} el así llamado *funcional de correlación e intercambio*.

---

[4] A pesar de la ausencia de interacción, los electrones siguen obedeciendo el Principio de Exclusión de Pauli, que indica que cada estado puede estar ocupado como máximo por dos electrones de espín opuesto.

[5] Por consiguiente, V_{KS} depende de la densidad electrónica no interactuantes. Esto complica extremadamente la búsqueda de los valores propios, ε_i^{KS}, y funciones propias, φ_i^{KS}, de $\widehat{H}_{KS}$ en (3), porque la forma de ésta última depende implícitamente de φ_i^{KS}.

Por un lado, encontrar la forma exacta de E_{XC} es posiblemente tan complicado como encontrar la forma exacta de F_{HK}. Por otro lado, $E_{XC}[\rho]$ es de una magnitud mucho menor que $F_{HK}[\rho]$, el cual esta dominado por la energía cinética de los electrones no interactuantes y su repulsión coulombica. De esta forma, cualquier aproximación hecha en E_{XC} tendrá un efecto mucho menor en el estado fundamental que las aproximaciones hechas en F_{HK}.

Modelización de catalizadores nanoparticulados

Como se ha discutido anteriormente la mayoría de los catalizadores estudiados experimentalmente y/o utilizados en la industria contienen el material activo en forma de nanopartículas, para así poder maximizar su área superficial reactiva. A menudo estas nanopartículas tienen tamaños de alrededor de decenas de nanómetros y contienen miles de átomos (Figura 8.4). Por lo tanto, con los métodos computacionales contemporáneos es casi imposible calcular directamente su estructura electrónica, por lo que habitualmente se necesitan aproximaciones de modelización.

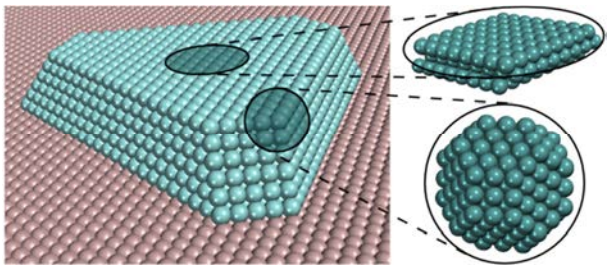

Figura 8.4. Representación esquemática de los catalizadores modelo estudiados experimentalmente, compuestos de nanopartículas metálicas bien definidas (cian) soportadas sobre una capa de óxido (marrón). Los recuadros (turquesa oscuro) abarcan los sitios activos en las zonas planas y ejes/aristas de las nanopartículas, correspondientes a los modelos de *slab* y partícula, respectivamente.

Para simular las aristas, esquinas y otros sitios superficiales, activos e irregulares de la superficie de la NP uno ha de no sólo reproducir en los cálculos su estructura local, sino también describir el conjunto envolvente de átomos (entorno). Un modo práctico de calcular de una manera eficiente la zona de entorno es excluir de ella aquellos átomos que no afecten de una manera crítica las propiedades investigadas. Como consecuencia, la modelización de la estructura electrónica de NPs de metales de transición soportadas en óxidos pasa por tener en cuenta sólo una parte de los átomos

metálicos que rodean el sitio activo y despreciar el efecto del óxido.[151,152] Esta última suposición se puede considerar válida para nanopartículas grandes soportadas en óxidos no reducibles y poco reactivos, porque en este caso solo una pequeña parte de los átomos de la nanopartícula está en contacto con el soporte. La validez de esta suposición se trata y discute debidamente en el Capítulo 4. Al mismo tiempo, puede ser necesario el uso de modelos más complejos para describir la interacción de las nanopartículas metálicas con soportes como TiO_2 y CeO_2,[55,153,154] incluyendo explícitamente el soporte y quizás también sus características a escala nanoscópica.[6]

Los estudios realizados en los Capítulos 4 y 5 se han llevado a cabo calculando NPs 3D de forma (principalmente) cubooctaédrica, cortada del interior del material (*bulk*), y optimizada. Las NPs diseñadas de esta forma tienen la disposición de los átomos como en el interior de un monocristal y sus caras están terminadas por superficies con índices de Miller bajos, tal y como se observa experimentalmente para NPs más grandes.[33,176] Debido a esto, la estructura de sitios de adsorción como caras, aristas y esquinas imitan los correspondientes sitios en catalizadores modelo. Por un lado estos modelos de NPs pueden no ser los mínimos globales para ese tamaño de partícula, aunque por otro lado los mínimos globales pueden no reproducir las características de un ordenamiento atómico como en el *bulk*, con unos sitios superficiales y una estructura electrónica parecidos a los del catalizador modelo. Así pues los cálculos utilizando NPs con la ordenación atómica del mínimo global pueden llevar a resultados variables frente al tamaño de las NPs, de manera que no se puedan extrapolar a NPs de mayor tamaño.

Además, la principal ventaja del modelo de NPs para metales de transición es que a pesar de ser un modelo con un tamaño computacionalmente tratable presenta una *escalabilidad con el tamaño* (SwS, *Scalability with Size*), que consiste en que las propiedades observables en NPs suficientemente grandes varían suave y monótonamente con el tamaño de NP.[151,177,178] De hecho, se ha demostrado que propiedades tales como la energía cohesiva, la distancia interatómica promedio de NPs (cubo)-octaédricas de Pd_N, Cu_N, Ag_N y Au_N[179–181] y también el centro de la banda *d* de NPs de Pd_N[182] dependen linealmente respecto la inversa del radio efectivo de la

[6] El efecto de la nanoestructuración en las propiedades del óxido de cerio se discute extensamente en el Capítulo 5.

nanopartícula, $N^{-1/3}$. También se ha demostrado que las energías de adsorción de CO en las caras de nanopartículas tridimensionales de Pd_N varían muy ligeramente con el tamaño para un número de átomos **N** igual o superior a 70 (Figura 8.5).[157,182] Por consiguiente, sabiendo las relaciones de escalabilidad uno puede extrapolar las propiedades de nanopartículas tratables computacionalmente y compuestas de 100-200 átomos a las de mayor tamaño constituidas por unos cuantos miles de átomos, típicamente presentes en los catalizadores modelo.

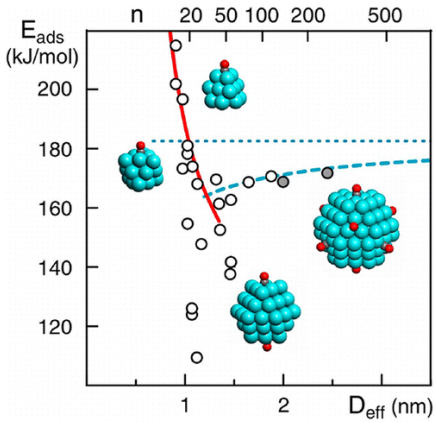

Figura 8.5. Dependencia de las energías de adsorción del CO en las caras {111} de nanopartículas de Pd en función del tamaño de nanopartícula.[182] Pd se muestra en cian, C en gris, O en rojo.

8.4 Nanopartículas de Metales de Transición no Soportadas

Objetivos de esta sección

Actualmente existe un número limitado de teóricos trabajando en el entendimiento de los nanoefectos dentro del marco de NPs de diferentes tamaños con propiedades SwS, así que todavía existen muchos efectos básicos aún por descubrir. Por otro lado, a pesar de que los estudios indicados han conducido a muchos avances en este campo, la mayoría de estos estudios se basan en ejemplos o pruebas conceptuales, es decir, carecen de una sistemática. Por lo tanto, es importante comprobar hasta qué punto los avances ya descubiertos son transferibles a otras especies u otros procesos. Esto dos aspectos, es decir, la exploración de nuevas formas de cómo la nanoestructuración puede afectar a las propiedades de NPs SwS no soportadas, así como un estudio sistemático de los nanoefectos ya descubiertos, son los objetivos de la investigación presentada en este capítulo.

De entre muchas posibilidades se escogió el Pd nanoparticulado para realizar la investigación de forma detallada, ya que este material y sus aleaciones son indispensables en catálisis heterogenia. Por ejemplo, el Pd cataliza la reacción de desplazamiento de agua en gas (*water gas shift*),[214] la formación de enlaces C-C[215] y varias reacciones de hidrogenación y deshidrogenación.[216] Además el Pd es capaz de catalizar la descomposición u oxidación de muchos hidrocarburos tales como el metano[7,217] o el metanol,[218] que pueden tener aplicaciones importantes como portadores de energía.

Adsorción en las aristas de las nanopartículas

Posiblemente la diferencia más obvia entre las nanopartículas y las superficies de Pd es la presencia de átomos con un número de coordinación inferior en las aristas de las primeras. En principio, se puede esperar que estos átomos formen enlaces más fuertes con las especies adsorbidas que el enlace que formaría el adsorbato con los átomos situados en las caras, debido a un mayor número de algo semejable a los orbitales desaparejados.

Para investigar este fenómeno, se realizó un estudio exhaustivo de la adsorción de los intermedios formados en la descomposición de metanol, es decir, especies CH_xO_y (x = 1–3, y = 0–1) en diversos lugares de adsorción de una nanopartícula SwS de 79

átomos de Pd (Figura 8.6 y Sección 3.1). Este conjunto particular de compuestos adsorbidos fue elegido debido a lo siguiente: 1) aparecen en muchas reacciones catalizadas por Pd, 2) se realizó previamente un estudio computacional y menos detallado de estas especies (utilizando el código de Paragauss) en dicha nanopartícula, que puede ser usados como referencia.[219]

Se encontró que la mayoría de las especies estudiadas eran más estables cuando se adsorbían en los átomos de las aristas de la NP de Pd_{79} en comparación con la adsorción en los átomos situados en las caras {111} de la nanopartícula. La única excepción fue el radical CH, que se une a un hueco tricoordinado de Pd en el centro de una cara con una energía 0.12 eV más fuerte que los mismos sitios tocando a las aristas. La estabilización más fuerte en las aristas se dio para los compuestos que formaban enlaces O-Pd, tales como CH_3O, CH_2O y CHO, con valores de entre 0.35 y 0.55 eV. Las especies metoxi cambiaron sus sitios preferenciales pasando de adsorberse en huecos tricoordinados en las caras a puentes bicoordinados en las aristas. La estabilización de las especies quimisorbidas a través de enlaces C-Pd fue de ~0.2 eV para CH_2OH, CH_3 y CH_2. La magnitud de esta estabilización puede afectar significativamente los perfiles de energía de varias reacciones que tienen lugar en catalizadores basados en nanopartículas de Pd.

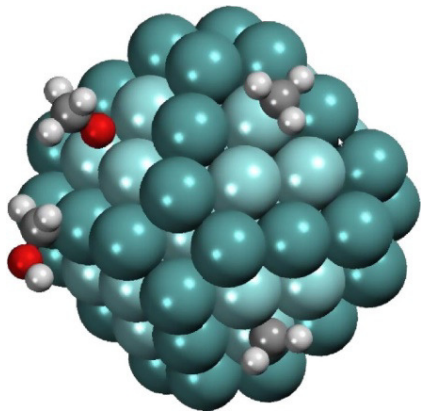

Figura 8.6. Nanopartícula de Pd_{79} con los radicales CH_2, CH_3, CH_2OH y CH_3O adsorbidos en ella. Los átomos de Pd se muestra en cian, H – blanco, C – gris, O – rojo. Los átomos más oscuros son los localizados en las aristas de la nanopartícula.

Actividad catalítica de las aristas de nanopartículas

Es esperable que las aristas de las nanopartículas no sólo cuenten con propiedades de adsorción diferentes, sino que la actividad catalítica en estos lugares de adsorción también varíe con respecto a los átomos en las caras de las nanopartículas o en las terrazas de los monocristales. Sin embargo, ya que los estudios que implican la búsqueda de estados de transición son computacionalmente más caros que los estudios de estructuras localmente estables, la existencia de estudios de propiedades catalíticas en las aristas de las nanopartículas es escasa. Un ejemplo es el estudio realizado por Viñes *et al.* donde investigaron la descomposición de metano en los bordes de la nanopartícula de Pt_{79} y se extendió el estudio, además, a la adsorción de metano sobre la superficie de Pt(111).[150] Una vez más se encontró que la actividad catalítica de los bordes de las nanopartículas de Pt es significativamente mayor que la actividad de las superficies (111), cosa que se confirmó mediante experimentos de haces moleculares.

Curiosamente, la actividad de las nanopartículas de Pd y Pt para la oxidación del metano depende de manera muy diferente con su tamaño.[200] Mientras que la frecuencia de repetición en nanopartículas de Pt permanece constante para los sistemas más grandes de 3 nm, aumenta con el tamaño de la nanopartícula hasta los 22 nm para nanopartículas de Pd. Este hecho hace que resulte muy interesante investigar si las nanopartículas de Pd y Pt se comportan de manera diferente en una reacción simple, como la descomposición del metano, que también puede llevarse a cabo utilizando catalizadores de Pd.[222] Para responder a esta pregunta se llevó a cabo un estudio computacional de esta reacción en las aristas de nanopartículas de 79 átomos de Pd y la superficie Pd(111) (Sección 3.2), y sus resultados se compararon con los obtenidos en Pt por Viñes *et al.*[150]

Curiosamente, el perfil de energía de reacción para la descomposición de metano calculada sobre Pd(111) era bastante similar al calculado por Viñes *et al.* sobre Pt(111).[150] Concretamente, la diferencia entre las barreras para la etapa limitante, la transformación de metano en metilo, fue sólo 0.05 eV, siendo la nanopartícula de Pt ligeramente más activa que la de Pd. Otras energías de activación calculadas presentaban diferencias mínimas, inferiores a 0.1 eV, y favorables a la superficie de Pt(111). A pesar de la aparente similitud entre las actividades catalíticas de las superficies {111} de Pd y Pt, hubo una diferencia significativa entre los perfiles de

energía de reacción calculados en las aristas de nanopartículas de Pd_{79} y Pt_{79}. Las energías de activación de las dos primeras etapas de la reacción disminuyeron a ~0.55 eV en el caso de Pd_{79} y ~0.3 eV para Pt_{79}. Por el contrario, las dos últimas barreras en la descomposición del metano son 0.23 y 0.07 eV más elevadas en Pt_{79} que en Pd_{79}. Por lo tanto, la nanoestructuración afecta a la actividad catalítica de ambos metales de manera cualitativamente similar (ambas nanopartículas son más activas que los monocristales), pero cuantitativamente diferente. Esta investigación contribuyó a la comprensión de la diferente la actividad de las nanopartículas de Pd y Pt, dependiendo de su tamaño, para la oxidación de metano.

Actividad catalítica de nanopartículas en función de las condiciones de reacción

Otra cuestión importante con relación a NPs SwS es si las propiedades de las caras de las NPs se mantienen iguales a las propiedades de los respectivos monocristales, o si cambian bajo ciertas condiciones. En principio, la definición de la escalabilidad con el tamaño requiere la posibilidad de *extrapolar* las propiedades de las caras de la NP a las caras de los monocristales, no a la similitud cuantitativa entre sus propiedades. Por el contrario, si la diferencia calculada entre NPs con caras de *e.g.* ~1.5 nm y sus respectivos monocristales es muy grande (aunque decayendo monótonamente con el tamaño de la NP), ésta puede ser un factor notable para NPs de pocos nm usadas en procesos catalíticos comunes.

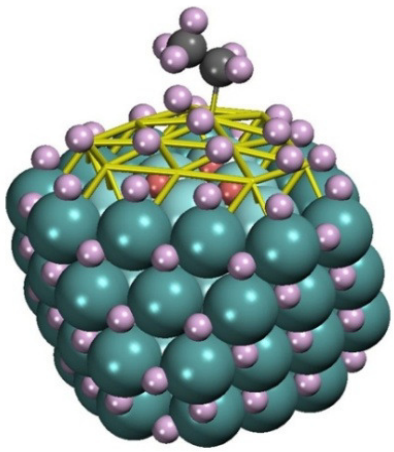

Figura 8.7. Etilo adsorbido en una nanopartícula de Pd_{79} con la superficie cubierta de H y algunos átomos de H situados también en la región bajo la superficie. Los átomos de Pd se presentan en cian, el H adsorbido en Pd o pertenecientes al etilo – rosa, H absorbidos – rojo, C – gris.

Uno de los fenómenos que pueden causar tales diferencias entre las caras de las NPs y los monocristales es la formación de hidruros cercanos a la superficie,[66,223,224] carburos,[186,225,226] (así como sus mezclas[52,227,228]) y óxidos[221,229,230] o las correspondientes impurezas bajo superficie.[185,231] Todos estos procesos ocurren fácilmente en catalizadores de Pd bajo diferentes condiciones de reacción y se conoce que son facilitados por la nanoestructuración del Pd.[186,232] En concreto, la hidrogenación de alquenos mantenida en el tiempo (especialmente el segundo paso de hidrogenación) es posible sólo en nanopartículas de Pd que contienen H subsuperficial.[52]

Con el fin de obtener un entendimiento a nivel atómico de la química involucrada, se realizó un estudio sistemático de la hidrogenación de etilo en caras {111} de Pd_{79} y Pd(111) a diferentes cantidades de H adsorbido y absorbido presente en el sistema (Figura 8.7 y Sección 3.3)

A recubrimientos bajos de H se encontró que la hidrogenación de etilo en monocristales de Pd(111) pasa por una barrera (de Gibbs) de 0.5 eV, lo que resulta en una constante de velocidad de la reacción de $k_{298} = 2\times10^{4}$ s^{-1}. La saturación de la superficie con H aumentó la constante a 2×10^{7} s^{-1} y la adición de un átomo de H en cada sitio tetraédrico subsuperficial (*tss'*) la aumentó a 2×10^{8} s^{-1}. Cuando se puso más H absorbido en la segunda capa de la subsuperficie, k_{298} continuó incrementando hasta 4×10^{9} s^{-1}. Así pues, incluso sobre la superficie de Pd(111) la constante de velocidad depende fuertemente de la concentración de H en el sistema. En la NP de Pd_{79} hay una dependencia similar pero mucho más acentuada de la k_{298} con respecto a la concentración de H en el sistema. La constante de velocidad aumentó según $2\times10^{4} \rightarrow 5\times10^{7} \rightarrow 8\times10^{11}$ s^{-1} para un bajo recubrimiento en H → recubrimiento completo de las caras {111} por H → llenando la capa subsuperficial con H. Vale la pena señalar la similitud de las constantes de reacción en Pd_{79} y Pd(111) sin H en la subsuperficie y cómo la formación de hidruros cercanos a la superficie elimina esta similitud. En un primer lugar esto significa que la diferencia entre las actividades catalíticas de monocristales y nanopartículas de Pd no es un artefacto de la simulación. En segundo lugar muestra la alta sensibilidad de las propiedades de la NP a las condiciones de reacción, lo que puede ser usado para modular la actividad catalítica.

Estrucutura de nanopartículas bimetálicas

Otra forma común de modificar las diversas propiedades de los catalizadores con metales de transición es hacer una aleación con otro metal. En algunos casos la relación entre los dos componentes puede agregar otro grado de libertad al sistema y permite modular la actividad y/o selectividad del catalizador en un proceso en particular. [67,240] Es muy importante saber el ordenamiento químico (distribución) de ambos componentes dentro de una nanopartícula bimetálica y, en particular, la estructura y composición de los sitios de superficie disponibles para una reacción. Sin este conocimiento es imposible realizar un estudio computacional de su actividad química y catalítica. Un método para analizar estas tendencias de manera cuantitativa podría arrojar luz sobre la naturaleza de la unión en diferentes aleaciones.

Para lograrlo, se ha propuesto un nuevo método basado en Hamiltonianos topológicos, H_{TOP}, (Sección 3.4). Estos Hamiltonianos tienen en cuenta la segregación de uno u otro de los elementos en caras, aristas y esquinas, así como la formación de enlaces heteroatómicos. Los parámetros energéticos en estos Hamiltonianos (más tarde conocidos como *descriptores*) fueron optimizados de forma individual para cada sistema en particular, basándose en resultados de cálculos de estructura electrónica de NPs con un determinado tamaño, forma y composición. Esto permitió una mayor precisión de los Hamiltonianos topológicos comparados con potenciales interatómicos optimizados usando una mayor cantidad de parámetros de ajuste.

El método de los Hamiltonianos topológicos se aplicó a la optimización del ordenamiento químico en nanopartículas $Pd_{70}X_{70}$ (X = Au, Ag, Cu y Zn), así como NPs de Pd_YAu_{79-Y} y Pd_YAu_{140-Y} de ~ 1.6 nm de tamaño. Las aleaciones de Pd-Au y Pd-Ag adoptan estructuras de núcleo recubierto con una segregación de Pd en el interior de las NPs (Figura 8.8). Las principales contribuciones a la energía de estas aleaciones provienen de la mayor estabilidad de los átomos de Au o Ag en sitios de baja coordinación (aristas y bordes), según se obtiene por los valores de los correspondientes descriptores. Se encontró que los enlaces heteroatómicos son de menor importancia para el ordenamiento químico. Por otra parte, los átomos de Cu son más estables en el interior de las nanopartículas de Pd-Cu que en su superficie. Sin embargo, la energía de los enlaces Pd-Cu heteroatómicos es suficiente para conducir una fracción significativa de los átomos de Cu a las caras, esquinas y aristas de las nanopartículas. El homótopo

energéticamente más estable de $Pd_{70}Cu_{70}$ tenía una estructura tipo matrioska o cebolla con una capa superficial rica en Pd, una subsuperficie rica en Cu y un núcleo de NP casi enteramente compuesto de Pd. El último caso, Pd-Zn, cuenta con enlaces heteroatómicos muy fuertes, que esencialmente definen el ordenamiento químico en este compuesto. El homótopo de $Pd_{70}Zn_{70}$ con el mayor número posible de enlaces heteroatómicos tenía una estructura con Pd y Zn átomos dispuestos en capas perpendiculares a la dirección [001] como en la estructura cristalográfica de PdZn.

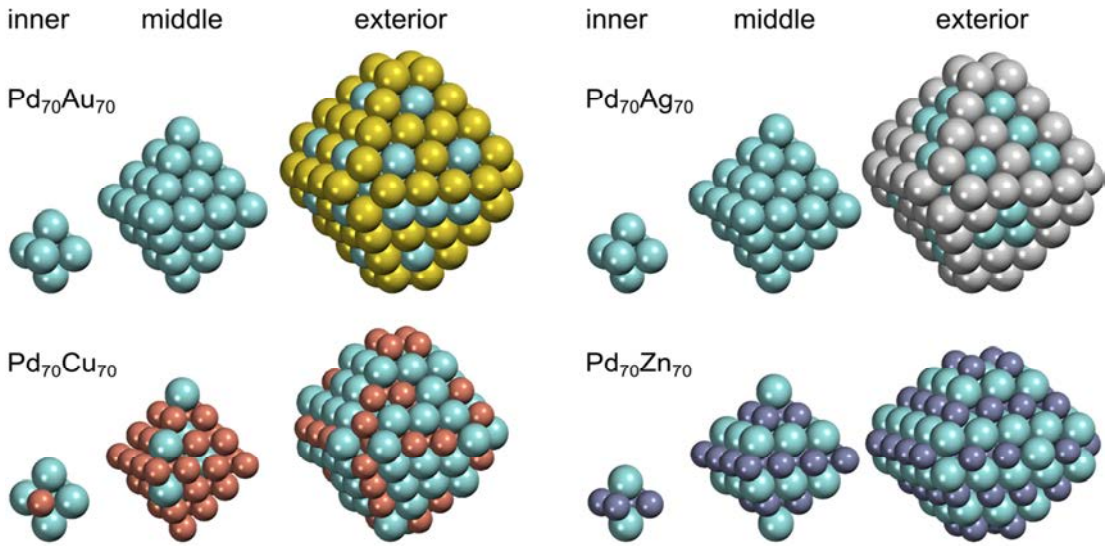

Figura 8.8. Capa interior, media y exterior de nanopartículas de $Pd_{70}X_{70}$ con un ordenamiento químico optimizado. Los átomos de Pd están representados en cian; Au – oro, Ag – plata, Cu – cobre, Zn – azul oscuro.

Con todo lo anteriormente expuesto, los Hamiltonianos topológicos parecen ser lo suficientemente potentes como para predecir de manera rigurosa los ordenamientos químicos en nanopartículas bimetálicas de diferentes tamaños. Se espera que este método permita una extensión del concepto de escalabilidad con el tamaño en nanoaleaciones y que haga posible estudios sistemáticos de estos sistemas del mismo modo que los estudios realizados en sus respectivas NPs monometálicas.

8.5 Nanopartículas de Metales de Transición Soportadas

Sólo es posible preparar y estudiar experimentalmente clústeres no soportados muy pequeños, mientras que las NPs de mayor tamaño tienen que ser estabilizadas en un soporte o en una solución. Estas NPs se utilizan para una gran variedad de aplicaciones. Actualmente existen una gran variedad de soportes para las NPs de metales de transición, mayormente basados en carburos u óxidos. Estos últimos son particularmente adecuados para su uso en condiciones de reacción duras y oxidantes.

Es harto conocido que el rendimiento de un catalizador de un metal de transición depende en gran medida del tipo de soporte que se utiliza (Figura 8.9).[19,246,247] Sin embargo es muy difícil de identificar la razón por la que las propiedades del catalizador cambian. De entre otros soportes, los óxidos reducibles tales como el CeO_2,[252–254] el TiO_2[154,255,256] o el Fe_2O_3,[32,34,206] son, por lo general, los que mayormente modifican las propiedades de las NPs soportadas. Se cree que otros soportes de óxido, como el MgO, el Al_2O_3 y, en menor medida, el SiO_2, tienen una influencia menor en los procesos catalíticos.[246,257,258] La única manera de verificar esta atribución es comparar la actividad de las nanopartículas soportadas en MgO o Al_2O_3 a la de NPs no soportadas del mismo tamaño. Esto último, sin embargo, es experimentalmente inaccesible y sólo se puede tratar en simulaciones (véase el Capítulo 3).

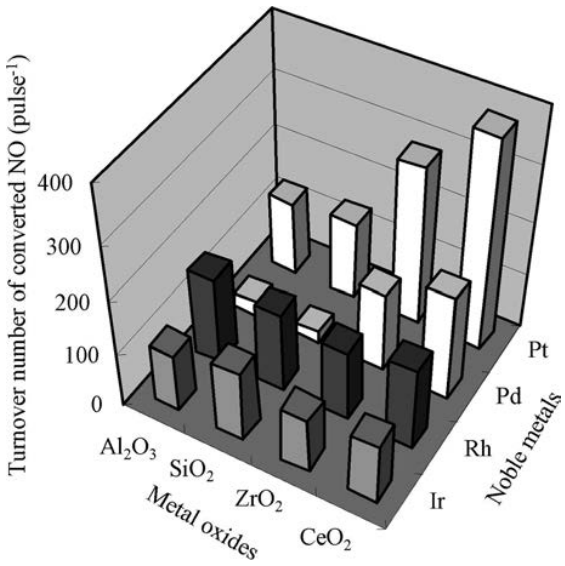

Figura 8.9. Efecto de diversos soportes óxidos sobre la actividad catalítica de metales de transición en la reducción de NO.[248] El Al_2O_3 y el SiO_2 se consideran inactivos, mientras que el ZrO_2 y el CeO_2 son capaces de alterar la actividad de algunos metales.

Es muy importante cuantificar el efecto del soporte en las propiedades de las NPs desde un punto de vista metodológico, ya que esto ayudará a responder a las siguientes preguntas interrelacionadas: ¿Se puede confiar en los resultados obtenidos para nanopartículas no soportadas? ¿Es siempre necesario considerar el soporte en estudios computacionales de NPs? ¿Cuán de adecuado es considerar nanopartículas SwS no soportadas como modelos para representar catalizadores modelo de NPs?

Los estudios en esta sección tratan de evaluar el papel del soporte óxido en las propiedades físicas, de adsorción y de absorción de las NPs de metales. Siguiendo la estrategia general adoptada en esta tesis nos centramos en nanopartículas de tamaño de alrededor de 1 nm o más que presentan una estructura similar a la estructura cristalina interna del material, ya que sólo éstas presentan escalabilidad con el tamaño.

En esta sección se considera no sólo la NP de Pd del Capítulo 3, sino también nanopartículas de Pt. La razón es que en la Sección 3.3 se mostró que las nanopartículas de Pt se comportan de forma similar a las de Pd en la hidrogenación de etilo, mientras que en la Sección 3.2 se discutió la diferencia entre las actividades de las NPs no soportadas de Pd y Pt en la descomposición del metano. Por lo tanto, es muy interesante ver si las NPs de estos dos materiales se verían afectadas de diferentes maneras por la presencia de un soporte de óxido. Además, de manera similar al Pd, el Pt es muy importante en muchas aplicaciones de catálisis heterogénea,[214,269,270] especialmente en pilas de combustible.[271–273] Dado que el H está presente en la mayoría de las reacciones catalizadas por Pd y Pt, es especialmente importante estudiar la adsorción y la absorción de H en éstos (visto en la Sección 3.3). En los estudios de las Secciones 4.2 y 4.3 se intenta aclarar el efecto del soporte óxido en la interacción del H con las NPs de Pd y Pt soportadas sobre MgO(100), otro de los objetivos de esta sección.

La superficie (100) de MgO se eligió como soporte para estas NPs por ser muy iónica, químicamente inerte y por las siguientes ventajas: 1) se puede esperar que el efecto del MgO(100) sea muy pequeño, por lo que este óxido puede servir como referencia para otros soportes; 2) el MgO tiene una sola fase cristalina y su superficie (100) tiene una estructura muy simple y bien caracterizada, que no es el caso, por ejemplo, en Al_2O_3 o SiO_2; 3) se ha hecho un gran esfuerzo experimental en caracterizar las formas de las nanopartículas Pd y Pt soportadas en MgO(100), así como en las respectivas interfaces entre las nanopartículas y el soporte.[38,40,274]

Efecto del óxido sobre la estructura y las propiedades físicas de las nanopartículas metálicas soportadas

Realizar una optimización global de estas NPs metálicas sobre un soporte es hoy en día todavía demasiado costoso, por lo que se utilizaron los potenciales interatómicos de la Ref. 276. Después de una evaluación de las diversas estructuras obtenidas, aquellas NPs de menor energía de entre 49 y 155 átomos que mantenían una disposición cúbica centrada en las caras (*fcc*) sin defectos de apilamiento fueron recalculadas con DFT. Se obtuvieron así modelos representativos de NPs de Pd y Pt sobre MgO(100) (Figura 8.10). Los estructuras son bastante similares a las formas de las NPs de Pd y Pt observadas experimentalmente (de mayor tamaño) soportadas sobre MgO(100).[38,278,279]

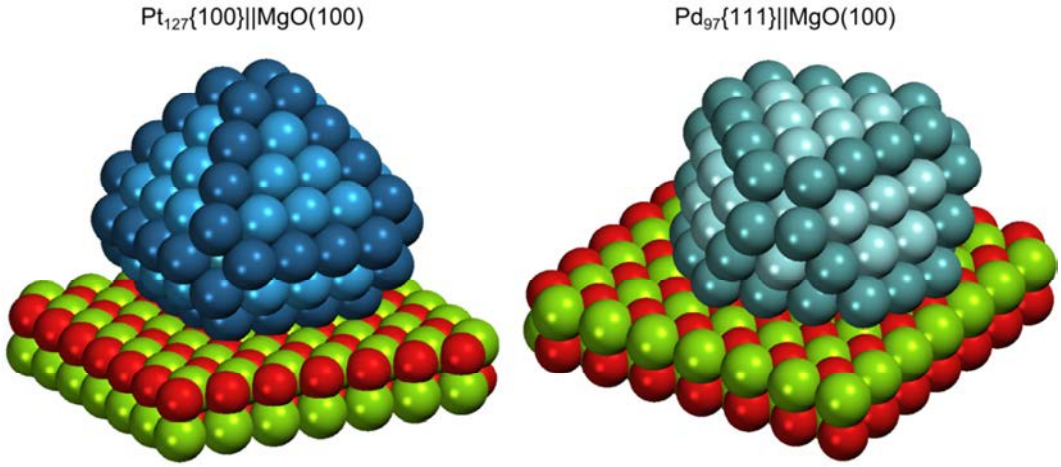

Figura 8.10. Estructuras energéticamente favorables de NPs de Pd y Pt en MgO(100). Los átomos de Pd se muestran en cian, Pt – azul, Mg – verde, O – rojo. Los átomos oscuros representan las aristas de las NPs.

Una vez se determinaron modelos realistas para las NPs de Pd y Pt soportadas en MgO(100) fue posible realizar un análisis de sus propiedades físicas para ver cómo éstas eran afectadas por la interacción con el soporte. En primer lugar se demostró que el soporte no afecta a la estructura geométrica de las nanopartículas —las diferencias entre las distancias interatómicas en NPs soportadas y no soportadas eran apenas visibles. En segundo lugar, el efecto del MgO en la estructura electrónica de las NPs de Pd y Pt soportadas parecía ser insignificante. Con todo, el efecto del soporte MgO(100) sobre las propiedades físicas de las NPs de Pd y Pt se encontró que era muy pequeño. A su vez esto sugiere que estas propiedades pueden ser simuladas con fiabilidad utilizando modelos de nanopartículas no soportadas.

Efecto del óxido en las propiedades de adsorción y absorción de nanopartículas soportadas

Usualmente las propiedades de adsorción de un sitio son más sensibles a su entorno que sus propiedades físicas, como la densidad de estados de los átomos que componen el sitio y la distancia entre ellos. Así, el leve efecto del MgO(100) sobre las propiedades de NPs de Pd y Pt, descritas en la Sección 4.1, no necesariamente significa que el efecto del soporte sobre las propiedades de adsorción sea también despreciable.

Se investigó en la Sección 4.2 la capacidad del MgO(100) para modificar las propiedades de adsorción y absorción de NPs de 1.5 nm de Pd_{127} y Pt_{127} usando las interacciones H-Pd y H-Pt como ejemplo. Se ha observado experimentalmente que las NPs de Pd se hidratan más rápido que los monocristales de Pd.[235,283,284] Al mismo tiempo sólo se han encontrado cantidades despreciables de H sobre Pt(111)[53] y sólo un artículo experimental informa de una pequeña adsorción de H sobre NPs de Pt.[235]

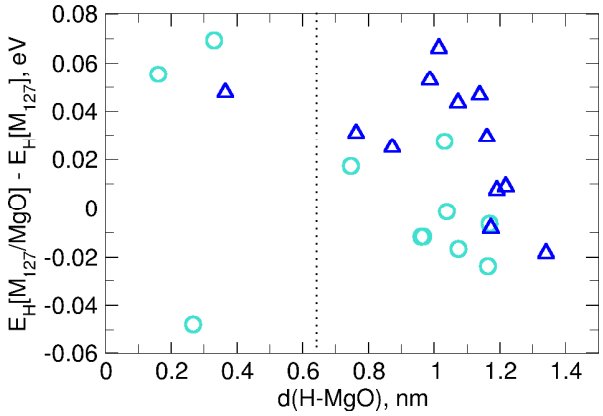

Figura 8.11. Efecto del soporte MgO(100) sobre las energías de adsorción y absorción de H en Pd_{127} (círculos turquesa) y Pt_{127} (triángulos azules) dependiendo de la distancia H-MgO. Las líneas punteadas separan los datos en caras inferiores o superiores.

Se encontró que el hidrógeno se adsorbe 0.08 eV más fuertemente en nanopartículas de Pd_{127} que en la superficie de Pd(111). Para el Pt la diferencia entre las energías de adsorción de la nanopartícula y el monocristal fue de 0.18 eV. Se encontró que la energía de unión dentro de la región de la subsuperficie era casi isoenergética con respecto a $½H_2$ y 0.04 eV más fuerte en Pd_{127} que sobre Pd(111). También se obtuvo que la absorción de H sobre Pt(111) era notablemente endotérmica, 0.43 eV, en donde la energía requerida para la absorción de H fue de 0.13 eV sobre NPs de Pt.

Se encontró que el efecto del soporte Mg (100) sobre las propiedades de adsorción y absorción de nanopartículas de Pd y Pt es muy pequeño, como mucho 0.07 eV (Figura 8.11). En muchos casos el efecto del soporte se limitó a la desestabilización local de sitios NP-óxido en la interfaz causados por la repulsión estérica entre H y MgO (100). En definitiva se encontró que el efecto del soporte en las propiedades de las nanopartículas de Pd y Pt fue más pequeño que la nanoestructura en sí misma.

Efecto del recubrimiento superficial en las propiedades de absorción de las nanopartículas soportadas

Los estudios descritos en la Sección 4.2 proporcionan una importante perspectiva en cuanto a la absorción de H en Pd y Pt nanoestructurado; sin embargo no aborda la situación experimental de manera exacta. Debido a que la absorción de H en Pd y Pt está energéticamente menos favorecida que la adsorción de H, ésta se realiza sólo cuando todos los sitios de la superficie están saturados por H (Figura 8.12). Según los resultados presentados en la Sección 4.2 es necesario realizar un estudio más realista (Sección 4.3), debido a que estos resultados no son suficientes para explicar la gran facilidad de absorción de H en NPs de Pd comparado con su monocristal, tal y como se observa experimentalmente.

Se encontró que el efecto de H superficial sobre la absorción de hidrógeno es más importante y cualitativamente igual sobre NPs de Pd y Pt y monocristales. Principalmente, el H adsorbido sobre la superficie M(111) (M = Pt o Pd) desestabiliza al hidrógeno absorbido en las posiciones de la subsuperficie ~0.13 eV, pero estabiliza el hidrógeno absorbido más profundamente en la nanopartícula ~0.08 eV. En las NPs de M_{127} el efecto desestabilizante del H adsorbido es de alrededor de 0.06 eV, *i.e.* un tanto menor a la superficie extendida (111), donde el efecto estabilizante está reforzado respecto a las nanopartículas por ~0.19 eV. Estos dos hallazgos muestran una mayor propensión de las nanopartículas de Pd y Pt a absorber H comparado con sus respectivos monocristales. En el caso de las nanopartículas de Pd la estabilización del H profundamente absorbido debido a las especies superficiales es suficiente para hacer de la absorción de H un paso un tanto exotérmico, por ~0.11 eV. El incremento en la exotermicidad del H absorbido permite una rápida formación de H absorbido en nanopartículas de Pd en condiciones normales de catálisis.

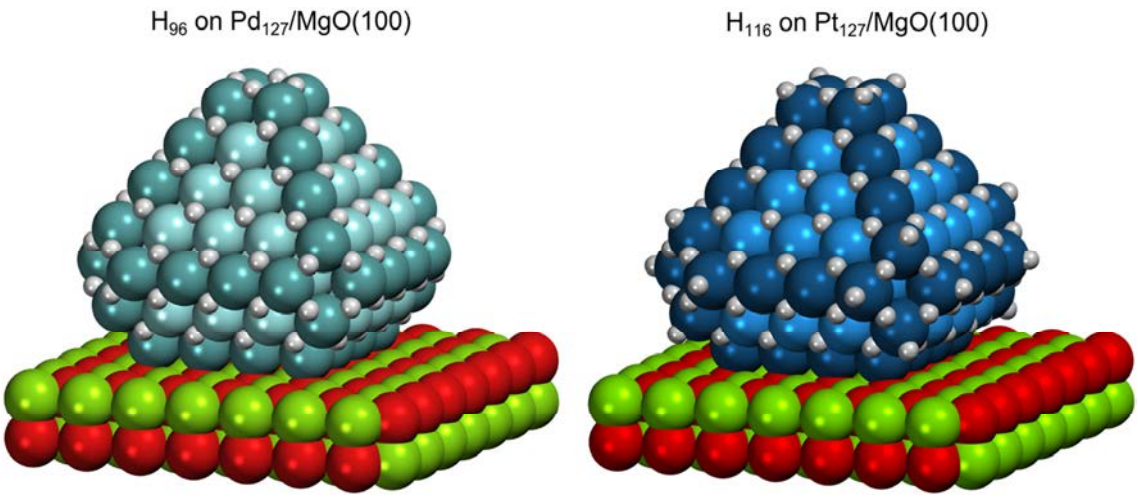

Figura 8.12. NPs de Pd y Pd soportadas en MgO(100) cubiertas por H. Las NPs de Pt son capaces de adsorber más hidrógeno debido a una mayor densidad de caras {100} situadas en las esquinas. Los átomos de Pd se muestran en azul turquesa, Pt – azul, Mg – verde, O – rojo. Los átomos más oscuros se localizan sobre las aristas de las NPs.

Se analizó el efecto de los hidrógenos superficiales sobre la distribución de las distancias interatómicas y la estructura electrónica de las nanopartículas de Pd y Pt soportado, en analogía con las consideraciones de la Sección 4.1. El promedio de las distancias interatómicas en las nanopartículas M_{127} incrementa un ~2% tras la saturación de la superficie por H y la densidad de estados proyectados sobre los átomos metálicos superficiales se mueve a menores energías unas décimas de eV.

Por tanto los efectos del H superficial en las propiedades físicas y de absorción en las nanopartículas de Pd y Pt es claramente mayor que el del soporte MgO(100). De estos hallazgos se puede concluir que en estudios catalíticos computacionales es mucho más importante precisar el modelo de especies co-adsorbidas sobre el catalizador nanoestructurado que precisar el soporte químicamente inerte.

8.6 Escalones en Superficies

En la escala subnanométrica, la rugosidad de una superficie se pone de manifiesto con la presencia de escalones entre terrazas más o menos extensas (Figura 8.13). De forma similar a lo que ocurre en los bordes de las nanopartículas, dichos escalones contienen algunos átomos con un número de coordinación más bajo de lo habitual, y, por tanto, constituyen otra forma importante de nanoestructuración intrínsecamente presente en la mayoría de muestras. En catálisis heterogénea, los escalones atómicos son ubicuos; en consecuencia, uno esperaría que también lo fueran en nanopartículas que actúen de catalizador[26,293,294] y en sus soportes.[295,296] En ambos casos, los escalones presentan a menudo una estructura electrónica diferente[289,297] debido a la presencia de átomos con un número de coordinación bajo. Por consiguiente, los escalones normalmente son capaces de adsorber distintas especies de forma más fuerte de lo que lo harían las terrazas.[295,298] A su vez, en materiales catalíticos, muchas reacciones ocurren preferentemente en escalones.[26,25,301] Por otro lado, los escalones en soportes podrían actuar como centros de nucleación de nanopartículas activas catalíticamente y, por tanto, podrían tener un efecto en las reacciones catalizadas.[296,302]

Dióxido de cerio en catálisis heterogénea

Con el fin de lograr una mayor coherencia en la tesis, se ha investigado los escalones de un único material, a saber, el CeO_2. Dichos escalones se han estudiado desde varios puntos de vista. El dióxido de cerio ha sido el sistema escogido para llevar a cabo un estudio detallado porque es relativamente abundante en la Tierra y tiene muchas y diversas aplicaciones,[303–305] entre las cuales cabe destacar su uso como soporte *activo* en catálisis heterogénea.[168,218,253] La capacidad que tiene el óxido de cerio para ejercer una influencia en reacciones catalíticas se atribuye normalmente a su capacidad de reducción, es decir, a la capacidad que tiene el cerio de adoptar dos estados de oxidación distintos (Ce^{3+} y Ce^{4+}) en óxidos CeO_x de diferente estequiometría.[59,309,310] Esta capacidad permite que los óxidos de cerio puedan actuar de reguladores de la cantidad de átomos de O[12,311,312] o que puedan participar en procesos de transferencia de carga en clústeres metálicos soportados.[261,313,314] La nanoestructuración del óxido de cerio es particularmente importante para sus propiedades[55,315] y, a menudo, conlleva una mejora en la actividad de los catalizadores que contienen dicho compuesto.[20,316,317] Algunos estudios relacionan la mayor actividad

del óxido de cerio nanoestructurado con su mayor capacidad de reducción, que se manifiesta en una menor energía de formación de vacantes de átomos de oxígeno $E_f(O_{vac})$.[55,318,319]

Debido a que los escalones en superficies constituyen también una forma de nanoestructuración, cabría esperar que dichos escalones presentes en la superficie más estable del dióxido de cerio, $CeO_2(111)$,[320,321] desempeñaran un papel importante en catálisis. Estos escalones son muy importantes, por ejemplo, en catalizadores del tipo Au/CeO_2,[20,271] puesto que actúan como centros de nucleación de nanopartículas de Au.[169,296] Los procesos de nucleación de nanopartículas de Rh y Pd también tienen lugar en los escalones de CeO_2.[322]

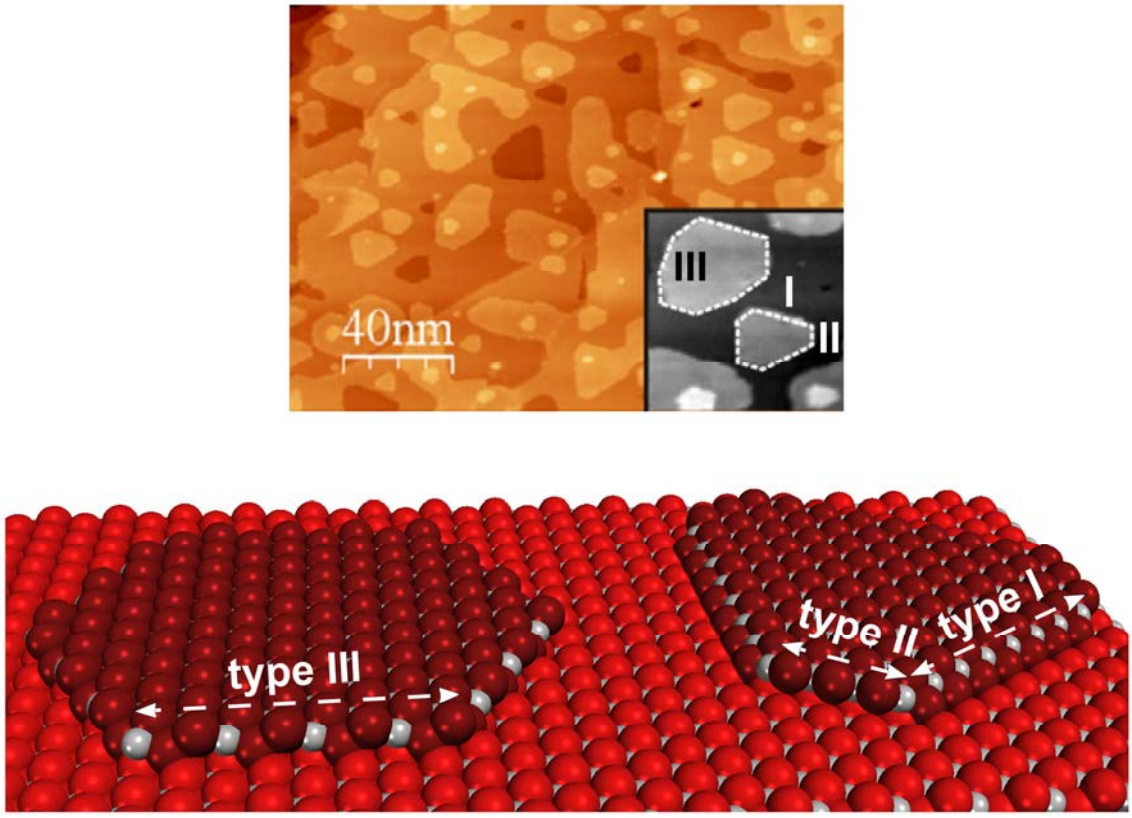

Figure 8.13. Imagen de microscopía de efecto túnel (STM) de un modelo atómico de $CeO_2(111)$ producido de forma controlable mediante recocido a altas temperaturas. Las islas nanométricas en la superficie muestran tres tipos distintos de escalones. El recuadro de la imagen muestra un área de 30×30 nm. Los átomos de oxígeno se muestran en rojo y los iones Ce en gris.

Objetivos de esta sección

Los estudios descritos en esta sección tienen como objetivo el proporcionar una caracterización de varias propiedades intrínsecas de los escalones de $CeO_2(111)$, es decir, de propiedades importantes para casi cada proceso que ocurra en ellos. Este objetivo implica, en primer lugar, determinar de forma unívoca las estructuras atómicas de los distintos tipos de escalones observados en $CeO_2(111)$, factor esencial para estudios posteriores. En segundo lugar se ha evaluado la estructura electrónica y la estabilidad energética de los distintos tipos de escalones. La estructura electrónica es especialmente interesante en vista al carácter iónico del CeO_2, que debería producir escalones con una polaridad no compensada. Finalmente, ya que muchas de las propiedades del óxido de cerio tienen su origen en su capacidad de reducción, se ha evaluado la capacidad que tienen estos escalones para formar vacantes de oxígeno, O_{vac}.

Estructura atómica y electrónica de los escalones en $CeO_2(111)$

En la Sección 5.1 los escalones en films de $CeO_2(111)$ o en Ru(0001) se prepararon mediante un recocido a altas temperaturas. Para temperaturas menores de 1000 K se observó que aparecían en la superficie islas hexagonales de tamaño nanométrico bordeadas por escalones perpendiculares a las direcciones <211>. Para temperaturas mayores de 1000 K, se observaron islas de forma hexagonal, y con escalones perpendiculares a las direcciones <110>.

Con el fin de determinar las estructuras atómicas de los escalones de $CeO_2(111)$, se simularon imágenes STM bajo la aproximación de Tersoff-Hamann a distintos voltajes, y se compararon con los experimentos.[338] Se observó que los escalones tipo I aparecen muy brillantes para voltajes bajos, de forma similar a lo que ocurre en las islas nanométricas producidas a T < 1000 K (Figure 8.14). Los escalones tipo II no deberían ser brillantes para ningún voltaje, como lo son los bordes cortos en los experimentos. En referencia a los escalones perpendiculares a las direcciones <110>, las simulaciones predicen que éstos tendrían que ser brillantes a voltajes elevados, resultado que encaja con las imágenes de conductancia diferencial para las islas nanométricas obtenidas para T > 1000 K. Finalmente, las simulaciones indican que los escalones de tipo II* tendrían que mostrarse de una forma extremadamente brillante en los experimentos incluso a voltajes bajos, aunque estos escalones brillantes nunca han sido observados.

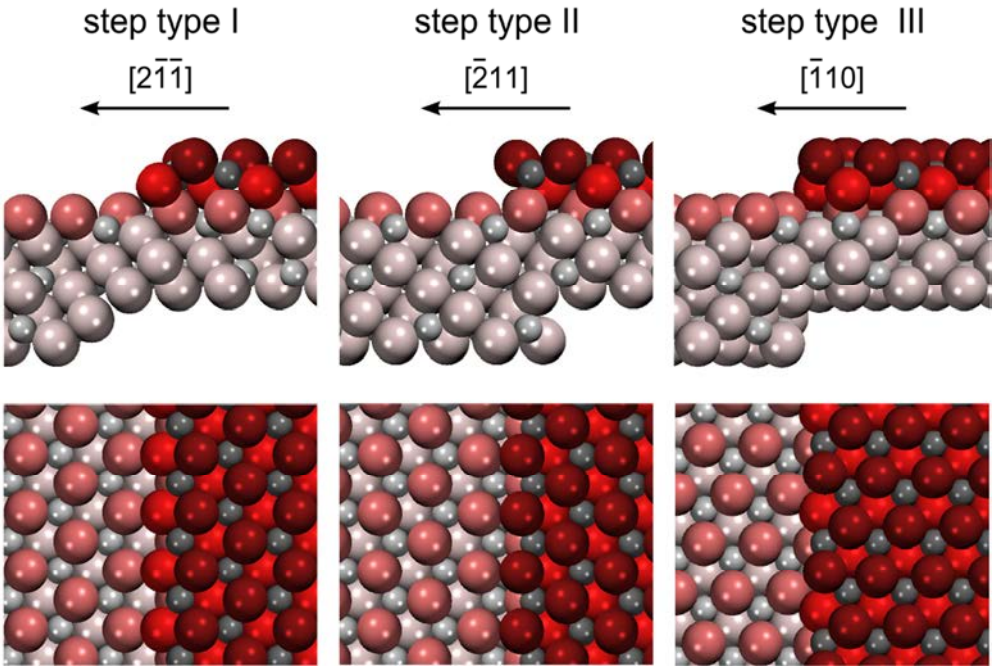

Figure 8.14. Escalones estables en CeO_2(111). Los aniones O están en rojo y los iones de Ce en gris. Los átomos con colores más oscuros se hallan en capas superficiales.

La estructura electrónica de los escalones explica por qué aparecen tan brillantes en las imágenes STM. Los escalones tipo I, III, y los de tipo II* dan lugar a estados específicos y separados en la banda vacía de orbitales 5*d* del Ce. A diferencia del resto de la banda, estos estados presentan contribuciones de orbitales tipo *s* y *p* que se acomodan mejor al potencial asimétrico electrostático de Madelung en los escalones. Como los orbitales tipo *s* y *p* son mucho más difusos que los orbitales *d*, son más accesibles a la corriente de efecto túnel, y por ello aparecen más en el STM.

Energías específicas de escalones en CeO_2 (111)

Una de las características más importantes de cualquier objeto es su energía específica, ya que ésta determina la abundancia de este objeto en equilibrio termodinámico. Sin embargo, raramente se determinan las energías específicas absolutas de escalones a partir de datos STM ya que esto requiere de un complejo análisis de las fluctuaciones de los escalones.[345–347]

En la Sección 5.2 se utilizaron tres métodos diferentes a fin de evaluar las energías específicas absolutas de los escalones en CeO_2(111). En el primer método, vecinal-γ, las energías de los escalones fueron derivadas en base a los análisis de las energías superficiales, como se utilizó en algunos estudios previos.[292,340,348] Por primera

vez se han propuesto otros dos métodos basados en la descomposición de la energía total de los modelos de *slab* con superficies vecinales en el método vecinal-*E* o en *slabs* con tiras de material en el método tira-*E*. Es importante destacar que todas las fórmulas involucradas fueron derivadas dentro del mismo marco teórico, el cual garantizó la consistencia entre diferentes métodos. A su vez, las energías de los escalones en CeO_2(111) calculadas con los tres métodos concuerdan bien entre ellas.

El método vecinal-γ dio lugar a una pobre precisión estadística (hasta un 20%) en las energías de escalón del CeO_2(111). Este grado de precisión hace que este método sea difícilmente aplicable en algunos casos, *e.g.* para escalones en TiO_2(101).[292] La precisión del método vecinal-*E* fue un 50% superior. Además, este método requirió cuatro veces menos cálculos que el método vecinal-γ, ya que utiliza las energías totales de los modelos de *slab* de superficies vecinales en vez de las energías superficiales correspondientes. El método tira-*E*, fue incluso más preciso que el método vecinal-*E*, a pesar de que requirió el mismo número de cálculos. La desventaja de este método, sin embargo, es que no da lugar a energías específicas de un único escalón, sino una suma de energías de escalones localizados a ambos lados de la tira.

Las energías específicas de escalones en CeO_2(111) calculadas estaban en línea con los resultados STM experimentales. Es decir, los escalones de tipo I tenían la menor energía calculada y son los más abundantes en la superficie cuando se lleva a cabo el recocido a T < 1000 K. Los escalones de tipo II tenían un ~30% más de energía a esta temperatura, lo cual estaba de acuerdo con el 25% de diferencia energética obtenida de datos experimentales a través de la reconstrucción de Wulff inversa. La energía específica de los escalones de tipo III fue muy similar a la energía de los escalones de tipo II, lo cual explica su aparición en experimentos a temperaturas de recocido superiores. A su vez, la energía específica de los escalones tipo II* fue aproximadamente el doble que las energías de otros tipos de escalones. Así no sorprende que no se detecte su presencia en los experimentos.

Formación de vacantes de oxígeno en escalones de CeO_2 (111)

Se cree que muchas propiedades ventajosas del óxido de cerio son debidas a su reducibilidad, la cual puede ser descrita por la energía de formación de vacantes de O, $E_f(O_{vac})$.[319] Curiosamente, la $E_f(O_{vac})$ calculada decrecía dramáticamente de 2.60 eV en

superficies extendidas de $CeO_2(111)$ a 0.46 eV en $Ce_{80}O_{160}$,[315] lo cual indica la incrementada reducibilidad del CeO_2 nanoestructurado en comparación con muestras más regulares. Por lo tanto, uno puede esperar también una mayor reducibilidad de las superficies escalonadas de óxido de cerio en comparación con el $CeO_2(111)$.

Los estudios computacionales de CeO_2 con vacantes de oxígeno (y de óxido de cerio parcialmente reducido[313,328,351]) son complicados por la presencia tanto de cationes Ce^{3+} y Ce^{4+} en el mismo sistema. Así, para que los estudios computacionales puedan representar la situación experimental energéticamente más estable la configuración O_{vac} + $2Ce^{3+}$ debe ser identificada de entre una multitud de posibilidades. Para sistemas con una compleja morfología la localización de la configuración más estable no puede ser alcanzada simplemente a *fuerza bruta* y se requieren métodos más sofisticados.

En la Sección 5.3 se considera la formación de vacantes de O y cationes Ce^{3+} en los escalones identificados experimentalmente en $CeO_2(111)$, y se presenta un nuevo procedimiento para encontrar la configuración de Ce^{3+} de inferior energía. Usando este procedimiento fue posible obtener las energías de formación de vacantes de O más bajas, $E_f(O_{vac})$, con una probabilidad superior al 97% para cada tipo de escalón. El procedimiento de precribado reduce el coste computacional ~un centenar de veces.

El procedimiento de precribado se basa en una correlación entre las energías relativas obtenidas en cálculos DFT+U con magnetización en iones Ce con cálculos sin correcciones de Hubbard U. En estos últimos cálculos el exceso de electrones formado por la O_{vac} aparece (de forma incorrecta) deslocalizado entre muchos cationes Ce, parcialmente reduciéndolos de Ce^{4+} a $Ce^{(4-\delta)+}$. Resulta que los iones Ce que están más (parcialmente) reducidos en un cálculo sin U son los mismos iones más fácilmente reducibles en un cálculo DFT+U. Así, un único cálculo CeO_2 defectuoso sin U permite elaborar una lista de estructuras que son propensas a dar lugar a bajas energías en cálculos DFT+U con el exceso de electrones localizado.

Este procedimiento permitió ver que los escalones en $CeO_2(111)$ eran de hecho más reducibles que el $CeO_2(111)$ limpio. Es decir, la energía de formación de vacantes de O calculada en escalones de tipo I, II y III fue 0.53 – 0.70 eV más baja que la de la superficie regular (111). Esta reducción en la $E_f(O_{vac})$ se encuentra en una gran multitud de reacciones que tengan lugar en los escalones.

8.7 Capas Gruesas a Escala Nanométrica

Las películas son estructuras extendidas en dos dimensiones (laterales) y confinadas en la tercera dirección (vertical) con una medida de hasta 100 nm. Una rica variedad de técnicas de superficies permite estudiarlas desde cualquier punto de vista,[46,290,366] que normalmente dan lugar a una caracterización precisa.

La simplicidad estructural de las capas nanométricas podría hacerlas unos modelos perfectos para estudios *e.g.* en catálisis heterogénea; sin embargo, también tienen sus puntos débiles. A diferencia de la catálisis industrial con superficies regulares sin defectos, éstas tienen una nanoestructura muy compleja, con un número más alto de átomos con baja coordinación. Por lo tanto la actividad de las películas puede no representar exactamente la actividad catalítica de los catalizadores reales.[368] Del mismo modo la estructura y actividad de las películas puede cambiar al exponerlos a reactivos, [369,370] mientras que muchas técnicas de superficie operan sólo en condiciones de ultra alto vacío o a presiones relativamente bajas.

Objetivos de esta sección

A pesar de que ha habido mucho progreso en los estudios de capas y se han determinado las estructuras de muchas con éxito, el continuo crecimiento del campo requiere de investigaciones adicionales. Normalmente una sola técnica de superficies es insuficiente para determinar la estructura de la película,[309,370,371] y aquí los estudios computacionales presentan un gran potencial esclarecedor.

Los estudios discutidos en esta Sección están dedicados a dos sistemas de considerable interés para la comunidad científica en catálisis y relacionados con los discutidos en la Sección 3.4 y el Capítulo 5. La primera investigación (Sección 6.1) se centra en películas de Ce_2O_3 que están siendo estudiadas como sistemas modelo para el óxido de cerio en condiciones reductoras presentes en muchas aplicaciones.[312,325,372] Después, en la Sección 6.2, se investigan capas de PdZn depositadas sobre Pd(111) en condiciones de ultra alto vacío y en atmósfera de CO, ya que se ha probado que éstas son muy útiles para entender los detalles del funcionamiento catalítico en catalizadores reales de PdZn.[42,58,373] En ambos estudios el objetivo ha sido explicar porque las estructuras observadas de las capas pueden diferir de las estructuras conocidas en las correspondientes estructuras cristalinas de *bulk*.

Posibles estructuras de películas de Ce_2O_3

El papel del óxido de cerio en catálisis heterogénea y otros campos ha sido resumido en la Sección 8.6. A causa de su fácil reducción en condiciones altamente reductoras[374] o altas temperaturas,[312] el óxido de cerio se presenta en una forma CeO_{2-x} parcialmente reducida. Para reducir la complejidad, se prepararon películas de óxido de cerio totalmente reducido, Ce_2O_3, en diferentes modelos de substratos. La estructura de las películas preparadas, sin embargo, cambia dependiendo del substrato o las condiciones de preparación. En algunos casos se prepararon con una red tipo-A (como en el *bulk* de Ce_2O_3),[375,376] mientras que en otros casos se obtuvieron películas de fase bixbyita,[377,378] a pesar que esta estructura no ha podido ser estabilizada en *bulks* de Ce_2O_3 (Figura 8.15). Además, cuando se depositaron películas de Ce_2O_3 sobre Pt(111) una nueva estructura apareció.[379,380] Esto sugiere que el substrato juega un papel importante en la estructura de la película.

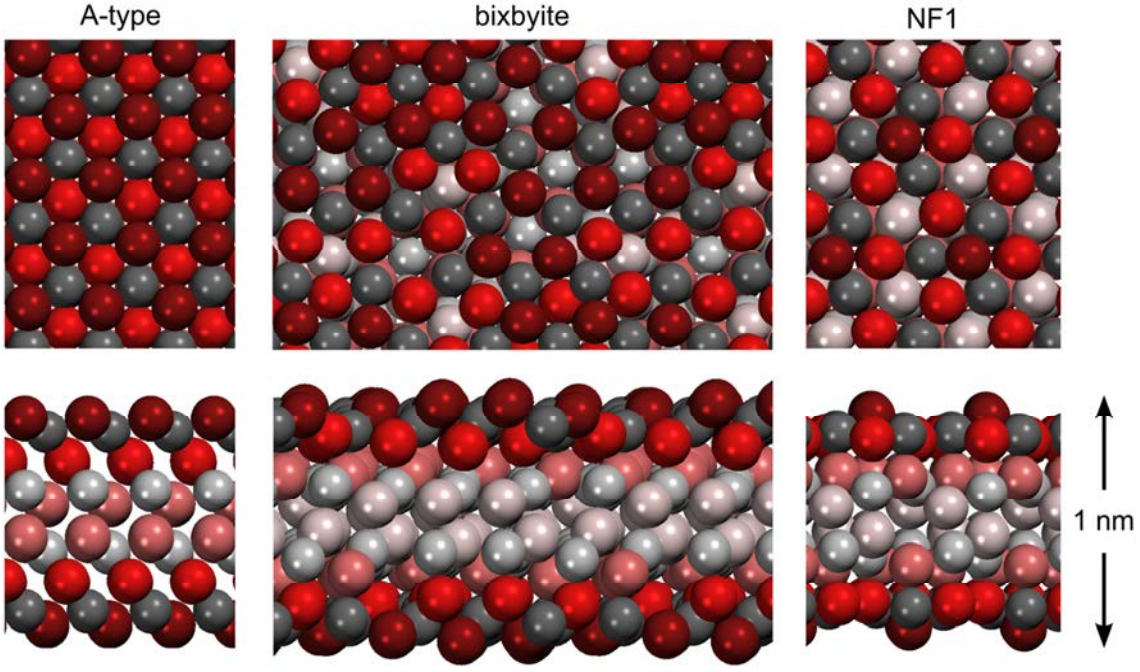

Figura 8.15. Estructuras de las películas de Ce_2O_3 de tipo-A, bixbyita y NF1. Los átomos de oxigeno están representados en rojo y los de cerio en gris. Los átomos más oscuros son los pertenecientes a las capas más superficiales.

Para investigar las diversas estructuras de películas de Ce_2O_3 se realizó un estudio combinando potenciales interatómicos y métodos DFT (Sección 6.1). Los potenciales interatómicos se utilizaron para testear el espacio configuracional de las

películas de Ce_2O_3 de 1 nm de grosor por medio de la técnica de simulación de recocido mecánico. Habiendo explorado el espacio configuracional de las películas de Ce_2O_3 con potenciales interatómicos, se utilizó DFT para estimar la estabilidad relativa de las películas de baja energía con una mayor exactitud.

La calculada preferencia por una u otra estructura de la película con dependencia al substrato estaba, en general, en concordancia con la bibliografía experimental disponible. Se ha encontrado que en sustratos que favorecen parámetros de red menores (< 386 pm) se favorece la estructura de tipo-A para capas de Ce_2O_3 depositados. Los sustratos con parámetros de celda intermedios (entre 390 y 406 pm) favorecerían la estructura bixbyita. Finalmente, la aparición de la nueva estructura NF1 se prevé para sustratos con parámetros de red por encima de 410 pm. La nueva estructura no se asemeja a ninguna estructura cristalina de ningún material con fórmula A_2B_3 y se ha visto que produce aniones de oxígeno que sobresalen de la superficie. Esto vaticina la existencia de interesantes propiedades químicas y, probablemente, altas reactividades en esta superficie.

Este estudio ha sido el primero en emplear un método de recocido mecánico para la optimización global (DFT) de estructuras en película. Esto muestra el potencial de este método para investigaciones sobre la estabilidad intrínseca de estructuras de películas plausibles y la predicción de nuevos polimorfismos.

Efecto de CO adsorbido sobre films de PdZn/Pd(111)

El PdZn es un compuesto bimetálico compuesto de un metal *d* y un elemento *sp*, que da lugar a enlaces heteroatómicos muy fuertes (Ref. 384 y Sección 3.4) y a una redistribución de cargas entre los elementos. La superficie más estable del material macroscópico de PdZn, la (111), expone átomos de Pd y Zn ordenados en filas alternadas. A su vez, esto da lugar a la ausencia de huecos tricoordinados compuestos de Pd o Zn en la superficie (presentes en PdZn(111)), los cuales pueden ser muy importantes para ciertas adsorciones o reacciones químicas.

A causa de la fuerte interacción química entre el Zn y Pd se ha encontrado que la densidad de estados proyectada sobre la superficie de los átomos de Pd en PdZn era más parecida a la del Cu que la propia del Pd.[58] Por lo tanto, no es ninguna sorpresa que la actividad y selectividad de los catalizadores basados en PdZn en reacciones tales como

el reformado de vapor de metanol (MSR) son muy parecidas a las de los catalizadores basados en Cu utilizados industrialmente.[58,258] A diferencia del Pd puro, que tiende a descomponer el metanol en hidrógeno y CO, el cobre (de modo parecido al PdZn) es, simultáneamente, activo y selectivo con el CO_2 en MSR (ver Sección 11.4). La ventaja más importante de los catalizadores de PdZn comparado con los basados en Cu para MSR es que los primeros[386–388] son más estables, menos propensos a la aglomeración y no pirofóricos, a diferencia de los segundos.[26,389,390]

En la Sección 6.2 se investigaron películas de PdZn sobre monocristales de Pd(111) a nivel teórico y experimental en presencia y ausencia de CO. En la Sección 6.2 se muestra como el CO adsorbido puede dar lugar a la reconstrucción de la superficie de PdZn y de este modo afectar considerablemente sus propiedades. Cálculos DFT han sido llevados a cabo sobre películas de una, dos y cuatro monocapas de grosor sobre un sustrato de Pd(111) con disposiciones de los átomos como las del material macroscópico (alternando filas de Pd y Zn) y también con disposiciones atómicas en zigzag (Figura 8.16). La adsorción de monóxido de carbono sobre cada una de estas estructuras fue simulada en condiciones de bajo y alto recubrimiento.

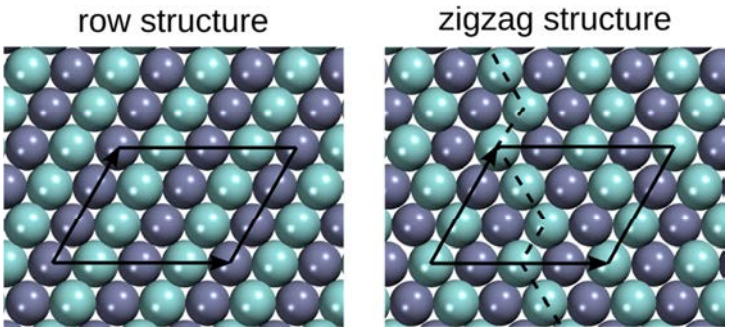

Figura 8.16. Estructuras en filas y en zigzag de la superficie de los films de la aleación PdZn sobre Pd(111). El Pd es representado en cian, Zn — azul teja.

Según los cálculos, la disposición alternativa de los átomos en zigzag resulta ser energéticamente más estable que la estructura convencional de filas para superficies de la aleación PdZn de una monocapa de grosor. La razón de este hecho es la mejor relajación superficial en la estructura menos simétrica en zigzag. En el caso de la saturación superficial con moléculas de CO la disposición de los átomos en superficie en zigzag se vuelve más estable que la disposición en filas para aleaciones de cualquier grosor. Esto se da por el hecho de que la estructura en zigzag permite mayores

distancias entre las moléculas de CO adyacentes en la superficie. A su vez, la repulsión entre moléculas adyacentes de CO en condiciones de alto recubrimiento se reduce.

La reconstrucción prevista de la superficie de PdZn/Pd(111) fue corroborada por descubrimientos experimentales. Primeramente, se predijo la adsorción de CO encima de átomos de Pd expuestos en PdZn con una disposición zigzag de los átomos superficiales, mientras que en el caso de la disposición por filas las posiciones interatómicas eran preferidas para la adsorción. A su vez, las frecuencias de vibración características del CO adsorbido directamente encima de un átomo fueron detectadas por espectroscopia de infrarrojos (IR). También, a causa de la menor repulsión entre moléculas de CO adyacentes en la estructura en zigzag, el recubrimiento de saturación, según los cálculos, era de un CO por átomo de Pd en la superficie. De diferente modo, la estructura convencional en filas ya se saturaba cuando dos moléculas de CO eran adsorbidas por cada tres átomos de Pd en la superficie. En experimentos de desorción a temperatura programada se midió el recubrimiento de saturación de una molécula de CO por átomo de Pd, lo cual corroboraba una vez más la existencia de la estructura superficial reconstruida.

Por lo tanto este estudio ha documentado un tipo muy interesante de reconstrucción superficial en películas de PdZn sobre Pd(111) inducida por la adsorción de moléculas de CO. En tal reconstrucción la composición y la estructura geométrica de la superficie se mantienen intactas. Es el orden relativo de átomos de Pd y Zn el que cambia de la estructura en filas a la estructura en zigzag. Dado que esta reconstrucción puede ser aperiódica, su detección por medio de ciertas técnicas superficiales se prevé complicada.

8.8 Conclusiones

Con los resultados presentados en los Capítulos 3-6 uno puede perfilar las siguientes conclusiones sobre los efectos de la nanoestructuración en las propiedades de materiales interesantes desde el punto de vista de la catálisis heterogénea:

- Las propiedades adsorbentes y catalíticas de nanopartículas de metales de transición escalables con el tamaño de partícula pueden diferir substancialmente de aquellas de los correspondientes monocristales. Primero, se ha visto que los filos de nanopartículas de Pd adsorben ciertas especies CH_xO_y significativamente más fuerte que las caras {111} de las nanopartículas. Además, los cálculos muestran que estos filos son catalíticamente más activos hacia la descomposición de metano que las superficies de Pd(111). Incluso se encuentra que las caras {111} de nanopartículas de Pd presentan una actividad catalítica mucho mayor para reacciones de hidrogenación comparadas a monocristales de Pd(111), siempre y cuando el sistema presenta H absorbido.

- Los resultados de los cálculos de la estructura electrónica permiten determinar la ordenación de componentes energéticamente más estable y, en particular, la composición superficial en nanopartículas bimetálicas de una manera eficiente. Esto se consigue mediante unos Hamiltonianos topológicos aquí propuestos y ajustados a energías totales calculadas a nivel DFT. Para las nanoaleaciones estudiadas se ha encontrado que la precisión de este método es del mismo orden que la energía térmica de una determinada nanopartícula a temperatura ambiente, cosa que es suficiente a efectos prácticos. Los parámetros obtenidos en los Hamiltonianos tienen interpretaciones claramente físicas y proporcionan importantes conocimientos sobre la naturaleza del enlace dentro de las nanopartículas bimetálicas.

- El efecto de soportes de óxidos químicamente bastante inertes (sin defectos) en las propiedades físicas y adsorbentes de nanopartículas metálicas de tamaño considerable puede ser insignificante. Esto se muestra de manera explícita para las nanopartículas Pd_{127} y Pt_{127} de 1.6 nm de tamaño soportadas sobre la superficie MgO(100). Se encuentra aquí que el efecto del óxido en la estructura electrónica y geométrica de las nanopartículas soportadas es débil. Además, su

efecto en las energía de adsorción y absorción de átomos de H en nanopartículas de Pd y Pt se limita sólo a cambios de cómo mucho 0.07 eV.

- El recubrimiento superficial puede cambiar las propiedades de las nanopartículas de metales de transición de una manera más significativa que el soporte óxido químicamente inerte. En particular, la saturación de la superficie de las nanopartículas Pd_{127} y Pt_{127} por átomos de H afecta a su estructura geométrica y electrónica mucho más que la presencia del soporte de MgO(100). Lo mismo se podría decir de la absorción de H en Pd y Pt nanoestructurado.

- Nanoislas formadas sobre la superficie $CeO_2(111)$ exponen escalones con una estructura electrónica modificada y una reducibilidad incrementada. El potencial electroestático de Madelung asimétrico que hay en los escalones se traduce en estados electrónicos específicos para ellos, como se identifica en los cálculos DFT así como en experimentos de microscopía y espectroscopia de efecto túnel. También con la ayuda de un nuevo procedimiento es posible testear diversas configuraciones $O_{vac} + 2Ce^{3+}$, encontrándose que las vacantes de O en escalones tienen energías de formación hasta 0.7 eV más bajas que dichas vacantes en la superficie limpia de $CeO_2(111)$. Esto pone de manifiesto una reducibilidad potenciada en los escalones comparada a las superficies regularmente extendidas.

- Las energías absolutas de los escalones que bordean las nanoislas se pueden calcular de una manera eficaz usando métodos DFT. Para ello se han propuesto dos nuevos métodos que requieren menos cálculos de la estructura electrónica y que a la vez proporcionan una exactitud estadística superior al método preexistente. La aplicación de estos métodos en los escalones de $CeO_2(111)$ da unos resultados concordes con los experimentos.

- Cuando la extensión del material en una sola dimensión se reduce alrededor de un nanómetro, la estructura de la capa obtenida puede resultar muy diferente de la estructura de la correspondiente fase cristalina por varias razones, tal y como se ha encontrado para capas de Ce_2O_3 y PdZn. La estructura de las capas de Ce_2O_3 dependen del substrato en que crecen. A saber, los resultados predicen capas con estructuras tipo A, bixbyita, y la nueva estructura NF1 cuando se

forman para parámetros de celda cortos, moderados, y largos, respectivamente. En cuanto las capas de PdZn sobre Pd(111), la razón de la mayor estabilidad energética de la estructura distorsionada en zigzag son unas distancias Pd-Pd más largas que en la convencional estructura en fila. Esto hace que la estructura zigzag sea la más estable para monocapas y para capas cubiertas por moléculas de CO.

Así pues, este trabajo resultó, por un lado, en un nuevo conocimiento básico sobre las diferencias entre la física y la química de materiales regularmente extendidos, y, por el otro, de nanopartículas, nanoislas, y capas finas del orden del nanómetro. Se han propuesto nuevos métodos de cómo optimizar el orden químico en nanopartículas bimetálicas, cómo calcular energías de peldaño absolutas en superficies, y cómo buscar la configuración de $O_{vac} + 2Ce^{3+}$ más baja en energía. Además la técnica del recocido mecánico simulado se aplicó, por primera vez, en la optimización global de capas. Los estudios llevados a cabo sobre nanopartículas de Pd y Pt soportadas en MgO servirán como un punto de referencia para futuras exploraciones de interacciones metal-soporte. Por último, se documentó, también por primera vez, la mayor sensibilidad de varias propiedades de nanopartículas de metales de transición a la presencia de adsorbatos (por ejemplo, H atómico). Todos estos estudios, *únicos en su especie*, tienen implicaciones a lago abasto para la nanociencia computacional y experimental, y pavimentan el camino de futuras investigaciones.

9 Bibliography

(1) Erisman, J.; Sutton, M.; Galloway, J.; Klimont, Z.; Winiwarter, W. How a Century of Ammonia Synthesis Changed the World. *Nat. Geosci.* **2008**, *1*, 636–639.

(2) Bosch, C. The Development of the Chemical High Pressure Method during the Establishment of the New Ammonia Industry. In *Nobel Lectures, Chemistry 1922-1941*; Elsevier: Amsterdam, 1966; pp. 197–241.

(3) Haber, F. The Synthesis of Ammonia from Its Elements. In *Nobel Lectures, Chemistry 1901-1921*; Elsevier: Amsterdam, 1966; pp. 326–340.

(4) Vermeiren, W.; Gilson, J.-P. Impact of Zeolites on the Petroleum and Petrochemical Industry. *Top. Catal.* **2009**, *52*, 1131–1161.

(5) Zaera, F. New Challenges in Heterogeneous Catalysis for the 21st Century. *Catal. Letters* **2012**, *142*, 501–516.

(6) Song, C. Fuel Processing for Low-Temperature and High-Temperature Fuel Cells Challenges, and Opportunities for Sustainable Development in the 21st Century. *Catal. Today* **2002**, *77*, 17–49.

(7) Gélin, P.; Primet, M. Complete Oxidation of Methane at Low Temperature over Noble Metal Based Catalysts: A Review. **2002**, *39*, 1–37.

(8) Choudhary, T. V; Banerjee, S.; Choudhary, V. R. Catalysts for Combustion of Methane and Lower Alkanes. **2002**, *234*, 1–23.

(9) Ab Rahim, M. H.; Forde, M. M.; Jenkins, R. L.; Hammond, C.; He, Q.; Dimitratos, N.; Lopez-Sanchez, J. A.; Carley, A. F.; Taylor, S. H.; Willock, D. J.; et al. Oxidation of Methane to Methanol with Hydrogen Peroxide Using Supported Gold-Palladium Alloy Nanoparticles. *Angew. Chem. Int. Ed. Engl.* **2013**, *52*, 1280–1284.

(10) Periana, R. A.; Mironov, O.; Taube, D.; Bhalla, G.; Jones, C. J. Catalytic, Oxidative Condensation of CH_4 to CH_3COOH in One Step via CH Activation. *Science* **2003**, *301*, 814–818.

(11) Huber, G. W.; Corma, A. Synergies between Bio- and Oil Refineries for the Production of Fuels from Biomass. *Angew. Chem. Int. Ed. Engl.* **2007**, *46*, 7184–7201.

(12) Sugiura, M. Oxygen Storage Materials for Automotive Catalysts : Ceria-Zirconia Solid Solutions. *Catal. Surv. from Asia* **2003**, *7*, 77–87.

(13) Cuenya, B. R. Synthesis and Catalytic Properties of Metal Nanoparticles: Size, Shape, Support, Composition, and Oxidation State Effects. *Thin Solid Films* **2010**, *518*, 3127–3150.

(14) Van Santen, R. A. Catalytic Paradigms: A Riddle and a Puzzle. *Angew. Chem. Int. Ed. Engl.* **2014**, *53*, 8618–8620.

(15) Tuxen, A. Atomic-Scale Investigations of MoS_2-Based Hydrotreating Model Catalysts, 2011, pp. 1–143.

(16) Bell, A. T. The Impact of Nanoscience on Heterogeneous Catalysis. *Science* **2003**, *299*, 1688–1691.

(17) Koper, M. Structure Sensitivity and Nanoscale Effects in Electrocatalysis. *Nanoscale* **2011**, *3*, 2054–2073.

(18) Green, I. X.; Tang, W.; Neurock, M.; Yates, J. T. Spectroscopic Observation of Dual Catalytic Sites during Oxidation of CO on a Au/TiO_2 Catalyst. *Science* **2011**, *333*, 736–739.

(19) Haruta, M. Size- and Support-Dependency in the Catalysis of Gold. *Catal. Today* **1997**, *861*, 153–166.

(20) Carrettin, S.; Concepción, P.; Corma, A.; López Nieto, J. M.; Puntes, V. F. Nanocrystalline CeO_2 Increases the Activity of Au for CO Oxidation by Two Orders of Magnitude. *Angew. Chem. Int. Ed. Engl.* **2004**, *43*, 2538–2540.

(21) Lu, X.; Li, X.; Qian, J.; Chen, Z. The Surfactant-Assisted Synthesis of CeO_2 Nanowires and Their Catalytic Performance for CO Oxidation. *Powder Technol.* **2013**, *239*, 415–421.

(22) Xu, C. W.; Wang, H.; Shen, P. K.; Jiang, S. P. Highly Ordered Pd Nanowire Arrays as Effective Electrocatalysts for Ethanol Oxidation in Direct Alcohol Fuel Cells. *Adv. Mater.* **2007**, *19*, 4256–4259.

(23) Lu, Y.; Chen, W. PdAg Alloy Nanowires: Facile One-Step Synthesis and High Electrocatalytic Activity for Formic Acid Oxidation. *ACS Catal.* **2012**, *2*, 84–90.

(24) Pieper, H. H.; Barth, C.; Reichling, M. Characterization of Atomic Step Structures on $CaF_2(111)$ by Their Electric Potential. *Appl. Phys. Lett.* **2012**, *101*, 051601.

(25) Dahl, S.; Logadottir, A.; Egeberg, R.; Larsen, J.; Chorkendorff, I.; Törnqvist, E.; Nørskov, J. Role of Steps in N_2 Activation on Ru(0001). *Phys. Rev. Lett.* **1999**, *83*, 1814–1817.

(26) Behrens, M.; Studt, F.; Kasatkin, I.; Kühl, S.; Hävecker, M.; Abild-Pedersen, F.; Zander, S.; Girgsdies, F.; Kurr, P.; Kniep, B.-L.; et al. The Active Site of Methanol Synthesis over $Cu/ZnO/Al_2O_3$ Industrial Catalysts. *Science* **2012**, *336*, 893–897.

(27) Quek, X.-Y.; Filot, I. A. W.; Pestman, R.; van Santen, R. A.; Petkov, V.; Hensen, E. J. M. Correlating Fischer-Tropsch Activity to Ru Nanoparticle Surface Structure as Probed by High-Energy X-Ray Diffraction. *Chem. Commun. (Camb).* **2014**, *50*, 6005–6008.

(28) Stamenkovic, V. R.; Mun, B. S.; Arenz, M.; Mayrhofer, K. J. J.; Lucas, C. A.; Wang, G.; Ross, P. N.; Markovic, N. M. Trends in Electrocatalysis on Extended and Nanoscale Pt-Bimetallic Alloy Surfaces. *Nat. Mater.* **2007**, *6*, 241–247.

(29) Wang, D.; Xin, H. L.; Hovden, R.; Wang, H.; Yu, Y.; Muller, D. A.; DiSalvo, F. J.; Abruña, H. D. Structurally Ordered Intermetallic Platinum-Cobalt Core-Shell Nanoparticles with Enhanced Activity and Stability as Oxygen Reduction Electrocatalysts. *Nat. Mater.* **2013**, *12*, 81–87.

(30) Freund, H.-J.; Nilius, N.; Risse, T.; Schauermann, S. A Fresh Look at an Old Nano-Technology: Catalysis. *Phys. Chem. Chem. Phys.* **2014**, *16*, 8148–8167.

(31) Nilius, N.; Risse, T.; Schauermann, S.; Shaikhutdinov, S.; Sterrer, M.; Freund, H.-J. Model Studies in Catalysis. *Top. Catal.* **2011**, *54*, 4–12.

(32) Freund, H.-J.; Heyde, M.; Nilius, N.; Schauermann, S.; Shaikhutdinov, S.; Sterrer, M. Model Studies on Heterogeneous Catalysts at the Atomic Scale: From Supported Metal Particles to Two-Dimensional Zeolites. *J. Catal.* **2013**, *308*, 154–167.

(33) Bäumer, M.; Freund, H. Metal Deposits on Well-Ordered Oxide Films. *Prog. Surf. Sci.* **1999**, *61*, 127–198.

(34) Willinger, M. G.; Zhang, W.; Bondarchuk, O.; Shaikhutdinov, S.; Freund, H.-J.; Schlögl, R. A Case of Strong Metal-Support Interactions: Combining Advanced Microscopy and Model Systems to Elucidate the Atomic Structure of Interfaces. *Angew. Chem. Int. Ed. Engl.* **2014**, *53*, 5998–6001.

(35) Pieper, H. H.; Derks, C.; Zoellner, M. H.; Olbrich, R.; Tröger, L.; Schroeder, T.; Neumann, M.; Reichling, M. Morphology and Nanostructure of CeO_2(111) Surfaces of Single Crystals and Si(111) Supported Ceria Films. *Phys. Chem. Chem. Phys.* **2012**, *14*, 15361–15368.

(36) Hausen, F.; Zimmet, J. A.; Bennewitz, R. Surface Structures and Frictional Properties of Au(100) in an Electrochemical Environment. *Surf. Sci.* **2013**, *607*, 20–24.

(37) Engelhardt, J. B.; Dabringhaus, H.; Wandelt, K. Atomic Force Microscopy Study of the CaF_2(111) Surface: From Cleavage via Island to Evaporation Topographies. *Surf. Sci.* **2000**, *448*, 187–200.

(38) Nolte, P.; Stierle, A.; Kasper, N.; Jin-Phillipp, N. Y.; Jeutter, N.; Dosch, H. Reversible Shape Changes of Pd Nanoparticles on MgO(100). *Nano Lett.* **2011**, *11*, 4697–4700.

(39) Revenant, C.; Leroy, F.; Lazzari, R.; Renaud, G.; Henry, C. Quantitative Analysis of Grazing Incidence Small-Angle X-Ray Scattering: Pd/MgO(001) Growth. *Phys. Rev. B* **2004**, *69*, 035411.

(40) Renaud, G.; Lazzari, R.; Revenant, C.; Barbier, A.; Noblet, M.; Ulrich, O.; Leroy, F.; Jupille, J.; Borensztein, Y.; Henry, C. R.; et al. Real-Time Monitoring of Growing Nanoparticles. *Science* **2003**, *300*, 1416–1419.

(41) Voogt, E. H.; Mens, A. J. M.; Gijzeman, O. L. J.; Geus, J. W. XPS Analysis of the Oxidation of Palladium Model Catalysts. **1999**, *47*, 321–323.

(42) Holzapfel, H. H.; Wolfbeisser, A.; Rameshan, C.; Weilach, C.; Rupprechter, G. PdZn Surface Alloys as Models of Methanol Steam Reforming Catalysts: Molecular Studies by LEED, XPS, TPD and PM-IRAS. *Top. Catal.* **2014**, *57*, 1218–1228.

(43) Rameshan, C.; Stadlmayr, W.; Penner, S.; Lorenz, H.; Mayr, L.; Hävecker, M.; Blume, R.; Rocha, T.; Teschner, D.; Knop-Gericke, A.; et al. In Situ XPS Study of Methanol Reforming on PdGa near-Surface Intermetallic Phases. *J. Catal.* **2012**, *290*, 126–137.

(44) Lipton-Duffin, J. A.; MacLeod, J. M.; Vondráček, M.; Prince, K. C.; Rosei, R.; Rosei, F. Thermal Evolution of the Submonolayer near-Surface Alloy of ZnPd on Pd(111). *Phys. Chem. Chem. Phys.* **2014**, *16*, 4764–4770.

(45) Rodriguez, J. A. Interactions in Bimetallic Bonding: Electronic and Chemical Properties of PdZn Surfaces. *J. Phys. Chem.* **1994**, *98*, 5758–5764.

(46) Freund, H.-J.; Nilius, N.; Risse, T.; Schauermann, S.; Schmidt, T. Innovative Measurement Techniques in Surface Science. *Chemphyschem* **2011**, *12*, 79–87.

(47) Pan, Y.; Cui, Y.; Stiehler, C.; Nilius, N.; Freund, H. Gold Adsorption on CeO_2 Thin Films Grown on Ru(0001). *J. Phys. Chem. C* **2013**, *117*, 21879–21885.

(48) Gamo, Y.; Nagashima, A.; Wakabayashi, M.; Terai, M.; Oshima, C. Atomic Structure of Monolayer Graphite Formed on Ni(111). *Surf. Sci.* **1997**, *374*, 61–64.

(49) Viñes, F.; Desikusumastuti, A.; Staudt, T.; Görling, A.; Libuda, J.; Neyman, K. M. A Combined Density-Functional and IRAS Study on the Interaction of NO with Pd Nanoparticles: Identifying New Adsorption Sites with Novel Properties. *J. Phys. Chem. C* **2008**, *112*, 16539–16549.

(50) Bäumer, M.; Libuda, J.; Neyman, K. M.; Rösch, N.; Rupprechter, G.; Freund, H.-J. Adsorption and Reaction of Methanol on Supported Palladium Catalysts: Microscopic-Level Studies from Ultrahigh Vacuum to Ambient Pressure Conditions. *Phys. Chem. Chem. Phys.* **2007**, *9*, 3541–3558.

(51) Wilde, M.; Fukutani, K. Hydrogen Detection near Surfaces and Shallow Interfaces with Resonant Nuclear Reaction Analysis. *Surf. Sci. Rep.* **2014**, *69*, 196–295.

(52) Wilde, M.; Fukutani, K.; Ludwig, W.; Brandt, B.; Fischer, J.-H.; Schauermann, S.; Freund, H.-J. Influence of Carbon Deposition on the Hydrogen Distribution in

Pd Nanoparticles and Their Reactivity in Olefin Hydrogenation. *Angew. Chem. Int. Ed. Engl.* **2008**, *47*, 9289–9293.

(53) Fukutani, K.; Itoh, A.; Wilde, M.; Matsumoto, M. Zero-Point Vibration of Hydrogen Adsorbed on Si and Pt Surfaces. *Phys. Rev. Lett.* **2002**, *88*, 116101.

(54) Dvořák, F.; Stetsovych, O.; Steger, M.; Cherradi, E.; Matolínová, I.; Tsud, N.; Skoda, M.; Skála, T.; Mysliveček, J.; Matolín, V. Adjusting Morphology and Surface Reduction of CeO_2(111) Thin Films on Cu(111). *J. Phys. Chem. C* **2011**, *115*, 7496–7503.

(55) Vayssilov, G. N.; Lykhach, Y.; Migani, A.; Staudt, T.; Petrova, G. P.; Tsud, N.; Skála, T.; Bruix, A.; Illas, F.; Prince, K. C.; et al. Support Nanostructure Boosts Oxygen Transfer to Catalytically Active Platinum Nanoparticles. *Nat. Mater.* **2011**, *10*, 310–315.

(56) Ertl, G. Reactions at Surfaces: From Atoms to Complexity. In *The Nobel Prizes 2007*; Grandin, K., Ed.; Nobel Foundation: Stockholm, 2008; pp. 116–139.

(57) Calle-Vallejo, F.; Koper, M. T. M. First-Principles Computational Electrochemistry: Achievements and Challenges. *Electrochim. Acta* **2012**, *84*, 3–11.

(58) Neyman, K. M.; Lim, K. H.; Chen, Z.-X.; Moskaleva, L. V; Bayer, A.; Reindl, A.; Borgmann, D.; Denecke, R.; Steinrück, H.-P.; Rösch, N. Microscopic Models of PdZn Alloy Catalysts: Structure and Reactivity in Methanol Decomposition. *Phys. Chem. Chem. Phys.* **2007**, *9*, 3470–3482.

(59) Paier, J.; Penschke, C.; Sauer, J. Oxygen Defects and Surface Chemistry of Ceria: Quantum Chemical Studies Compared to Experiment. *Chem. Rev.* **2013**, *113*, 3949–3985.

(60) Studt, F.; Sharafutdinov, I.; Abild-Pedersen, F.; Elkjær, C. F.; Hummelshøj, J. S.; Dahl, S.; Chorkendorff, I.; Nørskov, J. K. Discovery of a Ni-Ga Catalyst for Carbon Dioxide Reduction to Methanol. *Nat. Chem.* **2014**, *6*, 320–324.

(61) Greeley, J.; Jaramillo, T. F.; Bonde, J.; Chorkendorff, I. B.; Nørskov, J. K. Computational High-Throughput Screening of Electrocatalytic Materials for Hydrogen Evolution. *Nat. Mater.* **2006**, *5*, 909–913.

(62) Andersson, M. P.; Bligaard, T.; Kustov, A.; Larsen, K. E.; Greeley, J.; Johannessen, T.; Christensen, C. H.; Nørskov, J. K. Toward Computational Screening in Heterogeneous Catalysis: Pareto-Optimal Methanation Catalysts. *J. Catal.* **2006**, *239*, 501–506.

(63) Bligaard, T.; Nørskov, J. K.; Dahl, S.; Matthiesen, J.; Christensen, C. H.; Sehested, J. The Brønsted–Evans–Polanyi Relation and the Volcano Curve in Heterogeneous Catalysis. *J. Catal.* **2004**, *224*, 206–217.

(64) Wang, S.; Petzold, V.; Tripkovic, V.; Kleis, J.; Howalt, J. G.; Skúlason, E.; Fernández, E. M.; Hvolbæk, B.; Jones, G.; Toftelund, A.; et al. Universal Transition State Scaling Relations for (de)hydrogenation over Transition Metals. *Phys. Chem. Chem. Phys.* **2011**, *13*, 20760–20765.

(65) Logadottir, A.; Rod, T. H.; Nørskov, J. K.; Hammer, B.; Dahl, S.; Jacobsen, C. J. H. The Brønsted–Evans–Polanyi Relation and the Volcano Plot for Ammonia Synthesis over Transition Metal Catalysts. *J. Catal.* **2001**, *197*, 229–231.

(66) Studt, F.; Abild-Pedersen, F.; Bligaard, T.; Sørensen, R. Z.; Christensen, C. H.; Nørskov, J. K. On the Role of Surface Modifications of Palladium Catalysts in the Selective Hydrogenation of Acetylene. *Angew. Chem. Int. Ed. Engl.* **2008**, *47*, 9299–9302.

(67) Yoo, J. S.; Abild-Pedersen, F.; Nørskov, J. K.; Studt, F. Theoretical Analysis of Transition-Metal Catalysts for Formic Acid Decomposition. *ACS Catal.* **2014**, *4*, 1226–1233.

(68) Hammer, B.; Nørskov, J. Electronic Factors Determining the Reactivity of Metal Surfaces. *Surf. Sci.* **1995**, *343*, 211–220.

(69) Dahal, A.; Batzill, M. Graphene-Nickel Interfaces: A Review. *Nanoscale* **2014**, *6*, 2548–2562.

(70) Vojvodic, A.; Nørskov, J. K.; Abild-Pedersen, F. Electronic Structure Effects in Transition Metal Surface Chemistry. *Top. Catal.* **2013**, *57*, 25–32.

(71) Xin, H.; Vojvodic, A.; Voss, J.; Nørskov, J. K.; Abild-Pedersen, F. Effects of D-Band Shape on the Surface Reactivity of Transition-Metal Alloys. *Phys. Rev. B* **2014**, *89*, 115114.

(72) Boys, S. F. Electronic Wave Functions. I. A General Method of Calculation for the Stationary States of Any Molecular System. *Proc. R. Soc. A* **1950**, *200*, 542–554.

(73) Slater, J. C. The Theory of Complex Spectra. *Phys. Rev.* **1929**, *34*, 1293–1322.

(74) Schrödinger, E. An Undulatory Theory of the Mechanics of Atoms and Molecules. *Phys. Rev.* **1926**, *28*, 1049–1070.

(75) Kohn, W. Electronic Structure of Matter - Wave Functions and Density Functionals. In *Nobel Lectures, Chemistry 1996-2000*; Grenthe, I., Ed.; World Scientific Publishing: Singapore, 2003; pp. 213–237.

(76) Hohenberg, P.; Kohn, W. Inhomogeneous Electron Gas. *Phys. Rev.* **1964**, *136*, B864–B871.

(77) Levy, M. Electron Densities in Search of Hamiltonians. *Phys. Rev. A* **1982**, *26*, 1200–1208.

(78) Kohn, W.; Sham, L. J. Self-Consistent Equations Including Exchange and Correlation Effects. *Phys. Rev.* **1965**, *140*, 1133–1138.

(79) Dirac, P. A. M. Note on Exchange Phenomena in the Thomas Atom. *Math. Proc. Cambridge Philos. Soc.* **1930**, *26*, 376.

(80) Ceperley, D. M.; Alder, B. J. Ground State of the Electron Gas by a Stochastic Method. *Phys. Rev. Lett.* **1980**, *45*, 566–569.

(81) Perdew, J.; Burke, K.; Ernzerhof, M. Generalized Gradient Approximation Made Simple. *Phys. Rev. Lett.* **1996**, *77*, 3865–3868.

(82) Hammer, B.; Hansen, L.; Nørskov, J. K. Improved Adsorption Energetics within Density-Functional Theory Using Revised Perdew-Burke-Ernzerhof Functionals. *Phys. Rev. B* **1999**, *59*, 7413–7421.

(83) Perdew, J. P. Accurate Density Functional for the Energy: Real-Space Cutoff of the Gradient Expansion for the Exchange Hole. *Phys. Rev. Lett.* **1985**, *55*, 1665–1668.

(84) Kümmel, S.; Perdew, J. Optimized Effective Potential Made Simple: Orbital Functionals, Orbital Shifts, and the Exact Kohn-Sham Exchange Potential. *Phys. Rev. B* **2003**, *68*, 035103.

(85) Staroverov, V.; Scuseria, G.; Tao, J.; Perdew, J. Tests of a Ladder of Density Functionals for Bulk Solids and Surfaces. *Phys. Rev. B* **2004**, *69*, 075102.

(86) Ruzsinszky, A.; Csonka, G. I.; Scuseria, G. E. Regularized Gradient Expansion for Atoms, Molecules, and Solids. *J. Chem. Theory Comput.* **2009**, *5*, 763–769.

(87) Zhao, Y.; Truhlar, D. G. Construction of a Generalized Gradient Approximation by Restoring the Density-Gradient Expansion and Enforcing a Tight Lieb-Oxford Bound. *J. Chem. Phys.* **2008**, *128*, 184109.

(88) Perdew, J.; Ruzsinszky, A.; Csonka, G.; Vydrov, O.; Scuseria, G.; Constantin, L.; Zhou, X.; Burke, K. Restoring the Density-Gradient Expansion for Exchange in Solids and Surfaces. *Phys. Rev. Lett.* **2008**, *100*, 136406.

(89) Mori-Sánchez, P.; Cohen, A. J.; Yang, W. Many-Electron Self-Interaction Error in Approximate Density Functionals. *J. Chem. Phys.* **2006**, *125*, 201102.

(90) Tao, J.; Perdew, J.; Staroverov, V.; Scuseria, G. Climbing the Density Functional Ladder: Nonempirical Meta–Generalized Gradient Approximation Designed for Molecules and Solids. *Phys. Rev. Lett.* **2003**, *91*, 146401.

(91) Arbuznikov, A. V; Kaupp, M. The Self-Consistent Implementation of Exchange-Correlation Functionals Depending on the Local Kinetic Energy Density. *Chem. Phys. Lett.* **2003**, *381*, 495–504.

(92) Perdew, J. P.; Ernzerhof, M.; Burke, K. Rationale for Mixing Exact Exchange with Density Functional Approximations. *J. Chem. Phys.* **1996**, *105*, 9982.

(93) Adamo, C.; Barone, V. Toward Reliable Density Functional Methods without Adjustable Parameters: The PBE0 Model. *J. Chem. Phys.* **1999**, *110*, 6158.

(94) Heyd, J.; Scuseria, G. E.; Ernzerhof, M. Hybrid Functionals Based on a Screened Coulomb Potential. *J. Chem. Phys.* **2003**, *118*, 8207.

(95) Heyd, J.; Scuseria, G. E.; Ernzerhof, M. Erratum: "Hybrid Functionals Based on a Screened Coulomb Potential" [J. Chem. Phys. 118, 8207 (2003)]. *J. Chem. Phys.* **2006**, *124*, 219906.

(96) Becke, A. D. Density-Functional Thermochemistry. III. The Role of Exact Exchange. *J. Chem. Phys.* **1993**, *98*, 5648.

(97) Cramer, C. J.; Truhlar, D. G. Density Functional Theory for Transition Metals and Transition Metal Chemistry. *Phys. Chem. Chem. Phys.* **2009**, *11*, 10757–10816.

(98) Staroverov, V. N.; Scuseria, G. E.; Tao, J.; Perdew, J. P. Comparative Assessment of a New Nonempirical Density Functional: Molecules and Hydrogen-Bonded Complexes. *J. Chem. Phys.* **2003**, *119*, 12129.

(99) Eshuis, H.; Bates, J. E.; Furche, F. Electron Correlation Methods Based on the Random Phase Approximation. *Theor. Chem. Acc.* **2012**, *131*, 1084.

(100) Harl, J.; Kresse, G. Accurate Bulk Properties from Approximate Many-Body Techniques. *Phys. Rev. Lett.* **2009**, *103*, 056401.

(101) Ren, X.; Rinke, P.; Joas, C.; Scheffler, M. Random-Phase Approximation and Its Applications in Computational Chemistry and Materials Science. *J. Mater. Sci.* **2012**, *47*, 7447–7471.

(102) Schimka, L.; Harl, J.; Stroppa, A.; Grüneis, A.; Marsman, M.; Mittendorfer, F.; Kresse, G. Accurate Surface and Adsorption Energies from Many-Body Perturbation Theory. *Nat. Mater.* **2010**, *9*, 741–744.

(103) Dobson, J. F.; White, A.; Rubio, A. Asymptotics of the Dispersion Interaction: Analytic Benchmarks for van Der Waals Energy Functionals. *Phys. Rev. Lett.* **2006**, *96*, 073201.

(104) Cohen, A. J.; Mori-Sánchez, P.; Yang, W. Insights into Current Limitations of Density Functional Theory. *Science* **2008**, *321*, 792–794.

(105) Mori-Sánchez, P.; Cohen, A.; Yang, W. Localization and Delocalization Errors in Density Functional Theory and Implications for Band-Gap Prediction. *Phys. Rev. Lett.* **2008**, *100*, 146401.

(106) Hubbard, J. Electron Correlations in Narrow Energy Bands. *Proc. R. Soc. A Math. Phys. Eng. Sci.* **1963**, *276*, 238–257.

(107) Dudarev, S. L.; Manh, D. N.; Sutton, A. P. Effect of Mott-Hubbard Correlations on the Electronic Structure and Structural Stability of Uranium Dioxide. *Philos. Mag. Part B* **1997**, *75*, 613–628.

(108) Liechtenstein, A. I.; Anisimov, V. I.; Zaanen, J. Density-Functional Theory and Strong Interactions: Orbital Ordering in Mott-Hubbard Insulators. *Phys. Rev. B* **1995**, *52*, 5467–5471.

(109) Anisimov, V. I.; Zaanen, J.; Andersen, O. K. Band Theory and Mott Insulators: Hubbard U instead of Stoner I. *Phys. Rev. B* **1991**, *44*, 943–954.

(110) Dudarev, S. L.; Botton, G. A.; Savrasov, S. Y.; Humphreys, C. J.; Sutton, A. P. Electron-Energy-Loss Spectra and the Structural Stability of Nickel Oxide: An LSDA+U Study. *Phys. Rev. B* **1998**, *57*, 1505–1509.

(111) Cococcioni, M.; de Gironcoli, S. Linear Response Approach to the Calculation of the Effective Interaction Parameters in the LDA+U Method. *Phys. Rev. B* **2005**, *71*, 035105.

(112) Solovyev, I. V.; Dederichs, P. H.; Anisimov, V. I. Corrected Atomic Limit in the Local-Density Approximation and the Electronic Structure of D Impurities in Rb. *Phys. Rev. B* **1994**, *50*, 16861–16871.

(113) Anisimov, V. I.; Gunnarsson, O. Density-Functional Calculation of Effective Coulomb Interaction in Metals. *Phys. Rev. B* **1991**, *43*, 7570–7574.

(114) Loschen, C.; Carrasco, J.; Neyman, K.; Illas, F. First-Principles LDA+U and GGA+U Study of Cerium Oxides: Dependence on the Effective U Parameter. *Phys. Rev. B* **2007**, *75*, 035115.

(115) Zhao, Y.; Truhlar, D. G. Density Functionals with Broad Applicability in Chemistry. *Acc. Chem. Res.* **2008**, *41*, 157–167.

(116) Schultz, N. E.; Zhao, Y.; Truhlar, D. G. Databases for Transition Element Bonding: Metal-Metal Bond Energies and Bond Lengths and Their Use to Test Hybrid, Hybrid Meta, and Meta Density Functionals and Generalized Gradient Approximations. *J. Phys. Chem. A* **2005**, *109*, 4388–4403.

(117) Schultz, N. E.; Zhao, Y.; Truhlar, D. G. Density Functionals for Inorganometallic and Organometallic Chemistry. *J. Phys. Chem. A* **2005**, *109*, 11127–11143.

(118) Csonka, G.; Perdew, J.; Ruzsinszky, A.; Philipsen, P.; Lebègue, S.; Paier, J.; Vydrov, O.; Ángyán, J. Assessing the Performance of Recent Density Functionals for Bulk Solids. *Phys. Rev. B* **2009**, *79*, 155107.

(119) Singh-Miller, N. E.; Marzari, N. Surface Energies, Work Functions, and Surface Relaxations of Low-Index Metallic Surfaces from First Principles. *Phys. Rev. B* **2009**, *80*, 235407.

(120) Lejaeghere, K.; Speybroeck, V. Van; Oost, G. Van; Cottenier, S.; Introduction, I. Error Estimates for Solid-State Density-Functional Theory Predictions: An Overview by Means of the Ground-State Elemental Crystals. **2014**, 1–27.

(121) Gražulis, S.; Chateigner, D.; Downs, R. T.; Yokochi, A. F. T.; Quirós, M.; Lutterotti, L.; Manakova, E.; Butkus, J.; Moeck, P.; Le Bail, A. Crystallography Open Database - an Open-Access Collection of Crystal Structures. *J. Appl. Crystallogr.* **2009**, *42*, 726–729.

(122) Luo, S.; Zhao, Y.; Truhlar, D. G. Improved CO Adsorption Energies, Site Preferences, and Surface Formation Energies from a Meta-Generalized Gradient Approximation Exchange–Correlation Functional, M06-L. *J. Phys. Chem. Lett.* **2012**, *3*, 2975–2979.

(123) Paier, J.; Marsman, M.; Kresse, G. Why Does the B3LYP Hybrid Functional Fail for Metals? *J. Chem. Phys.* **2007**, *127*, 024103.

(124) Harvey, J. N. On the Accuracy of Density Functional Theory in Transition Metal Chemistry. *Annu. Reports Sect. "C"* **2006**, *102*, 203–226.

(125) Zhao, Y.; Truhlar, D. G. A New Local Density Functional for Main-Group Thermochemistry, Transition Metal Bonding, Thermochemical Kinetics, and Noncovalent Interactions. *J. Chem. Phys.* **2006**, *125*, 194101.

(126) Peverati, R.; Truhlar, D. G. An Improved and Broadly Accurate Local Approximation to the Exchange-Correlation Density Functional: The MN12-L Functional for Electronic Structure Calculations in Chemistry and Physics. *Phys. Chem. Chem. Phys.* **2012**, *14*, 13171–13174.

(127) Peverati, R.; Truhlar, D. G. Screened-Exchange Density Functionals with Broad Accuracy for Chemistry and Solid-State Physics. *Phys. Chem. Chem. Phys.* **2012**, *14*, 16187–16191.

(128) Peverati, R.; Truhlar, D. G. Performance of the M11-L Density Functional for Bandgaps and Lattice Constants of Unary and Binary Semiconductors. *J. Chem. Phys.* **2012**, *136*, 134704.

(129) Sousa, S. F.; Fernandes, P. A.; Ramos, M. J. General Performance of Density Functionals. *J. Phys. Chem. A* **2007**, *111*, 10439–10452.

(130) Ross, P. D.; Subramanian, S. Thermodynamics of Protein Association Reactions: Forces Contributing to Stability. *Biochemistry* **1981**, *20*, 3096–3102.

(131) Plata, J. J.; Collico, V.; Márquez, A. M.; Sanz, J. F. Analysis of the Origin of Lateral Interactions in the Adsorption of Small Organic Molecules on Oxide Surfaces. *Theor. Chem. Acc.* **2012**, *132*, 1311.

(132) Silvestrelli, P. L.; Ambrosetti, A. Including Screening in van Der Waals Corrected Density Functional Theory Calculations: The Case of Atoms and Small Molecules Physisorbed on Graphene. *J. Chem. Phys.* **2014**, *140*, 124107.

(133) Vanin, M.; Mortensen, J. J.; Kelkkanen, A. K.; Garcia-Lastra, J. M.; Thygesen, K. S.; Jacobsen, K. W. Graphene on Metals: A van Der Waals Density Functional Study. *Phys. Rev. B* **2010**, *81*, 081408.

(134) Sutter, P. W.; Flege, J.-I.; Sutter, E. A. Epitaxial Graphene on Ruthenium. *Nat. Mater.* **2008**, *7*, 406–411.

(135) Grüneis, A.; Vyalikh, D. Tunable Hybridization between Electronic States of Graphene and a Metal Surface. *Phys. Rev. B* **2008**, *77*, 193401.

(136) Gotterbarm, K.; Steiner, C.; Bronnbauer, C.; Bauer, U.; Steinrück, H.-P.; Maier, S.; Papp, C. Graphene-Templated Growth of Pd Nanoclusters. *J. Phys. Chem. C* **2014**, *118*, 15934–15939.

(137) Ortmann, F.; Bechstedt, F.; Schmidt, W. Semiempirical van Der Waals Correction to the Density Functional Description of Solids and Molecular Structures. *Phys. Rev. B* **2006**, *73*, 205101.

(138) Grimme, S. Accurate Description of van Der Waals Complexes by Density Functional Theory Including Empirical Corrections. *J. Comput. Chem.* **2004**, *25*, 1463–1473.

(139) Grimme, S.; Antony, J.; Ehrlich, S.; Krieg, H. A Consistent and Accurate Ab Initio Parametrization of Density Functional Dispersion Correction (DFT-D) for the 94 Elements H-Pu. *J. Chem. Phys.* **2010**, *132*, 154104.

(140) Tkatchenko, A.; Scheffler, M. Accurate Molecular Van Der Waals Interactions from Ground-State Electron Density and Free-Atom Reference Data. *Phys. Rev. Lett.* **2009**, *102*, 073005.

(141) Tkatchenko, A.; DiStasio, R. A.; Car, R.; Scheffler, M. Accurate and Efficient Method for Many-Body van Der Waals Interactions. *Phys. Rev. Lett.* **2012**, *108*, 236402.

(142) Dion, M.; Rydberg, H.; Schröder, E.; Langreth, D. C.; Lundqvist, B. I. Van Der Waals Density Functional for General Geometries. *Phys. Rev. Lett.* **2004**, *92*, 246401.

(143) Lee, K.; Murray, É. D.; Kong, L.; Lundqvist, B. I.; Langreth, D. C. Higher-Accuracy van Der Waals Density Functional. *Phys. Rev. B* **2010**, *82*, 081101.

(144) Klimeš, J.; Bowler, D. R.; Michaelides, A. Chemical Accuracy for the van Der Waals Density Functional. *J. Phys. Condens. Matter* **2010**, *22*, 022201.

(145) Klimeš, J.; Bowler, D. R.; Michaelides, A. Van Der Waals Density Functionals Applied to Solids. *Phys. Rev. B* **2011**, *83*, 195131.

(146) Dobson, J. F.; Mclennan, K.; Rubio, A.; Wang, J.; Gould, T.; Le, H. M.; Dinte, B. P. Prediction of Dispersion Forces : Is There a Problem ? *Aust. J. Chem.* **2001**, *54*, 513–257.

(147) Bianchini, F.; Patera, L. L.; Peressi, M.; Africh, C.; Comelli, G. Atomic Scale Identification of Coexisting Graphene Structures on Ni(111). *J. Phys. Chem. Lett.* **2014**, *5*, 467–473.

(148) Mostafa, S.; Behafarid, F.; Croy, J. R.; Ono, L. K.; Li, L.; Yang, J. C.; Frenkel, A. I.; Cuenya, B. R. Shape-Dependent Catalytic Properties of Pt Nanoparticles. *J. Am. Chem. Soc.* **2010**, *132*, 15714–15719.

(149) Peter, M.; Flores Camacho, J. M.; Adamovski, S.; Ono, L. K.; Dostert, K.-H.; O'Brien, C. P.; Roldan Cuenya, B.; Schauermann, S.; Freund, H.-J. Trends in the Binding Strength of Surface Species on Nanoparticles: How Does the Adsorption Energy Scale with the Particle Size? *Angew. Chem. Int. Ed. Engl.* **2013**, *52*, 5175–5179.

(150) Viñes, F.; Lykhach, Y.; Staudt, T.; Lorenz, M. P. A.; Papp, C.; Steinrück, H.-P.; Libuda, J.; Neyman, K. M.; Görling, A. Methane Activation by Platinum: Critical Role of Edge and Corner Sites of Metal Nanoparticles. *Chem. A Eur. J.* **2010**, *16*, 6530–6539.

(151) Neyman, K. M.; Illas, F. Theoretical Aspects of Heterogeneous Catalysis: Applications of Density Functional Methods. *Catal. Today* **2005**, *105*, 2–16.

(152) Yudanov, I. V.; Genest, A.; Rösch, N. DFT Studies of Palladium Model Catalysts: Structure and Size Effects. *J. Clust. Sci.* **2011**, *22*, 433–448.

(153) Cargnello, M.; Doan-Nguyen, V. V. T.; Gordon, T. R.; Diaz, R. E.; Stach, E. A.; Gorte, R. J.; Fornasiero, P.; Murray, C. B. Control of Metal Nanocrystal Size Reveals Metal-Support Interface Role for Ceria Catalysts. *Science* **2013**, *341*, 771–773.

(154) Green, I. X.; Tang, W.; Neurock, M.; Yates, J. T. Low-Temperature Catalytic H_2 Oxidation over Au nanoparticle/TiO_2 Dual Perimeter Sites. *Angew. Chem. Int. Ed. Engl.* **2011**, *50*, 10186–10189.

(155) Whitten, J. L.; Yang, H. Theory of Chemisorption and Reactions on Metal Surfaces. *Surf. Sci. Rep.* **1996**, *24*, 55–124.

(156) Häkkinen, H.; Yoon, B.; Landman, U.; Li, X.; Zhai, H.; Wang, L.; Box, P. O. On the Electronic and Atomic Structures of Small Au_N^-(N = 4 - 14) Clusters: A Photoelectron Spectroscopy and Density-Functional Study. *J. Phys. Chem. A* **2003**, *107*, 6168–6175.

(157) Yudanov, I. V.; Sahnoun, R.; Neyman, K. M.; Rösch, N. Metal Nanoparticles as Models of Single Crystal Surfaces and Supported Catalysts: Density Functional Study of Size Effects for CO/Pd(111). *J. Chem. Phys.* **2002**, *117*, 9887.

(158) Kua, J.; Goddard III, W. A. Oxidation of Methanol on 2nd and 3rd Row Group VIII Transition Metals (Pt, Ir, Os, Pd, Rh, and Ru): Application to Direct Methanol Fuel Cells. *J. Am. Chem. Soc.* **1999**, *121*, 10928–10941.

(159) Jacob, T.; Goddard III, W. A. Chemisorption of (CH_x and C_2H_y) Hydrocarbons on Pt(111) Clusters and Surfaces from DFT Studies. *J. Phys. Chem. B* **2005**, *109*, 297–311.

(160) Pettersson, L. G. M.; Faxen, T. Massively Parallel Direct SCF Calculations on Large Metal Clusters: Ni_5-Ni_{481}. *Theor. Chim. Acta* **1993**, *85*, 345–361.

(161) Triguero, L.; Pettersson, L. G. M.; Minaev, B.; Ågren, H. Spin Uncoupling in Surface Chemisorption of Unsaturated Hydrocarbons. *J. Chem. Phys.* **1998**, *108*, 1193–1205.

(162) Huang, P.; Carter, E. A. Advances in Correlated Electronic Structure Methods for Solids, Surfaces, and Nanostructures. *Annu. Rev. Phys. Chem.* **2008**, *59*, 261–290.

(163) Sushko, P. V.; Shluger, A. L.; Catlow, C. R. A. Relative Energies of Surface and Defect States: Ab Initio Calculations for the MgO (001) Surface. *Surf. Sci.* **2000**, *450*, 153–170.

(164) Nasluzov, V. A.; Rivanenkov, V. V.; Gordienko, A. B.; Neyman, K. M.; Birkenheuer, U.; Rösch, N. Cluster Embedding in an Elastic Polarizable Environment: Density Functional Study of Pd Atoms Adsorbed at Oxygen Vacancies of MgO(001). *J. Chem. Phys.* **2001**, *115*, 8157–8171.

(165) Catlow, C. R. A.; Bromley, S. T.; Hamad, S.; Mora-Fonz, M.; Sokol, A. A.; Woodley, S. M. Modelling Nano-Clusters and Nucleation. *Phys. Chem. Chem. Phys.* **2010**, *12*, 786–811.

(166) Johnston, R. L. Evolving Better Nanoparticles: Genetic Algorithms for Optimising Cluster Geometries. *Dalt. Trans.* **2003**, 4193–4207.

(167) Baletto, F.; Ferrando, R. Structural Properties of Nanoclusters: Energetic, Thermodynamic, and Kinetic Effects. *Rev. Mod. Phys.* **2005**, *77*, 371–423.

(168) Bruix, A.; Rodriguez, J. A.; Ramírez, P. J.; Senanayake, S. D.; Evans, J.; Park, J. B.; Stacchiola, D.; Liu, P.; Hrbek, J.; Illas, F. A New Type of Strong Metal-Support Interaction and the Production of H_2 through the Transformation of Water on Pt/CeO_2(111) and Pt/CeO_x/TiO_2(110) Catalysts. *J. Am. Chem. Soc.* **2012**, *134*, 8968–8974.

(169) Kim, H. Y.; Henkelman, G. CO Oxidation at the Interface of Au Nanoclusters and the Stepped- CeO_2(111) Surface by the Mars−van Krevelen Mechanism. **2013**, *2*, 2–7.

(170) Chretien, S.; Buratto, S.; Metiu, H. Catalysis by Very Small Au Clusters. *Curr. Opin. Solid State Mater. Sci.* **2007**, *11*, 62–75.

(171) Chen, Y.; Crawford, P.; Hu, P. Recent Advances in Understanding CO Oxidation on Gold Nanoparticles Using Density Functional Theory. *Catal. Letters* **2007**, *119*, 21–28.

(172) Heiz, U.; Sanchez, A.; Abbet, S.; Schneider, W. Catalytic Oxidation of Carbon Monoxide on Monodispersed Platinum Clusters: Each Atom Counts. *J. Am. Chem. Soc.* **1999**, *121*, 3214–3217.

(173) Rösch, N.; Petrova, G. P.; Petkov, P. St.; Genest, A.; Krüger, S.; Aleksandrov, H. A.; Vayssilov, G. N. Impurity Atoms on Small Transition Metal Clusters. Insights from Density Functional Model Studies. *Top. Catal.* **2011**, *54*, 363–377.

(174) Pyykkö, P. Theoretical Chemistry of Gold. III. *Chem. Soc. Rev.* **2008**, *37*, 1967–1997.

(175) Vilhelmsen, L. B.; Hammer, B. Identification of the Catalytic Site at the Interface Perimeter of Au Clusters on Rutile TiO_2(110). *ACS Catal.* **2014**, *2*, 1626–1631.

(176) Freund, H.-J. Model Studies in Heterogeneous Catalysis. *Chemistry* **2010**, *16*, 9384–9397.

(177) Pacchioni, G.; Chung, S.-C.; Krüger, S.; Rösch, N. On the Evolution of Cluster to Bulk Properties: A Theoretical LCGTO-LDF Study of Free and Coordinated Ni_n Clusters (n=6-147). *Chem. Phys.* **1994**, *184*, 125–137.

(178) Häberlen, O. D.; Chung, S.-C.; Stener, M.; Rösch, N. From Clusters to Bulk: A Relativistic Density Functional Investigation on a Series of Gold Clusters Au_n, n = 6,…,147. *J. Chem. Phys.* **1997**, *106*, 5189–5201.

(179) Roldán, A.; Viñes, F.; Illas, F.; Ricart, J. M.; Neyman, K. M. Density Functional Studies of Coinage Metal Nanoparticles: Scalability of Their Properties to Bulk. *Theor. Chem. Acc.* **2008**, *120*, 565–573.

(180) Yudanov, I. V; Metzner, M.; Genest, A.; Rösch, N. Size-Dependence of Adsorption Properties of Metal Nanoparticles: A Density Functional Study on Palladium Nanoclusters. *J. Phys. Chem. C* **2008**, *112*, 20269–20275.

(181) Viñes, F.; Illas, F.; Neyman, K. M. Density Functional Calculations of Pd Nanoparticles Using a Plane-Wave Method. *J. Phys. Chem. A* **2008**, *112*, 8911–8915.

(182) Yudanov, I. V; Genest, A.; Schauermann, S.; Freund, H.-J.; Rösch, N. Size Dependence of the Adsorption Energy of CO on Metal Nanoparticles: A DFT Search for the Minimum Value. *Nano Lett.* **2012**, *12*, 2134–2139.

(183) Neyman, K. M.; Inntam, C.; Gordienko, A. B.; Yudanov, I. V; Rösch, N. Adsorption of Carbon on Pd Clusters of Nanometer Size: A First-Principles Theoretical Study. *J. Chem. Phys.* **2005**, *122*, 174705.

(184) Neyman, K. M.; Go, A. Carbon on Platinum Substrates : From Carbidic to Graphitic Phases on the (111) Surface. **2009**, 11963–11973.

(185) Yudanov, I. V; Neyman, K. M.; Rösch, N. Density Functional Study of Pd Nanoparticles with Subsurface Impurities of Light Element Atoms. *Phys. Chem. Chem. Phys.* **2004**, *6*, 116–123.

(186) Viñes, F.; Loschen, C.; Illas, F.; Neyman, K. M. Edge Sites as a Gate for Subsurface Carbon in Palladium Nanoparticles. *J. Catal.* **2009**, *266*, 59–63.

(187) Li, L.; Larsen, A. H.; Romero, N. A.; Morozov, V. A.; Glinsvad, C.; Abild-pedersen, F.; Greeley, J.; Jacobsen, K. W.; Nørskov, J. K. Investigation of Catalytic Finite-Size-Effects of Platinum Metal Clusters. *J. Phys. Chem. Lett.* **2013**, *4*, 222–226.

(188) Roldán, A.; Ricart, J. M.; Illas, F.; Pacchioni, G. O_2 Adsorption and Dissociation on Neutral, Positively and Negatively Charged Au_n (n = 5-79) Clusters. *Phys. Chem. Chem. Phys.* **2010**, *12*, 10723–10729.

(189) Kleis, J.; Greeley, J.; Romero, N. A.; Morozov, V. A.; Falsig, H.; Larsen, A. H.; Lu, J.; Mortensen, J. J.; Dułak, M.; Thygesen, K. S.; et al. Finite Size Effects in Chemical Bonding: From Small Clusters to Solids. *Catal. Letters* **2011**, *141*, 1067–1071.

(190) Loschen, C.; Bromley, S. T.; Neyman, K. M.; Illas, F. Understanding Ceria Nanoparticles from First-Principles Calculations. *J. Phys. Chem. C* **2007**, *111*, 10142–10145.

(191) Loschen, C.; Migani, A.; Bromley, S. T.; Illas, F.; Neyman, K. M. Density Functional Studies of Model Cerium Oxide Nanoparticles. *Phys. Chem. Chem. Phys.* **2008**, *10*, 5730–5738.

(192) Migani, A.; Neyman, K. M.; Bromley, S. T. Octahedrality versus Tetrahedrality in Stoichiometric Ceria Nanoparticles. *Chem. Commun. (Camb).* **2012**, *48*, 4199–4201.

(193) Migani, A.; Loschen, C.; Illas, F.; Neyman, K. M. Towards Size-Converged Properties of Model Ceria Nanoparticles: Monitoring by Adsorbed CO Using DFT+U Approach. *Chem. Phys. Lett.* **2008**, *465*, 106–109.

(194) Pozun, Z. D.; Tran, K.; Shi, A.; Smith, R. H.; Henkelman, G. Why Silver Nanoparticles Are Effective for Olefin/Paraffin Separations. *J. Phys. Chem. C* **2011**, *115*, 1811–1818.

(195) Kietzmann, H.; Morenzin, J.; Bechthold, P.; Ganteför, G.; Eberhardt, W.; Yang, D.-S.; Hackett, P.; Fournier, R.; Pang, T.; Chen, C. Photoelectron Spectra and Geometric Structures of Small Niobium Cluster Anions. *Phys. Rev. Lett.* **1996**, *77*, 4528–4531.

(196) Ganteför, G.; Eberhardt, W. Localization of 3d and 4d Electrons in Small Clusters: The "Roots" of Magnetism. *Phys. Rev. Lett.* **1996**, *76*, 4975–4978.

(197) Apsel, S.; Emmert, J.; Deng, J.; Bloomfield, L. Surface-Enhanced Magnetism in Nickel Clusters. *Phys. Rev. Lett.* **1996**, *76*, 1441–1444.

(198) Molina, L. M.; Lee, S.; Sell, K.; Barcaro, G.; Fortunelli, A.; Lee, B.; Seifert, S.; Winans, R. E.; Elam, J. W.; Pellin, M. J. Size-Dependent Selectivity and Activity of Silver Nanoclusters in the Partial Oxidation of Propylene to Propylene Oxide and Acrolein: A Joint Experimental and Theoretical Study. *Catal. Today* **2011**, *160*, 116–130.

(199) Shao, M.; Peles, A.; Shoemaker, K. Electrocatalysis on Platinum Nanoparticles: Particle Size Effect on Oxygen Reduction Reaction Activity. *Nano Lett.* **2011**, *11*, 3714–3719.

(200) Stakheev, A. Y.; Batkin, A. M.; Teleguina, N. S.; Bragina, G. O.; Zaikovsky, V. I.; Prosvirin, I. P.; Khudorozhkov, A. K.; Bukhtiyarov, V. I. Particle Size Effect on CH_4 Oxidation Over Noble Metals: Comparison of Pt and Pd Catalysts. *Top. Catal.* **2013**, *56*, 306–310.

(201) Kaden, W. E.; Wu, T.; Kunkel, W. A.; Anderson, S. L. Electronic Structure Controls Reactivity of Size-Selected Pd Clusters Adsorbed on TiO_2 Surfaces. *Science* **2009**, *326*, 826–829.

(202) Fischer-Wolfarth, J.-H.; Hartmann, J.; Farmer, J. A.; Flores-Camacho, J. M.; Campbell, C. T.; Schauermann, S.; Freund, H.-J. An Improved Single Crystal Adsorption Calorimeter for Determining Gas Adsorption and Reaction Energies on Complex Model Catalysts. *Rev. Sci. Instrum.* **2011**, *82*, 024102.

(203) Fischer-Wolfarth, J.-H.; Farmer, J. A.; Flores-Camacho, J. M.; Genest, A.; Yudanov, I. V.; Rösch, N.; Campbell, C. T.; Schauermann, S.; Freund, H.-J. Particle-Size Dependent Heats of Adsorption of CO on Supported Pd Nanoparticles as Measured with a Single-Crystal Microcalorimeter. *Phys. Rev. B* **2010**, *81*, 241416.

(204) Flores-Camacho, J. M.; Fischer-Wolfarth, J.-H.; Peter, M.; Campbell, C. T.; Schauermann, S.; Freund, H.-J. Adsorption Energetics of CO on Supported Pd Nanoparticles as a Function of Particle Size by Single Crystal Microcalorimetry. *Phys. Chem. Chem. Phys.* **2011**, *13*, 16800–16810.

(205) Peter, M.; Adamovsky, S.; Flores Camacho, J. M.; Schauermann, S. Energetics of Elementary Reaction Steps Relevant for CO Oxidation: CO and O_2 Adsorption on Model Pd Nanoparticles and Pd(111). *Faraday Discuss.* **2013**, *162*, 341.

(206) Schauermann, S.; Nilius, N.; Shaikhutdinov, S.; Freund, H.-J. Nanoparticles for Heterogeneous Catalysis: New Mechanistic Insights. *Acc. Chem. Res.* **2013**, *46*, 1673–1681.

(207) Hansen, P. L.; Wagner, J. B.; Helveg, S.; Rostrup-Nielsen, J. R.; Clausen, B. S.; Topsøe, H. Atom-Resolved Imaging of Dynamic Shape Changes in Supported Copper Nanocrystals. *Science* **2002**, *295*, 2053–2055.

(208) Krüger, S.; Vent, S.; Nörtemann, F.; Staufer, M.; Rösch, N. The Average Bond Length in Pd Clusters Pd_n, n=4–309: A Density-Functional Case Study on the Scaling of Cluster Properties. *J. Chem. Phys.* **2001**, *115*, 2082.

(209) Yudanov, I. V; Sahnoun, R.; Neyman, K. M.; Rösch, N.; Hoffmann, J.; Schauermann, S.; Johánek, V.; Unterhalt, H.; Rupprechter, G.; Libuda, J.; et al. CO Adsorption on Pd Nanoparticles: Density Functional and Vibrational Spectroscopy Studies. *J. Phys. Chem. B* **2003**, *107*, 255–264.

(210) Allian, A. D.; Takanabe, K.; Fujdala, K. L.; Hao, X.; Truex, T. J.; Cai, J.; Buda, C.; Neurock, M.; Iglesia, E. Chemisorption of CO and Mechanism of CO Oxidation on Supported Platinum Nanoclusters. *J. Am. Chem. Soc.* **2011**, *133*, 4498–4517.

(211) Mamatkulov, M.; Filhol, J.-S. Intrinsic Electrochemical and Strain Effects in Nanoparticles. **2013**, *117*, 2334–2343.

(212) Calle-Vallejo, F.; Martínez, J. I.; García-Lastra, J. M.; Sautet, P.; Loffreda, D. Fast Prediction of Adsorption Properties for Platinum Nanocatalysts with Generalized Coordination Numbers. *Angew. Chem. Int. Ed. Engl.* **2014**, 8316–8319.

(213) Li, H.-J.; Yeh, C.-H.; Ho, J.-J. The Highly Effective Catalytic Behavior of a Metal Nanocluster Ru_{79} on the Dissociation of a N_2 molecule—A Quantum-Chemical Calculation. *Catal. Commun.* **2014**, *52*, 5–9.

(214) Bunluesin, T.; Gottea, R. J.; Grahamb, G. W. Studies of the Water-Gas-Shift Reaction on Ceria-Supported Pt, Pd, and Rh: Implications for Oxygen-Storage Properties. **1998**, *15*, 107–114.

(215) Biffis, A.; Zecca, M.; Basato, M. Palladium Metal Catalysts in Heck C-C Coupling Reactions. *J. Mol. Catal. A Chem.* **2001**, *173*, 249–274.

(216) Blaser, H.; Indolese, A.; Schnyder, A.; Steiner, H.; Studer, M. Supported Palladium Catalysts for Fine Chemicals Synthesis. **2001**, *173*, 3–18.

(217) Anderson, R. B.; Stein, K. C.; Feenan, J. J.; Hofer, L. J. E. Catalytic Oxidation of Methane. *Ind. Eng. Chem.* **1961**, *53*, 809–812.

(218) Usami, Y.; Kagawa, K.; Kawazoe, M.; Sakurai, H.; Haruta, M. Catalytic Methanol Decomposition at Low Temperatures over Palladium Supported on Metal Oxides. *Appl. Catal. A Gen.* **1998**, *171*, 123–130.

(219) Yudanov, I. V; Matveev, A. V; Neyman, K. M.; Rösch, N. How the C-O Bond Breaks during Methanol Decomposition on Nanocrystallites of Palladium Catalysts. *J. Am. Chem. Soc.* **2008**, *130*, 9342–9352.

(220) Jennings, P. C.; Aleksandrov, H. A.; Neyman, K. M.; Johnston, R. L. A DFT Study of Oxygen Dissociation on Platinum Based Nanoparticles. *Nanoscale* **2014**, *6*, 1153–1165.

(221) Hellman, A.; Resta, A.; Martin, N. M.; Gustafson, J.; Trinchero, A.; Carlsson, P.-A.; Balmes, O.; Felici, R.; Rijn, R. Van; Frenken, J. W. M.; et al. The Active Phase of Palladium during Methane Oxidation. *J. Phys. Chem. Lett.* **2012**, *3*, 678–682.

(222) Peskov, N. V; Slinko, M. M.; Bychkov, V. Y.; Korchak, V. N. Mathematical Modelling of Oscillatory Behaviour during Methane Oxidation over Palladium Catalysts. *Chem. Eng. Sci* **2012**, *84*, 684–694.

(223) Savara, A.; Ludwig, W.; Schauermann, S. Kinetic Evidence for a Non-Langmuir-Hinshelwood Surface Reaction: H/D Exchange over Pd Nanoparticles and Pd(111). *Chemphyschem* **2013**, *14*, 1686–1695.

(224) Ludwig, W.; Savara, A.; Brandt, B.; Schauermann, S. A Kinetic Study on the Conversion of Cis-2-Butene with Deuterium on a Pd/Fe_3O_4 Model Catalyst. *Phys. Chem. Chem. Phys.* **2011**, *13*, 966–977.

(225) Gabasch, H.; Hayek, K.; Klötzer, B.; Knop-Gericke, A.; Schlögl, R. Carbon Incorporation in Pd(111) by Adsorption and Dehydrogenation of Ethene. *J. Phys. Chem. B* **2006**, *110*, 4947–4952.

(226) Schauermann, S.; Hoffmann, J.; Johánek, V.; Hartmann, J.; Libuda, J.; Freund, H.-J. Catalytic Activity and Poisoning of Specific Sites on Supported Metal Nanoparticles. *Angew. Chem. Int. Ed. Engl.* **2002**, 2532–2535.

(227) Teschner, D.; Borsodi, J.; Wootsch, A.; Révay, Z.; Hävecker, M.; Knop-Gericke, A.; Jackson, S. D.; Schlögl, R. The Roles of Subsurface Carbon and Hydrogen in Palladium-Catalyzed Alkyne Hydrogenation. *Science* **2008**, *320*, 86–89.

(228) Teschner, D.; Révay, Z.; Borsodi, J.; Hävecker, M.; Knop-Gericke, A.; Schlögl, R.; Milroy, D.; Jackson, S. D.; Torres, D.; Sautet, P. Understanding Palladium Hydrogenation Catalysts: When the Nature of the Reactive Molecule Controls the Nature of the Catalyst Active Phase. *Angew. Chem. Int. Ed. Engl.* **2008**, *47*, 9274–9278.

(229) Leisenberger, F. P.; Koller, G.; Sock, M.; Surnev, S.; Ramsey, M. G.; Netzer, F. P.; Klötzer, B.; Hayek, K. Surface and Subsurface Oxygen on Pd(111). *Surf. Sci.* **2000**, *445*, 380–393.

(230) Zemlyanov, D.; Klötzer, B.; Gabasch, H.; Smeltz, A.; Ribeiro, F. H.; Zafeiratos, S.; Teschner, D.; Schnörch, P.; Vass, E.; Hävecker, M.; et al. Kinetics of Palladium Oxidation in the Mbar Pressure Range: Ambient Pressure XPS Study. *Top. Catal.* **2013**, *56*, 885–895.

(231) Kozlov, S. M.; Yudanov, I. V; Aleksandrov, H. A.; Rösch, N. Theoretical Study of Carbon Species on Pd(111): Competition between Migration of C Atoms to

the Subsurface Interlayer and Formation of C_n Clusters on the Surface. *Phys. Chem. Chem. Phys.* **2009**, *11*, 10955–10963.

(232) Ludwig, W.; Savara, A.; Dostert, K.-H.; Schauermann, S. Olefin Hydrogenation on Pd Model Supported Catalysts: New Mechanistic Insights. *J. Catal.* **2011**, *284*, 148–156.

(233) Neyman, K. M.; Schauermann, S. Hydrogen Diffusion into Palladium Nanoparticles: Pivotal Promotion by Carbon. *Angew. Chem. Int. Ed. Engl.* **2010**, *49*, 4743–4746.

(234) Teschner, D.; Vass, E.; Havecker, M.; Zafeiratos, S.; Schnorch, P.; Sauer, H.; Knopgericke, A.; Schlogl, R.; Chamam, M.; Wootsch, A. Alkyne Hydrogenation over Pd Catalysts: A New Paradigm. *J. Catal.* **2006**, *242*, 26–37.

(235) Yamauchi, M.; Kobayashi, H.; Kitagawa, H. Hydrogen Storage Mediated by Pd and Pt Nanoparticles. *Chemphyschem* **2009**, *10*, 2566–2576.

(236) Kobayashi, H.; Morita, H.; Yamauchi, M.; Ikeda, R.; Kitagawa, H.; Kubota, Y.; Kato, K.; Takata, M. Nanosize-Induced Hydrogen Storage and Capacity Control in a Non-Hydride-Forming Element: Rhodium. *J. Am. Chem. Soc.* **2011**, *133*, 11034–11037.

(237) Daley, S. P.; Utz, A. L.; Trautman, T. R.; Ceyer, S. T. Ethylene Hydrogenation on Ni(111) by Bulk Hydrogen. *J. Am. Chem. Soc.* **1994**, *116*, 6001–6002.

(238) Henkelman, G.; Arnaldsson, A.; Jónsson, H. Theoretical Calculations of CH_4 and H_2 Associative Desorption from Ni(111): Could Subsurface Hydrogen Play an Important Role? *J. Chem. Phys.* **2006**, *124*, 044706.

(239) Li, G.; Kobayashi, H.; Taylor, J. M.; Ikeda, R.; Kubota, Y.; Kato, K.; Takata, M.; Yamamoto, T.; Toh, S.; Matsumura, S.; et al. Hydrogen Storage in Pd Nanocrystals Covered with a Metal – Organic Framework. *Nat. Mater.* **2014**, *13*, 802–806.

(240) Greeley, J.; Nørskov, J. K. A General Scheme for the Estimation of Oxygen Binding Energies on Binary Transition Metal Surface Alloys. *Surf. Sci.* **2005**, *592*, 104–111.

(241) Ferrando, R.; Jellinek, J.; Johnston, R. L. Nanoalloys: From Theory to Applications of Alloy Clusters and Nanoparticles. *Chem. Rev.* **2008**, *108*, 845–910.

(242) Bochicchio, D.; Ferrando, R. Morphological Instability of Core-Shell Metallic Nanoparticles. *Phys. Rev. B* **2013**, *87*, 165435.

(243) Bruma, A.; Ismail, R.; Paz-Borbón, L. O.; Arslan, H.; Barcaro, G.; Fortunelli, A.; Li, Z. Y.; Johnston, R. L. DFT Study of the Structures and Energetics of 98-Atom AuPd Clusters. *Nanoscale* **2013**, *5*, 646–652.

(244) Negreiros, F. R.; Barcaro, G.; Kuntová, Z.; Rossi, G.; Ferrando, R.; Fortunelli, A. Structures of AgPd Nanoclusters Adsorbed on MgO(100): A Computational Study. *Surf. Sci.* **2011**, *605*, 483–488.

(245) Barcaro, G.; Fortunelli, A.; Polak, M.; Rubinovich, L. Patchy Multishell Segregation in Pd-Pt Alloy Nanoparticles. *Nano Lett.* **2011**, *11*, 1766–1769.

(246) Mărginean, P.; Olariu, A. Influence of Metal Oxides on the Catalytic Activity of Nickel. *Appl. Catal. A Gen.* **1997**, *165*, 241–248.

(247) Jin, M.; Park, J.-N.; Shon, J. K.; Kim, J. H.; Li, Z.; Park, Y.-K.; Kim, J. M. Low Temperature CO Oxidation over Pd Catalysts Supported on Highly Ordered Mesoporous Metal Oxides. *Catal. Today* **2012**, *185*, 183–190.

(248) Okumura, K.; Motohiro, T.; Sakamoto, Y.; Shinjoh, H. Effect of Combination of Noble Metals and Metal Oxide Supports on Catalytic Reduction of NO by H_2. *Surf. Sci.* **2009**, *603*, 2544–2550.

(249) Chua, Y. P. G.; Gunasooriya, G. T. K. K.; Saeys, M.; Seebauer, E. G. Controlling the CO Oxidation Rate over Pt/TiO_2 Catalysts by Defect Engineering of the TiO_2 Support. *J. Catal.* **2014**, *311*, 306–313.

(250) Persson, K.; Ersson, A.; Colussi, S.; Trovarelli, A.; Järås, S. G. Catalytic Combustion of Methane over Bimetallic Pd–Pt Catalysts: The Influence of Support Materials. *Appl. Catal. B Environ.* **2006**, *66*, 175–185.

(251) Thevenin, P.; Alcalde, A.; Pettersson, L. J.; Järås, S. G.; Fierro, J. L. G. Catalytic Combustion of Methane over Cerium-Doped Palladium Catalysts. *J. Catal.* **2003**, *215*, 78–86.

(252) Phatak, A. A.; Koryabkina, N.; Rai, S.; Ratts, J. L.; Ruettinger, W.; Farrauto, R. J.; Blau, G. E.; Delgass, W. N.; Ribeiro, F. H. Kinetics of the Water–gas Shift Reaction on Pt Catalysts Supported on Alumina and Ceria. *Catal. Today* **2007**, *123*, 224–234.

(253) Fouladvand, S.; Schernich, S.; Libuda, J.; Grönbeck, H.; Pingel, T.; Olsson, E.; Skoglundh, M.; Carlsson, P.-A. Methane Oxidation Over Pd Supported on Ceria–Alumina Under Rich/Lean Cycling Conditions. *Top. Catal.* **2013**, *56*, 410–415.

(254) Groppi, G.; Cristiani, C.; Lietti, L.; Ramella, C.; Valentini, M.; Forzatti, P. Effect of Ceria on Palladium Supported Catalysts for High Temperature Combustion of CH4 under Lean Conditions. *Catal. Today* **1999**, *50*, 399–412.

(255) Chenakin, S. P.; Melaet, G.; Szukiewicz, R.; Kruse, N. XPS Study of the Surface Chemical State of a Pd/(SiO_2+TiO_2) Catalyst after Methane Oxidation and SO_2 Treatment. *J. Catal.* **2014**, *312*, 1–11.

(256) Liu, Z.-P.; Gong, X.-Q.; Kohanoff, J.; Sanchez, C.; Hu, P. Catalytic Role of Metal Oxides in Gold-Based Catalysts: A First Principles Study of CO Oxidation on TiO_2 Supported Au. *Phys. Rev. Lett.* **2003**, *91*, 266102.

(257) Iwasa, N.; Mayanagi, T.; Ogawa, N.; Sakata, K.; Takezawa, N. New Catalytic Functions of Pd–Zn, Pd–Ga, Pd–In, Pt–Zn, Pt–Ga and Pt–In Alloys in the Conversions of Methanol. **1998**, *54*, 119–123.

(258) Iwasa, N.; Takezawa, N. New Supported Pd and Pt Alloy Catalysts for Steam Reforming and Dehydrogenation of Methanol. *Top. Catal.* **2003**, *22*, 215–224.

(259) Liu, Y.; Chen, J.; Zhang, J. Effects of the Supports on Activity of Supported Nickel Catalysts for Hydrogenation of M-Dinitrobenzene to M-Phenylenediamine. *Chinese J. Chem. Eng.* **2007**, *15*, 63–67.

(260) Han, Y.; Ferrando, R.; Li, Z. Y. Atomic Details of Interfacial Interaction in Gold Nanoparticles Supported on MgO(001). *J. Phys. Chem. Lett.* **2014**, *5*, 131–137.

(261) Bruix, A.; Migani, A.; Vayssilov, G. N.; Neyman, K. M.; Libuda, J.; Illas, F. Effects of Deposited Pt Particles on the Reducibility of CeO_2(111). *Phys. Chem. Chem. Phys.* **2011**, *13*, 11384–11392.

(262) Barcaro, G.; Fortunelli, A.; Nita, F.; Ferrando, R. Diffusion of Palladium Clusters on Magnesium Oxide. *Phys. Rev. Lett.* **2005**, *95*, 246103.

(263) Barcaro, G.; Fortunelli, A.; Rossi, G.; Nita, F.; Ferrando, R. Epitaxy, Truncations, and Overhangs in Palladium Nanoclusters Adsorbed on MgO(001). *Phys. Rev. Lett.* **2007**, *98*, 156101.

(264) Hu, C. H.; Chizallet, C.; Mager-Maury, C.; Corral-Valero, M.; Sautet, P.; Toulhoat, H.; Raybaud, P. Modulation of Catalyst Particle Structure upon Support Hydroxylation: Ab Initio Insights into Pd_{13} and Pt_{13}/γ-Al_2O_3. *J. Catal.* **2010**, *274*, 99–110.

(265) Wang, J. G.; Hammer, B. Oxidation State of Oxide Supported Nanometric Gold. *Top. Catal.* **2007**, *44*, 49–56.

(266) Li, Z.; Li, Y.; Li, J. Support Effects on the Dissociation of Hydrogen over Gold Clusters on ZnO(101) Surface: Theoretical Insights. *J. Chem. Phys.* **2012**, *137*, 234704.

(267) Eichler, A. Chemical Characterization of a Zirconia-Supported Pt Cluster. *Phys. Rev. B* **2005**, *71*, 125418.

(268) Corral Valero, M.; Raybaud, P.; Sautet, P. Interplay between Molecular Adsorption and Metal–support Interaction for Small Supported Metal Clusters: CO and C_2H_4 Adsorption on Pd_4/γ-Al_2O_3. *J. Catal.* **2007**, *247*, 339–355.

(269) Vendelbo, S. B.; Elkjær, C. F.; Falsig, H.; Puspitasari, I.; Dona, P.; Mele, L.; Morana, B.; Nelissen, B. J.; Rijn, R. Van; Creemer, J. F.; et al. Visualization of Oscillatory Behaviour of Pt Nanoparticles Catalysing CO Oxidation. *Nat. Mater.* **2014**, 1–7.

(270) Casalongue, H. S.; Kaya, S.; Viswanathan, V.; Miller, D. J.; Friebel, D.; Hansen, H. A.; Nørskov, J. K.; Nilsson, A.; Ogasawara, H. Direct Observation of the Oxygenated Species during Oxygen Reduction on a Platinum Fuel Cell Cathode. *Nat. Commun.* **2013**, *4*, 2817.

(271) Ciftci, A.; Ligthart, D. A. J. M.; Pastorino, P.; Hensen, E. J. M. Nanostructured Ceria Supported Pt and Au Catalysts for the Reactions of Ethanol and Formic Acid. *Appl. Catal. B Environ.* **2013**, *130-131*, 325–335.

(272) Jacobs, G.; Keogh, R.; Davis, B. Steam Reforming of Ethanol over Pt/ceria with Co-Fed Hydrogen. *J. Catal.* **2007**, *245*, 326–337.

(273) Takezawa, N.; Iwasa, N. Steam Reforming and Dehydrogenation of Methanol: Difference in the Catalytic Functions of Copper and Group VIII Metals. *Catal. Today* **1997**, *36*, 45–56.

(274) Olander, J.; Lazzari, R.; Jupille, J.; Mangili, B.; Goniakowski, J.; Renaud, G. Size- and Temperature-Dependent Epitaxy for a Strong Film-Substrate Mismatch: The Case of Pt/MgO(001). *Phys. Rev. B* **2007**, *76*, 075409.

(275) Ferrando, R.; Rossi, G.; Levi, A. C.; Kuntová, Z.; Nita, F.; Jelea, A.; Mottet, C.; Barcaro, G.; Fortunelli, A.; Goniakowski, J. Structures of Metal Nanoparticles Adsorbed on MgO(001). I. Ag and Au. *J. Chem. Phys.* **2009**, *130*, 174702.

(276) Goniakowski, J.; Jelea, A.; Mottet, C.; Barcaro, G.; Fortunelli, A.; Kuntová, Z.; Nita, F.; Levi, A. C.; Rossi, G.; Ferrando, R. Structures of Metal Nanoparticles Adsorbed on MgO(001). II. Pt and Pd. *J. Chem. Phys.* **2009**, *130*, 174703.

(277) Viñes, F.; Illas, F.; Neyman, K. M. On the Mechanism of Formation of Metal Nanowires by Self-Assembly. *Angew. Chem. Int. Ed. Engl.* **2007**, *46*, 7094–7097.

(278) Graoui, H.; Giorgio, S.; Henry, C. R. Shape Variations of Pd Particles under Oxygen Adsorption. **1998**, *417*, 350–360.

(279) Gatel, C.; Baules, P.; Snoeck, E. Morphology of Pt Islands Grown on MgO(001). *J. Cryst. Growth* **2003**, *252*, 424–432.

(280) Renaud, G.; Barbier, A.; Robach, O. Growth, Structure, and Morphology of the Pd/MgO(001) Interface: Epitaxial Site and Interfacial Distance. *Phys. Rev. B* **1999**, *60*, 5872–5882.

(281) Fornander, H.; Hultman, L.; Birch, J.; Sundgren, J. Initial Growth of Pd on MgO(001). *J. Cryst. Growth* **1998**, *186*, 189–202.

(282) Aleksandrov, H. A.; Viñes, F.; Ludwig, W.; Schauermann, S.; Neyman, K. M. Tuning the Surface Chemistry of Pd by Atomic C and H: A Microscopic Picture. *Chem. A Eur* **2013**, *19*, 1335–1345.

(283) Bardhan, R.; Hedges, L. O.; Pint, C. L.; Javey, A.; Whitelam, S.; Urban, J. J. Uncovering the Intrinsic Size Dependence of Hydriding Phase Transformations in Nanocrystals. *Nat. Mater.* **2013**, *12*, 905–912.

(284) Wilde, M.; Fukutani, K.; Naschitzki, M.; Freund, H.-J. Hydrogen Absorption in Oxide-Supported Palladium Nanocrystals. *Phys. Rev. B* **2008**, *77*, 113412.

(285) Markovic, N. M.; Grgur, B. N.; Lucas, C. A.; Ross, P. N. Surface Electrochemistry of CO on Pt(110)-(1x2) and Pt(110)-(1x1) Surfaces. *Surf. Sci.* **1997**, *384*, L805–L814.

(286) Martins, M. E.; Zinola, C. F.; Andreasen, G.; Salvarezza, R. C.; Arvia, A. J. The Possible Existence of Subsurface H-Atom Adsorbates and H_2 Electrochemical Evolution Reaction Intermediates on Platinum in Acid Solutions. *J. Electroanal. Chem.* **1998**, *445*, 135–154.

(287) Greeley, J.; Mavrikakis, M. Surface and Subsurface Hydrogen: Adsorption Properties on Transition Metals and near-Surface Alloys. *J. Phys. Chem. B* **2005**, *109*, 3460–3471.

(288) Nobuhara, K.; Nakanishi, H.; Kasai, H.; Okiji, A. Interactions of Atomic Hydrogen with Cu(111), Pt(111), and Pd(111). *J. Appl. Phys.* **2000**, *88*, 6897.

(289) Niimi, Y.; Matsui, T.; Kambara, H.; Tagami, K.; Tsukada, M.; Fukuyama, H. Scanning Tunneling Microscopy and Spectroscopy of the Electronic Local Density of States of Graphite Surfaces near Monoatomic Step Edges. *Phys. Rev. B* **2006**, *73*, 085421.

(290) Diebold, U. The Surface Science of Titanium Dioxide. *Surf. Sci. Rep.* **2003**, *48*, 53–229.

(291) Stausholm-Møller, J.; Kristoffersen, H. H.; Martinez, U.; Hammer, B. A Density Functional Theory Study of Atomic Steps on Stoichiometric Rutile TiO_2(110). *J. Chem. Phys.* **2013**, *139*, 234704.

(292) Gong, X.-Q.; Selloni, A.; Batzill, M.; Diebold, U. Steps on Anatase TiO_2(101). *Nat. Mater.* **2006**, *5*, 665–670.

(293) Chang, L. Y.; Barnard, A. S.; Gontard, L. C.; Dunin-Borkowski, R. E. Resolving the Structure of Active Sites on Platinum Catalytic Nanoparticles. *Nano Lett.* **2010**, *10*, 3073–3076.

(294) Van Santen, R. Complementary Structure Sensitive and Insensitive Catalytic Relationships. *Acc. Chem. Res.* **2009**, *42*, 57–66.

(295) Bruix, A.; Lykhach, Y.; Matolínová, I.; Neitzel, A.; Skála, T.; Tsud, N.; Vorokhta, M.; Stetsovych, V.; Sevčíková, K.; Myslivecek, J.; et al. Maximum Noble-Metal Efficiency in Catalytic Materials: Atomically Dispersed Surface Platinum. *Angew. Chem. Int. Ed. Engl.* **2014**, *53*, 10525–10530.

(296) Lu, J.-L.; Gao, H.-J.; Shaikhutdinov, S.; Freund, H.-J. Gold Supported on Well-Ordered Ceria Films: Nucleation, Growth and Morphology in CO Oxidation Reaction. *Catal. Letters* **2007**, *114*, 8–16.

(297) Setvin, M.; Hao, X.; Daniel, B.; Pavelec, J.; Novotny, Z.; Parkinson, G. S.; Schmid, M.; Kresse, G.; Franchini, C.; Diebold, U. Charge Trapping at the Step Edges of TiO_2 Anatase (101). *Angew. Chem. Int. Ed. Engl.* **2014**, *53*, 4714–4716.

(298) Trinchero, A.; Hellman, A.; Grönbeck, H. Methane Oxidation over Pd and Pt Studied by DFT and Kinetic Modeling. *Surf. Sci.* **2013**, *616*, 206–213.

(299) Castellani, N. J.; Branda, M. M.; Neyman, K. M.; Illas, F. Density Functional Theory Study of the Adsorption of Au Atom on Cerium Oxide: Effect of Low-Coordinated Surface Sites. *J. Phys. Chem. C* **2009**, *113*, 4948–4954.

(300) Fei Tan, K.; Xu, J.; Chang, J.; Borgna, A.; Saeys, M. Carbon Deposition on Co Catalysts during Fischer–Tropsch Synthesis: A Computational and Experimental Study. *J. Catal.* **2010**, *274*, 121–129.

(301) Papp, C.; Tränkenschuh, B. Influence of Steps on the Adsorption of Methane on Platinum Surfaces. *J. Phys. Chem. C* **2007**, *111*, 2177–2184.

(302) Lin, W.-C.; Chang, H.-Y.; Lin, Y.-Y.; Hu, Y.-C.; Hsu, C.-H.; Kuo, C.-C. Nucleation of Fe Nanoparticle Chains and Nanostripes on Au(111) Stepped Surface. *J. Appl. Phys.* **2010**, *107*, 014301.

(303) Fergus, J. W. Electrolytes for Solid Oxide Fuel Cells. *J. Power Sources* **2006**, *162*, 30–40.

(304) Tarnuzzer, R. W.; Colon, J.; Patil, S.; Seal, S. Vacancy Engineered Ceria Nanostructures for Protection from Radiation-Induced Cellular Damage. *Nano Lett.* **2005**, *5*, 2573–2577.

(305) Feng, X.; Sayle, D. C.; Wang, Z. L.; Paras, M. S.; Santora, B.; Sutorik, A. C.; Sayle, T. X. T.; Yang, Y.; Ding, Y.; Wang, X.; et al. Converting Ceria Polyhedral Nanoparticles into Single-Crystal Nanospheres. *Science* **2006**, *312*, 1504–1508.

(306) Bernal, S.; Blanco, G.; Calvino, J. J.; Gatica, J. M.; Pérez Omil, J. A.; Pintado, J. M. Characterisation of Three-Way Automotive Aftertreatment Catalysts and Related Model Systems. *Top. Catal.* **2004**, *28*, 31–45.

(307) Matam, S. K.; Chiarello, G. L.; Lu, Y.; Weidenkaff, A.; Ferri, D. PdO_X/Pd at Work in a Model Three-Way Catalyst for Methane Abatement Monitored by Operando XANES. *Top. Catal.* **2013**, *56*, 239–242.

(308) Golunski, S. E.; Hatcher, H. A.; Rajaram, R. R.; Truex, T. J. Origins of Low-Temperature Three-Way Activity in Pt/CeO_2. *Appl. Catal. B Environ.* **1995**, *5*, 367–376.

(309) Wilkens, H.; Schuckmann, O.; Oelke, R.; Gevers, S.; Reichling, M.; Schaefer, A.; Bäumer, M.; Zoellner, M. H.; Niu, G.; Schroeder, T.; et al. Structural Transitions of Epitaxial Ceria Films on Si(111). *Phys. Chem. Chem. Phys.* **2013**, *15*, 18589–18599.

(310) Duchoň, T.; Dvořák, F.; Aulicka, M.; Stetsovych, V.; Vorokhta, M.; Mazur, D.; Veltruska, K.; Skála, T.; Mysliveček, J.; Matolínová, I.; et al. Ordered Phases of Reduced Ceria as Epitaxial Films on Cu (111). *J. Phys. Chem. C* **2014**, *118*, 357.

(311) Trovarelli, A.; de Leitenburg, C.; Dolcetti, G.; Llorca, J. CO_2 Methanation under Transient and Steady-State Conditions over Rh/CeO_2 and CeO_2-Promoted Rh/SiO_2: The Role of Surface and Bulk Ceria. *J. Appl. Phys.* **1995**, *151*, 111–124.

(312) Chueh, W. C.; Falter, C.; Abbott, M.; Scipio, D.; Furler, P.; Haile, S. M.; Steinfeld, A. High-Flux Solar-Driven Thermochemical Dissociation of CO_2 and H_2O Using Nonstoichiometric Ceria. *Science* **2010**, *330*, 1797–1801.

(313) Negreiros, F. R.; Fabris, S. Role of Cluster Morphology in the Dynamics and Reactivity of Sub-Nm Pt Clusters Supported on Ceria Surfaces. *J. Phys. Chem. C* **2014**, *118*, 21014–21020.

(314) Óvári, L.; Krick Calderon, S.; Lykhach, Y.; Libuda, J.; Erdőhelyi, A.; Papp, C.; Kiss, J.; Steinrück, H.-P. Near Ambient Pressure XPS Investigation of the Interaction of Ethanol with Co/CeO2(111). *J. Catal.* **2013**, *307*, 132–139.

(315) Migani, A.; Vayssilov, G. N.; Bromley, S. T.; Illas, F.; Neyman, K. M. Dramatic Reduction of the Oxygen Vacancy Formation Energy in Ceria Particles: A Possible Key to Their Remarkable Reactivity at the Nanoscale. *J. Mater. Chem.* **2010**, *20*, 10535.

(316) Zhou, K.; Wang, X.; Sun, X.; Peng, Q.; Li, Y. Enhanced Catalytic Activity of Ceria Nanorods from Well-Defined Reactive Crystal Planes. *J. Catal.* **2005**, *229*, 206–212.

(317) Cargnello, M.; Delgado Jaén, J. J.; Hernández Garrido, J. C.; Bakhmutsky, K.; Montini, T.; Calvino Gámez, J. J.; Gorte, R. J.; Fornasiero, P. Exceptional Activity for Methane Combustion over Modular $Pd@CeO_2$ Subunits on Functionalized Al_2O_3. *Science* **2012**, *337*, 713–717.

(318) Migani, A.; Vayssilov, G. N.; Bromley, S. T.; Illas, F.; Neyman, K. M. Greatly Facilitated Oxygen Vacancy Formation in Ceria Nanocrystallites. *Chem. Commun. (Camb).* **2010**, *46*, 5936–5938.

(319) Botu, V.; Ramprasad, R.; Mhadeshwar, A. B. Ceria in an Oxygen Environment: Surface Phase Equilibria and Its Descriptors. *Surf. Sci.* **2014**, *619*, 49–58.

(320) Branda, M. M.; Ferullo, R. M.; Caus, M.; Illas, F. Relative Stabilities of Low Index and Stepped CeO_2 Surfaces from Hybrid and GGA + U Implementations of Density Functional Theory. *J. Phys. Chem. C* **2011**, *115*, 3716–3721.

(321) Jiang, Y.; Adams, J. B.; van Schilfgaarde, M. Density-Functional Calculation of CeO_2 Surfaces and Prediction of Effects of Oxygen Partial Pressure and Temperature on Stabilities. *J. Chem. Phys.* **2005**, *123*, 64701.

(322) Zhou, J.; Baddorf, A. P.; Mullins, D. R.; Overbury, S. H. Growth and Characterization of Rh and Pd Nanoparticles on Oxidized and Reduced CeO_x(111) Thin Films by Scanning Tunneling Microscopy. *J. Phys. Chem. C* **2008**, *112*, 9336–9345.

(323) Mudiyanselage, K.; Kim, H. Y.; Senanayake, S. D.; Baber, A. E.; Liu, P.; Stacchiola, D. Probing Adsorption Sites for CO on Ceria. *Phys. Chem. Chem. Phys.* **2013**, *15*, 15856–15862.

(324) Jerratsch, J.-F.; Shao, X.; Nilius, N.; Freund, H.-J.; Popa, C.; Ganduglia-Pirovano, M. V.; Burow, A. M.; Sauer, J. Electron Localization in Defective Ceria Films: A Study with Scanning-Tunneling Microscopy and Density-Functional Theory. *Phys. Rev. Lett.* **2011**, *106*, 246801.

(325) Shahed, S. M. F.; Hasegawa, T.; Sainoo, Y.; Watanabe, Y.; Isomura, N.; Beniya, A.; Hirata, H.; Komeda, T. STM and XPS Study of CeO_2(111) Reduction by Atomic Hydrogen. *Surf. Sci.* **2014**, *628*, 30–35.

(326) Nolan, M. Hybrid Density Functional Theory Description of Oxygen Vacancies in the CeO_2 (110) and (100) Surfaces. *Chem. Phys. Lett.* **2010**, *499*, 126–130.

(327) Ganduglia-Pirovano, M.; Da Silva, J.; Sauer, J. Density-Functional Calculations of the Structure of Near-Surface Oxygen Vacancies and Electron Localization on CeO_2(111). *Phys. Rev. Lett.* **2009**, *102*, 026101.

(328) Migani, A.; Neyman, K. M.; Illas, F.; Bromley, S. T. Exploring Ce^{3+}/Ce^{4+} Cation Ordering in Reduced Ceria Nanoparticles Using Interionic-Potential and Density-Functional Calculations. *J. Chem. Phys.* **2009**, *131*, 064701.

(329) Nolan, M.; Parker, S. C.; Watson, G. W. The Electronic Structure of Oxygen Vacancy Defects at the Low Index Surfaces of Ceria. *Surf. Sci.* **2005**, *595*, 223–232.

(330) Branda, M. M.; Castellani, N. J.; Grau-Crespo, R.; de Leeuw, N. H.; Hernandez, N. C.; Sanz, J. F.; Neyman, K. M.; Illas, F. On the Difficulties of Present Theoretical Models to Predict the Oxidation State of Atomic Au Adsorbed on Regular Sites of CeO_2(111). *J. Chem. Phys.* **2009**, *131*, 094702.

(331) Fabris, S.; Vicario, G.; Balducci, G.; de Gironcoli, S.; Baroni, S. Electronic and Atomistic Structures of Clean and Reduced Ceria Surfaces. *J. Phys. Chem. B* **2005**, *109*, 22860–22867.

(332) Nolan, M.; Fearon, J.; Watson, G. Oxygen Vacancy Formation and Migration in Ceria. *Solid State Ionics* **2006**, *177*, 3069–3074.

(333) Perdew, J. P.; Wang, Y. Accurate and Simple Analytic Representation of the Electron-Gas Correlation Energy. *Phys. Rev. B* **1992**, *45*, 13244–13249.

(334) Preda, G.; Migani, A.; Neyman, K. M.; Bromley, S. T.; Illas, F.; Pacchioni, G. Formation of Superoxide Anions on Ceria Nanoparticles by Interaction of Molecular Oxygen with Ce^{3+} Sites. *J. Phys. Chem. C* **2011**, *115*, 5817–5822.

(335) Puchin, V. E.; Puchina, A. V.; Huisinga, M.; Reichling, M. Theoretical Modelling of Steps on the CaF_2(111) Surface. *J. Phys. Condens. Matter* **2001**, *13*, 2081–2094.

(336) Shahed, S. M. F.; Sainoo, Y.; Komeda, T. Scanning Tunneling Microscope Study of Surface Morphology Variation of CeO_2(111) with Changing Annealing Condition. *Jpn. J. Appl. Phys.* **2011**, *50*, 08LB05.

(337) Gritschneder, S.; Namai, Y.; Iwasawa, Y.; Reichling, M. Structural Features of CeO_2(111) Revealed by Dynamic SFM. *Nanotechnology* **2005**, *16*, S41–S48.

(338) Tersoff, J.; Hamann, D. R. Theory of the Scanning Tunneling Microscope. *Phys. Rev. B* **1985**, *31*, 805–813.

(339) Jeong, H.-C.; Williams, E. D. Steps on Surfaces: Experiment and Theory. *Surf. Sci. Rep.* **1999**, *34*, 171–294.

(340) Frenken, J. W. M.; Stoltze, P. Are Vicinal Metal Surfaces Stable ? *Phys. Rev. Lett.* **1999**, *82*, 3500–3503.

(341) Goniakowski, J.; Noguera, C. Atomic and Electronic Structure of Steps and Kinks on MgO(100) and MgO(110). *Surf. Sci.* **1995**, *340*, 191–204.

(342) Yu, B. D.; Scheffler, M. Ab Initio Study of Step Formation and Self-Diffusion on Ag(100). *Phys. Rev. B* **1997**, *55*, 13916–13924.

(343) Kern, G.; Hafner, J. Ab Initio Calculations of the Atomic and Electronic Structure of Diamond (111) Surfaces with Steps. *Phys. Rev. B* **1998**, *58*, 2161–2169.

(344) Giesen, M. Step and Island Dynamics at Solid/Vacuum and Solid/Liquid Interfaces. *Prog. Surf. Sci.* **2001**, *68*, 1–153.

(345) Kodambaka, S.; Petrova, V.; Khare, S.; Johnson, D.; Petrov, I.; Greene, J. Absolute TiN(111) Step Energies from Analysis of Anisotropic Island Shape Fluctuations. *Phys. Rev. Lett.* **2002**, *88*, 146101.

(346) Ikonomov, J.; Starbova, K.; Ibach, H.; Giesen, M. Measurement of Step and Kink Energies and of the Step-Edge Stiffness from Island Studies on Pt(111). *Phys. Rev. B* **2007**, *75*, 245411.

(347) Schulze Icking-Konert, G.; Giesen, M.; Ibach, H. Novel Method for the Experimental Determination of Step Energies. *Phys. Rev. Lett.* **1999**, *83*, 3880–3883.

(348) Hardcastle, T. P.; Seabourne, C. R.; Brydson, R. M. D.; Livi, K. J. T.; Scott, A. J. Energy of Step Defects on the TiO_2 Rutile (110) Surface: An Ab Initio DFT Methodology. *J. Phys. Chem. C* **2013**, *117*, 23766–23780.

(349) Boettger, J. C. Nonconvergence of Surface Energies Obtained from Thin-Film Calculations. *Phys. Rev. B* **1994**, *49*, 16798–16800.

(350) Fiorentini, V.; Methfessel, M. Extracting Convergent Surface Energies from Slab Calculations. *J. Phys. Condens. Matter* **1996**, *8*, 6525–6529.

(351) Bruix, A.; Neyman, K. M.; Illas, F. Adsorption, Oxidation State, and Diffusion of Pt Atoms on the CeO_2(111) Surface. *J. Phys. Chem. C* **2010**, *114*, 14202–14207.

(352) Kugai, J.; Miller, J. T.; Guo, N.; Song, C. Oxygen-Enhanced Water Gas Shift on Ceria-Supported Pd–Cu and Pt–Cu Bimetallic Catalysts. *J. Catal.* **2011**, *277*, 46–53.

(353) Zhang, Q.; Farrauto, R. J. A PdZn Catalyst Supported on Stabilized Ceria for Stoichiometric Methanol Steam Reforming and Hydrogen Production. *Appl. Catal. A Gen.* **2011**, *395*, 64–70.

(354) Gritschneder, S.; Reichling, M. Structural Elements of CeO2(111) Surfaces. *Nanotechnology* **2007**, *18*, 044024.

(355) Fuente, S.; Branda, M. M.; Illas, F. Role of Step Sites on Water Dissociation on Stoichiometric Ceria Surfaces. *Theor. Chem. Acc.* **2012**, *131*, 1190.

(356) Fronzi, M.; Piccinin, S.; Delley, B.; Traversa, E.; Stampfl, C. Water Adsorption on the Stoichiometric and Reduced CeO_2(111) Surface: A First-Principles Investigation. *Phys. Chem. Chem. Phys.* **2009**, *11*, 9188–9199.

(357) Du, N.; Zhang, H.; Chen, B.; Ma, X.; Yang, D. Ligand-Free Self-Assembly of Ceria Nanocrystals into Nanorods by Oriented Attachment at Low Temperature. *J. Phys. Chem. C* **2007**, *111*, 12677–12680.

(358) Liu, X.; Zhou, K.; Wang, L.; Wang, B.; Li, Y. Oxygen Vacancy Clusters Promoting Reducibility and Activity of Ceria Nanorods. *J. Am. Chem. Soc.* **2009**, *131*, 3140–3141.

(359) Anwar, M. S.; Kumar, S.; Ahmed, F.; Arshi, N.; Kil, G.-S.; Park, D.-W.; Chang, J.; Koo, B. H. Hydrothermal Synthesis and Indication of Room Temperature Ferromagnetism in CeO_2 Nanowires. *Mater. Lett.* **2011**, *65*, 3098–3101.

(360) Mai, H.-X.; Sun, L.-D.; Zhang, Y.-W.; Si, R.; Feng, W.; Zhang, H.-P.; Liu, H.-C.; Yan, C.-H. Shape-Selective Synthesis and Oxygen Storage Behavior of Ceria

Nanopolyhedra, Nanorods, and Nanocubes. *J. Phys. Chem. B* **2005**, *109*, 24380–24385.

(361) Tana; Zhang, M.; Li, J.; Li, H.; Li, Y.; Shen, W. Morphology-Dependent Redox and Catalytic Properties of CeO_2 Nanostructures: Nanowires, Nanorods and Nanoparticles. *Catal. Today* **2009**, *148*, 179–183.

(362) Sayle, T. X. T.; Cantoni, M.; Bhatta, U. M.; Parker, S. C.; Hall, S. R.; Möbus, G.; Molinari, M.; Reid, D.; Seal, S.; Sayle, D. C. Strain and Architecture-Tuned Reactivity in Ceria Nanostructures; Enhanced Catalytic Oxidation of CO to CO_2. *Chem. Mater.* **2012**, *24*, 1811–1821.

(363) Faraday, M. The Bakerian Lecture: Experimental Relations of Gold (and Other Metals) to Light. *Philos. Trans. R. Soc. London* **1857**, *147*, 145–181.

(364) Thirsk, H. R. A Note on the Orientated Overgrowths of Metal Films on Single Crystal Inorganic Substrates. *Proc. Phys. Soc.* **1950**, *63*, 834–839.

(365) Goche, O.; Wilman, H. The Structure of Silver Films. *Proc. Phys. Soc.* **1939**, *51*, 625–651.

(366) Freund, H.-J. Clusters and Islands on Oxides: From Catalysis via Electronics and Magnetism to Optics. *Surf. Sci.* **2002**, *500*, 271–299.

(367) Jiang, J.; Jung, H.-J.; Yoon, S.-G. Epitaxial PMN–PT Thin Films Grown on Buffered Si Substrates Using Ceramic and Single-Crystal Targets. *J. Alloys Compd.* **2011**, *509*, 6924–6929.

(368) Armbrüster, M.; Behrens, M.; Föttinger, K.; Friedrich, M.; Gaudry, E.; Matam, S. K.; Sharma, H. R. The Intermetallic Compound ZnPd and Its Role in Methanol Steam Reforming. *Catal. Rev. Sci. Eng.* **2013**, *55*, 289–367.

(369) González, S.; Neyman, K. M.; Shaikhutdinov, S.; Freund, H.-J.; Illas, F. On the Promoting Role of Ag in Selective Hydrogenation Reactions over Pd-Ag Bimetallic Catalysts: A Theoretical Study. *J. Phys. Chem. C* **2007**, *111*, 6852–6856.

(370) Gabasch, H.; Knop-Gericke, A.; Schlögl, R.; Penner, S.; Jenewein, B.; Hayek, K.; Klötzer, B. Zn Adsorption on Pd(111): ZnO and PdZn Alloy Formation. *J. Phys. Chem. B* **2006**, *110*, 11391–11398.

(371) Zheng, G.; Altman, E. I. The Oxidation Mechanism of Pd(100). *Surf. Sci.* **2002**, *504*, 253–270.

(372) Yang, F.; Graciani, J.; Evans, J.; Liu, P.; Hrbek, J.; Sanz, J. F.; Rodriguez, J. a. CO Oxidation on Inverse CeO_x/Cu(111) Catalysts: High Catalytic Activity and Ceria-Promoted Dissociation of O_2. *J. Am. Chem. Soc.* **2011**, *133*, 3444–3451.

(373) Rameshan, C.; Stadlmayr, W.; Weilach, C.; Penner, S.; Lorenz, H.; Hävecker, M.; Blume, R.; Rocha, T.; Teschner, D.; Knop-Gericke, A.; et al. Subsurface-

Controlled CO_2 Selectivity of PdZn near-Surface Alloys in H_2 Generation by Methanol Steam Reforming. *Angew. Chem. Int. Ed. Engl.* **2010**, *49*, 3224–3227.

(374) Vilé, G.; Bridier, B.; Wichert, J.; Pérez-Ramírez, J. Ceria in Hydrogenation Catalysis: High Selectivity in the Conversion of Alkynes to Olefins. *Angew. Chem. Int. Ed. Engl.* **2012**, *51*, 8620–8623.

(375) Matolín, V.; Libra, J.; Matolínová, I.; Nehasil, V.; Sedláček, L.; Šutara, F. Growth of Ultra-Thin Cerium Oxide Layers on Cu(111). *Appl. Surf. Sci.* **2007**, *254*, 153–155.

(376) Xiao, W.; Guo, Q.; Wang, E. G. Transformation of CeO_2(111) to Ce_2O_3(0001) Films. **2003**, *368*, 527–531.

(377) Stetsovych, V.; Pagliuca, F.; Dvořák, F.; Duchoň, T.; Vorokhta, M.; Aulická, M.; Lachnitt, J.; Schernich, S.; Matolínová, I.; Veltruska, K.; et al. Epitaxial Cubic Ce_2O_3 Films via Ce–CeO_2 Interfacial Reaction. *J. Phys. Chem. Lett.* **2013**, *4*, 866–871.

(378) Flege, J. I.; Kaemena, B.; Gevers, S.; Bertram, F.; Wilkens, T.; Bruns, D.; Bätjer, J.; Schmidt, T.; Wollschläger, J.; Falta, J. Silicate-Free Growth of High-Quality Ultrathin Cerium Oxide Films on Si(111). *Phys. Rev. B* **2011**, *84*, 235418.

(379) Luches, P.; Pagliuca, F.; Valeri, S. Structural and Morphological Modifications of Thermally Reduced Cerium Oxide Ultrathin Epitaxial Films on Pt(111). *Phys. Chem. Chem. Phys.* **2014**, *16*, 18848–18857.

(380) Berner, U.; Schierbaum, K.-D. Cerium Oxides and Cerium-Platinum Surface Alloys on Pt(111) Single-Crystal Surfaces Studied by Scanning Tunneling Microscopy. *Phys. Rev. B* **2002**, *65*, 235404.

(381) Luches, P.; Pagliuca, F.; Valeri, S.; Boscherini, F. Structure of Ultrathin CeO_2 Films on Pt(111) by Polarization- Dependent X-Ray Absorption Fine Structure. *J. Phys. Chem. C* **2013**, *117*, 1030–1036.

(382) Marchini, S.; Günther, S.; Wintterlin, J. Scanning Tunneling Microscopy of Graphene on Ru(0001). *Phys. Rev. B* **2007**, *76*, 075429.

(383) Sangthong, W.; Limtrakul, J.; Illas, F.; Bromley, S. T. Persistence of Magic Cluster Stability in Ultra-Thin Semiconductor Nanorods. *Nanoscale* **2010**, *2*, 72–77.

(384) Chen, Z.-X.; Neyman, K.; Gordienko, A.; Rösch, N. Surface Structure and Stability of PdZn and PtZn Alloys: Density-Functional Slab Model Studies. *Phys. Rev. B* **2003**, *68*, 075417.

(385) Friedrich, M.; Ormeci, A.; Grin, Y.; Armbrüster, M. PdZn or ZnPd: Charge Transfer and Pd-Pd Bonding as the Driving Force for the Tetragonal Distortion of the Cubic Crystal Structure . *Zeitschrift für Anorg. und Allg. Chemie* **2010**, *636*, 1735–1739.

(386) Penner, S.; Jenewein, B.; Gabasch, H.; Klotzer, B.; Wang, D.; Knop-Gericke, A.; Schlogl, R.; Hayek, K. Growth and Structural Stability of Well-Ordered PdZn Alloy Nanoparticles. *J. Catal.* **2006**, *241*, 14–19.

(387) Dagle, R. A.; Platon, A.; Palo, D. R.; Datye, A. K.; Vohs, J. M.; Wang, Y. PdZnAl Catalysts for the Reactions of Water-Gas-Shift, Methanol Steam Reforming, and Reverse-Water-Gas-Shift. *Appl. Catal. A Gen.* **2008**, *342*, 63–68.

(388) Conant, T.; Karim, A.; Lebarbier, V.; Wang, Y.; Girgsdies, F.; Schlogl, R.; Datye, A. Stability of Bimetallic Pd–Zn Catalysts for the Steam Reforming of Methanol. *J. Catal.* **2008**, *257*, 64–70.

(389) Günter, M. M.; Ressler, T.; Jentoft, R. E.; Bems, B. Redox Behavior of Copper Oxide/Zinc Oxide Catalysts in the Steam Reforming of Methanol Studied by in Situ X-Ray Diffraction and Absorption Spectroscopy. *J. Catal.* **2001**, *203*, 133–149.

(390) Kurtz, M.; Wilmer, H.; Genger, T.; Hinrichsen, O.; Muhler, M. Deactivation of Supported Copper Catalysts for Methanol Synthesis. *Catal. Letters* **2003**, *86*, 77–80.

(391) Friedrich, M.; Teschner, D.; Knop-Gericke, A.; Armbrüster, M. Influence of Bulk Composition of the Intermetallic Compound ZnPd on Surface Composition and Methanol Steam Reforming Properties. *J. Catal.* **2012**, *285*, 41–47.

(392) Lebarbier, V.; Dagle, R.; Datye, A.; Wang, Y. The Effect of PdZn Particle Size on Reverse-Water–gas-Shift Reaction. *Appl. Catal. A Gen.* **2010**, *379*, 3–6.

(393) Bollmann, L.; Ratts, J. L.; Joshi, A. M.; Williams, W. D.; Pazmino, J.; Joshi, Y. V.; Miller, J. T.; Kropf, A. J.; Delgass, W. N.; Ribeiro, F. H. Effect of Zn Addition on the Water–gas Shift Reaction over Supported Palladium Catalysts. *J. Catal.* **2008**, *257*, 43–54.

(394) Tew, M. W.; Emerich, H.; van Bokhoven, J. A. Formation and Characterization of PdZn Alloy: A Very Selective Catalyst for Alkyne Semihydrogenation. *J. Phys. Chem. C* **2011**, *115*, 8457–8465.

(395) Laider, K. J. A Glossary of Terms Used in Chemical Kinetics, Including Reaction Dynamics. *Pure Appl. Chem.* **1996**, *68*, 149–192.

(396) Born, M.; Oppenheimer, R. Zur Quantentheorie Der Molekeln. *Ann. Phys.* **1927**, *84*, 0457–0484.

(397) Jacob, C. R.; Reiher, M. Spin in Density-Functional Theory. *Int. J. Quantum Chem.* **2012**, *112*, 3661–3684.

(398) Kurth, S.; Perdew, J. P.; Blaha, P. Molecular and Solid-State Tests of Density Functional Approximations: LSD, GGAs, and Meta-GGAs. *Int. J. Quantum Chem.* **1999**, *75*, 889–909.

(399) Chai, J.-D.; Head-Gordon, M. Systematic Optimization of Long-Range Corrected Hybrid Density Functionals. *J. Chem. Phys.* **2008**, *128*, 084106.

(400) Soini, T. M.; Krüger, S.; Rösch, N. The DFT+Umol Method and Its Application to the Adsorption of CO on Platinum Model Clusters. *J. Chem. Phys.* **2014**, *140*, 174709.

(401) Kresse, G.; Gil, A.; Sautet, P. Significance of Single-Electron Energies for the Description of CO on Pt(111). *Phys. Rev. B* **2003**, *68*, 073401.

(402) Gajdoš, M.; Hafner, J. CO Adsorption on Cu(111) and Cu(001) Surfaces: Improving Site Preference in DFT Calculations. *Surf. Sci.* **2005**, *590*, 117–126.

10 List of Publications

Main Results:

S. M. Kozlov, G. F. Cabeza, K. M. Neyman

Bonding and vibrations of CH_xO and CH_x species (x = 1–3) on a palladium nanoparticle representing model catalysts

Chemical Physics Letters, 2011, 506, 92-97

H. A. Aleksandrov, S. M. Kozlov, S. Schauermann, G. N. Vayssilov, K. M. Neyman

How Absorbed Hydrogen Affects Catalytic Activity of Transition Metals

Angewandte Chemie International Edition 2014, DOI: 10.1002/anie.201405738

S. M. Kozlov, H. A. Aleksandrov, J. Goniakowski, K. M. Neyman

Effect of MgO(100) support on structure and properties of Pd and Pt nanoparticles with 49-155 atoms

Journal of Chemical Physics, 2013, 139, 084701

S. M. Kozlov, H. A. Aleksandrov, K. M. Neyman

Adsorbed and Subsurface Absorbed Hydrogen Atoms on Bare and MgO(100)-Supported Pd and Pt Nanoparticles

The Journal of Physical Chemistry C, 2014, 118, 15242−15250

N. Nilius, S. M. Kozlov, J.-F. Jerratsch, M. Baron, X. Shao, F. Viñes, S. Shaikhutdinov, K. M. Neyman, H.-J. Freund

Formation of One-Dimensional Electronic States along the Step Edges of CeO_2(111)

ACS Nano, 2012, 6, 1126-1133

S. M. Kozlov, F. Viñes, N. Nilius, S. Shaikhutdinov, K. M. Neyman

Absolute Surface Step Energies: Accurate Theoretical Methods Applied to Ceria Nanoislands

The Journal of Physical Chemistry Letters, 2012, *3*, **1956–1961**

S. M. Kozlov, K. M. Neyman

O Vacancies on Steps on CeO_2(111) Surface

Physical Chemistry Chemical Physics, 2014, 16, 7823-7829

C. Weilach, S. M. Kozlov, H. H. Holzapfel, K. Föttinger, K. M. Neyman, G. Rupprechter

Geometric Arrangement of Components in Bimetallic PdZn/Pd(111) Surfaces Modified by CO Adsorption: A Combined Study by Density Functional Calculations, Polarization-Modulated Infrared Reflection Absorption Spectroscopy, and Temperature-Programmed Desorption

The Journal of Physical Chemistry C, **2012**, *116*, 18768–18778.

Outlook:

P. Janthon, S. M. Kozlov, F. Viñes, J. Limtrakul, F. Illas

Establishing the Accuracy of Broadly Used Density Functionals in Describing Bulk Properties of Transition Metals

Journal of Chemical Theory and Computation, 2013, 9, 1631-1640

P. Janthon, S. (A.) Luo, S. M. Kozlov, F. Viñes, J. Limtrakul, D. G. Truhlar, F. Illas

Bulk Properties of Transition Metals: A Challenge for the Design of Universal Density Functionals

Journal of Chemical Theory and Computation, 2014, 10, 3832-3839.

P. Janthon, F. Viñes, S. M. Kozlov, J. Limtrakul, F. Illas

Theoretical assessment of graphene- metal contacts

Journal of Chemical Physics, 2013, 138, 244701

S. M. Kozlov, H. A. Aleksandrov, L. V. Moskaleva, M. Bäumer and K. M. Neyman, in Comprehensive Inorganic Chemistry (2nd edition), eds. J. Reedijk and K. Poeppelmeier, Elsevier, Amsterdam, 2013; vol. 7: Surface Inorganic Chemistry and Heterogeneous Catalysis, eds. R. Schlögl and J. W. Niemantsverdriet, pp. 475-503.

S. M. Kozlov, K. M. Neyman

Catalysis from First Principles: Towards Accounting for the Effects of Nanostructuring

Topics in Catalysis, 2013, 56, 867-873

Y. Lykhach, V. Johánek, H. A. Aleksandrov, S. M. Kozlov, M. Happel, T. Skála, P. St. Petkov, N. Tsud, G. N. Vayssilov, K. C. Prince, K. M. Neyman, V. Matolín, J. Libuda

Water chemistry on model ceria and Pt/ceria catalysts

The Journal of Physical Chemistry C, 2012, *116*, 12103–12113

M. A. Sk, S. M. Kozlov, A. Migani, K. H. Lim, K. M. Neyman

Oxygen Vacancies in Self-Assemblies of Ceria Nanoparticles

Journal of Materials Chemistry A, 2014, 2, 18329-18338.

11 Appendix

Section 11.1

JCTC Journal of Chemical Theory and Computation

Article

pubs.acs.org/JCTC

Establishing the Accuracy of Broadly Used Density Functionals in Describing Bulk Properties of Transition Metals

Patanachai Janthon,[†,‡,§,∥] Sergey M. Kozlov,[†] Francesc Viñes,[†] Jumras Limtrakul,[‡,§,∥] and Francesc Illas*[,†]

[†]Departament de Química Física and Institut de Química Teòrica i Computacional (IQTCUB), Universitat de Barcelona, c/Martí i Franquès 1, 08028, Barcelona, Spain

[‡]Department of Chemistry and Center of Nanotechnology, Kasetsart University, Bangkok 10900, Thailand

[§]Center for Advanced Studies in Nanotechnology and Its Applications in Chemical, Food and Agricultural Industries, Kasetsart University, Bangkok 10900, Thailand

[∥]NANOTEC Center for the Design of Nanoscale Materials for Green Nanotechnology Kasetsart University, Bangkok 10900, Thailand

Supporting Information

ABSTRACT: The performance of various commonly used density functionals is established by comparing calculated values of atomic structure data, cohesive energies, and bulk moduli of all transition metals to available experimental data. The functionals explored are the Ceperley–Alder (CA), Vosko–Wilk–Nussair (VWN) implementation of the Local Density Approximation (LDA); the Perdew–Wang (PW91) and Perdew–Burke–Ernzerhof (PBE) forms of the Generalized Gradient Approximation (GGA), and the RPBE and PBEsol modifications of PBE, aimed at better describing adsorption energies and bulk solid lattice properties, respectively. The present systematic study shows that PW91 and PBE consistently provide the smallest differences between the calculated and experimental values. Additional calculations of the (111) surface energy of several face centered cubic (*fcc*) transition metals reveal that LDA produces the most accurate results, while all other functionals significantly underestimate the experimental values. RPBE severely underestimates surface energy, which may be the origin for the reduced surface chemical activity and the better performance of RPBE describing adsorption energies.

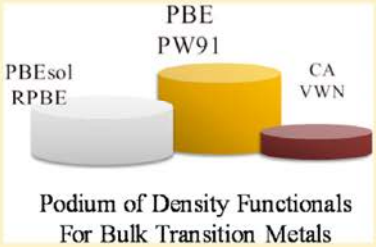

1. INTRODUCTION

Density Functional Theory (DFT) based methods[1,2] are nowadays routinely used in a variety of fields, encompassing quantum chemistry,[3] solid state physics,[4] materials science,[5] and heterogeneous catalysis,[6] just to mention a few. This is due to the nicely balanced accuracy versus computational cost ratio and the increasing improvement of highly parallelized implementations.[7,8] Nevertheless, these methods rely on approximations to the universal, yet unknown, exact exchange-correlation functional, and so, several questions still remain open.[9] Consequently, it is difficult to assess *a priori* which electron density functional is more adequate for a given problem. Usually, the suitability is concluded *a posteriori* after a comparison of test calculations to experimentally available data, and several data sets have been posed for this purpose, mostly focusing on molecular systems.[10−12] Indeed, a systematic evaluation of the accuracy of various density functionals for different systems is of the utmost importance in the field of electronic structure calculations: On the one hand, they guide the users on the choice of a functional to properly describe a particular property, and on the other hand, they assess the developers on detecting what are the main drawbacks of current functionals.

Nowadays, it is well established that hybrid functionals such as the popular Becke–Lee–Yang–Parr (B3LYP)[13] or subsequent improvements, scuh as those developed by Truhlar and co-workers,[11,14] Adamo and Barone,[15] and Scuseria et al.,[16,17] are required to describe molecular systems and their thermochemistry within the chemical accuracy of 1 kcal mol^{-1}. However, the situation in materials science is quite different since calculations on extended periodic systems still often rely on exchange-correlation functionals based either in the Local Density Approximation (LDA) or the Generalized Gradient Approximation (GGA).[1,4,5] The reason is the significantly higher computational cost, compared to LDA or GGA functionals of hybrid density functionals in periodic calculations, especially when using plane wave basis sets, a common choice for periodic systems. Another more fundamental reason is that, while hybrid functionals are essential to reproduce the band gap and electronic structure of oxides,[18−22] manganites,[23] and cuprates,[24−26] they fail in describing metals, which is related to the slow decay of nonlocal Fock exchange with the interelectronic distance.[27] The difficulties hybrid functionals have dealing with transition metals have been very recently pointed out by Tran et al.[28] in their study on the application of the screened hybrid functional YS-PBE0 to bulk Rh, Pd, and Pt. These authors found that this

Received: November 22, 2012
Published: February 19, 2013

hybrid functional incorrectly predicts a ferromagnetic ground state on these metals, in clear contradiction to reality.

An important distinction between molecular and extended systems is the different types and extent of databases used for the calibration of the exchange-correlation potentials. Whereas for isolated systems the studies assessing the performance of various functionals on carefully constructed reference databases are abundant,[11,12,29] on solids these studies are relatively scarce. Moreover, even in the available studies concerning the accuracy of density functional theory based methods in periodic calculations,[27,28,30−58] transition metals are poorly represented although they are crucial components in heterogeneous catalysis and electrochemistry and are of paramount importance in environmental chemistry. In particular, a few transition metal elements concentrate most of the scientific attention, as schematically shown in Figure 1. The majority of the studies

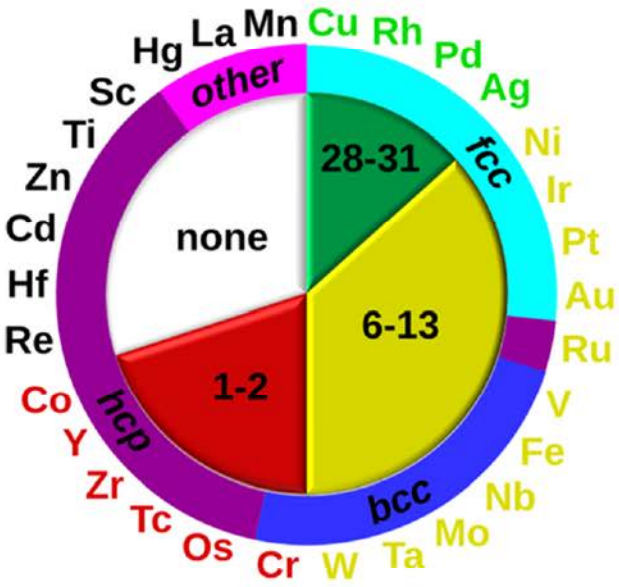

Figure 1. Graphical distribution indicating the number of studies dealing with the accuracy of various exchange correlation functionals on transition metal bulk properties, together with their crystal structure. The distribution is based on 31 references published from 1999 to 2012.[27,30−58] Note that for those metals considered in 1−2 papers, not all of the discussed observables (metal−metal distances, bulk moduli, cohesive energies) have been published.

only focus on Cu, Rh, Pd, and Ag, largely because these elements are often used as benchmarks when developing new exchange-correlation functionals to assess the DFT accuracy.[41,48] Besides, these studies encompass metals with a face centered cubic (*fcc*) crystallographic structure (CS). This is due to the fact that their lattice constants have been experimentally measured near or thermally corrected to 0 K, and relativistic effects for such heavy transition metal elements, though minor, are also known.[59] Thus, it is likely that some of the present density functionals are somewhat biased toward the accurate description of these four transition metals and their particular spatial arrangement, hoping that an equally accurate description will be achieved for the rest of the transition metals, regardless of their crystallographic structure. Interestingly, even Fe, Ni, and Pt, which are very important in industrial catalysis, are often neglected in this type of study. There are more systematic studies dedicated to testing various functionals, although these usually cover only half of the transition metals, mostly sampling, with the caveat of Ru, *fcc* or body centered cubic (*bcc*) structures. There is only one study[50] dealing with a rather broad set containing 19 out of the 30 transition metals and a significant number of *fcc*, *bcc*, and hexagonal closed packed (*hcp*) structures. Unfortunately, even in this study only atomic radii and bulk moduli were examined with various functionals, and hence, some reference data are still missing for Cr, Co, Y, Zr, Tc, and Os. Finally, none of the systematic studies in the literature include Sc, Ti, Mn, Zn, Cd, La, Hf, Re, or Hg in the research scope. All in all, the performance of various density functionals has not been sufficiently studied for half of the transition metal elements of the periodic table. This may lead to significant errors when dealing with these systems due to the different occupation of the d orbitals and to their degree of delocalization, aspects that make each transition metal exhibit its own particular chemistry.

In this work, we assess the performance of ubiquitously used exchange correlation density functionals within LDA and GGA: From LDA, we examined Ceperley−Alder[60] (CA) and Vosko−Wilk−Nussair[61] (VWN) parametrizations and from GGA, the broadly used Perdew−Wang (PW91)[62] and Perdew−Burke−Ernzerhof (PBE)[63] implementations. In addition, we considered the revised version of the PBE (RPBE)[64] functional aimed at providing better chemisorption energies and, furthermore, a revision of PBE designed to provide a better description of lattice properties of solid structures (PBEsol).[47] It should be noted that RPBE was initially proposed on the basis of a few test systems ranging from the adsorption of atomic and molecular oxygen, CO, and NO on Ni(100), Ni(111), Rh(100), Pd(100), and Pd(111) surfaces. Since then, it has been used in a very large number of studies, although none of them focused extensively on the performance of the functional on bulk properties such as metal−metal distances, cohesive energies, and bulk moduli. However, despite the better description of metal−adsorbate interactions, RPBE is thought to yield a poorer description of the binding within a metallic substrate.[49] A similar situation is found for PBEsol, a functional designed to revamp the description of solids by eliminating the bias of PBE toward the description of free atom energies, which is achieved by restoring the first-principles gradient expansion for the exchange part of the functional. The resulting PBEsol was tested for a variety of solids but included Cu, Rh, Pd, and Ag only as representatives of the transition metal series. Despite this, PBEsol is increasingly often chosen for studies involving solids, including transition metals.

The inability to correctly describe both adsorption properties and surface/bulk properties at the same time seems to be a general feature of the broadly used density functional based methods.[49] In spite of the considerations presented above and of the fact that the RPBE and PBEsol versions of the GGA are increasingly used in computational materials science and heterogeneous catalysis studies, it seems necessary to better establish the accuracy of these and other commonly used approaches on a comprehensive series of systems through the simultaneous examination of various properties. In this work, we provide a systematic study of the performance of the above-mentioned LDA and GGA approaches, including also RPBE and PBEsol. The accuracy of these six functionals is established by comparing calculated and experimental results of the interatomic distances, cohesive energies, and bulk moduli of the most stable crystal structure of the 30 transition metal elements in the periodic table. Last but not least, we report

surface related properties for the *fcc* subset of transition metals, and we discuss the effect of the inaccuracy of bulk properties on the surface chemical activity.

2. COMPUTATIONAL DETAILS

DFT calculations have been carried out using the Vienna Ab Initio Simulation Package VASP,[65] employing periodic boundary conditions and sampling CA, VWN, PW91, PBE, RPBE, and PBEsol exchange-correlation functionals. Valence electron density was expanded in a plane-wave basis set with a 415 eV cutoff for the kinetic energy. This ensured variations of total energy below 1 meV with respect to further basis set improvement. Optimizations were performed using the tetrahedron smearing method of Blöchl et al.[66] with an energy width of 0.2 eV to speed up convergence; however, final energy values were corrected to 0 K (no smearing). The effect of the atomic cores into the electron density has been described through the Projector Augmented Wave (PAW) method,[67] using the pseudopotentials recommended in the documentation. Note that scalar relativistic effects may affect bulk properties, especially for heavy elements. These effects are most important in the core electrons, exhibiting very large kinetic energy values, and can be easily incorporated through pseudopotentials, model core potentials, and effective core potential approaches. In the present work, scalar relativistic effects are included through the PAW description of the atomic core region. Previous calculations have shown that explicit inclusion of relativistic effects for the valence electrons of heavy transition metals leads to negligible deviations from present standard PAW approximation, i.e., interatomic distances changes ranging 0.2−0.5 pm and differences in bulk moduli of 3−5 GPa.[59] The electronic structure calculations were nonspin polarized, with the exception of the calculation of isolated metal atoms (in an appropriate box surrounded by a large enough vacuum width) and of magnetic Fe, Ni, and Co bulks. An optimal Monkhorst−Pack[68] grid of 7 × 7 × 7 special **k**-points dimensions was found to be sufficient for accurate total energy calculations in the most stringent metals—those with the smallest unit cell—and so this set has been systematically used for all bulk calculations. Note that energy variations due to the usage of denser **k**-points grids were always below 30 meV. When computing atoms in a vacuum, a broken symmetry cell of 9 × 10 × 11 Å dimensions was employed to ensure proper occupancy of degenerated orbitals. These calculations were carried out at the Γ point. Reference atomic values are included in the Supporting Information. In the case of slab calculations, a 7 × 7 × 1 grid was used to sample the reciprocal space. In bulk calculations, ionic positions and cell volumes were optimized using the conjugate gradient algorithm until pressures and total energies were converged within 0.01 GPa and 10 meV, respectively.

Cohesive energies, E_{coh}, were calculated as follows:

$$E_{coh} = E_{at} - \frac{E_{bulk}}{N} \quad (1)$$

where E_{at} is the energy of the isolated metal atom in a vacuum and E_{bulk} is the energy of the bulk unit cell containing N atoms. Within this definition, the larger the positive values of cohesive energies, the stronger is the chemical bonding within the solid. Bulk modulus (B_0) measures the volume variation of the solid (V) due to an external pressure (P), defined as

$$B_0 = -V_0\left(\frac{\partial P}{\partial V}\right)_{T,Vo} \quad (2)$$

where the negative sign shows that volume decreases when a positive external pressure is applied. Variation of the external pressure versus volume is gained via linear regression using the value at equilibrium geometry plus four single point calculations with ±0.05 and ±0.10 Å modifications of the lattice constants. More details of the procedure are detailed elsewhere.[69]

Under normal conditions, most of the 30 transition metals exhibit either *fcc*, *bcc*, or *hcp* crystallographic structures (see the Supporting Information for illustrative pictures). However, there are three exceptions to this: La and solid Hg present hexagonal (h) and rhombohedral (r) unit cells, respectively, and Mn features a cubic unit cell (c) containing 58 atoms, distributed as two Mn_{29} clusters centered in the cell origin and center—thus, similar to a *bcc* structure. In the following, the shortest interatomic distance within a crystal cell, δ, will be compared to the experimental values. However, note that δ depends on the lattice parameter a; in the *fcc* structure, it equals $a/\sqrt{2}$, while for *bcc* it equals $a\sqrt{3}/2$. In the case of *hcp* and h structures, δ depends on two lattice parameters, a and c. In the *hcp* structure, δ may either equal a or $\sqrt{(c^2/4 + a^2/3)}$ depending on the c/a ratio. Finally, for h structures, δ may equal either a or $\sqrt{(c^2/16 + a^2/3)}$, again depending on the c/a ratio, which is always kept constant. In r structures, both δ and a are the same quantity.

Last but not least, in order to connect surface chemical activity with a degree of accuracy in bulk description, we calculated the (111) surface energies of all transition metal elements with the *fcc* crystal structure (Rh, Ir, Ni, Pd, Pt, Cu, Ag, and Au), often encountered as components of heterogeneous catalysts. Surface energies, γ, were derived in two different ways: On one hand, surface energies of either the fixed or relaxed surface can be gained from the relaxation of a six layer slab optimizing the three outermost layers while freezing the remaining ones to the corresponding optimized bulk, following the usual general procedure.[69] A second procedure involves the definition of the slab total energy, E_{slab}, as

$$E_{slab} = N\varepsilon + 2\gamma A \quad (3)$$

where N is the number of atoms composing the slab unit cell, ε is the total energy of each atom in the slab, and A is the surface area of each of the two exposed surfaces. Within this methodology,[70,71] one has to consider a set of slabs with different thicknesses and to perform a linear regression of E_{slab} as a function of N. Surface energy is simply gained from the intercept which equals $2\gamma A$, and the slope gives the bulk energy ε. In the present work, thicknesses from four to nine layers were used for the linear regressions. The linear regression method is able to avoid erroneous results depending on the computational parameters.[72] Also its statistical accuracy can be estimated by 95% confidence intervals.

Due to the large number of studied systems and functionals used, we analyze the results profiting from standard error analysis, i.e., not only Mean Error (ME) but also Mean Absolute Error (MAE), which counteracts possible cancellation of errors in ME. Finally, the Mean Absolute Percentage Error (MAPE) provides the degree of inaccuracy of the functional under study. The MAE, ME, and MAPE values were calculated using standard definitions.

3. RESULTS AND DISCUSSION

The results for the 30 transition metal elements calculated with VWN, PBE, RPBE, and PBEsol exchange-correlation functionals explored in this work are reported in Tables 1−3 for interatomic distances, cohesive energies, and bulk moduli, respectively. The complete sets of calculated data, including CA and PW91 results, are provided in Tables S1−S3 of the Supporting Information. Nevertheless, one must point out that CA and PW91 essentially provided similar results to VWN and PBE exchange-correlation functionals, respectively. Accordingly, CA and PW91 results are not further discussed in detail, and only general trends and significant mean differences are discussed. In the following, we will discuss the sampled functionals performance for each property with the error analysis summarized in Table 4 and graphically displayed in Figure 2. The results concerning surface energies are reported in Table 5 and will be discussed at the end of this section. Nevertheless, one must be aware of the fact that, because of their peculiar crystal structure, results for Mn, La, and Hg will be discussed separately. Including Mn, La, and Hg in the error analysis results in larger deviations and distorts the conclusions, although the relative trends are similar. Finally, we do not compare our results with previous studies in the literature since the main goal here is to establish the accuracy of the six density functionals above-described with respect to experimental data, including all transition metal elements. Nevertheless, it is worth mentioning that the present results follow the trend of those reported in the quite complete study of Ropo et al.[50] and in excellent quantitative agreement with the values reported in the reference paper of Perdew et al.[41] with differences in interatomic distances and cohesive energies with respect to the present values being within 1.2 pm and 0.03 eV, respectively.

Table 1. Calculated and Experimental Shortest Interatomic Distances (δ in pm) of Bulk 3*d*, 4*d*, and 5*d* Transition Metals[a]

element	CS	VWN	PBE	RPBE	PBEsol	exp.
Sc	*hcp*	311.6	321.4	325.7	316.8	325.4[b]
Ti	*hcp*	281.6	288.4	290.8	285.0	289.7[c]
V	*bcc*	251.9	257.7	259.2	254.6	261.3[d]
Cr	*bcc*	241.0	245.9	247.0	243.3	249.8[c]
Mn[e]	*c*	209.0	213.0	215.0	211.0	224.0[f]
Fe	*bcc*	238.5	245.3	247.5	241.6	246.0[g]
Co	*hcp*	240.1	247.0	249.4	243.3	249.7[c]
Ni	*fcc*	242.1	248.9	251.2	244.6	249.3[h]
Cu	*fcc*	249.0	256.7	259.8	252.2	255.6[d]
Zn	*hcp*	278.0	289.0	294.2	281.8	291.3[c]
Y	*hcp*	344.1	354.3	358.5	348.8	355.6[c]
Zr	*hcp*	314.7	319.7	321.3	316.2	317.9[c]
Nb	*bcc*	281.9	287.3	288.6	284.0	285.9[i]
Mo	*bcc*	271.0	274.9	275.8	272.3	272.5[j]
Tc	*hcp*	268.3	272.2	272.7	269.6	271.0[k]
Ru	*hcp*	261.5	265.8	266.6	263.0	265.0[c]
Rh	*fcc*	266.4	271.7	272.9	268.2	253.9[l]
Pd	*fcc*	272.4	279.4	281.6	274.8	275.3[m]
Ag	*fcc*	283.8	294.1	298.1	287.6	288.9[n]
Cd	*hcp*	315.4	330.6	339.5	320.7	329.4[c]
La	*h*	354.5	372.0	378.0	360.9	373.9[c]
Hf	*hcp*	305.7	313.9	315.7	309.7	313.1[c]
Ta	*bcc*	281.8	287.5	288.6	284.2	286.0[c]
W	*bcc*	271.5	275.1	275.4	272.7	274.1[o]
Re	*hcp*	272.1	275.5	275.8	273.2	256.7[p]
Os	*hcp*	265.7	269.4	270.0	267.1	267.5[c]
Ir	*fcc*	270.0	274.1	274.8	271.4	271.5[c]
Pt	*fcc*	276.2	281.1	282.2	277.6	277.2[q]
Au	*fcc*	287.2	295.0	297.5	289.8	287.9[n]
Hg	*r*	309.8	353.2	397.5	321.8	301.0[k]

[a]CS stands for crystal structure (*hcp*, hexagonal close packed; *fcc*, face centered cubic; *bcc*, body centered cubic; *c*, cubic; *h*, hexagonal; *r*, rhombic). [b]Ref 74. [c]Ref 75. [d]Ref 76. [e]Due to the complex unit cell, only the shortest Mn−Mn distance is reported. [f]Ref 77. [g]Ref 78. [h]Ref 79. [i]Ref 80. [j]Ref 81. [k]Ref 82. [l]Ref 83. [m]Ref 84. [n]Ref 85. [o]Ref 86. [p]Ref 87. [q]Ref 88.

Table 2. Calculated and Experimental Cohesive Energies (E_{coh} in eV/atom) of Bulk 3*d*, 4*d*, and 5*d* Transition Metals

element	CS	VWN	PBE	RPBE	PBEsol	exp.[a]
Sc	*hcp*	4.86	4.12	3.72	4.52	3.90
Ti	*hcp*	6.37	5.45	4.96	6.06	4.84
V	*bcc*	7.36	6.03	5.39	6.73	5.30
Cr	*bcc*	5.51	4.00	3.39	4.65	4.09
Mn	*c*	5.42	3.86	3.38	4.61	2.92
Fe	*bcc*	6.41	4.87	4.24	5.61	4.28
Co	*hcp*	6.61	5.27	4.49	5.86	4.43
Ni	*fcc*	6.04	4.87	4.22	5.53	4.44
Cu	*fcc*	4.50	3.48	3.12	4.03	3.48
Zn	*hcp*	1.90	1.12	0.75	1.59	1.35
Y	*hcp*	4.87	4.13	3.75	4.56	4.39
Zr	*hcp*	7.34	6.16	6.27	6.94	6.29
Nb	*bcc*	8.46	6.98	6.39	7.68	7.44
Mo	*bcc*	7.95	6.21	5.57	7.01	6.80
Tc	*hcp*	8.70	6.85	6.17	7.82	7.13
Ru	*hcp*	8.68	6.67	5.92	7.69	6.74
Rh	*fcc*	7.55	5.62	5.19	6.81	5.72
Pd	*fcc*	5.02	3.71	3.09	4.43	3.90
Ag	*fcc*	3.60	2.49	1.98	3.03	2.94
Cd	*hcp*	1.53	0.73	0.33	1.20	1.16
La	*h*	5.09	4.18	3.70	4.72	4.47
Hf	*hcp*	7.53	6.40	5.90	7.07	6.42
Ta	*bcc*	9.63	8.27	7.66	9.09	8.09
W	*bcc*	10.57	9.07	8.42	9.96	8.79
Re	*hcp*	9.61	7.82	7.09	8.79	8.02
Os	*hcp*	10.21	8.29	7.56	9.40	8.17
Ir	*fcc*	9.22	7.32	6.63	8.42	6.92
Pt	*fcc*	7.13	5.50	4.83	6.41	5.85
Au	*fcc*	4.27	2.99	2.40	3.66	3.81
Hg	*r*	0.93	0.15	0.49	0.51	0.62

[a]Ref 90.

3.A. Interatomic Distances. We begin the discussion by comparing the shortest interatomic distances δ of the transition metals calculated with different functionals, compared to the available experimental values, see Table 1. Most recent experimental crystallographic interatomic distances have been collected via the Crystallographic Open Database,[73] and the original sources are also included in the reference list for completeness.[74−88] Note that in general terms the experimental interatomic distances suffer from measurement error bars below ±0.03 pm, and so below the order of magnitude of the significant figures here discussed. Only in a few cases are the experimental bond length error bars on the same order, with Re being the case displaying the worst precision.[87] Nevertheless, for Re the error bars are of ±0.46 pm and, as shown afterwards,

Table 3. Calculated and Experimental Bulk Moduli (B_0 in GPa) of Bulk 3*d*, 4*d*, and 5*d* Transition Metals

element	CS	VWN	PBE	RPBE	PBEsol	exp.[a]
Sc	*hcp*	62.9	55.0	51.2	57.9	54.6
Ti	*hcp*	129.4	113.5	103.8	120.7	106.0
V	*bcc*	219.4	183.1	175.0	200.1	155.0
Cr	*bcc*	302.0	261.2	237.6	284.5	160.0
Mn	*c*	333.7	281.9	264.2	311.2	90.4
Fe	*bcc*	256.9	195.3	159.1	216.1	163.0
Co	*hcp*	270.1	212.5	189.0	238.3	186.0
Ni	*fcc*	254.7	193.9	173.2	233.6	179.0
Cu	*fcc*	188.2	146.9	122.3	165.2	133.0
Zn	*hcp*	107.3	78.4	66.4	96.2	64.8
Y	*hcp*	44.2	40.7	38.6	42.6	41.0
Zr	*hcp*	102.6	95.5	92.9	104.2	94.9
Nb	*bcc*	173.8	171.1	164.7	183.5	169.0
Mo	*bcc*	296.8	261.3	254.2	288.9	261.0
Tc	*hcp*	349.6	307.6	294.8	333.8	297.0
Ru	*hcp*	365.2	308.2	295.7	349.1	303.0
Rh	*fcc*	317.7	256.4	238.1	290.8	282.0
Pd	*fcc*	215.6	169.4	151.2	203.8	189.0
Ag	*fcc*	138.7	83.3	74.6	117.4	98.8
Cd	*hcp*	79.7	49.6	39.1	68.9	49.8
La	*h*	30.6	25.1	23.1	27.8	26.6
Hf	*hcp*	124.6	108.0	104.3	114.3	108.0
Ta	*bcc*	213.7	195.3	188.3	209.2	191.0
W	*bcc*	351.7	316.2	306.1	334.8	308.0
Re	*hcp*	415.8	372.1	363.6	405.6	360.0
Os	*hcp*	254.5	402.6	388.4	439.2	418.0
Ir	*fcc*	406.1	347.3	333.4	387.8	358.0
Pt	*fcc*	309.4	250.9	233.5	291.7	277.0
Au	*fcc*	187.2	138.4	120.7	171.9	166.0
Hg	*r*	45.3	9.7	1.9	20.0	28.2

[a]Ref 90.

well below the differences of accuracy of different types of exchange-correlation functionals explored in the present work. Experimental data are chosen whenever possible at temperatures close or extrapolated to 0 K. Nevertheless, transition metal thermal expansion coefficients are on the order of $\sim 10^{-5}$ K^{-1}, and so lattice constant expansions at room temperature would systematically decrease the experimental values of interatomic distances, but not significantly enough to affect the conclusions of this study. Last but not least, a recent study has shown that inclusion of zero-point anharmonic phonon correction on lattice constants little reduces the error statistics of density functionals, by 0.1−0.2% in transition metals.[32]

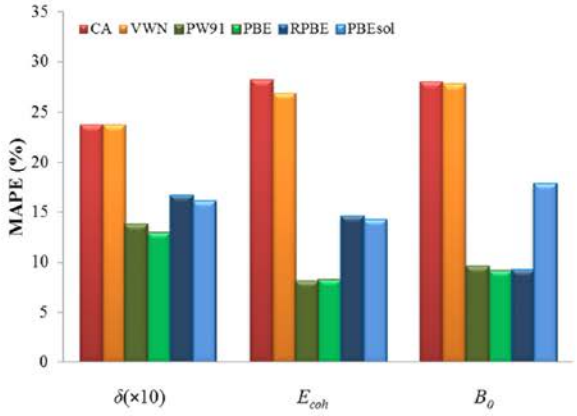

Figure 2. Summary of Mean Absolute Percentage Error (MAPE) for the interatomic distances, δ; cohesive energies, E_{coh}; and bulk moduli, B_0, of the 3d, 4d, and 5d transition metals series excluding metals with particular crystallographic structure: Mn, La, and Hg. MAPE in δ has been multiplied by a factor of 10 for a better visualization.

From the error analysis in Table 4, restricted to the 27 transition metal elements obtained by excluding Mn, La, and Hg, it seems clear that the PBE provides the most accurate description of the atomic structure of bulk transition metals closely followed by PW91. This result is already somewhat surprising because it contradicts the common belief, mostly from molecular systems and organometallic chemistry,[89] that LDA yields significantly better interatomic distances than GGA functionals of broad applicability such as PW91 and PBE. We find that this is the case only for Mo, Rh, Pd, Re, Ir, Pt, and Au (also for Hg). However, when considering the set of 27 transition metals, one can clearly see that GGA performs better. In fact, the MAE of PBE and PW91 functionals for the optimized interatomic distances is of ~3.5−3.7 pm only, whereas it is considerably larger (~6.7 pm) in the case of both CA and VWN parametrizations of LDA. Nevertheless, the mean (signed) average error (ME) of interatomic distances for the complete set of 27 transition metal elements corresponding to PW91 and PBE is of only 1.95 and 2.01 pm, respectively. As expected, LDA underestimates all of the interatomic distances (27 transition metals set) by 4.6 pm on average as expected from the well-known tendency of LDA to overestimate binding interactions.

The PBEsol functional designed to reproduce experimental distances between metal atoms in the bulk[47] yields the most accurate results for 6 out of 27 (even 30) transition metal

Table 4. Error Analysis of the Results Corresponding to the Interatomic Distance (δ in pm except for MAPE), Cohesive Energy (E_{coh} in eV atom^{-1} except for MAPE), and Bulk Modulus (B_0 in GPa except for MAPE) of Bulk 3d, 4d, and 5d Transition Metals Excluding Mn, La, and Hg (See Text)

property		CA	VWN	PW91	PBE	RPBE	PBEsol
δ	ME	−4.60	−4.59	1.95	2.01	4.19	−1.98
	MAE	6.67	6.66	3.72	3.49	4.56	4.42
	MAPE	2.38	2.38	1.37	1.29	1.66	1.60
E_{coh}	ME	1.44	1.36	0.02	−0.01	−0.57	0.74
	MAE	1.44	1.36	0.33	0.34	0.59	0.75
	MAPE	28.24	26.94	8.11	8.29	14.49	14.16
B_0	ME	36.12	35.74	7.46	5.21	−7.89	28.79
	MAE	48.23	47.85	16.13	15.66	15.73	28.79
	MAPE	28.06	27.84	9.57	9.17	9.21	17.72

Table 5. Surface Energies (in J m^{-2}) Calculated with Various Functionals and Using Either Direct Calculation (dc) or Calculated through Linear Regression (lr)[a]

	CA		VWN		PW91		PBE		RPBE		PBEsol		exp.[b]
	dc	lr	dc	lr	dc	lr	dc	lr	dc	lr	dc	lr	
Ni	2.56	2.48 ± 0.05	2.55	2.48 ± 0.05	1.92	1.89 ± 0.05	1.93	1.92 ± 0.06	1.68	1.65 ± 0.08	2.32	2.28 ± 0.05	2.45
Cu	1.83	1.74 ± 0.17	1.83	1.74 ± 0.17	1.30	1.29 ± 0.11	1.31	1.30 ± 0.11	1.07	1.09 ± 0.10	1.65	1.59 ± 0.17	1.83
Rh	2.53	2.57 ± 0.14	2.53	2.57 ± 0.14	1.94	1.97 ± 0.12	1.94	1.98 ± 0.12	1.72	1.75 ± 0.11	2.42	2.37 ± 0.14	2.70
Pd	1.81	1.79 ± 0.07	1.81	1.79 ± 0.07	1.25	1.27 ± 0.05	1.25	1.27 ± 0.04	1.02	1.05 ± 0.03	1.60	1.60 ± 0.05	2.05
Ag	1.18	1.16 ± 0.03	1.18	1.16 ± 0.03	0.74	0.75 ± 0.03	0.73	0.74 ± 0.03	0.52	0.55 ± 0.02	1.01	1.00 ± 0.03	1.25
Ir	2.81	2.83 ± 0.10	2.81	2.83 ± 0.10	2.25	2.27 ± 0.11	2.27	2.27 ± 0.10	2.06	2.07 ± 0.09	2.65	2.67 ± 0.10	3.00
Pt	1.96	1.95 ± 0.10	1.96	1.95 ± 0.10	1.45	1.44 ± 0.07	1.52	1.46 ± 0.08	1.24	1.25 ± 0.07	1.54	1.80 ± 0.10	2.48
Au	1.19	1.16 ± 0.11	1.19	1.16 ± 0.11	0.74	0.73 ± 0.09	0.74	0.73 ± 0.09	0.54	0.54 ± 0.08	1.02	1.00 ± 0.11	1.50
ME	−0.17	−0.20	−0.17	−0.20	−0.71	−0.71	−0.70	−0.70	−0.93	−0.91	−0.38	−0.37	
MAE	0.20	0.21	0.20	0.21	0.71	0.71	0.70	0.70	0.93	0.91	0.38	0.37	
MAPE	9.55	10.07	9.50	10.07	34.52	34.38	34.00	34.11	45.34	44.71	18.50	18.25	

[a]ME and MAE are in J m^{-2}, whereas MAPE is in %. [b]Ref 91.

elements (Mo, Pd, Ag, Os, Ir, and Pt), whereas, at the same time, the accuracy of the calculated distances for 14 elements (Ni, Fe, Cu, Zn, Y, Zr, Nb, Tc, Ru, Cd, La, Hf, Ta, and W) is clearly inferior to that of PW91 or PBE. A closer inspection of the data in Table 1 reveals that PBEsol improves the PBE parent functional for *fcc* metals only (see deviation analysis for different CSs in the Supporting Information), while its performance is similar for *hcp* and clearly worse for *bcc* metals. Note that PBEsol was developed considering Cu, Rh, Ag, and Pd, all exhibiting *fcc* structure. This provides one more indication of the need to consider a sufficiently broad number of cases when designing and testing new functionals. From the accuracy analysis in Table 4, one finds that, regarding interatomic distances, the MAE of PBEsol is 4.42 pm, which is somewhat higher than those of PW91 and PBE values. It is also rather surprising to find that the performance of the RPBE potential is the worst among considered GGA functionals with a MAE of 4.56 pm. It is also worth pointing out that RPBE systematically tends to overestimate interatomic distances by 4.2 pm on average. Note again that the performance of the different exchange-correlation functionals examined in this work depends on the lattice type of a metal under consideration. For example, PBEsol produces more accurate interatomic distances of *fcc* metals while *bcc* and *hcp* metals are best described with PBE. Surprisingly, RPBE yields relatively accurate results for metals with the *bcc* lattice. See the Supporting Information for more details.

For the special cases of Mn, La, and Hg, the trends are similar, although the errors are larger than on the rest of transition metal cases. Indeed, RPBE provides the best description of Mn, although with an error of 9 pm. PBE almost reproduces the experimental value for La, whereas both CA and VWN underestimate it by 19 pm, and the rest of the functionals provide results within 2−12 pm. Finally, for Hg one finds that CA and VWN perform the best, with an error of 9 pm but overestimating the bond length, which is opposite to the behavior encountered in the rest of the metals.

3.B. Cohesive Energies. The accurate prediction of the cohesive energies of the whole transition metal series represents a stringent test for the different exchange-correlation functionals since it implies the breaking of all the different bonds depending on the crystal structure of a given element. Calculated E_{coh} values are displayed in Table 2 together with tabulated experimental data.[90] Results show that, as expected from the self-interaction error in the Coulomb contribution to the total energy, both CA and VWN implementation of LDA significantly overestimate the binding energy. In fact, these two functionals provide the worst results for a large fraction of the transition metal series. The mean absolute errors for CA and VWN on the 27 transition metals are 1.44 and 1.36 eV, respectively. The values corresponding to the standard GGA functionals (PW91 and PBE) represent a noteworthy improvement on the LDA values, expected from the more physically grounded nature of these exchange-correlation functionals. This is due, as commented above, to the fact that the electron density of transition metals largely deviates from that of simple metals which, in turn, is sufficiently well represented by the homogeneous electron gas model. Thus, PW91 and PBE provide, in general, the most accurate cohesive energies with a MAE of ∼0.34 eV and a MAPE of ∼8%. Finally, we consider the accuracy of RPBE and PBEsol functionals on predicting cohesive energies. Both functionals exhibit better behavior than LDA functionals, but none of them present any improvement

with respect to the GGA ones. This result is not unexpected for PBEsol since the restoration of the gradient expansion for slowly varying densities implies a poor description of exchange energies, vital to gaining good estimates of dissociation and cohesive energies.[47] The accuracy of RPBE and PBEsol is characterized by MAE values of 0.59 and 0.75 eV, respectively, which correspond both to a MAPE of ∼14%, almost doubling the MAPE exhibited by the other GGA functionals. Moreover, it is worth pointing out that, on average, RPBE tends to underestimate cohesive energies by 0.57 eV, whereas PBEsol overestimates them by 0.74 eV, in line with the trends in calculated interatomic distances discussed in the previous subsection. Nevertheless, one has to realize that for some metals, either RPBE (Sc, Ti, V, Mn, Fe, Co, Ni, Zr, and Ir) or PBEsol (Y, Nb, Mo, Ag, Cd, Au, and Hg) yields surprisingly good cohesive energies. This is an argument in favor of testing the accuracy of newly developed methods using a sufficiently large database of available experimental results.

It is noteworthy that, at variance with the situation concerning interatomic distance, the performance of the functionals here explored does not significantly depend on the type of crystal structure, clearly showing that the accuracies of PW91 and PBE functionals are especially good when computing the cohesive energy of metals, as shown in the Supporting Information. Only RPBE seems to be similarly adequate to PW91 and PBE for *bcc* metals. For the special cases of Mn, La, and Hg, the mean error is surprisingly small for some functionals and quite large for others. For instance, in the case of Mn, RPBE provides the best estimate with an error of 0.5 eV, and LDA errors are almost 100%. For La, the GGA functionals deviate only ∼0.1 eV from experimental values, while RPBE performs even worse than LDA. A different situation is found for Hg; here PBEsol provides the best description and PBE and PW91 the worst.

3.C. Bulk Moduli. Estimations of B_0 for the different metals under scope are listed in Table 3 together with the tabulated experimental data.[90] This is quite a difficult property, although, surprisingly, the error exhibited by all methods is similar to that corresponding to the cohesive energy. Hence, consistently with the situation already commented on for interatomic distances and cohesive energies, both LDA type functionals overestimate bulk moduli by a ME of ∼36 GPa, whereas, once again, the best performance is exhibited by the GGA functionals with ME values of 7.5 and 5.2 GPa for PW91 and PBE, respectively, although the MAE values are larger (∼16 GPa for both PW91 and PBE), indicating some sort of error compensation along the series. Here, the accuracy of RPBE is similar to that exhibited by PW91 and PBE and consistently better for *bcc* metals and somewhat worse for *fcc* metals, as detailed in the Supporting Information. However, it is interesting to point out that while PW91 and PBE systematically tend to overestimate this property, the RPBE functional exhibits an opposite behavior with a tendency to underestimate the bulk moduli of transition metals by 8 GPa, but with a MAE of 16 GPa. Finally, the PBEsol performance is closer to LDA and, therefore, worse than that of PW91 and PBE. In terms of MAPE, it is worth pointing out that PW91, PBE, and RPBE deviate from experiment by 10% and CA and VWN by 28%, and finally, PBEsol exhibits an intermediate behavior (18%).

Among the special cases (Mn, La, and Hg), Mn exhibits the largest deviations from experimental values with errors greater than 200 GPa regardless of the functional. On the contrary, in the case of La, all functionals are found to perform with a similar accuracy, although with errors below 6 GPa or ∼20%. Finally, in the case of Hg, LDA provides the best values, a behavior which has also been found for the cohesive energy and interatomic distances.

3.D. Surface Energies of Selected Metals. In this subsection, we investigate how the accuracy of a given functional in describing bulk properties affects surface energies, and ultimately, the magnitude of adsorption energy. Clearly, one has to restrict the study to a few metals and to the most stable surface only. Here, we choose to study the (111) surface of a set of transition metals with the common feature of exhibiting *fcc* crystal structure and for which experimental values are also available,[91] even if one must admit that accurate measurements of this property are extremely difficult. Nevertheless, note that the reported experimental error bars are below the significant figures here treated.[92] In addition, these are the metals commonly encountered in heterogeneous catalysts and, therefore, the ones for which the knowledge of this information appears to be most essential.

From the summary of results in Table 5, one can readily see that results obtained via linear regression of slab energies tend to be as accurate as those arising from the straightforward method involving bulk calculations. With respect to the accuracy of the different DFT methods explored in this work, the error analysis shows that all exchange-correlation functionals underestimate the surface energies with the exception of LDA for Cu and Ni. The lowest value of the MAE (0.2 J m^{-2}) corresponds to the LDA methods and is hardly consistent with the well-known tendency to overestimate bonding interactions. Naively, one would expect that an overestimated value of the cohesive energy results also in a larger value of the surface energy simply because the cost to create the surface will also be higher. GGA functionals exhibit a few times more pronounced deviations (MAEs) than the LDA methods. In fact, the MAPE values for LDA are ∼10%, whereas the GGA methods have a noticeable value of ∼35%. Interestingly, RPBE produces an even larger MAPE value of ∼45%, whereas here PBEsol presents the best performance among GGAs with a MAPE of roughly 20%. This finding is in line with the known anticorrelation between the accuracy of a GGA functional for the calculation of surface energies and adsorption energies, the case of the CO molecule adsorption being the typical example.[37,49] This can be easily understood from the following arguments: Methods overestimating/underestimating the bonding interactions such as LDA/GGA will predict larger/smaller surface energies simply because the cost to break a bond is larger/smaller. Consequently, the surface is less/more stable and tends to interact more/less with incoming adsorbates. This is likely to be the reason why RPBE provides CO adsorption energies which improve the PBE ones.[64] This trend on the surface energy is likely to be transferred to the energy profiles of surface reactions, affecting the thermodynamics and kinetics of a given process.[93,94]

■ CONCLUSIONS

Interatomic distances, cohesive energies, and bulk moduli of the three transition metal series (3d, 4d, and 5d) in the periodic table in their most stable crystal structures have been obtained using several exchange-correlation potentials. These are the CA and VWN implementation of LDA, the GGA type PW91 and PBE functionals, and the RPBE and PBEsol revisions of PBE. From the analysis of calculated results for these metals and from comparison to the available experimental data, it is

possible to obtain a rather complete picture concerning the performance of these functionals. This is done, however, by excluding the cases of Mn, La, and Hg, which for some or all properties present errors significantly larger than for the rest of the transition metals and bias the mean deviations. On the basis of the research scope, we present compelling evidence that (*i*) PW91 and PBE produce similar results for the majority of transition metals and yield the best overall accuracy for structural data, cohesive energies, and bulk moduli, as shown in Figure 2, based on MAPE. (*ii*) Except for a few elements, LDA yields less accurate interatomic distances, cohesive energies, and bulk moduli than the typical GGA functionals. At the same time, as a consequence of the overestimation of bond interactions, LDA does not underestimate the surface energies so strongly as the other considered functionals. (*iii*) PBEsol, designed to yield good results for lattice parameters of solids, improves it over PBE only for six transition metals, while its performance for 14 other bulks is clearly inferior to those of PW91 or PBE. In general, PBEsol appears to exhibit a performance in between that of GGA and LDA. In this sense, it overestimates binding energies more than PBE or PW91 but less than LDA. (*iv*) The overall performance of RPBE for lattice parameters, cohesive, and surface energies of transition metals is worse than that of PW91 and PBE, although results for bulk moduli are of comparable quality. The better performance of RPBE in describing chemisorption energies seems to result from a severe underestimation of cohesive energies, and consequently, an overestimation of the surface stability, which hinders its chemical activity. (*v*) The bulk crystal structure seems to be a factor to take into account when using a given functional and certain properties. Cohesive energies seem to be unaffected by the type of crystal structure, although interatomic distances of *fcc* are better reproduced with PBEsol, and *bcc* and *hcp* interatomic distances are better reproduced by GGA and RPBE functionals, respectively. Concerning bulk moduli, RPBE is especially good when describing the bulk moduli of *hcp* and *bcc* solids.

Finally, even if among the explored exchange-correlation potentials the average performance of PBE results to be the best, one must be aware that non-negligible errors with respect to experimental results still remain. The origin of these errors has to be traced to approximations in the form of the exchange-correlation functional. On the one hand, it is likely that the *d* orbitals suffer from the self-interaction error as is the case in transition metal oxides and also in *f* orbitals in rare earth elements and their oxides. In principle, this can be remedied through self-interaction corrected DFT methods.[95] A second source of error, especially for the heavier transition metal elements, is the lack of explicit nonscalar relativistic effects such as spin−orbit interactions. Nevertheless, the precise contribution of these effects remains an open question.

To summarize, whereas PW91 and PBE functionals represent a significant improvement over the LDA type functional, the RPBE and PBEsol do not necessarily improve over either PW91 or PBE and should be used with caution because improvement in some property is at the cost of worsening the description of others. Likewise, one must insist that because of the peculiarities and particular chemistry of each transition metal element, it is advisable to test the performance of newly developed functionals for the whole series rather than concentrating on a few cases only.

■ ASSOCIATED CONTENT

Supporting Information

Figure S1 shows schematic representations of the lattice structures discussed in the work. Tables S1−S3 display interatomic distances, cohesive energies, and bulk moduli, respectively, analogous to Tables 1−3 but including CA and PW91 results. Tables S4−S6 include an error analysis analogous to that of Table 4 but carried out exclusively for *fcc*, *bcc*, or *hcp* metals. Table S7 contains atomic configuration and atomic energy reference data. This information is available free of charge via the Internet at http://pubs.acs.org/.

■ AUTHOR INFORMATION

Corresponding Author

*E-mail: francesc.illas@ub.edu.

Notes

The authors declare no competing financial interest.

■ ACKNOWLEDGMENTS

This work was supported by the Spanish MICINN FIS2008-02238 and MINECO CTQ2012-30751 grants, *Generalitat de Catalunya* (grants 2009SGR1041 and XRQTC), and, in part, by grants from the National Science and Technology Development Agency (NSTDA Chair Professor and NANOTEC Center for the Design of Nanoscale Materials for Green Nanotechnology), the Kasetsart University Research and Development Institute (KURDI), the Commission on Higher Education, Ministry of Education ("the National Research University Project of Thailand (NRU)" and "Postgraduate Education and Research Programs in Petroleum and Petrochemicals and Advanced Materials"). P.J. would like to thank the Office of the Higher Education Commission, Thailand for supporting him with a grant under the program Strategic Scholarships for Frontier Research Network for the Ph.D. Program Thai Doctoral degree and the Graduate School of Kasetsart University for his research. F.V. thanks the Spanish MICINN for the postdoctoral grant under the program *Juan de la Cierva* (JCI-2010-06372). S.M.K. is grateful to the Spanish *Ministerio de Educación, Cultura y Deporte* for the predoctoral FPU Grant AP2009-3379, and F.I. acknowledges additional support through the ICREA Academia award for excellence in research.

■ REFERENCES

(1) Parr, R. G.; Yang, W. *Density Functional Theory of Atoms and Molecules*; Oxford University Press: Oxford, U. K., 1989.
(2) McWeeny, R. *Methods of Molecular Quantum Mechanics*; Academic Press: London, U. K., 1992.
(3) Cramer, C. J.; Truhlar, D. G. *Phys. Chem. Chem. Phys.* **2009**, *11*, 10757.
(4) Payne, M. C.; Teter, M. P.; Allan, D. C.; Arias, T. A.; Joannopolos, J. D. *Rev. Mod. Phys.* **1992**, *64*, 1045−1097.
(5) Huang, P.; Carter, E. A. *Annu. Rev. Phys. Chem.* **2008**, *59*, 261.
(6) van Santen, R. A.; Neurock, M. *Molecular Heterogeneous Catalysis*; Wiley-VCH: Weinheim, Germany, 2006.
(7) Valiev, M.; Bylaska, E. J.; Govind, N.; Kowalski, K.; Straatsma, T. P.; Van Dam, H. J. J.; Wang, D.; Nieplocha, J.; Apra, E.; Windus, T. L.; de Jong, W. *Comput. Phys. Commun.* **2010**, *181*, 1477−1489.
(8) Iwata, J. I.; Takahashi, D.; Oshiyama, A.; Boku, T.; Shiraishi, K.; Okada, S.; Yabana, K. *J. Comput. Phys.* **2010**, *229*, 2339−2363.
(9) Cohen, A. J.; Mori-Sanchez, P.; Yang, W. *Chem. Rev.* **2012**, *112*, 289.
(10) Yang, K.; Zheng, J. J.; Zhao, Y.; Truhlar, D. G. *J. Chem. Phys.* **2010**, *132*, 164117.

(11) Zhao, Y.; Truhlar, D. G. *Theor. Chem. Acc.* **2008**, *120*, 215−241.
(12) Boese, A. D.; Martin, J. M. L. *J. Chem. Phys.* **2004**, *121*, 3405−3416.
(13) Becke, A. D. *J. Chem. Phys.* **1993**, *98*, 5648−5652.
(14) Peverati, R.; Truhlar, D. G. *Phys. Chem. Chem. Phys.* **2012**, *14*, 13171−13174.
(15) Adamo, C.; Barone, V. *J. Chem. Phys.* **1999**, *110*, 6158.
(16) Vydrov, O. A.; Scuseria, G. E. *J. Chem. Phys.* **2006**, *125*, 234109.
(17) (a) Heyd, J.; Scuseria, G. E.; Ernzernhof, M. *J. Chem. Phys.* **2003**, *518*, 8207;(b) *ibid.* **2006**, *124*, 219906(E).
(18) Moreira, I. de P. R.; Illas, F.; Martin, R. L. *Phys. Rev. B* **2002**, *65*, 155102.
(19) Feng, X. B.; Harrison, N. M. *Phys. Rev. B* **2004**, *69*, 035114.
(20) Bredow, T.; Gerson, A. R. *Phys. Rev. B* **2000**, *61*, 5194.
(21) Muscat, J.; Wander, A.; Harrison, N. M. *Chem. Phys. Lett.* **2001**, *342*, 397.
(22) Kudin, K. N.; Scuseria, G. E.; Martin, R. L. *Phys. Rev. Lett.* **2002**, *89*, 266402.
(23) Muñoz, D.; Harrison, N. M.; Illas, F. *Phys. Rev. B* **2004**, *69*, 085115.
(24) Perry, J. K.; Tahir-Kheli, J.; Goddard, W. A. *Phys. Rev. B* **2001**, *63*, 144510.
(25) Feng, X.; Harrison, N. M. *Phys. Rev. B* **2004**, *70*, 092402.
(26) Moreira, I. de P. R.; Dovesi, R. *Int. J. Quantum Chem.* **2004**, *99*, 811.
(27) Paier, J.; Marsman, M.; Kresse, G. *J. Chem. Phys.* **2007**, *127*, 024103.
(28) Tran, F.; Koller, D.; Blaha, P. *Phys. Rev. B* **2012**, *86*, 134406.
(29) Zhao, Y.; Truhlar, D. G. *Acc. Chem. Res.* **2008**, *41*, 157−167.
(30) Luo, S.; Zhao, Y.; Truhlar, D. G. *J. Phys. Chem. Lett.* **2012**, *3*, 2975−2979.
(31) Ruzsinszky, A.; Sun, J.; Xiao, B.; Csonka, G. I. *J. Chem. Theory Comput.* **2012**, *8*, 2078−2087.
(32) Hao, P.; Fang, Y.; Sun, J.; Csonka, G. I.; Philipsen, P. H. T.; Perdew, J. P. *Phys. Rev. B* **2012**, *85*, 014111.
(33) Sun, J.; Marsman, M.; Csonka, G. I.; Ruzsinszky, A.; Hao, P.; Kim, Y.-S.; Kresse, G.; Perdew, J. P. *Phys. Rev. B* **2011**, *84*, 035117.
(34) Schimka, L.; Harl, J.; Kresse, G. *J. Chem. Phys.* **2011**, *134*, 024116.
(35) Sun, J.; Marsman, M.; Ruzsinszky, A.; Kresse, G.; Perdew, J. P. *Phys. Rev. B* **2011**, *83*, 121410.
(36) Haas, P.; Tran, F.; Blaha, P.; Schwarz, K. *Phys. Rev. B* **2011**, *83*, 205117.
(37) Schimka, L.; Harl, J.; Stroppa, A.; Grüneis, A.; Marsman, M.; Mittendorfer, F.; Kresse, G. *Nat. Mater.* **2010**, *9*, 741−744.
(38) Harl, J.; Schimka, L.; Kresse, G. *Phys. Rev. B* **2010**, *81*, 115126.
(39) Haas, P.; Tran, F.; Blaha, P.; Pedroza, L. S.; da Silva, A. J. R.; Odashima, M. M.; Capelle, K. *Phys. Rev. B* **2010**, *81*, 125136.
(40) Harl, J.; Kresse, G. *Phys. Rev. Lett.* **2009**, *103*, 056401.
(41) Perdew, J. P.; Ruzsinszky, A.; Csonka, G. I.; Constantin, L. A.; Sun, J. *Phys. Rev. Lett.* **2009**, *103*, 026403.
(42) Haas, P.; Tran, F.; Blaha, P. *Phys. Rev. B* **2009**, *79*, 085104.
(43) Ruzsinszky, A.; Csonka, G. I.; Scuseria, G. E. *J. Chem. Theory Comput.* **2009**, *5*, 763−769.
(44) Csonka, G. I.; Perdew, J. P.; Ruzsinszky, A.; Philipsen, P. H. T.; Lebègue, S.; Paier, J.; Vydrov, O. A.; Ángyán, J. G. *Phys. Rev. B* **2009**, *79*, 155107.
(45) Perdew, J. P.; Ruzsinszky, A.; Csonka, G. I.; Vydrov, O. A.; Scuseria, G. E.; Constantin, L. A.; Zhou, Z.; Burke, K. *Phys. Rev. Lett.* **2008**, *101*, 239702.
(46) Marsman, M.; Paier, J.; Stroppa, A.; Kresse, G. *J. Phys.: Condens. Matter* **2008**, *20*, 064201.
(47) Perdew, J. P.; Ruzsinszky, A.; Csonka, G. I.; Vydrov, O. A.; Scuseria, G. E.; Constantin, L. A.; Zhou, X.; Burke, K. *Phys. Rev. Lett.* **2008**, *100*, 136406.
(48) Zhao, Y.; Truhlar, D. G. *J. Chem. Phys.* **2008**, *128*, 184109.
(49) Stroppa, A.; Kresse, G. *New J. Phys.* **2008**, *10*, 063020.
(50) Ropo, M.; Kokko, K.; Vitos, L. *Phys. Rev. B* **2008**, *77*, 195445.
(51) Mattsson, A. E.; Armiento, R.; Paier, J.; Kresse, G.; Wills, J. M.; Mattsson, T. R. J. *Chem. Phys.* **2008**, *128*, 084714.
(52) Madsen, G. K. *Phys. Rev. B* **2007**, *75*, 195108.
(53) Tran, F.; Laskowski, R.; Blaha, P.; Schwarz, K. *Phys. Rev. B* **2007**, *75*, 115131.
(54) Wu, Z.; Cohen, R. E. *Phys. Rev. B* **2006**, *73*, 235116.
(55) Paier, J.; Marsman, M.; Hummer, K.; Kresse, G.; Gerber, I. C.; Ángyán, J. G. J. *Chem. Phys.* **2006**, *124*, 154709.
(56) Gajdo, M.; Eichler, A.; Hafner, J. *J. Phys.: Condens. Matter* **2004**, *16*, 1141−1164.
(57) Staroverov, V. N.; Scuseria, G. E.; Tao, J.; Perdew, J. P. *Phys. Rev. B* **2004**, *69*, 075102.
(58) Kurth, S.; Perdew, J. P.; Blaha, P. *Int. J. Quantum Chem.* **1999**, *75*, 889−909.
(59) Grabowski, B.; Hickel, T.; Neugebauer, J. *Phys. Rev. B* **2007**, *76*, 024309.
(60) Ceperley, D. M.; Alder, B. J. *Phys. Rev. Lett.* **1980**, *45*, 566−569.
(61) Vosko, S. H.; Wilk, L.; Nusair, M. *Can. J. Phys.* **1980**, *58*, 1200−1211.
(62) Perdew, J. P.; Wang, Y. *Phys. Rev. B* **1992**, *45*, 13244−13249.
(63) Perdew, J. P.; Burke, K.; Ernzerhof, M. *Phys. Rev. Lett.* **1996**, *77*, 3865−3868.
(64) Hammer, B.; Hansen, L. B.; Nørskov, J. K. *Phys. Rev. B* **1999**, *59*, 7413−7421.
(65) Kresse, G.; Furthmuller, J. *Phys. Rev. B* **1996**, *54*, 11169−11186.
(66) Blöchl, P. E.; Jepsen, O.; Andersen, O. K. *Phys. Rev. B* **1994**, *49*, 16223−16233.
(67) Blöchl, P. E. *Phys. Rev. B* **1994**, *50*, 17953−17979.
(68) Monkhorst, H. J.; Pack, J. D. *Phys. Rev. B* **1976**, *13*, 5188−5192.
(69) Viñes, F.; Sousa, C.; Liu, P.; Rodriguez, J. A.; Illas, F. *J. Chem. Phys.* **2005**, *122*, 174709.
(70) Boettger, J. C. *Phys. Rev. B* **1994**, *49*, 16798−16800.
(71) Kozlov, S. M.; Viñes, F.; Nilius, N.; Shaikhutdinov, S.; Neyman, K. M. *J. Phys. Chem. Lett.* **2012**, *3*, 1956−1961.
(72) Da Silva, J. L. F.; Stampfl, C.; Scheffler, M. *Surf. Sci.* **2006**, *600*, 703−715.
(73) Gražulis, S.; Chateigner, D.; Downs, R. T.; Yokochi, A. T.; Quiros, M.; Lutterotti, L.; Manakova, E.; Butkus, J.; Moeck, P.; Le Bail, A. *J. Appl. Crystallogr.* **2009**, *42*, 726−729.
(74) Saw, C. K.; Beaudry, B. J.; Stassis, C. *Phys. Rev. B* **1983**, *27*, 7013−7017.
(75) Wyckoff, R. W. G. *Crystal Structures*, 2nd ed.; Interscience Publishers: New York, 1963; pp 7−83.
(76) Smura, C. F.; Parker, D. R.; Zbiri, M.; Johnson, M. R.; Gál, Z. A.; Clarke, S. J. *J. Am. Chem. Soc.* **2011**, *133*, 2691−2705.
(77) Bradley, A. J.; Thewlis, J. *Proc. R. Soc. London, Ser. A* **1927**, *115*, 456−471.
(78) Neale, J. W.; Walker, A. M.; Marshall, W. G.; Tucker, M. G.; Francis, D. J.; Stone, H. J.; McCammon, C. A. *J. Appl. Crystallogr.* **2008**, *41*, 886−896.
(79) Jørgensen, J.-E.; Smith, R. I. *Acta Crystallogr., Sect. B* **2006**, *62*, 987−992.
(80) Ling, C. D.; Avdeev, M.; Kharton, V. V.; Yaremchenko, A. A.; Macquart, R. B.; Hoelzel, M. *Chem. Mater.* **2010**, *22*, 532−540.
(81) Bernuy-Lopez, C.; Allix, M.; Bridges, C. A.; Claridge, J. B.; Rosseinsky, M. J. *Chem. Mater.* **2007**, *19*, 1035−1043.
(82) Kittel, C. *Introduction to Solid State Physics*, 8th ed.; John Wiley & Sons: New York, 2005; p 20.
(83) Moshopoulou, E. G.; Ibberson, R. M.; Sarrao, J. L.; Thompson, J. D.; Fisk, Z. *Acta Crystallogr., Sect. B* **2006**, *62*, 173−189.
(84) Ellner, M. *J. Less-Common Met.* **1981**, *78*, 21−32.
(85) Suh, I.-K.; Ohta, H.; Waseda, Y. *J. Mater. Sci.* **1988**, *23*, 757−760.
(86) Dubrovinsky, L. S.; Saxena, S. K. *Phys. Chem. Miner.* **1997**, *24*, 547−550.
(87) Koichi, S.; Taku, T.; Shigeaki, S. *Acta Crystallogr., Sect. B* **2003**, *59*, 701−708.
(88) Davey, W. P. *Phys. Rev.* **1925**, *25*, 753−761.

(89) Görling, A.; Trickey, S. B.; Gisdakis, P.; Rösch, N. In *Topics in Organometallic Chemistry*; Brown, J., Hofmann, P., Eds.; Springer: Heidelberg, Germany, 1999; Vol. *4*, pp 109−163.
(90) Young, D. A. *Phase Diagrams of the Elements*; University of California Press: Berkeley, CA, 1991; pp 273−381.
(91) de Boer, F. R.; Boom, R.; Mattens, W. C. M.; Miedama, A. R.; Niessen, A. K. *Cohesion in Metals*; North-Holland: Amsterdam, 1988.
(92) Tyson, W. R.; Miller, W. A. *Surf. Sci.* **1977**, *62*, 267−276.
(93) Fajin, J. L. C.; Illas, F.; Gomes, J. R. B. *J. Chem. Phys.* **2009**, *130*, 224702.
(94) Roldán, A.; Ricart, J. M.; Illas, F. *Theor. Chem. Acc.* **2009**, *123*, 119−126.
(95) Svane, A. *Phys. Rev. B* **1996**, *53*, 4275−4286.

Section 11.2

JCTC Journal of Chemical Theory and Computation

ACS Editors' Choice

Article

pubs.acs.org/JCTC

Terms of Use

Bulk Properties of Transition Metals: A Challenge for the Design of Universal Density Functionals

Patanachai Janthon,[†,‡,§] Sijie (Andy) Luo,[∥] Sergey M. Kozlov,[†] Francesc Viñes,[†] Jumras Limtrakul,[‡,§] Donald G. Truhlar,[∥] and Francesc Illas*[,†]

[†]Departament de Química Física & Institut de Química Teòrica i Computacional (IQTCUB), Universitat de Barcelona, c/Martí i Franquès 1, 08028, Barcelona, Spain

[‡]Department of Chemistry and NANOTEC Center for Nanoscale Materials Design for Green Nanotechnology, Kasetsart University, Bangkok 10900, Thailand

[§]PTT Group Frontier Research Center, PTT Public Company Limited, 555 Vibhavadi Rangsit Road, Chatuchak, Bangkok 10900, Thailand

[∥]Department of Chemistry, Chemical Theory Center, and Supercomputing Institute, University of Minnesota, Minneapolis, Minnesota 55455-0431, United States

Supporting Information

ABSTRACT: Systematic evaluation of the accuracy of exchange-correlation functionals is essential to guide scientists in their choice of an optimal method for a given problem when using density functional theory. In this work, accuracy of one Generalized Gradient Approximation (GGA) functional, three meta-GGA functionals, one Nonseparable Gradient Approximation (NGA) functional, one meta-NGA, and three hybrid GGA functionals was evaluated for calculations of the closest interatomic distances, cohesive energies, and bulk moduli of all 3d, 4d, and 5d bulk transition metals that have face centered cubic (fcc), hexagonal closed packed (hcp), or body centered cubic (bcc) structures (a total of 27 cases). Our results show that including the extra elements of kinetic energy density and Hartree−Fock exchange energy density into gradient approximation density functionals does not usually improve them. Nevertheless, the accuracies of the Tao−Perdew−Staroverov−Scuseria (TPSS) and M06-L meta-GGAs and the MN12-L meta-NGA approach the accuracy of the Perdew−Burke−Ernzerhof (PBE) GGA, so usage of these functionals may be advisable for systems containing both solid-state transition metals and molecular species. The N12 NGA functional is also shown to be almost as accurate as PBE for bulk transition metals, and thus it could be a good choice for studies of catalysis given its proven good performance for molecular species.

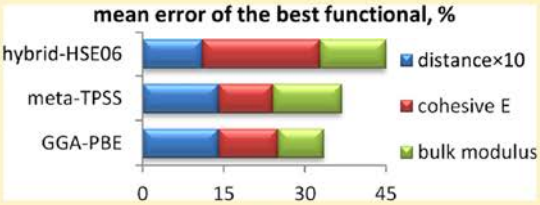

1. INTRODUCTION

Kohn−Sham Density Functional Theory (KS-DFT) has become a workhorse for treating complex problems in both the gaseous and condensed phases. The accuracy of KS-DFT rests entirely on the accuracy of one's approximation to the exchange-correlation (xc) functional. Functional development has considered a wide range of application targets. In particular, there are numerous validation studies for atoms and molecules, many more than for condensed-phase quantum chemistry and solid-state physics. A particularly important area that still needs further study in its own right, in addition to its importance for studying heterogeneous catalysis and electrochemistry,[1] is the accuracy of available xc functionals for transition metal solids.

One route to improving xc functionals is to add more elements, which takes one to a higher rung on the Jacob's ladder[2] of xc functionals. The first rung is the Local Spin Density Approximation (LSDA), where the xc functional depends on only local spin densities. Including dependences not only on spin densities but also on their gradients yields gradient approximations, such as the Generalized Gradient Approximation[3,4] (GGA) or Nonseparable Gradient Approximation[5] (NGA), which constitute the second rung; further addition of kinetic energy density leads to meta functionals, such as meta-GGAs and meta-NGAs, which form the third rung, and, finally, including Hartree−Fock (HF) exchange leads to hybrid functionals, in particular hybrid gradient approximations and hybrid meta approximations, which form the fourth rung. Through the third rung, the exchange-correlation energy density depends only on local variables, but hybrid functionals are nonlocal.

One tentative conclusion about xc functionals that has been advanced is that adding elements from the third and fourth rungs has not (with some exceptions) led to better performance for molecules containing metals,[6,7] and various studies have been carried out with gradient approximations that provide further experience related to this issue.[7−9] Furthermore, although hybrid functionals are justifiably the most popular

Received: June 20, 2014
Published: August 6, 2014

kind of functionals in molecular chemistry[10] (because of their good performance), for extended systems they have increased computational demands as compared to local functionals due to the long range of the exchange in real space programs and to the requirement for dense Brillouin zone sampling in plane wave programs.[11] Hybrid functionals also have the disadvantage of bringing in HF static correlation error, which is important for many molecular and solid-state transition metal compounds.[6−9,12,13] In fact, when one tries to estimate the optimal percentage of HF exchange in a hybrid functional suitable for transition metal solids, the resulting fraction is close to zero,[14,15] leading to the conclusion that the inclusion of HF exchange is detrimental for the accuracy of xc functionals for solid transition metals. The problems with Hartree−Fock exchange for metals are in fact well-known in that Hartree−Fock exchange for free electrons (which constitute the zeroth-order model of a metal) leads to an unphysical density of states such that there is a singularity in the electron group velocity at the Fermi level, although this defect is eliminated if the Hartree−Fock exchange is screened by correlation effects.[16]

As a result of the above kinds of issues with including Hartree−Fock exchange—cost, performance, and an incorrect treatment of the density of states—local functionals have remained the most popular choice for solid-state transition metal investigations even though hybrid functionals by construction reduce self-interaction error. A similar situation pertains even when the choice of xc functionals is restricted to local ones, where, although meta functional also has the potential to reduce self-interaction error,[17] gradient approximations have been preferred to meta functionals partly for the greater simplicity of popular GGAs, but also because meta functionals have not always seemed to significantly improve the accuracy. However, this situation seems unsatisfactory because both hybrid functionals and meta functionals have better performance than GGAs on molecules composed of atoms lighter than the transition metals.[18−21] Thus, there is a strong interest in certain fields, such as heterogeneous catalysis, nanotechnology, and materials chemistry, to use meta or hybrid functionals because these research lines often deal with the interaction between transition metal surfaces and light main-group compounds. Meta and hybrid functionals also yield more accurate band gaps,[15,22,25] which may be important for metal-oxide systems that are ubiquitous as supports in catalysis, photocatalysis, and nanotechnology. In light of these practical considerations, there is a need for a more systematic investigation of the accuracy of meta and hybrid functionals for various properties of transition metal solids.

In this article, we assess the accuracy of several meta and hybrid functionals for bulk transition metals. Namely, we consider shortest interatomic distances, δ, cohesive energies, E_{coh}, and bulk moduli, B_0, of all 27 bulk transition metals that have face centered cubic (fcc), hexagonal closed packed (hcp), or body centered cubic (bcc) structures. We present new results for the following functionals: GGA: SOGGA11;[26] NGA: N12;[5] meta-GGAs: Tao−Perdew−Staroverov−Scuseria (TPSS),[27] revised Tao−Perdew−Staroverov−Scuseria (revTPSS),[28] and meta M06-L;[29] meta-NGA: MN12-L;[30] hybrid gradient approximations with unscreened Hartree−Fock exchange: Perdew−Burke−Ernzerhof (PBE0),[31,32] and Lee−Yang−Parr B3LYP;[32] and hybrid gradient approximation with screened Hartree−Fock exchange: Heyd−Scuseria−Ernzerhof (HSE06).[33]

We compare the new results obtained here to the results obtained previously[34] with PBE, a GGA functional that performed best in a previous study of two LSDA functionals [the Perdew−Zunger functional (PZ81)[35] based on Ceperley−Alder (CA) numerical results[36] and the Vosko−Wilk−Nusair functional (VWN, usually denoted also as VWN5)][37] and four gradient approximations [PBE,[38] PBEsol,[39] RPBE,[40] and PW91[41]]. Note that the performance of the PW91 GGA was found to be close to that of PBE.

2. COMPUTATIONAL DETAILS

The computational procedures were kept as close as possible to those used in a previous work by Janthon et al.[34] Calculations were performed using a locally modified version of the Vienna Ab Initio Simulation Package (VASP).[42] The atomic cores were described by the Projector Augmented Wave (PAW) method,[43] using the potentials recommended in the documentation (see Table S1 in the Supporting Information for full specification) which take account of kinetic energy density dependencies when present. An optimized Monkhorst−Pack[44] **k**-points grid of 7 × 7 × 7 was used in all bulk calculations, which was found to be sufficient for accurate total energy calculations with the smallest unit cell. A kinetic energy cutoff of 415 eV for the plane-wave basis set was employed throughout, guaranteeing variations of total energy below 1 meV with respect to more complete basis sets.

Scalar relativistic effects in the core region are included in the PAW potentials. Previous calculations have shown that relativistic effects on the valence electrons of heavy transition metals lead to negligible deviations from this standard PAW approximation, i.e., interatomic distance changes in the 0.002−0.005 Å range and differences in bulk moduli of 3−5 GPa.[45]

The electronic structure calculations were not spin polarized, with the exception of the calculations on the ferromagnetic Fe, Ni, and Co bulk systems and on isolated metal atoms. Although it is a digression, we note in passing that some of the calculated magnetic moments agree nicely with experimental values. For instance, the PBE values of 2.21, 1.55, and 0.59 μ_B agree well with experimental values of 2.2, 1.7, and 0.6 μ_B for Fe, Co, and Ni, respectively.[46] Values predicted by TPSS are very close to the PBE ones with differences smaller than 0.02 μ_B, whereas HSE06 overestimates the magnetic moments with predicted values of 2.89, 1.85, and 0.82 μ_B for Fe, Co, and Ni, respectively. Note also that, even though a nearly degenerate antiferromagnetic solution for the bulk structure of Cr with a magnetic moment of of 0.92 μ_B has been reported from calculations at the PW91 level,[47] the present calculations for Cr correspond to a nonmagnetic solution.

Optimizations were performed using the tetrahedron smearing method of Blöchl et al.[48] with an energy width of 0.2 eV to speed up convergence with the final energies extrapolated to zero smearing. In bulk calculations, ionic positions and cell volumes were optimized using the conjugate gradient algorithm until pressures and total energies were converged within 0.01 GPa and 10 meV, respectively.

Calculated cohesive energies are sensitive to the treatment adopted for calculating the energies of the atoms. The isolated atoms were placed in a large unit cell with a broken symmetry of 9 × 10 × 11 Å dimensions to ensure proper occupancy of orbitals. When needed, orbital occupancy was imposed to match that of the isolated atom; further details concerning atomic configuration and energies are found in a previous article.[34] The large unit cell allows one to sufficiently suppress

Table 1. Calculated and Experimental Shortest Interatomic Distances (δ, in Å) for Bulk Transition Metals

		GGA		NGA	meta-GGA			meta-NGA	hybrid				
	CS	PBE	SOGGA11	N12	TPSS	revTPSS	M06-L	MN12-L	PBE0	HSE06	B3LYP	exptl.	exptl. corr.[a]
Sc	hcp	3.214	3.066	3.194	3.198	3.192	3.149	3.013	3.238	3.252	3.230	3.254	3.244
Ti	hcp	2.884	2.806	2.864	2.862	2.855	2.859	2.850	2.862	2.865	2.883	2.897	2.889
V	bcc	2.577	2.561	2.582	2.559	2.554	2.581	2.559	2.548	2.548	2.573	2.613	2.606
Cr	bcc	2.459	2.479	2.467	2.442	2.435	2.457	2.428	2.429	2.428	2.457	2.498	2.485
Fe	bcc	2.453	2.498	2.457	2.431	2.424	2.484	2.598	2.502	2.522	2.517	2.460	2.450
Co	hcp	2.470	2.496	2.438	2.444	2.438	2.472	2.489	2.452	2.482	2.498	2.497	2.488
Ni	fcc	2.489	2.506	2.455	2.453	2.443	2.419	2.370	2.471	2.480	2.510	2.493	2.484
Cu	fcc	2.567	2.502	2.551	2.517	2.499	2.476	2.485	2.563	2.564	2.606	2.556	2.544
Zn	hcp	2.644	2.558	2.658	2.522	2.465	2.490	2.552	2.638	2.640	2.781	2.665	2.645
Y	hcp	3.543	3.419	3.511	3.522	3.518	3.562	3.615	3.554	3.559	3.565	3.556	3.548
Zr	hcp	3.197	3.144	3.166	3.179	3.171	3.218	3.195	3.187	3.185	3.213	3.179	3.174
Nb	bcc	2.873	2.882	2.871	2.862	2.852	2.888	2.871	2.860	2.857	2.888	2.859	2.854
Mo	bcc	2.749	2.716	2.692	2.734	2.729	2.748	2.726	2.724	2.721	2.755	2.725	2.721
Tc	hcp	2.722	2.707	2.685	2.700	2.689	2.706	2.689	2.679	2.677	2.717	2.710	2.705
Ru	hcp	2.658	2.643	2.627	2.637	2.624	2.649	2.623	2.608	2.610	2.649	2.650	2.642
Rh	fcc	2.717	2.695	2.683	2.689	2.674	2.702	2.676	2.674	2.672	2.723	2.539	2.532
Pd	fcc	2.794	2.756	2.766	2.761	2.742	2.794	2.755	2.768	2.765	2.827	2.753	2.745
Ag	fcc	2.941	2.861	2.901	2.890	2.867	2.940	2.899	2.924	2.925	2.992	2.889	2.877
Cd	hcp	2.990	2.941	3.018	2.920	2.880	2.883	3.002	2.964	2.971	3.139	2.979	2.959
Hf	hcp	3.139	3.067	3.110	3.114	3.100	3.151	3.099	3.123	3.151	3.148	3.131	3.126
Ta	bcc	2.875	2.875	2.854	2.857	2.844	2.886	2.839	2.864	2.861	2.886	2.860	2.856
W	bcc	2.751	2.761	2.746	2.736	2.724	2.744	2.718	2.725	2.724	2.761	2.741	2.738
Re	hcp	2.755	2.756	2.723	2.742	2.730	2.742	2.724	2.721	2.720	2.759	2.567	2.562
Os	hcp	2.694	2.700	2.673	2.685	2.673	2.688	2.656	2.660	2.661	2.698	2.675	2.671
Ir	fcc	2.741	2.747	2.712	2.727	2.710	2.733	2.705	2.712	2.711	2.759	2.715	2.710
Pt	fcc	2.811	2.809	2.780	2.789	2.769	2.806	2.771	2.778	2.777	2.835	2.772	2.766
Au	fcc	2.950	2.921	2.912	2.912	2.888	2.945	2.913	2.922	2.919	2.992	2.879	2.870

[a]ZPE and finite temperature corrections to experimental values adapted from Lejaeghere et al.[52]

spurious interactions between periodic images (<1 meV). Calculations of isolated atoms were carried out at the Γ point in reciprocal space.

For the purpose of comparing calculations on bulk metals to calculations on metal dimers and clusters, it is more physical to consider shortest interatomic distances in a crystal than to consider lattice constants. For fcc and bcc structures, the shortest interatomic distances, δ, within a crystal cell may be calculated from the lattice parameter a. For the fcc structures δ equals $a/\sqrt{2}$, while for bcc it equals $\sqrt{3}a/2$. In the case of hcp, δ depends on lattice parameters a and c, and δ may equal a or $(c^2/4 + a^2/3)$ depending on the c/a ratio.

Cohesive energies, E_{coh}, were expressed as an energy difference per atom as follows:

$$E_{coh} = E_{at} - \frac{E_{bulk}}{N}$$

where E_{at} is the energy of the isolated metal atom in a vacuum and E_{bulk} is the energy of the bulk unit cell containing N atoms. With this definition, the larger the positive values of cohesive energies, the stronger is the chemical bonding within the solid.

The bulk modulus, B_0, is defined as

$$B_0 = -V_0\left(\frac{\partial P}{\partial V}\right)_{T,Vo}$$

where V is the volume of the solid, P is an external pressure, and the negative sign is used because the volume decreases when a positive external pressure is applied. Bulk modulus is obtained as the slope of linear regression of P versus V using the volumes at the equilibrium geometry and at geometries with ±0.05 and ±0.10 Å variations of the lattice constants. A more accurate procedure would be the adjustment of energy points to a Murnaghan equation of state.[49] Bulk moduli obtained at the PBE level with a similar calculation setup but through the adjustment to the Murnaghan equation are ~5 GPa lower than those calculated here.[11]

In the present work, we consider the 27 transition metals that exhibit close-packed structures, which may display fcc, hcp, or that exhibit a bcc structure. We specifically exclude La and solid Hg, which have hexagonal and rhombohedral unit cells, respectively, and Mn, which has a cubic unit cell containing 58 atoms, although it is similar to a bcc structure. The reason for these exclusions is that preliminary work showed that metals exhibiting these structures can exhibit different trends than the typical metals, and specialized consideration is required to do them justice.

In the following, as in the previous work,[34] in addition to cohesive energy and bulk modulus, the shortest interatomic distance within a crystal cell, δ, will be compared to the experimental values. We present results for individual metals, and to more clearly see some trends, we also present mean errors, in particular mean signed error (MSE), mean absolute error (MAE), and mean absolute percentage error (MAPE).

3. COMPARISON BETWEEN EXPERIMENTAL AND THEORETICAL RESULTS

To compare calculated results to the available experimental data in a reasonable fashion, we must take account of experimental variability and the differences between the measurements and

Table 2. Calculated and Experimental Cohesive Energies (E_{coh}, in eV/atom) of Bulk Transition Metals

		GGA		NGA	meta-GGA			meta-NGA	hybrid				
	CS	PBE	SOGGA11	N12	TPSS	revTPSS	M06-L	MN12-L	PBE0	HSE06	B3LYP	exptl.	exptl. corr.[a]
Sc	hcp	4.12	3.63	4.53	4.21	4.28	5.77	5.32	3.42	3.52	2.76	3.90	3.93
Ti	hcp	5.45	5.37	5.78	5.47	5.52	6.40	6.85	4.00	4.08	3.35	4.84	4.88
V	bcc	6.03	5.12	5.77	5.73	5.94	6.30	5.75	3.40	3.48	3.25	5.30	5.34
Cr	bcc	4.00	4.37	4.21	4.21	4.44	4.55	4.33	1.54	1.57	1.57	4.09	4.15
Fe	bcc	4.87	4.96	4.65	5.23	5.48	5.39	5.13	3.22	3.29	2.81	4.28	4.32
Co	hcp	5.27	4.28	5.32	6.21	6.51	5.66	4.54	3.24	3.31	2.86	4.43	4.47
Ni	fcc	4.87	4.11	4.96	5.40	5.24	5.75	6.15	3.19	3.26	2.85	4.44	4.48
Cu	fcc	3.48	3.32	3.36	3.73	4.06	4.39	4.42	3.01	3.06	2.54	3.48	3.51
Zn	hcp	1.12	0.86	1.14	1.34	1.59	1.67	1.58	1.12	1.17	0.44	1.35	1.38
Y	hcp	4.13	4.56	4.59	4.23	4.38	4.96	5.78	3.74	3.85	3.00	4.39	4.42
Zr	hcp	6.16	7.43	6.73	6.30	6.50	6.75	5.15	5.60	5.70	4.69	6.29	6.32
Nb	bcc	6.98	7.86	7.23	7.20	7.42	8.02	7.40	5.96	6.12	5.59	7.44	7.47
Mo	bcc	6.21	6.95	6.89	6.59	6.91	6.90	6.82	5.10	5.19	4.82	6.80	6.84
Tc	hcp	6.85	8.52	7.34	7.18	7.58	7.15	7.04	5.41	5.54	4.90	7.13	7.17
Ru	hcp	6.67	8.00	7.21	7.10	7.52	6.76	6.79	5.06	5.21	4.56	6.74	6.80
Rh	fcc	5.62	7.00	6.00	6.22	6.61	6.12	6.33	4.39	4.54	3.92	5.72	5.76
Pd	fcc	3.71	4.54	3.55	4.01	4.40	4.24	4.70	2.85	2.96	2.43	3.90	3.93
Ag	fcc	2.49	3.20	2.49	2.73	3.04	3.28	3.60	2.28	2.35	1.87	2.94	2.96
Cd	hcp	0.73	1.72	0.76	0.96	1.21	1.37	1.06	0.78	0.85	0.18	1.16	1.18
Hf	hcp	6.40	7.61	6.84	6.53	6.78	7.32	5.78	6.04	6.12	5.02	6.42	6.44
Ta	bcc	8.27	8.45	8.26	8.51	8.84	8.99	7.58	7.63	7.74	6.58	8.09	8.11
W	bcc	9.07	9.16	9.02	8.81	9.19	9.86	8.43	7.76	7.79	7.29	8.79	8.83
Re	hcp	7.82	7.97	7.89	8.25	8.68	7.97	9.45	6.75	6.85	5.89	8.02	8.06
Os	hcp	8.29	8.72	7.84	8.46	8.80	8.32	9.46	7.20	7.34	6.24	8.17	8.22
Ir	fcc	7.32	8.31	7.74	7.71	8.21	7.03	7.35	6.19	6.36	5.28	6.92	6.96
Pt	fcc	5.50	6.58	5.71	5.79	6.25	5.97	6.17	4.69	4.83	3.99	5.85	5.87
Au	fcc	2.99	3.86	3.03	3.28	3.62	3.61	3.79	2.80	2.88	2.23	3.81	3.83

[a]ZPE and finite temperature corrections to experimental values adapted from Lejaeghere et al.[52]

the calculations. First of all, significant differences can be found between experimental values reported for cohesive energies and bulk moduli in different sources, and on average, different entries in the Crystallographic Open Database[50] yield the shortest interatomic distances with variations of ~0.05 Å. Among many entries in the database, we selected the most recent ones, as was done previously.[34] For cohesive energies and bulk moduli, we picked experimental values from the handbook by Young.[51] However, in a recent study by Lejaeghere et al.[52] assessing the performance of the PBE functional for almost all elemental solids in the periodic table, alternative sets of experimental values are used, mostly from Kittel or Villars and Daams.[53,54] See Tables S2–S4 in the Supporting Information for more details. With some exceptions, the experimental values used in the present work compare nicely to the values used in Lejaeghere et al., with median discrepancies for δ, E_{coh}, and B_0 being 0.004 Å, 0.06 eV, and 5 GPa, respectively. If we used the same set of experimental values as in ref 52, the reported MAPE would change by less than 0.5% for δ, 0.25% for E_{coh}, and 2% for B_0, and such changes have a negligible effect on our conclusions.

The second type of complication comes from the fact that experiments are typically performed at room temperature, whereas the calculations reported here reflect the internal energies at minima of potential energy surfaces. Results measured at room temperature differ from the calculated values mainly by inclusion of zero-point phonon energy and thermal phonon energy. Rather than account for these effects in each computation, reverse corrections are applied to the experimental values. Here, we apply the same corrections as in Lejaeghere et al.,[52] which decrease δ by 0.003–0.022 Å, increase E_{coh} by 0.01–0.06 eV, and increase B_0 by 1–17 GPa. In general, these corrections move experimental values closer to calculated ones, typically decreasing average MAPEs by 0.04%, 0.2%, and 2% for δ, E_{coh}, and B_0, respectively. For a clearer comparison with other studies, we list both corrected and uncorrected experimental values, but only corrected ones were used to calculate errors and draw conclusions.

4. RESULTS AND DISCUSSION

4.1. Interatomic Distances. In most of the cases studied here, the accuracy of KS-DFT for lattice constants is rather high. Table 1 shows ~1% discrepancies between the calculated and the experimental data. One can compare the present results with previous computational studies carried out for a reduced set of metals. For instance, the present PBE results nicely correlate with previous calculations on Cu, Rh, Pd, and Ag fcc metals, with deviations below 0.01 Å.[11] Another suitable comparison with a previous study with over a dozen fcc and bcc transition metals revealed lattice parameter deviations of ~0.03 Å for the PBE functional and below 0.02 Å for the TPSS functional,[55] corroborating the precision of the present calculations. Surprisingly, the most accurate xc functionals for interatomic distances are HSE06 and PBE0, which both slightly overestimate δ on average. Nevertheless, with the exception of HSE06 for Sc, all considered functionals underestimate interatomic distances of the lightest transition metals, Sc, Ti, V, and Cr. The present calculations reveal a nice match of HSE06 for Cr interatomic distances, whereas—for reasons that we do not understand—a previous study showed a considerable

Table 3. Calculated and Experimental Bulk Moduli (B_0, in GPa) of Bulk Transition Metals[a]

		GGA	meta-GGA			meta-NGA	hybrid				
	CS	PBE	TPSS	revTPSS	M06-L	MN12-L	PBE0	HSE06	B3LYP	exptl.	exptl. corr.[a]
Sc	hcp	55.0	59.4	57.9	71.6	82.5	57.2	56.2	51.4	54.6	55.6
Ti	hcp	113.5	119.1	122.6	129.4	125.4	132.4	125.2	120.0	106.0	108.3
V	bcc	183.1	198.9	212.0	193.3	199.1	225.9	214.9	199.1	155.0	158.9
Cr	bcc	261.2	274.4	293.3	268.6	298.4	290.7	291.8	271.8	160.0	174.5
Fe	bcc	195.3	218.5	232.8	169.8	77.2	165.1	176.7	151.1	163.0	169.8
Co	hcp	212.5	236.3	244.2	236.4	172.7	222.4	203.5	204.1	186.0	193.0
Ni	fcc	193.9	226.4	239.6	262.9	323.2	226.3	216.4	169.4	179.0	185.5
Cu	fcc	146.9	184.3	198.7	183.4	181.5	135.2	133.8	113.4	133.0	140.3
Zn	hcp	78.4	106.4	124.9	109.2	92.0	88.0	76.5	62.8	64.8	69.7
Y	hcp	40.7	44.4	42.1	47.0	34.5	39.9	41.5	42.5	41.0	41.7
Zr	hcp	95.5	98.3	98.7	96.9	96.3	88.0	99.0	94.4	94.9	95.9
Nb	bcc	171.1	178.9	190.6	170.4	179.2	190.6	183.7	176.7	169.0	172.0
Mo	bcc	261.3	278.2	285.3	262.9	286.8	288.4	295.7	262.8	261.0	264.7
Tc	hcp	307.6	324.1	336.5	307.2	333.3	357.2	355.4	310.2	297.0	303.1
Ru	hcp	308.2	334.8	347.6	312.5	349.5	366.3	361.9	314.1	303.0	317.7
Rh	fcc	256.4	282.8	298.5	258.8	287.6	294.0	284.7	241.2	282.0	288.7
Pd	fcc	169.4	192.1	207.9	153.3	181.4	176.0	163.3	138.8	189.0	195.4
Ag	fcc	83.3	110.2	120.9	93.6	98.3	89.9	83.6	71.2	98.8	103.8
Cd	hcp	49.6	61.1	68.0	64.1	37.9	58.1	55.3	38.9	49.8	53.8
Hf	hcp	108	112.6	115.4	116.2	114.8	112.3	115.7	111.7	108.0	109.7
Ta	bcc	195.3	205.9	212.6	201.2	210.5	217.4	205.8	193.3	191.0	193.7
W	bcc	316.2	329.8	335.7	320.1	348.2	347.0	356.4	315.9	308.0	312.3
Re	hcp	372.1	393.1	407.1	402.2	396.7	428.7	424.8	376.9	360.0	368.8
Os	hcp	402.6	426.4	449.9	427.7	482.4	460.9	460.9	396.9	418.0	424.6
Ir	fcc	347.3	367.0	391.8	339.6	396.9	397.1	392.8	328.1	358.0	365.2
Pt	fcc	250.9	272.6	290.2	250.7	273.9	278.1	275.6	225.4	277.0	284.2
Au	fcc	138.4	162.7	174.9	140.3	143.4	141.2	146.6	112.0	166.0	174.8

[a]ZPE and finite temperature corrections to experimental values adapted from Lejaeghere et al.[52]

overestimation (23%) by this functional for bulk Cr.[56] Moreover, interatomic distances of magnetic Fe, Co, and Ni are nicely described by hybrid functionals. Calculated and experimental lattice parameters are given in Table S8 of the Supporting Information.

The accuracy of all meta functionals is noticeably lower for the δ of Zn, Cd, and Re. The least accurate results, among the eight functionals considered here, are obtained by the SOGGA11 and B3LYP functionals. Upon a careful inspection of the present values and previous data,[34] one could conclude that B3LYP is even less accurate than LSDA functionals for structural data of bulk transition metals. Finally, despite satisfactory overall performance, MN12-L yields poor results for Sc and Fe.

The performance of revTPSS is not superior to that of TPSS. The reason may be that revTPSS is based on PBEsol, which was parametrized to predict better lattice constants of solid state materials, while TPSS is based on the more versatile PBE. However, for solid transition metals the performance of PBEsol is worse than that of PBE (even for interatomic distances),[34] and so is the performance of revTPSS compared to the accuracy of TPSS. In fact, revTPSS tends to be more accurate than TPSS only for heavy and late transition metals, i.e. from Zr to Cd (except Tc and Ru) and from Re to Au.

The table does show some correlation between the accuracy of the functional and the type of crystal structure. For example, M06-L and the hybrid functionals are somewhat less accurate for fcc metals with absolute errors 0.01−0.02 Å higher than average; see Tables S5−S7 in the Supporting Information for more details. At the same time, PBE0 and HSE06 are more accurate for hcp metals (MAE of only 0.014 to 0.016 Å, respectively), while M06-L, TPSS, revTPSS, and B3LYP are more accurate for bcc metals with absolute errors lower by 0.016−0.025 Å than average.

4.2. Cohesive Energies. Cohesive energies are generally harder than interatomic distances to predict correctly,[21] and Table 2 shows that many functionals are systematically biased toward overestimation or underestimation of the energies. For example, in most of the cases, the hybrid functionals considered here strongly underestimate E_{coh} by ∼1 to 1.7 eV, which renders them the least accurate functionals for this quantity (B3LYP is even less accurate than LSDA). The most accurate results come from PBE, TPSS, and N12 (MAEs of ∼0.35 eV), followed by revTPSS and SOGGA11 (MAEs of 0.52 eV).

As for interatomic distances, there are certain materials for which all meta functionals show lower accuracy. Cohesive energies of Ni, Co, and Fe are overestimated by 0.75−2 eV (except MN12-L for Co). M06-L and MN12-L also overestimate E_{coh} of Cu, Sc, and Ti. The correlation between the functional accuracy and the crystal structure is rather weak in this case, but we find that MN12-L is quite accurate for bcc metals (MAE of 0.35 eV), while PBE0 and HSE06 are particularly bad for them (MSE of ∼−1.4 eV).

4.3. Bulk Moduli. Bulk moduli are also quite hard to calculate correctly, and almost all the considered meta and hybrid functionals (except B3LYP) overestimate them, as shown in Table 3. The most accurate results are produced by PBE, followed by TPSS, while the least accurate functionals for this property are MN12-L and revTPSS.

Table 4. Statistical Analysis of Differences between the Experimental Results Extrapolated to 0 K and Corrected for Zero-Point Vibrations and the Calculated Values: Interatomic Distances (δ, in Å), Cohesive Energies (E_{coh}, in eV/atom), and Bulk Moduli (B_0, in GPa)[a]

		GGA		NGA	meta-GGA			meta-NGA	hybrid		
		PBE	SOGGA11	N12	TPSS	revTPSS	M06-L	MN12-L	PBE0	HSE06	B3LYP
δ	MSE	0.03	0.00	−0.02	0.00	−0.01	0.01	0.00	0.01	0.01	0.05
	MAE	0.04	0.05	0.05	0.04	0.04	0.05	0.05	0.03	0.03	0.06
	MAPE	1.4	1.9	1.8	1.4	1.5	1.9	2.0	1.2	1.1	2.2
	rank	3	7	6	3	5	7	9	2	**1**	10
E_{coh}	MSE	−0.04	0.40	0.12	0.21	0.50	0.46	0.40	−1.08	−0.99	−1.66
	MAE	0.34	0.52	0.36	0.35	0.52	0.49	0.64	1.08	0.99	1.66
	MAPE	10.9	11.4	8.6	10.0	11.2	10.6	13.7	24.0	21.7	37.7
	rank	4	6	**1**	2	5	3	7	9	8	10
B_0	MSE	−0.4			17.5	28.7	9.8	17.7	20.3	17.5	−8.6
	MAE	15.1			20.0	28.7	23.4	32.4	27.2	24.9	22.4
	MAPE	8.4			12.7	17.6	15.4	19.6	14.2	12.2	12.9
	rank	**1**			3	7	6	8	5	2	4
average rank	2.7	6.5	3.5	2.7	5.7	5.3	8.0	5.3	3.7	8.0	

[a]MAPE values are given in percent.

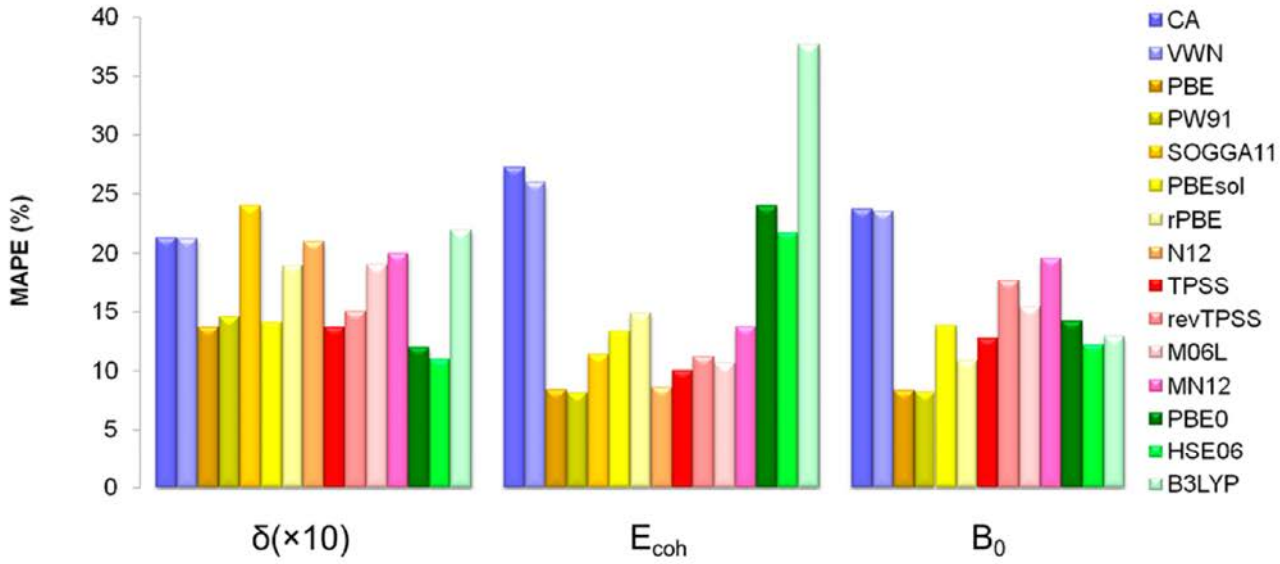

Figure 1. Mean Absolute Percentage Errors (MAPE) for the interatomic distances, δ; cohesive energies, E_{coh}; and bulk moduli, B_0, of 27 transition metals with respect to experimental values extrapolated to 0 K and adjusted to remove zero-point vibrational contributions. MAPE of δ has been multiplied by a factor of 10 for a better presentation. Data for LDA xc functionals, PBE, PW91, PBEsol, and RPBE are adapted from Janthon et al.[34]

All considered functionals significantly overestimate the bulk moduli of V, Ni, Re, and especially Cr (except B3LYP for Ni). Also, all meta functionals show lower accuracy for B_0 of Cu and Zn. The PBE and HSE06 hybrid functionals, in general, have an accuracy similar to that of meta functionals, but their performance is less satisfactory for Tc, Ru, and heavy transition metals from W to Ir.

Bulk moduli exhibit a strong correlation of functional accuracy with the crystal structure. For example, MN12-L, TPSS, revTPSS, PBE0, and HSE06 suffer a 60−70% increase in MAPE for the metals with bcc crystal structure. M06-L and B3LYP have lower accuracy for fcc metals (by 60 and 90%, respectively) but are somewhat more accurate for hcp metals (by 40 and 65%, respectively). Finally, PBE0 is 35% more accurate for B_0 of fcc metals, while HSE06 is 30% better for transition metals with hcp structure.

4.4. Overall Performance. Average discrepancies between theoretical and corrected experimental values are listed in Table 4 (for comparison with uncorrected experimental values, see Tables S2−S4, and for particular metals and properties, see Figure S1 and Tables S5−S7 in the Supporting Information). For the sake of better presentation, MAPE values are also displayed in Figure 1.

Table 4 shows the best performance is obtained for the PBE gradient approximation and for the TPSS meta functional, with HSE06, N12, M06-L, and PBE0 performing moderately well and revTPSS, B3LYP, SOGGA11, and MN12-L performing least well. TPSS is slightly more accurate than PBE for cohesive energies, while it tends to significantly overestimate bulk moduli. Both PBE and TPSS MAPE values are in line with previous calculations with a restricted set of transition metals.[55] As expected, TPSS corrects the tendency of PBE to overestimate interatomic distances by eliminating the diverging

exchange potential at the nuclei.[21] The use of TPSS may be favorable when molecular systems are also to be considered in the same study.[21] Nevertheless, when one is only interested in the accurate prediction of lattice parameters, hybrid functionals such as PBE0 or HSE06 may be preferred. However, HSE06 always shows a performance slightly better than that of PBE0, which may reflect the higher suitability of Hartree−Fock exchange restricted only to short range for the treatment of solid-state systems, although it may also result from cancellation of errors.

On the other hand, if one is mainly interested in accurate energetics, then the N12 gradient approximation is a good choice, especially when one considers its good performance for both cohesive energies and molecular species. The poor performance of the hybrid functionals considered here for the cohesive energies of bulk transition metals may be related to a poorer description of the gas-phase atoms used as energy references.[11] However, this does not explain the mediocre accuracy of the bulk moduli calculations with PBE0, HSE06, and B3LYP.

Although no solid-state data were used in designing M06-L, whereas solid-state data were used for designing MN12-L, it is interesting that M06-L shows better performance in the present tests. We note in passing that M06-L was found to properly describe the difficult case of CO adsorption on Pt(111), which strengthens its usefulness even in complex systems.[57] B3LYP turns out to be the least accurate hybrid functional of those studied here for transition metal solids. In most of the cases, it overestimates interatomic distances and underestimates cohesive energies, being even less accurate than LSDA. Earlier, this poor performance was explained by the LYP correlation functional not satisfying the homogeneous electron gas limit and by the inappropriateness of unscreened HF exchange for metals.[58,59]

5. CONCLUSIONS

The accuracy of selected meta and hybrid functionals for solid transition metals has been assessed by comparing calculated interatomic distances, cohesive energies, and bulk moduli to experimental values. We assess the accuracy based on the set of 27 bulk transition metals having fcc, hcp, or bcc structures. For proper comparison, the measured values were corrected for finite temperature and zero-point vibrations as in Lejaeghere et al.[52] The obtained results are also compared to those from a previous study by Janthon et al.,[34] where the performance of LSDA and GGA functionals was assessed in a very similar manner.

Table 5 presents average discrepancies between theory and experiment averaged over members of a given functional type: Gradient Approximations (GA), meta functionals, and hybrid functionals. The present results show that meta and hybrid functionals present, on average, no improvement in accuracy over gradient approximation functionals for transition metal solids. TPSS is found to be the most accurate among meta exchange-correlation functionals, but even it essentially matches the accuracy of PBE for interatomic distances and cohesive energies, while being somewhat less accurate for bulk moduli. M06-L was found to be moderately accurate as well. Given that N12, TPSS, M06-L, and MN12-L functionals are more accurate for molecular systems than PBE, one could foresee their successful application to processes involving both solid state metals and molecular species, e.g. those in surface science, heterogeneous catalysis, etc. Hybrid functionals (except B3LYP, maybe due to the uniform gas limit violation[58]) were found to be the most accurate methods for calculations of interatomic distances in bulk transition metals. However, the performance of all the hybrid functionals considered here for cohesive energies is disappointing, and their accuracy for the bulk moduli is just moderate, as expected from the known problem of HF exchange static correlation error, which is critical for the description of transition metals.

Table 5. Statistical Analysis of Differences between the Experimental Results As in Table 4 but Grouping Functionals by Type

		GA[a]	meta[b]	hybrid[c]
δ (Å)	MSE	0.00	0.00	0.03
	MAE	0.05	0.05	0.04
	MAPE	1.7	1.7	1.5
E_{coh} (eV/atom)	MSE	0.16	0.39	−1.24
	MAE	0.42	0.50	1.24
	MAPE	10.3	11.4	27.8
B_0 (GPa)	MSE	−0.4	18.4	9.7
	MAE	15.1	26.1	24.8
	MAPE	8.4	16.3	13.1

[a]Averaged over PBE, N12, and SOGGA11. [b]Averaged over TPSS, revTPSS, M06-L, and MN12-L. [c]Averaged over PBE0, HSE06, and B3LYP.

■ ASSOCIATED CONTENT

Supporting Information

Table S1 provides details of the pseudopotentials used in the calculations. Tables S2−S4 display experimental lists of interatomic distances, cohesive energies, and bulk moduli (un)corrected for ZPE and finite-temperature values, as well as differences from the two sources. Tables S5−S7 are analogous to Table 4 but considering only fcc, bcc, or hcp metals. Table S8 is analogous to Table 1 but displaying lattice constants. Figure S1 sketches the most accurate functional(s) from those studied in the description of interatomic distances, cohesive energies, and bulk moduli across the transition metals. This material is available free of charge via the Internet at http://pubs.acs.org.

■ AUTHOR INFORMATION

Corresponding Author

*E-mail: francesc.illas@ub.edu.

Notes

The authors declare no competing financial interest.

■ ACKNOWLEDGMENTS

This work was supported by Spanish *Ministerio* grants (FIS2008-02238, CTQ2012-30751) and *Generalitat de Catalunya* grants (2014SGR97 and XRQTC) and, in part, by grants from the National Science and Technology Development Agency (NSTDA Chair Professor and NANOTEC Center for the Design of Nanoscale Materials for Green Nanotechnology), the Kasetsart University Research and Development Institute (KURDI), and the Commission on Higher Education, Ministry of Education ("the National Research University Project of Thailand (NRU)" and "Postgraduate Education and Research Programs in Petroleum and Petrochemicals and Advanced Materials"). P.J. would like to thank the Office of the Higher Education Commission, Thailand for supporting him with a grant under the program Strategic Scholarships for Frontier

Research Network for the Ph.D. Program Thai Doctoral degree and the Graduate School of Kasetsart University for his research. S.M.K. thanks the *Spanish Ministerio de Educacion* for a predoctoral grant AP2009-3379. F.V. thanks the Spanish MICINN for the postdoctoral grants under the programs *Juan de la Cierva* and *Ramón y Cajal* (JCI-2010-06372 and RYC-2012-10129), and F.I. acknowledges additional support through the ICREA Academia award for excellence in research. This work was also supported in part by the Air Force Office of Scientific Research under grant number FA9550-11-1-0078.

■ REFERENCES

(1) Cramer, C. J.; Truhlar, D. G. *Phys. Chem. Chem. Phys.* **2009**, *11*, 10757.
(2) Perdew, J. P.; Schmidt, K. *AIP Conf. Proc.* **2001**, *577*, 1.
(3) Langreth, D. D.; Mehl, M. J. *Phys. Rev. B* **1983**, *28*, 1809.
(4) Perdew, J. P.; Wang, Y. *Phys. Rev. B* **1986**, *33*, 8800.
(5) Peverati, R.; Truhlar, D. G. *J. Chem. Theory Comput.* **2012**, *8*, 2310.
(6) Schultz, N. E.; Zhao, Y.; Truhlar, D. G. *J. Chem. Phys.* **2006**, *124*, 224105.
(7) Schultz, N. E.; Zhao, Y.; Truhlar, D. G. *J. Phys. Chem. A* **2005**, *109*, 11127.
(8) Harvey, J. N. *Annu. Rep. Prog. Chem., Sect. C* **2006**, *102*, 203.
(9) Schultz, N. E.; Zhao, Y.; Truhlar, D. G. *J. Phys. Chem. A* **2005**, *109*, 4388.
(10) Sousa, S. F.; Fernandes, P. A.; Ramos, M. J. *J. Phys. Chem. A* **2007**, *111*, 10439.
(11) Paier, J.; Marsman, M.; Hummer, K.; Kresse, G.; Gerber, I. C.; Ángyán, J. G. *J. Chem. Phys.* **2006**, *124*, 154709.
(12) (a) Polo, V.; Kraka, E.; Cremer, D. *Mol. Phys.* **2002**, *100*, 1771. (b) Grafenstein, J.; Kraka, E.; Cremer, D. *Phys. Chem. Chem. Phys.* **2004**, *6*, 1096. (c) Ellis, J. K.; Martin, R. L. *J. Chem. Theory Comput.* **2013**, *9*, 2857.
(13) (a) Jiang, W.; DeYonker, N. J.; Determann, J. J.; Wilson, A. K. *J. Phys. Chem. A* **2011**, *116*, 870. (b) Zhang, W.; Truhlar, D. G.; Tang, M. J. *J. Chem. Theory Comput.* **2013**, *9*, 3965.
(14) Perdew, J. P.; Ernzerhof, M.; Burke, K. *J. Chem. Phys.* **1996**, *105*, 9982.
(15) Marques, M. A. L.; Vidal, J.; Oliveira, M. J. T.; Reining, L.; Botti, S. *Phys. Rev. B* **2011**, *83*, 035119.
(16) Ashcroft, N. W.; Mermin, N. D. *Solid State Physics*; Saunders College Publishing: Orlando, FL, 1976; p 335.
(17) Becke, A. D. *J. Chem. Phys.* **1998**, *109*, 2092.
(18) Staroverov, V. N.; Scuseria, G. E.; Tao, J.; Perdew, J. P. *J. Chem. Phys.* **2003**, *119*, 12129.
(19) Mardirossian, N.; Parkhill, J. A.; Head-Gordon, M. *Phys. Chem. Chem. Phys.* **2011**, *13*, 19325.
(20) Peverati, R.; Truhlar, D. G. *Phys. Chem. Chem. Phys.* **2012**, *14*, 16187.
(21) Peverati, R.; Truhlar, D. G. *Philos. Trans. R. Soc., A* **2014**, *372*, 20120476.
(22) Muscat, J.; Wander, A.; Harrison, N. M. *Chem. Phys. Lett.* **2001**, *342*, 397.
(23) Tomiæ, S.; Montanari, B.; Harrison, N. M. *Phys. E* **2008**, *40*, 2125.
(24) Zhao, Y.; Truhlar, D. G. *J. Chem. Phys.* **2009**, *130*, 074103.
(25) Peverati, R.; Truhlar, D. G. *J. Chem. Phys.* **2012**, *136*, 134704.
(26) Peverati, R.; Zhao, Y.; Truhlar, D. G. *J. Phys. Chem. Lett.* **2011**, *2*, 1991.
(27) Tao, J.; Perdew, J. P.; Staroverov, V. N.; Scuseria, G. E. *Phys. Rev. Lett.* **2003**, *91*, 146401.
(28) Perdew, J. P.; Ruzsinszky, A.; Csonka, G. I.; Constantin, L. A.; Sun, J. *Phys. Rev. Lett.* **2009**, *103*, 026403.
(29) Zhao, Y.; Truhlar, D. G. *J. Chem. Phys.* **2006**, *125*, 194101.
(30) Peverati, R.; Truhlar, D. G. *Phys. Chem. Chem. Phys.* **2012**, *14*, 13171.
(31) Adamo, C.; Barone, V. *J. Chem. Phys.* **1999**, *110*, 6158.
(32) Becke, A. D. *J. Chem. Phys.* **1993**, *98*, 5648.
(33) Krukau, A. V.; Vydrov, O. A.; Izmaylov, A. F.; Scuseria, G. E. *J. Chem. Phys.* **2006**, *125*, 224106.
(34) Janthon, P.; Kozlov, S. M.; Viñes, F.; Limtrakul, J.; Illas, F. *J. Chem. Theory Comput.* **2013**, *9*, 1631.
(35) Perdew, J. P.; Zunger, A. *Phys. Rev. B* **1981**, *23*, 5048.
(36) Ceperley, D. M.; Alder, B. J. *Phys. Rev. Lett.* **1980**, *45*, 566.
(37) Vosko, S. H.; Wilk, L.; Nusair, M. *Can. J. Phys.* **1980**, *58*, 1200.
(38) Perdew, J. P.; Burke, K.; Ernzerhof, M. *Phys. Rev. Lett.* **1996**, *77*, 3865.
(39) Perdew, J. P.; Ruzsinszky, A.; Csonka, G. I.; Vydrov, O. A.; Scuseria, G. E.; Constantin, L. A.; Zhou, X.; Burke, K. *Phys. Rev. Lett.* **2008**, *100*, 136406.
(40) Hammer, B.; Hansen, L. B.; Nørskov, J. K. *Phys. Rev. B* **1999**, *59*, 7413.
(41) Perdew, J. P.; Wang, Y. *Phys. Rev. B* **1992**, *45*, 13244.
(42) Kresse, G.; Furthmüller, J. *Phys. Rev. B* **1996**, *54*, 11169.
(43) Blöchl, P. E. *Phys. Rev. B* **1994**, *50*, 17953.
(44) Monkhorst, H. J.; Pack, J. D. *Phys. Rev. B* **1976**, *13*, 5188.
(45) Grabowski, B.; Hickel, T.; Neugebauer, J. *Phys. Rev. B* **2007**, *76*, 024309.
(46) Billas, I. M. L.; Châtelain, A.; de Heer, W. A. *Science* **1994**, *265*, 1682.
(47) Hafner, R.; Spišák, D.; Lorenz, R.; Hafner, J. *Phys. Rev. B* **2002**, *65*, 184432.
(48) Blöchl, P. E.; Jepsen, O.; Andersen, O. K. *Phys. Rev. B* **1994**, *49*, 16223.
(49) Murnaghan, F. D. *Proc. Natl. Acad. Sci. U. S. A.* **1944**, *30*, 244.
(50) Gražulis, S.; Chateigner, D.; Downs, R. T.; Yokochi, A. T.; Quiros, M.; Lutterotti, L.; Manakova, E.; Butkus, J.; Moeck, P.; Le Bail, A. J. *Appl. Crystallogr.* **2009**, *42*, 726.
(51) Young, D. A. *Phase Diagrams of the Elements*; University of California Press: Berkeley, CA, 1991; p 273.
(52) Lejaeghere, K.; Van Speybroeck, V.; Van Oost, G.; Cottenier, S. *Crit. Rev. Solid State Mater. Sci.* **2014**, *39*, 1.
(53) Kittel, C. *Introduction to Solid State Physics*, 8th ed.; John Wiley & Sons, Inc.: New York, 2005; p 20.
(54) Villars, P.; Daams, J. *J. Alloys Compd.* **1993**, *197*, 177.
(55) Haas, P.; Tran, F.; Blaha, P. *Phys. Rev. B* **2009**, *79*, 085104.
(56) Chevrier, V. L.; Ong, S. P.; Armiento, R.; Chan, M. K. Y.; Ceder, G. *Phys. Rev. B* **2010**, *82*, 075122.
(57) Luo, S.; Zhao, Y.; Truhlar, D. G. *J. Phys. Chem. Lett.* **2012**, *3*, 2975.
(58) Kurth, S.; Perdew, J. P.; Blaha, P. *Int. J. Quantum Chem.* **1999**, *75*, 889.
(59) Paier, J.; Marsman, M.; Kresse, G. *J. Chem. Phys.* **2007**, *127*, 024103.

Section 11.3

Theoretical assessment of graphene-metal contacts

Patanachai Janthon,[1,2,3,4] Francesc Viñes,[1,a)] Sergey M. Kozlov,[1] Jumras Limtrakul,[2,3,4] and Francesc Illas[1]

[1]*Departament de Química Física and Institut de Química Teòrica i Computacional (IQTCUB), Universitat de Barcelona, c/ Martí i Franquès 1, 08028 Barcelona, Spain*
[2]*Department of Chemistry and Center of Nanotechnology, Kasetsart University, Bangkok 10900, Thailand*
[3]*Center for Advanced Studies in Nanotechnology and Its Applications in Chemical, Food and Agricultural Industries, Kasetsart University, Bangkok 10900, Thailand*
[4]*PTT Group Frontier Research Center, PTT Public Company Limited, 555 Vibhavadi Rangsit Road, Chatuchak, Bangkok 10900, Thailand*

(Received 27 March 2013; accepted 13 May 2013; published online 24 June 2013)

Graphene-metal contacts have emerged as systems of paramount importance in the synthesis of high-quality and large-size patches of graphene and as vital components of nanotechnological devices. Herein, we study the accuracy of several density functional theory methods using van der Waals functionals or dispersive forces corrections when describing the attachment of graphene on Ni(111). Two different experimentally observed chemisorption states, top-fcc and bridge-top, were put under examination, together with the hcp-fcc physisorption state. Calculated geometric, energetic, and electronic properties were compared to experimental data. From the calculations, one finds that (i) predictions made by different methodologies differ significantly and (ii) optB86b-vdW functional and Grimme dispersion correction seem to provide the best balanced description of stability of physisorption and chemisorption states, the attachment strength of the latter on Ni(111) surface, the graphene-Ni(111) separation, and the bandstructure of chemisorbed graphene. The collation suggests that accurate and affordable theoretical studies on technologies based on graphene-metal contacts are already at hand. © *2013 AIP Publishing LLC*. [http://dx.doi.org/10.1063/1.4807855]

I. INTRODUCTION

Since its discovery in 2004,[1] graphene — a 2D carbon network displaying sp^2 hybridization — has become the hub for a variety of future electronic technologies, mostly due to its amazing electronic, magnetic, and mechanical properties.[1–3] The posed applications range from standard electronics,[4] to biosensors,[4] energy devices (Li-ion batteries, supercapacitors, etc.),[4,5] transparent electrodes,[4,6] and spintronic devices.[7] The interaction of graphene with given substrates has become of utmost importance in the recent years basically due to its role during graphene synthesis or in graphene-based devices. This has spurred atomic scale research on the interaction of graphene sheets with silicon carbide,[8] silicon oxide,[9] and late transition metal surfaces.[10]

As far as metal surfaces are concerned, the growth of graphene thereon has become a major approach for producing high-quality and large-area patches used afterwards for material production,[11] electronic measurements,[12] and device fabrication.[13] Newly developed graphene synthesis techniques such as Chemical Vapor Deposition (CVD),[10,11,14] bulk-dissolved carbon segregation on Ni,[15] and epitaxial growth on SiC[16] allow nowadays gaining high-quality graphene sheets up to a few cm in size, compatible with chip fabrication processes.[17] Very recently, CVD and epitaxial growth techniques have been adapted to effectively *n*-dope graphene, thus incrementing the charge carrier concentration, e.g., by using N-containing precursors in CVD,[18] or by exposing/bombarding the graphene layer with N_2 during/after the graphene formation.[19,20]

Aside from the synthetic aspects, late transition metal surfaces can be divided into two distinct groups according to their specific role on the graphene electronic and conductivity properties, which are correlated to the graphene attachment strength. On the one hand, graphene weakly interacts with Ir, Pt, Au, or Cu metal surfaces,[21–24] and, in these cases, the points of contact between valence and conduction bands, also known as Dirac cones, remain intact. This bonding mechanism is commonly referred to the physisorption state of graphene, where binding is essentially driven by dispersive interactions.[25,26] On the other hand, the interaction of graphene with some metals such as Ni, Ru, Co, and Pd is sensibly stronger,[14,27–29] resulting in a strong hybridization between metal *d*- and graphene π-bands, which eventually tears apart the graphene Dirac cones.[14,25] This is frequently referred as the chemisorbed state of graphene.[25,26,30] A recent detailed Density Functional Theory (DFT) study on graphene/Ni(111) interface discriminated between electronic and van der Waals (vdW) contributions to the attachment energy, by simply subtracting the dispersion term from total energy obtained using a dispersive forces correction (DFT-D) method (see below).[25] This strategy allowed to observe that Pauli repulsion between chemisorbed graphene and the metal surface is counteracted by a donation/back-donation bonding

a)Author to whom correspondence should be addressed. Electronic mail: francesc.vines@ub.edu

contribution of similar magnitude, leaving the adsorption strength again to be strongly determined by vdW forces.

Consequently, it is not surprising that recent studies on graphene/metal interfaces highlighted the importance of including a proper description of dispersive forces when studying them by first-principles methods. In particular, the theoretical description of vdW forces within a DFT calculation scheme has permitted to understand the Moiré patterns of graphene on the Ru(0001) surface as observed with Scanning Tunneling Microscopy (STM),[31] due to a surface lattice incommensurability and the simultaneous coexistence of regions with physisorption and chemisorption states of graphene. In addition, this has served to identify, by means of theoretically aided assignment of High-Resolution X-Ray Photoemission Spectroscopy (HR-XPS) core level shifts, two coexisting chemisorbed structures of graphene on Ni(111),[20] namely, top-fcc and bridge-top. Finally, it helped in uncovering the crucial role of Ni(111) substrate in the healing of Stone-Wales defects, as observed by STM images.[32]

During the last decade, a plethora of methods has bloomed to properly account for dispersive forces within DFT in an accurate yet computationally affordable fashion. It is worth highlighting the so-called DFT-D methods, in which a dispersive force correction based on interatomic potentials of the $C^6 \cdot R^{-6}$ form is added to a standard DFT exchange-correlation functional —allowing for a facile energy decomposition to vdW and electronic parts. Representatives of DFT-D methods are the implementations of Ortmann,[33] Grimme,[34] and Tkatchenko.[35] Aside from these, various exchange-correlation functionals have been developed with the goal of including a proper description of vdW forces, the so-called van der Waals functionals (vdW-DFT), initially developed by Dion and co-workers.[36] The initial functional baptized as revPBE-vdW has suffered different modifications afterwards in order to solve drawbacks in its accuracy. This resulted in different vdW-DFT flavors, such as the rPW86-vdW,[37] optPBE-vdW and optB88-vdW,[38] and the most recent, the optB86b-vdW.[39] Note that most of these functionals and corrections are parameterized using specifically designed benchmark datasets — with the risks this procedure implies — although some are based on a theoretically derived ansatz, and so, *a priori* physically sound. Very recent studies rely on the correct treatment of dispersive interactions by more sophisticated yet computationally expensive methods, such as the Random Phase Approximation (RPA),[40,41] or the meta Generalized Gradient Approximation (metaGGA) functional M06,[42] where the suitability of few representatives of the above-commented DFT-D and/or vdW-DFT methods was examined by comparing their accuracy to RPA, assumed to be a golden standard for graphene-metal contacts given its accuracy describing vdW interactions.[43,44]

These last works focused however on the reproducibility of RPA results rather than targeting available experimental data, and, furthermore, centred most of the study on the top-fcc chemisorbed state, in this sense disregarding the competitive bridge-top surface conformation.[20] A comprehensive, systematic, and comparative study of the accuracy of diverse DFT-D and vdW-DFT methodologies towards the geometry, energetics, and electronic structure of graphene on metal contacts is a must. The ultimate goal is to identify accurate yet affordable computational strategies suited not only to assess surface science techniques aimed at characterizing graphene-metal contacts, such as STM,[31] Scanning Tunneling Spectroscopy (STS),[45] or Atomic Force Microscopy (AFM),[46] but well beyond to properly model technologically relevant processes such as graphene epitaxial growth,[47] defect healing,[32] hole reknitting,[48] doping,[49] and metal intercalation.[50]

Here we provide such a study by tackling the performance of the above-listed DFT-D and vdW-DFT methods in describing the structure, energy, and bandstructure of graphene attached to Ni(111). This substrate has been chosen as a representative late transition metal surface for multiple reasons. First, it does not only exhibit chemisorption states typical for Ru, Co, and Pd, but also less stable physisorption states similar to those on Ir, Cu, Pt, and Au.[25] Second, for most of the properties under scrutiny there is available, reproducible, and accurate enough — for the present purposes — experimental information. Besides most of the previous theoretical studies in the field used graphene/Ni(111) as a benchmark case. Finally, the high-degree of graphene-Ni(111) surface commensurability allowed its investigation with all sort of DFT-based methods, to which present results are compared.

II. COMPUTATIONAL DETAILS

Three adsorption conformations have been investigated (Figure 1); the chemisorbed top-fcc and bridge-top states,[14] and hcp-fcc as a representative case of physisorption contact,[25] have been explicitly addressed. The Perdew-Burke-Erzenhof (PBE) exchange-correlation functional,[51] a representative of the functionals within the Generalized Gradient Approximation (GGA), has been used as the basis for the DFT-D corrections, since, as shown in the supplementary material,[72] it provides excellent results for the graphene and Ni lattice structures in particular, and for transition metals in general.[52]

Spin-polarized DFT calculations were carried out with the VASP calculation package.[53] The projector augmented wave method was used to treat interactions between core and valence electrons.[54] A plane-wave basis set was used with a

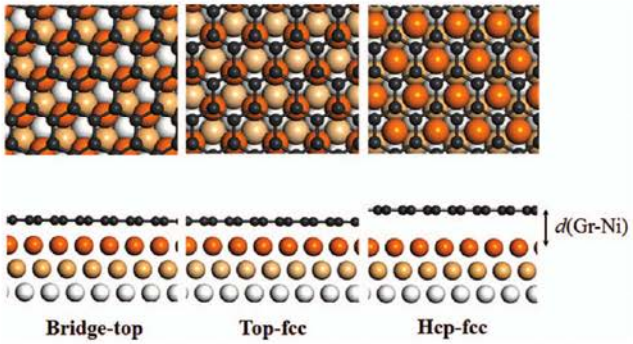

FIG. 1. Adsorption conformations of graphene on Ni(111). Top and bottom images show top and side views, respectively. C and Ni atoms are displayed as grey and orange spheres, respectively. The darkness of Ni atomic spheres reduces when moving towards bulk material.

kinetic cut-off energy of 415 eV was found to be optimal as differences in energy below 1 meV were found when using a larger basis set. The reciprocal space was sampled with an optimal Monkhorst-Pack[55] **k**-point grid of 7 × 7 × 1 size, although a denser grid of 9 × 9 × 1 **k**-points was used when evaluating graphene bandstructures. Optimizations were performed using the tetrahedron smearing of Blöchl,[56] with an energy width of 0.2 eV to speed up convergence; however, final energy values were corrected to 0 K (no smearing). A six layer $p(1 \times 1)$ Ni(111) slab unit cell was used in the calculations. During the geometry optimizations, the three bottom layers were fixed to bulk-optimized (Self-Consistent (SC)) or experimental (E) Ni positions, while the three top layers were relaxed—so-called 3 + 3 approximation. The adjacent slabs were separated in the vacuum direction by at least 1 nm. Geometry optimizations were performed until all forces acting on relaxed atoms became less than 0.03 eV $Å^{-1}$. The adsorption energy of graphene on Ni(111), E_{ads}, was calculated by subtracting the energy of the adsorption complex, $E_{Gr/Ni}$, from the energies of a pristine Ni(111) slab, E_{Ni}, and of a free-standing graphene, E_{Gr}, i.e., $E_{ads} = -E_{Gr/Ni} + (E_{Gr} + E_{Ni})$. With this definition, more positive adsorption energies indicate stronger bonding, and *vice versa*. The graphene height with respect to the Ni(111) surface, *d*(Gr-Ni), was calculated from the mean plane of graphene sheet and the Ni(111) surface plane. Standard parameterizations for the DFT-D corrections, e.g., particularities of the damping function, the C^6 values used, etc., were taken as suggested in the original studies.[33–35]

III. RESULTS AND DISCUSSION

A. Graphene and graphite

Initially, we assess the suitability of the methods under the scope for the description of bulk Ni, graphene, and graphite, with results listed in Tables S1 and S2 of the supplementary material.[72] In a nutshell, all the examined DFT-D and vdW-DFT methods provided an excellent agreement with respect to the lattice cell parameter *a* of graphene, with deviations below ∼1 pm, i.e., within the chemical accuracy, with optB88-vdW functional and Tkatchenko DFT-D correction matching the experimental value. The same degree of accuracy is achieved for *a* graphite parameter, where optB88-vdW, optB86b-vdW, and even PBE match the experimental value.[57] On graphite, the differences raise on the description of *c* lattice parameter, i.e., graphite sheets interlayer distance δ. Here, PBE clearly overestimates it due to its lack of description of dispersive forces. The examined DFT-D approaches tend to counteract such deficiency, with deviations of 1–5 pm. For the vdW-DFT, a similar situation is found, in most cases with a systematic overestimation of δ by 5–13 pm. Both strategies have outstanding representatives, namely, Grimme for DFT-D, with an overestimation of δ by only 1.1 pm — at chemical accuracy — closely followed by revPBE-vdw, with an overestimation of 2.4 pm. Concerning graphite exfoliation energy, PBE incorrectly predicts no bonding between sheets, while other methods — revPBE-vdW and optB88-vdW functionals, and the DFT-D corrections of Ortmann and Tkatchenko — slightly overestimate it, although by only 1–5 kJ mol^{-1}. The rest of the studied methods accord perfectly well to the rather broad range of experimental values of exfoliation energies.

B. The graphene-Ni contact: Structure and energetics

Let us now move forward and tackle the graphene-Ni contact. When comparing the lattice mismatch (see Table S2 in the supplementary material[72]), there are significant deviations among the studied methods. For instance, while PBE, optPBE-vdW, and optB88-vdW provide a lattice mismatch similar to the experimental value of ∼1%, some other accentuate it —rPW86-vdW—, some other attenuate it to almost no mismatch — revPBE-vdW, optB86-vdW, and Grimme — and the weirdest case comes from Tkatchenko DFT-D which yields to an inversion of the lattice mismatch, i.e., with a Ni(111) *a* lattice parameter 4.6 pm shorter than that of graphene, contrary to the empiric observations. Due to these disagreements, and in order to delve into the effect of the lattice mismatch on the graphene attachment, two sets of calculations have been carried out according to the employed Ni(111) *a* lattice parameter: The first set, hereafter named SC, uses the *a* lattice parameter of Ni(111) as optimized by the level of calculation under examination. The second set uses the experimental (E) Ni(111) *a* lattice parameter—which happens to match the PBE optimized value. In any set, the *a* lattice of graphene was expanded/contracted to match that of either SC or E Ni(111) surface. However, except for a few cases the two data sets lead to similar conclusions, and thus only the E set is discussed in detail in the manuscript, while all the SC information is provided in Tables S3 and S4 of the supplementary material.[72]

The structures were optimized according to the procedure described in Sec. II. The estimations of the adsorption energy per C atom, E_{ads}, and the distance between graphene and the Ni(111) surface, *d*(Gr-Ni), are encompassed in Table I. Regardless of the functional and method employed, negligible rumpling well below 1 pm was found for the graphene layer. The computed values are compared to reliable experimental estimations for the structure and energetics. In this sense, the chemisorption distances are compared to the experimental value by Gamo *et al.* of 211 ± 7 pm—in other words ranging 204–218 pm,[58] supported by a more recent measurement of 201 ± 10 pm by Kawanowa *et al.*,[59] although exhibiting a slightly larger standard deviation.

As long as the graphene adsorption energy is concerned, there is unfortunately no direct measurement. However, an estimate can be inferred from the work of Shelton *et al.* concerning the graphite segregation to a Ni(111) surface.[60] The authors found that interaction strength between the Ni(111) surface and a monolayer graphite film was ∼4.8 kJ mol^{-1} stronger than the exfoliation energy of graphite.[60] In turn, according to previous measurements graphite exfoliation energy ranges 2.4–6.4 kJ mol^{-1}.[61–63] Therefore, one can suggest that the final range of adsorption energy of graphene on Ni(111) is 7.2–11.2 kJ mol^{-1}. This range of values must be taken with caution since it relies on a single measurement,[60] and further experiments are needed to confirm it. In any case, the

TABLE I. Distance between the graphene sheet and the Ni(111) surface, d(Gr-Ni), and adsorption energies per C atom, E_{ads}, as obtained using various vdW-DFT, DFT-D, and GGA functionals.

		d(Gr-Ni) (pm)	E_{ads} (kJ mol^{-1})
Expt.		[204–218][a]	[7.2–11.2][b]
PBE	Top-fcc	213	−4.9
	Bridge-top	207	−4.7
	Hcp-fcc	413	−0.9
revPBE-vdW	Top-fcc	207	12.8
	Bridge-top	201	13.6
	Hcp-fcc	330	3.1
rPW86-vdW	Top-fcc	377	0.6
	Bridge-top	370	0.6
	Hcp-fcc	383	0.4
optPBE-vdW	Top-fcc	222	0.9
	Bridge-top	215	0.7
	Hcp-fcc	356	4.4
optB88-vdW	Top-fcc	217	3.9
	Bridge-top	212	4.2
	Hcp-fcc	356	4.9
optB86b-vdW	Top-fcc	211	6.6
	Bridge-top	205	7.1
	Hcp-fcc	344	2.6
Grimme	Top-fcc	209	8.3
	Bridge-top	206	8.5
	Hcp-fcc	306	2.6
Tkatchenko	Top-fcc	203	5.0
	Bridge-top	210	5.6
	Hcp-fcc	339	0.7
Ortmann	Top-fcc	212[c]	12.5[c]
	Bridge-top	206[c]	12.2[c]
	Hcp-fcc	353[c]	8.8[c]

[a]Reference 58.
[b]References 60–63.
[c]Reference 25.

stronger bonding to Ni(111) with respect to graphite exfoliation is definitely well-established. Furthermore, it is back-supported by the experimentally observed shorter heights over the metal surface of chemisorbed graphene (on Co, Ni, and Pd) compared to larger heights of physisorbed graphene (on Ag, Au, Cu, and Pt), and separation between graphene sheets in graphite. Last but not least, the stronger interaction is indirectly manifested by the larger extent of graphene-metal hybridization observed for chemisorbed graphene on the former metals.[65]

The data thresholds allow discarding certain methods of calculation, given that they provide wrong results for the structure and/or energetics. In principle, a suitable method must satisfy the following: (i) Describe correctly the structure and energetics of the two chemisorption states of graphene on Ni(111). Despite HR-XPS experiments perhaps point for a slightly higher stability of the top-fcc conformation,[14] these studies are non-conclusive, and therefore a calculation level shall be considered adequate when structure and energetics of both top-fcc and bridge-top conformations fall within the range of experimental values. (ii) The method must capture the physisorption state of hcp-fcc, which, in concordance with other transition metals (Ir, Pt, Cu, Au),[21–24] must display a d(Gr-Ni) of 300–360 pm. Note that there is no experimental physisorption energy for graphene on Ni(111), although the physisorption state must be clearly disfavored with respect to the chemisorption states. (iii) The method has to deliver an interaction energy of graphene on Ni(111) larger than the graphite exfoliation energy, and it should be also able to reproduce the exfoliation energy of graphite as listed in Table S1 of the supplementary material.[72]

A careful examination of the data collected in Table I shows that there are significant differences between the predictions made by the different vdW-DFT functionals and DFT-D corrections. Let us consider first the last of the above-listed requirements: At this stage, only five methods provide adsorption energies of graphene attached to Ni(111) surface larger than the calculated exfoliation energies of graphite: PBE, revPBE-vdW and optB86b-vdW vdW-DFT functionals, and Grimme and Ortmann DFT-D corrections. Among these only the optB86b-vdW functional and the dispersion correction of Grimme deliver graphite exfoliation energies within the experimental value range, as shown in Table S1 of the supplementary material.[72] Regardless of this first evaluation, a proper examination of the different methods is presented below.

Let us begin with the PBE, which, not surprisingly, is not a suitable method to study graphene-metal contacts, simply because of its lack of dispersive interaction description. This is translated into incorrect endothermic chemisorption energies for both top-fcc and bridge-top modes. Note, however, that the adsorption height for these two modes is close to the experimental value, as previously found for top-fcc and top-hcp structures.[30,41,42] Furthermore, PBE is completely unable to describe the physisorption energies, which are exclusively governed by vdW interactions.[25]

When focusing on the vdW-DFT functionals, it is notorious how rPW86-vdW fails on each observable under the scope, in accordance with previous tests on top-fcc and top-hcp.[41,64] It does not only miss in capturing the structure and bond strength of the two chemisorption states, but also the physisorption states are located significantly farther from the Ni(111) surface. It is however worth pointing out that, in relation with a sensibly high lattice mismatch (see the supplementary material[72]), the E results yield sensibly better adsorption strengths than SC, that are, nevertheless, far from reaching the experimental values. The original revPBE-vdW seems rather adequate in predicting stable geometries, a surprising finding since previous studies on the attachment of graphene on Ni(111) on top-fcc or top-hcp geometries reported no chemisorption state, and only a slightly bounded physisorption point.[40,41,64,65] Nevertheless, revPBE-vdW sensibly overestimates the chemisorption strength, and its use is therefore not advisable.

The newer vdW-DFT functionals — optPBE-vdW, optB88-vdW, and optB86b-vdW — seem to deliver more balanced results, particularly on geometries. Only optPBE-vdW produces a graphene chemisorption height for the top-fcc conformation, which is slightly above, by ∼4 pm, the upper experimental limit. Nevertheless, this does not apply on the energy criterion: The optPBE-vdW incorrectly predicts the physisorption state to be clearly more stable than the chemisorption states, plus none of the attachment energies

fits into the experimental measured range. This happens as well for the optB88-vdW, yet here both chemisorption and physisorption states seem to be isoenergetic. This behavior was found to basically match RPA calculations of Mittendorfer and co-workers, who consequently proposed it as a computationally affordable alternative method with similar accuracy to RPA, they are considered as a golden standard.[41] However, such a statement has to be taken with caution, since other RPA-based calculation on the same system provided a slightly higher stability by ∼1 kJ mol^{-1} for the physisorbed state, which is unlikely.[40] Nonetheless, in this latter study it was stated that RPA, while providing an excellent description of graphite, is in principle underestimating the chemisorption minimum, attributed to the known deficiencies of RPA on properly weighting the atomization energies, i.e., breaking of non-dispersive bonds. Indeed, from the here contemplated vdW-DFT functionals, the optB86b-vdW seems to be a particularly appropriate one, as it provides a correct description for geometries and adsorption energies of chemisorbed and physisorbed states, and, additionally, clearly favors chemisorption over physisorption on Ni(111). Nevertheless, one could criticize that the adsorption energies are still slightly below, by 0.1–0.6 kJ mol^{-1}, the experimental range.

The situation is qualitatively different for the DFT-D approaches. Present and previous[25] values using the Ortmann scheme support its usage to describe the graphene-metal interface, particularly appropriate for the structural data, while binding energies are slightly overestimated. In this sense, Grimme parameterization seems to be more adequate, as long as it provides excellent results for both structural and energetic observables. This is in line with very recent calculations on the top-fcc chemisorption state using a GGA functional and adding Grimme parameterization for vdW interactions.[66] However, one has to be cautious since other recent studies yielded slightly different results. For instance, Voloshina and co-workers, using PBE+Grimme, found an overestimation of the chemisorption strength for the top-fcc state of ∼4.7 kJ mol^{-1}.[67] Furthermore, a recent study by Adamska *et al.* using PBE+Grimme provided similar values for the top-fcc chemisorption state, though quite substantially underestimating the bridge-top stability to the point of being, not yet chemisorbed, less stable than the physisorbed hcp-fcc state.[68] Last but not least, Tkatchenko yields graphene heights for both chemisorption states within the measurements, although binding energies are ∼2 kJ mol^{-1} below the experimental range. Only in the SC set the binding energies fit to the experiments, although at the expense of incorrectly conferring to the hcp-fcc physisorption conformation a higher stability, see the supplementary material.[72]

It is worth inspecting whether simple Local Density Approximation (LDA) exchange-correlation functionals were already suited to describe graphene-metal contacts. Usually LDA tends to provide a reasonable description of systems where vdW interactions do play a role, simply due to its well-known bond strength overestimation. However, one has to keep in mind that LDA provides a good description for clearly the wrong reason, this is, the presence of self-interaction error. Nevertheless, many studies contemplated its usefulness by studying top-fcc and top-hcp contact conformations,[26,40,41,65,68,69] though many aspects discourage its use. For instance, in many cases LDA was unable to capture the physisorption state of graphene on Ni(111),[40,41,65] with the exception of Adamska *et al.* who found not only the physisorption state of hcp-fcc, but also the competitive chemisorption of bridge-top.[68] However, their interaction strengths, well above 30 kJ mol^{-1}, are clearly overestimating the experimental values. Indeed, this overestimation spreads to other studies, always finding E_{ads} to be above 17 kJ mol^{-1},[40,41] with concomitant *d*(Gr-Ni) values around or even below 200 pm. Other LDA works feature more reasonable graphene heights, and a graphene-Ni(111) bond strength only 1–2 kJ mol^{-1} above the available experimental measurement.[26,65,69]

Last but not least, it is worth mentioning other previously sampled calculation methods. Hamada and Otani[64] tested variants of revPBE-vdW and rPW86-vdW using the Cooper exchange functional C09, explicitly developed for the vdW-DFT functionals.[70] Both modifications produced results similar to LDA, that is, they allowed the location of the chemisorption top-hcp state with an excellent match with respect to graphene height, although the interaction energies, ranging 13.6–17.6 kJ mol^{-1}, are slightly above the present experimental estimates ranging 7.2–11.2 kJ mol^{-1}. Another work by Andersen *et al.* examined the usage of the metaGGA M06 functional on the top-fcc conformation,[42] correctly finding the physisorption and the chemisorption state, although with a sensibly larger height of the latter, by 11–19 pm. Accordingly, the chemisorption binding strength was calculated to be of 4.2–6.2 kJ mol^{-1}, thus below the experimental range. Similar to RPA results, both physisorption and chemisorption minima were found to be in the same range of energies.

C. Electronic structure analysis

Let us address now the reproducibility of the chemisorbed graphene electronic structure, with special attention towards certain **k**-points of its bandstructure when chemisorbed on Ni(111). Many previous experimental studies using Angle-Resolved Photoemission Electron Spectroscopy (ARPES) on graphene chemisorbed on Ni(111) showed the so-called σ and π graphene bands, see Figure 2. Indeed, the strong hybridization of Nickel *d* orbitals with the graphene π-band is responsible of the disruption of Dirac cones originally located at **K** point and Fermi energy. By means of ARPES, the dispersion of these two bands across the Brillouin space is easily detected.[18,50,67,71] For a proper comparison, we will focus on the well-defined eigenvalues of σ- and π-bands at two high-symmetry **k**-points, namely, **Γ** and **K**, on which σ- and π-bands feature maximum or minimum energy. Note that as briefly commented, the eigenvalue, ϵ, of π-band at **K**, i.e., the original Dirac points referred as ϵ_{π}^{K}, is disrupted due to the chemisorption, and so, no proper value is deliverable. Thus, we shall focus on the eigenvalues of σ-band at **Γ** and **K**, $\epsilon_{\sigma}^{\Gamma}$ and ϵ_{σ}^{K}, respectively, and the value of π-band at **Γ**, ϵ_{π}^{Γ}. According to a variety of recent ARPES

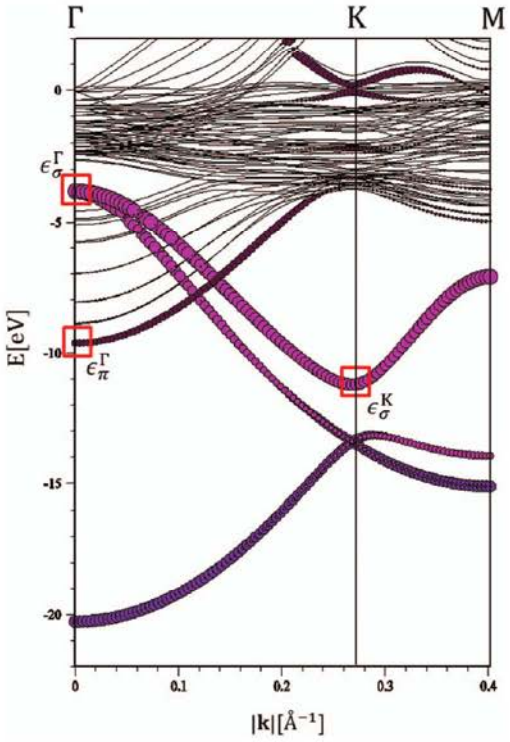

FIG. 2. Bandstructure of graphene adsorbed on Ni(111). The contributions of carbon orbitals to bands are colored violet (2*s*), mauve ($2p_x$, $2p_y$), and maroon ($2p_z$). The points in band structures whose energy shifts are analyzed in detail are marked by red squares.

TABLE II. Eigenvalues of σ- and π-bands of graphene at **Γ** and **K** **k**-points of the Brillouin space, in eV, as obtained using various vdW-DFT, DFT-D, and GGA functionals using experimental Ni(111) lattice values.

		ϵ_σ^Γ (eV)	ϵ_π^Γ (eV)	ϵ_σ^K (eV)
Expt.[a]		[4.3–4.5]	[10.2–10.4]	[12.3–12.5]
PBE	Top-fcc	4.3	10.0	11.7
	Bridge-top	4.6	10.3	11.8
revPBE-vdW	Top-fcc	4.3	10.1	11.8
	Bridge-top	4.5	10.5	11.9
rPW86-vdW	Top-fcc	3.3	7.4	10.2
	Bridge-top	3.3	7.3	10.2
optPBE-vdW	Top-fcc	4.4	9.7	11.4
	Bridge-top	4.5	10.1	11.6
optB88-vdW	Top-fcc	4.5	9.8	11.7
	Bridge-top	4.6	10.2	11.7
optB86b-vdW	Top-fcc	4.4	10.0	11.7
	Bridge-top	4.5	10.3	11.8
Grimme	Top-fcc	4.4	10.0	11.8
	Bridge-top	4.4	10.3	11.8
Tkatchenko	Top-fcc	4.3	10.0	11.8
	Bridge-top	4.2	10.1	11.9
Ortmann[b]	Top-fcc	4.2	9.8	11.5
	Bridge-top	4.1	9.8	11.6

[a]References 18, 50, 66 and 70.
[b]Reference 25.

experiments, ϵ_σ^Γ encompasses values of 4.3–4.5 eV, while ϵ_σ^K is located at 12.3–12.5 eV. The π-band at **Γ** ranges values of 10.2–10.4 eV.

The estimated Kohn-Sham eigenvalues at the sampled **k**-points are listed in Table II for the bridge-top and top-fcc chemisorbed states using the experimental Ni lattice parameter — E dataset — whereas the results for the SC set are reported in Table S4 in the supplementary material.[72] In general terms, with the exception of rPW86-vdW, all vdW functionals and dispersive corrections tend to deliver reasonable dispersion of graphene σ- and π-bands, that is, band energy values in the order of those experimentally observed. However, none of them is systematically targeting the band energy ranges. In other words, regardless of the SC or E sets, at least one band position of either bridge-top and top-fcc conformations is over- or underestimated. Note in passing that such deviations are sometimes of ∼0.1 eV, and so could be acceptable given the broad dispersion of the observed bands and the associated difficulty in establishing a clear maximum or minimum energy point.[18,50,67,71]

Nevertheless, the comparison allows discarding some vdW-DFT functionals such as the rPW86-vdW, which, in accordance to the results in Table I, is unable to describe any chemisorption state, and so the band energy points are highly different to the observed ones, hence resembling those of quasi freestanding graphene.[18] Furthermore, optPBE-vdW and optB88-vdW sensibly underestimate ϵ_π^Γ on top-fcc conformation by 0.4–0.5 eV, and ϵ_σ^K by 0.6–0.9 eV. This also happens, to a lower degree, on PBE values. Concerning revPBE-vdW, the only weak point is the overestimation of ϵ_π^Γ by 0.3 eV in the SC set of calculations. The optB86b-vdW scheme seems again to be the best compromise among vdW-DFT functionals, proven that only overestimates ϵ_π^Γ in E set by barely 0.2 eV, and the divergence of ϵ_σ^K is reduced to 0.4–0.6 eV. Concerning the DFT-D corrections, Tkatchenko seems to be somewhat affected when carrying out the calculations in a self-consistent manner, see Table S4 in the supplementary material.[72] There ϵ_σ^Γ on top-fcc is underestimated by 0.3 eV, although with reasonable estimates for the rest of the eigenvalues. By imposing the experimental Ni lattice — in other words, getting rid of the spurious inverse mismatch as predicted by Tkatchenko — the divergences of ϵ_σ^Γ seem to be attenuated, yet now ϵ_π^Γ results are underestimated by at most 0.2 eV, and those of ϵ_σ^K risen to 0.4–0.5 eV. As far as Ortmann parameterization is concerned, all the eigenvalues seem to be systematically underestimated, by ∼0.3 eV at **Γ**, and σ-band at **K** by 0.7–0.9 eV.[18,25] Only Grimme's approach, one more time, seems to deliver the most adjusted estimates, with only slight deviations. For instance, in the SC set (Table S4 in the supplementary material[72]), ϵ_π^Γ of bridge-top conformation is overestimated by 0.3 eV, whereas when using the experimental Ni lattice constant, its value for the top-fcc is underestimated by 0.2 eV. The σ-band value at **K** is reasonably near the experimental range in the SC set (Table S4), although it suffers from divergences of 0.4–0.5 eV in the E set.

Concerning the suitability of other previously addressed computational levels, LDA tends to underestimate the eigenvalues of σ- and π-bands for top-fcc and top-hcp chemisorption conformations by 0.1–0.3 eV.[64,66] On the same systems, PBE studies also seemed to underestimate the band eigenvalues by 0.2–0.4 eV.[40,41] The metaGGA M06 functional indeed behaves rather similar to PBE in this particular property.[42]

There are only two recent works where the band structure of graphene attached on Ni(111) was investigated employing vdW-DFT functionals, although in one case, the revPBE-vdW was found only to capture the physisorbed state, and so, the resulting bandstructure resembled very much to that of quasi freestanding graphene. Only in the work of Hamada and Otani,[64] the usage of C09 functional on the rPW86-vdW scheme seemed to be rather appropriate, with a faint underestimation of ∼0.2 eV for the ϵ_{π}^{Γ} band and of ∼0.5 eV for the ϵ_{σ}^{K} band.

From the preceding discussion one can state that, in general terms, with the exception of rPW86-vdW, all vdW functionals and dispersive corrections tend to deliver reasonable dispersion of graphene σ- and π-bands, that is, band energy values in the order of those experimentally observed. However, none of them is systematically targeting the band energy ranges. In other words, at least one band position of either bridge-top or top-fcc conformations is over- or underestimated. Nevertheless, it is worth pointing out also that optB86b-vdW and Grimme correction seem to deliver better results with somewhat smaller deviations. Note in passing that such deviations are sometimes of ∼0.1 eV, and so could be acceptable given the broad dispersion of the observed bands and the associated difficulty in establishing a clear maximum or minimum energy point.[18,50,67,71]

IV. CONCLUSIONS

In summary, the accuracy of several vdW-DFT functionals — revPBE-vDW, rPW86-vdW, optPBE-vdW, optB88-vdW, and optB86b-vdW — and DFT-D corrections — Grimme, Ortmann, and Tkatchenko flavours added to PBE basis functional — has been tested on describing the attachment of graphene on Ni(111) —a text-book case featuring the chemisorption and physisorption states characteristic of late transition metals. Two sets of models were studied, one with experimental Ni(111) *a* lattice parameter and the other with the lattice parameter derived from a respective bulk Ni optimization, finding that overall results for both sets tend to agree. Different chemisorption states, namely, top-fcc and bridge-top, were put under examination, together with the so-called hcp-fcc physisorption state. Geometric, energetic, and electronic properties were compared to broad sets of experimental data, concluding that optB86b-vdW functional and Grimme dispersive corrections provide the best balanced results with respect to the relative stability of physisorption and chemisorption states, the attachment strength of the latter, the graphene-Ni(111) separation, and the supported graphene electronic structure. In particular, they yield a more accurate description than previous LDA, metaGGA, and RPA studies. However, this hint should be further confirmed with future experiments aimed at measuring the graphene attachment energy and height on many transition metals, accompanied with a systematic evaluation of the here-tested methodologies on them. In any case the present study evidences significant differences between the predictions arising from current vdW-DFT functionals and DFT-D corrections, and paves the way for future accurate and affordable theoretical studies of nanotechnologic devices based on graphene-metal contacts.

ACKNOWLEDGMENTS

This work was supported by the Spanish MICINN grants FIS2008-02238 and CTQ2012-30751, *Generalitat de Catalunya* (grants 2009SGR1041 and XRQTC), and, in part, by grants from the National Science and Technology Development Agency (NSTDA Chair Professor and NANOTEC Center for the Design of Nanoscale Materials for Green Nanotechnology), the Kasetsart University Research and Development Institute (KURDI), the Commission on Higher Education, Ministry of Education ("the National Research University Project of Thailand (NRU)" and "Post-graduate Education and Research Programs in Petroleum and Petrochemicals and Advanced Materials"). S.M.K. and F.V. are thankful to Red Star community for fruitful discussions. P.J. would like to thank the Office of the Higher Education Commission, Thailand for supporting him with a grant under the program Strategic Scholarships for Frontier Research Network for the Ph.D. Program Thai Doctoral degree and the Graduate School of Kasetsart University for his research. F.V. thanks the Spanish MICINN for the postdoctoral grant under the program *Juan de la Cierva* (JCI-2010-06372). S.M.K. is grateful to the Spanish *Ministerio de Educación, Cultura y Deporte* for the predoctoral FPU grant AP2009-3379, and F.I. acknowledges additional support through the ICREA Academia award for excellence in research.

[1] K. S. Novoselov, A. K. Geim, S. V. Morozov, D. Jiang, Y. Zhang, S. V. Dubonos, I. V. Grigorieva, and A. A. Firsov, Science **306**, 666 (2004).
[2] V. Singh, D. Jounga, L. Zhaia, S. Dasa, S. I. Khondakera, and S. Seal, Prog. Mater. Sci. **56**, 1178 (2011).
[3] S. D. Sarma, S. Adam, E. H. Hwang, and E. Rossi, Rev. Mod. Phys. **83**, 407 (2011).
[4] H. Bai, C. Li, and G. Shi, Adv. Mater. **23**, 1089 (2011).
[5] S. Guo and S. Dong, Chem. Soc. Rev. **40**, 2644 (2011).
[6] K. S. Kim, Y. Zhao, H. Jang, S. Y. Lee, J. M. Kim, K. S. Kim, J.-H. Ahn, P. Kim, J. Y. Choi, and B. H. Hong, Nature (London) **457**, 706 (2009).
[7] N. Trombos, C. Jozsa, M. Popinciuc, H. T. Jonkman, and J. van Wees, Nature (London) **448**, 571 (2007).
[8] S. Y. Zhou, G.-H. Gweon, A. V. Fedorov, P. N. First, W. A. De Heer, D.-H. Lee, F. Guinea, A. H. Castro Neto, and A. Lanzara, Nature Mater. **6**, 770 (2007).
[9] M. Ishigami, J. H. Chen, W. G. Cullen, M. S. Fuhrer, and E. D. Williams, Nano Lett. **7**, 1643 (2007).
[10] M. Batzill, Surf. Sci. Rep. **67**, 83 (2012).
[11] X. Li, W. Cai, J. An, S. Kim, J. Nah, D. Yang, R. Piner, A. Velamakanni, I. Jung, E. Tutuc, S. K. Banerjee, L. Colombo, and R. S. Ruoff, Science **324**, 1312 (2009).
[12] B. Huard, N. Stander, J. A. Sulpizio, and D. Goldhaber-Gordon, Phys. Rev. B **78**, 121402(R) (2008).
[13] X. Wang, Y. Ouyang, X. Li, H. Wang, J. Guo, and H. Dai, Phys. Rev. Lett. **100**, 206803 (2008).
[14] W. Zhao, S. M. Kozlov, O. Höfert, K. Gotterbarm, M. P. A. Lorenz, F. Viñes, C. Papp, A. Görling, and H.-P. Steinrück, J. Phys. Chem. Lett. **2**, 759 (2011).
[15] Q. Yu, J. Lian, S. Siriponglert, H. Li, Y. P. Chen, and S.-S. Pei, Appl. Phys. Lett. **93**, 113103 (2008).
[16] C. Berger, Z. M. Song, T. B. Li, X. B. Li, Y. Ogbazghi, R. Feng, Z. T. Dai, A. N. Marchenkov, E. H. Conrad, P. N. First, and W. A. De Heer, J. Phys. Chem. B **108**, 19912 (2004).
[17] Y. Wang, C. Miao, B. Huang, J. Zhu, W. Liu, Y. Park, Y. Xie, and J. C. S. Woo, IEEE Trans. Electron Devices **57**, 3472 (2010).
[18] R. J. Koch, M. Weser, W. Zhao, F. Viñes, K. Gotterbarm, S. M. Kozlov, O. Höfert, M. Ostler, C. Papp, J. Gebhardt, H.-P. Steinrück, A. Görling, and Th. Seyller, Phys. Rev. B **86**, 075401 (2012).
[19] E. Velez-Fort, C. Mathieu, E. Pallecchi, M. Pigneur, M. G. Silly, R. Belkhou, M. Marangolo, A. Shukla, F. Sirotti, and A. Ouerghi, ACS Nano **6**, 10893 (2012).

[20]W. Zhao, O. Höfert, K. Gotterbarm, J. F. Zhu, C. Papp, and H.-P. Steinrück, J. Phys. Chem. C **116**, 5062 (2012).
[21]F. Viñes, K. M. Neyman, and A. Görling, J. Phys. Chem. A **113**, 11963 (2009).
[22]C. Busse, P. Lazic, R. Djemour, J. Coraux, T. Gerber, N. Atodiserei, V. Cadiuc, R. Brako, A. T. N'Diaye, S. Blugel, J. Zegenhagen, and T. Michely, Phys. Rev. Lett. **107**, 036101 (2011).
[23]J. Gebhardt, F. Viñes, and A. Görling, Phys. Rev. B **86**, 195431 (2012).
[24]I. Jeon, H. Yang, S.-H. Lee, J. Heo, D. H. Seo, J. Shin, U.-I. Chung, Z. G. Kim, H.-J. Chung, and S. Seo, ACS Nano **5**, 1915–1920 (2011).
[25]S. M. Kozlov, F. Viñes, and A. Görling, J. Phys. Chem. C **116**, 7360–7366 (2012).
[26]C. Gong, G. Lee, B. Shan, E. M. Vogel, R. M. Wallace, and K. Cho, J. Appl. Phys. **108**, 123711 (2010).
[27]W. Moritz, B. Wang, M.-L. Bocquet, T. Brugger, T. Greber, J. Wintterlin, and S. Günther, Phys. Rev. Lett. **104**, 136102 (2010).
[28]S.-Y. Kwon, C. V. Ciobanu, V. Petrova, V. B. Shenoy, J. Bareo, V. Gambin, I. Petrov, and S. Kodambacka, Nano Lett. **9**, 3985 (2009).
[29]D. Eom, D. Prezzi, K. T. Rim, H. Zhou, M. Lefenfeld, S. Xiao, C. Nuckolls, M. S. Hybertsen, T. F. Heinz, and G. W. Flynn, Nano Lett. **9**, 2844 (2009).
[30]X. Li, J. Feng, E. Wang, S. Meng, J. Klimeš, and A. Michaelides, Phys. Rev. B **85**, 085425 (2012).
[31]D. Stradi, S. Barja, C. Díaz, M. Garnica, B. Borca, J. J. Hinarejos, D. Sánchez-Portal, M. Alcamí, A. Arnau, A. L. Vázquez de Parga, B. Miranda, and F. Martín, Phys. Rev. Lett. **106**, 186102 (2011).
[32]P. Jacobson, B. Stöger, A. Garhofer, G. S. Parkinson, M. Schmid, R. Caudillo, F. Mittendorfer, J. Redinger, and U. Diebold, J. Phys. Chem. Lett. **3**, 136–139 (2012).
[33]F. Ortmann, F. Bechstedt, and W. G. Schmidt, Phys. Rev. B **73**, 205101 (2006).
[34]S. Grimme, J. Comput. Chem. **27**, 1787 (2006).
[35]A. Tkatchenko and M. Scheffler, Phys. Rev. Lett. **102**, 073005 (2009).
[36]M. Dion, H. Rydberg, E. Schröder, D. C. Langreth, and B. I. Lundqvist, Phys. Rev. Lett. **92**, 246401 (2004).
[37]K. Lee, E. D. Murray, L. Kong, B. I. Lundqvist, and D. C. Langreth, Phys. Rev. B **82**, 081101 (2010).
[38]J. Klimeš, D. R. Bowler, and A. Michaelides, J. Phys.: Condens. Matter **22**, 022201 (2012).
[39]J. Klimeš, D. R. Bowler, and A. Michaelides, Phys. Rev. B **83**, 195131 (2011).
[40]T. Olsen, J. Yan, J. J. Mortensen, and K. S. Thygesen, Phys. Rev. Lett. **107**, 156401 (2011).
[41]F. Mittendorfer, A. Garhofer, J. Redinger, J. Klimeš, J. Harl, and G. Kresse, Phys. Rev. B **84**, 201401 (2011).
[42]M. Andersen, L. Hornekær, and B. Hammer, Phys. Rev. B **86**, 085405 (2012).
[43]S. Lebègue, J. Harl, T. Gould, J. G. Ángyán, G. Kresse, and J. F. Dobson, Phys. Rev. Lett. **105**, 196401 (2010).
[44]J. Harl and G. Kresse, Phys. Rev. Lett. **103**, 056401 (2009).
[45]D. Stradi, S. Barja, C. Díaz, M. Garnica, B. Borca, J. J. Hinarejos, D. Sánchez-Portal, M. Alcamí, A. Arnau, A. L. Vázquez de Parga, R. Miranda, and F. Martín, Phys. Rev. B **85**, 121404 (2012).
[46]P. Lazar, S. Zhang, K. Safarova, Q. Li, J. P. Froning, J. Granatier, P. Hobza, R. Zboril, F. Besenbacher, M. Dong, and M. Otyepka, ACS Nano **7**, 1646 (2013).
[47]Y. Zhang, L. Gomez, F. N. Ishikawa, A. Madaria, K. Ryu, C. Wang, A. Badmaev, and C. Zhou, J. Phys. Chem. Lett. **1**, 3101 (2010).
[48]R. Zan, Q. M. Ramasse, U. Bangert, and K. S. Novoselov, Nano Lett. **12**, 3936 (2012).
[49]D. Usachov, O. Vilkov, A. Grüneis, D. Haberer, A. Fedorov, V. K. Adamchuk, A. B. Preobrajenski, P. Dudin, A. Barinov, M. Oehzelt, C. Laubschat, and D. V. Vyalikh, Nano Lett. **11**, 5401 (2011).
[50]A. Varykhalov, J. Sánchez-Barriga, A. M. Shikin, C. Biswas, E. Vescovo, A. Rybkin, D. Marchenko, and O. Rader, Phys. Rev. Lett. **101**, 157601 (2008).
[51]J. P. Perdew and K. Burke, Phys. Rev. Lett. **77**, 3865 (1996).
[52]P. Janthon, S. M. Kozlov, F. Viñes, J. Limtrakul, and F. Illas, J. Chem. Theory Comput. **9**, 1631 (2013).
[53]G. Kresse and J. Furthmüller, Comput. Mater. Sci. **6**, 15 (1996).
[54]P. E. Blöchl, Phys. Rev. B **50**, 17953 (1994).
[55]H. J. Monkhorst and J. D. Pack, Phys. Rev. B **13**, 5188 (1976).
[56]P. E. Blöchl, O. Jepsen, and O. K. Andersen, Phys. Rev. B **49**, 16223 (1994).
[57]F. Tuinstra and J. L. Koenig, J. Chem. Phys. **53**, 1126 (1970).
[58]Y. Gamo, A. Nagashima, M. Wakabayashi, M. Terai, and C. Oshima, Surf. Sci. **374**, 61 (1997).
[59]H. Kawanowa, H. Ozawa, T. Yazaki, Y. Gotoh, and R. Souda, Jpn. J. Appl. Phys. **41**, 6149 (2002).
[60]J. C. Shelton, H. R. Patil, and J. M. Blakely, Surf. Sci. **43**, 493 (1974).
[61]R. Zacharia, H. Ulbricht, and T. Hertel, Phys. Rev. B **69**, 155406 (2004).
[62]L. A. Girifalco and R. A. Lad, J. Chem. Phys. **25**, 693 (1956).
[63]L. X. Benedict, N. G. Chopra, M. L. Cohen, Z. Zettl, S. G. Louie, and V. H. Crespi, Chem. Phys. Lett. **286**, 490 (1998).
[64]I. Hamada and M. Otani, Phys. Rev. B **82**, 153412 (2010).
[65]M. Vanin, J. J. Mortensen, A. K. Kelkkanen, J. M. Garcia-Lastra, K. S. Thygesen, and K. W. Jacobsen, Phys. Rev. B **81**, 081408 (2010).
[66]P. Błonski and J. Hafner, J. Chem. Phys. **136**, 074701 (2012).
[67]E. N. Voloshina, A. Generalov, M. Weser, S. Böttcher, K. Horn, and Y. S. Dedkov, New J. Phys. **13**, 113028 (2011).
[68]L. Adamska, Y. Lin, A. J. Ross, M. Batzill, and I. I. Oleynik, Phys. Rev. B **85**, 195443 (2012).
[69]G. Giovannetti, P. A. Khomyakov, G. Brocks, V. M. Karpan, J. van den Brink, and P. J. Kelly, Phys. Rev. Lett. **101**, 026803 (2008).
[70]V. R. Cooper, Phys. Rev. B **81**, 161104 (2010).
[71]A. Grüneis, J. Phys.: Condens. Matter. **25**, 043001 (2013).
[72]See supplementary material at http://dx.doi.org/10.1063/1.4807855 for the following material: Graphite structure parameters and exfoliation energy estimates are provided in Table S1 for the different calculation methods under examination. Their estimated mismatch between graphene and Ni(111) surface lattice is provided in Table S2. Tables S3 and S4 complement Tables I and II, respectively, including the SC data.

Section 11.4

7.18 From Static to Reacting Systems on Transition-Metal Surfaces

SM Kozlov, Universitat de Barcelona, Barcelona, Spain
HA Aleksandrov, Universitat de Barcelona, Barcelona, Spain; University of Sofia, Sofia, Bulgaria
LV Moskaleva and M Bäumer, Universität Bremen, Bremen, Germany
KM Neyman, Universitat de Barcelona, Barcelona, Spain; Institució Catalana de Recerca i Estudis Avançats (ICREA), Barcelona, Spain

Abbreviations

Acrolein	2-Propenal	**Crotonaldehyde**	2-Butenal
BEP	Brønsted–Evans–Polanyi (relationship)	**DFT**	Density functional theory (method)
		Ethylidene	$CH_3CH=$

Comprehensive Inorganic Chemistry II: From Elements to Applications, (2013), vol. 7, pp. 475-503

Ethylidyne	$CH_3C\equiv$
kMC	Kinetic Monte Carlo (simulation)
LEED	Low-energy electron diffraction
ML	Monolayer
MSR	Methanol steam reforming
NP	Nanoparticle
np-Au	Nanoporous gold
PBE	Perdew–Burke–Ernzerhof (exchange-correlation functional)
PM-IRAS	Polarization modulated infrared reflection absorption spectroscopy
Prenal	3-Methyl-2-butenal
PW91	Perdew–Wang 1991 (exchange-correlation functional)
SAL	Saturated aldehyde
SOL	Saturated alcohol
STM	Scanning tunneling microscropy
TM	Transition metal
TPD	Temperature programmed desorption
TS	Transition state
UAL	α,β-Unsaturated aldehyde
UHV	Ultra-high vacuum
UOL	Unsaturated alcohol
vdW	van der Waals
Vinyl	CH_2CH
Vinylidene	CH_2C
ZPE	Zero-point energy (correction)

Symbols

*	Adsorbed species
ΔH	Reaction enthalpy
$E^{\neq}$	Activation energy
$E_0^{\neq}$	Activation energy including ZPE corrections
E^{ads}	Adsorption energy
E_0^{ads}	Adsorption energy including ZPE corrections

7.18.1 Introduction

7.18.1.1 Historical Aspects and Outline of the Chapter

Chemical reactions on inorganic surfaces have long been the exclusive dominion of experimental surface science and catalysis. However, already in the beginning of the 1990s it has become evident that 'computer experiments' modeling surface structures and processes can also furnish very useful data, some of which would otherwise be hard, if not impossible, to obtain. This change in the general attitude of the scientific community resulted from the amazing progress achieved in the performance and accuracy of first-principles quantum-mechanical methods. Such a progress has become possible due to both the rapid and steady growth of the computing power and the groundbreaking developments of computational approaches. Among the latter, electronic structure methods based on density functional theory (DFT) became especially favored as powerful computational tools for complementing and aiding interpretation of experimental data in many areas of modern physics, chemistry, materials science, and biology in general[1,2] and in those of surface science and heterogeneous catalysis in particular.

By the end of the twentieth century, amazing achievements in understanding surface structures and processes from DFT-based studies were documented.[3,4] Nevertheless, that period of computational research on surface phenomena dealt much more with structural (static) aspects than directly with reactivity problems. The subsequent rapid development of the surface-related computational research areas during the past decade clearly demonstrated deep and wide-ranging insights in understanding the reactivity on numerous solid surfaces and catalysts.[5–14] The present chapter aims to illustrate this remarkable progress – from static to reacting systems – and the current status of the first-principles computational description of surface reactivity and heterogeneous catalysis.

Obviously, only a very small fraction of the pertinent literature on electronic structure modeling of surface reactions can be discussed here because of space limitations. We have restricted ourselves to rather simple representative reactions on surfaces of either pure or alloyed transition or noble metals. The main reasons for this choice are that (1) such metals are considered to be crucial components of many widely used or emerging catalysts and (2) DFT description is known to be quite good for transition-metal (TM) catalysts, whereas it may be less accurate for other types of catalysts[14] and related systems,[15] for example, those based on strongly correlated oxides and their composites.[16,17]

The multitude of primary surface reaction types on metals is still too wide to be covered in the present chapter. This volume contains chapters entirely devoted to DFT studies of certain reaction types vital for industry, energy, and environment metal-catalyzed processes such as car exhaust cleaning (Chapter 7.19), ammonia synthesis (Chapter 7.17), and Fischer–Tropsch synthesis (Chapter 7.20). These processes are not discussed here despite their paramount importance. Instead, we consider four other groups of representative surface catalytic reactions in the following.

The next section addresses theoretical insights into the (de-) hydrogenation of double C=C and triple C≡C bonds in hydrocarbons on Pd, Pt, and Rh surfaces and accompanying processes. Then, such important transformations of methanol as steam reforming and decomposition on Pd, PdZn, and Cu surfaces are reviewed in Section 7.18.3. These two closely related processes were exhaustively studied because they allow on-board production of H_2, the fuel for hydrogen energy technologies. Methanol steam reforming (MSR) is also an example of a reaction where different elementary steps control the rate and the selectivity of the process. After that, achievements and remaining problems in the DFT modeling of selective hydrogenation of α,β-unsaturated aldehydes (UALs) on chosen mono- and bimetallic surfaces are described. Significance of this kind of reactions is not only restricted to their practical use in synthesis of fine chemicals[18] and biomass conversion[19] but they are also very instructive for demonstrating how to address theoretically the competition between

different functional groups of comparable reactivity, just one of which has to be selectively transformed.[19–21] Next, theoretical aspects of low-temperature CO oxidation on unsupported porous gold catalysts with residual silver impurities remained during the sample preparation by selective leaching of silver from Au–Ag alloys are outlined in Section 7.18.5. Finally, overall achievements and challenges for utilizing theoretical approaches in studies of surface reactivity and in heterogeneous catalysis by TMs are summarized in Section 7.18.6.

Before turning to the discussion of particular surface systems and reactions, it is appropriate to briefly comment on selected methodology and modeling aspects of surface reactivity and catalysis as described by means of DFT calculations. The rest of this section is devoted to these issues.

7.18.1.2 Contemporary Modeling Approaches in a Nutshell

One of the greatest challenges of computational quantum chemistry in catalysis is to design new catalysts from first principles.[14] A crucial prerequisite for that is the development of concepts that enable understanding of (at least) trends in the activities of various types of catalysts in a given reaction. The description of binding between a surface and molecules interacting with it is fundamental for understanding chemical reactivity on surfaces and in catalysis. A simple but very utile and widely applicable tool in surface chemistry is a correlation found between the position of d-band center of TM substrates and the stabilization of various species and transition state (TS) complexes on the metal surface.[22] As various adsorption and activation energies correlate with the same electronic structure features of a surface, correlations between adsorption and TS energies are established for surface chemistry of TMs[14] (see Chapter 7.15 for more details on the so-called scaling laws and descriptors). The correlations open a way to efficiently approach kinetics of a chosen catalytic reaction on various surfaces, bypassing prohibitively demanding direct DFT calculations of all reaction and activation (Gibbs free) energies of all involved elementary steps as a function of surface coverage and considering the great variety of conceivable structures of the active sites. This approach is rapidly becoming very popular in pre-screening of materials to propose new catalysts using microkinetic models alongside the catalytic properties evaluated for numerous structures and compositions of catalysts.[14] Note, however, that to establish a scaling law one usually has to calculate a set of activation energies on the basis of DFT used for fitting that scaling law. Also, the limited accuracy of scaling laws (i.e., deviations from the values obtained using first-principles calculations) makes their application most appropriate for rapid pre-screening of potential catalysts, leaving detailed investigations of a given reaction to the domain of explicit DFT calculations. Finally, in applications of the scaling laws, the surfaces (and the corresponding active sites) of each metal under scrutiny are commonly restricted to a few regular low-index surfaces, basically neglecting the surface roughness of the real nanoscopic catalysts where low-coordinated defect sites are abundant.

A more traditional approach in the first-principles description of reactive and catalytic properties of a given surface is to quantify pertinent reaction energies and activation barriers (together with the corresponding structures of surface complexes) for elementary steps in question by more demanding yet more rigorous direct DFT calculations. In this approach, the question of how adequately the active sites on the surface of the catalyst are modeled (their atomic and electronic structure, interaction with the reacting species, proximity of other surface species, overall surface coverage, etc.) is important. For example, quite disordered metal nanoparticles (NPs) in common catalysts with large surface area abundantly expose edges, kinks, and other structural irregularities composed of undercoordinated atoms, often assumed to be more reactive. Such sites are absent on regular single-crystal metal surfaces. Thus, the actual catalyst activity may deviate significantly from the activity of extended metal surfaces. This is a well-known problem of the material gap between surface science and catalysis.[23] Experimentally, the material gap was successfully bridged by the introduction of so-called model catalysts[24,25] usually composed of well-characterized supported metal (or alloy) NPs. Quite surprisingly, this material gap largely remains out of the scope of quantum mechanical computational studies related to heterogeneous catalysis.[5–14] Slab models, that is, infinite in two dimensions slices of material with a width of several atomic layers, continue to be the main 'working horse' in catalysis-related applications of first-principles theories. Apparently, metal NPs in catalysts are mostly described by slab models instead of NP models not because of exceedingly high cost of calculating the latter. In fact, DFT calculations of metal NPs large enough to serve as realistic models in heterogeneous catalysis can nowadays be performed almost routinely.[26–31] Here, the term 'large enough' does not mean that the size of computed NPs coincides with that of many thousand metal atoms constituting NPs commonly investigated experimentally, which are still too big for DFT calculations. It should be sufficient for many purposes to computationally study metal NPs belonging to a so-called 'scalable' regime, where certain observables vary smoothly and monotonically with the particle size.[26] It appears that for such a catalytically important TM as Pd, NP models with about 100 atoms in the form of 3D cuts from the metal bulk already satisfy these requirements for adsorption energy and related surface properties.[26,27]

Employment of the NPs from scalable size range to theoretically mimic (larger) metal NPs present in common catalysts is a visible step toward more realistic models in catalysis compared to the slab models. The NP models allow one to quantify the reactivity of both extended regular terraces and more specific surface active sites formed by low-coordinated atoms and featuring inherently nanoscopic properties. It is well known that 'chemistry' on such special sites may be very different from what takes place on flat surface terraces. Here, it is appropriate to briefly mention just one example of dramatically changed reactivity of Pt(111) surface compared to nanoparticulate Pt to dehydrogenate methane, calculated in excellent agreement with observations of molecular beam and photoelectron spectroscopy experiments.[32] Not surprisingly, a NP Pt_{79} was found to be much more catalytically active than the Pt(111) surface (see Figure 1). For instance, a strong decrease of the activation energy on the Pt NP by ~ 60 kJ mol^{-1} was calculated for the first step of methane dehydrogenation to methyl, usually considered as the rate-limiting one of the whole chain of the dehydrogenation reactions.[33]

The emerging research on catalysis by (size-selected) subnanoscale metal particles containing up to one to two dozens

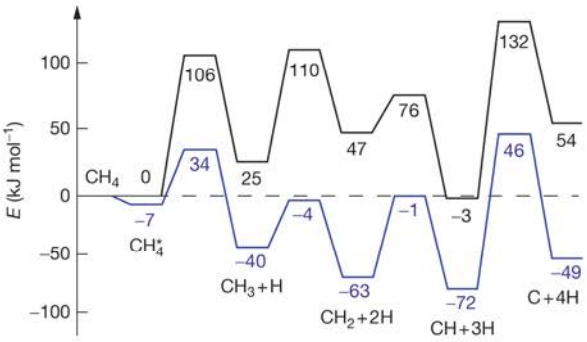

Figure 1 Energy profiles of methane decomposition on a Pt(111) slab model (black) and a Pt_{79} nanoparticle (blue) calculated by Viñes, F.; Lykhach, Y.; Staudt, T.; Lorenz, M. P. A.; Papp, C.; Steinrück, H.-P.; Libuda, J.; Neyman, K. M.; Görling, A. *Chem. Eur. J.* **2010**, *16*, 6530–6539. Relative stability of the reaction intermediates and the product species is given with respect to the total energy sum of the bare metal substrate and gas-phase methane.

of atoms[34–38] deals with the opposite to the 'scalable' regime situation for the adsorption and catalytic activity – in these NPs, 'each atom counts.'[34] Obviously, different approaches are required to theoretically explore the reactivity of such catalysts, which have to include the variation of the metal particle size atom by atom in the range of sizes under scrutiny. Another type of catalysts with active sites composed of noble metal ions has recently attracted great attention,[39–41] also theoretically.[41,42] These two above-mentioned prospective types of catalytic systems are not discussed in the present chapter.

Before closing this section, one has to mention that heterogeneous catalysts are often viewed as quite rigid complex solids, exposing a variety of surface structures located on terraces, edges, corners, point defects, modifiers, etc. (the active sites), where catalytic reactions take place more rapidly than on the other parts of the surface. The active sites are assumed to be created when a catalyst is prepared and remain unaltered in the course of the catalytic cycle. This view on the static structure of catalysts is an oversimplification, at least for processes requiring activation time, during which the catalytic performance is developed concomitantly with modifications of the surface structure of the catalysts. There, the active sites are created *in situ*, during the reaction, which makes their characterization very complicated. So far, theoretical chemistry of surface reactions mainly dealt with the question of how the structure of a given surface site controls the catalytic reaction. However, recent DFT studies also succeeded to describe the formation of actual active sites triggered by reacting species in several catalytic processes. Examples of such transformations of metal catalysts are given in the following sections.

7.18.2 Hydrogenation and Dehydrogenation of Unsaturated Hydrocarbons

Olefins are an important class of organic compounds with numerous industrial applications in petrochemistry, organic, and polymer chemistry.[43] Various TMs are used as catalysts for converting olefins (and other molecules with C=C bond) to a range of valuable chemicals. Being the simplest member of the class, ethylene is frequently used as a model for studying reactions of compounds containing C=C bonds with TM surfaces.[44,45] Hence, it is well justified that most of the studies outlined in this section address surface reactions of ethylene mediated by TMs. In particular, some of the theoretical achievements in exploring the chemistry of ethylene and its derivatives under dehydrogenation and hydrogenation conditions are considered. Two other industrially important processes of selective (partial) hydrogenation of 1,3-butadiene[46] and acetylene[47] are also dealt with. This section includes a discussion of such extensive and branching reaction chains as ethylene and ethylidyne decomposition and butadiene hydrogenation.

7.18.2.1 Dehydrogenation of Alkenes

7.18.2.1.1 Conversion of ethylene to ethylidyne on Pd(111), Pt(111), and Rh(111) surfaces

Although the present chapter is focused on the reactivity issues, it is worth mentioning that ethylene and other C_2H_x ($x=0-5$) species usually prefer adsorption configurations on TMs with both C atoms sp^3-hybridized, as in the C_2H_6 molecule, so that the missing bonds with H atoms are replaced by interactions with the underlying surface metal atoms. When ethylene is adsorbed on surfaces such as Pd(111),[48–53] Pt(111),[54–58] Rh(111),[59] Ir(111),[60] and Ru(0001)[61] at room temperature, the surface is densely covered by a stable phase of ethylidyne, CH_3C, species. The exact mechanism of this reaction could not be unequivocally determined experimentally and several theoretical studies briefly surveyed below used the tools of modern DFT and kinetic Monte Carlo (kMC) simulations to identify accessible reaction pathways and to determine the preferred reaction route at given experimental conditions.

7.18.2.1.1.1 Pd(111)

It is appropriate to begin with the discussion of ethylene conversion to ethylidyne on the Pd(111) surface, which seems to be one of the theoretically best explored surface reactions of ethylene. The following three conceivable reaction pathways for ethylene transformations on TMs proposed in the literature are described below: ethylene → vinyl → ethylidene → ethylidyne (Mechanism 1); ethylene → vinyl → vinylidene → ethylidyne (Mechanism 2); ethylene → ethyl → ethylidene → ethylidyne (Mechanism 3). Figure 2 shows the complex reaction network and the various species involved in the transformation of ethylene to ethylidyne. Experimental studies on Pt(111)[57,58,62,63] supposed that the most plausible pathway includes a direct isomerization of ethylene to ethylidene followed by a dehydrogenation of ethylidene to ethylidyne: ethylene → ethylidene → ethylidyne. As shown in Section 7.18.2.1.1.3, hydrogen-shift reactions require very high activation barriers and alternatively can be replaced by dehydrogenation–hydrogenation reactions as in Mechanism 1. On Pd(111), the latter mechanism was first considered theoretically by Pallassana et al.[64] assuming a very high coverage of 1/3 monolayer (ML). They found that the first step, ethylene dehydrogenation to vinyl, has the highest barrier, 151 kJ mol^{-1}, while the third one, dehydrogenation of ethylidene to ethylidyne, has the lowest barrier of 75 kJ mol^{-1}. Later, Moskaleva et al.[65] revisited this mechanism using more elaborate models and more

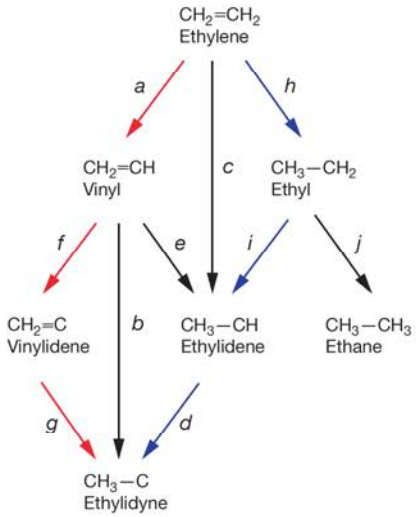

Figure 2 Proposed reaction pathways of ethylene conversion to ethylidyne over Pt group metals. Arrows pointing to the left, to the right, and vertically down indicate dehydrogenation steps, hydrogenation steps, and 1,2 H shift, respectively. Mechanism 1 (pathway *a–e–d*), Mechanism 2 (pathways *a–f–g*), and Mechanism 3 (pathways *h–i–d*) are addressed in the text.[67] Reprinted from Moskaleva, L. V.; Aleksandrov, H. A.; Basaran, D.; Zhao, Z.-J.; Rösch, N. *J. Phys. Chem. C* **2009**, *113*, 15373–15379, with permission. Copyright 2009 American Chemical Society.

precise computational strategy (thicker slab with larger structural flexibility, denser k-point grid, and stricter convergence criteria). They found the same sequence of the barrier heights as in the previous theoretical study;[64] however, the barriers were predicted significantly lower, by 32–47 kJ mol^{-1} for the same coverage of 1/3 ML. They also found that the coverage effect is important for the modeled reactions and can change the reaction barriers by up to 25 kJ mol^{-1} when the coverage is decreased to 1/9 ML. Similarly, coverage effects were found to be very important during the production of vinyl acetate from ethylene and acetate on Pd.[66]

Further, Moskaleva et al.[67] considered by means of periodic DFT calculations all three reaction pathways of ethylene transformation to ethylidyne on Pd(111) at different surface coverage. Again, the highest activation barrier, 100–117 kJ mol^{-1}, was found for the dehydrogenation of ethylene to vinyl. Hence, the Mechanisms 1 and 2 involve the highest reaction barrier for the same step. It was shown that depending on the coverage, one of the two mechanisms can become more plausible than the other. Interestingly, the barrier heights of the three elementary reactions of Mechanism 3 (at most 88 kJ mol^{-1}) are lower than the rate-limiting barriers of Mechanisms 1 and 2. Nevertheless, Mechanism 3 was concluded unlikely, since its first reaction step is ethylene hydrogenation, which implies notable concentration of hydrogen on the surface. However, if the latter were the case, ethyl species can be also hydrogenated to ethane, instead of being dehydrogenated to ethylidene species. Indeed, significantly lower barrier was found for the ethyl → ethane reaction step, 51 kJ mol^{-1}, than for the ethyl → ethylidene one, >80 kJ mol^{-1}. Although DFT calculations suggested plausible mechanisms of ethylene conversion to ethylidyne, the authors were unable to ultimately identify a dominating pathway since the information on the heights of activation barriers was insufficient for that; also the answer could change depending on particular experimental conditions.

Further clarification of the mechanistic picture can be achieved by kinetic modeling with macroscopic rate equations or, preferably, by kMC simulations. The latter allow one to track explicitly the behavior of all surface species as a function of time and process conditions.[68–73] Aleksandrov et al.[74] performed such kMC simulations, employing a first-principles kinetic database, constructed from the DFT results of Moskaleva et al.[67] in combination with a parametrized semi-empirical model for lateral interactions to account for the effects of local environment on reaction kinetics.[68,69] It was found that Mechanism 2, via vinyl and vinylidene, should be the most plausible under hydrogen-deficient conditions. The other two, Mechanisms 1 and 3, proceed via the rate-limiting formation of ethylidene from vinyl or ethyl, respectively. Those reaction steps are significantly slower than the rate-limiting step of Mechanism 2, ethylene dehydrogenation to vinyl. It was also noted that the determination of the fastest route of the overall process and of the associated rate-limiting steps cannot be unequivocally predicted from activation energies only. The reaction rates depend also on the initial conditions, for example, in the present case on the concentration of H atoms on the surface. In the simulations discussed, the hydrogenation steps were found to be slow due to the limited production of adsorbed H atoms. This leads to the somewhat counterintuitive result that in several cases, for example, ethylene hydrogenation to ethyl or ethyl hydrogenation to ethane, hydrogenation steps are slower than dehydrogenation steps with similar or even higher barriers.

All studies discussed above used idealized computational models, but catalytic reactions are known to often occur preferentially at defects of surfaces, such as step-edge sites.[75–79] This issue is partially addressed in the study of Andersin et al.[80] where ethylene conversion to ethylidyne was considered on flat and stepped Pd surfaces. Their results showed that at low-coverage transformations of ethylene are the most likely processes on both types of surfaces. This differs from the case of Ni, for which a more pronounced effect of steps in terms of the selectivity for the activation of C—H or C—C bond-breaking processes was observed and calculated.[81]

7.18.2.1.1.2 Pt(111)

The three possible mechanisms of ethylene conversion to ethylidyne on Pt(111) were modeled by Zhao et al.[82] at three different coverages using periodic DFT calculations. Similarly to their findings for the same reaction on Pd(111),[67] Mechanisms 1 and 2 seemed to be equally plausible on Pt(111), at low coverage and in the absence of co-adsorbed hydrogen. For all three considered mechanisms the highest barriers are similar, ~80 kJ mol^{-1}. As mentioned above, Zaera et al.[57,58,62,63] proposed ethylidene as one of the most probable intermediates in this reaction. Zhao et al. found that the barrier of ethylidene conversion to ethylidyne is remarkably low, only ~20–30 kJ mol^{-1}, which implies that ethylidene species will be rapidly converted to ethylidyne and should not be detected experimentally. kMC simulations of ethylene dehydrogenation have also been performed on Pt(111).[74] Similar to the results on

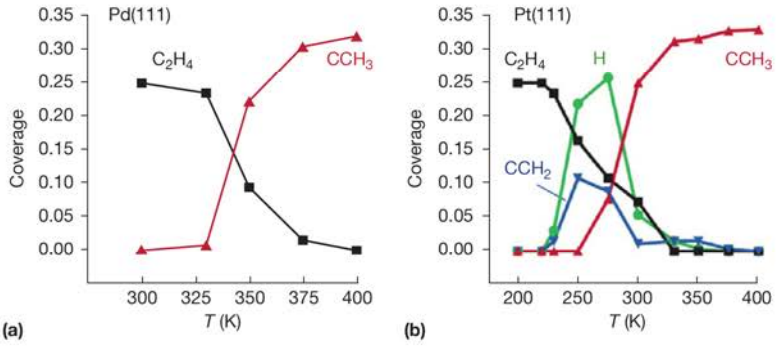

Figure 3 Temperature dependence of the coverages θ of species detected on the surface ($\theta > 0.01$) after 60 s of kinetic Monte Carlo simulation of ethylene conversion to ethylidyne on (a) Pd(111) and (b) Pt(111). Reproduced from Aleksandrov, H. A.; Moskaleva, L. V.; Zhao, Z.-J.; Basaran, D.; Chen, Z.-X.; Mei, D.; Rösch, N. *J. Catal.* **2012**, *285*, 187–195, with permission. Copyright 2012 Elsevier.

Pd(111), Mechanism 2 was found to be the most plausible on Pt(111), with the faster rate-limiting step than that in the other two mechanisms. A notable difference between these two metals is that on Pt(111), the rate-limiting step in Mechanism 2 is the last one, the hydrogenation of vinylidene to ethylidyne, whereas on Pd(111) it is the first step, ethylene dehydrogenation to vinyl. Hence, vinylidene and hydrogen species were theoretically found to accumulate on Pt(111) surface at low temperatures, while no intermediates were calculated on Pd(111) surface (Figure 3). In agreement with experimental evidence,[83] the kMC simulations also predict that the conversion of ethylene to ethylidyne occurs at significantly lower temperatures on Pt(111) than on Pd(111). Like on Pd, reaction steps of Mechanism 2 have similar barriers on Pt(111) and Pt(211).[84]

7.18.2.1.1.3 Rh(111)

Li et al.[85] modeled ethylene conversion to ethylidyne on Rh (111) using periodic DFT approach. Similar to the situation on Pd and Pt, they found that the most plausible is again Mechanism 2, via vinyl and vinylidene intermediates. Vinylidene hydrogenation to ethylidyne with the barrier of 64 kJ mol^{-1} was calculated to be rate limiting. Mechanism 1 with a conversion rate at least 10^4 times lower than that in Mechanism 2 seems to be not operative. Mechanism 3 is unlikely due to the high barrier of ethyl dehydrogenation to ethylidene and the low barriers for ethyl conversions to ethane and/or ethylene.

Finally, it should be mentioned that direct isomerization processes of ethylene to ethylidene and vinyl to ethylidyne via 1,2 H-shifts on Pd(111),[65,80] Pt(111),[82,84] Pt(110),[86] and Rh (111)[85] surfaces were theoretically found to have very high reaction barriers and thus unlikely to occur under relevant experimental conditions.

7.18.2.1.2 Decomposition of ethylidyne

Experimental studies reveal that ethylene on Pd(111) is converted at room temperature to ethylidyne, which after further heating to ~425 K decomposes to C_1 species, yielding hydrogen.[51] This is in agreement with the results of Chen et al.[87] and Andersin and Honkala,[88] who calculated barriers for ethylidyne decomposition by ~50 kJ mol^{-1} higher than those for ethylene conversion to ethylidyne. DFT calculations show that direct C—C bond scission, $CH_3C \rightarrow CH_3 + C$, is unlikely on Pd(111) due to a very high barrier of almost 200 kJ mol^{-1}, and large endothermicity, 116 kJ mol^{-1}.[87] According to Chen et al., two other more complex reaction schemes seem to be more plausible on Pd(111): (1) $CH_3C \rightarrow CH_2C \rightarrow CHC \rightarrow CH + C$ and (2) $CH_3C \rightarrow CH_2C \rightarrow CHCH \rightarrow CH + CH$, with the barriers of similar heights, ~140 kJ mol^{-1}.[87] The pathway (1) was also proposed by Andersin and Honkala[88] to be the most probable on Pd (111). On the Pd(211) stepped surface similar reaction chain was proposed,[88] but with a different final part, $CHC \rightarrow CC \rightarrow C + C$, due to a decreased by 50 kJ mol^{-1} dehydrogenation barrier of CHC to CC. If ethylene is heated rapidly to 400 K, other pathways (not only those via ethylidyne) may be involved, for example, $CH_2CH_2 \rightarrow CH_2CH \rightarrow CH_2C \rightarrow CHC \rightarrow CH + C$ and $CH_2CH_2 \rightarrow CH_2CH \rightarrow CHCH \rightarrow CHC \rightarrow CH + C$. In most cases it seems that the preferred final steps should be $CH_2C \rightarrow CHC \rightarrow CH + C$.[87] This finding is in good agreement with experiments, which also documented the formation of CHC species during ethylidyne decomposition on Pd(111)[89,90] and Pt(111).[91,92]

7.18.2.1.3 Comparison between different TM surfaces

In order to compare the catalytic activity of four most commonly studied (111) TM surfaces of Pd, Pt, Rh, and Ni, the simplest pathway of ethylene decomposition, $CH_2CH_2 \rightarrow CH_2CH \rightarrow CHCH \rightarrow CHC \rightarrow CC \rightarrow C + C$, was considered on them using periodic slab model DFT calculations (Figure 4).[93] It was found that the dehydrogenation reactions occur easier, both kinetically and thermodynamically, on Ni(111) and Rh(111) than on Pd(111) and Pt(111).

Trends of reaction energies and barriers on the various metals are controlled mainly by the difference between the binding energy values of the reactant C_2H_x ($x = 1$–4) and product C_2H_{x-1} species of the corresponding reaction step. On all four metals studied, the first two dehydrogenation steps, $CH_2CH_2 \rightarrow CH_2CH \rightarrow CHCH$, are kinetically and thermodynamically more favorable than the dehydrogenation of the species with lower H content (CHCH, CHC). As discussed above (see Section 7.18.2.1.2), C—C bond breaking in CHC may be competitive with that in C_2.[87,88] As Ni is very cheap

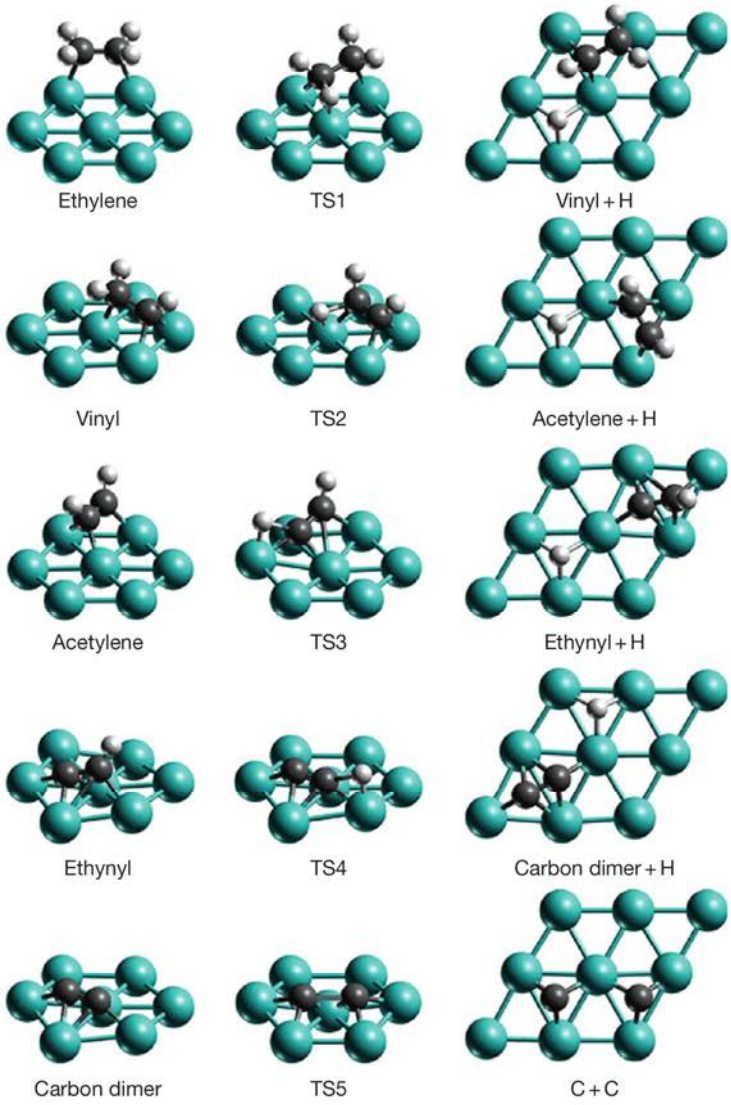

Figure 4 Structures of initial, transition, and final states at 1/9 ML coverage of the model decomposition of ethylene which includes five reaction steps: $C_2H_4 \rightarrow TS1 \rightarrow C_2H_3 + H$, $C_2H_3 \rightarrow TS2 \rightarrow C_2H_2 + H$, $C_2H_2 \rightarrow TS3 \rightarrow C_2H + H$, $C_2H \rightarrow TS4 \rightarrow C_2 + H$, and $C_2 \rightarrow TS5 \rightarrow C + C$ on Pd(111).[93] Reproduced from Basaran, D.; Aleksandrov, H. A.; Chen, Z.-X.; Zhao, Z.-J.; Rösch, N. *J. Mol. Catal. A: Chem.* **2011**, *344*, 37–46, with permission. Copyright 2011 Elsevier.

compared with the other three metals under scrutiny, it would be attractive if this 3d-metal could replace the noble metals as a catalyst in various hydrocarbon transformations including dehydrogenation reactions. However, coke formation on Ni presents a serious problem that significantly reduces its potential applicability in catalytic processes such as hydrogenation and dehydrogenation, stream reforming, and catalytic partial oxidation of natural gas.[44,94] One possibility for improving the coking resistance of Ni-based catalysts is promotion with boron.[95,96]

Finally, it is appropriate to comment on the effect of zero-point energy (ZPE) corrections for the activation barriers, which are central quantities defining the reaction kinetics. In general, ZPE corrections are found to be not very sensitive to the metal and to moderately reduce the barriers: for C—H bond breaking by ~10–15 kJ mol^{-1} on Pd(111),[87] Ni(111), and Pt(111)[97] and up to 18 kJ mol^{-1} on Rh(111)[85]; for C–C scission barriers the corrections are even smaller, 5–8 kJ mol^{-1}.[87]

7.18.2.2 Hydrogenation of Alkenes

Hydrogenation of the C═C double bond is a very important reaction with various applications in petrochemistry, synthesis of fine chemicals, food chemistry, etc.[45] The Horiuti–Polanyi model is generally accepted to describe olefin hydrogenation.[98] According to this model, hydrogenation reactions of the double C═C and triple C≡C bonds proceed in a stepwise fashion via a series of consecutive additions of H atoms.

The process was demonstrated to crucially depend not only on the presence of adsorbed hydrogen species but also on the presence of H absorbed in the subsurface region of the TM catalyst.[99,100] It was found experimentally[101] that the first

hydrogenation step of ethylene, to form ethyl, on Pd(111) surface is characterized by a higher activation barrier than that for the second step, ethyl to ethane. A more recent molecular beam investigation of *cis*-2-butene hydrogenation on a supported NP catalyst Pd/Fe_3O_4,[102] however, indicated the activation barrier for the second step to be rate limiting. The argumentation behind this claim was based on the observed in the latter work increase in the butane formation rates with temperature despite of the concomitant decrease in the concentration of the butyl intermediate. The slow part could be either butyl hydrogenation to butane itself or the activation of H atoms diffusion between the surface and the subsurface regions of Pd. However, the available experimental results do not directly confirm any of these scenarios. It was found that when ethylene hydrogenation reaction occurs on NPs or rough surfaces, low-coordinated sites are crucial for the efficiency of hydrogenation.[103] Apparently, theoretical calculations are required in order to clarify some of the above-mentioned experimental observations.

7.18.2.2.1 Hydrogenation of ethylene

Hansen and Neurock carried out kMC studies of ethylene hydrogenation to ethane on Pd(100).[68,69] In their reaction diagram with the energies of initial, transition, intermediate, and final states, determined from their own DFT calculations and literature estimates, both reaction steps have very similar barriers of $\sim$60 kJ mol^{-1}. Using their database, they simulated apparent activation barriers and kinetic reaction orders in close agreement with experimental results and found that those quantities were significantly affected by lateral surface interactions.

Cluster and periodic slab models of the Pd(111) surface were employed by Neurock and van Santen in order to investigate ethylene hydrogenation on Pd(111).[104] At low surface coverage, they found the barriers for the first and second hydrogenation steps to be again essentially the same, $\sim$70 kJ mol^{-1}, while the reaction energies of both steps were found to be near zero.

Ten years later, ethylene hydrogenation to ethane on the Pd(111) surface was also studied theoretically by Moskaleva et al.,[67] Garcia-Mota et al.,[105] and Tiruppathi et al.[106] using periodic DFT calculations with advanced models and improved computational strategies. These more recent calculations revealed that the barrier for ethylene hydrogenation to ethyl strongly depends on the coverage and increases with decreasing the coverage – 64 kJ mol^{-1} (1/3 ML),[67] 71 kJ mol^{-1} (1/4 ML),[105] 85 kJ mol^{-1} (1/9 ML),[67] and 93 kJ mol^{-1} (1/16 ML).[106] (All barriers in this paragraph are for the hydrogenation of di-σ-ethylene; the values for π-ethylene are similar.[67]) In agreement with experiments by Stacchiola et al. using Pd(111),[101] theoretical works found that the second hydrogenation step has a lower barrier than the first one. The former was calculated to be 44 kJ mol^{-1} (at 1/4 ML)[105] and 51 kJ mol^{-1} (at 1/3 and 1/9 ML),[67] and it became as high as 77 kJ mol^{-1} at 1/16 ML coverage.[106] The reason for the notable difference in the results for this barrier in Moskaleva et al.[67], Garcia-Mota et al.,[105] and Tiruppathi et al.[106] is not clear, since details for the located TS structures are not provided. The change of barrier heights could be either due to a large difference in the TS structures or due to the different initial state structures used in different studies.[107] The three studies also found that the first hydrogenation step is endothermic by up to 44 kJ mol^{-1}, depending on the coverage, while the second step is exothermic by 20–37 kJ mol^{-1}.

The calculations reviewed above provide a realistic picture of ethylene hydrogenation on Pd(111) only assuming a very low H coverage, when ethylene most readily transforms to ethylidyne (see Section 7.18.2.1.1). Under 'real' catalytic hydrogenation conditions, however, various additional factors can influence the kinetics and thermodynamics of alkene hydrogenation, for example, a high amount of adsorbed hydrogen (on the surface itself and in the subsurface area), the presence of additional alkyl groups in the case of larger alkenes, nanostructuring effect (the influence of low-coordinated sites), and the co-presence of various surface (ethylidyne, vinylidene) or subsurface (carbon) modifiers. Tiruppathi et al.[106] considered the influence of subsurface H on the kinetics and the thermodynamics of ethylene hydrogenation. It was found that in the presence of subsurface H, the barriers of both the first and the second hydrogenation steps were lowered by $\sim$25 kJ mol^{-1} and both reaction steps became more exothermic. Somewhat unrealistic in their models was the saturation of the subsurface area by H atoms, while the surface H coverage was assumed low. However, when hydrogen is dosed on Pd, first Pd surface becomes densely covered by H and only after that H starts to penetrate in the subsurface region, this process being thermodynamically driven.[108,109] Hence, it would be more instructive to investigate a balanced combination of surface and subsurface H coverage together. The influence of subsurface C was also addressed in the same publication[106] and its presence was found not to affect the first hydrogenation barrier but to lower the second one by almost 30 kJ mol^{-1}. It was further shown that subsurface C decreased the binding energy of ethylene, which is important for the selective hydrogenation of acetylene to ethylene (see Section 7.18.2.3).[105,106]

On Pt(111), just a slightly larger barrier for the first hydrogenation step of ethylene was found, 108 kJ mol^{-1}, than for the second one, 98 kJ mol^{-1}.[84] This tendency toward a higher first hydrogenation barrier is more pronounced on the stepped Pt(211) surface, where the barrier for the first hydrogenation step, 102 kJ mol^{-1}, is 16 kJ mol^{-1} higher than for the second one.[84] Despite hydrogenation barriers being higher on Pt(111) than on Pt(211), reactions are less endothermic on Pt(111), 30 and 46 kJ mol^{-1}, than on Pt(211), 60 and 78 kJ mol^{-1}, for the first and second hydrogenation steps, respectively. The DFT-predicted barriers for hydrogenation of ethylene on Pt(111) are higher than those on Pd(111) discussed above. This is in agreement with experimetal[57,54,110] and kMC[74] data, indicating that hydrogen atoms produced during ethylene conversion to ethylidyne react to ethane rather than form H_2 on Pd(111), while the situation on Pt(111) is reversed and H_2 is formed easier than C_2H_6.

7.18.2.2.2 Hydrogenation of larger alkene molecules

For larger alkenes, such as 2-butene, hydrogenation and isomerization processes compete with each other.[100,102] Belelli et al.[111] studied the hydrogenation of *cis*- and *trans*-2-butene, as well as their isomerization on the Pd(111) surface, using periodic DFT slab calculations. They found that the alkyl intermediate for *cis*-2-butene hydrogenation is less stable than that for *trans*-2-butene by $\sim$40 kJ mol^{-1}. The addition of the first H atom was calculated to be rate limiting, with barrier heights around 60 kJ mol^{-1}. This finding contradicts with the already-mentioned experimental results of Ludwig et al.[102] which may

be an indication that some other factors, such as (sub)surface hydrogen coverage and defects, can influence the hydrogenation barriers of larger alkenes. The activation barrier for *cis*- to *trans*-2-butene isomerization is found to be as low as 11 kJ mol^{-1} but it should depend significantly on the hydrogen coverage.[111]

Selective isomerization of *trans*-olefins to their less thermodynamically favorable *cis*-counterparts is a very important process with many applications in the food industry,[112] the manufacturing of vitamins,[113] etc. It was found to occur on the Pt(111) surface, whereas the selectivity is reversed on more open Pt surfaces.[114] DFT calculations performed in that work suggested that an extra stability of *cis*-olefins on hydrogen-saturated Pt(111) surfaces may be due to a lesser degree of surface reconstruction, a factor found to be significant in the adsorption on close-packed Pt surfaces.

Industrially produced butene usually contains butadiene impurities,[46,115,116] which should be partially hydrogenated to obtain pure butene necessary for polymerization processes. Usually Pd[46,116] and Pt[115,116] catalysts are used for partial hydrogenation of butadiene and the selectivity is significantly higher in the case of Pd. Valcarcel et al.[117] investigated the hydrogenation of 1,3-butadiene on both metals using DFT calculations and slab models. **Figure 5** summarizes the hydrogenation reaction network of 1,3-butadiene to C_4H_8 species – butan-1,3-diyl, butan-1,4-diyl, 1-butene, and 2-butene.

According to **Figure 5**, 1-butene and 2-butene can be formed via 1–2 or 1–4 attack of 1,3-butadiene by H atoms. The 1–3 (or 2–4) attack leads to a diradical species, butan-1,3-diyl, which is very unstable in the gas phase.[117] This diradical is strongly stabilized by interaction with metal surfaces (especially, Pt(111)). Calculations[117] also revealed that on Pt, the pathway toward butan-1,3-diyl radical is competitive with those leading to butenes. The formed butene will desorb when butadiene is present in the gas phase, since the adsorption of butadiene is preferred by more than 60 kJ mol^{-1}. The diradical species will be further hydrogenated, leading to the formation of a side product, butane, thus lowering the selectivity to butene. This is in good agreement with the partial selectivity (60%) toward butene observed on Pt(111) and with the appearance of butane right from the beginning of the reaction.[118]

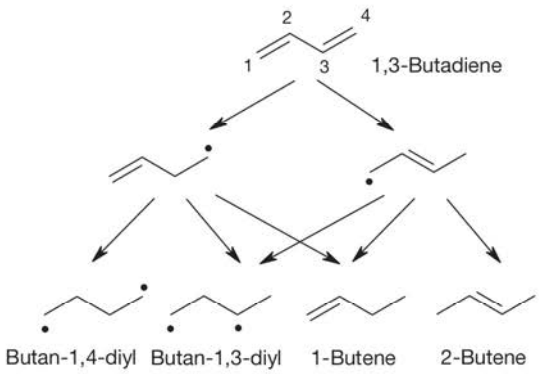

Figure 5 Hydrogenation of 1,3-butadiene to C_4H_8 species via the Horiuti–Polanyi mechanism.[117] Adapted from Valcarcel, A.; Clotet, A.; Ricart, J. M.; Delbecq, F.; Sautet, P. *J. Phys. Chem. B* **2005**, *109*, 14175–14182, with permission. Copyright 2005 American Chemical Society.

The situation on Pd(111) is different: the pathway toward butan-1,3-diyl radical is not favorable, since the TS energy for its formation is ~40 kJ mol^{-1} higher than that for the formation of 1-butene. Hence, in agreement with experimental data,[116] the calculations[117] predicted a full selectivity to butene on Pd(111) and that the pathway to 1-butene involves lower activation barriers than the paths to 2-butene on both metals.

Recently, Delbecq et al.[119] have shown theoretically that the hydrogenation of 1,3-butadiene on Pt_2Sn/Pt(111) can occur via a mechanism different from the commonly accepted Horiuti–Polanyi one: instead of hydrogenation of a fully adsorbed butadiene molecule, the latter can first partially desorb from the surface by detachment of one of the C=C groups, whereby the activation barrier for the hydrogenation of the latter reduces by 19 kJ mol^{-1} (**Figure 6**).

7.18.2.3 Partial Hydrogenation of Alkynes

Ethylene used for polymerization processes typically contains 1% of acetylene, which can poison the polymerization catalyst.[120] In order to prevent catalyst deactivation, concentration of acetylene needs to be lowered to <5 ppm by volume.[47,121] One method to achieve this is the selective hydrogenation of acetylene to ethylene, which also enhances the amount of ethylene feedstock.[122] This process requires highly optimized catalysts that are very selective, since any ethylene that is hydrogenated together with the acetylene results in losses.

Palladium-based catalysts modified with other metals are often used industrially, for example, Pd–Ag alloys are widely used,[123] and also less often Pd–Au,[124] Pd–Ga,[125] Pd–Pb,[126,127] and Pd–Zn.[128] Among the main factors determining the

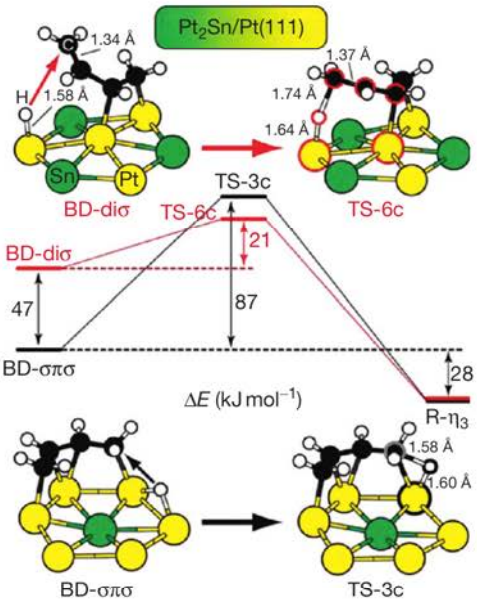

Figure 6 Hydrogenation of butadiene on Pt_2Sn/Pt(111) from the adsorbed (BD-σπσ) or partially de-coordinated (BD-diσ) butadiene reactant, via a three-center transition state (TS-3c) or a six-center one (TS-6c), forming 2-butenyl in an η_3 mode (R-η_3).[119] Reprinted from Delbecq, F.; Loffreda, D.; Sautet, P. *J. Phys. Chem. Lett.* **2010**, *1*, 323–326, with permission. Copyright 2010 American Chemical Society.

selectivity are the adsorption energies of ethylene and acetylene. For instance, periodic DFT slab-model calculations permitted to establish and quantify the effects of alloying Pd with Ag on the binding energies of various C_1H_x and C_2H_y ($x=0$–3, $y=0$–6) intermediates and to determine the overall hydrogenation reaction energies for these intermediates.[129] It was found that, due to both electronic and geometric effects, addition of Ag to a Pd(111) surface weakens the binding energies for all considered intermediates – the binding becomes progressively weaker with increasing of the surface Ag content. The weaker the adsorption of ethylene, the more selective the catalyst should be. On the other hand, weaker adsorption of acetylene should make the catalyst less reactive. Hence, one needs to search for a balance: the best catalyst will be a compromise between the selectivity and activity.

This idea was exploited by Studt et al.[14,130,131] in their search for new potentially selective catalysts. The adsorption energies of acetylene and ethylene were found to scale linearly with the carbon–metal bond energy, represented by the adsorption energy of CH_3 on the corresponding metal surface as a descriptor. Using this strategy, the authors were able to identify Ni–Zn alloys as a new promising cheap catalyst. Indeed, this catalyst was then experimentally confirmed to be significantly more selective than the pure Ni catalyst.[131] Recently, it was also shown theoretically that doping of Ni with Au and Ag should enhance the selectivity of ethylene formation, whereas the selectivities of Cu-doped Ni and pure Ni catalysts are similar.[122]

A similar analysis of ethylene and acetylene adsorption energies was done for Pd systems containing C,[130] used as a catalyst for selective hydrogenation of acetylene.[132] Elemental carbon in a Pd catalyst can originate from the decomposition of C_2H_x species to CH_x ($x=0$–3) at temperatures above 400 K (see **Section 7.18.2.1.2**).[89] The ability of atomic C to migrate from the surface sites on Pd into subsurface or deeper absorption sites is well documented both experimentally[132–135] and theoretically.[27,136,137,138] It was found by DFT calculations that the binding energy of methyl group decreases progressively, when the concentration of subsurface C atoms on Pd(111) increases.[130] This weaker binding of methyl group is indicative of a weaker adsorption of acetylene and ethylene (according to scaling laws, see **Chapter 7.15**) and in general Pd/C systems showed the same scaling as (mono- and bi-) metallic surfaces. It seems that the effect of the subsurface carbon on Pd is comparable to the effect of the addition of Ag to the Pd catalyst.[130]

Studt et al.[14,131] also modeled acetylene and ethylene hydrogenation reactions on Pd(111) and PdAg(111) surfaces. First, acetylene is adsorbed and sequentially hydrogenated to ethylene. Once ethylene is formed, it can desorb or be hydrogenated to ethyl. The competition between the barriers of these two events should determine the selectivity of the catalyst. Both events have comparable barriers on Pd, while on PdAg the desorption barrier is lower, manifesting a higher selectivity of PdAg catalysts in acetylene hydrogenation to ethylene than that of pure Pd.

Another important aspect of selective acetylene hydrogenation is that catalysts should be able to dissociate H_2. For instance, H_2 dissociation on Au, Cu, and Ag has high activation barriers. Depending on the hydrogen coverage the respective activation energies are 95[139]–133,[140] 91,[140] and 71–107[141] kJ mol^{-1}, and the reaction is weakly exothermic for Cu and endothermic for Au and Ag.[140] On the contrary, the activation barrier for H_2 dissociation on Ni and Pd is much lower, ~15–20 kJ mol^{-1},[142] and the reactions are exothermic.[143] The dissociation barrier of H_2 on the alloys between Pt-group and coinage metals depends on the concentration of both metals. For instance, the dissociative adsorption of H_2 becomes less favorable with increasing surface Ag content in Pd.[129] On the other hand, the barriers for the first hydrogenation step of propyne were found to be relatively low, ~75 kJ mol^{-1}, on both Au and Cu.[143] This is due to the weaker adsorbed atomic hydrogen on these surfaces. On Ni and Pd, the first hydrogenation step has notably higher barriers, around 95 kJ mol^{-1}. The second hydrogenation step shows lower barriers in all cases, 58, 39, 87, and 48 kJ mol^{-1} for Au, Cu, Pd, and Ni, respectively. Hence, an optimum balance between the amounts of dopant, such as Au and Cu, on one side and the main component, Pd or Ni, on the other side is needed for reaching desired activity and selectivity of a bimetallic catalyst.

Another way for increasing the selectivity of acetylene hydrogenation is the use of molecular modifiers. One of the most commonly used modifiers is carbon monoxide.[105,144,145] It tends to enhance the selectivity to ethylene and suppress the production of fully hydrogenated species. It was shown[105,144,145] that CO enhances alkene production due to the following effects: the suppression of subsurface H formation; the reduction of the total amount of surface hydrogen; the reduction to almost zero of ethylene adsorption energy on Pd surface while keeping the adsorption energy of acetylene notable, 120 kJ mol^{-1}; and the separation of the reacting alkyne molecules, so that they cannot couple to generate side products, such as oligomers. This effect of CO is reversible, that is, it disappears when CO feeding is stopped.[146]

7.18.2.4 Summary of the Achievements of Theoretical Studies

One of the main goals of theoretical chemistry is to understand complex mechanisms of chemical reactions. In most of the studies addressed in this section, DFT periodic calculations are employed for this purpose to model transformations of hydrocarbons on TM surfaces. In many cases, these calculations have shown very good agreement with available experimental data and have provided crucial complementary information that cannot be derived only by experimental means. The considered surface reactions demonstrated general reliability of the DFT-based computational methods, which decisively help to clarify reaction mechanisms, to delineate the detailed role of the catalyst and its various modifiers, and thus to efficiently assist in searching for novel, improved catalysts. For instance, mechanistic details of ethylene conversion to ethylidyne on Pd(111), Pt(111), and Rh(111) surfaces have been established by means of DFT calculations in combination with kMC simulations. Also, reaction pathways for ethylidyne decomposition have been identified. Furthermore, the roles of bimetallic catalysts, of subsurface C or H atoms or CO modifiers during selective alkyne hydrogenation have been clarified.

The activation energy is a key parameter that controls the rate of each elementary step and ultimately determines the reaction path. Location of TS structures is usually a difficult task, which requires significant computational effort. A significantly less-expensive alternative is the usage of the Brønsted–Evans–Polanyi relationship (BEP).[147,148] It establishes a relationship between a reaction barrier (hence, the reaction kinetic parameters) and the reaction energy (i.e., thermodynamic parameters) by stipulating a linear dependence between these quantities, thus allowing one to estimate barriers from the much easier obtainable reaction energies. In many of the above-mentioned studies, it was found that the BEP approach can be applied successfully.

7.18.3 Decomposition and Steam Reforming of Methanol on Pd, PdZn, and Cu Catalysts

To meet humanity's growing demand for energy in this century, several breakthrough technologies are being developed. One of them, electricity generation using fuel cells, allows efficient (up to 80% including heat utilization)[149] and intensive energy production from hydrogen-rich fuels, such as methane and methanol. The latter is not only bio-renewable but also liquid under ambient conditions, which makes it particularly attractive for application in mobile devices. Molecular hydrogen, which is necessary for many types of fuel cells, may be produced from methanol in the course of two reactions discussed in this section – methanol decomposition and MSR. The former reaction yields as a product CO molecules or carbonaceous deposits, which are detrimental to fuel cell electrodes.[149] MSR, in turn, produces more environmentally friendly CO_2 instead of CO, but only if performed on a highly selective catalyst.

The current section is focused on theoretical investigations of these reactions catalyzed by Cu, Pd, and bimetallic PdZn. Presently, Cu/ZnO catalysts are used industrially for MSR but they are pyrophoric[150] and prone to sintering.[151] At the same time, Cu surfaces were shown to be inactive in complete methanol decomposition (i.e., to CO and H_2), which proceeds on these metals only up to CH_3O or CH_2O.[152,153] Palladium is active for methanol decomposition,[154] but is unselective in MSR.[155,156] Finally, PdZn-based systems (Pd/ZnO[156–158] or Zn/Pd[159]) recently emerged as stable catalysts[160] for MSR. Nevertheless, their selectivity[155,158] strongly depends on the preparation conditions[161] and such subtle characteristics as composition of subsurface layers.[159] A good selectivity of PdZn is often explained by a similarity of its electronic structure to that of selective in MSR copper.[162]

Due to space limitations, this chapter does not describe water dissociation on metal surfaces, which is an important part of MSR. The structure of water–metal interfaces is an extremely intensely studied topic, with many questions yet to be answered.[163–165] This issue is rather complex because of the following considerations: (1) experimental studies are mostly limited to ultra-high vacuum (UHV) and low-temperature conditions, $T < 200$ K; (2) adsorbed water molecules tend to form clusters, which modify their chemical properties[166]; (3) the apparent activation energies of water dissociation may be decreased by up to 50% due to tunneling through the reaction barrier[167]; and (4) the full interplay between methanol decomposition, MSR, and water dissociation may be rigorously considered only via very laborious kMC simulations, which have not yet been accomplished. However, even without taking into account water dissociation on metal surfaces, studies that elucidate activation energies of various elementary steps provide an important insight into methanol transformations on catalytically active surfaces and explain the experimental trends. In general, the dissociation of isolated water molecules is calculated to be slightly exothermic on Cu(111) and PdZn(111), slightly endothermic on Pd(111), and to occur with (classical) activation barriers around 100 kJ mol^{-1}.[166,168]

7.18.3.1 Structure of Pd, Cu, and PdZn Catalysts

Before performing large-scale theoretical studies of a given catalyst, it is important to design an appropriate model reflecting the actual structure of an experimentally prepared catalyst. In the case of monometallic Pd and Cu catalysts, theoretical studies should at least consider which surfaces are present in experiment. For bimetallic PdZn one also has to consider possible variations in local concentrations of one or the other component on the surface (surface segregation) and their relative structural arrangement. There are indications that to model processes on Cu/ZnO catalysts one should also somehow address the influence of the support on the catalyst properties,[169,170] but this issue is still mostly out of the scope of contemporary theoretical studies.

7.18.3.1.1 Structure of monometallic Cu and Pd catalysts

According to thermodynamic considerations, the abundance of different surface planes (or terraces) exposed in experimental samples should be related to their surface energies. Theoretical studies suggest that surface energies of Cu(100), Cu(110), and Cu(111) are quite different, with the ratios $\gamma_{100}:\gamma_{110}:\gamma_{111} = 1.14:1.18:1$.[171] However, all these surfaces were observed experimentally for copper NPs on ZnO.[172] The order of surface stabilities in these experiments was found to be the same, as above but the ratios between surface energies were found to be closer to one, namely, $\gamma_{100}:\gamma_{110}:\gamma_{111} = 1.08:1.11:1$. The ratios were also found to depend on the reaction atmosphere. For example, the presence of water decreases the surface energies differently, by 50–60% depending on the surface type, and makes Cu(110) the most stable.[172] Similarly, adsorbed sulfur was calculated to decrease the surface energies roughly by a factor of 2 and to make again Cu(110) the most stable surface at high S coverage.[173] Thus, for comprehensive theoretical studies of copper reactivity, all three surfaces should be considered.

The ratios between calculated energies of Pd surfaces $\gamma_{100}:\gamma_{110}:\gamma_{111} = 1.11:1.17:1$ suggest that the (111) terraces should be abundant in experimental nanoparticulate samples and also a fraction of the (100) terraces should be present.[171]This was, indeed, observed for Pd NPs deposited on alumina film[174] and on MgO(100) surface.[175,176] Other surfaces of Pd may appear under certain experimental conditions. For example, {112} facets were found to emerge on the NP surface in O_2 atmosphere[175] and {100} facets were bordering Pd nanocubes synthesized in an aqueous solution.[177] Because {111} facets dominate the samples

interface at least in UHV conditions, most of the theoretical studies were performed on the Pd(111) slabs and also on {111} facets of Pd_{79}–Pd_{140} NPs, which allowed one to account for catalyst structure on the nanoscale.

7.18.3.1.2 Structure of bimetallic PdZn catalysts

Unlike Cu and Pd, which have the face-centered cubic (fcc) crystal structure, PdZn crystals have tetragonal CuAu-type structure with measured lattice parameters $a = 288.78$ and $c = 336.22$ pm.[178] This system appears to be an intermetallic compound with a rather strong covalent contribution to the formed Pd—Zn bonds. This is reflected by untypical for common TM bimetallic systems calculated charge redistribution, $Pd^{-0.4}Zn^{+0.4}$,[178] which is supported by a shift of Pd 4d band upon the alloy formation.[162] Theoretically, calculated ratios between energies of PdZn surfaces, $\gamma_{100}:\gamma_{001}:\gamma_{110}:\gamma_{111} = 1.05:1.41:1.34:1$, suggest that (100) and (111) facets should be dominant in nonsingle-crystal samples.[171] However, presently many investigations are performed on ordered PdZn films grown on Pd surfaces by Zn deposition and subsequent annealing. If one deposits Zn on Pd(110) surface the resulting alloy is terminated by PdZn(101),[179] and if Pd(111) is chosen as a substrate PdZn(111) surface is formed.[180] The latter, at 1:1 Pd:Zn stoichiometry, is composed of alternating rows of Pd and Zn atoms with ~25 pm Pd-in/Zn-out corrugation of multilayer surface alloys and none or reverse corrugation of very thin alloys.[181,182] Under MSR conditions, this surface was predicted to be free of adsorbed H, OH, and O.[183] Hence, many of the theoretical studies are performed assuming a bare surface.

7.18.3.1.3 Homotopy in bimetallic PdZn catalysts

Surface segregation, that is, surface enrichment by one or the other component, is a common phenomenon in bimetallic systems, which among other effects governs the catalytic activity of a given surface. Surface segregation in PdZn was calculated to depend on alloy composition and underlying support.[184] In the case of self-supported stoichiometric PdZn alloys, the segregation was found to be energetically unfavorable. At the same time, in Pd_3Zn_1 and Pd_1Zn_3 alloys the prevalent component is prone to segregate to the surface. A similar trend is calculated for stoichiometric PdZn films on Pd(111) and Zn(0001): Pd atoms are more prone to segregate in the Pd-supported film and Zn atoms in the Zn-supported film. This behavior may be rationalized by comparing relative strengths of interatomic bonds estimated to be $E(\text{Pd–Pd}) = 30$ kJ mol^{-1}, $E(\text{Pd–Zn}) = 36$ kJ mol^{-1}, and $E(\text{Zn–Zn}) = 17$ kJ mol^{-1} based on the respective bulk cohesive energies.[184] Because of $E(\text{Pd–Zn}) > \frac{1}{2}E(\text{Pd–Pd}) + \frac{1}{2}E(\text{Zn–Zn})$, the most thermodynamically stable alloy configuration is that with the maximum number of Pd—Zn bonds. Thus, to increase the number of heteroatomic bonds, the less abundant component should migrate to deeper alloy layers. Note that, no surface segregation is predicted for perfectly stoichiometric PdZn alloys.

Even when the ratio between the components on the surface is known, one still has to determine the arrangement of components on the surface (Figure 7). With the help of low-energy electron diffraction (LEED) and scanning tunneling microscopy (STM) studies at room temperature in UHV, the surface structure of PdZn grown on Pd(111) was shown to be alternating rows of Pd and Zn atoms.[180] At the same time, Monte Carlo simulations done with interatomic potentials concluded that at 300 K, due to numerous irregularities, the rows of Pd and Zn atoms should appear as zigzags.[185] Zigzag arrangement of atoms on PdZn/Pd(111) was also suggested in a very recent combined DFT, polarization-modulated infrared reflection absorption spectroscopy (PM-IRAS), and temperature programmed desorption (TPD) study.[186] There, it was found that the considered zigzag-like arrangement is more stable than the conventional arrangement of Pd and Zn atoms in rows in the presence of an overlayer of adsorbed CO. Also, in agreement with PM-IRAS study, CO was found to adsorb preferentially at top sites on the alloy surface with the zigzag arrangement; in agreement with TPD experiments, the saturation coverage of CO on the zigzag structure was calculated to be 0.5 ML. The conventional row structure of PdZn/Pd(111) was calculated to adsorb CO preferentially on the bridge sites with the saturation coverage of 0.33 ML, which was found to be in clear disagreement with experiment. The PM-IRAS study illustrated that the arrangement of atoms on the surface in a bimetallic catalyst (in particular PdZn) is prone to change depending on the reaction atmosphere. However, this phenomenon has not yet been included into consideration in theoretical studies of PdZn activity.

7.18.3.2 Methanol Dehydrogenation

Methanol dehydrogenation, $CH_3OH \rightarrow CO + 2H_2$, which may take place parallel with MSR, is an endothermic process with the reaction enthalpy $\Delta H = 91$ kJ mol^{-1}. In fact, as shown in Section 7.18.3.4, these two reactions have the same rate-limiting steps, methanol dehydrogenation to formaldehyde through CH_3O or CH_2OH. Note that methanol and formaldehyde are

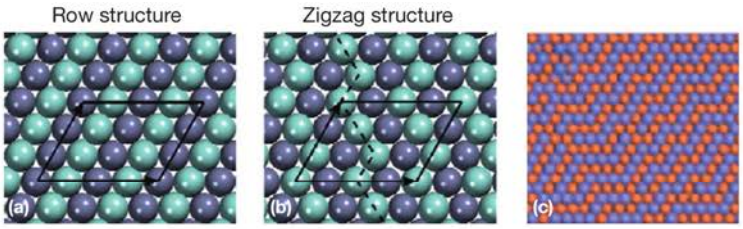

Figure 7 Arrangements of Pd and Zn atoms on PdZn/Pd(111). (a) Row (determined in UHV studies) and (b) proposed zigzag structures. Adapted from Weilach, C.; Kozlov, S. M.; Holzapfel, H.; Föttinger, K.; Neyman, K. M.; Rupprechter, G. *J. Phys. Chem. C.* **2012**, *116*, 18768–18778, with permission. Copyright 2012 American Chemical Society. (c) Results of Monte Carlo simulation based on interatomic potentials at 300 K exhibiting zigzag-like pattern. Adapted from He, X. A.; Huang, Y. C.; Chen, Z.-X. *Phys. Chem. Chem. Phys.* **2011**, *13*, 107–109. Reproduced by permission of the PCCP Owner Societies.

often weakly bound to the metal substrate and may desorb from the surface before reacting. Thus, their adsorption energies are also important to determine the reactivity of a given surface.

7.18.3.2.1 Cu

7.18.3.2.1.1 Cu(111)

Methanol dehydrogenation on Cu(111), $CH_3OH^* \rightarrow CO^* + 4H^*$ (here, stars indicate adsorbed species), is calculated to be endothermic by 222 kJ mol^{-1}.[187] The most stable intermediate of methanol decomposition on Cu(111), the thermodynamic sink, appears to be either the adsorbed methanol molecules or methoxy species, whose stabilities were calculated to be close to each other: $\Delta H(CH_3OH^* \rightarrow CH_3O^* + H^*) = -23$ to 24 kJ mol^{-1}.[187,188] Despite many studies assume the first dehydrogenation step of methanol to methoxy to be fast, its calculated activation energy on Cu(111) is substantial, $E^{\neq} = 103$–135 kJ mol^{-1}.[188–191] This value is much higher than the adsorption energy of methanol on Cu(111), $E^{ads} = 15$–21 kJ mol^{-1},[187,189,192] making its desorption much more likely than dehydrogenation. The activation energy of the second dehydrogenation step of CH_3O to formaldehyde also appears to be high, $E^{\neq} = 112$–178 kJ mol^{-1},[187–191,193,194] and in many studies it is concluded to be the rate-limiting step of the reaction. In Gu and Li[189] also the alternative path of formaldehyde formation through CH_2OH was predicted to be unfavorable due to 12 kJ mol^{-1} higher activation energy of the first dehydrogenation step than in the case of CH_3O path. The barriers for consequent dehydrogenation steps are significantly lower. For $CH_2O \rightarrow CHO + H$ they were calculated[187–189,195] to be $E^{\neq} = 54$–84 kJ mol^{-1} and for $CHO \rightarrow CO + H$ only $E^{\neq} = 17$–31 kJ mol^{-1}.[187,188,195] However, while CHO is a strongly adsorbed species, $E^{ads} = 111$–167 kJ mol^{-1},[187,189,192,195] formaldehyde is prone to desorb,[187–190,192,194–196] $E^{ads} = 1$–17 kJ mol^{-1} before further dehydrogenation. Note that ZPE corrections may lower activation energies of dehydrogenation steps by 15–17 kJ mol^{-1} and the respective reaction energies by 7–11 kJ mol^{-1} (making the reactions more exothermic).[195] All in all, despite certain numerical discrepancies, all DFT studies agree that the rate of methanol decomposition on Cu(111) is limited by the first two dehydrogenations steps. The activation energy of the subsequent dehydrogenation of formaldehyde is significantly lower, which nevertheless greatly exceeds the adsorption energy of formaldehyde on Cu(111) and makes formaldehyde desorb before reacting.[152,153]

7.18.3.2.1.2 Cu(110) and Cu(100)

The reaction profile of methanol decomposition is significantly different on more open Cu(100). First, the barrier of the first step in methanol dehydrogenation is greatly decreased on Cu(100), $E^{\neq} = 33$[197] and 48[198] kJ mol^{-1}, which makes it comparable to methanol adsorption energy, $E^{ads} = 20$[198] and 39[197] kJ mol^{-1} (without taking into account the van der Waals (vdW) attraction) and drastically facilitates the formation of methoxy species. The energy barrier for methoxy dehydrogenation still remains significant, $E^{\neq} = 96$,[198] 133[197] kJ mol^{-1}, so that it is the rate-limiting step of MSR in this case. Another bottleneck of the reaction on Cu(111), formaldehyde dehydrogenation, is again facilitated on Cu(100) by stronger binding of CH_2O. In Schbib et al.[47] the formaldehyde adsorption energy is calculated to be 108[198] kJ mol^{-1} (68 kJ mol^{-1} in Sakong and Groß[197]), which is higher than the barrier of its dehydrogenation from the same study, $E^{\neq} = 86$ kJ mol^{-1}.[198] The last dehydrogenation step of CHO to CO is calculated to proceed with the barrier of only 52 kJ mol^{-1}, that is, much faster than the other reaction steps.[198] Thus, theoretical studies suggest that methanol decomposition to CO is possible on Cu (100) and was calculated to occur in 27 s after methanol deposition at room temperature in an adaptive kMC simulation (**Figure 8**).[198] In agreement with the calculated barriers the rate-limiting step was found to be the dehydrogenation of methoxy species.

Interestingly, even more open Cu(110) is not active in methanol decomposition. On this surface methanol desorption, $E^{ads} = 40$[197] and 53[199] kJ mol^{-1}, is more likely than methoxy formation, $E^{\neq} = 70$[197] and 66[199] kJ mol^{-1}. The barriers for methoxy dehydrogenation are 116[197] and 107[199] kJ mol^{-1}, while that for formaldehyde dehydrogenation, $E^{\neq} = 66$ kJ mol^{-1}, is 16 kJ mol^{-1} higher than the formaldehyde adsorption energy.[199] Thus, on Cu(110) the reaction is limited (but not so severely) by the same bottlenecks as on Cu(111) and proceeds only until the formation of formaldehyde.

7.18.3.2.2 Pd

7.18.3.2.2.1 Pd(111) single crystals

In contrast with Cu surfaces, methanol decomposition is exothermic on Pd(111) slabs by $\Delta H = 135$–251[191,200,201] kJ mol^{-1} (without taking into account reagent adsorption and product desorption). Moreover, the elementary steps of methanol dehydrogenation were found to become more exothermic by 9,[195] 9–17,[201] and 12–35,[202] kJ mol^{-1} if one includes ZPE corrections, which makes the overall reaction more exothermic by 54[201] kJ mol^{-1}. Many studies agree that the first step of methanol dehydrogenation on Pd(111) is C—H bond cleavage leading to formation of CH_2OH, $E^{\neq} = 53$,[189] 118,[202] 133,[200] kJ mol^{-1}. Note that the significant variation of the activation energies is not due to different exchange-correlation functionals (all of these

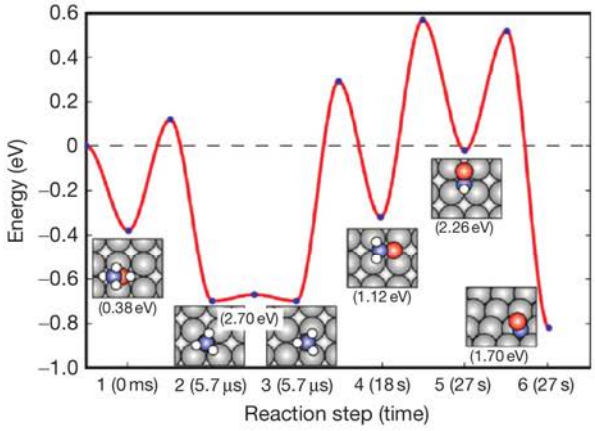

Figure 8 Timeline of methanol decomposition on Cu(100) obtained in the course of Monte Carlo simulation based on DFT-calculated reaction barriers. Energy reference is chosen to be methanol molecule in the gas phase, and adsorption energies of different species are given in parentheses.[108] Reprinted with permission from Xu, L.; Mei, D.; Henkelman, G. *J. Chem. Phys.* **2009**, *131*, 244520. Copyright 2009, American Institute of Physics.

studies used Perdew–Wang 1991 (PW91)[203] one), but probably due to relatively loose force convergence criterion in Jiang et al.[202] and relatively small plane-wave basis set cut-off in Yang et al.[200] (force convergence criteria were not reported). CH_2OH is further dehydrogenated to formaldehyde with moderate activation energies, $E^{\neq} = 67–92$ kJ mol^{-1}.[189,200,202] At the same time, other studies[193–195,201,204] are focused on the dehydrogenation pathway through CH_3O, because methoxy species are experimentally observed on Pd(111) after methanol deposition.[205,206] This discrepancy between theoretical and experimental results was attributed to low methanol coverage in the theoretical studies and to high methanol coverage in the experimental setups.[202] Irrespective of the pathway, the first dehydrogenation barrier appears to be significantly higher than the methanol desorption energy by 29–90 kJ mol^{-1},[189,200–202,207] which means that it is one of the reaction's bottlenecks. When formaldehyde is formed, the further dehydrogenation steps have smaller barriers, up to 51–60 kJ mol^{-1},[195,200–202] which makes these steps significantly faster than the first step of methanol dehydrogenation. The calculated adsorption energies of formaldehyde on Pd(111) are also noticeable 39–52 kJ mol^{-1} (without taking into account vdW attraction),[195,200–202,204] which is only up to 15 kJ mol^{-1} below the respective calculated dehydrogenation barriers. Inclusion of ZPE corrections into consideration again facilitates methanol dehydrogenation on Pd(111) by decreasing the activation energies of the elementary steps by 14–19,[195] 15–22,[201] and 15–24[202] kJ mol^{-1}. Thus, theoretical studies suggest that on Pd(111) the reaction proceeds until the formation of CO, but also many of the adsorbed methanol molecules would desorb before reacting. The reasons for higher activity of Pd than Cu in methanol dehydrogenation are stabilization of CH_2O and CH_2OH on the surface, which facilitates dehydrogenation of weakly adsorbed methanol and formaldehyde.

7.18.3.2.2.2 Scalable with size Pd NPs

The adsorption of various intermediates of methanol dehydrogenation was also considered on truncated octahedral Pd NPs, which belong to the scalable to bulk regime (see Section 7.18.1.2.). Certain species were found to be significantly more stable at the edges between {111} facets than on {111} facets themselves. Species such as CH_3O, CH_2O, and CHO are stabilized on the edges of Pd_{79} NP in comparison with {111} terraces by 46, 50, and 34 kJ mol^{-1}, respectively.[208] However, other species such as CH_2OH on Pd_{79} and CO on Pd_{140} NPs are stabilized on the edges by $\leq$20 kJ mol^{-1}.[208,209] The stabilization of the intermediates in methanol dehydrogenation on the edges may change the reaction energies of various elementary steps by up to 20 kJ mol^{-1} and also change the main reaction pathway from CH_2OH route to CH_3O route, due to significant stabilization of the latter.

7.18.3.2.2.3 Pd(100)

More open Pd(100) surface dehydrogenates methanol significantly faster than Pd(111).[210] The rate-limiting step was found to be methanol dehydrogenation with barriers $E^{\neq} > 94$ kJ mol^{-1} (Figure 9).[210] This barrier height exceeds methanol adsorption energy, which was measured at 45 kJ mol^{-1} [211] and calculated to be $E_0^{ads} = 50$ kJ mol^{-1}.[210] This is in line with the experimental findings that majority of methanol molecules desorb from Pd(100) before dehydrogenating.[211] Nevertheless, the calculated (with the same method) difference between the activation and desorption energies on Pd(111), $E^{\neq} - E^{ads} = 59$ kJ mol^{-1},[202] is larger than that on Pd(100) surface, 44 kJ mol^{-1},[210] explaining the higher activity of the latter. At low temperature, the reaction on Pd(100) proceeds through CH_2OH pathway, but at higher temperatures (500 K) the CH_3O pathway also becomes feasible due to rapid CH_3O dehydrogenation, $E^{\neq} = 35$ kJ mol^{-1}.[210] The adsorption energy of formaldehyde is by 27 kJ mol^{-1} higher on Pd(100) than on Pd(111), which makes its dehydrogenation rate higher than the desorption rate.[210]

7.18.3.2.3 PdZn-based systems

7.18.3.2.3.1 PdZn(111)

It is known that the electronic structure[162] and the catalytic activity[155,158] of PdZn in MSR are similar to that of Cu. Thus, many studies[193,195,204] assumed that the reaction pathway of methanol dehydrogenation is also the same, that is, $CH_3OH \rightarrow CH_3O \rightarrow CH_2O \rightarrow CHO \rightarrow CO$. However, only recently it was theoretically confirmed that CH_3O pathway has activation energy by 32 kJ mol^{-1} lower than the pathway through CH_2OH.[212] The similarity between Cu and PdZn is supported by the calculated activation energies of methoxy dehydrogenation, 113 and 112 kJ mol^{-1}, and formaldehyde dehydrogenation, 78 and 80 kJ mol^{-1}, on PdZn(111) and Cu(111), respectively.[204] However, the reaction energies of these elementary steps are by 36 and 45 kJ mol^{-1} lower on PdZn(111) than on Cu(111) facilitating the dehydrogenation. Also the activation energy of the first step of methanol dehydrogenation is calculated to be only 85 kJ mol^{-1} on PdZn(111)[212] compared to more than 100 kJ mol^{-1} on Cu(111).[189,191] However, the

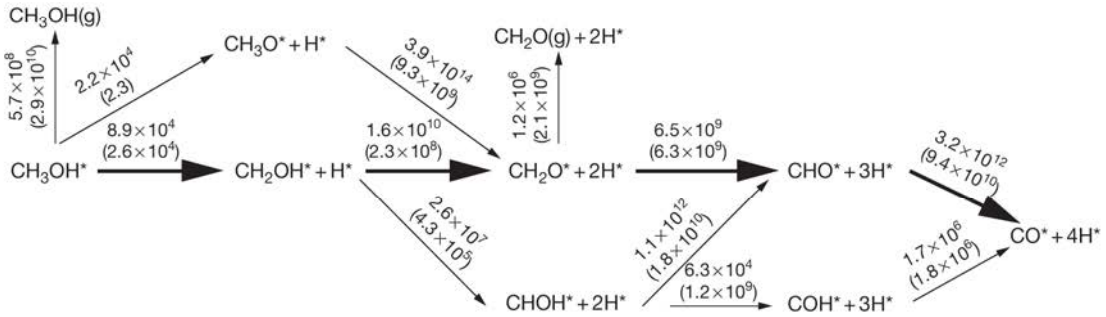

Figure 9 Reaction rates (s^{-1}) of various processes involved in methanol decomposition on Pd(100) and Pd(111) (values in parentheses) calculated based on DFT activation energies and prefactors from harmonic approximation at 500 K. Reproduced from Jiang, R.; Guo, W.; Li, M.; Lu, Z.; Yuan, J.; Shan, H. *Phys. Chem. Chem. Phys.* **2010**, *12*, 7794–7803, with permission from the PCCP Owner Societies.

dehydrogenation barrier of methanol still exceeds its adsorption energy, $E^{ads} = 31$ kJ mol^{-1}.[212] In contrast with the higher catalytic activity of PdZn in the mentioned processes, the final step, dehydrogenation of CHO, has lower activation energy and higher exothermicity on Cu(111) than on PdZn(111), but this step is far from being rate limiting.

7.18.3.2.3.2 PdZn structures on Pd(111)

Some theoretical studies consider ultrathin (up to four atomic layers) PdZn films on Pd(111),[185,186,201] because these systems are experimentally employed for model studies of PdZn catalytic activity.[159,204] The results calculated with VASP package[213] and PW91[203] exchange-correlation functional on bilayer PdZn films on Pd(111)[201] and on PdZn(111)[204] compare nicely to each other, reflecting the similarities of the two systems. For example, the activation energies on PdZn/Pd(111) of sequential dehydrogenation steps $CH_3O \rightarrow CH_2O \rightarrow CHO \rightarrow CO$ (the values calculated on PdZn(111) in parenthesis) were calculated to be 109 (113), 53 (88), and 37 (38) kJ mol^{-1}. The reaction energies of these steps were found to agree within 6 kJ mol^{-1}. Among the reaction steps on PdZn/Pd(111) only methoxy dehydrogenation requires activation energy of more than 100 kJ mol^{-1}, which makes it the rate-limiting step of the reaction. However, like on Cu(111), the activation energy of the first step of methanol dehydrogenation on PdZn/Pd(111), $E^{\neq} = 88$ kJ mol^{-1}, exceeds the desorption energy of methanol, $E^{ads} = 23$ kJ mol^{-1}. The situation is similar for formaldehyde; its adsorption energy, $E^{ads} = 47$ kJ mol^{-1}, is just 6 kJ mol^{-1} lower than the activation energy for the dehydrogenation.[201]

Methanol dehydrogenation was also studied on two-layer-thick PdZn films on Pd(111) with various distributions of Zn atoms among layers.[201] It was found that the adsorption energy of methoxy species roughly linearly increases from 203 to 248 kJ mol^{-1} with increasing Zn content on the surface. Its favorable adsorption site also changes from Pd_3 threefold hollow, to Pd_2Zn and $PdZn_2$ sites on Zn-rich surfaces. In variation, with that the adsorption energies of CH_2O and CHO almost linearly decrease by 14 and 29 kJ mol^{-1} with the growing number of Zn atoms in the subsurface layer. This illustrates that certain adsorbates are sensitive to the surface composition of PdZn (ensemble effect), while others are more sensitive to the structure of subsurface layers (ligand effect). However, no clear trends were observed for the considered activation energies.

If only low quantities of Zn are deposited on Pd(111), clusters made of Zn or Pd and Zn atoms may form on the surface.[185,214] The adsorption energies of formaldehyde on such clusters may exceed 97 kJ mol^{-1},[214] which is in line with the high-temperature peak in TPD of formaldehyde on Pd(111) with deposited 0.03–0.06 ML of Zn.[215] These clusters were found to be inactive in formaldehyde dehydrogenation,[214] which may explain why Pd with small amounts of deposited Zn is not active in formaldehyde and methanol dehydrogenation.[215]

7.18.3.2.3.3 PdZn(100) and PdZn(221)

Only initial steps of methanol dehydrogenation were studied on PdZn(100).[212,216] It was again found that CH_3O pathway of methanol dehydrogenation is preferred to CH_2OH pathway, but both pathways have activation energies >70 kJ mol^{-1}, which exceed the adsorption energy of methanol on PdZn (100), $E^{ads} = 34$ kJ mol^{-1}.[212] The activation energy $E_0^{\neq}$ of CH_3O dehydrogenation on PdZn(100) is also significant, ≥90 kJ mol^{-1}.[212,216]

Only dehydrogenation of methoxy was studied on stepped (221) surfaces of PdZn.[195,204,217] On PdZn(221) terminated by Pd steps the first step of methoxy dehydrogenation proceeds with the activation energy of 68 kJ mol^{-1}, which is in between the values for PdZn(111), $E^{\neq} = 113$ kJ mol^{-1}, and Pd(111), $E^{\neq} = 33$ kJ mol^{-1}.[195,204] However, like on PdZn(111) and on Cu(111), the next dehydrogenation step from CH_2O to CHO is less favorable, $E^{\neq} = 76$ kJ mol^{-1}, than formaldehyde desorption, $E^{ads} = 43$ kJ mol^{-1}. Few reaction steps were also calculated on PdZn(211) terminated by Zn steps.[212,217] Methanol desorption, $E_0^{ads} = 38$ kJ mol^{-1}, was found to be more facile than methanol dehydrogenation, $E_0^{\neq} = 57$ kJ mol^{-1}.[212] Furthermore, the activation energy of methoxide dehydrogenation on PdZn(211) with Zn steps was calculated to be even higher than on PdZn(111).[195] Thus, it was concluded that PdZn is inactive in methanol dehydrogenation irrespective of surface orientation. Hence, the small amounts of CO observed in experiment[218] are attributed to the activity of defect sites in PdZn catalysts.[195]

7.18.3.3 C—O Bond Cleavage in Methanol and Formation of C Deposits

Depending on the catalyst, methanol decomposition may yield not only CO but also atomic C (or CH)[219] as a final product in addition to H_2. The yield of atomic C, which eventually leads to the catalyst poisoning if not removed, is possible if C—O bond cleavage takes place as a side reaction in one of the intermediates on the surface.[219,220] This process was extensively studied on Pd, where C deposits were found to alter the activity of Pd catalysts.[100,132,134] Notwithstanding a special attention that should be devoted to this process, it is still seldom taken into account in theoretical studies.

7.18.3.3.1 Cu

By performing potential energy surface mapping without relying on chemical intuition (by TS search via dimer[221] method starting almost from initial state), it was found that on Cu(110) the cleavage of C—O bond is most likely to occur in adsorbed CH_3O species, $E^{\neq}(CH_3O \rightarrow CH_3 + O) = 161$ kJ mol^{-1} versus $E^{\neq}(CH_3O \rightarrow CH_2O + H) = 107$ kJ mol^{-1}.[199] The difference between activation energies of C—O bond cleavage and dehydrogenation step (or desorption) was calculated to be larger for other intermediates of methanol decomposition on Cu(110). In the case of Cu(100) the breaking of C—O bond is more likely to happen in CH_3O and CHO species with activation energies of 157 and 101 kJ mol^{-1}, which are 62 and 49 kJ mol^{-1} higher than the respective dehydrogenation barriers.[198] On Cu(111) cleavage of C—O bond was calculated only in methoxyde species, which appears to be the most abundant reaction intermediate on the surface.[193] The activation energy of the scission was predicted to be 203 kJ mol^{-1}, that is, 85 kJ mol^{-1} higher than the respective dehydrogenation barrier.

7.18.3.3.2 Pd

C—O bond cleavage in the intermediates of methanol dehydrogenation was studied in detail on truncated octahedral scalable with size Pd_{79} NPs.[222,223] However, the activation energies of C—O bond scission in methoxide, $E^{\neq} \sim 140$ kJ mol^{-1},

calculated using this model are not much different from the values obtained on Pd(111) slabs, $E^{\neq}=146$[193] and 172[207] kJ mol^{-1}. Among all intermediates, the barrier of C—O bond cleavage (in parentheses, in kJ mol^{-1}) was found to correlate with the degree of dehydrogenation and increase in a sequence

$$CH_2OH\ (128) < CH_3O\ (135) < CH_2O\ (194) < CHO\ (206) < CO\ (414)$$

which renders CH_2OH and CH_3O as the most likely candidates for the cleavage.[223] Experimentally it was impossible to determine, in which of the CH_xO intermediates C—O bond dissociation actually takes place.[219]

7.18.3.3.3 PdZn

On PdZn surfaces cleavage of C—O bond was considered only in adsorbed methoxy species by Chen et al.[193,216,217] It was found that among PdZn surfaces the most active for C—O bond scission are (100) surfaces, $E_0^{\neq}=158$ kJ mol^{-1}, while other surfaces, such as PdZn(111) and PdZn(211) with either Pd or Zn steps, exhibited ZPE-corrected activation energies around 210 kJ mol^{-1}. These barriers are at least 70 kJ mol^{-1} higher than methoxy dehydrogenation barriers calculated in the respective studies, which renders C—O bond scission unlikely on PdZn catalysts.

7.18.3.4 Methanol Steam Reforming

MSR, $CH_3OH+H_2O\rightarrow CO_2+3H_2$, is endothermic by 50 kJ mol^{-1}, that is, almost twice less endothermic than methanol decomposition. Nevertheless, this endothermicity may be compensated by adding small amounts of O_2 to the feed (O_2:$H_2O\approx1$:6) and oxidizing methanol (the so-called autothermal reforming).[224,225] Two more reactions may take place on the catalyst surface during MSR: methanol dehydrogenation (described earlier) and water–gas shift reaction. Some of the earlier studies proposed that, on commercial Cu-based catalysts, MSR actually proceeds through sequential methanol dehydrogenation followed by water–gas shift.[226,227] However, more recent studies concluded that methanol dehydrogenation is much slower than MSR and the role of water–gas shift reaction is limited to somewhat shifting the CO/CO_2 ratio toward thermal equilibrium.[225,228] Some other studies also suggested methyl formate as one of the reaction intermediates in MSR, but there still seems to be a lack of definitive evidence.[229,230]

7.18.3.4.1 Cu(111)

All present theoretical studies agree that the first two elementary steps in MSR on Cu(111) are methanol dehydrogenation to formaldehyde.[169,188–190,192] Moreover, one of these steps, methoxy dehydrogenation, is considered to be the rate-limiting step in both methanol decomposition and steam reforming.[231,232] The details of these steps were discussed in Section 7.18.3.2.1.1. Upon formation, adsorbed formaldehyde readily reacts with OH species to form CH_2OOH with activation energy, $E^{\neq}=0$–17 kJ mol^{-1},[188,189,196] lower than the adsorption energy of formaldehyde (some theoretical studies report higher values $E^{\neq}=81$ kJ mol^{-1},[192] and $E_0^{\neq}=73$[192] and 49[169] kJ mol^{-1}). CH_2OOH species then dehydrogenate to CO_2 and H_2 with O—H bond scission taking place in either CH_2OOH or CHOOH.[196] Note that the latter species do not adsorb strongly on Cu(111), $E^{ads}=23$ kJ mol^{-1}.[189,196] Barriers of further C—H bond scissions do not exceed 74–91 kJ mol^{-1},[188,189,196] which are significantly lower than the barriers of rate-limiting steps (methanol and methoxy dehydrogenation) in the respective studies. Barriers of O—H bond cleavage may be significant, but were found to be dramatically reduced, if co-adsorbed OH species are involved, that is, reactions $CH_xOOH+OH\rightarrow CH_xOO+H_2O$ have activation energies less than 15 kJ mol^{-1}.[196] At the same time no promoting effect of OH species on C—H bond dissociation was predicted. Finally, it was recently concluded that methyl formate is an intermediate of minor importance for MSR on Cu(111).[233]

7.18.3.4.2 Pd(111)

Because Pd catalysts are known to produce no CO_2 in MSR,[155,156] there is a lack of systematic theoretical studies of this reaction on Pd surfaces. From the available data it seems that the reaction of formaldehyde with OH group has a higher activation energy, $E^{\neq}=56$ kJ mol^{-1}, than the dehydrogenation of the former, $E^{\neq}=35$ kJ mol^{-1}, making MSR pathway unlikely.[189]

7.18.3.4.3 PdZn(111)

The activity of PdZn(111) in MSR is quite similar to that of Cu (111). Again it is assumed that the reaction proceeds, first, through methanol dehydrogenation to formaldehyde (the rate-limiting part) and then formaldehyde rapidly reacts with OH groups, $E^{\neq}=16$ kJ mol^{-1}, and dehydrogenates further to form CO_2.[234] The dehydrogenation of CH_2OOH may proceed either through CHOOH or through CH_2OO to form CHOO with barriers $\sim$60 kJ mol^{-1} for C—H bond cleavage and $<$35 kJ mol^{-1} for O—H bond cleavage promoted by a co-adsorbed OH group. In the next step CHOO species on PdZn (111) move from the more stable bi-dentate adsorption mode to the mono-dentate one, $E^{\neq}\approx\Delta H=53$ kJ mol^{-1}, and dissociate, $E^{\neq}=36$ kJ mol^{-1}.[234] Similar to methanol decomposition, ZPE corrections decrease activation energies by up to 14 kJ mol^{-1} and change reaction energies by up to 17 kJ mol^{-1}.[234] Note that, the differences between activation energies of the discussed elementary steps on PdZn(111) and Cu(111) surfaces may be as high as 31 kJ mol^{-1}; nevertheless, the activities of these catalysts in MSR are similar because these steps are not rate-limiting ones. Similar to Cu(111), recent theoretical studies showed that methyl formate pathway is unimportant for the reactivity of PdZn(111) in MSR, because methyl formate is more prone to desorb than to react.[235]

7.18.3.5 Concluding Remarks on Methanol Decomposition and Steam Reforming

Methanol decomposition and MSR attract so much attention because of their high yield of hydrogen for environmentally friendly energy generation. These two reactions may take place simultaneously on a catalyst surface and have the same rate-limiting steps: dehydrogenation of methanol to methoxy and subsequent dehydrogenation of methoxy to formaldehyde. Depending on the employed catalysts, formaldehyde species either decompose to CO (decomposition pathway on Pd) or react with OH species and decompose to CO_2 (steam reforming on Cu and PdZn). Thus, the ratio between these two

activation energies (and, to a lesser extent, the adsorption energy of formaldehyde) governs the catalyst selectivity in MSR.

Theoretical studies of methanol decomposition are more abundant than those concerning MSR, for which only the activities of (111) surfaces of Cu, Pd, and PdZn were investigated. More surface types were considered for methanol decomposition. It was found that more open Cu(100), Cu (110), and Pd(100) surfaces are more active than Cu(111) and Pd(111) ones, respectively. However, the desorption of formaldehyde was still predicted to be more favorable than its dehydrogenation on Cu(110) and Pd(100). PdZn(100) exhibits lower activation energy for C—O bond cleavage in adsorbed methoxy than PdZn(111), but the activity of both surfaces in dehydrogenation reactions is quite similar. At variance, stepped PdZn(211) is more active than Pd(111) in dehydrogenation of methoxy, but exhibits similar activation energy for C—O bond cleavage.

7.18.4 Selective Hydrogenation of α,β-UALs on Mono- and Bimetallic Surfaces

Selectivity aspects play a central role in chemistry in general and in heterogeneous catalysis in particular. Indeed, the design of highly selective, active, and long-working catalysts is a major challenge in heterogeneous catalysis. In previous sections, the surface selectivity has been mainly addressed from the viewpoint of a preferred chemical transformation of quite a simple reactant in comparison to its other possible transformation pathways. When several conceivable transformation routes of the same molecule were addressed, their kinetics were usually sufficiently different, in most cases allowing for identification of the main reaction path. The current section is devoted to even more intricate processes, which involve reactants with two conjugated functional groups, C=C and C=O, both of them being capable of competitive (regioselective) transformations over metal surfaces.[236]

Selective hydrogenation of such bifunctional reactants – α,β-UALs – is industrially important for synthesis of unsaturated alcohols (UOLs). These are valuable chemicals for producing perfumes, flavoring materials, and pharmaceuticals. Recently, the similarities between the selective hydrogenation of UALs and the refining of present in biomass unsaturated oxygenates, crucial for production of biofuels, have been reviewed.[19] Surface science experiments and DFT modeling of the selective hydrogenation of UALs, which belong to the best studied multifunctional reactants, provided a firm basis for the knowledge-driven design of more selective catalysts. In the following, the achievements of theoretical chemistry studies in deepening our understanding of this class of reactions are outlined. Also, some limitations in the DFT description of regioselectivity on metal catalysts are addressed.

Three lowest α,β-UALs R′RC=CH–CH=O (see **Figure 10**) have been a subject of theoretical studies of their selective hydrogenation: acrolein (2-propenal, R′=R=H), crotonaldehyde (2-butenal, R=CH_3, R′=H), and prenal (3-methyl-2-butenal, R′=R=CH_3). Transformations of species pertinent to the stepwise gas-phase hydrogenation of acrolein were studied by means of DFT calculations using PW91 functional.[237] In that work, the target UOL CH_2=CH–CH_2–OH was found to be strongly destabilized, by ~80 kJ mol^{-1}, compared to the competing undesired product, saturated aldehyde (SAL) CH_3–CH_2–CH=O. This result, on the one hand, illustrates the difficulty to hydrogenate preferentially the C=O and not the C=C bond in UALs. On the other hand, it shows that the same reaction could proceed completely differently on a metal surface, in which case, unlike in the gas-phase, the selective production of UOLs can be achieved. It is worth noting that, the substitution of the R′=R=H atoms in acrolein by bulkier CH_3 groups in crotonaldehyde and prenal could affect the adsorption geometry of UALs on metal surfaces, for example, by elongating the contacts of the C=C bond with the substrate and thus possibly increasing the selectivity of the heavier UALs toward the target UOLs.

Reviewed below are DFT-based studies performed for the two main types of TM surfaces mediating the selective hydrogenation processes of α,β-UALs (and related molecules). As Pt is widely used to catalyze various reactions of unsaturated hydrocarbons (see **Section 7.18.2.**), one could anticipate its high activity in the hydrogenation of the C=C bonds of UOLs. Indeed, catalytic surfaces based on Pt, which bind pertinent reactants and products quite strongly, belong to the first, most studied type of metal substrates (**Section 7.18.4.1**).[19] In order to partly counteract the too strong binding of the products and to enhance the selectivity, an introduction of a second metal,

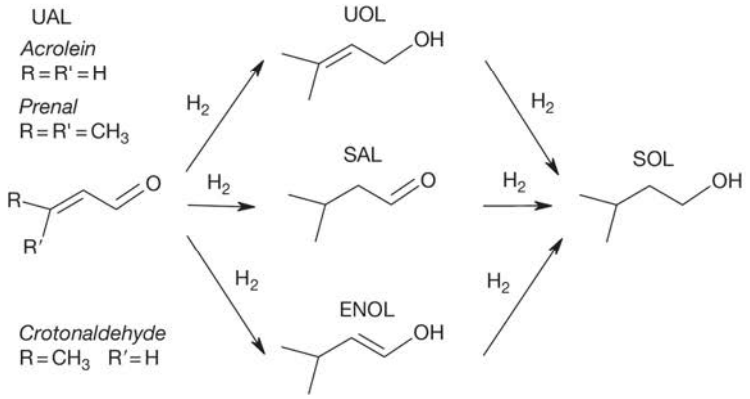

Figure 10 Three lowest α,β-unsaturated aldehydes and products of their hydrogenation.

such as Sn, Ni, Co, or Cu, is often beneficial. The second type of substrates are coinage metals Ag and Au that expose surfaces less conventional for catalytic hydrogenation single-crystal studies, thus showing a somewhat different chemistry.[238]

7.18.4.1 Reactivity of Pt-Based Catalysts

7.18.4.1.1 Pt(111) and Pt(211)

DFT studies of UOLs transformations on the Pt(111) surface were pioneered by Delbecq et al.[239] First, they computed the structures of adsorption complexes of acrolein, crotonaldehyde, and prenal that were assumed to govern the hydrogenation selectivity on Pt(111) surface.[20,239,240] In particular, a stepwise addition of methyl substituents at the C_3 atom of the $C_3{=}C_2{-}C_1{=}O$ frame resulted in consecutively weaker adsorption. Calculated predominant binding of acrolein to the surface via the C=C bond was suggested to explain its experimentally observed preferential hydrogenation. On the other hand, the CH_3 substituents gradually facilitate a detachment of the C=C bond from the surface, thus acting to reduce its reactivity compared to the C=O bond. Furthermore, at high coverage, bulkier prenal molecules were found to be oriented vertically and bound to the surface solely via an O atom, whereas acrolein remained interacting via the C=C bond. Such a vertical structure that should hinder the hydrogenation of the C=C bond was the first tentative rationalization of the more selective surface hydrogenation to UOLs of prenal compared to acrolein, substantiated by first-principles calculations. However, the authors emphasized a possibly important role of co-adsorption of H and of the surface modification by fragmentation products in the course of hydrogenation reactions, thus significantly limiting the predictive power of the adsorption studies on model surfaces, without a detailed direct quantification of competitive reaction routes.[239]

The latter issue became a subject of subsequent publications of the same group.[20,240] There, DFT calculations of elementary reaction steps (including reaction and activation energies) combined with kinetic modeling were performed to comprehensively explore the hydrogenation of acrolein on the Pt(111) surface, which can competitively produce either the target UOL product, propenol, or the undesired SAL, propanal. Note that among the typical UALs, the selective hydrogenation of acrolein to propenol is considered to be most difficult, whereas the overall selectivity of UALs to the UOLs on such representative metal catalyst as Pt is low, around 2% only. The theoretical studies questioned the traditional assumption that, on TM surfaces, the C=C bond of UALs is more reactive than the C=O bond, that is, that the low selectivity to UALs on Pt surfaces originates from the stronger interaction of the C=C group with the metal substrate and its more rapid reaction with surface H than that of its conjugated C=O group. Briefly, according to the results of density functional calculations, the attack of the C=O functional group of acrolein on Pt(111) by H appears to be kinetically favored over the attack of the C=C group, even when the molecule is adsorbed via the latter. The reason for a lower activation barrier is that attack at the atom O by adsorbed atom H involves a remarkable metastable precursor state –CH=O···H, in which the –CH=O group is essentially noninteracting with the surface, other than indirectly via a bond with surface H. This never-before-identified type of adsorption and reaction was described as an intermediate between the Langmuir–Hinshelwood and Eley–Rideal classical schemes. At the same time, the hydrogenation of the adsorbed C=C group takes place via the conventional Langmuir–Hinshelwood mechanism.

Interestingly, these quite counterintuitive findings for the kinetics of the surface hydrogenation steps still nicely agree with the experimental observations of very low yield associated with the target propenol product of acrolein hydrogenation on Pt catalysts. In order to see that, one needs to consider the last elementary step of hydrogenation – the desorption of UOL and SAL.[20,240] Although the former species is rapidly formed on the Pt(111) surface, its calculated desorption barrier is very high, over 100 kJ mol^{-1}, whereas the corresponding SAL, with the desorption barrier only slightly over 20 kJ mol^{-1}, desorbs orders of magnitude faster. Thus, the final yield of UOL appears to be strongly hindered by the desorption step. This implies the existence of opportunities to improve the selectivity toward the target UOL by modifying Pt substrates, so that a more facile desorption of UOL could be enabled (see Section 7.18.4.1.2).

Very recently, the reaction mechanism of crotonaldehyde hydrogenation using a Pt(111) slab model has been investigated theoretically by Hu et al.[241] by means of density functional calculations of Gibbs free reaction and activation energies of all elementary steps in combination with microkinetic modeling. Among the important findings of that work, one should mention that for crotonaldehyde molecule adsorbed on Pt(111) the dominant reaction channel of each considered product starts from the surface hydrogenation of the O atom. Thus, the selectivity is governed by the subsequent hydrogenation steps of C atoms. The similar heights of the calculated activation barriers for the dominant pathways to three conceivable final hydrogenation products of crotonaldehyde on Pt(111) prevent the achievement of a high selectivity toward the desired UOL product.[241] Note that microkinetic analysis combined with the DFT study of partial hydrogenation of crotonaldehyde on Pt(111) surface revealed the importance of ZPE corrections, in particular, for multistep hydrogenation processes.[242]

The importance of low-coordinated Pt active sites for the hydrogenation of acrolein to propenol, propanal, and enol has been studied by density functional calculations on the stepped Pt(211) surface.[243] Different from the fourfold adsorption structure communicated for acrolein on the flat Pt(111) surface,[20,240] acrolein on Pt(221) was calculated to be bound to three Pt atoms of the step edge with $E^{ads} = 157$ kJ mol^{-1}, that is, $\sim$55 kJ mol^{-1} stronger than on Pt(111). This finding implies that the more favorable for acrolein adsorption step site could also be the active site for its hydrogenation on Pt. The three hydrogenation products of acrolein, E^{ads}(propenol) = 140 kJ mol^{-1}, E^{ads}(propanal) = 76 kJ mol^{-1}, and E^{ads}(enol) = 124 kJ mol^{-1}, prefer the adsorption on the step in a di-σ configuration, in line with earlier DFT results.[240] The TS structure of the first hydrogenation step of O atom is calculated to be very similar to that of Pt(111),[20,240] that is, the O atom is lifted from its adsorption position and the reacting H is located on top of the edge Pt atom below O.[243] Overall, even though the formation of adsorbed propenol on Pt(221) was calculated to be more favorable than that of propanal, the reaction barrier of enol formation was found 19 kJ mol^{-1} lower than that of propenol. Because enol is also weaker adsorbed than propenol,

the formation of enol product was concluded to be both kinetically and thermodynamically favored on Pt.

Before closing this subsection, a recent DFT work on selective hydrogenation to UOLs of two α,β-unsaturated ketones, benzalacetone and methyl vynil ketone, on model Pt(111) and Ru(0001) surfaces is worth mentioning.[244] This study was performed in combination with a comprehensive experimental study that also included the hydrogenation of UALs on supported Pd, Pt, Ru, and Au catalysts. In these experiments the Pt and Ru catalysts were able to produce UOLs from UALs but not from unsaturated ketones. The calculations suggested that the observed selectivity over Ru and Pt should be controlled by the significantly higher activation barriers to hydrogenate the C=O bond than the C=C bond. Both primary reaction products, the UOL and the saturated ketone, are strongly bound to Ru and can react to the respective saturated alcohols (SOLs). The calculated lower hydrogenation barriers on Pt compared with Ru are in line with the higher turnover frequencies observed for the hydrogenation on Pt. A bulky phenyl α-substituent at the C=C bond of benzalacetone did increase the barrier for the C=C hydrogenation over that of methyl vynil ketone, but this barrier increase was insufficient to reverse the selectivity ratio in favor of the UOL.

7.18.4.1.2 Bimetallic Pt–M surfaces

As already alluded to above, the reactivity of Pt surfaces toward selective hydrogenation of UALs could be favorably changed by the addition of a second metal M = Sn,[245–248] Ni,[249–251] Co,[251] and Cu.[251] Such an oxophilic modifier as Sn is expected to interact mainly with the O atom and thus to improve the desired selectivity toward UOLs by facilitating activation of the C=O bond. In reality, however, as suggested by recent experimental and theoretical results, the general role of Sn in Pt–Sn surface alloys appears to be different: Sn weakens the adsorption of UALs by favoring the η^1 or η^2 coordination on bimetallic surfaces compared to the stronger adsorbed η^4 binding mode prevalent on Pt(111). Although, on Sn-modified Pt, the η^2-adsorption of crotonaldehyde via a C=O group is still favored over the adsorption via a C=C group,[246,247] the weakened binding of the latter does enhance the selectivity of the C=O hydrogenation by facilitating the desorption of the desired UOL product crotyl alcohol. Notably, there is only very limited Sn-induced change in the adsorption strength of acrolein, the adsorption through the C=C bond being predominant.[245] This rationalizes the only slightly altered selectivity of acrolein hydrogenation on alloyed Pt–Sn compared to pure Pt. For prenal, on the contrary, a parallel to the surface UAL adsorption is favored on Pt but solely the atop mode is formed on the alloys, thus explaining a larger amount of UOL in the products over the Pt–Sn alloys.[245,246]

Chen et al. have investigated acrolein hydrogenation on a variety of Pt-based bimetallic surfaces.[249,250] They observed UHV formation of propenol via acrolein hydrogenation on a Pt/Ni/Pt(111) surface,[249] where Ni prefers to be located in the first subsurface layer, while Pt composes the surface layer. DFT calculations helped to establish that the subsurface Ni layer weakens the binding of adsorbates on the surface and disfavors the adsorption of highly coordinated η^4-acrolein.[252,253] The adsorption of the C=O group was found to become energetically competitive with that of the C=C group. On the other hand, a Ni/Pt(111) surface alloy was observed to strongly adsorb acrolein in an η^4 configuration, with no propenol product detected. The propensity to form propenol was related to the position of the surface d-band center, lying deeper for the Pt/Ni/Pt(111) slab model than for Pt(111) and Ni/Pt(111). This finding suggests the possibility of using the position of the surface d-band center as a parameter to search for other bimetallic surfaces appropriate for catalyzing the selective hydrogenation of acrolein. Furthermore, the surface concentration of co-adsorbed H atoms was concluded to be of major importance for the selectivity and the adsorbed structure of acrolein: adsorption via the C=O group being stabilized when Pt/Ni/Pt(111) surface was covered with H.[249]

These studies have been lately extended to other Pt-3d surface alloys Pt/Co/Pt(111), Co/Pt(111), Pt/Cu/Pt(111), and Cu/Pt(111),[251] which also revealed an enhanced propenol yield compared with Pt(111), though the propenol production was higher on Pt/Ni/Pt(111). DFT calculations suggest that the different hydrogenation activities of the subsurface and the surface structures could be related to the differences in the binding energy of acrolein on the corresponding bimetallic surfaces. Overall, these investigations corroborate the usefulness of the strategy to weaken the binding of UALs on Pt-based surfaces by alloying with 3d TMs in order to enhance the selectivity of UOL formation.

7.18.4.2 Reactivity of Catalysts Based on Coinage Metals

Pt is a well-known hydrogenation catalyst. Thus, it is not particularly surprising that the just overviewed Pt-based systems are used for the selective hydrogenation of UALs with the conjugated C=C and C=O bonds.[18] By contrast, coinage metals Ag and Au exhibit in general a considerably lower reactivity than Pt and many other TMs. Among the few catalytic applications of Ag, and, more recently, of nanoparticulate Au, are oxidation reactions. Remarkably, supported Ag and Au NPs have also been found experimentally not only active but also very selective (Ag: 42%[254]; Au modified by In: 63%[255]) in the hydrogenation of UALs.[236,238] In the following, insights from published DFT studies aimed to clarify the factors affecting the catalytic function of Ag and Au in hydrogenation of UALs are summarized.

7.18.4.2.1 Ag(111), Ag(110), and Ag(221)

The experimentally identified key features of UALs hydrogenation on supported Ag catalysts are[256] (1) UOLs are not observed below a threshold pressure of ~100 mbar; (2) the presence of defects significantly improves the selectivity to UOLs, which is <10% over bulk Ag materials; (3) the activity depends on the number of (possibly electron-deficient) sites that can activate H_2; and (4) O incorporated in Ag catalysts in the reaction course promotes H_2 activation and increases both the activity and the selectivity of UALs hydrogenation.[21] The state of the catalysts was noticed to depend on the reaction conditions, for example, oxygen pre-treatment improves the activity and selectivity of Ag/SiO_2 catalysts to UOLs.[257] This dependence of the reactivity on catalyst preparation conditions makes the task of establishing structure–reactivity relations very challenging.

In fact, the activity of even clean Ag surfaces appears to be surprising because of the weak adsorption of UALs[258,259] that hardly weakens the C=C and C=O bonds and because of the low probability to activate H_2 revealed by experimental[260,261] and theoretical[262–265] studies. The dissociation of H_2 on clean Ag surfaces is calculated to be endothermic, although such an absolutely O-free silver surface may be difficult to obtain in practice.[261] The presence of oxygen can make the dissociation of hydrogen exothermic,[141] which agrees with the experimental observation of H_2 dissociation on silver catalysts.[261]

Recently, DFT investigations demonstrated how different forms of oxygen on silver surface can lower the activation barrier for the dissociative adsorption of H_2 and render the dissociation strongly exothermic due to very stable products formed.[264,265] Not only water and OH groups but also active (atomic) hydrogen species can be formed when H_2 reacts with an oxygen-modified Ag surface.[264]

Neyman, Rösch et al. performed a comprehensive DFT study of the mechanisms of selective hydrogenation of UALs on silver catalysts, focusing on the description of bulky catalyst particles modeled by the two limiting situations – the regular clean Ag (110) surface and the O_{sub}/Ag(111) surface with incorporated subsurface oxygen atoms.[21] Acrolein was considered as a representative reactant. Reaction and activation energies of numerous elementary steps involved in the hydrogenation of acrolein on the two model silver surfaces were quantified and the structures of the corresponding surface complexes were optimized and analyzed (see **Figure 11**). Acrolein was found to be much weaker adsorbed on Ag surfaces, $E^{ads} < 20$ kJ mol^{-1},[21] than on Pt-based catalysts, where the calculated adsorption energies were up to 100 kJ mol^{-1}.[239] This difference is emphasized because the strength of interaction and the adsorption mode are considered important for the hydrogenation selectivity. The calculations implied that on the Ag(110) surface the undesired product, propanal, should be prevalent. On the contrary, the O_{sub}/Ag (111) model system revealed a very high selectivity to the desired allyl alcohol, although its activity was predicted to be lower than that of clean Ag. At variance with Pt(111), where the selectivity of UOLs is greatly decreased by the high adsorption energy of the latter, both allyl alcohol and propanal products are calculated to be easily desorbed from the Ag(110) and O_{sub}/Ag(111).

The DFT results yielded a low selectivity for allyl alcohol on the regular Ag(110) surface (<9%), in good agreement with the experimental data for bulky silver catalysts, which also point to a low selectivity of ~10%.[256] In the case of O_{sub}/Ag (111), calculations predicted a very high selectivity, ~90%. This provided a rationalization to the experimentally observed selectivity enhancement toward propenol on Ag catalysts after pretreatment with O.[256] Of conceptual importance for estimating the overall reliability of the theoretical analysis of regioselectivity in catalysis are the following considerations.[21] Due to inherent DFT and surface model approximations, even relative reaction and activation energies are expected to be calculated with a precision of at most 5–10 kJ mol^{-1}. Altering the calculated barriers by 5–10 kJ mol^{-1} would strongly affect the resulting selectivity. For instance, lowering the barrier for the step H→C1 of acrolein hydrogenation on the Ag(110) surface (**Figure 11**) by 10 kJ mol^{-1} would increase the selectivity to allyl aldehyde from 9% to 47%.[21] This example illustrates how

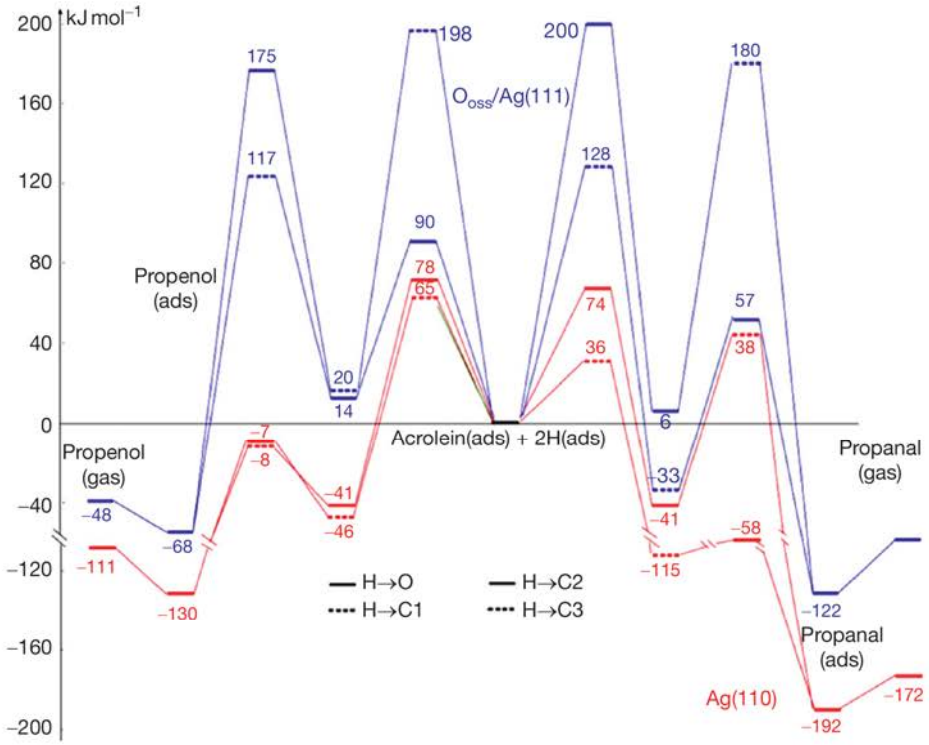

Figure 11 Comparison of reaction profiles of the partial hydrogenation of acrolein (C3=C2–C1=O) on model surfaces Ag(110) and O_{sub}/Ag(111) from DFT calculations.[21]

the limitations of contemporary first-principles approaches, for example, lacking dispersive components of the interactions in common exchange-correlation density functionals, as well as usual oversimplification of the catalyst active sites in the model calculations can prevent a quantitative description of the chemo-selectivity of reactions with comparable rates.

It was concluded[21] that more theoretical and experimental work is required for building a detailed enough microscopic picture of the unusual hydrogenating activity of silver catalysts. In particular, deeper insights are expected from further improving the still rather limited understanding of the nature of surface sites capable of delivering atomic H as well as from identifying those catalyst sites (possibly, low-coordinated) that are directly responsible for the hydrogenation steps. Also, the selectivity of acrolein hydrogenation to propenol on supported Ag catalysts under high-pressure conditions is known to be significantly higher than that of the low-pressure process on single-crystal Ag surfaces.[254] Thus, one should be cautious about the material and pressure gaps when comparing UHV surface science results with those for supported catalysts obtained at ambient conditions.

7.18.4.2.2 Au

Oxide-supported gold NPs were also shown to catalyze the hydrogenation of UALs to UOLs.[236,238] Acrolein was found experimentally to be transformed to the desired product allyl alcohol mainly on low-coordinated (edge and possibly corner) sites of Au NPs, whereas the {111} and {100} facets of the NPs were concluded to be active in the preferrential production of propanal.[255] It was also demonstrated there that the selectivity of acrolein hydrogenation to allyl alcohol can be significantly, up to more than 60%, enhanced by indium additives to the above-mentioned gold catalysts. This was rationalized by the blocking effect of less selective terrace sites by In atoms, thus efficiently forcing the hydrogenation to take place on the more selective sites at NP edges. However, a recent DFT study[266] questioned this interpretation. There, acrolein adsorption and the subsequent hydrogenation were modeled on the pure and decorated by indium Au(110) surfaces, employing a Au_{20} particle to represent edge sites of the metal substrate. The calculations corroborated preferential location of In admixtures in the surface plane of Au terrace sites. Nevertheless, the calculated activation barriers revealed that the hydrogenation of the C=O bond should be facilitated compared to that of the C=C bond on both the Au(110) and the Au–In(110) surfaces. According to the interpretation of He et al.,[266] due to the strong In–O interactions, the presence of In significantly strengthens the adsorption of acrolein on the Au–In(110) surface, which leads to higher concentration of acrolein at terrace sites, where the hydrogenation of the C=O group is favored, and concomitantly reduces the accumulation of this reactant at edge sites, more active in the hydrogenation of the C=C bond.

7.18.5 Toward Green Chemistry: CO Oxidation on Nanoporous Au and the Role of Ag Residues

Au-based oxidation catalysis is attracting continuously growing interest at present,[267,268] especially in the context of industrial sustainability,[269] which implies the development of more efficient processes operating under milder reaction conditions (thus reducing energy consumption) and using cleaner and safer technologies. Metallic gold was for a long time considered inert until the discovery by Haruta et al.[270] that supported Au NPs can be very active in aerobic oxidation reactions, that is, using air or molecular oxygen as oxidant. In contrast to supported Au NPs, whose inherent tendency to sinter limits their practical applications, nanoporous Au (np-Au), also referred to as gold sponges or foams, is a different form of a nanostructured Au catalyst – a monolithic high-surface-area material. Np-Au manufactured by selective dealloying of Au/Ag alloys[271,272] presents an attractive alternative to Au NP-based catalysts and is therefore expected to have a high impact on improving the sustainability of chemical production and on 'green' chemistry. For instance, np-Au was shown to be a quite effective catalyst for the aerobic oxidation of methanol to methyl formate[273] and of benzyl alcohol to benzaldehyde[274] as well as for the oxidation of organosilanes with water.[275] This nanostructured catalyst holds additional advantages owing to its easy preparation, handling, recovery, and recycling. Aside from potential practical applications, np-Au seems to be a perfect target system for fundamental studies of intrinsic catalytic properties of nanostructured gold, owing to the absence of oxide support.

7.18.5.1 Surface Ag Atoms and O_2 Activation on Model Single-Crystal Au Surfaces

Catalytic activity of Au NPs and nanostructured Au, in general, has been often connected to the nature of surface metal atoms, many of which are under-coordinated.[276,277] Direct or indirect promoting role of the oxide support has been discussed in connection to the activity of Au NPs[278] but is excluded for unsupported np-Au catalysts. For the latter, trace amounts of Ag still remaining in the material after dealloying could be an additional factor probably responsible for the high catalytic activity toward oxidation reactions.[271,279] In computational modeling of monolithic catalysts such as np-Au, well-defined stepped surfaces seem to offer a good model for studying the mechanistic details of Au oxidation catalysis at the atomic scale. Reviewed below are theoretical studies relevant to dissociative adsorption of moleclular oxygen on several single-crystal Au surfaces and to the reaction of atomic oxygen with CO.

Gold single-crystal surfaces are known to be chemically inert. There is a general consent that the catalytic activity of gold single crystals in aerobic oxidation reactions is hindered by the low adsorption energy of O_2 and by a relatively high barrier for O_2 dissociation even at stepped Au surfaces, which expose under-coordinated Au atoms (with coordination numbers 6 or 7). Molecular oxygen does not bind to the flat Au(111) surface according to theoretical[280–282] as well as experimental[283] studies. Weak binding of O_2 on steps of Au (211),[281] Au(221),[282] and Au(321),[284,285] with adsorption energies between 5 and 16 kJ mol^{-1}, was predicted from DFT calculations. The calculated high barrier for O_2 dissociation, at least 90 kJ mol^{-1},[281,284,285] suggests that the dissociation even at stepped surfaces should be difficult at room temperature. This is in agreement with experimental studies, showing that

neither the stepped Au(211),[286] Au(310),[287] and Au(755)[288] surfaces nor polycrystalline surfaces[289] are able to dissociate molecular oxygen even at high pressure conditions. By contrast, Au substrates with pre-adsorbed atomic oxygen using, for example, oxygen sputtering, can become very reactive.[290–293] Different from extended Au surfaces, supported Au NPs do not require pre-adsorption of atomic O to become active catalysts at ambient temperature; in other words, they are able to activate molecular oxygen chemically. This marked contrast to Au single crystals has been attributed not only to the small size and abundance of under-coordinated metal centers in Au NPs but also to the direct or indirect involvement of the oxide support. Remarkably, O_2 can also be activated on nanoporous gold foams (with no oxide support present) which is evident from pronounced catalytic activity of np-Au toward aerobic oxidation reactions.[271–274]

Undeniably, the question of whether indeed pure gold can be catalytically active is central to gold catalysis. This is why recent reports on the catalytic activity of unsupported gold systems (including np-Au as well as specially prepared Au powders and nanotubes[279,294–296]) have stirred some controversy and triggered discussions in the literature.[271,297–299] Apparently, these findings suggested that the activity of nanostructured gold should mainly come from a special nature of Au atoms in these catalysts, such as the high fraction of low-coordinated Au atoms or a change in the electronic structure of gold. On the other hand, some of the authors have noted[279,294] that trace amounts of a second metal (silver or copper, perhaps in the oxidized form) present in all unsupported Au catalysts as a result of their manufacturing could play a role in the activation of O_2. The latter hypothesis was also supported by reports[294,300,301] showing a strong influence of Ag content in Au–Ag particles of submicron size on their catalytic activity. Very recently, Rousset and coworkers reported a synthesis of extremely pure nanoporous gold using a different manufacturing process starting from Au–Zr intermetallic alloy via a mild oxidation (by air at room temperature) and subsequent dissolution of zirconia in HF.[299] This material showed very poor catalytic performance toward CO oxidation. Strikingly, the activity increased by some orders of magnitude, when analogously prepared np-Au contained just 2 atom % Ag. Hence, these recent findings further support the crucial role of Ag impurities for the catalytic activity of np-Au.

Moskaleva et al.[284] discussed the role of Ag in facilitating the dissociation of molecular oxygen using periodic DFT approach along with the GGA-PBE functional and employing the kinked Au(321) surface as a model. The authors substituted two to eight Au atoms at the O_2 binding site with Ag, corresponding to surface Ag concentrations of 20–80 atom %, and analyzed the change in the binding energy and O_2 dissociation barrier (**Figure 12**). It was shown that the replacement of only up to three Au atoms with Ag did increase the magnitude of the binding strength of O_2 to about 30 kJ mol^{-1}; however, the O_2 dissociation barrier remained above 100 kJ mol^{-1}. A replacement of four to eight atoms around the reactive center with Ag gradually lowered the dissociation barrier to 70 kJ mol^{-1} and increased the binding energy of O_2 to 43 kJ mol^{-1}, indicating that O_2 dissociation on small silver patches is a plausible reaction pathway.

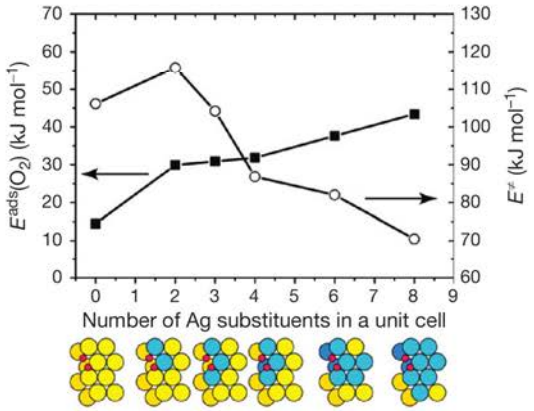

Figure 12 Adsorption energies of O_2 (squares) and the barrier height for O_2 dissociation (circles) as a function of the number of Ag substituents in a unit cell. Transition state structures adapted from Moskaleva, L. V.; Röhe, S.; Wittstock, A.; Zielasek, V.; Klüner, T.; Neyman, K. M.; Bäumer, M. *Phys. Chem. Chem. Phys.* **2011**, *13*, 4529–4539 are schematically depicted. Reproduced by permission of the PCCP Owner Societies.

A similar conclusion was reached by Fajín et al.[302] in a periodic GGA-PW91 study using planar Au(111) doped with Ag and stepped Au(110) and Au(321) surfaces partially substituted with Ag. They found the molecular oxygen dissociation barrier to decrease somewhat upon substitution of Au by Ag though a significant lowering to ~60 kJ mol^{-1} was achieved only for selected structures where entire rows of metal atoms were replaced by Ag. Further Fajín et al. observed that model surfaces with deposited Ag adatoms showed much lower activation energies for O_2 dissociation and, hence, should be more active than those obtained through atomic substitution.

Hence, it could be speculated on the basis of the mentioned computational studies that on Ag-modified corrugated Au surfaces (such as those pertinent to np-Au) the strengthened O_2 adsorption and the decreased activation barrier to O_2 dissociation can in certain cases afford the dissociative adsorption at room temperature and the spillover of atomic O to most favorable surface sites; most likely, such dissociation occurs at Ag particles or ad-rows deposited on Au or on small surface-embedded Ag islands.

7.18.5.2 Adsorption of Atomic O on Au Surfaces with or without Ag Impurities

It is convenient to express the energy of adsorbed atomic O relative to half of the O_2 molecule in the gas phase and the clean metal surface. With this reference state, the adsorption of O at the Au(111) surface is calculated 7–14 kJ mol^{-1} endothermic,[284] which suggests that the thermodynamically favorable route should be a recombination of adsorbed oxygen atoms into molecular oxygen. The latter should easily desorb from the surface due to a negligible binding energy. Nevertheless, this does not happen at room temperature because of the high activation barrier for the recombination to O_2; its desorption temperature for various Au and Ag surfaces reported in the literature lies in the range 490–650 K.[286,303–306]

On the flat Au(111) surface, adsorbed O atoms prefer the fcc threefold hollow site.[281,282,307] Stepped Au surfaces offer several possibilities for binding of atomic O. Not surprisingly, positions in direct contact to coordinatively unsaturated metal atoms at step edges (hollow or 'bridge' sites) were found energetically preferred.[281,282,284,285] On the Au(321) kinked surface, O atoms adsorbed at most favorable positions were found ~30 kJ mol^{-1} stronger bound than O atoms adsorbed inside (111) terraces.[284,285]

Moskaleva et al.[284] examined the influence of Ag impurities on the binding energies of atomic oxygen to the Ag-substituted Au(111) and Au(321) surfaces. Up to three metal atoms confining the threefold adsorption site of atomic O were substituted with Ag impurities. As a result, the binding strength of O increased by up to 35 kJ mol^{-1} with respect to pure Au surfaces. Interestingly, the direct contact of O to the impurity atom was not necessary for increasing the binding energy of the former; rather, it was important that O atom be located reasonably near to the impurity. On the kinked Au(321) surface, hollow sites on the border of the step closest to the impurity remained energetically preferred unless Ag substituents were placed far from the step edge.

7.18.5.3 Co-Adsorption of CO with Atomic O on Au Surfaces

CO adsorption studies on catalytically active np-Au foam using TPD[284] revealed the existence of a stronger bound CO state (states) corresponding to CO desorption above 200 K in addition to two lower lying desorption peaks, at 120–145 K and 170–185 K. The latter two desorption peaks are similar to those earlier observed in the TPD of CO adsorbed on Au single crystals,[308,309] supported Au particles,[310,311] and on Au(111) roughened by sputtering.[312] They were interpreted in terms of CO adsorption on top of sixfold- and sevenfold-coordinated Au atoms.[312] The higher binding energy of CO on np-Au needed clarification. Interestingly, CO_2 desorption was detected concomitantly with the CO desorption state at ~200 K indicating that the newly observed CO desorption state could be linked to the catalytic activity of np-Au.

Moskaleva et al.[284] investigated theoretically the direct influence of Ag impurities on CO adsorption energy using both Au(111) and Au(321) model substrates but no significant increase in the CO binding strength was found upon placing Ag impurities in the vicinity of the CO-binding Au atom; the adsorption directly on top of Ag was found even less favorable than on top of Au. Hence, it was further checked, whether co-adsorbed oxygen could increase the binding energy of CO at certain favorable surface sites.

Studies of CO and O co-adsorption on the flat Au(111) surface[284] indicated that the presence of O in a 'vicinal' position to adsorbed CO (i.e., CO and O are separated by one empty hollow site) could stabilize adsorbed CO by up to 30 kJ mol^{-1}. On the kinked Au(321) surface, which should be a better model for a corrugated ligament surface of np-Au, two main types of stabilized co-adsorption structures were identified. In the first one, which is analogous to the favorable co-adsorption structure on Au(111), CO and O are separated by just one hollow site (see an example in Figure 13 (top left panel)) and were referred to as 'vicinal'.[313] Vicinal complexes on Au(321) are stabilized by up to 9 kJ mol^{-1} with respect to separately adsorbed CO and O. In

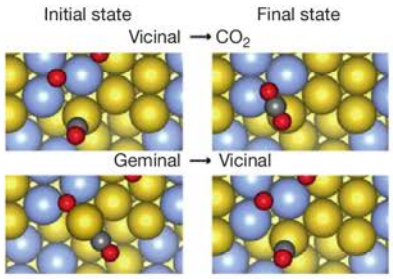

Figure 13 Representative structures for co-adsorption and reaction of CO and O on the Au(321) surface with Ag impurities. Au, Ag, C, and O are indicated by yellow, blue, gray, and red spheres, respectively. Adapted from Moskaleva, L. V.; Zielasek, V.; Klüner, T.; Neyman, K. M.; Bäumer, M. *Chem. Phys. Lett.* **2012**, 525–526, 87–91, with permission. Copyright 2012 Elsevier.

the other type of favorably co-adsorbed complexes on Au(321) CO and O are bound to the same Au atom (see an example in Figure 13 (bottom left panel)). Such co-adsorption complexes were named 'geminal' by Moskaleva et al.[313]. These are quite remarkable structures containing a characteristic linear O–Au–C–O unit and strongly stabilized by 15–20 kJ mol^{-1} with respect to separately adsorbed CO and O. Interestingly, the magnitude of stabilization of both vicinal and geminal structures with respect to individually adsorbed CO and O remained about the same regardless of the presence of Ag impurities at the O binding site.

Most likely, co-adsorption structures discussed above are not just special for the Au(321) surface but can also be encountered on irregular rough Au surfaces containing sixfold-coordinated Au atoms, such as on np-Au. Hence, interaction of CO with O species on the np-Au surface could be a plausible explanation for the high-temperature state observed in the desorption studies of CO from np-Au. The calculated stabilization of geminal complexes, ~20 kJ mol^{-1}, agrees well with the energy difference between the two most stable adsorption states estimated from TPD.

7.18.5.4 Reaction of CO with Atomic O on Au(321)

Moskaleva et al.[313] subsequently analyzed possible reaction routes for CO_2 formation on the kinked Au(321) surface and identified the corresponding TS structures. Possible initial states correspond to vicinal and geminal CO + O co-adsorption complexes introduced above and are schematically depicted in Figure 14. It was found that the most strongly bound geminal CO + O complexes cannot directly form CO_2; they first need to rearrange to a vicinal geometry (with calculated barriers between 43 and 57 kJ mol^{-1}). In contrast, vicinal complexes with less strongly bound CO form CO_2 at almost no energy cost. These theoretical results are in line with the experimentally observed high activity of atomic oxygen bound on single-crystal gold for CO oxidation.[314–319] The authors of Moskaleva et al.[313] attempted to generalize their finding for the Au(321) surface to np-Au in order to interpret the TPD spectrum of CO adsorbed on gold sponges. Most likely, the desorption signals below 185 K could be largely attributed to CO species not interacting with surface oxygen, in analogy to Au single-crystal surfaces[308,309] and Ar-ion sputtered Au(111).[312] Vicinal

CO + O complexes should be present on the np-Au surface in a lower concentration than more thermodynamically favorable geminal complexes. Vicinal structures react and form CO_2 already at low T, from ~100 K. For geminal CO + O complexes desorption at ~200 K competes with a two-step CO_2 formation, the rate-limiting step being the isomerization to a vicinal CO + O structures.

Moskaleva et al.[313] further note that there is another possibility for CO_2 formation from geminal CO + O complexes, which could come into play when surface O is present in excess, for instance, if it is pre-adsorbed onto the Au surface using methods such as O^+/O_2^+ bombardment[290,291] or pre-treatment with O_3.[303,320]Carbon dioxide can be formed via an abstraction of CO from a geminal complex by another surface O, located at a vicinal position with respect to CO (see an example in Figure 15). The activation barrier for this step was calculated to be very low. Hence, O atom migration on Au surfaces (with the barrier 40–50 kJ mol^{-1}) should be the rate-limiting step for CO_2 formation via this channel.

As far as the influence of Ag impurities on the reaction kinetics is concerned, Ag atoms replacing Au at the reactive sites did not change the barrier heights of considered reaction channels by more than 22 kJ mol^{-1}. Generally, the activation energy of CO_2 formation from geminal complexes increased when Ag impurities were introduced. Hence, Ag impurities seem not to be responsible for lowering the energy barrier of the CO + O reaction but rather they promote the dissociation of molecular oxygen on np-Au foams, which is the limiting factor of aerobic oxidation reactions on np-Au.

Importantly, theoretical results of Moskaleva et al.[313] suggest that the abundance of geminal complexes, where CO and O species are adsorbed in immediate vicinity on the same Au atom at a step, is thermodynamically and kinetically favored over more reactive vicinal complexes. Hence, a large fraction of CO + O co-adsorption complexes can survive without reacting with each other up to relatively high temperature. Their immediate reaction is prevented by an activation barrier, which shifts the formation of CO_2 into the experimentally observed temperature range above 200 K.

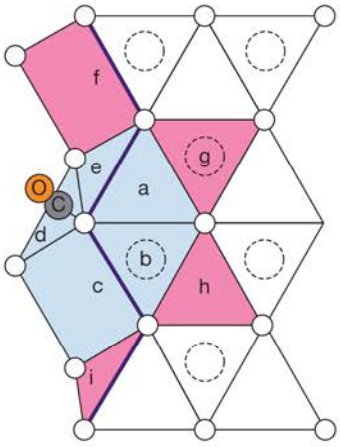

Figure 14 A (111) terrace of the Au(321) surface and various co-adsorption arrangements of CO and O are shown schematically. The border of a step is indicated by a thick dark line. Metal atoms of the surface layer are indicated by open white circles. CO is always placed on top of a sixfold-coordinated Au atom. Labels a–i mark hollow sites on the terrace and on the step investigated for O co-adsorption. Dashed circles denote hcp sites. Light blue and pink areas indicate geminal and vicinal co-adsorption complexes, respectively, see text. Adapted from Moskaleva, L. V.; Zielasek, V.; Klüner, T.; Neyman, K. M.; Bäumer, M. *Chem. Phys. Lett.* **2012**, 525–526, 87–91, with permission. Copyright 2012 Elsevier.

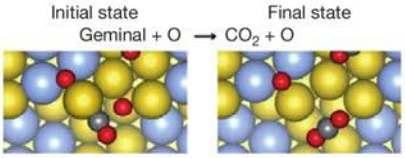

Figure 15 Representative structures for abstraction reaction of CO from a geminal complex by a neighbor O on the Au(321) surface with Ag impurities. Color notations are the same as in Figure 13. Adapted from Moskaleva, L. V.; Zielasek, V.; Klüner, T.; Neyman, K. M.; Bäumer, M. *Chem. Phys. Lett.* **2012**, 525–526, 87–91, with permission. Copyright 2012 Elsevier.

7.18.6 Conclusion

In Sections 7.18.2–7.18.4 of this chapter we presented an overview of recent theoretical studies on such representative reactions at catalytically active TM surfaces as transformations of unsaturated hydrocarbons, methanol, and UALs. These processes were extensively studied because of their pivotal importance either for hydrogen energy technologies, polymer, organic and food chemistry or for pharmaceuticals. In the core of all these reactions is the cleavage or formation of C—H bonds, which is a fundamental issue in chemistry in general. Depending on the catalyst, the formation or scission of C—H bonds may be faster or slower than those of O—H bonds, which may change either the decomposition pathway (Section 7.18.3) or the selectivity of a hydrogenation catalyst (Section 7.18.4). At the same time in the considered processes on TM catalysts these reactions are significantly faster than C—O (Section 7.18.3) or C—C bond scissions (Section 7.18.2). In Section 7.18.5, another process important in energy production, CO oxidation on nanoporous gold (an unsupported Au catalyst), is discussed with a focus on the role of silver impurities for the remarkable activity of np-Au.

Contemporary theoretical investigations of TM catalysts' activities (in most cases) are not only able to reproduce experimental findings but also shed light on many details of reaction mechanisms that would be impossible to extract from experimental evidence alone. In particular, theoretical studies are useful for analyzing which reaction intermediates are formed on the surface and what are their (reactive) properties without any constraints on the intermediate lifetimes.

Numerous examples of insights gained by theoretical methods, which complement the available experimental observations and deepen the understanding of underlying phenomena, are provided in this chapter. Several decades ago, experimental studies[57,58,62,63] suggested that ethylene converts to ethylidyne on Pt(111) through ethylene isomerization to ethylidene and subsequent dehydrogenation of the latter (Section 7.18.2.1.1.2). Theoretical studies found that a reaction pathway via ethylidene could be operative at high coverages, and clarified that it proceeds through consecutive dehydrogenation–hydrogenation reactions rather than a 1,2 H-shift.[82,84] Moreover, a competing mechanism

through vinyl and vinylidene was found to be plausible in kMC studies based on the DFT reaction barriers especially at lower coverages.[74] In agreement with experimental evidence,[83] the kMC simulations[74] also predicted that the conversion of ethylene to ethylidyne occurs at significantly lower temperatures on Pt(111) than on Pd(111). Another example comes from ethylene decomposition on Pd(111), which is observed to proceed until formation of C_1 species at ~425 K (Section 7.18.2.1.2).[51] Only with the help of theoretical studies it was possible to conclude that C—C bond cleavage takes place either in CHC or CHCH species.[87] Also, the experimental studies on model Pd catalysts suggested an involvement of subsurface H in hydrogenation reactions, but could not provide a direct evidence.[102] This evidence was obtained by theoretical means by showing that the presence of subsurface H lowers activation energies of hydrogenation steps by ~25 kJ mol^{-1} (Section 7.18.2.2.1).[106]

Experimentally, methanol decomposition and MSR have been investigated on Cu, Pd, and PdZn-based catalysts for several decades (Section 7.18.3). It was found that Pd catalysts are active in methanol decomposition,[154] but they produce CO under MSR conditions,[155,156] while Cu[152,153] and PdZn[155,156,158,159,161] catalysts do not decompose methanol completely (to CO) and are highly selective to CO_2 in MSR. The available theoretical studies on Cu(111),[189,204] Cu(110),[199] Pd(111),[189,201,202,204] Pd(100),[210] PdZn(111),[204,234] PdZn(211),[204] and PdZn/Pd(111)[201] are in agreement with experimental findings. Theoretical studies also revealed certain details in the reaction mechanisms that were impossible to obtain experimentally. For example, theoretical studies revealed that methanol dehydrogenation to formaldehyde on Pd(111) actually proceeds through a CH_2OH intermediate,[189,200,202] while CH_3O species are observed in experiment due to their higher kinetic stability (Section 7.18.3.2.2).[205,206] Theoretical studies were also able to determine that among all reaction intermediates on nanoparticulate Pd, C—O bond scission (a process much slower than dehydrogenation but nevertheless important as produced C_1 species may lead to catalyst poisoning) is more likely to occur in CH_2OH or CH_3O species (Section 7.18.3.3.2).[222,223] However, the exact mechanism of C_1 species formation was impossible to be determined using sum frequency generation and X-ray photoelectron spectroscopy experimental techniques.[219]

Another example comes from the studies of selectivity of UALs hydrogenation (Section 7.18.4.1). It is known experimentally that when acrolein hydrogenation is performed on Pt(111) the yield of propenol is very low. However, DFT studies revealed that this is not due to kinetically hindered propenol production – the relevant activation energies are rather low – but due to its very slow desorption, $E^{ads} > 100$ kJ mol^{-1}. At the same time, the corresponding SAL has an adsorption energy of ~20 kJ mol^{-1}, which makes its desorption (and yield) favorable.[20,240] Theoretical studies also shed light on important details of hydrogenation reactions on Ag surfaces (Section 7.18.4.2). Pristine Ag surfaces were calculated to be unable to dissociate adsorbed H_2,[260] which appeared to be in disagreement with experimental findings on Ag catalysts.[261] To reconcile the experimental results and theory the effect of residual O atoms on adsorptive properties of Ag should be taken into account. The latter were calculated to make the formation of OH groups and H species strongly exothermic on oxygen-modified Ag surfaces.[263] This finding also explained the promoting effect of oxygen pre-treatment on the activity of Ag/SiO_2 catalysts.[257]

Finally, theoretical studies helped to shed some light on the mechanism of CO oxidation on nanoporous gold, a process in which Ag impurities seem to play a crucial role. Because extremely pure np-Au is known to be chemically inactive in CO oxidation, the activity of np-Au prepared by dealloying could in some way be related to the presence of ~1–2 atom % of a less-noble component, such as silver.[271–273,279] It was possible to explain this phenomenon in a theoretical study revealing that Ag impurities are necessary for O_2 dissociation on stepped Au surfaces.[284,313] DFT data also helped in interpretation of TPD experiments performed on np-Au, which found that some CO species desorbed at $T \sim 200$ K, an unusually high T, when compared to Au single-crystal surfaces, suggestive of a stronger-bound CO species present on np-Au. This process was accompanied by a CO_2 yield, establishing the relation between these species and CO oxidation.[284] With the help of DFT studies, the structure of this species was attributed to strongly interacting geminal CO + O coadsorption complexes, which may survive up to ~200 K, at which point they may start to desorb or transform to vicinal CO + O complexes and produce CO_2.[313]

Despite that in many cases, the agreement between theoretical and experimental studies was achieved, discrepancies between simulation and practice are also often present. They may be either due to intrinsic inaccuracy of modern DFT-based calculations or due to inadequate models used in theoretical studies (or due to inappropriate experimental or computational techniques, of course). Presently one cannot expect more than 5–10 kJ mol^{-1} accuracy in calculations of activation energies on heterogeneous catalysts. As a rule, this degree of uncertainty does not change the qualitative conclusions of theoretical studies. However, when strong competition between two reaction pathways is involved, for example, in the case of hydrogenation of UALs (Section 7.18.4), this inaccuracy may prevent one from drawing a definitive conclusion about catalyst selectivity from theoretical studies. Nevertheless, the development of better exchange-correlation functionals is steadily progressing,[321–323] so that the intrinsic accuracy of DFT will be eventually improved. At the same time, due to constant increase in computational power there are many more opportunities for improving the complexity of employed models and for making them more realistic. There are two significant discrepancies between currently widespread slab models and typical experimental systems: (1) perfect periodicity of the slab models versus common supported nanoparticulate samples and (2) small surface coverage and the absence of co-adsorbed species in theoretical investigation versus saturated surface in many experiments. The nanostructured models in the scalable with size form up to now have been employed to study only very few processes, such as methane decomposition on Pt,[32] the formation of subsurface C in Pd,[108] and C—O bond scission[222,223] in methanol decomposition intermediates. The former two processes were found to be greatly facilitated on NP edges, illustrating how important the precise catalyst structure is for its activity. Theoretical studies considering reactions at varied surface coverage are also not very common. In a study of ethylene conversion to ethylidyne on Pd(111) it was found that barriers may change by up to

25 kJ mol^{-1} depending on surface coverage.[65] Also the barriers of ethylene hydrogenation to ethyl were calculated[67,105,106] to be from 64 to 93 kJ mol^{-1} in correlation with the surface coverage in respective studies. Surface coverage was also calculated to critically affect the dynamics of C impurities on Pd(111).[137] As for the co-adsorbed species, the presence of OH species was found to greatly facilitate the scission of O—H bond in MSR intermediates in the reaction $CH_xOOH + OH \rightarrow CH_xOO + H_2O$.[196] Finally, the presence of adsorbed CO was found to change the arrangement of components on the surface of bimetallic PdZn films on Pd (111), which may be capable of changing its catalytic properties.[186] One can expect more theoretical investigations with models more realistically representing experimental situations regarding nanoparticulate nature of catalysts and effects of surface coverage on the activity to appear in the next years.

Also one could notice significant differences between reaction or activation energies of a given process published in various theoretical papers that cannot be explained by different surface coverage or other physical phenomena. This is exemplified for dehydrogenation of methanol on Cu(111) and Pd(111) studied by a handful of different groups (**Section 7.18.3.1**). In some cases, the variation of calculated values may be as high as 60 kJ mol^{-1} for $E^{\neq}$ ($CH_3O \rightarrow CH_2O + H$) on Cu(111) or even 80 kJ mol^{-1} for $E^{\neq}$ ($CH_3OH \rightarrow CH_2OH + H$) on Pd(111). Often, such large differences are due to loosely chosen computational parameters in some of the papers, which requires one to consider calculated values (especially from older publications) with some precaution. Nevertheless, even with these discrepancies, it is often possible to draw unambiguous qualitative conclusions like in the considered case of methanol decomposition on TM catalysts. Typical variations of values calculated in different studies do not exceed 20–30 kJ mol^{-1}, which expands the reliability of DFT for qualitative analysis of a broader set of processes.

References

1. Parr, R. G.; Yang, W. *Ann. Rev. Phys. Chem.* **1995**, *46*, 701–728.
2. Koch, W.; Holthausen, M. C. *A Chemist's Guide to Density Functional Theory*. Wiley-VCH: Weinheim, 2000.
3. Neurock, M.; van Santen, R. A. *Catal. Today* **1999**, *50*, 445–450.
4. Hammer, B.; Nørskov, J. K. In *Advances in Catalysis, Impact of Surface Science on Catalysis*; Gates, B. C., Knözinger, H., Eds.; Elsevier: San Diego, CA, 2000; Vol. 45, pp 71–129.
5. Kroes, G. J.; Gross, A.; Baerends, E. J.; Scheffler, M.; McCormack, D. A. *Acc. Chem. Res.* **2002**, *35*, 193–200.
6. Greeley, J.; Nørskov, J. K.; Mavrikakis, M. *Ann. Rev. Phys. Chem.* **2002**, *53*, 319–348.
7. Neyman, K. M.; Illas, F. *Catal. Today* **2005**, *105*, 2–16.
8. Nørskov, J. K.; Scheffler, M.; Toulhoat, H. *MRS Bull.* **2006**, *31*, 669–674.
9. Hammer, B. *Top. Catal.* **2006**, *37*, 3–16.
10. Raybaud, P. *Appl. Catal. A: Gen.* **2007**, *322*, 76–91.
11. van Santen, R. A. *Acc. Chem. Res.* **2009**, *42*, 57–66.
12. Sautet, P.; Delbecq, F. *Chem. Rev.* **2010**, *110*, 1788–1806.
13. van Santen, R. A.; Neurock, M.; Shetty, S. G. *Chem. Rev.* **2010**, *110*, 2005–2048.
14. Nørskov, J. K.; Abild-Pedersen, F.; Studt, F.; Bligaard, T. *Proc. Natl. Acad. Sci. U.S.A* **2011**, *108*, 937–943.
15. Cohen, A. J.; Mori-Sánchez, P.; Yang, W. *Chem. Rev.* **2012**, *112*, 289–320.
16. Pacchioni, G. *J. Chem. Phys.* **2008**, *128*, 182505.
17. Chrétien, S.; Metiu, H. *J. Chem. Phys.* **2008**, *129*, 074705.
18. Ponec, V. *Appl. Catal. A* **1997**, *149*, 27–48.
19. Medlin, J. W. *ACS Catal.* **2011**, *1*, 1284–1297.
20. Loffreda, D.; Delbecq, F.; Vigné, F.; Sautet, P. *J. Am. Chem. Soc.* **2006**, *128*, 1316–1323.
21. Lim, K. H.; Mohammad, A. B.; Yudanov, I. V.; Neyman, K. M.; Bron, M.; Claus, P.; Rösch, N. *J. Phys. Chem. C* **2009**, *113*, 13231–13240.
22. Hammer, B.; Nørskov, J. K. *Nature* **1995**, *376*, 2238–2240.
23. Freund, H.-J.; Kuhlenbeck, H.; Libuda, J.; Rupprechter, G.; Bäumer, M.; Hamann, H. *Top. Catal.* **2001**, *15*, 201–209.
24. Bäumer, M.; Freund, H.-J. *Prog. Surf. Sci.* **1999**, *61*, 127–198.
25. Valden, M.; Lai, X.; Goodman, D. W. *Science* **1998**, *281*, 1647–1650.
26. Yudanov, I. V.; Sahnoun, R.; Neyman, K. M.; Rösch, N. *J. Chem. Phys.* **2002**, *117*, 9887–9896.
27. Viñes, F.; Loschen, C.; Illas, F.; Neyman, K. M. *J. Catal.* **2009**, *266*, 59–63.
28. Viñes, F.; Neyman, K. M.; Görling, A. *J. Phys. Chem. A* **2009**, *113*, 11963–11973.
29. Pozun, Z. D.; Tran, K.; Shi, A.; Smith, R. H.; Henkelman, G. *J. Phys. Chem. C* **2011**, *115*, 1811–1818.
30. Allian, A. D.; Takanabe, K.; Fujdala, K. L.; Hao, X.; Truex, T. J.; Cai, J.; Buda, C.; Neurock, M.; Iglesia, E. *J. Am. Chem. Soc.* **2011**, *133*, 4498–4517.
31. Yudanov, I. V.; Genest, A.; Schauermann, S.; Freund, H.-J.; Rösch, N. *Nano Lett.* **2012**, *12*, 2134–2139.
32. Viñes, F.; Lykhach, Y.; Staudt, T.; Lorenz, M. P. A.; Papp, C.; Steinrück, H.-P.; Libuda, J.; Neyman, K. M.; Görling, A. *Chem. Eur. J.* **2010**, *16*, 6530–6539.
33. Wei, J.; Iglesia, E. *J. Phys. Chem. B* **2004**, *108*, 4094–4103.
34. Heiz, U.; Sanchez, A.; Abbet, S.; Schneider, W.-D. *J. Am. Chem. Soc.* **1999**, *121*, 3214–3217.
35. Abbet, S.; Sanchez, A.; Heiz, U.; Schneider, W. D.; Ferrari, A. M.; Pacchioni, G.; Rösch, N. *J. Am. Chem. Soc.* **2000**, *122*, 3453–3457.
36. Chrétien, S.; Buratto, S. K.; Metiu, H. *Curr. Opin. Solid State Mater. Sci.* **2007**, *11*, 62–75.
37. Chen, Y.; Crawford, P.; Hu, P. *Catal. Lett.* **2007**, *119*, 21–28.
38. Lei, Y.; Mehmood, F.; Lee, S.; Greeley, J.; Lee, B.; Seifert, S.; Winans, R. E.; Elam, J. W.; Meyer, R. J.; Redfern, P. C.; Teschner, D.; Schlögl, R.; Pellin, M. J.; Curtiss, L. A.; Vajda, S. *Science* **2010**, *328*, 224–228.
39. Hegde, M. S.; Madras, G.; Patil, K. C. *Acc. Chem. Res.* **2009**, *42*, 704–712.
40. Fu, Q.; Saltsburg, H.; Flytzani-Stephanopoulos, M. *Science* **2003**, *301*, 935–938.
41. Zhai, Y.; Pierre, D.; Si, R.; Deng, W.; Ferrin, P.; Nilekar, A.; Peng, G.; Herron, J. A.; Bell, D.; Saltsburg, H.; Mavrikakis, M.; Flytzani-Stephanopoulos, M. *Science* **2010**, *329*, 1633–1636.
42. Colussi, S.; Gayen, A.; Farnesi Camellone, M.; Boaro, M.; Llorca, J.; Fabris, S.; Trovarelli, A. *Angew. Chem. Int. Ed.* **2009**, *48*, 8481–8484.
43. Matar, S.; Hatch, L. F. In *Chemistry of Petrochemical Processes*, Chapter 7, 2nd ed.; Gulf Professional Publishing: Houston, 2001 pp 188–212.
44. Ponec, V.; Bond, G. C. *Catalysis by Metals and Alloys*. Elsevier: Amsterdam, 1995.
45. Bond, G. C. *Metal-Catalysed Reactions of Hydrocarbons*. Springer: New York, 2005.
46. Alves, J. A.; Bressa, S. P.; Martinez, O. M.; Barreto, G. F. *J. Ind. Eng. Chem.* **2012**, *18*, 1353–1365.
47. Schbib, N. S.; Garcia, M. A.; Gigola, C. E.; Errazu, A. F. *Ind. Eng. Chem. Res.* **1996**, *35*, 1496–1505.
48. Stacchiola, D.; Calaza, F.; Zheng, T.; Tysoe, W. T. *J. Mol. Catal. A* **2005**, *228*, 35–45.
49. Tysoe, W. T.; Nyberg, G. L.; Lambert, R. M. *J. Phys. Chem.* **1984**, *88*, 1960–1963.
50. Kesmodel, L. L.; Gates, J. A. *Surf. Sci.* **1981**, *111*, L747–L754.
51. Stacchiola, D.; Kaltchev, M.; Wu, G.; Tysoe, W. T. *Surf. Sci.* **2000**, *470*, L32–L38.
52. Beebe, T. P., Jr.; Yates, J. T. *J. Am. Chem. Soc.* **1986**, *108*, 663–671.
53. Sock, M.; Eichler, A.; Surnev, S.; Andersen, J. N.; Klötzer, B.; Hayek, K.; Ramsey, M. G.; Netzer, F. P. *Surf. Sci.* **2003**, *545*, 122–136.
54. Steininger, H.; Ibach, H.; Lehwald, S. *Surf. Sci.* **1982**, *117*, 685–698.
55. Hugenschmidt, M. B.; Dolle, P.; Jupille, J.; Cassuto, A. *J. Vac. Sci. Technol. A* **1989**, *7*, 3312–3316.
56. Cremer, P. S.; Somorjai, G. A. *J. Chem. Soc. Faraday Trans.* **1995**, *91*, 3671–3677.
57. Zaera, F.; Bernstein, N. *J. Am. Chem. Soc.* **1994**, *116*, 4881–4887.
58. Zaera, F. *Langmuir* **1996**, *12*, 88–94.
59. Koestner, R. J.; van Hove, M. A.; Somorjai, G. A. *Surf. Sci.* **1982**, *121*, 321–337.
60. Marinova, Ts.S.; Kostov, K. L. *Surf. Sci.* **1987**, *181*, 573–585.
61. Hills, M. M.; Parmeter, J. E.; Mullins, C. B.; Weinberg, W. H. *J. Am. Chem. Soc.* **1986**, *108*, 3554–3562.
62. Zaera, F.; French, C. R. *J. Am. Chem. Soc.* **1999**, *121*, 2236–2243.
63. Zaera, F.; Janssens, T. V. W.; Öfner, H. *Surf. Sci.* **1996**, *368*, 371–376.
64. Pallassana, V.; Neurock, M.; Lusvardi, V. S.; Lerou, J. J.; Kragten, D. D.; van Santen, R. A. *J. Phys. Chem. B* **2002**, *106*, 1656–1669.
65. Moskaleva, L. V.; Chen, Z.-X.; Aleksandrov, H. A.; Mohammed, A. B.; Sun, Q.; Rösch, N. *J. Phys. Chem. C* **2009**, *113*, 2512–2520.
66. Calaza, F.; Stacchiola, D.; Neurock, M.; Tysoe, W. T. *J. Am. Chem. Soc.* **2010**, *132*, 2202–2207.

67. Moskaleva, L. V.; Aleksandrov, H. A.; Basaran, D.; Zhao, Z.-J.; Rösch, N. *J. Phys. Chem. C* **2009**, *113*, 15373–15379.
68. Hansen, E. W.; Neurock, M. *Chem. Eng. Sci.* **1999**, *54*, 3411–3421.
69. Hansen, E. W.; Neurock, M. *J. Catal.* **2000**, *196*, 241–252.
70. Zhdanov, V. P. *Elementary Physicochemical Processes on Solid Surfaces*. Plenum Press: New York, 1991.
71. Reuter, K. In *Modeling Heterogeneous Catalytic Reactions: From the Molecular Process to the Technical System*; Deutschmann, O., Ed.; Wiley-VCH: Weinberg, 2009.
72. Reuter, K.; Scheffler, M. *Phys. Rev. B* **2006**, *73*, 045433.
73. Sendner, C.; Sakong, S.; Groß, A. *Surf. Sci.* **2006**, *600*, 3258–3265.
74. Aleksandrov, H. A.; Moskaleva, L. V.; Zhao, Z.-J.; Basaran, D.; Chen, Z.-X.; Mei, D.; Rösch, N. *J. Catal.* **2012**, *285*, 187–195.
75. Somorjai, G. A. *Surface Chemistry and Catalysis*. Wiley: New York, 1994.
76. Yates, J. T., Jr. *J. Vac. Sci. Technol. A* **1995**, *13*, 1359–1367.
77. Zambelli, T.; Wintterlin, J.; Trost, J.; Ertl, G. *Science* **1996**, *273*, 1688–1690.
78. Dahl, S.; Logadottir, A.; Egeberg, R. C.; Larsen, J. H.; Chorkendorff, I.; Törnqvist, E.; Nørskov, J. K. *Phys. Rev. Lett.* **1999**, *83*, 1814–1817.
79. Nørskov, J. K.; Bligaard, T.; Logadottir, A.; Bahn, S.; Hansen, L. B.; Bollinger, M.; Bengaard, H.; Hammer, B.; Sljivancanin, Z.; Mavrikakis, M.; Xu, Y.; Dahl, S.; Jacobsen, C. J. H. *J. Catal.* **2002**, *209*, 275–278.
80. Andersin, J.; Lopez, N.; Honkala, K. *J. Phys. Chem. C* **2009**, *113*, 8278–8286.
81. Vang, R. T.; Honkala, K.; Dahl, S.; Vestergaard, E. K.; Schnadt, J.; Lægsgaard, E.; Clausen, B. S.; Nørskov, J. K.; Besenbacher, F. *Surf. Sci.* **2006**, *600*, 66–77.
82. Zhao, Z.-J.; Moskaleva, L. V.; Aleksandrov, H. A.; Basaran, D.; Rösch, N. *J. Phys. Chem. C* **2010**, *114*, 12190–12201.
83. Wang, L. P.; Tysoe, W. T.; Ormerod, R. M.; Lambert, R. M.; Hoffmann, H.; Zaera, F. *J. Phys. Chem.* **1990**, *94*, 4236–4239.
84. Chen, Y.; Vlachos, D. G. *J. Phys. Chem. C* **2010**, *114*, 4973–4982.
85. Li, M.; Guo, W.; Jiang, R.; Zhao, L.; Lu, X.; Zhu, H.; Fu, D.; Shan, H. *J. Phys. Chem. C* **2010**, *114*, 8440–8448.
86. Anghel, A. T.; Wales, D. J.; Jenkins, S. J.; King, D. A. *Chem. Phys. Lett.* **2005**, *413*, 289–293.
87. Chen, Z.-X.; Aleksandrov, H. A.; Basaran, D.; Rösch, N. *J. Phys. Chem. C* **2010**, *114*, 17683–17692.
88. Andersin, J.; Honkala, K. *Surf. Sci.* **2010**, *604*, 762–769.
89. Gabasch, H.; Hayek, K.; Klötzer, B.; Knop-Gericke, A.; Schlögl, R. *J. Phys. Chem. B* **2006**, *110*, 4947–4952.
90. Jungwirthova, I.; Kesmodel, L. L. *J. Phys. Chem. B* **2001**, *105*, 674–680.
91. Deng, R.; Herceg, E.; Trenary, M. *Surf. Sci.* **2004**, *573*, 310–319.
92. Deng, R.; Herceg, E.; Trenary, M. *J. Am. Chem. Soc.* **2005**, *127*, 17628–17633.
93. Basaran, D.; Aleksandrov, H. A.; Chen, Z.-X.; Zhao, Z.-J.; Rösch, N. *J. Mol. Catal. A: Chem.* **2011**, *344*, 37–46.
94. Twigg, M. V. *Catalyst Handbook*, 2nd edn; Manson Pub.: London, 1996.
95. Xu, J.; Saeys, M. *J. Catal.* **2006**, *242*, 217–226.
96. Xu, J.; Saeys, M. *J. Phys. Chem. C* **2009**, *113*, 4099–4106.
97. Nave, S.; Tiwari, A. K.; Jackson, B. *J. Chem. Phys.* **2010**, *132*, 054705.
98. Horiuti, J.; Polanyi, M. *Trans. Faraday Soc.* **1934**, *30*, 1164–1172.
99. Doyle, A. M.; Shaikhutdinov, S. K.; Jackson, S. D.; Freund, H.-J. *Angew. Chem. Int. Ed.* **2003**, *42*, 5240–5243.
100. Wilde, M.; Fukutani, K.; Ludwig, W.; Brandt, B.; Fischer, J.-H.; Schauermann, S.; Freund, H.-J. *Angew. Chem. Int. Ed.* **2008**, *47*, 9289–9293.
101. Stacchiola, D.; Azad, S.; Burkholder, L.; Tysoe, W. T. *J. Phys. Chem. B* **2001**, *105*, 11233–11239.
102. Ludwig, W.; Savara, A.; Brandt, B.; Schauermann, S. *Phys. Chem. Chem. Phys.* **2011**, *13*, 966–977.
103. Dohnalek, Z.; Kim, J.; Kay, B. D. *J. Phys. Chem. C* **2008**, *112*, 15796–15801.
104. Neurock, M.; van Santen, R. A. *J. Phys. Chem. B* **2000**, *104*, 11127–11145.
105. Garcia-Mota, M.; Bridier, B.; Perez-Ramirez, J.; Lopez, N. *J. Catal.* **2010**, *273*, 92–102.
106. Tiruppathi, P.; Low, J. J.; Chan, A. S. Y.; Bare, S. R.; Meyer, R. J. *Catal. Today* **2011**, *165*, 106–111.
107. Andersin, J.; Parkkinen, P.; Honkala, K. *J. Catal.* **2012**, *290*, 118–125.
108. Neyman, K. M.; Schauermann, S. *Angew. Chem. Int. Ed.* **2010**, *49*, 4743–4746.
109. Aleksandrov, H. A.; Viñes, F.; Ludwig, W.; Schauermann, S.; Neyman, K. M. *Chem. Eur. J.* **2013**, *19*, 1335–1345.
110. Berlowitz, P.; Megiris, C.; Butt, J. B.; Kung, H. H. *Langmuir* **1985**, *1*, 206–212.
111. Belelli, P. G.; Castellani, N. J. *Surf. Rev. Lett.* **2008**, *15*, 259.
112. Simopoulos, A. P. In *Handbook of Lipids in Human Nutrition*; Spiller, G. A., Ed.; CRC Press: Boca Raton, 1996; pp 91–99.
113. Mercier, C.; Chabardes, P. *Pure Appl. Chem.* **1994**, *66*, 1509–1518.
114. Lee, I.; Delbecq, F.; Morales, R.; Albiter, M. A.; Zaera, F. *Nat. Mater.* **2009**, *8*, 132–138.
115. Yoon, C.; Yang, M. X.; Somorjai, G. A. *Catal. Lett.* **1997**, *46*, 37–41.
116. Tourillon, G.; Cassuto, A.; Jugnet, Y.; Massadier, J.; Bertolini, J. C. *J. Chem. Soc. Faraday Trans.* **1996**, *92*, 4835–4841.
117. Valcarcel, A.; Clotet, A.; Ricart, J. M.; Delbecq, F.; Sautet, P. *J. Phys. Chem. B* **2005**, *109*, 14175–14182.
118. Boitiaux, J. P.; Cosyns, J.; Robert, E. *Appl. Catal.* **1987**, *35*, 193–209.
119. Delbecq, F.; Loffreda, D.; Sautet, P. *J. Phys. Chem. Lett.* **2010**, *1*, 323–326.
120. Derrien, M. L. In *Studies in Surface Science and Catalysis. Catalytic Hydrogenation*; Cerveny, L., Ed.; Elsevier: Amsterdam, 1986; Vol. 27, pp 613–666.
121. Jin, Y.; Datye, A. K.; Rightor, E.; Gulotty, R.; Waterman, W.; Smith, M.; Holbrook, M.; Maj, J.; Blackson, J. *J. Catal.* **2001**, *203*, 292–306.
122. Yang, B.; Burch, R.; Hardacre, C.; Headdock, G.; Hu, P. *ACS Catal.* **2012**, *2*, 1027–1032.
123. Johnson, M. M.; Walker, D. W.; Nowack, G. P. Selective Hydrogenation Catalyst. U.S. Patent 4,404,124, 1983
124. Sarkany, A.; Geszti, O.; Safran, G. *Appl. Catal. A: Gen.* **2008**, *350*, 157–163.
125. Armbrüster, M.; Kovnir, K.; Behrens, M.; Teschner, D.; Grin, Y.; Schlögl, R. *J. Am. Chem. Soc.* **2010**, *132*, 14745–14747.
126. Volpe, M. A.; Rodriguez, P.; Gigola, C. E. *Catal. Lett.* **1999**, *61*, 27–32.
127. Garcia-Mota, M.; Gomez-Diaz, J.; Novell-Leruth, G.; Vargas-Fuentes, C.; Bellarosa, L.; Bridier, B.; Perez-Ramirez, J.; Lopez, N. *Theor. Chem. Acc.* **2011**, *128*, 663–673.
128. Tew, M. W.; Emerich, H.; van Bokhoven, J. A. *J. Phys. Chem. C* **2011**, *115*, 8457–8465.
129. Sheth, P. A.; Neurock, M.; Smith, C. M. *J. Phys. Chem. B* **2005**, *109*, 12449–12466.
130. Studt, F.; Abild-Pedersen, F.; Bligaard, T.; Sørensen, R. Z.; Christensen, C. H.; Nørskov, J. K. *Angew. Chem. Int. Ed.* **2008**, *47*, 9299–9302.
131. Studt, F.; Abild-Pedersen, F.; Bligaard, T.; Sørensen, R. Z.; Christensen, C. H.; Nørskov, J. K. *Science* **2008**, *320*, 1320–1322.
132. Teschner, D.; Borsodi, J.; Wootsch, A.; Révay, Z.; Hävecker, M.; Knop-Gericke, A.; Jackson, S. D.; Shlögl, R. *Science* **2008**, *320*, 86–89.
133. Teschner, D.; Vass, E.; Hävecker, M.; Zafeiratos, S.; Schnörch, P.; Sauer, H.; Knop-Gericke, A.; Schlögl, R.; Chamam, M.; Wootsch, A.; Canning, A. S.; Gamman, J. J.; Jackson, S. D.; McGregor, J.; Gladden, L. F. *J. Catal.* **2006**, *242*, 26–37.
134. Teschner, D.; Révay, Z.; Borsodi, J.; Hävecker, M.; Knop-Gericke, A.; Shlögl, R.; Milroy, D.; Jackson, S. D.; Torres, D.; Sautet, P. *Angew. Chem. Int. Ed.* **2008**, *47*, 9274–9278.
135. Gabasch, H.; Kleimenov, E.; Teschner, D.; Zafeiratos, S.; Havecker, M.; Knop-Gericke, A.; Schlögl, R.; Zemlyanov, D.; Aszalos-Kiss, B.; Hayek, K.; Klötzer, B. *J. Catal.* **2006**, *242*, 340–348.
136. Yudanov, I. V.; Neyman, K. M.; Rösch, N. *Phys. Chem. Chem. Phys.* **2004**, *6*, 116–123.
137. Kozlov, S. M.; Yudanov, I. V.; Aleksandrov, H. A.; Rösch, N. *Phys. Chem. Chem. Phys.* **2009**, *11*, 10955–10963.
138. Nykanen, L.; Andersin, J.; Honkala, K. *Phys. Rev. B* **2010**, *81*, 075417.
139. Gomez, T.; Florez, E.; Rodriguez, J. A.; Illas, F. *J. Phys. Chem. C* **2011**, *115*, 11666–11672.
140. Hammer, B.; Norskov, J. K. *Nature* **1995**, *376*, 238–240.
141. Xu, Y.; Greeley, J.; Mavrikakis, M. *J. Am. Chem. Soc.* **2005**, *127*, 12823–12827.
142. Lopez, N.; Łodziana, Z.; Illas, F.; Salmeron, M. *Phys. Rev. Lett.* **2004**, *93*, 146103.
143. Bridier, B.; Lopez, N.; Perez-Ramirez, J. *Dalton Trans.* **2010**, *39*, 8412–8419.
144. Lopez, N.; Vargas-Fuentes, C. *Chem. Commun.* **2012**, *48*, 1379–1391.
145. Lopez, N.; Bridier, B.; Perez-Ramirez, J. *J. Phys. Chem. C* **2008**, *112*, 9346–9350.
146. Molnar, A.; Sarkany, A.; Varga, M. *J. Mol. Catal. A: Chem.* **2001**, *173*, 185–221.
147. Brønsted, J. N. *Chem. Rev.* **1928**, *5*, 231–338.
148. Evans, M. G.; Polanyi, M. *Trans. Faraday Soc.* **1938**, *34*, 0011–0023.
149. Song, C. S. *Catal. Today* **2002**, *77*, 17–49.
150. Schuyten, S.; Guerrero, S.; Miller, J. T.; Shibata, T.; Wolf, E. E. *Appl. Catal. A: Gen.* **2009**, *352*, 133–144.
151. Kurtz, M.; Wilmer, H.; Genger, T.; Hinrichsen, O.; Muhler, M. *Catal. Lett.* **2003**, *86*, 77–80.
152. Wachs, I. E.; Madix, R. J. *J. Catal.* **1978**, *53*, 208–227.
153. Bowker, M.; Madix, R. J. *Surf. Sci.* **1980**, *95*, 190–206.
154. Usami, Y.; Kagawa, K.; Kawazoe, M.; Matsumura, Y.; Sakurai, H.; Haruta, M. *Appl. Catal. A: Gen.* **1998**, *171*, 123–130.
155. Suwa, Y.; Ito, S.; Kameoka, S.; Tomishige, K.; Kunimori, K. *Appl. Catal. A: Gen.* **2004**, *267*, 9–16.
156. Takezawa, N.; Iwasa, N. *Catal. Today* **1997**, *36*, 45–56.
157. Föttinger, K.; van Bokhoven, J. A.; Nachtegaal, M.; Rupprechter, G. *J. Phys. Chem. Lett.* **2011**, *2*, 428–433.

158. Chin, Y.-H.; Dagle, R.; Hu, J.; Dohnalkova, A. C.; Wang, Y. *Catal. Today* **2002**, *77*, 79–88.
159. Rameshan, C.; Stadlmayr, W.; Weilach, C.; Penner, S.; Lorenz, H.; Hävecker, M.; Blume, R.; Rocha, T.; Teschner, D.; Knop-Gericke, A.; Schlögl, R.; Memmel, N.; Zemlyanov, D.; Rupprechter, G.; Klötzer, B. *Angew. Chem. Int. Ed.* **2010**, *49*, 3224–3227.
160. Conant, T.; Karim, A. M.; Lebarbier, V.; Wang, Y.; Girgsdies, F.; Schlögl, R.; Datye, A. *J. Catal.* **2008**, *257*, 64–70.
161. Friedrich, M.; Teschner, D.; Knop-Gericke, A.; Armbrüster, M. *J. Catal.* **2012**, *285*, 41–47.
162. Bayer, A.; Flechtner, K.; Denecke, R.; Steinrück, H. P.; Neyman, K. M.; Rösch, N. *Surf. Sci.* **2006**, *600*, 78–94.
163. Carrasco, J.; Hodgson, A.; Michaelides, A. *Nat. Mater.* **2012**, *11*, 667–674.
164. Henderson, M. A. *Surf. Sci. Rep.* **2002**, *46*, 1–308.
165. Hodgson, A.; Haq, S. *Surf. Sci. Rep.* **2009**, *64*, 381–451.
166. Huang, Y.; Chen, Z.-X. *J. Phys. Chem. C* **2011**, *115*, 18752–18760.
167. German, E. D.; Sheintuch, M. *J. Phys. Chem. C* **2010**, *114*, 3089–3097.
168. Phatak, A. A.; Delgass, V. N.; Ribeiro, F. H.; Schneider, W. F. *J. Phys. Chem. C* **2009**, *113*, 7269–7276.
169. Behrens, M.; Studt, F.; Kasatkin, I.; Kühl, S.; Hävecker, M.; Abild-Pedersen, F.; Zander, S.; Girgsdies, F.; Kurr, P.; Kniep, B.-L.; Tovar, M.; Fischer, R. W.; Nørskov, J. K.; Schlögl, R. *Science* **2012**, *336*, 893–897.
170. Gunter, M. M.; Ressler, T.; Jentoft, R. E.; Bems, B. *J. Catal.* **2001**, *203*, 133–149.
171. Chen, Z.-X.; Neyman, K. M.; Gordienko, A. B.; Rösch, N. *Phys. Rev. B* **2003**, *68*, 075417.
172. Hansen, P. L.; Wagner, J. B.; Helveg, S.; Rostrup-Nielsen, J. R.; Clausen, B. S.; Topsøe, H. *Science* **2002**, *295*, 2053–2055.
173. Inoğlu, N.; Kitchin, J. R. *J. Catal.* **2009**, *261*, 188–194.
174. Meusel, I.; Hoffmann, J.; Hartmann, J.; Heemeier, M.; Bäumer, M.; Libuda, J.; Freund, H.-J. *Catal. Lett.* **2001**, *71*, 5–13.
175. Nolte, P.; Stierle, A.; Kasper, N.; Jin-Phillipp, N. Y.; Jeutter, N.; Dosch, H. *Nano Lett.* **2011**, *11*, 4697–4700.
176. Renaud, G.; Lazzari, R.; Revenant, C.; Barbier, A.; Noblet, M.; Ulrich, O.; Leroy, F.; Jupille, J.; Borensztein, Y.; Henry, C. R.; Deville, J.-P.; Scheurer, F.; Mane-Mane, J.; Fruchart, O. *Science* **2003**, *300*, 1416–1419.
177. Fan, F.-R.; Attia, A.; Sur, U. K.; Chen, J.-B.; Xie, Z.-X.; Li, J. F.; Ren, B.; Tian, Z.-Q. *Cryst. Growth Des.* **2009**, *9*, 2335–2340.
178. Friedrich, M.; Ormeci, A.; Grin, Y.; Armbrüster, M. *Z. Anorg. Allg. Chem.* **2010**, *636*, 1735–1739.
179. Stadlmayr, W.; Klötzer, B.; Penner, S.; Memmel, N. *J. Phys. Chem. C* **2012**, *116*, 3635–3644.
180. Weirum, G.; Kratzer, M.; Koch, H. P.; Tamtögl, A.; Killmann, J.; Bako, I.; Winkler, A.; Surnev, S.; Netzer, F. P.; Schennach, R. *J. Phys. Chem. C* **2009**, *113*, 9788–9796.
181. Stadlmayr, W.; Rameshan, C.; Weilach, C.; Lorenz, H.; Hävecker, M.; Blume, R.; Rocha, T.; Teschner, D.; Knop-Gericke, A.; Zemlyanov, D.; Penner, S.; Schlögl, R.; Rupprechter, G.; Klötzer, B.; Memmel, N. *J. Phys. Chem. C* **2010**, *114*, 10850–10856.
182. Stadlmayr, W.; Penner, S.; Klötzer, B.; Memmel, N. *Surf. Sci.* **2009**, *603*, 251–255.
183. Lim, K. H.; Moskaleva, L. V.; Rösch, N. *Chem. Phys. Chem.* **2006**, *7*, 1802–1812.
184. Chen, Z.-X.; Neyman, K. M.; Rösch, N. *Surf. Sci.* **2004**, *548*, 291–300.
185. He, X. A.; Huang, Y. C.; Chen, Z.-X. *Phys. Chem. Chem. Phys.* **2011**, *13*, 107–109.
186. Weilach, C.; Kozlov, S. M.; Holzapfel, H.; Föttinger, K.; Neyman, K. M.; Rupprechter, G. J. *Phys. Chem. C.* **2012**, *116*, 18768–18778.
187. Greeley, J.; Mavrikakis, M. *J. Catal.* **2002**, *208*, 291–300.
188. Grabow, L. C.; Mavrikakis, M. *ACS Catal.* **2011**, *1*, 365–384.
189. Gu, X.-K.; Li, W.-X. *J. Phys. Chem. C* **2010**, *114*, 21539–21547.
190. Yang, Y.; Evans, J.; Rodriguez, J. A.; White, M. G.; Liu, P. *Phys. Chem. Chem. Phys.* **2010**, *12*, 9909–9917.
191. Tao, S.-X.; Wang, G.-C.; Bu, X.-H. *J. Phys. Chem. B* **2006**, *110*, 26045–26054.
192. Zhao, Y.-F.; Yang, Y.; Mims, C.; Peden, C. H. F.; Li, J.; Mei, D. *J. Catal.* **2011**, *281*, 199–211.
193. Chen, Z. X.; Neyman, K. M.; Lim, K. H.; Rösch, N. *Langmuir* **2004**, *20*, 8068–8077.
194. Ren, R.; Niu, C.; Bu, S.; Zhou, Y.; Lv, Y.; Wang, G. *J. Nat. Gas Chem.* **2011**, *20*, 90–98.
195. Lim, K. H.; Chen, Z. X.; Neyman, K. M.; Rösch, N. *J. Phys. Chem. B* **2006**, *110*, 14890–14897.
196. Lin, S.; Johnson, R. S.; Smith, G. K.; Xie, D.; Guo, H. *Phys. Chem. Chem. Phys.* **2011**, *13*, 9622–9631.
197. Sakong, S.; Groß, A. *J. Catal.* **2005**, *231*, 420–429.
198. Xu, L.; Mei, D.; Henkelman, G. *J. Chem. Phys.* **2009**, *131*, 244520.
199. Mei, D. H.; Xu, L. J.; Henkelman, G. *J. Phys. Chem. C* **2009**, *113*, 4522–4537.
200. Yang, J.; Zhou, Y.; Su, H.; Jiang, S. *J. Electroanal. Chem.* **2011**, *662*, 251–256.
201. Huang, Y.; Chen, Z.-X. *Langmuir* **2010**, *26*, 10796–10802.
202. Jiang, R.; Guo, W.; Li, M.; Fu, D.; Shan, H. *J. Phys. Chem. C* **2009**, *113*, 4188–4197.
203. Perdew, J. P.; Wang, Y. *Phys. Rev. B* **1992**, *45*, 13244.
204. Neyman, K. M.; Lim, K. H.; Chen, Z. X.; Moskaleva, L. V.; Bayer, A.; Reindl, A.; Borgmann, D.; Denecke, R.; Steinrück, H.-P.; Rösch, N. *Phys. Chem. Chem. Phys.* **2007**, *9*, 3470–3482.
205. Levis, R. J.; Zhicheng, J.; Winograd, N. *J. Am. Chem. Soc.* **1989**, *111*, 4605–4612.
206. Chen, J. J.; Jiang, Z. C.; Zhou, Y.; Chakraborty, B. R.; Winograd, N. *Surf. Sci.* **1995**, *328*, 248–262.
207. Zhang, J.; Hu, P. *J. Chem. Phys.* **2001**, *115*, 7182–7186.
208. Kozlov, S. M.; Cabeza, G. F.; Neyman, K. M. *Chem. Phys. Lett.* **2011**, *506*, 92–97.
209. Yudanov, I. V.; Sahnoun, R.; Neyman, K. M.; Rösch, N.; Hoffmann, J.; Schauermann, S.; Johánek, V.; Unterhalt, H.; Rupprechter, G.; Libuda, J.; Freund, H.-J. *J. Phys. Chem. B* **2003**, *107*, 255–264.
210. Jiang, R.; Guo, W.; Li, M.; Lu, Z.; Yuan, J.; Shan, H. *Phys. Chem. Chem. Phys.* **2010**, *12*, 7794–7803.
211. Christmann, K.; Demuth, J. E. *J. Chem. Phys.* **1982**, *76*, 6308–6317.
212. Smith, G. K.; Lin, S.; Lai, W. Z.; Datye, A.; Xie, D. Q.; Guo, H. *Surf. Sci.* **2011**, *605*, 750–759.
213. Kresse, G.; Hafner, J. *Phys. Rev. B* **1994**, *49*, 14251.
214. Huang, Y. C.; He, X.; Chen, Z.-X. *J. Chem. Phys.* **2011**, *134*, 184702.
215. Jeroro, E.; Vohs, J. M. *J. Am. Chem. Soc.* **2008**, *130*, 10199–10207.
216. Chen, Z.-X.; Lim, K. H.; Neyman, K. M.; Rösch, N. *Phys. Chem. Chem. Phys.* **2004**, *6*, 4499–4504.
217. Chen, Z.-X.; Lim, K. H.; Neyman, K. M.; Rösch, N. *J. Phys. Chem. B* **2005**, *109*, 4568–4574.
218. Bera, P.; Vohs, J. M. *J. Phys. Chem. C* **2007**, *111*, 7049–7057.
219. Morkel, M.; Kaichev, V. V.; Rupprechter, G.; Freund, H.-J.; Prosvirin, I. P.; Bukhtiyarov, V. I. *J. Phys. Chem. B* **2004**, *108*, 12955–12961.
220. Schauermann, S.; Hoffmann, J.; Johánek, V.; Hartmann, J.; Libuda, J.; Freund, H.-J. *Angew. Chem. Int. Ed.* **2002**, *41*, 2532–2535.
221. Henkelman, G.; Jónsson, H. *J. Chem. Phys.* **1999**, *111*, 7010–7022.
222. Yudanov, I. V.; Matveev, A. V.; Neyman, K. M.; Rösch, N. *J. Am. Chem. Soc.* **2008**, *130*, 9342–9352.
223. Yudanov, I. V.; Neyman, K. M.; Rösch, N. *Phys. Chem. Chem. Phys.* **2006**, *8*, 2396–2401.
224. Geissler, K.; Newson, E.; Vogel, F.; Truong, T.-B.; Hottinger, P.; Wokaun, A. *Phys. Chem. Chem. Phys.* **2001**, *3*, 289–293.
225. Agrell, J.; Birgersson, H.; Boutonnet, M. *J. Power. Sources* **2002**, *106*, 249–257.
226. Pour, V.; Bartoň, J.; Benda, A. *Collect. Czech. Chem. Commun.* **1975**, *40*, 2923–2934.
227. Amphlett, J. C.; Evans, M. J.; Mann, R. F.; Weir, R. D. *Can. J. Chem. Eng.* **1985**, *63*, 605–611.
228. Jiang, C. J.; Trimm, D. L.; Wainwright, M. S.; Cant, N. W. *Appl. Catal. A: Gen.* **1993**, *93*, 245–255.
229. Takahashi, K.; Takezawa, N.; Kobayashi, H. *Appl. Catal.* **1982**, *2*, 363–366.
230. Jiang, C. J.; Trimm, D. L.; Wainwright, M. S.; Cant, N. W. *Appl. Catal. A: Gen.* **1993**, *97*, 145–158.
231. Peppley, B. A.; Amphlett, J. C.; Kearns, L. M.; Mann, R. F. *Appl. Catal. A: Gen.* **1999**, *179*, 31–49.
232. Asprey, S. P.; Wojciechowski, B. W.; Peppley, B. A. *Appl. Catal. A: Gen.* **1999**, *179*, 51–70.
233. Lin, S.; Xie, D.; Guo, H. *ACS Catal.* **2011**, *1*, 1263–1271.
234. Lin, S.; Xie, D. Q.; Guo, H. *J. Phys. Chem. C* **2011**, *115*, 20583–20589.
235. Lin, S.; Xie, D.; Guo, H. *J. Mol. Catal. A: Chem.* **2012**, *356*, 165–170.
236. Önal, Y.; Claus, P. In *Handbook of Heterogeneous Catalysis*; Ertl, G., Knözinger, H., Schüth, F., Weitkamp, J., Eds.; Wiley-VCH: Weinheim, 2007; pp 3308–3329.
237. Kang, G.-J.; Ma, J.; Chen, Z.-X. *Catal. Lett.* **2012**, *142*, 287–293.
238. Claus, P. *Top. Catal.* **1998**, *5*, 51–62.
239. Delbecq, F.; Sautet, P. *J. Catal.* **2002**, *211*, 398–406.
240. Loffreda, D.; Delbecq, F.; Vigné, F.; Sautet, P. *Angew. Chem. Int. Ed.* **2005**, *44*, 5279–5282.
241. Cao, X.-M.; Burch, R.; Hardacre, C.; Hu, P. *J. Phys. Chem. C* **2011**, *115*, 19819–19827.
242. Cao, X. M.; Burch, R.; Hardacre, C.; Hu, P. *Catal. Today* **2011**, *165*, 71–79.
243. Yang, B.; Wang, D.; Gong, X.-Q.; Hu, P. *Phys. Chem. Chem. Phys.* **2011**, *13*, 21146–21152.

244. Ide, M. S.; Hao, B.; Neurock, M.; Davis, R. J. *ACS Catal.* **2012**, *2*, 671–683.
245. Delbecq, F.; Sautet, P. *J. Catal.* **2003**, *220*, 115–126.
246. Haubrich, J.; Loffreda, D.; Delbecq, F.; Sautet, P.; Jugnet, Y.; Krupski, A.; Becker, C.; Wandelt, K. *J. Phys. Chem. C* **2008**, *112*, 3701–3718.
247. Haubrich, J.; Loffreda, D.; Delbecq, F.; Sautet, P.; Jugnet, Y.; Becker, C.; Wandelt, K. *J. Phys. Chem. C* **2010**, *114*, 1073–1084.
248. Haubrich, J.; Loffreda, D.; Delbecq, F.; Sautet, P.; Jugnet, Y.; Krupski, A.; Becker, C.; Wandelt, K. *Phys. Chem. Chem. Phys.* **2011**, *13*, 6000–6009.
249. Murillo, L. E.; Goda, A. M.; Chen, J. G. *J. Am. Chem. Soc.* **2007**, *129*, 7101–7105.
250. Zheng, R.; Humbert, M. P.; Zhu, Y.; Chen, J. G. *Catal. Sci. Technol.* **2011**, *1*, 638–643.
251. Murillo, L. E.; Menning, C. A.; Chen, J. G. *J. Catal.* **2009**, *268*, 335–342.
252. Kitchin, J. R.; Khan, N. A.; Barteau, M. A.; Chen, J. G.; Yakshinksiy, B.; Madey, T. E. *Surf. Sci.* **2003**, *544*, 295–308.
253. Kitchin, J. R.; Norskov, J. K.; Barteau, M. A.; Chen, J. G. *J. Chem. Phys.* **2004**, *120*, 10240–10246.
254. Bron, M.; Teschner, D.; Knop-Gericke, A.; Steinhauer, B.; Scheybal, A.; Hävecker, M.; Wang, D.; Födisch, R.; Hönicke, D.; Wootsch, A.; Schlögl, R.; Claus, P. *J. Catal.* **2005**, *234*, 37–47.
255. Mohr, C.; Hofmeister, H.; Radnik, J.; Claus, P. *J. Am. Chem. Soc.* **2003**, *125*, 1905–1911.
256. Bron, M.; Teschner, D.; Knop-Gericke, A.; Jentoft, F. C.; Kröhnert, J.; Hohmeyer, J.; Volckmar, C.; Steinhauer, B.; Schlögl, R.; Claus, P. *Phys. Chem. Chem. Phys.* **2007**, *9*, 3559–3569.
257. Bron, M.; Teschner, D.; Wild, U.; Steinhauer, B.; Knop-Gericke, A.; Volckmar, C.; Wootsch, A.; Schlögl, R.; Claus, P. *Appl. Catal. A* **2008**, *341*, 127–132.
258. Lim, K. H.; Chen, Z.-X.; Neyman, K. M.; Rösch, N. *Chem. Phys. Lett.* **2006**, *420*, 60–64.
259. Ferullo, R.; Branda, M. M.; Illas, F. *J. Phys. Chem. Lett.* **2010**, *1*, 2546–2549.
260. Christmann, K. *Surf. Sci. Rep.* **1988**, *9*, 1–163.
261. Hohmeyer, J.; Kondratenko, E. V.; Bron, M.; Kröhnert, J.; Jentoft, F. C.; Schlögl, R.; Claus, P. *J. Catal.* **2010**, *269*, 5–14.
262. Greeley, J.; Mavrikakis, M. *J. Phys. Chem. B* **2005**, *109*, 3460–3471.
263. Montoya, A.; Schlunke, A.; Haynes, B. S. *J. Phys. Chem. B* **2006**, *110*, 17145–17154.
264. Mohammad, A. B.; Yudanov, I. V.; Lim, K. H.; Neyman, K. M.; Rösch, N. *J. Phys. Chem. C* **2008**, *112*, 1628–1635.
265. Mohammad, A. B.; Lim, K. H.; Yudanov, I. V.; Neyman, K. M.; Rösch, N. *Phys. Chem. Chem. Phys.* **2007**, *9*, 1247–1254.
266. He, X.; Chen, Z.-X.; Kang, G.-J. *J. Phys. Chem. C* **2009**, *113*, 12325–12330.
267. Carabineiro, S. A. C.; Nieuwenhuys, B. E. *Gold Bull.* **2009**, *42*, 288–301.
268. Carabineiro, S. A. C.; Nieuwenhuys, B. E. *Gold Bull.* **2010**, *43*, 252–266.
269. Ishida, T.; Haruta, M. *Angew. Chem. Int. Ed.* **2007**, *46*, 7154–7156.
270. Haruta, M.; Yamada, N.; Kobayashi, T.; Iijima, S. *J. Catal.* **1989**, *115*, 301–389.
271. Wittstock, A.; Neumann, B.; Schaefer, A.; Dumbuya, K.; Kübel, C.; Biener, M. M.; Zielasek, V.; Steinrück, H.-P.; Gottfried, J. M.; Biener, J.; Hamza, A.; Bäumer, M. *J. Phys. Chem. C* **2009**, *113*, 5593–5600.
272. Wittstock, A.; Biener, J.; Bäumer, M. *Phys. Chem. Chem. Phys.* **2010**, *12*, 12919–12930.
273. Wittstock, A.; Zielasek, V.; Biener, J.; Friend, C. M.; Bäumer, M. *Science* **2010**, *327*, 319–322.
274. Han, D.; Xu, T.; Xu, X.; Ding, Y. *ChemCatChem* **2010**, *2*, 383–386.
275. Asao, N.; Ishikawa, Y.; Hatakeyama, N.; Menggenbateer, Y.; Yamamoto, Y.; Chen, M.; Zhang, W.; Inoue, A. *Angew. Chem. Int. Ed.* **2010**, *49*, 10093–10095.
276. Lopez, N.; Janssens, T. V. W.; Clausen, B. S.; Xu, Y.; Mavrikakis, M.; Bligaard, T.; Nørskov, J. K. *J. Catal.* **2004**, *223*, 232–235.
277. Campbell, C. T. *Science* **2004**, *306*, 234–235.
278. Janssens, T. V. W.; Clausen, B. S.; Hvolbæk, B.; Falsig, H.; Christensen, C. H.; Bligaard, T.; Nørskov, J. K. *Top. Catal.* **2007**, *44*, 15–26 and references therein.
279. Zielasek, V.; Jürgens, B.; Schulz, C.; Biener, J.; Biener, M. M.; Hamza, A. V.; Bäumer, M. *Angew. Chem. Int. Ed.* **2006**, *45*, 8241–8244.
280. Mills, G.; Gordon, M. S.; Metiu, H. *J. Chem. Phys.* **2003**, *118*, 4198–4205.
281. Xu, Y.; Mavrikakis, M. *J. Phys. Chem. B* **2003**, *107*, 9298–9307.
282. Liu, Z.-P.; Hu, P.; Alavi, A. *J. Am. Chem. Soc.* **2002**, *124*, 14770–14779.
283. Bond, G. C.; Thompson, D. T. *Catal. Rev. Sci. Eng.* **1999**, *41*, 319–388.
284. Moskaleva, L. V.; Röhe, S.; Wittstock, A.; Zielasek, V.; Klüner, T.; Neyman, K. M.; Bäumer, M. *Phys. Chem. Chem. Phys.* **2011**, *13*, 4529–4539.
285. Fajín, J. L. C.; Cordeiro, M. N. D. S.; Gomes, J. R. B. *J. Phys. Chem. C* **2007**, *111*, 17311–17321.
286. Kim, J.; Samano, E.; Koel, B. E. *Surf. Sci.* **2006**, *600*, 4622–4632.
287. Vinod, C. P.; Hans, J. W. N.; Nieuwenhuys, B. E. *Appl. Catal. A* **2005**, *291*, 93–97.
288. Chesters, M. A.; Somorjai, G. A. *Surf. Sci.* **1975**, *52*, 21–28.
289. Jiang, P.; Porsgaard, S.; Borondics, F.; Köber, M.; Caballero, A.; Bluhm, H.; Besenbacher, F.; Salmeron, M. *J. Am. Chem. Soc.* **2010**, *132*, 2858–2859.
290. Gottfried, J. M.; Elghobashi, N.; Schroeder, S. L. M.; Christmann, K. *Surf. Sci.* **2003**, *523*, 89–102.
291. Biener, J.; Biener, M. M.; Nowitzki, T.; Hamza, A. V.; Friend, C. M.; Zielasek, V.; Bäumer, M. *ChemPhysChem* **2006**, *7*, 1906–1908.
292. Baber, A. E.; Torres, D.; Müller, K.; Nazzarro, M.; Liu, P.; Starr, D. E.; Stacchiola, D. J. J. *Phys. Chem. C.* **2012**, *116*, 18292–18299.
293. Baker, T. A.; Liu, X.; Friend, C. M. *Phys. Chem. Chem. Phys.* **2011**, *13*, 34–46.
294. Iizuka, Y.; Kawamoto, A.; Akita, K.; Date, M.; Tsubota, S.; Okumura, M.; Haruta, M. *Catal. Lett.* **2004**, *97*, 203–208.
295. Sanchez-Castillo, M. A.; Couto, C.; Kim, W. B.; Dumesic, J. A. *Angew. Chem. Int. Ed.* **2004**, *43*, 1140–1142.
296. Xu, C.; Su, J.; Xu, X.; Liu, P.; Zhao, H.; Tian, F.; Ding, Y. *J. Am. Chem. Soc.* **2007**, *129*, 42–43.
297. U, C.; Xu, X.; Su, J.; Ding, Y. *J. Catal.* **2007**, *252*, 243–248.
298. Haruta, M. *ChemPhysChem* **2007**, *8*, 1911–1913.
299. Déronzier, T.; Morfin, F.; Massin, L.; Lomello, M.; Rousset, J.-L. *Chem. Mater.* **2011**, *23*, 5287–5289.
300. Wang, A. Q.; Liu, J. H.; Lin, S. D.; Lin, T. S.; Mou, C. Y. *J. Catal.* **2005**, *233*, 186–197.
301. Jürgens, B.; Kübel, C.; Schulz, C.; Nowitzki, T.; Zielasek, V.; Biener, J.; Biener, M. M.; Hamza, A. V.; Bäumer, M. *Gold Bull.* **2007**, *40*, 142–149.
302. Fajín, J. L. C.; Cordeiro, M. N. D. S.; Gomes, J. R. B. *Chem. Commun.* **2011**, *47*, 8403–8405.
303. Saliba, N.; Parker, D. H.; Koel, B. E. *Surf. Sci.* **1998**, *410*, 270–282.
304. Gottfried, J. M.; Schmidt, K. J.; Schroeder, S. L. M.; Christmann, K. *Surf. Sci.* **2003**, *525*, 184–196.
305. Campbell, C. T. *Surf. Sci.* **1985**, *157*, 43–60.
306. Raukema, A.; Butler, D. A.; Kleyn, A. W. *J. Phys. Condens. Matter* **1996**, *8*, 2247–2263.
307. Torres, D.; Neyman, K. M.; Illas, F. *Chem. Phys. Lett.* **2006**, *429*, 86–90.
308. Ruggiero, C.; Hollins, P. *J. Chem. Soc. Faraday Trans.* **1996**, *92*, 4829–4834.
309. Weststrate, C. J.; Lundgren, E.; Andersen, J. N.; Rienks, E. D. L.; Gluhoi, A. C.; Bakker, J. W.; Groot, I. M. N.; Nieuwenhuys, B. E. *Surf. Sci.* **2009**, *603*, 2152–2157.
310. Lemire, C.; Meyer, R.; Shaikhutdinov, S.; Freund, H.-J. *Angew. Chem. Int. Ed.* **2004**, *43*, 118–121.
311. Nowitzki, T.; Nickut, P.; Deiter, C.; Wollschläger, J.; Al-Shamery, K.; Bäumer, M. *Surf. Sci.* **2006**, *600*, 3595–3599.
312. Yim, W.-L.; Nowitzki, T.; Necke, M.; Schnars, H.; Nickut, P.; Biener, J.; Biener, M. M.; Zielasek, V.; Al-Shamery, K.; Klüner, T.; Bäumer, M. *J. Phys. Chem. C* **2007**, *111*, 445–451.
313. Moskaleva, L. V.; Zielasek, V.; Klüner, T.; Neyman, K. M.; Bäumer, M. *Chem. Phys. Lett.* **2012**, *525–526*, 87–91.
314. Outka, D. A.; Madix, R. J. *Surf. Sci.* **1987**, *179*, 351–360.
315. Gottfried, J. M.; Christmann, K. *Surf. Sci.* **2004**, *566–568*, 1112–1117.
316. Min, B. K.; Alemozafar, A. R.; Pinnaduwage, D.; Deng, X.; Friend, C. M. *J. Phys. Chem. B* **2006**, *110*, 19833–19838.
317. Min, B. K.; Friend, C. M. *Chem. Rev.* **2007**, *107*, 2709–2724.
318. Samano, E.; Kim, J.; Koel, B. E. *Catal. Lett.* **2009**, *128*, 263–267.
319. Gong, J. L.; Mullins, C. B. *Acc. Chem. Res.* **2009**, *42*, 1063–1073.
320. Biener, J.; Wittstock, A.; Biener, M. M.; Nowitzki, T.; Hamza, A. V.; Bäumer, M. *Langmuir* **2010**, *26*, 13736–13740.
321. Eshuis, H.; Bates, J. E.; Furche, F. *Theor. Chem. Acc.* **2012**, *131*, 1084.
322. Klimeš, J.; Bowler, D. R.; Michaelides, A. *Phys. Rev. B* **2011**, *83*, 195131.
323. Zhang, I. Y.; Xu, X. *Int. Rev. Phys. Chem.* **2012**, *30*, 115–160.

Section 11.5

Top Catal
DOI 10.1007/s11244-013-0050-1

ORIGINAL PAPER

Catalysis from First Principles: Towards Accounting for the Effects of Nanostructuring

Sergey M. Kozlov · Konstantin M. Neyman

Abstract The article deals with an issue of density-functional description of heterogeneous catalysts by nanoparticle models instead of still commonly employed slab models. Typically, active (metal) components are present in catalysts as nano-aggregates formed of many thousands atoms, remaining due to their size inaccessible even for modern first-principles computations. However, such species could be rather realistically represented by notably smaller computationally tractable model nanoparticles, whose surface sites only marginally change the reactivity with increasing particle size. Herein presented results are mainly related to methane dehydrogenation on Pt catalysts, methanol decomposition on Pd catalysts and the composition of active sites on Pt/ceria catalysts. They document the feasibility of taking nanostructuring effects into account in density-functional modeling (at least for transition metals) and, more importantly, demonstrate that ignoring the nanoeffects in these systems leads to misrepresentation of their catalytic properties.

Keywords Density-functional calculations · Surface reactivity · Slab models · Nanoparticles · Heterogeneous catalysis

S. M. Kozlov · K. M. Neyman
Departament de Química Física and Institut de Química Teòrica i Computacional (IQTCUB), Universitat de Barcelona, c/Martí i Franquès, 1, 08028 Barcelona, Spain

K. M. Neyman (✉)
Institució Catalana de Recerca i Estudis Avançats (ICREA), 08010 Barcelona, Spain
e-mail: konstantin.neyman@icrea.cat

Published online: 14 May 2013

1 Introduction

Heterogeneous catalysis is an area of nanoscience established a long time before the prefix "nano" became fashionable and indicative of cutting-edge research and technology [1, 2]. Indeed, typical "real" catalysts are complex materials made of several components and containing metal nanoparticles (NPs), which are considered to be essential for the catalytic action [3]. The NPs inherently expose edge, kink and other sites involving under-coordinated atoms, whose reactivity may differ significantly from that of the corresponding metal surfaces. Yet, the understanding of structure–activity relationships of catalysts at the atomic scale has long been relied mainly on the reactivity studies of single-crystal metal surfaces [4]; the problem is referred to as the materials gap between surface science and catalysis [5].

Design of model catalysts composed of well-characterized metal NPs supported on oxide films [6, 7] enabled more than a decade ago to successfully bridge this gap experimentally. In principle, already on model catalysts prepared in such a way one may observe many important phenomena that are absent on single-crystal surfaces. Among them are strong metal support interaction (SMSI) and spillover or reverse spillover processes. Also the model catalyst approach allows one to tune the size of metal NPs and, thus, the fraction of edge, corner and other low-coordinated sites on their surface in a controllable way. Moreover, despite that moderately thin oxide films reproduce well the properties of bulk oxides, they are still able to conduct electrons to substrate via tunneling and defects and, thus, allow one to use the whole arsenal of surface science techniques on them.

Despite significant advances in this direction from the side of experiment, the material gap problem is ignored

(with only few exceptions) in first-principles computational studies related to heterogeneous catalysis [8–11]: there, so-called slab models still remain the "working horse". Questions arise, why metal NPs in catalysts have to be simulated by slabs featuring atoms arranged as on extended surfaces rather than by appropriate NP models? Are electronic structure calculations of models realistic enough to mimic heterogeneous catalysts with NPs containing several hundreds or thousands metal atoms still prohibitively expensive? Density-functional (DF) studies of NPs composed of a hundred transition or noble metal atoms pioneered almost two decades ago [12–15] imply that the computational cost is not a severe limitation. Instead, crucial is to ensure that the accuracy of employed NP models to describe adsorptive and reactivity features of key active sites on (larger) experimentally studied NPs is only insignificantly affected by the increase of model size [16, 17].

In the next section we will outline methodological aspects of relevant to heterogeneous catalysis DF studies that employed NP models made of $\sim$100 atoms and emphasize main advantages and limitations of this computational approach. Afterwards, we will address the microscopic effects of nanostructuring on the properties of selected catalytic systems investigated in detail computationally. These case studies, where the nanoeffects range from strong to dramatic, include (1) methane dehydrogenation on the surface of Pt, (2) structure, bonding and infrared (IR) spectra of adsorbed CH_xO_y intermediates of methanol decomposition on Pd NPs, (3) initial stage of formation of subsurface C deposits in Pd catalysts, and finally (4) electronic and chemical state of Pt species deposited on CeO_2 support. We hope that this article will convince the reader of the necessity and feasibility of theoretical studies using nanostructured models of catalytic systems that mimic experimental situations more realistically.

2 Methodology

Calculations of supported metal NPs that consist of thousands of atoms are still not feasible with electronic structure methods, e.g. DF ones, even on modern computers. A practical way to treat this type of problems is to consider either (1) moderately big unsupported NPs (>75 atoms) or (2) unrealistically small sub-nanoscale supported species (often <20 atoms). In this work we focus on the former approach, because (as will be shown later) it allows one to estimate properties of much bigger unsupported NPs. Also we believe that certain relatively unreactive supports, such as MgO or Al_2O_3, do not alter significantly the catalytic activity of sizeable NPs deposited on them. However, one should note that sometimes the approach (2) also yields results in a good agreement with experiments performed on much larger NPs [18, 19].

2.1 Scalability with Size

An attractive way to investigate properties of up to 10 nm large NPs typically present in experiment [20, 21] could be to calculate much smaller, computationally feasible models and to extrapolate the obtained results to bigger systems. However, one should exercise caution while doing this, because the extrapolation is possible only when the property under investigation changes smoothly and monotonically with the NP size. NPs that fulfill this condition for a given property are called scalable (with size) [22].

Several DF studies [8, 12–14, 16, 23–25] have demonstrated that various properties of truncated octahedral transition metal NPs of $\sim$100 and more atoms including interatomic distances, cohesive energies, and adsorptive properties indeed vary smoothly and monotonically with NP size. Thus, it is proven that these models are suitable to simulate the properties of much bigger NPs. In contrast, smaller NPs [25] and metal clusters with other shapes [26–28] (not in line with Wulff construction) exhibit significant fluctuations of their properties with minor changes in their size. Thus, these NPs belong to the so-called "every atom counts" regime [22]. Such NPs cannot be reliably used to predict properties of bigger species typically present in experiment.

It is essential to establish if a model NP considered in a computational study belongs to the "every atom counts" or "scalable" regime. Moreover, the transition between the regimes depends on material composing the NPs and property under investigation. Here we will focus only on the dependency of NP interactions with adsorbates on NP size, a property which governs the catalytic activity. For example, it was shown that truncated octahedral Pd NPs of $\geq$70 atoms yield scalable with size CO adsorption energies on NP terraces [16, 25, 29] and NO adsorption energies on NP edges [30]. However, to produce scalable with size adsorption energies of stronger bound adsorbates, such as atomic C, bigger Pd and Pt NPs of 140 atoms were found to be required [31, 32]. A special case is Au NPs, for which scalability of adsorption energies on species up to 225 atoms could not be established [33]. Only recently Au_{561} (2.7 nm in size) and bigger NPs were found to be sufficiently big to yield atomic O and CO adsorption energies close to the values calculated on slabs [34].

One should note that scalability with size has not been sufficiently studied for nonmetallic NPs. Few studies indicate that cohesive energies of $(ZnO)_N$, $(SiO_2)_N$ and $(CeO_2)_N$ clusters indeed exhibit scalable behavior starting from $N = 13$ [22]. Nevertheless, due to the scarcity of available studies [35] it is hard to conclude at which NP

size adsorptive properties of these systems become representative for the properties of similar sites on larger NPs. A study that considered such an important for catalysis property as the O vacancy formation energy in CeO_2 NPs implied that even $Ce_{80}O_{160}$ species may not yet behave as scalable with size [36, 37].

2.2 Comparison to Slab Studies

An important and advantageous feature of scalable with size models is that results calculated for processes on their terraces can be often extrapolated to the corresponding results for slab models. Such agreement indicates that the two computational approaches are consistent. From the practical point of view, this means that the properties of certain active sites on bigger experimentally studied NPs may be predicted not only via extrapolation of results calculated on smaller NPs, but also via interpolation of results calculated on smaller NPs to those calculated on slab models.

Presently, there are only few studies published that compare adsorption energies calculated on terraces of scalable with size NPs to those calculated with the same method on extended surfaces. For example, NO adsorption energies on Pd_{79} NPs were calculated to be just 9 % higher than on Pd(111) slabs [30] and the adsorption energies of C atoms on Pd_{79} and Pt_{79} NPs were calculated to be only ~4 % different from the values on respective (111) slabs [32, 38].

Because of the scarcity of such studies, it is worth commenting a systematic DF investigation where adsorption properties of (111) terraces, edges, and corners of metal (Ag, Au, Cu, Ni, Pd, Pt) NPs were compared to the properties of (111) terraces, edges, and kinks of respective metal slabs [39]. There it was found that (111) facets of Cu, Ni, and Pd NPs consisting of 79 atoms were big enough to adequately represent the adsorption of a single ethylene molecule on the corresponding infinite surfaces. The differences between respective adsorption energies of ethylene on the centre of a (111) nanofacet of M_{79} and on M(111) slabs (M = Cu, Ni, Pd) were found to be less than 10 kJ/mol. Agreement of the same quality was found for M_{140} NPs (M = Cu, Ni, Pd). However, M_{38} NPs displayed deviations up to ~20 kJ/mol in the ethylene adsorption energies in comparison with the respective slabs. In contrast, metals, such as Au and Pt, showed much slower convergence of ethylene adsorption energies with NP size towards the slab values. In this case, differences between the adsorption energies on the slabs and respective (111) nanofacets of M_{79} (M = Au, Pt) were found to be up to 40 kJ/mol; the agreement was improved to better than 10 kJ/mol on M_{140} NPs. For Ag NPs it was impossible to study the adsorption of ethylene on (111) facets because of weak chemisorptive interaction.

Similar trends were observed for ethylene adsorption on NP edges and step sites on surfaces vicinal to (111) terraces [39]. In this case, Ag, Cu, Ni and Pd NPs of 79 atoms were found to be sufficient to produce results close enough to those obtained on slabs, with deviations <12 kJ/mol. Slightly better agreement was observed between the adsorption energies on the edges of M_{140} NPs (M = Ag, Cu, Ni, and Pd) and step sites on slabs of the respective metals. However, for Au and Pt only M_{140} NPs yielded the ethylene adsorption energies close to those obtained on the respective slab systems (deviations of less than ~10 kJ/mol), while NPs of 79 atoms showed deviations up to 32 kJ/mol. Corner sites seem to be sufficiently well represented even on the smallest considered M_{38} NPs of Ag, Pd and Pt. Differences between respective ethylene adsorption energies on the corners of M_{38} species and kinks on rough M slabs (M = Ag, Pd, Pt) do not exceed 5 kJ/mol. However, to model the adsorption of ethylene on corners of some other metals (Au, Cu, Ni), bigger NPs of 79 atoms or more may be required [39].

3 Reaction Profile of Methane Decomposition on Pt Nanoparticles

A very convincing example of how nanostructuring alters catalyst properties was given by Viñes et al., who considered methane decomposition on Pt(111) slab and edges of truncated octahedral Pt_{79} NP [40]. On edges of Pt NPs the reaction was calculated to be almost 8 times more exothermic than on Pt(111) and proceed through significantly lower activation barriers for the rate-limiting steps (Fig. 1). This finding was confirmed by a complementary molecular beam/high-resolution photoelectron spectroscopy investigation, which found the reaction to occur even at 100 K on

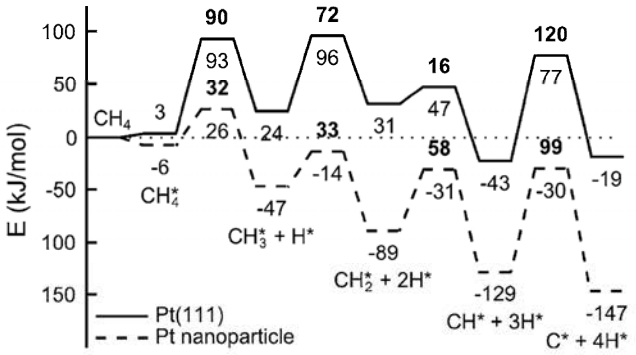

Fig. 1 Energy profiles of methane decomposition on a Pt(111) slab model (*solid line*) and Pt_{79} NP (*dashed line*) after zero point energy corrections as calculated in Ref. [40]. Relative stability of the reaction intermediates and the products is given with respect to the total energy sum of the bare metal substrate and gas-phase methane. Activation barriers (in *bold*) are also given

Pt NPs [40]. At the same time, on Pt(111) single-crystal the reaction required temperatures of 260 K to proceed [41].

The reason for Pt activation by nanostructuring is because CH_3 and CH_2 species are stabilized on NP edges by 48 and 76 kJ/mol, respectively, which converts the first two steps of methane decomposition from endothermic on Pt(111) to exothermic on Pt_{79}. Moreover, the stabilization significantly lowers the activation energies of the first two steps, from 90 and 72 kJ/mol to ~33 kJ/mol both. The exothermicity of the two last steps of methane decomposition is also higher on edges of Pt NPs than on Pt(111). However, only the barrier of the last step, $CH \rightarrow C + H$, is decreased by 21 kJ/mol, while the activation energy of $CH_2 \rightarrow CH + H$ is increased to 58 kJ/mol. The latter increase may be explained by significant stabilization of the initial state, CH_2 species, on the edges. The higher activity of edge Pt atoms was rationalized by their lower coordination and higher flexibility. The latter is especially important in the case of strongly bound adsorbates such as C atoms. This study clearly demonstrated that in some cases the studies performed on extended surfaces yield qualitatively different results from those obtained on nanostructured models mimicking industrial catalysts.

4 Adsorption and IR Spectra of Methanol Decomposition Intermediates on Pd Nanoparticles

The change of adsorptive properties of a catalyst due to nanostructuring was illustrated by a computational investigation of CO, CH_xO and CH_x ($x = 1$–3) species on Pd_{79} NPs [17, 42]. Majority of the considered species were found to be stabilized by 17–50 kJ/mol on the edge sites of Pd_{79} NP in comparison with terrace sites (Fig. 2). In general, the strongest stabilization occurs when species adsorb on the bridge sites on the edges, then the stabilization may be ~20 kJ/mol (CH_2, CO) or even >35 kJ/mol (CH_3O, CH_2O, CHO) [42]. In some cases (CH_3O, CHO, and CO), the type of adsorption site on the NP edge is not the same as that on the terrace. This may occur when species prefer to adsorb on the three-fold hollow sites of NP terraces, because these sites cannot be composed of edge atoms alone. Also, unlike the bridge sites, the three-fold hollow sites are not significantly stabilized next to the edges in comparison with terraces.

The difference between structures of adsorption complexes in the cases of edge and terrace adsorption is reflected in IR spectra of adsorbed species, which are often useful for species identification in experiment [43, 44]. For instance, a combined theoretical and experimental study made it possible to document differences between vibrations of CO molecules adsorbed on terraces and on edges of Pd NPs [17]. Analysis of calculated vibrational frequencies of CH_x and CH_xO ($x = 1$–3) adsorbates on various sites of NP Pd_{79} suggests that these differences are sufficient to experimentally distinguish species adsorbed on edges and on terraces [42]. For example, the O–H stretching frequency of CH_2OH and C–H stretching frequency in edge adsorbed species were calculated to be 46 and 53 cm^{-1} different from those of the species adsorbed on (111) facets. More pronounced changes are noticed for CHO, which exhibits the C–H stretching frequency 100 cm^{-1} higher and the C–O stretching frequency 208 cm^{-1} lower when it is adsorbed on the edges than when it is adsorbed on the NP facets. Previously, the difference of 23 cm^{-1} between stretching frequencies of edge and terrace adsorbed CO species was found to be enough to distinguish between them in a joint theoretical and experimental investigation [17].

However, even for the adsorbates that have very close vibrational frequencies on the terraces and the edges (CH_3O, CH_2O, CH_3 and CH) one could determine their location on NPs by monitoring relative intensities of various peaks. Species adsorbed on the NP edges may exhibit very different tilting to the metal surface compared to the adsorbates located on the terraces. Thus, due to the surface selection rules, new vibrational modes may become visible in the IR spectra of those species. At the same time, intensities of the IR peaks that were strong enough to be observed in the spectra of the adsorbates on the terraces may be decreased or even vanish. This concept is illustrated by alterations of the IR intensities of the molecular vibrations of CH_2OH, CH_3O and CH_3 species [42]. In the case of CH_2OH, the H–C–H scissor mode is computed to be IR-active only for adsorption on a NP edge, while the peak intensity of the C–O–H bending mode is greatly decreased in this case. For CH_3 species adsorbed on NP edges, some of the asymmetric deformations of C–H bonds may become IR-active, yielding IR peaks in the region around 1400 cm^{-1}. Finally, CH_3O molecules located on the edges are strongly inclined to one of the NP facets and thus do not exhibit IR-active modes with frequencies >1200 cm^{-1}. In general, appearance of modes that were IR-inactive on terraces due to the surface selection rules may serve as a good indicator of the edge adsorption.

5 Effect of Flexibility of Nanoparticulate Pd on Adsorption and Subsurface Absorption of C Impurities

Peculiar properties of metal NPs are caused not only by altered chemical properties of low coordinated atoms, but also by somewhat shorter average interatomic distances in small NPs [16, 24] and higher flexibility of their structure and consequently easier stress relief within NP. The higher flexibility may affect not only adsorptive properties of sites

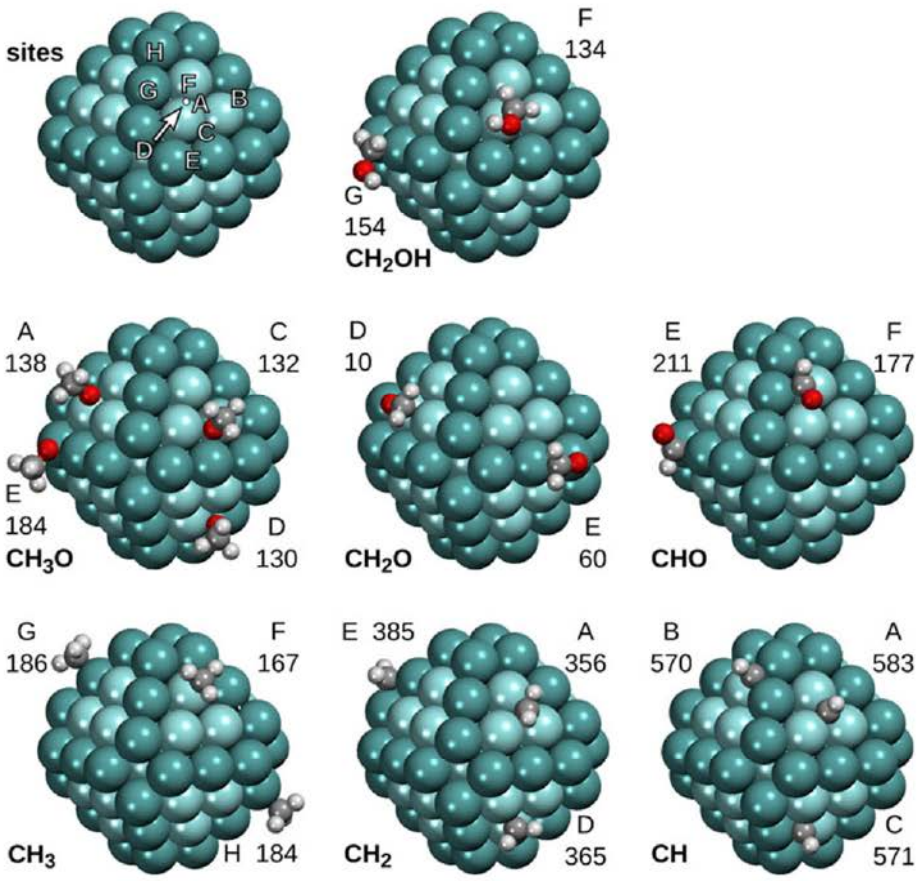

Fig. 2 Calculated adsorption energies (in kJ/mol) of CH_x and CH_xO species ($x = 1$–3) on various sites of Pd_{79} nanoparticles. Note that only one species was adsorbed at a time. Reprinted from Kozlov et al. [42], Copyright (2011), with permission from Elsevier

involving low-coordinated atoms but, more importantly, terrace sites at some distance from the edges. This effect is more pronounced for adsorbates strongly bound to the NP, when substrate relaxation is substantial. Atomic C on Pd is one of such adsorbates. Presently, it attracts special attention because it is a side product in methanol decomposition and dehydrogenation reactions [21, 45, 46], which is able to modify catalyst properties upon exothermic migration into subsurface region [38, 47–49].

Adsorption energies of C atom on the fcc and hcp sites of sizeable Pd_{140} NPs were calculated to be 28 and 14 kJ/mol higher than on respective sites of Pd(111) surface [38]. The energies of C absorption into the tetrahedral (tss) or octahedral (oss) subsurface sites are also increased by $\sim$15 kJ/mol on Pd_{140} in comparison with Pd(111). The most drastic effect of higher flexibility of Pd NPs is on migration barriers of C from surface to subsurface sites, a process that involves passing of C through stretched triangle of surface Pd atoms. On extended surfaces the barriers of fcc$\rightarrow$oss and hcp$\rightarrow$tss migrations to subsurface are calculated to be 63 and 48 kJ/mol, respectively. It should be noted, the values decrease dramatically at high C coverages [50]. At the same time, on the (111) terraces of Pd_{140} NPs the activation energies are only 43 and 14 kJ/mol, respectively [38]. In the vicinity of the NPs edges these barriers decrease even further to 12 and $\sim$0 kJ/mol. Thus, the effect of nanostructuring on catalyst properties is shown not to be located only on the edges, but to extend to terrace sites at some distance from them.

6 Effect of Nanostructuring on Strong Metal-Support Interaction in Pt/CeO_2 Catalysts

Interactions of metal particles with materials on which they are supported can radically modify the catalytic performance. Such effects—either deactivating or promoting—become really prominent in the case of "strong metal-support interaction", which implies exceptionally intimate contacts between metal and support and is actively discussed for decades [51–54]. In this case, nanostructuring of both active component and support may open new channels in SMSI.

Due to the great complexity of the catalytic materials under consideration and of the phenomena involved, the origin of such interactions commonly remains a mystery at the microscopic level. However, recently a combination of DF calculations with synchrotron-radiation experiments on models of industrially important Pt-ceria catalysts succeeded to uncover atomic details of interactions in this complex

system and unique properties revealed exclusively at the nanoscale [55–57].

In that study, interactions of sub-nanoscale Pt_8 cluster with $Ce_{21}O_{42}$ and $Ce_{40}O_{80}$ model ceria NPs [56] as well as with $CeO_2(111)$ slab model [57] have been computationally explored applying a so-called GGA + U DF approach. The former two models of the ceria support were employed to represent Pt-ceria nano-composites, whereas the latter (111) slab model mimicked a catalyst, where Pt is supported on bulk-like ceria samples that expose fairly extended terraces. The presence of an O vacancy in each of the aforementioned models of ceria support, on which the Pt_8 species had been deposited, was also considered [56, 57].

These calculations identified two types of oxidative Pt-ceria interactions (Fig. 3): (1) electron transfer from the Pt particle to the support and (2) oxygen transport from ceria to Pt [55]. The electron transfer appeared to be favorable on ceria supports, irrespective of their morphology. Remarkably, the oxygen transfer (often referred to as the "reverse spillover") was shown to require the presence of Pt in close contact with nanostructured ceria, where oxygen is dramatically more mobile than on ordered extended ceria surfaces [36, 37]. Thus, the reverse spillover is inherently a nanostructure sensitive effect. Both effects (1) and (2) were experimentally detected by monitoring the Ce^{3+}/Ce^{4+} ratio using resonant photoelectron spectroscopy on well-defined Pt-CeO_2 model catalysts [55]. These findings enabled to propose the formation mechanism of Pt–O species on ceria

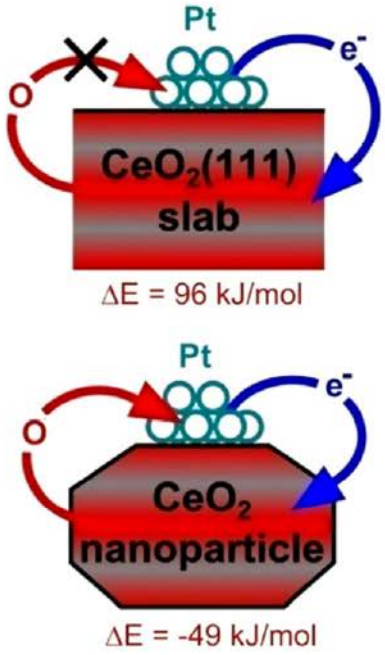

Fig. 3 Sketch of the calculated similarities and differences in the properties of a Pt/ceria model catalyst as a function of nanostructuring of their CeO_2 support. ΔE are the energy values (*negative* means exothermic) of the O transfer process from ceria to Pt_8 models

and to shed light on the observed extraordinary structure–activity relationship of ceria-based catalysts in general.

7 Summary

To summarize, this article outlines the advanced, based on DF methodology, computational approach of representing nanocomposite heterogeneous catalysts by nanoparticulate models, which are more realistic than conventional surface slab models. It documents the feasibility of DF studies of model NPs that (at least for transition metals) are large enough to possess surface reactivity changing predictably with increasing particle size and thus appropriate to describe the reactivity of larger experimentally studied particles. The discussed examples reveal very significant differences in the surface reactivity derived from customary slab-model calculations and those employing pertinent NP models. The latter expose a variety of active sites, whose structure and geometric flexibility notably better mimic those of the sites present under experimental conditions. In fact, ignoring the nano-effects in these systems leads to misrepresentation of their catalytic properties. Thus, we advocate much broader usage of suitable nanoparticulate models in "catalysis from first principles" and expect it to become a standard approach in the near future.

Acknowledgments Financial support from the Spanish Ministerio de Economía y Competitividad (grants FIS2008-02238, CTQ2012-34969) and the Generalitat de Catalunya (grant 2009SGR1041) is gratefully acknowledged. SMK thanks the Spanish Ministerio de Educación for a pre-doctoral grant AP2009-3379. The work is also supported by the COST Action CM1104 "Reducible oxide chemistry, structure and functions". Computer resources, technical expertise and assistance were partly provided by the Red Española de Supercomputación.

References

1. Bell AT (2003) Science 299:1688
2. Schlögl R, Abd Hamid SB (2004) Angew Chem Int Ed 43:1628
3. Ertl G, Knözinger H, Schüth F, Weitkamp J (eds) (2008) Handbook of heterogeneous catalysis, 2nd edn. Wiley-VCH, Weinheim
4. Ertl G (2008) Angew Chem Int Ed 47:3524
5. Jaeger NI (2001) Science 293:1601
6. Bäumer M, Freund HJ (1999) Progr Surf Sci 61:127
7. Freund HJ, Kuhlenbeck H, Libuda J, Rupprechter G, Bäumer M, Hamann H (2001) Top Catal 15:201
8. Neyman KM, Illas F (2005) Catal Today 105:2
9. Nørskov JK, Scheffler M, Toulhoat H (2006) MRS Bull 31:669
10. Hammer B (2006) Top Catal 37:3
11. Nørskov JK, Bligaard T, Rossmeisl J, Christensen CH (2009) Nat Chem 1:37
12. Pacchioni G, Chung SC, Krüger S, Rösch N (1994) Chem Phys 184:125
13. Häberlen OD, Chung SC, Stener M, Rösch N (1997) J Chem Phys 106:5189
14. Krüger S, Vent S, Nörtemann F, Staufer M, Rösch N (2001) J Chem Phys 115:2082

15. Nava P, Sierka M, Ahlrichs R (2003) Phys Chem Chem Phys 5:3372
16. Yudanov IV, Sahnoun R, Neyman KM, Rösch N (2002) J Chem Phys 117:9887
17. Yudanov IV, Sahnoun R, Neyman KM, Rösch N, Hoffmann J, Schauermann S, Johánek V, Unterhalt H, Rupprechter G, Libuda J, Freund HJ (2003) J Phys Chem B 107:255
18. Green IX, Tang W, Neurock M, Yates JT Jr (2011) Science 333:736
19. Green IX, Tang W, Neurock M, Yates JT Jr (2011) Angew Chem Int Ed 50:10186
20. Meusel I, Hoffmann J, Hartmann J, Heemeier M, Bäumer M, Libuda J, Freund HJ (2001) Catal Lett 71:5
21. Schauermann S, Hoffmann J, Johánek V, Hartmann J, Libuda J, Freund HJ (2002) Angew Chem Int Ed 41:2532
22. Bromley ST, de PR Moreira I, Neyman KM, Illas F (2009) Chem Soc Rev 38:2657
23. Baletto F, Ferrando R (2005) Rev Mod Phys 77:371
24. Roldán A, Viñes F, Illas F, Ricart JM, Neyman KM (2008) Theor Chem Acc 120:565
25. Yudanov IV, Genest A, Schauermann S, Freund HJ, Rösch N (2012) Nano Lett 12:2134
26. Pettersson LGM, Faxen T (1993) Theor Chim Acta 85:345
27. Kua J, Goddard WA III (1999) J Am Chem Soc 121:10928
28. Jacob T, Goddard WA III (2005) J Phys Chem B 109:297
29. Yudanov IV, Metzner M, Genest A, Rösch N (2008) J Phys Chem C 112:20269
30. Viñes F, Desikusumastuti A, Staudt T, Görling A, Libuda J, Neyman KM (2008) J Phys Chem C 112:16539
31. Neyman KM, Inntam C, Gordienko AB, Yudanov IV, Rösch N (2005) J Chem Phys 122:174705
32. Viñes F, Neyman KM, Görling A (2009) J Phys Chem A 113:11963
33. Roldán A, Ricart JM, Illas F (2011) Theor Chem Acc 128:675
34. Kleis J, Greeley J, Romero NA, Morozov VA, Falsig H, Larsen AH, Lu J, Mortensen JJ, Dułak M, Thygesen KS, Nørskov JK, Jacobsen KW (2011) Catal Lett 141:1067
35. Migani A, Loschen C, Illas F, Neyman KM (2008) Chem Phys Lett 465:106
36. Migani A, Vayssilov GN, Bromley ST, Illas F, Neyman KM (2010) Chem Commun 46:5936
37. Migani A, Vayssilov GN, Bromley ST, Illas F, Neyman KM (2010) J Mater Chem 20:10535
38. Viñes F, Loschen C, Illas F, Neyman KM (2009) J Catal 266:59
39. Pozun ZD, Tran K, Shi A, Smith RH, Henkelman G (2011) J Phys Chem C 115:1811
40. Viñes F, Lykhach Y, Staudt T, Lorenz MPA, Papp C, Steinrück HP, Libuda J, Neyman KM, Görling A (2010) Chem Eur J 16:6530
41. Fuhrmann T, Kinne M, Tränkenschuh B, Papp C, Zhu JF, Denecke R, Steinrück HP (2005) New J Phys 7:107
42. Kozlov SM, Cabeza GF, Neyman KM (2011) Chem Phys Lett 506:92
43. Morkel M, Kaichev VV, Rupprechter G, Freund HJ, Prosvirin IP, Bukhtiyarov VI (2004) J Phys Chem B 108:12955
44. Borasio M, Rodríguez de la Fuente O, Rupprechter G, Freund HJ (2005) J Phys Chem B 109:17791
45. Rebholz M, Kruze N (1991) J Chem Phys 95:7745
46. Yudanov IV, Matveev AV, Neyman KM, Rösch N (2008) J Am Chem Soc 130:9342
47. Wilde M, Fukutani K, Ludwig W, Brandt B, Fischer JH, Schauermann S, Freund HJ (2008) Angew Chem Int Ed 47:9289
48. Teschner D, Vass E, Hävecker M, Zafeiratos S, Schnörch P, Sauer H, Knop-Gericke A, Schlögl R, Chamam M, Wootsch A, Canning AS, Gamman JJ, Jackson SD, McGregor J, Gladden LF (2006) J Catal 242:26
49. Tiruppathi P, Low JJ, Chan ASY, Bare SR, Meyer R (2011) Catal Today 165:106
50. Kozlov SM, Yudanov IV, Aleksandrov HA, Rösch N (2009) Phys Chem Chem Phys 11:10955
51. Tauster SJ, Fung SC, Garten RL (1978) J Am Chem Soc 100:170
52. Tauster SJ (1987) Acc Chem Res 20:389
53. Conner WC, Falconer JL (1995) Chem Rev 95:759
54. Bruix A, Rodriguez JA, Ramírez PJ, Senanayake SD, Evans J, Park JB, Stacchiola D, Liu P, Hrbek J, Illas F (2012) J Am Chem Soc 134:8968
55. Vayssilov GN, Lykhach Y, Migani A, Staudt T, Petrova GP, Tsud N, Skála T, Bruix A, Illas F, Prince KC, Matolin V, Neyman KM, Libuda J (2011) Nat Mater 10:310
56. Vayssilov GN, Migani A, Neyman K (2011) J Phys Chem C 115:16081
57. Bruix A, Migani A, Vayssilov GN, Neyman KM, Libuda J, Illas F (2011) Phys Chem Chem Phys 13:11384

Section 11.6

THE JOURNAL OF PHYSICAL CHEMISTRY C

Article

pubs.acs.org/JPCC

Water Chemistry on Model Ceria and Pt/Ceria Catalysts

Yaroslava Lykhach,*[,†] Viktor Johánek,[‡] Hristiyan A. Aleksandrov,[§,⊥] Sergey M. Kozlov,[⊥] Markus Happel,[†] Tomáš Skála,[∥,‡] Petko St. Petkov,[§] Nataliya Tsud,[‡] Georgi N. Vayssilov,[§] Kevin C. Prince,[∥,#] Konstantin M. Neyman,[⊥,▽] Vladimír Matolín,[‡] and Jörg Libuda[†,◆]

[†]Lehrstuhl für Physikalische Chemie II, Friedrich-Alexander-Universität Erlangen-Nürnberg, Egerlandstrasse 3, 91058 Erlangen, Germany

[‡]Charles University, Faculty of Mathematics and Physics, Department of Surface and Plasma Science, V Holešovičkách 2, 18000 Prague, Czech Republic

[§]Faculty of Chemistry and Pharmacy, University of Sofia, 1126 Sofia, Bulgaria

[⊥]Departament de Quimica Fisica and Institut de Quimica Teorica i Computacional (IQTCUB), Universitat de Barcelona, C/Marti Franques 1, 08028 Barcelona, Spain

[∥]Sincrotrone Trieste SCpA, Strada Statale 14, km 163.5, 34149 Basovizza-Trieste, Italy

[#]IOM, Strada Statale 14, km 163.5, 34149 Basovizza-Trieste, Italy

[▽]Institucio Catalana de Recerca i Estudis Avançats (ICREA), 08010 Barcelona, Spain

[◆]Erlangen Catalysis Resource Center, Friedrich-Alexander-Universität Erlangen-Nürnberg, Egerlandstrasse 3, 91058 Erlangen, Germany

ABSTRACT: We have studied the interaction of water with stoichiometric $CeO_2(111)/Cu(111)$, partially reduced $CeO_{2-x}/Cu(111)$, and $Pt/CeO_2/Cu(111)$ model catalysts by means of synchrotron−radiation photoelectron spectroscopy (SRPES), resonant photoemission spectroscopy (RPES) at the Ce 4d edge, infrared reflection absorption spectroscopy (IRAS), and density functional (DF) calculations. The principal species formed during adsorption of water at 160 K on $CeO_2(111)$ films is chemisorbed molecular water. On the surface of CeO_{2-x} water partially dissociates yielding hydroxyl groups. By use of core-level PES, differentiation between chemisorbed water and hydroxyl groups is complicated by the overlap of the corresponding spectral features. Nevertheless, we determined three characteristic indicators for OH groups on ceria: (i) the presence of 1π and 3σ states in valence band (VB) PES; (ii) an increase of the binding energy (BE) separation between the O 1s spectral components of lattice oxygen and OH/H_2O; (iii) an increase of the amplitude of the Ce^{3+} resonance in RPES. Chemisorbed water desorbs below 400 K and hydroxyl groups vanish at 500 K. The most favorable configurations of chemisorbed water and hydroxyl groups have been investigated by DF calculations. Both $CeO_2(111)$ and CeO_{2-x} involve strongly tilted H_2O and OH species which complicate their detection by IRAS. On Pt/CeO_2, water adsorbs molecularly at 160 K but undergoes partial dissociation during annealing. The dissociation of water is accompanied by spillover of hydrogen to ceria and formation of hydroxyl groups between 180 and 250 K. Above 250 K, decomposition of hydroxyl groups and reverse spillover of hydrogen from ceria to Pt occurs, followed by desorption of molecular water.

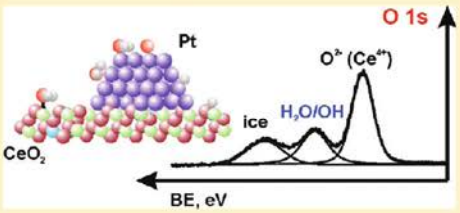

1. INTRODUCTION

Microscopic understanding of the water interaction with ceria-based catalysts has significant implications for numerous chemical processes, e.g., the steam reforming of hydrocarbons or the water gas shift (WGS) reaction. The fundamental aspects of the water interaction with various solid surfaces has been reviewed in detail, e.g., by Thiel and Madey[1] and by Henderson.[2] In general, it was reported that water interacts more strongly with oxide surfaces compared to noble metal surfaces. On most metal oxide surfaces, water interacts with the cation site via its $3a_1$ orbital. Depending on the structure and stoichiometry of the oxide, the water molecule may then adsorb either molecularly or dissociatively.[1,2]

On the stoichiometric $CeO_2(111)$ surface, water molecules adsorb above cerium ions[3−7] without dissociation, and Kumar and Shelling[6] predicted tilted adsorption geometries of the molecule based on density functional (DF) calculations. As a result, the water molecule forms single[6,7] or double[5] hydrogen bonds with surface oxygen ions. Dissociation of water occurs on reduced or partially reduced CeO_{2-x} surfaces.[8−12] It has been suggested that the water molecule dissociates forming OH groups, which fill the oxygen vacancies and are hydrogen bound to surface oxygens.[5,7] Filling of oxygen vacancies by hydroxyl groups on ceria has been confirmed experimentally by Gritschneder and Reichling[4] using dynamic atomic force microscopy. However, discrepancies remain in the literature

Received: March 7, 2012
Revised: May 17, 2012
Published: May 17, 2012

regarding the impact of water on the cerium oxidation state. For instance, Kundakovic et al.[8] reported desorbed H_2 to be the main product of *irreversible* water dissociation on reduced ceria on Ru(0001), but they observed no significant alteration of the oxidation state of cerium, neither upon adsorption nor desorption. In contrast, Henderson et al.[9] reported that dissociation of water on reduced ceria on yttria-stabilized $ZrO_2(111)$ is *reversible*, i.e., occurs without release of H_2 into the gas phase. The authors attributed weak reduction of ceria upon water adsorption at elevated temperatures to redistribution of oxygen vacancies from the bulk to the surface. Berner et al.[10] observed reduction of noncontinuous CeO_x deposits on Pt(111) during adsorption of water at 300 K without significant formation of hydroxyl groups. An apparent reduction of ceria induced by water has also been observed on stoichiometric $CeO_2(111)$ films on Cu(111) by Matolín et al.[12] The authors suggested[12] that the water molecule triggers a redistribution of charge within the cerium ion, yielding a charge depletion in 5d and a charge accumulation in 4f states. DF studies[6] imply another explanation of the observed effect: they predict a strong attractive interaction between water and bulk oxygen vacancies, causing rapid diffusion of vacancies to the surface. Both experimental[8−12] and theoretical[7] studies agree that water tends to reduce rather than reoxidize ceria, at least for the systems and conditions investigated.

Dissociation of water on noble metal surfaces occurs less readily.[1,2] Shavorskiy et al.[13] investigated the reactivity of water on hexagonal Pt-group metals and found higher reactivity for the 4d metals (Ru, Rh, Pd) as compared to 5d (Ir, Pt). Generally, Pt(111) and Pt stepped surfaces are considered particularly inert toward water dissociation. However, adding a small amount of oxygen to the surface facilitates dissociation of water on Pt(111).[13−15] In the presence of thick ice layers, the dissociation of a buried monolayer of water on Pt(111) has also been reported.[16]

Establishing whether a water molecule adsorbs molecularly or dissociatively on the catalyst's surface may represent a challenge to many surface diagnostic tools.[1,2] The problems arise from many similarities in the properties of molecular H_2O and OH species or from overlaps of distinctive spectral features, e.g., in photoelectron spectroscopy. Characterization of mixed molecular and dissociative adsorption is especially difficult in the case of reversible dissociation.

In this paper, we perform a comprehensive study of water adsorption and dissociation on well-ordered stoichiometric $CeO_2(111)$, partially reduced CeO_{2-x}, and $Pt/CeO_2(111)$ model catalysts prepared on Cu(111) single crystal. We combine synchrotron radiation photoelectron spectroscopy (SRPES), resonant photoemission spectroscopy (RPES), and infrared reflection absorption spectroscopy (IRAS) with DF calculations. The complementarity of these methods largely resolves the above-mentioned difficulties and provides insight into the water chemistry on ceria based catalysts and the related redox processes.

2. EXPERIMENTAL METHODS

2.1. SRPES and RPES. High-resolution SRPES was performed at the Materials Science Beamline at the Elettra synchrotron facility in Trieste, Italy. The radiation source was a bending magnet producing synchrotron light in the energy range of 21−1000 eV. The ultrahigh vacuum (UHV) end-station (base pressure 1×10^{-10} mbar) was equipped with a multichannel electron energy analyzer (Specs Phoibos 150), a rear-view low-energy electron diffraction (LEED) optics, an argon sputter gun, and a gas inlet system. The basic setup of the chamber includes a dual Mg/Al X-ray source used for energy calibration of the synchrotron light and for off-line work. Additionally, two electron-beam evaporators for Ce and Pt deposition were installed. A single crystal Cu(111) disk (MaTecK GmbH, 99.999%) was used as a substrate for $CeO_2(111)$, CeO_{2-x}, and $Pt/CeO_2(111)$. First, Cu(111) was cleaned by several cycles of Ar^+ sputtering (300 K, 60 min) and annealing (723 K, 5 min) until no traces of carbon or any other contaminant were found in the photoelectron spectra. Epitaxial layers of CeO_2 were prepared on clean Cu(111) by physical vapor deposition (PVD) of Ce metal (Goodfellow, 99.99%) in an oxygen atmosphere ($p_{O_2} = 5 \times 10^{-7}$ mbar, Linde, 99.999%) at 523 K, followed by annealing of the films at 523 K in an oxygen atmosphere at the same pressure for 10 min. The preparation method[17,18] yields a continuous, stoichiometric $CeO_2(111)$ film with a thickness in the range of 1.9−2.1 nm as determined from the attenuation of the Cu $2p_{3/2}$ intensity. LEED observations of the prepared films confirm the epitaxial growth of $CeO_2(111)$ with the characteristic (1.5×1.5) superstructure relative to the Cu(111) substrate.[17] According to previous scanning tunneling microscopy (STM) studies, flat $CeO_2(111)$ terraces are separated by steps and contain extended rough patches composed of small ceria particles.[19,20] Partially reduced ceria film (CeO_{2-x}) was prepared by exposing a stoichiometric $CeO_2(111)$ film to 45 L (Langmuir, 1 L = 1.33×10^{-6} mbar × s) of methanol by backfilling the chamber at a sample temperature of 700 K, followed by annealing at 700 K in UHV for 30 min. The procedure yields partially reduced CeO_{2-x} films, where $x = 0.16$.[21] Pt was deposited by means of PVD from a Pt wire (0.5 mm in diameter, Goodfellow, 99.99%) onto CeO_2/Cu(111) at 300 K. The nominal thickness of the deposited Pt layer was 0.4 nm as determined from the attenuation of the Cu $2p_{3/2}$ intensity. The structure and thermal stability of the Pt/CeO_2 systems have been discussed before.[22] Briefly, Pt nanoparticles grown at 300 K preferentially nucleate at rough patches of the ceria surface. Typically, the density of Pt particles is $(5.4 \pm 1.0) \times 10^{23}$ cm^{-2}, and the average size of Pt particles is 3.3 ± 0.3 nm for the Pt/CeO_2 system with a nominal thickness of the Pt deposit of 0.5 nm.

VB spectra were acquired at three different photon energies (PEs), 121.4, 124.8, and 115.0 eV, that correspond to the resonant enhancements in Ce^{3+}, Ce^{4+} ions, and to off-resonance conditions, respectively. Analysis of the spectra obtained with these photon energies forms the basis of RPES.[21] Core level spectra of O 1s, C 1s, and Pt 4f were acquired at 650, 410, and 180 eV, respectively. The BEs in the spectra acquired with synchrotron radiation were calibrated with respect to the Fermi level. Additionally, Al Kα radiation (1486.6 eV) was used to measure the core levels of O 1s, C 1s, Pt 4f, Ce 3d, and Cu $2p_{3/2}$. All spectra were acquired at constant pass energy and at an emission angle for the photoelectrons of 20 or 0° with respect to the sample normal, while using the X-ray source or synchrotron radiation, respectively. The total spectral resolutions achieved were 1 eV (Al Kα), 200 meV (PE = 115−180 eV), 400 meV (PE = 410 eV), and 650 meV (PE = 650 eV). The core level spectra were fitted with a Doniach-Šunjić (DS) function convoluted with Gaussian (Pt 4f) or Voigt (O 1s, C 1s) profiles after proper background subtraction. All SRPES and PES data were processed using KolXPD fitting software.[23]

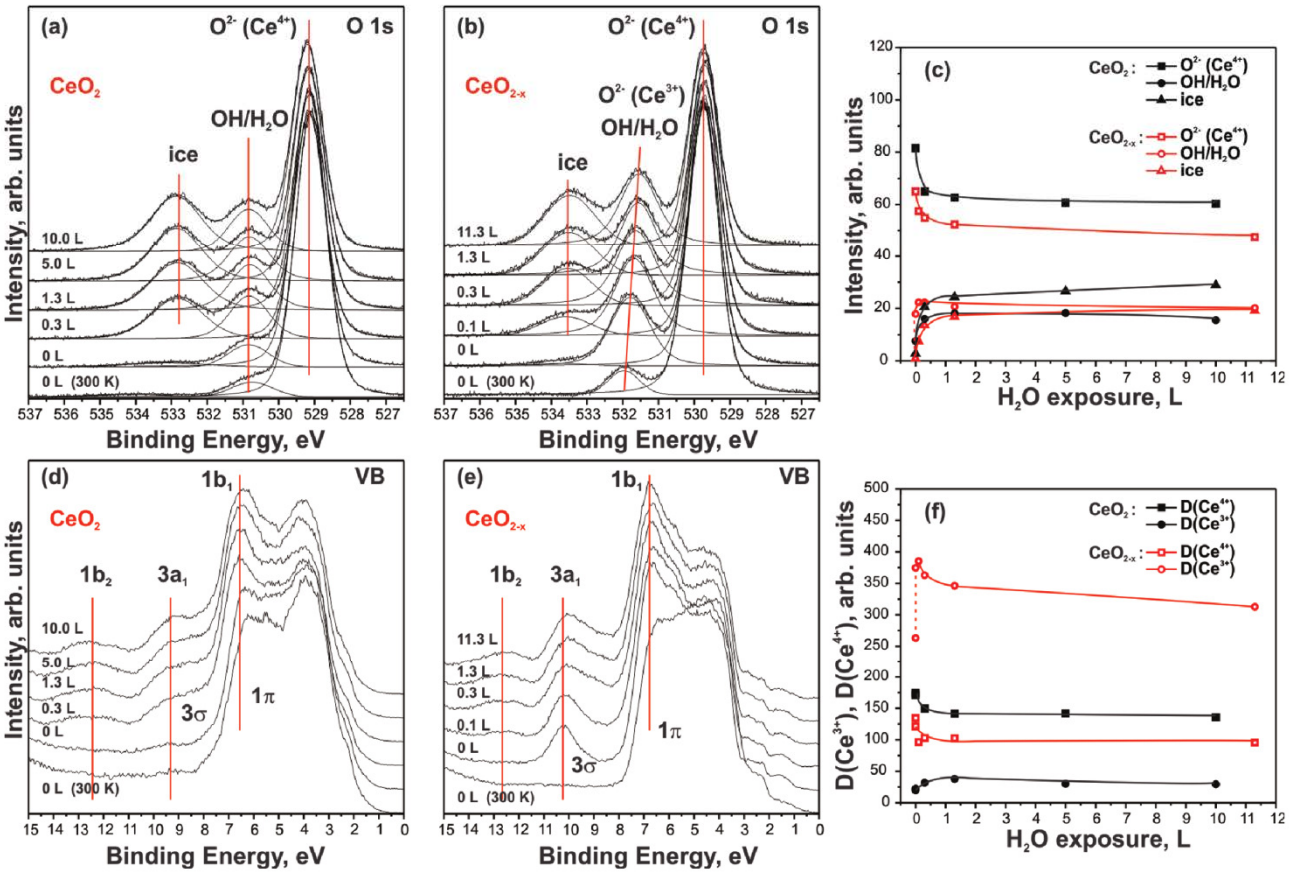

Figure 1. O 1s core level (a–b) and VB (d–e) spectra obtained from $CeO_2(111)$ (a, d) and CeO_{2-x} (b, e) during exposure to increasing doses of H_2O at 160 K. The bottom spectra were obtained from as-prepared samples at 300 K. The O 1s (a–b) and the VB (d–e) spectra were acquired with photon energies of 650 and 115 eV, respectively. Integrated intensities of O 1s spectral components (c) and $D(Ce^{3+})$ and $D(Ce^{4+})$ resonant enhancement (f) as functions of H_2O exposure on $CeO_2(111)$ (black) and CeO_{2-x} (red).

During the experiment the sample temperature was controlled by a DC power supply passing a current through Ta wires holding the sample. Temperatures were measured by a K-type thermocouple attached to the rear surface of the sample. Stable temperature and fast cooling after the annealing steps were achieved by simultaneous resistive heating and cooling of the manipulator with liquid nitrogen. The investigated samples were exposed in consecutive doses to a total amount of 10 - 11 L of H_2O at 160 K by backfilling the UHV chamber.

2.2. Molecular Beams (MB) and IRAS. The MB/IRAS measurements were performed in an UHV apparatus at the Friedrich-Alexander-University Erlangen-Nuremberg, Germany. The setup allows exposure of the sample surface to up to four effusive beams and one supersonic beam. A beam monitor is used that permits exact MB alignment and calibration. In addition, the system is equipped with a vacuum Fourier transform IR (FTIR) spectrometer (Bruker IFS 66/v), two quadrupole mass spectrometers (QMS), a vacuum transfer system, and a high-pressure cell.

A Cu(111) single crystal (MaTecK GmbH, 99.999%) was used as a substrate for $CeO_2(111)$, CeO_{2-x}, and Pt/CeO_2 films. Well-ordered $CeO_2(111)$ and Pt/CeO_2 films were prepared according to the procedures described in section 2.1. The deposition rates of Ce (1.5–2.0 nm per hour) and Pt (0.3 nm per hour) were calibrated using a quartz crystal microbalance (QCM). The resulting thickness of the $CeO_2(111)$ film was 1.2–1.5 nm, and the nominal thickness of the deposited Pt layer was 0.4 nm. A partially reduced ceria film (CeO_{2-x}) was produced by means of sputtering of the $CeO_2(111)$ film at 300 K with Ar^+ ions at energy of 0.7 kV and ion current density 2.5 $\mu A/cm^2$ for 5 min. The procedure results in increased step density and formation of oxygen vacancies on the terraces.[12]

The $CeO_2(111)$ and CeO_{2-x} films were exposed to deuterated water, D_2O, (Sigma-Aldrich, 99.96%) at 110 K, while $Pt/CeO_2(111)$ was exposed to D_2 (Linde, 99.9%) at 150 K. The deuterated water was used in order to distinguish between the OH vibrations of the water adsorbed on ceria and the residual water in the IR detector. Both gases, D_2O and D_2, were dosed via the room-temperature MB nozzle. Argon was used as a carrier gas for D_2O, and the amount of D_2O in the gas stream calibrated by the QMS and beam monitor was 3.6%. Pressures of D_2 and D_2O + Ar at the surface of the samples were 1.2×10^{-6} mbar and 2.0×10^{-6} mbar, respectively.

The IR spectra were acquired as follows: First background spectra of the clean samples were taken. Then the samples were exposed to defined doses of D_2O using the MB, and then the IR spectrum was recorded. The total exposures of D_2O and D_2 on the samples were ~24 and 50 L, respectively. Finally, the samples were flashed to the desired temperature and cooled down to 110 K again in order to acquire temperature dependent spectra.

2.3. Density Functional Modeling. To model surface complexes on CeO_2, we used the plane-wave VASP code[24,25] employing a generalized gradient approximation (GGA) in the form of the PW91 exchange-correlation functional.[26] In accord with earlier studies,[27−29] the Hubbard scheme (GGA+U) with the on-site Coulomb correction U_{eff} = 4 eV was applied to all Ce 4f orbitals to reinforce their localization. The core−valence interaction was treated with the projector augmented wave method (plane wave energy cutoff 415 eV).[30,31] Because of the considerable size of the unit cell, the calculations were performed only at the Γ-point of reciprocal space. The total energy threshold defining the self-consistency of the electron density was set to 10^{-4} eV and all structures were optimized until forces acting on the relaxed atoms were smaller than 0.2 eV/nm. Spin-polarized calculations were performed when a single H atom was adsorbed on CeO_2, while spin-restricted calculations were performed when H_2O was adsorbed or dissociated on CeO_2. For all optimized structures we determined the relative stability and calculated the harmonic vibrational frequencies that justified their true local energy-minimum character.

We represented the experimentally treated rough ceria surfaces by a model of a stepped $CeO_2(111)$ surface.[32] Step edges running along the $\langle 2\bar{1}1 \rangle$ direction were modeled with stoichiometric O−Ce−O stripes located on top of a double-trilayer $CeO_2(111)$ slab. To minimize mutual interactions between adjacent steps we used a unit cell that consists of 60 Ce and 120 O atoms (first trilayer, $Ce_{12}O_{24}$; second and third trilayers, $Ce_{24}O_{48}$ each). The size of the unit cell is 1.322 × 1.984 nm^2 with an angle between both directions of 60°. The slabs are separated by more than 1.2 nm of vacuum from their nearest periodic images. The present stepped model has been recently validated by its accurate representation of STM images of nanoislands observed on $CeO_2(111)$ films.[32]

3. RESULTS AND DISCUSSION

3.1. Adsorption of Water on Stoichiometric $CeO_2(111)$ and Partially Reduced CeO_{2-x}. The O 1s core level spectra obtained from stoichiometric $CeO_2(111)/Cu(111)$ and partially reduced $CeO_{2-x}/Cu(111)$ during exposure to increasing doses of water at 160 K are shown in parts a and b of Figure 1, respectively. The spectra obtained from as-prepared samples at 300 K are shown at the bottom of each figure. The main components in the O 1s spectra at BEs of 529.3 eV (CeO_2) and 529.7 eV (CeO_{2-x}) emerge due to lattice oxygen anions located near Ce^{4+} cations, $O^{2-}(Ce^{4+})$.[8,33,34] A small contribution from O^{2-} located near Ce^{3+}, $O^{2-}(Ce^{3+})$, appears at 532.0 eV in the O 1s spectrum obtained from partially reduced CeO_{2-x}.[34] Cooling the samples to 160 K triggers development of an additional small peak at 530.9 eV (CeO_2) and growth of the peak at 532.0 eV (CeO_{2-x}). These changes are induced by adsorption of water from the residual background gas of the UHV chamber. Subsequent exposure of the samples to water resulted in a further increase of the peaks at 530.9 (CeO_2) and 532.0 eV (CeO_{2-x}) as well as in the emergence of new peaks at 532.9 eV (CeO_2) and 533.5 eV (CeO_{2-x}). In parallel, the intensities of the features associated with lattice oxygen are attenuated with increasing doses of water on both samples.

The peaks at 532.9 eV (CeO_2) and 533.5 eV (CeO_{2-x}) are associated with formation of multilayers of water (ice) on the surfaces of both samples.[8,12] The individual assignment of the peaks at 530.9 (CeO_2) and at 532.0 eV (CeO_{2-x}) is less straightforward, however. According to the literature,[8] either peak may contain contributions from both chemisorbed water (H_2O) and hydroxyl groups (OH). As mentioned above,[8,12] water adsorbs molecularly on stoichiometric CeO_2 but undergoes partial dissociation on reduced CeO_{2-x} surfaces.[8,10,12] BEs of the two surface species are too close to be resolved experimentally.[8] By use of a nonlinear least-squares fitting procedure, Kundakovic et al.[8] identified two components separated by 0.7 eV on reduced $CeO_x(111)/Ru(0001)$. The authors assigned the lower BE component to chemisorbed water and the higher BE component to hydroxyl groups. However, in order to avoid any misinterpretation of the peaks at 530.9 (CeO_2) and 532.0 eV (CeO_{2-x}), we hereafter assign both peaks to unresolved contributions from chemisorbed water and hydroxyl groups.

The evolution of the integrated intensities of the O 1s features as a function of water exposure is shown in Figure 1c for both CeO_2 (black) and CeO_{2-x} (red). It is seen that exposures of less than 2 L are sufficient to saturate the OH/H_2O signal and generate ice contributions on the CeO_2 and CeO_{2-x} surfaces. Unlike on CeO_2, on reduced ceria the OH/H_2O component shifts gradually toward lower BE with increasing water dose. Such shifts could indeed point to the presence of two spectral components in the peak, i.e., OH and chemisorbed H_2O.

Evidence for the dissociation of water and formation of OH groups on ceria can be derived from the VB of the two samples. As reviewed by Thiel and Madey[1] and Henderson,[2] molecular water has three occupied states in the VB region assigned to the $1b_1$, $3a_1$, and $1b_2$ molecular orbitals. In contrast, surface OH gives rise to only two features that correspond to the 1π and 3σ states. The VB spectra obtained from CeO_2 and CeO_{2-x} samples are shown in parts d and e of Figure 1, respectively. Note that the presented VBs were acquired with a photon energy of 115 eV, which corresponds to the off-resonance condition and is not sensitive to any resonant features in the VB of ceria.[21,35] The bottom spectra in both figures show the VB spectra obtained at 300 K from the as-prepared samples, whose principal features were discussed earlier by Mullins et al.[34] The authors assigned two broad features at 4.5 and 6.5 eV to the O 2p orbitals hybridized with the Ce 4f and 5d orbitals, respectively. Additional spectral features emerge in the VBs of both samples, CeO_2 and CeO_{2-x}, upon cooling to 160 K and subsequent adsorption of water. On CeO_2 (Figure 1d), three features develop at 6.5, 9.3, and 12.5 eV that correspond to the $1b_1$, $3a_1$, and $1b_2$ states of molecular water. Our DF calculations also reveal two VB peaks for adsorbed OH groups and three peaks for adsorbed water molecules, which are split similarly to the experimental features. The calculated splittings between the corresponding electronic bands $1b_1-3a_1$ and $3a_1-1b_2$ for the H_2O/CeO_2 models are 1.8 and 3.8 eV, respectively, in line with the splittings between the experimental peaks.

On CeO_{2-x} (Figure 1e), the corresponding three peaks appear at 6.7, 10.2, and 12.6 eV. The most important difference between the two samples is the clear dominance of only two spectral features at 6.7 and 10.2 eV in the VB of CeO_{2-x} during the initial stage of water adsorption. We assign these peaks to the 1π and 3σ states of hydroxyl groups, indicating facile dissociation at low exposure. Above 0.3 L (see Figure 1e), the $3a_1/3\sigma$ component develops a small shoulder on the low BE side suggesting the formation of a mixed hydroxyl/molecular water layer on partially reduced ceria.

The influence of water on the oxidation state of ceria can be effectively monitored by RPES, and the fundamentals of the

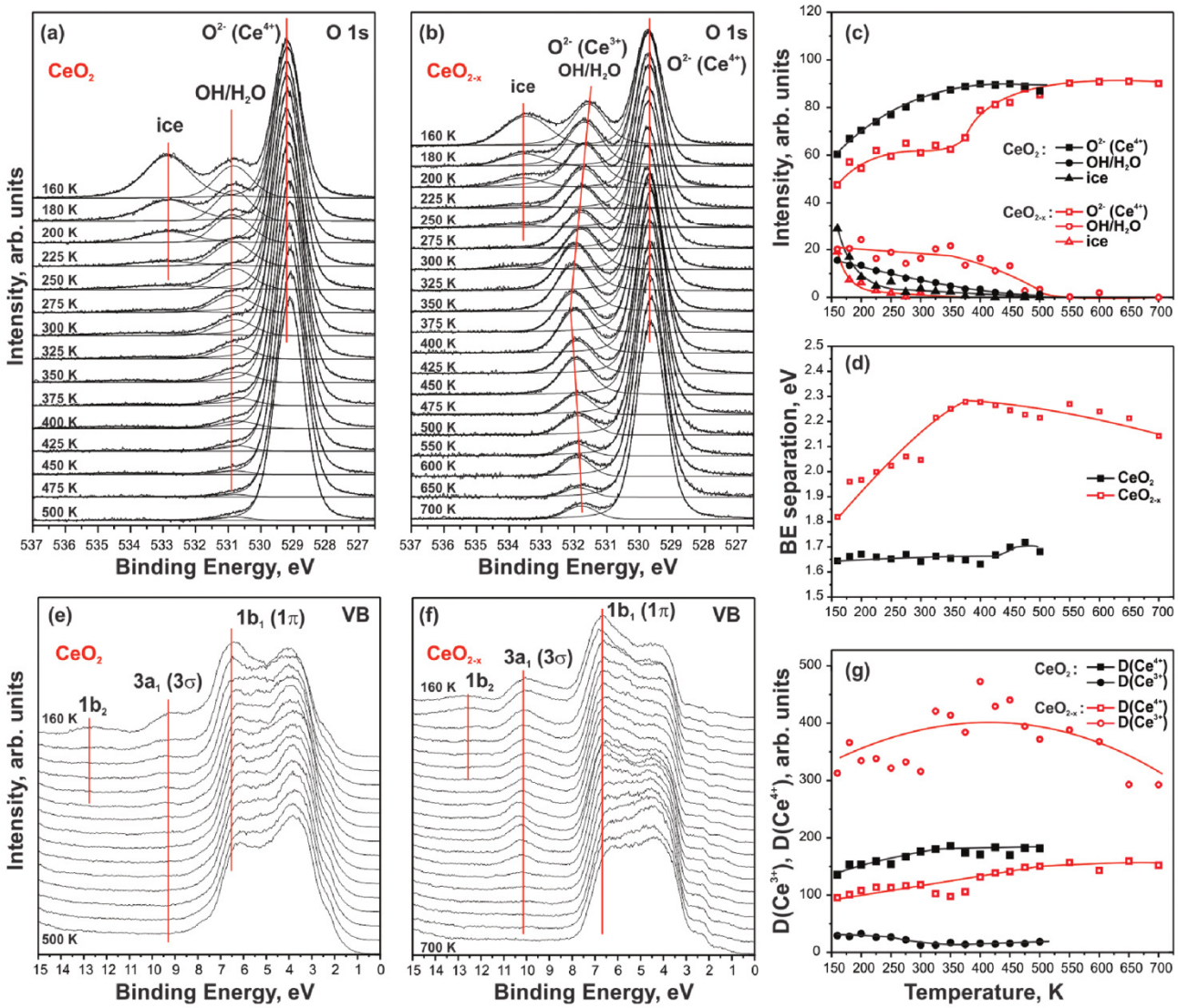

Figure 2. O 1s core level (a–b) and VB (e–f) spectra during annealing of CeO_2(111) (a, e) and CeO_{2-x} (b, f) exposed to total doses of 10 and 11.3 L of H_2O at 160 K, respectively. The O 1s (a–b) and the VB (e–f) spectra were acquired with photon energies of 650 and 115 eV, respectively. Integrated intensities of O 1s spectral components (c), BE separation between $O^{2-}(Ce^{4+})$ and OH/H_2O components (d), and $D(Ce^{3+})$ and $D(Ce^{4+})$ resonant enhancement (g) as functions of temperature on CeO_2(111) (black) and CeO_{2-x} (red).

method are described elsewhere.[21,35] Briefly, RPES is based on measuring VB photoemission spectra at photon energies corresponding to the 4d→4f resonance either for the Ce^{3+} or the Ce^{4+} ions. The Ce^{3+} resonance at a photon energy of 121.4 eV is caused by a super-Coster–Kronig decay involving electron emission from the Ce 4f states located about 1.4 eV below the Fermi edge. The Ce^{4+} resonance at photon energy of 124.8 eV involves emission of electrons from O 2p states hybridized with Ce 4f states in the VB around 4.0 eV. Additionally, the VB spectrum at photon energy of 115 eV (off-resonance) is measured. Resonant enhancements for Ce^{3+}, $D(Ce^{3+})$ and for Ce^{4+}, $D(Ce^{4+})$ are quantified by calculating the intensity difference between the corresponding features in- and off-resonance. The amplitudes of $D(Ce^{3+})$ and $D(Ce^{4+})$ are directly proportional to the concentrations of Ce^{3+} and Ce^{4+} ions in the sample, respectively.

The development of $D(Ce^{3+})$ and $D(Ce^{4+})$ during adsorption of water on CeO_2 (black) and CeO_{2-x} (red) is shown in Figure 1f. It is seen that, upon water adsorption on CeO_2, $D(Ce^{3+})$ slightly increases. On CeO_{2-x}, an initial increase of $D(Ce^{3+})$ after cooling (see dashed line) and adsorption of 0.1 L of water is followed by a decrease. At the same time, $D(Ce^{4+})$ on both samples is attenuated by the adsorbed water in a similar manner. The origin of the observed increase of $D(Ce^{3+})$ as a result of the interaction with water is not clear. Simple dissociation of water into OH^- and H^+ should not change the oxidation state of ceria.[1,2] The observed effect could be explained in terms of a strong attractive interaction between the water molecule and subsurface or bulk oxygen vacancies[5,6] or by a change of the electronic configuration of the Ce^{3+} ion as a result of the interaction with the OH group.[12] According to our observations, the change of the electronic structure on partially reduced ceria is directly related to the formation of OH groups and, therefore, may indicate water dissociation. A slighter reduction of stoichiometric CeO_2 could

thus be explained by dissociation of a small fraction of water at defects or steps (see Section 3.2.2).

3.2. Desorption and Dissociation of Water during Annealing on Stoichiometric CeO_2(111) and Partially Reduced CeO_{2-x}. *3.2.1. Identification of Adsorbed Species.* The development of the O 1s spectra during annealing of CeO_2(111) and CeO_{2-x} pre-exposed to water at 160 K is shown in parts a and b of Figure 2, respectively. It is seen that the peaks associated with ice on CeO_2 (532.9 eV) and CeO_{2-x} (533.5 eV) gradually decrease until they vanish on both samples at 275 K. The peaks associated with OH/H_2O on CeO_2 (530.9 eV) and CeO_{2-x} (532.0 eV) gradually decrease while the peaks associated with lattice oxygen, $O^{2-}(Ce^{4+})$ increase. The evolution of the integrated intensities of the peaks in the O 1s spectra obtained from CeO_2 (black) and CeO_{2-x} (red) as a function of temperature is shown in Figure 2c. Note that the OH/H_2O peak contains a small contribution from O^{2-} near Ce^{3+} ions on CeO_{2-x}, which is not resolved in Figure 2a but subtracted from the integrated intensities in Figure 2c. The figure demonstrates that the thermal stability of the OH/H_2O surface species differs for the two samples. The signals from OH/H_2O species disappear at 400 K for CeO_2 and at 500 K for CeO_{2-x} (see Figure 2c). Unlike on CeO_2, the intensity of OH/H_2O is almost constant up to 350 K on CeO_{2-x}. Another difference between the two samples is the effect of annealing on the BE of the OH/H_2O peak. Its position does not change on CeO_2, whereas it shifts to higher BE on CeO_{2-x} (compare parts a and b of Figure 2). In Figure 2d, the separation between the BEs of the lattice oxygen ($O^{2-}(Ce^{4+})$) and OH/H_2O is plotted as a function of temperature for both samples. It is seen that annealing has little effect on the BE separation between the two peaks on CeO_2. In contrast, the peak separation increases by ~0.5 eV upon annealing of CeO_{2-x} to 350 K.

The development of the VB during annealing of CeO_2(111) and CeO_{2-x} after exposure to water at 160 K and subsequent annealing is shown in parts e and f of Figure 2, respectively. As discussed above, three peaks at 6.5, 9.3, and 12.5 eV corresponding to the $1b_1$, $3a_1$, and $1b_2$ states of molecular water are resolved on CeO_2(111). We observe that the intensities of all three features decrease gradually upon annealing. Above 200 K, the $1b_2$ state completely disappears whereas two weak features at 6.5 and 9.3 eV can be traced in the spectra up to 400 K (see Figure 2e). Similarly to stoichiometric CeO_2, the $1b_2$ state also disappears from the VB of CeO_{2-x} above 200 K. However, two strong bands at 6.7 and 10.2 eV remain visible until 500 K on CeO_{2-x}, indicating high thermal stability of hydroxyl groups on partially reduced CeO_{2-x}.

In Figure 2g, the evolution of the $D(Ce^{3+})$ and $D(Ce^{4+})$ resonances for CeO_2(111) (black) and CeO_{2-x} (red) is plotted as a function of temperature. On CeO_2, $D(Ce^{3+})$ decreases, and $D(Ce^{4+})$ increases to values similar to the as-prepared sample at about 350 K. This behavior is consistent with decomposition/desorption of the OH group in this temperature range. The growth of $D(Ce^{3+})$ on CeO_{2-x} indicates increasing dissociation of water and formation of hydroxyl groups with increasing temperature. $D(Ce^{3+})$ reaches a maximum at about 380 K; note that the BE separation between $O^{2-}(Ce^{4+})$) and OH/H_2O (see Figure 2d) peaks reaches a maximum at the same temperature. The gradual increase of $D(Ce^{4+})$ is consistent with desorption/decomposition of water/hydroxyl on both samples.

It appears that the majority of hydroxyl groups are formed immediately upon adsorption of water at 160 K, on both CeO_2(111) and partially reduced CeO_{2-x}. Since hardly any change in $D(Ce^{3+})$ is observed upon annealing of CeO_2(111) we conclude that practically all defect sites active for water dissociation react upon adsorption at low temperature. The amount of hydroxyl groups formed on CeO_2(111) is, however, insufficient to contribute significantly to either the intensity or the BE of the OH/H_2O component. Contrary to this, hydroxyl groups are the principal species on CeO_{2-x}. An increase in $D(Ce^{3+})$ and BE separation indicated a further increase in the concentration of hydroxyl groups during annealing.

In summary, three characteristic experimental indications of water dissociation and formation of hydroxyl groups are identified in the O 1s spectra, VB spectra, and RPES on CeO_2(111) and partially reduced CeO_{2-x}: (i) the presence of 1π and 3σ states in the VB; (ii) the increase of the BE separation between the lattice oxygen, O^{2-} (Ce^{4+}), and OH/H_2O; (iii) the increase of $D(Ce^{3+})$ resonance.

3.2.2. IRAS and DFT Studies: Geometry of Water and OH on Ceria. The IR absorption spectra obtained from CeO_2 and CeO_{2-x} after exposure to 24 L of D_2O at 110 K are shown in parts a and b of Figure 3. Two bands emerge in the spectral regions of both samples at 2525 and 2730 cm^{-1}. The band at 2525 cm^{-1} corresponds to the OD stretching vibration of hydrogen (deuterium)-bound OD within multilayer water (ice).[36,37] The band at 2730 cm^{-1} is associated with dangling OD groups of water molecules in 3D ice islands.[37−39]

Surprisingly, the bands at 2525 and 2730 cm^{-1} disappear after annealing to 200 K on both samples. In view of the O 1s spectra described in section 3.2.1, a substantial amount of surface species, either in the form of chemisorbed water or hydroxyl groups, should be left on the surfaces of both samples, CeO_2 and CeO_{2-x}, under these conditions. Only the multilayer water (ice) layer should have desorbed (see parts a−c of Figure 2). However, the remaining species are apparently not detectable in the IRAS experiment. We attribute the remarkable insensitivity of IRAS experiment to surface OD/D_2O to an unfavorable inclined geometry and small dynamic dipole moment of the surface species on ceria leading to a very low relative absorption signal.[40−42]

The configuration of water molecules on extended CeO_2(111) surfaces has been extensively modeled by DFT methods.[5−7] Since CeO_2(111) films prepared on Cu(111) are rather rough,[19,20] we performed a complementary DF GGA+U study (see section 2.3 for details) of water adsorption on stepped CeO_2(111) surface. A slab consisting of two O−Ce−O trilayers with a stripe of a single O−Ce−O trilayer atop[32] was used to represent a step edge running along the $\langle 2\bar{1}1 \rangle$ direction on the (111) surface plane (see Figure 4a; the other panels of Figure 4 display the structures of all studied adsorption complexes b−m). The adsorption of water, estimated by the adsorption energy, $E_{ad}(H_2O)$, at the terrace, site b, and at the step, site c, is exothermic, suggesting that both sites can be populated upon water adsorption. For site b we obtained $E_{ad}(H_2O)$ = −0.50 eV, very close to the values of −0.52 and −0.49 eV reported by Marrocchelli and Yildiz[43] and by Fronzi et al.[5] At the step site c the water molecule is more strongly bound by 0.39 eV, with $E_{ad}(H_2O)$ = −0.89 eV.

In both these cases, the water molecules are strongly tilted with respect to the surface normal. This adsorption geometry will decrease the perpendicular component of the dynamic dipole moment of the O−D stretching mode in the limit of low coverage. Note that the metal surface selection rule (MSSR) requires a component of the dynamic dipole moment normal to

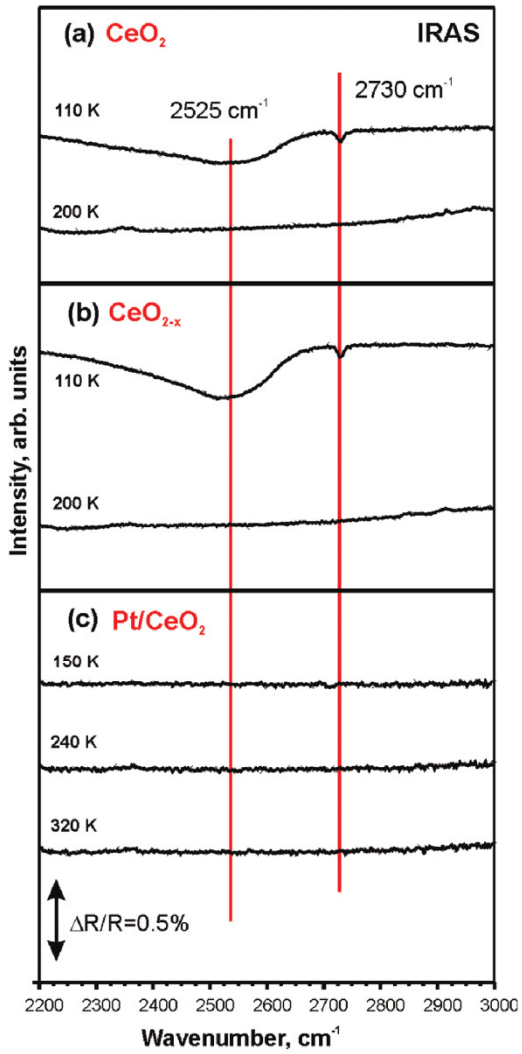

Figure 3. IRAS spectra obtained from $CeO_2(111)$ (a) and CeO_{2-x} (b) exposed to a total dose of 24 L of D_2O at 110 K and subsequently annealed to 200 K. IRAS spectra obtained from $Pt/CeO_2(111)$ (c) exposed to a total dose of 24 L of D_2 at 110 K and subsequently annealed to 240 and 320 K.

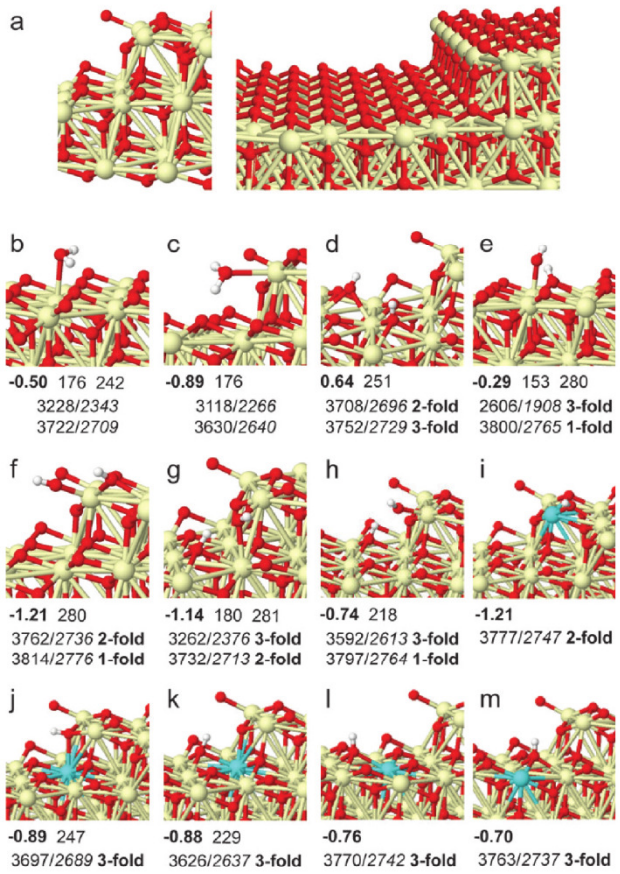

Figure 4. Sketches of the optimized models of the stepped $CeO_2(111)$ surface (a) bare surface, the surface with one intact (b–c) or dissociated (d–h) adsorbed water molecule (surface OH groups) or adsorbed hydrogen atom (i–m). Below each panel are displayed: adsorption energy of H_2O (b–c), dissociation energy of H_2O with respect to the gas-phase molecule (d–h), adsorption energy of H with respect to $^1/_2$ H_2 in the gas phase (i–m), in eV (all the numbers are in bold); the length of hydrogen bonds (if formed; next to the energy values), in pm; bottom lines correspond to O–H/*O–D* vibrational frequencies, in cm^{-1}, and coordination type of O atoms in OH groups with respect to Ce ions. Color coding: Ce^{4+}, ivory; Ce^{3+}, blue; O, red; H, white.

the surface in a vibrational mode for the detection of the respective IR peak.[42] The MSSR also holds for both $CeO_2(111)/Cu(111)$ and $CeO_{2-x}/Cu(111)$ systems because the thicknesses of the oxide films are much smaller than the IR wavelengths.[44] We assume that at higher coverage building of water clusters will result in hydrogen bond formation which strongly broadens and, therefore, obscures the O–D bands.

In addition to molecular adsorption, we also considered heterolytic dissociation of H_2O at terraces, sites d and e, and step edges, sites f–h, on stoichiometric $CeO_2(111)$. We found that water dissociation from the gas phase at the terrace sites depends strongly on the type of formed surface hydroxyl groups, from endothermic, 0.64 eV (site d), to slightly exothermic, −0.29 eV (site e). However, with respect to the adsorbed water molecule, the process on site e is endothermic by 0.21 eV in agreement with Fronzi et al.[5] In contrast, the dissociation at these steps becomes favorable with respect to both the gas phase, −1.21 and −1.14 eV, and adsorbed H_2O molecules, −0.32 and −0.25 eV, for configurations f and g, respectively. In the most stable configuration f, the released proton forms an OH group with 2-fold coordinated oxygen, while the OH^- remains coordinated to one of the Ce^{4+} ions. The O–H vibrational frequency of the 2-fold OH group, 3762 cm^{-1} (*2736* cm^{-1}; here and in the following the corresponding calculated O–D stretching frequencies are given in italics), is close to that of the isolated one i, while the frequency of the 1-fold group is calculated to be about 50 cm^{-1} higher.

According to Fronzi et al.,[5] formation of hydroxyl groups from water on reduced CeO_{2-x}, can be modeled as adsorption of hydrogen atoms on stoichiometric ceria. This assumption has been validated experimentally by Gritschneder and Reichling,[4] who observed that OH^- groups occupy the exact positions of the missing lattice oxygen. In each of our models, shown in Figure 4, configurations i–m, the hydroxyl group was produced by attachment of a single H atom at the corresponding surface O center; concomitantly, one of the surface Ce^{4+} ions in proximity of the OH group is reduced to Ce^{3+} (labeled in blue in Figure 4). This is similar to the

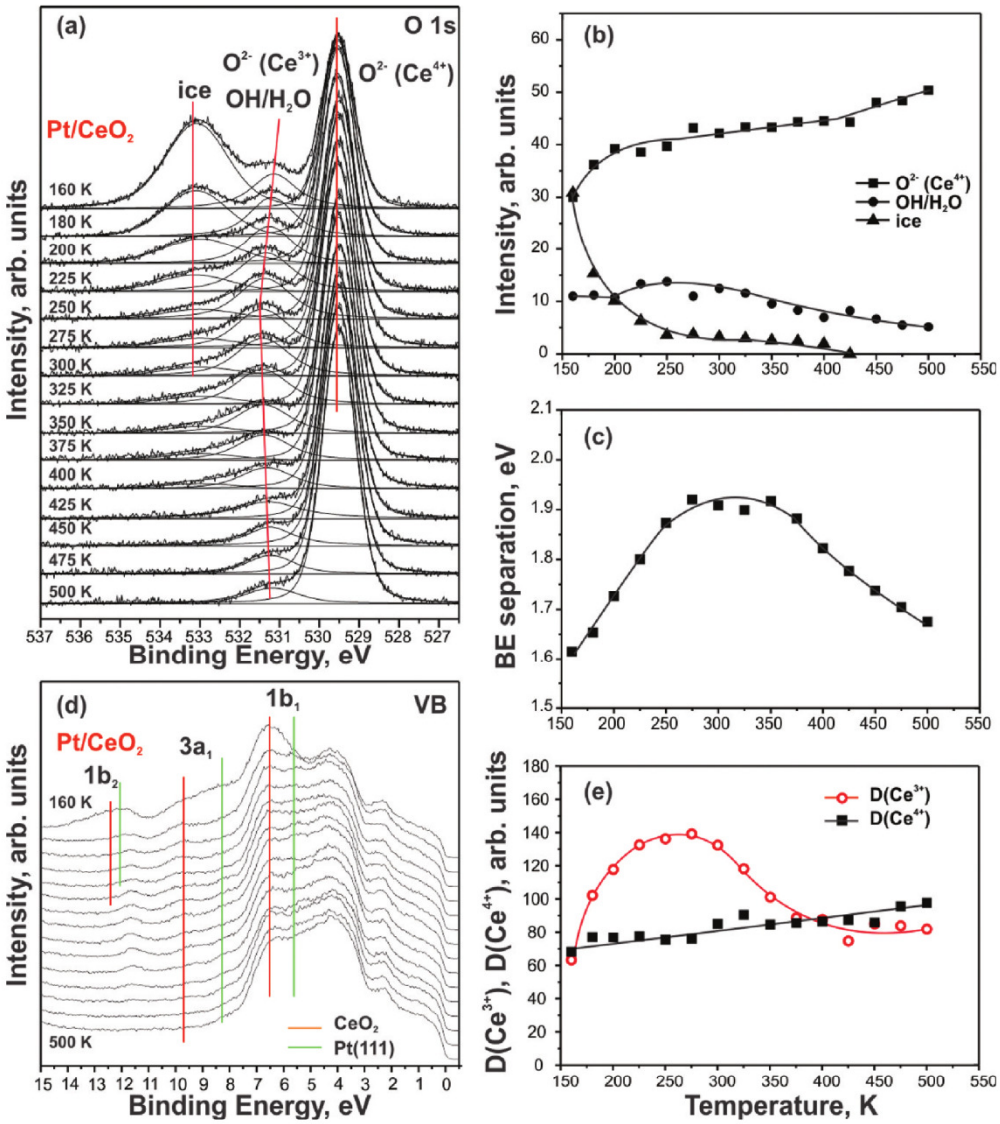

Figure 5. O 1s core level (a) and VB (d) spectra during annealing of Pt/CeO_2(111) exposed to the total doses of 10 L of H_2O at 160 K. The O 1s (a) and the VB (d) spectra were acquired with photon energies of 650 and 115 eV, respectively. Integrated intensities of O 1s spectral components (b), BE separation between $O^{2-}(Ce^{4+})$ and OH/H_2O components (c), and $D(Ce^{3+})$ and $D(Ce^{4+})$ resonant enhancement (e) as functions of temperature.

experimental conditions for water dissociation at the CeO_{2-x} sample since the formation of hydroxyl groups by dissociation of H_2O on it does not cause reoxidation of Ce^{3+} to Ce^{4+}, as discussed in sections 3.1 and 3.2.1.

Attachment of H to a 3-fold O center in the configurations l and m provides stabilization (computed with respect to $^1/_2$ H_2) by −0.76 and −0.70 eV, respectively. The corresponding terrace OH groups do not form hydrogen bonds with nearest oxygen ions. On the contrary, the 3-fold OH groups in the proximity of the step form weak hydrogen bonds with nearest oxygen ions, configurations j and k, which are stabilized by −0.89 eV. Thus, one can estimate the energy of these hydrogen bonds to be 0.1−0.2 eV.

The hydroxyl group at the 2-fold coordinated oxygen at the step, site i, stabilized by −1.21 eV, is found to be the most favorable energetically. It suggests preferential formation of the 2-fold hydroxyls over the 3-fold ones.

According to our calculations, the OH axis of the 2-fold hydroxyl group is tilted by 70° away from the surface normal. Such an arrangement of a hydroxyl group on reduced CeO_{2-x} or stoichiometric CeO_2(111) surfaces (in addition to its inherently small dynamic dipole moment) explains the missing O−D stretching bands in IRAS above 200 K. Indeed, the calculated IR intensity of the O−H vibration even for structure l, where the OH group is perpendicular to the CeO_2(111) surface, is small. For instance, it is about 40 times smaller than the intensity of the C−O stretching mode of a CO molecule adsorbed on Pt(111). The energetically favorable inclination of the OH group from the surface normal (such as in structure i) further reduces the small IR intensity of OH group. Note that calculated stretching O−H (*O−D*) vibrational frequencies for both 2- and 3-fold hydroxyl groups are within the narrow range of 3763−3777 (*2737−2747*) cm^{-1}. The difference in the O−H stretching frequencies between species d−m in the range of

70−140 cm^{-1} is caused by formation of weak hydrogen bonds (the frequency shift may be overestimated in the calculations, in particular for stronger hydrogen bonds[45]). The only case with strong hydrogen bond, characterized by the bond distance 153 pm and stretching frequency 2606 (*1908*) cm^{-1}, is found for water dissociation on the terrace (structure e), which is, however, energetically disfavored with respect to the non-dissociative adsorption (structure b).

3.3. Dissociation of Water on Pt/CeO_2. In the final step we investigated the interaction of water with Pt nanoparticles supported on CeO_2(111) films.[22,29] The O 1s spectra obtained from Pt/CeO_2 exposed to a total dose of 10 L of H_2O at 160 K and subsequently annealed stepwise to 500 K are plotted in Figure 5a.

As discussed in section 3.1, the O 1s spectrum at 160 K contains spectral contributions from lattice oxygen in ceria, (O^{2-}(Ce^{4+})), at 529.5 eV, the multilayer water (ice) at 533.0 eV, and unresolved contributions from OH and chemisorbed H_2O, OH/H_2O, at 531.1 eV. Because of the large width of the peaks at 533.0 and 531.1 eV, however, the corresponding species adsorbed on ceria and those on Pt particles cannot be resolved. Therefore, the intensity of the components shown in Figure 5b contains contributions from the species on both ceria and Pt particles. Since deposition of Pt on stoichiometric CeO_2(111) gives rise to immediate formation of a small fraction of Ce^{3+} ions,[29] the contribution from O^{2-}(Ce^{3+}) to the intensity of the peak at 531.1 eV should not be ignored. The BE separation between O^{2-}(Ce^{4+}) and OH/H_2O is shown in Figure 5c.

The VB spectra obtained from Pt/CeO_2 exposed to a total dose of 10 L of water at 160 K and subsequently annealed stepwise to 500 K are shown in Figure 5d. The VB at 160 K contains contributions from water, molecularly adsorbed on both ceria and Pt particles. The red and green lines in the VB indicate the positions of the VB features of water on CeO_2(111) (see Figure 1d) and Pt(111).[13,15,46−48] The amplitudes of D(Ce^{3+}) and D(Ce^{4+}) resonant enhancements as a function of temperature are plotted in Figure 5e.

According to the literature,[13,15,46−50] water does not dissociate on Pt(111) or stepped Pt(111) surfaces. Note that Pt/CeO_2 was flashed only to 500 K prior to water adsorption. Annealing to higher temperature will lead to stronger reverse oxygen spillover from ceria to Pt.[29] Even if a small amount of oxygen reverse spillover occurred, the resulting oxygen coverage on the Pt particles would be extremely small.[22,29] This is important as spilt-over oxygen could, in turn, trigger dissociation of water.[13−15] Since we did not observe any increase of D(Ce^{3+}) (data not shown) during the adsorption of water, we assume that the principal species on the surface of Pt/CeO_2 at 160 K are chemisorbed water and ice.

During annealing to 500 K (see Figure 5b), the intensity of the peak at 533.0 eV (ice) gradually decreases while that at 529.5 eV (O^{2-}(Ce^{4+})) increases. The intensity change of both peaks is caused by desorption of water. In parallel, the intensity of the feature at 531.1 eV (OH/H_2O) decreases above 350 K, while its BE gradually shifts to higher values (see Figure 5a). The BE separation between the peaks associated with OH/H_2O and O^{2-}(Ce^{4+}) reaches the highest values between 250 and 350 K before it decreases again above 350 K. In parallel, we observe a substantial increase of D(Ce^{3+}) above 180 K (see Figure 5e), reaching a maximum at about 250 K, and then decreasing to a value similar to that of the as-prepared sample.

In view of the discussion in the previous sections, the observed behavior suggests that the majority of hydroxyl groups formed during annealing to 350 K are located on ceria rather than on Pt: if most of the hydroxyl groups were formed on Pt the BE separation between the OH/H_2O and O^{2-}(Ce^{4+}) peaks would decrease rather than increase.[13]

A possible pathway for the formation of hydroxyl groups on ceria involves the dissociation of water on the surface of the Pt particle or at the Pt/ceria interface followed by spillover of hydrogen to the support. Earlier we observed a similar reduction and reoxidation of ceria during annealing of Pt/CeO_2 upon exposure to hydrogen at low temperature and subsequent annealing.[35] Hydroxyl species were suggested to be formed by spillover of hydrogen and were shown to be stable up to 260 K.[35]

The unequal amounts of the OH groups on Pt and CeO_2 suggest a rather complex chemistry. Simple dissociation of water into OH and H on Pt followed by hydrogen spillover to CeO_2 would yield equal amounts of OH groups on both Pt and CeO_2. There must be additional processes that may lead to an increase of hydroxyl groups on ceria. Such processes may involve (1) dissociation of OH to oxygen and hydrogen on Pt followed by spillover of hydrogen to ceria; (2) spillover of OH groups from Pt to ceria; (3) OH recombination on Pt to oxygen and water followed by desorption or subsequent dissociation of water. According to Grabow et al.,[51] processes 1 and 2 involve high activation barriers and therefore are very unlikely to occur under our experimental conditions. In contrast, the OH recombination occurs almost spontaneously and may fully account for the reduced concentration of OH groups on Pt.[51]

In view of the lack of sensitivity of the IRAS experiment to low coverages of surface OH groups (see section 3.2) it is not surprising that these species are not observed in IRAS. The corresponding spectra obtained from Pt/CeO_2 after adsorption of 50 L of D_2 at 150 K followed by annealing to 240 and 320 K are shown in Figure 3c. Upon deuterium spillover from Pt to ceria, an OD band should appear around 2700 cm^{-1}; however, the spectrum remains featureless after annealing to 240 and 320 K. As SRPES and RPES provide clear proof of spillover, we attribute the lack of sensitivity of the IRAS experiment to the low dynamic dipole moment and the strongly tilted and hydrogen bond nature of the hydroxyl groups formed. Note that vibrational bands for dissociatively adsorbed D_2 on Pt[52] (as on other metals[53−55]) appear at low frequency and are not accessible in the present experiment.

The decrease of D(Ce^{3+}) above 260 K (see Figure 5e) is consistent with the decomposition of OH groups on ceria and reverse spillover of hydrogen from ceria to Pt. As discussed in detail in our previous work,[35] hydrogen spillover becomes reversible in this temperature region. Therefore it may recombine with OH groups or atomic oxygen left on Pt and desorb as water. After complete water removal at 500 K the peak at 529.5 eV (O^{2-}(Ce^{4+})) had intensity similar to that of before adsorption of water. The small shoulder left in the O 1s spectrum at 500 K (see Figure 5a) corresponds to the small amount of O^{2-}(Ce^{3+}) also present on the as-prepared sample.

4. CONCLUSIONS

We investigated the chemistry of water on well-ordered stoichiometric CeO_2(111), partially reduced CeO_{2-x}, and Pt/CeO_2 combining SRPES, RPES, IRAS, and DF calculations.

We have found that adsorption of H_2O at 160 K is mostly molecular on $CeO_2(111)$ and partially dissociative on CeO_{2-x}. Formation of hydroxyl (OH) groups has been observed during adsorption and annealing on both samples. We find three typical characteristics that can be used to identify OH groups on ceria: (i) the presence of 1π and 3σ states in VB; (ii) the increase of the BE separation between the O 1s spectral components of lattice oxygen, O^{2-} (Ce^{4+}), and OH/H_2O; (iii) the increase of $D(Ce^{3+})$ resonance.

The results of DF calculations show that the energetically most favorable surface species on stoichiometric CeO_2 terraces is adsorbed water, while dissociation is disfavored by about 0.2 eV. At the steps, the adsorption energy of water is higher than on the terraces but there dissociation of water was found to dominate the molecular adsorption.

Dissociation of water and formation of OH groups readily takes place on partially reduced CeO_{2-x}. Hydroxyl groups at 2-fold oxygen sites (with respect to cerium ions) were calculated to be more stable than those at 3-fold oxygen sites. However, all favorable configurations of chemisorbed H_2O and OH exhibit strong tilting away from the surface normal on both types of calculated systems (without or with Ce^{3+} ions) that model $CeO_2(111)$ and CeO_{2-x} samples. This adsorption geometry, in combination with the small dynamic dipole moment of the OH stretch, makes it extremely difficult to detect these species in IRAS, and explains the featureless IR spectra above 200 K, i.e., after desorption of multilayer water.

The interaction of water with CeO_{2-x} does not cause any detectable reoxidation of Ce^{3+} into Ce^{4+}. The dissociation of water is fully reversible, yielding either molecular water (recombination of OH groups) or release of hydrogen and oxygen into the gas phase. The oxidation state of CeO_{2-x} after desorption/decomposition of H_2O/OH is fully recovered to that before water adsorption.

Adsorption of water on Pt/CeO_2 is molecular at 160 K. We find partial dissociation of water, either on Pt or at Pt/ceria interface, followed by spillover of hydrogen to the support in the temperature interval between 180 and 250 K. This leads to formation of hydroxyl groups on ceria in this temperature region. Above 250 K, decomposition of hydroxyl groups on ceria and reverse spillover of hydrogen to Pt occurs, followed by desorption of molecular water. Whereas initial spillover of hydrogen leads to a significant alteration of the oxidation state of cerium, reverse-spillover of hydrogen and subsequent desorption of water up to 500 K fully restores the oxidation state of ceria on the Pt/CeO_2 model catalyst.

AUTHOR INFORMATION

Corresponding Author

*E-mail: Yaroslava.Lykhach@chemie.uni-erlangen.de. Fax: +49-9131-8528867.

Notes

The authors declare no competing financial interest.

ACKNOWLEDGMENTS

The authors gratefully acknowledge financial support by the Deutsche Forschungsgemeinschaft (DFG), by the Ministry of Education of the Czech Republic (LG12003 and LA08022), and by the Spanish MICINN (FIS2008-02238) and the Generalitat de Catalunya (2009SGR1041). We acknowledge additional support from the DFG within the excellence cluster "Engineering of Advanced Materials" in the framework of the Excellence Initiative as well as the support from the COST Action CM1104 "Reducible oxide chemistry, structure and functions". M.H. gratefully acknowledges support by a grant of the "Fonds der Chemischen Industrie". Travel support by the DAAD (Project No. 50755695) is gratefully acknowledged. H.A.A., P.S.P., and G.N.V. are grateful to the Bulgarian National Science Fund (DTK 02/36 and DCVP 02/1) and FP7 project BeyondEverest for support. H.A.A. is grateful for postdoctoral Grant No. SB2010-0172 (Spain). We thank the Bulgarian Supercomputer Center and the Red Española de Supercomputación for provided computational resources and assistance. S.M.K. is grateful to the Spanish Ministerio de Economia y Competitividad for the predoctoral FPU grant AP2009-3379. Y.L., V.J., N.T., and K.C.P. thank Elettra for excellent working conditions.

REFERENCES

(1) Thiel, P. A.; Madey, T. E. *Surf. Sci. Rep.* **1987**, *7*, 211−385.
(2) Henderson, M. A. *Surf. Sci. Rep.* **2002**, *46*, 1−308.
(3) Gritschneder, S.; Iwasawa, Y.; Reichling, M. *Nanotechnology* **2007**, *18*, 044025.
(4) Gritschneder, S.; Reichling, M. *Nanotechnology* **2007**, *18*, 044024.
(5) Fronzi, M.; Piccinin, S.; Delley, B.; Traversa, E.; Stampfl, C. *Phys. Chem. Chem. Phys.* **2009**, *11*, 9188−9199.
(6) Kumar, S.; Schelling, P. K. *J. Chem. Phys.* **2006**, *125*, 204704.
(7) Yang, Z.; Wang, Q.; Wei, S.; Ma, D.; Sun, Q. *J. Phys. Chem. C* **2010**, *114*, 14891−14899.
(8) Kundakovic, L.; Mullins, D. R.; Overbury, S. H. *Surf. Sci.* **2000**, *457*, 51−62.
(9) Henderson, M. A.; Perkins, C. L.; Engelhard, M. H.; Thevuthasan, S.; Peden, C. H. F. *Surf. Sci.* **2003**, *526*, 1−18.
(10) Berner, U.; Schierbaum, K.; Jones, G.; Wincott, P.; Haq, S.; Thornton, G. *Surf. Sci.* **2000**, *467*, 201−213.
(11) Zhao, X.; Ma, S.; Hrbek, J.; Rodriguez, J. A. *Surf. Sci.* **2007**, *601*, 2445−2452.
(12) Matolín, V.; Matolínová, I.; Dvořák, F.; Johánek, V.; Mysliveček, J.; Prince, K. C.; Skála, T.; Stetsovych, O.; Tsud, N.; Václavů, M.; Šmíd, B. *Catal. Today* **2012**, *181*, 124−132.
(13) Shavorskiy, A.; Gladys, M. J.; Held, G. *Phys. Chem. Chem. Phys.* **2008**, *10*, 6150−6159.
(14) Fisher, G. B.; Sexton, B. A. *Phys. Rev. Lett.* **1980**, *44*, 683−686.
(15) Fisher, G. B.; Gland, J. L. *Surf. Sci.* **1980**, *94*, 446−455.
(16) Lilach, Y.; Iedema, M. J.; Cowin, J. P. *Phys. Rev. B* **2007**, *98*, 016105.
(17) Šutara, F.; Cabala, M.; Sedláček, L.; Skála, T.; Škoda, M.; Matolín, V.; Prince, K. C.; Cháb, V. *Thin Solid Films* **2008**, *516*, 6120−6124.
(18) Matolín, V.; Libra, J.; Matolínová, I.; Nehasil, V.; Sedláček, L.; Šutara, F. *Appl. Surf. Sci.* **2007**, *254*, 153−155.
(19) Staudt, T.; Lykhach, Y.; Hammer, L.; Schneider, M. A.; Matolin, V.; Libuda, J. *Surf. Sci.* **2009**, *603*, 3382−3388.
(20) Dvořák, F.; Stetsovych, O.; Steger, M.; Cherradi, E.; Matolínová, I.; Tsud, N.; Škoda, M.; Skála, T.; Mysliveček, J.; Matolín, V. *J. Phys. Chem. C* **2011**, *115*, 7496.
(21) Staudt, T.; Lykhach, Y.; Tsud, N.; Skala, T.; Prince, K. C.; Matolín, V.; Libuda, J. *J. Catal.* **2010**, *275*, 181.
(22) Lykhach, Y.; Staudt, T.; Lorenz, M. P. A.; Streber, R.; Bayer, A.; Steinrück, H. P.; Libuda, J. *ChemPhysChem* **2010**, *11*, 1496−1504.
(23) http://www.kolibrik.net/science/kolxpd/.
(24) Kresse, G.; Hafner, J. *Phys. Rev. B* **1994**, *49*, 14251.
(25) Kresse, G.; Furthmüller, J. *Comput. Mater. Sci.* **1996**, *6*, 15.
(26) Perdew, J. P.; Wang, Y. *Phys. Rev. B* **1992**, *45*, 13244.
(27) Loschen, C.; Carrasco, J.; Neyman, K. M.; Illas, F. *Phys. Rev. B* **2007**, *75*, 035115.
(28) Migani, A.; Vayssilov, G. N.; Bromley, S. T.; Illas, F.; Neyman, K. M. *J. Mater. Chem.* **2010**, *20*, 10535.

(29) Vayssilov, G. N.; Lykhach, Y.; Migani, A.; Staudt, T.; Petrova, G. P.; Tsud, N.; Skála, T.; Bruix, A.; Illas, F.; Prince, K. C.; Matolín, V.; Neyman, K. M.; Libuda, J. *Nat. Mater.* **2011**, *10*, 310−315.
(30) Blöchl, P. E. *Phys. Rev. B* **1994**, *50*, 17953.
(31) Kresse, G.; Joubert, D. *Phys. Rev. B* **1999**, *59*, 1758.
(32) Nilius, N.; Kozlov, S. M.; Jerratsch, J.-F.; Baron, M.; Shao, X.; Viñes, F.; Shaikhutdinov, S.; Neyman, K. M.; Freund, H.-J. *ACS Nano* **2012**, *6*, 1126−1133.
(33) Trovarelli, A. *Catalysis by Ceria and Related Metals*; Imperial College Press: London, 2002.
(34) Mullins, D. R.; Overbury, S. H.; Huntley, D. R. *Surf. Sci.* **1998**, *409*, 307−319.
(35) Lykhach, Y.; Staudt, T.; Vorokhta, M.; Skála, T.; Johánek, V.; Prince, K. C.; Matolín, V.; Libuda, J. *J. Catal.* **2012**, *285*, 6−9.
(36) Ogasawara, H.; Yoshinobu, J.; Kawai, M. *Chem. Phys. Lett.* **1994**, *231*, 188−192.
(37) Leist, U.; Ranke, W.; Al-Shamery, K. *Phys. Chem. Chem. Phys.* **2003**, *5*, 2435−2441.
(38) Ogasawara, H.; Yoshinobu, J.; Kawai, M. *J. Chem. Phys.* **1999**, *111*, 7003−7009.
(39) Daschbach, J. L.; Dohnálek, Z.; Liu, S.-R.; Smith, R. S.; Kay, B. D. *J. Phys. Chem. B* **2005**, *109*, 10362−10370.
(40) Xu, C.; Goodman, D. W. *Chem. Phys. Lett.* **1997**, *265*, 341−346.
(41) Hugenschmidt, M. B.; Gamble, L.; Campbell, C. T. *Surf. Sci.* **1994**, *302*, 329−340.
(42) Hoffmann, F. M. *Surf. Sci. Rep.* **1983**, *3*, 107−192.
(43) Marrocchelli, D.; Yildiz, B. *J. Phys. Chem. C* **2012**, *116*, 2411−2424.
(44) Bermudez, V. M. *J. Vac. Sci. Technol. A* **1992**, *10*, 152−157.
(45) Kolev, S. K.; Petkov, P. S.; Rangelov, M. A.; Vayssilov, G. N. *J. Phys. Chem. A* **2011**, *115*, 14054.
(46) Ranke, W. *Surf. Sci.* **1989**, *209*, 57−76.
(47) Ranke, W.; Kuhr, H. J. *Phys. Rev. B* **1989**, *39*, 1595−1601.
(48) Langenbach, E.; Spitzer, A.; Lüth, H. *Surf. Sci.* **1984**, *147*, 179−190.
(49) Ibach, H.; Lehwald, S. *Surf. Sci.* **1980**, *91*, 187−197.
(50) Ogasawara, H.; Brena, B.; Nordlung, D.; Nyberg, M.; Pelmenschikov, A.; Pettersson, L. G. M.; Nilsson, A. *Phys. Rev. Lett.* **2002**, *89*, 276102.
(51) Grabow, L. C.; Gokhale, A. A.; Evans, S. T.; Dumesic, J. A.; Mavrikakis, M. *J. Phys. Chem. C* **2008**, *112*, 4608−4617.
(52) Baró, A. M.; Ibach, H.; Bruchmann, H. D. *Surf. Sci.* **1979**, *88*, 384−398.
(53) Gruyters, M.; Jacobi, K. *J. Electron Spectrosc. Relat. Phenom.* **1993**, *64*−*65*, 591−598.
(54) Sayers, C. M. *Surf. Sci.* **1984**, *136*, 582−593.
(55) Nordlander, P.; Holloway, S.; Norskov, J. K. *Surf. Sci.* **1984**, *136*, 59−81.

Section 11.7

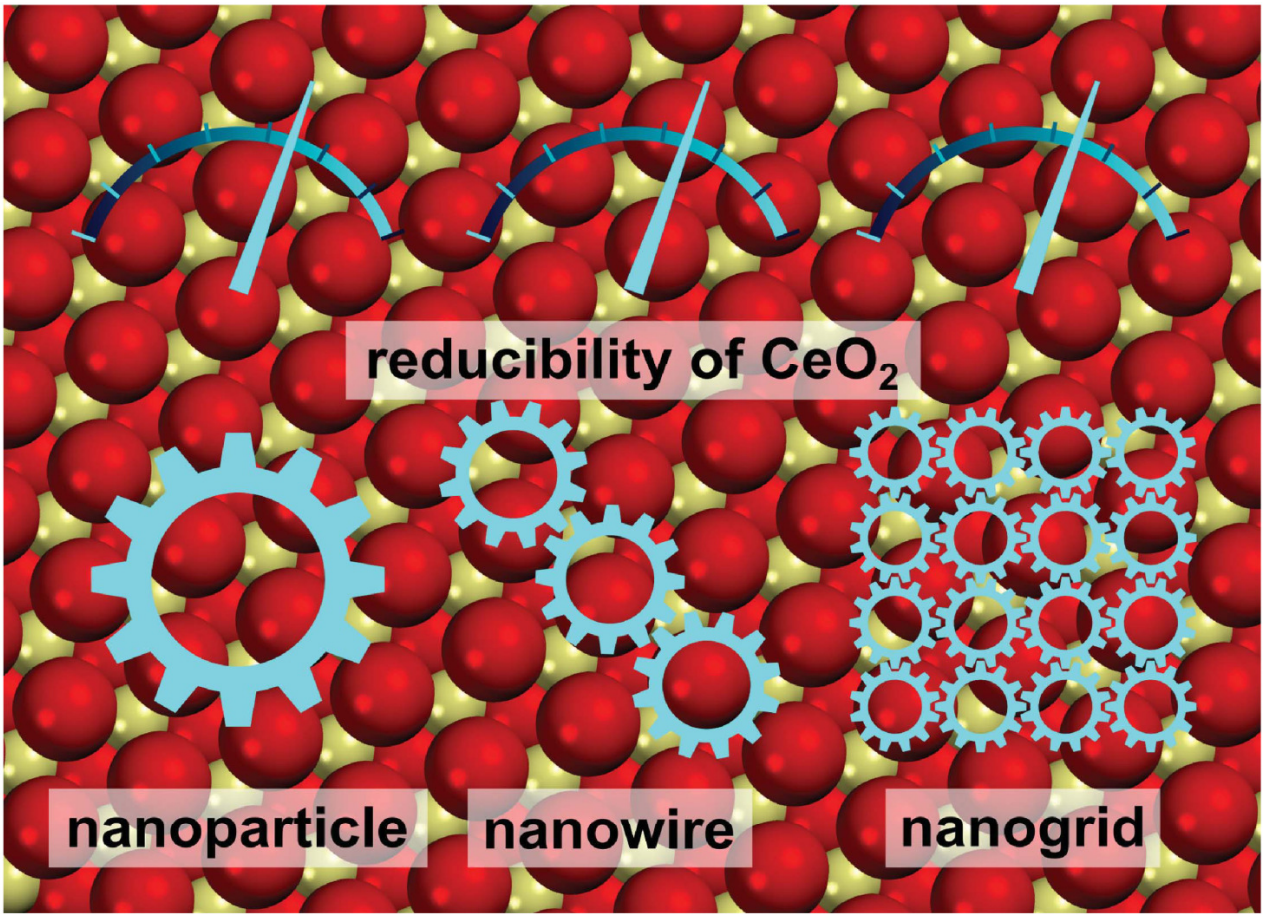

Showcasing the work on CeO_2 nanoarrays presented by Dr. Annapaola Migani at Consejo Superior de Investigaciones Científicas and Institut Català de Nanociència i Nanotecnologia, Prof. Kok Hwa Lim at Singapore Institute of Technology, and Prof. Konstantin Neyman at Institució Catalana de Recerca i Estudis Avançats and Universitat de Barcelona.

Title: Oxygen vacancies in self-assemblies of ceria nanoparticles

Agglomeration of CeO_2 nanoparticles in one- and two-dimensional (1D and 2D) nanoarchitectures has a large effect on their properties. Judging by the electronic structures and formation energies of oxygen vacancies, the 1D $Ce_{80}O_{160}$ and 2D $Ce_{40}O_{80}$ arrays are more similar to a larger-sized nanoparticle $Ce_{140}O_{280}$ than to their building blocks.

As featured in:

See Kok Hwa Lim, Annapaola Migani *et al.*, *J. Mater. Chem. A*, 2014, **2**, 18329.

ROYAL SOCIETY OF CHEMISTRY

www.rsc.org/MaterialsA

Registered charity number: 207890

Journal of Materials Chemistry A

PAPER

View Article Online
View Journal | View Issue

Cite this: J. Mater. Chem. A, 2014, 2, 18329

Oxygen vacancies in self-assemblies of ceria nanoparticles†

Mahasin Alam Sk,[a] Sergey M. Kozlov,[b] Kok Hwa Lim,*[ac] Annapaola Migani*[de] and Konstantin M. Neyman[bf]

Received 2nd May 2014
Accepted 10th August 2014

DOI: 10.1039/c4ta02200a

www.rsc.org/MaterialsA

Cerium dioxide (CeO_2, ceria) nanoparticles possess size-dependent chemical properties, which may be very different from those of the bulk material. Agglomeration of such particles in nanoarchitectures may further significantly affect their properties. We computationally model the self-assembly of Ce_nO_{2n} particles (n = 38, 40, 80) – zero-dimensional (0D) structures – in one- and two-dimensional (1D and 2D) nanoarchitectures by employing density-functional methods. The electronic properties of 1D $Ce_{80}O_{160}$ and 2D $Ce_{40}O_{80}$ resemble those of larger 0D crystallites, $Ce_{140}O_{280}$, rather than those of their building blocks. These 0D, 1D and 2D nanostructures are employed to study the size dependence of the formation energy of an oxygen vacancy, $E_f(O_{vac})$, a central property in ceria chemistry. We rationalize within a common electronic structure framework the variations of the $E_f(O_{vac})$ values, which are computed for the Ce_nO_{2n} nanostructures with different sizes and dimensionalities. We identify: (i) the bandwidth of the unoccupied density of states projected onto the Ce 4f levels as an important factor, which controls $E_f(O_{vac})$; and (ii) the corner Ce atoms as the structural motif essential for a noticeable reduction of $E_f(O_{vac})$. These results help to understand the size dependent behaviour of $E_f(O_{vac})$ in nanostructured ceria.

Introduction

Cerium dioxide (ceria) is an indispensable component of a broad variety of materials for industrial applications, ranging from oxygen sensors and permeation membranes to bio- and medical materials.[1] Usage of ceria in catalysis alone represents a very rapidly growing area with a huge market.[2] Remarkably, some properties of ceria change considerably when the size of its crystallites is decreased to nanoscale.[1,3] For example, ceria nanoparticles (NPs) of ~3–4 nm were shown to improve the catalytic performance of supported gold species by orders of magnitude compared to the situation when the support is less dispersed.[4,5] These experimental observations were rationalized by means of calculations based on density-functional theory (DFT), which showed that the formation of an oxygen vacancy (O_{vac}) is greatly facilitated in ceria NPs[6,7] with respect to the bulk material.[8]

A combined DFT and synchrotron-radiation photoelectron spectroscopy study showed that oxygen spillover to Pt species deposited on ceria requires the presence of nanostructured ceria.[9] This indicates that oxygen transfer through the ceria–Pt boundary is a nanoscale effect, and that nanostructured ceria is crucial to form key catalytic sites such as Pt–O.[10] Very recently it has been shown that nanostructured ceria leads to remarkable stabilization of platinum deposited in an atomically dispersed form. This finding enables maximum usage of this precious metal in catalytic materials.[11]

Strong size- and shape-dependence of the properties of the ceria nanostructures boosted intense experimental efforts, which resulted in the preparation of various ceria nano-polyhedra (truncated octahedra, cubes, *etc.*).[12,13] Zero-dimensional (0D) ceria nanopolyhedra can form structures extended in one (1D, *e.g.* nanowires, rods and tubes) and two dimensions (2D, *e.g.* nanogrids), either by self-assembly[13,14] or in the course of direct synthesis.[12,15] These 1D and 2D nanoarchitectures expose not only the most stable (111) planes of ceria but also more reactive (100) and (110) planes. Thus, the reactivity of nanoscale ceria can be tuned in a controllable fashion.[1]

[a]School of Chemical and Biomedical Engineering, Nanyang Technological University, Singapore 639798

[b]Departament de Química Física and Institut de Química Teòrica i Computacional (IQTCUB), Universitat de Barcelona, 08028 Barcelona, Spain

[c]Singapore Institute of Technology, 10 Dover Drive, Singapore 138683. E-mail: KokHwa.Lim@SingaporeTech.edu.sg

[d]CSIC - Consejo Superior de Investigaciones Científicas, Campus UAB, ICN2 Building, 08193 Bellaterra, Spain. E-mail: Annapaola.Migani@cin2.es

[e]ICN2 - Institut Català de Nanociència i Nanotecnologia, Campus UAB, ICN2 Building, 08193 Bellaterra, Spain

[f]Institució Catalana de Recerca i Estudis Avançats (ICREA), 08010 Barcelona, Spain

† Electronic supplementary information (ESI) available: Figure for $Ce_{40}O_{80}$ and $Ce_{40}O_{80}'$. $E_f(O_{vac})$ results for additional Ce^{3+} configurations for the Ce_nO_{2n} (n = 38, 40, 80) NPs and their self-assemblies. $E_f(O_{vac})$ results for regular and three (I–III) vicinal stepped $CeO_2(111)$ surface models. Cartesian coordinates for the Ce_nO_{2n} (n = 38, 40, 80, 140) NPs. See DOI: 10.1039/c4ta02200a

Recent atomistic simulations using interatomic potentials explored the strain and architecture-tuned reactivity of ceria nanostructures to oxidize CO to CO_2.[16] These studies revealed that the tension is an activating factor, whereas the compression hinders the reaction. To the best of our knowledge, no results of DFT-based studies of 1D or 2D nanostructures formed *via* the self-assembly of ceria NPs have been published yet.

Herein, we computationally model the directional[17,18] self-assembly of Ce_nO_{2n} particles (n = 38, 40, 80) in 1D and 2D nanoarchitectures employing density-functional methods. We use the Perdew–Wang[19–21] functional augmented with a Hubbard-type term U = 4 eV[22] for the Ce 4f electrons (PW91+4 approximation).[23,24] We address the formation of the most stable single oxygen vacancy in the Ce_nO_{2n} particles and their self-assemblies, focusing on the dependence of the formation energy of an oxygen vacancy, $E_f(O_{vac})$, on the size and dimensionality. To this end, the $E_f(O_{vac})$ values of the 1D and 2D structures are compared to those of their respective building blocks. Moreover, the electronic properties and the $E_f(O_{vac})$ values of the Ce_nO_{2n} particles ($n \leq 80$) and their nanoarchitectures are compared to those of a ~2.4 nm large $Ce_{140}O_{280}$ nanocrystallite.[25]

Finally, we address the reliability of the trends derived for $E_f(O_{vac})$ in ceria nanostructures from contemporary electronic structure calculations. For this purpose, we evaluate $E_f(O_{vac})$ for ceria nanostructures with 40 CeO_2 units, including the previously reported $Ce_{40}O_{80}'$ model,[6,7] with the HSE06 variant of the Heyd–Scuseria–Ernzerhof hybrid functional.[26–29] These values are used in conjunction with the HSE06 $E_f(O_{vac})$ values computed for suitably small regular[30,31] and vicinal stepped[31] $CeO_2(111)$ surface models and the $Ce_{21}O_{42}$[6,7] model to derive general oxygen mobility trends in ceria.

Computational methods

Periodic DFT calculations were carried out using the VASP[32,33] package and employing the Perdew–Wang[19–21] (PW91) implementation of the generalized gradient approximation (GGA) for the exchange-correlation functional. An effective on-site Coulomb correction U_{eff} = 4 eV[22] was applied to the Ce 4f levels within the GGA + U scheme[23,24] (referred to as PW91+4). The computationally very demanding hybrid exchange correlation functional by Heyd–Scuseria–Ernzerhof (HSE),[26,27] previously tested for partially reduced $CeO_2(111)$ surfaces[8,34] and (in a slightly modified form) for Ce_2O_3 bulk,[35] was also used to obtain alternative supposedly more accurate[8] comparative $E_f(O_{vac})$ estimates. The HSE functional was used with the screening parameter of 2 nm^{-1} corresponding to the HSE06 scheme. Following the procedure adopted in ref. 6 and 7, HSE06 single-point energy calculations were carried out at the PW91+4 optimized pristine and oxygen atom defective geometries. Importantly, the position of the Ce^{3+} pair of atoms of the oxygen defective geometries is the same in the corresponding PW91+4 and HSE06 calculations. This procedure is expected to reproduce O activity trends derived from computationally exceedingly expensive HSE06 optimizations although some numerical differences may exist.

A plane-wave basis with a 415 eV cut-off for the kinetic energy and projector–augmented wave[36] description of core-valence electron interactions were employed. The calculations were done at the Γ-point. Single-point total energy convergence tolerance at the self-consistency was set to 10^{-6} eV. The structures were optimized until a maximum force less than 2 eV pm^{-1} was obtained.

In the spin-polarized calculations of the oxygen atom defective nanostructures, the ferromagnetic alignment of the two localized Ce 4f electrons resulting in a total magnetic moment $\mu = 2\ \mu_B$ was assumed. For the regular and vicinal $CeO_2(111)$ surface models an antiferromagnetic alignment of the two localized Ce 4f electrons resulting in a total magnetic moment $\mu = 0\ \mu_B$ was sometimes obtained. The charge of the O and Ce atoms forming the Ce–O_4 and Ce_4–O_4 contacts between NPs was characterized by topological Bader analysis.[37] The $E_f(O_{vac})$ energies are calculated from the total energies of the stoichiometric and O defective systems with respect to 1/2 of the O_2 molecule triplet state energy, $E(O_2) = -9.82$ (−17.03) eV with PW91+4 (HSE06).

A unit cell of 2.5 nm × 2.5 nm × 2.5 nm was used for the 0D $Ce_{40}O_{80}$ building block. 0D $Ce_{40}O_{80}$ (Fig. 1) has two equatorial Ce corner atoms, which can interact with the O_4 unit located at the axial position in the *x*- and *y*-directions, upon decreasing the *a* and *b* cell parameters, respectively. The 1D $Ce_{40}O_{80}$ structure was constructed by gradually decreasing the cell parameter *a* and optimizing the atomic positions. The lowest energy was obtained in this procedure for a unit cell of 1.612 nm × 2.5 nm × 2.5 nm, which identifies the optimized geometry for the 1D $Ce_{40}O_{80}$ nanowire. Starting from the 1.612 nm × 2.5 nm × 2.5 nm unit cell of 1D $Ce_{40}O_{80}$, a similar procedure was repeated to construct the 2D $Ce_{40}O_{80}$ nanogrid, by repeatedly shrinking the cell parameter *b* and optimizing the atomic positions. The lowest energy was obtained for a unit cell of 1.612 nm × 1.607 nm × 2.5 nm, which corresponds to the 2D $Ce_{40}O_{80}$ optimized geometry.

Similarly, the 0D $Ce_{80}O_{160}$ building block has one Ce corner atom (Fig. 1), which can interact with the O_4 unit located at the axial position in the self-assembling *x*-direction. The unit cell for the 0D $Ce_{80}O_{160}$ building block is 3 nm × 2.5 nm × 2.5 nm, and for the optimized 1D $Ce_{80}O_{160}$ nanostructure is 2.145 nm × 2.5 nm × 2.5 nm. The unit cell for the 0D $Ce_{38}O_{76}$ nanostructure is 2.2 nm × 2.5 nm × 2.5 nm, and for the optimized 1D $Ce_{38}O_{76}$ nanowire is 1.303 nm × 2.5 nm × 2.5 nm. The unit cell for the $Ce_{140}O_{280}$ NP is 2.487 nm × 2.487 nm × 2.902 nm. The cells employed ensure an inter-particle distance of ≥1 nm in each direction for the building blocks and in each not connected direction for the 1D and 2D nanoarchitectures, and an inter-particle distance of ≥0.6 nm in each direction for $Ce_{140}O_{280}$.

The average energy of the 4f levels, ε_{4f}, corresponds to the first moment of the density of states projected (PDOS) onto the Ce 4f levels, $\rho_{4f}(\varepsilon)$, *i.e.*, $\varepsilon_{4f} = \dfrac{\int_{\varepsilon_{Fermi}}^{+\infty} \varepsilon \rho_{4f}(\varepsilon) d\varepsilon}{\int_{\varepsilon_{Fermi}}^{+\infty} \rho_{4f}(\varepsilon) d\varepsilon}$. The average energy of the 4f levels of the Ce atom *i* (*i* = corner 1, corner 2, edge,

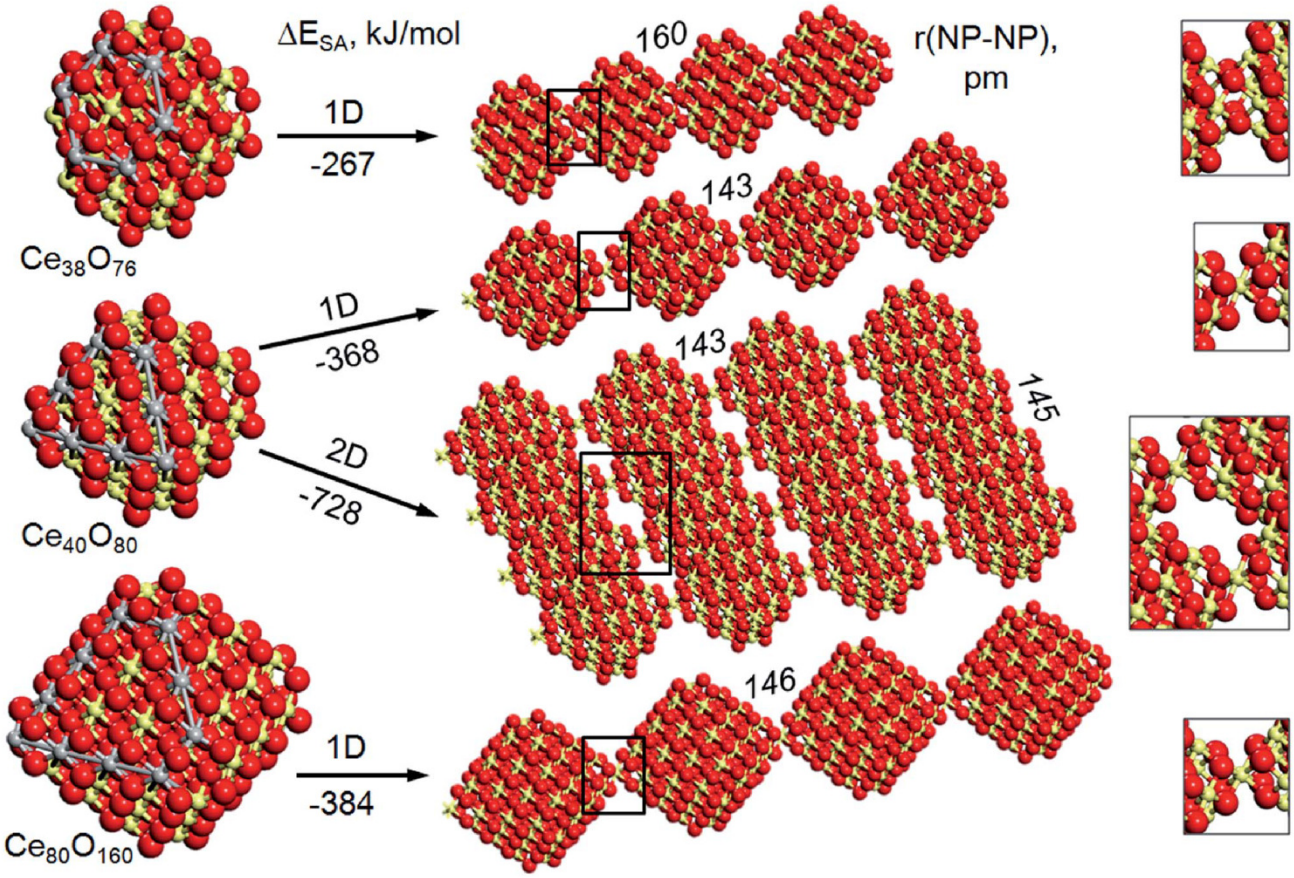

Fig. 1 Sketches of stoichiometric ceria NPs Ce_nO_{2n}, $n = 38$, 40, 80, and their self-assemblies generated *via* the binding of the four O atoms of the {100} facet to four corner Ce atoms ($n = 38$) or one corner Ce atom ($n = 40$, 80), as detailed in the insets. Ce^{4+} cations – light beige spheres, O^{2-} anions – red spheres, and edges of one {111} facet – grey spheres. The ΔE_{SA} [kJ mol^{-1}] values are the PW91+4 self-assembly energies; the r(NP-NP) [pm] values are the optimized heights of the corner Ce atoms over the O_4 planes.

facet), ε_{4f}^{i}, corresponds to the first moment of the corresponding PDOS. The ε_{4f} and ε_{4f}^{i} values are shifted with respect to the vacuum level, ε_{vacuum}, to enable comparison between different structures. The bandwidth of the 4f levels, W_{4f}, is estimated as the full width at half maximum of a Gaussian distribution with standard deviation equals to the square root of the Ce 4f PDOS variance, σ_{4f}, *i.e.*, $W_{4f} \sim 2\sqrt{2 \ln 2}\sigma_{4f}$ where $\sigma_{4f} = \sqrt{\frac{\int_{\varepsilon_{Fermi}}^{+\infty} (\varepsilon - \varepsilon_{4f})^2 \rho_{4f}(\varepsilon) d\varepsilon}{\int_{\varepsilon_{Fermi}}^{+\infty} \rho_{4f}(\varepsilon) d\varepsilon}}$. ε_{4f} and W_{4f} are analogous[38] to the d band center and d bandwidth commonly used as descriptors for bulk and surface systems.

The convergence with respect to the k-point density was examined for 2D $Ce_{40}O_{80}$ with a Monkhorst-Pack $3 \times 3 \times 1$ k-point mesh. This calculation gives ε_{4f} and $\varepsilon_{4f}^{corner\ 1}$ values identical within the given accuracy to the Γ-point calculation values, and a total energy within 0.02 eV with respect to the Γ-point calculation energy. The convergence with respect to the vacuum thickness was checked for the $Ce_{40}O_{80}'$ particle (Fig. S1†). The $\varepsilon_{4f} = -3.67$ eV and $\varepsilon_{4f}^{corner\ 1} = -3.80$ eV values in Table 1 are obtained from a calculation, which employed a 2.2 nm × 1.9 nm × 1.9 nm cell (inter-particle separation ≥0.6 nm).[6,7] Similar results ($\varepsilon_{4f} = -3.69$ eV and $\varepsilon_{4f}^{corner\ 1} = -3.82$ eV) are obtained from a calculation, which employs a 2.5 nm × 2.5 nm × 2.5 nm cell (inter-particle separation ≥1 nm).

The regular $CeO_2(111)$ surface and the vicinal surfaces with type I, II, and III steps were modelled by three O–Ce–O tri-layer thick slabs.[31] To model $CeO_2(111)$, we used a hexagonal $p(3 \times 3)$ unit cell of 1.150 nm × 1.150 nm × 1.935 nm. For type I, II, and III steps, we employed the 0.763 nm × 1.479 nm × 3 nm ($\alpha = 102.17°$, $\beta = 90.00°$, $\gamma = 82.58°$), 0.763 nm × 1.266 nm × 3 nm ($\alpha = 75.74°$, $\beta = 90.00°$, $\gamma = 81.33°$), and 0.661 nm × 1.376 nm × 3 nm ($\alpha = 76.95°$, $\beta = 90.00°$, $\gamma = 94.59°$) unit cells, respectively. These unit cells were constructed using the experimental lattice constant for CeO_2 bulk, 541 pm,[39,40] and ensuring a vacuum layer thickness of ≥ 1 nm. During the geometry optimization all three O–Ce–O tri-layers were relaxed for the stepped surfaces, while only the top two O–Ce–O tri-layers were relaxed for the regular surface. Type I and II unit cells have composition $3 \times Ce_8O_{16}$, and the type III unit cell has composition $3 \times Ce_7O_{14}$.

Results and discussion

Self-assembly of ceria nanoparticles in 1D and 2D structures

Experiments show that NPs with diameter ∅ ~3÷10 nm commonly have truncated octahedral morphologies enclosed by

Table 1 Calculated PW91+4 data for the 0D, 1D and 2D Ce_nO_{2n} nanostructures: excess energy per CeO_2 unit with respect to the energy of ceria bulk (ΔE), average energy of the 4f levels of the connecting corner Ce atom 1, ($\varepsilon_{4f}^{corner\ 1}$), average energy of the 4f levels of the connecting corner Ce atom 2, ($\varepsilon_{4f}^{corner\ 2}$), average energy of the total 4f levels, (ε_{4f}), bandwidth of the PDOS on the 4f levels, (W_{4f}), energy of the highest energy peak of the PDOS on the 2p levels of the O_4 site, from which the O_{2c} atom is removed upon vacancy formation, ($\varepsilon_{2p}^{O_{2c}}$). O 2p HOMO and Ce 4f LUMO energy difference, ($\Delta\varepsilon$), and the lowest O_{2c} vacancy formation energy, ($E_f(O_{vac})$). The $\varepsilon_{4f}^{corner\ 1}$, $\varepsilon_{4f}^{corner\ 2}$, ε_{4f} and $\varepsilon_{2p}^{O_{2c}}$ values are with respect to the vacuum level, ε_{vacuum}

Building block	System	ΔE, kJ mol^{-1}	$\varepsilon_{4f}^{corner\ 1}$, eV	$\varepsilon_{4f}^{corner\ 2}$, eV	ε_{4f}, eV	W_{4f}, eV	$\varepsilon_{2p}^{O_{2c}}$, eV	$\Delta\varepsilon$, eV	$E_f(O_{vac})$, kJ mol^{-1}
$Ce_{38}O_{76}$[a]	0D	121.9	−4.21	—	−3.89	0.82	−5.67	0.74	5
	1D	114.9	−4.10	—	−4.03	0.38	−6.05	1.52	149
$Ce_{40}O_{80}'$	0D	107.8	−3.80	−3.80	−3.67	0.35	−5.55	1.49	77[b]
$Ce_{40}O_{80}$	0D[c]	109.2	−3.97	−3.97	−3.85	0.54	−5.55	0.97	39
	1D	100.0	−3.68	−4.05	−3.84	0.49	−5.68	1.15	57
	2D	91.0	−3.85	−3.85	−3.86	0.24	−5.83	1.76	157
$Ce_{80}O_{160}$	0D	81.1	−4.24	—	−3.87	0.54	−5.60	0.98	45[b]
	1D	76.3	−3.89	—	−3.87	0.26	−5.71	1.63	103
$Ce_{140}O_{280}$	0D	64.5	—	—	−3.83	0.26	−5.68	1.63	145

[a] See ref. 25 for the global minimum structure. [b] Ref. 6 and 7. [c] See text for description on how the building block has been designed by rearrangement of the $Ce_{40}O_{80}'$ model (Fig. S1†).

extended {111} facets and small (up to four atom width)[41] {100} facets.[42] The morphology emerging from the simulations based on interatomic potentials is in full accord with the experiment.[25,43] The truncated octahedral Ce_nO_{2n} (n = 38, 40, 80 and 140) models in the ~1.5 ÷ 2.4 nm size range generated by global optimization[25] all have apical {100} facets made of four oxygen atoms, the O_4 site. Compared with the bulk octahedral cuts,[44,45] the Ce_nO_{2n} (n = 40, 80 and 140) models have an increasing number of missing Ce atoms (four, five and six, respectively) at the vertices of the octahedra.

Here the $Ce_{40}O_{80}$ (∅ ~1.5 nm) and $Ce_{80}O_{160}$ (∅ ~1.9 nm) NPs are used as building blocks for the self-assembly of higher-order 1D and 2D nanoarchitectures through a corner-to-facet interaction (Fig. 1). The $Ce_{80}O_{160}$ building block has one corner Ce atom and an O_4 site directly across from each other. A regular 1D $Ce_{80}O_{160}$ wire is formed through the binding of the corner Ce atom of a NP with the O_4 site of another NP with a similar orientation, *i.e.*, Ce–O_4 binding.

The $Ce_{40}O_{80}$ and $Ce_{40}O_{80}'$ NPs are structural isomers with truncated octahedral shape (Fig. S1†). $Ce_{40}O_{80}$ is 55 kJ mol^{-1} higher in energy (Table 1) than $Ce_{40}O_{80}'$. In $Ce_{40}O_{80}'$ the two corner Ce atoms are directly across from each other. In this arrangement they cannot be used to connect NPs with a similar orientation. In the $Ce_{40}O_{80}$ NP the two corner Ce atoms are directly across from O_4 sites. In this case, the NP can interact with another similarly oriented NP in one or two directions *via* Ce–O_4 binding. The binding in one direction leads to the formation of the 1D $Ce_{40}O_{80}$ wire and the concurrent Ce–O_4 binding in the two orthogonal directions leads to the creation of the 2D $Ce_{40}O_{80}$ grid.

Among the truncated octahedral structures, the somewhat smaller (∅ ~1.1 nm) $Ce_{38}O_{76}$ particle is also interesting as it can be used as a building block to form a 1D wire through a facet-to-facet binding mechanism (Fig. 1). The $Ce_{38}O_{76}$ NP corresponds to a sub-system of the $Ce_{40}O_{80}$ NP.[46] When $Ce_{40}O_{80}$ is reduced in size by removing a CeO_4 unit from one corner and an additional Ce corner atom to maintain the stoichiometry, a {100} facet with four four-coordinated Ce atoms is formed. These open Ce sites can interact with the four O atoms of a {100} facet of another similarly oriented $Ce_{38}O_{76}$ NP to form a 1D wire, *i.e.*, Ce_4–O_4 binding.

The energy gained in the self-assembly, ΔE_{SA}, of the Ce_nO_{2n} (n = 38, 40, 80) building blocks is reported in Fig. 1. The "reaction" coordinate is given by the inter-particle separation, r(NP-NP), measured as the height of the corner Ce atom over the O_4 plane of the Ce–O_4 or Ce_4–O_4 contact formed between contiguous NPs. The self-assembled structure corresponds to the energy minimum in the interacting particle energy profile along the r(NP-NP) reaction coordinate at 160 and 143–146 pm (Fig. 1) for the facet-to-facet and corner-to-facet self-assembly, respectively. The self-assembly energy profile has no barrier and decreases slowly in a first stage (r(NP-NP) ~0.6 nm) as the building blocks approach each other, and rapidly decreases afterwards until the energy minimum. A similar energy profile was found based on DFT calculations for 1D Pd_n nanowires constructed from isolated cuboctahedral Pd_n (n = 38, 79, 140, 225) species.[18]

ΔE_{SA} depends only weakly on the size of the building blocks but depends noticeably on the type of connector. Despite the size difference, the self-assembly energies computed for the 1D $Ce_{40}O_{80}$ and $Ce_{80}O_{160}$ nanowires (−368 and −384 kJ mol^{-1} per Ce–O_4 corner-to-facet contact, respectively) are close to each other. This indicates that for the Ce–O_4 corner-to-facet interaction ΔE_{SA} is converged with respect to the size of the Ce_nO_{2n} building block within ≤ 20 kJ mol^{-1} for $n \geq 40$. This size agrees with the size required to obtain adsorption energies for weakly interacting probe molecules (*i.e.*, CO) on Ce_nO_{2n} NPs converged with respect to the NP size.[47]

The geometry difference in the $Ce_{40}O_{80}$ template, which has an additional corner Ce atom compared to the $Ce_{80}O_{160}$ NP, seems not to significantly change ΔE_{SA} for 1D $Ce_{40}O_{80}$ *vs.* 1D $Ce_{80}O_{160}$. Likewise, the energy gained in the creation of the

second Ce–O_4 corner-to-facet contact in 2D $Ce_{40}O_{80}$ (−360 kJ mol^{-1}) is almost the same as the energy gained in the creation of the first Ce–O_4 contact. These all are indications of a rather local character of the inter-particle interaction, which is hardly affected by more distant atoms of the NP.

On the other hand, ΔE_{SA} for $Ce_{38}O_{76}$ is notably smaller (−267 kJ mol^{-1}) despite the small difference in size with $Ce_{40}O_{80}$. This lower energy gain is attributable to the longer Ce–O bonds between the Ce and O atoms in the Ce_4–O_4 contact as compared to the Ce–O_4 contact. In 1D $Ce_{38}O_{76}$ the contact is provided by an O_4 unit, which is bound to two equivalent Ce_4 units on opposite sides. In this configuration, the O atoms are four-coordinated and have four equivalent Ce–O bond lengths (251 pm), while the Ce atoms are six-coordinated. The Ce atom of the Ce–O_4 contact is equivalently bound to two O_4 units, and therefore is eight-coordinated with eight equivalent Ce–O 243 pm long bonds.

A Bader charge analysis[37] shows that the driving force for the self-assembly principally originates from electrostatic factors. The positive charge of the corner Ce atom changes upon formation of the Ce–O_4 contact from the value of a four-coordinated corner Ce atom (2.14|e|) to a typical charge value of a bulk eight-coordinated Ce atom (2.37|e|) in the Ce–O_4 contact. This is compensated by an increment of negative charge (from −1.09|e| to −1.15|e|) of each of the four O atoms involved in the corner-to-facet interaction. In the facet-to-facet binding, there is an increment of the negative charge by 0.12|e| per O atom (from −1.10|e| to −1.22|e|) for the O atoms of the Ce_4–O_4 contact. This is counterbalanced by an increment of the positive charge (from 2.16|e| to 2.23|e|) per Ce atom for the two Ce_4 units on opposite sides of the O_4 unit. The smaller increment of the positive charge per Ce atom in the Ce_4–O_4 contact as compared to the Ce–O_4 contact reflects the smaller coordination number of the Ce atoms in the Ce_4–O_4 contact (six) as compared to the Ce–O_4 contact (eight). Similarly, the larger increment of negative charge per O atom in the Ce_4–O_4 contact as compared to the Ce–O_4 contact is due to the larger coordination number of the O atoms in the Ce_4–O_4 contact (four) as compared to the Ce–O_4 contact (three).

The structural changes induced by the formation of the contacts between the NPs are local and involve a minority of atoms. Nevertheless they have a noticeable impact on the global electronic structure of the nanoarrays. In order to understand this effect, in Fig. 2 we report the occupied total DOS, and the unoccupied PDOS on the total 4f levels, which essentially coincides with the unoccupied total DOS in this energy range, for the Ce_nO_{2n} (n = 38, 40, 80) NPs, their 1D and 2D self-assemblies, $Ce_{40}O_{80}'$ and $Ce_{140}O_{280}$.[48] Moreover, we consider the unoccupied PDOS on the 4f levels of one corner Ce atom, and the occupied PDOS on the 2p levels of the binding O_4 site for all structures except $Ce_{40}O_{80}'$ and $Ce_{140}O_{280}$. Note that it is sufficient to analyse only one of the Ce corner atoms because of symmetry. We use different colors to differentiate the PDOS of the free (blue) and connected (green) corner Ce atom and O_4 site. The vertical blue (green) line indicates the average energy of the 4f levels of the free (connected) corner Ce atom, $\varepsilon_{4f}^{corner\ 1}$ and $\varepsilon_{4f}^{corner\ 2}$. We consider the shift of $\varepsilon_{4f}^{corner\ 1}$ and

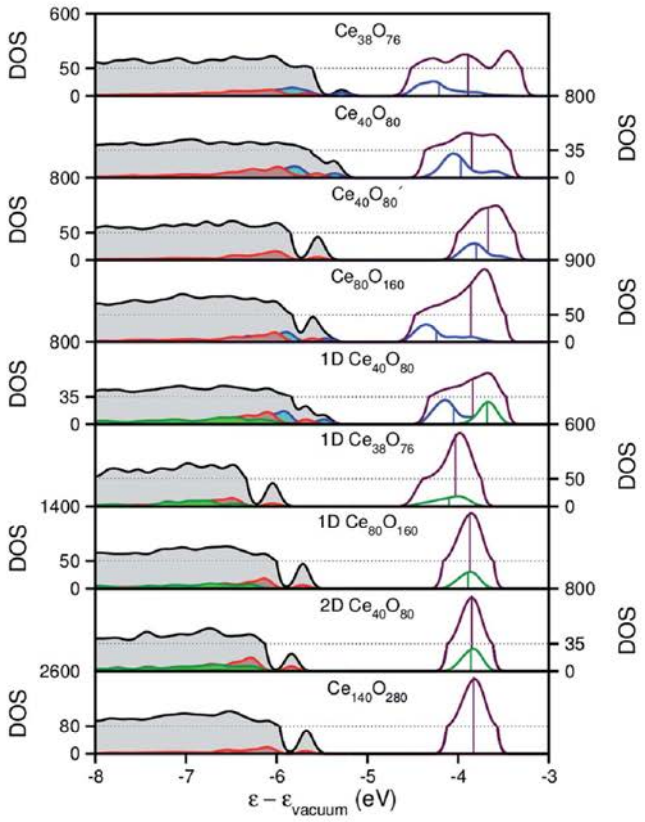

Fig. 2 Occupied total DOS (black) and PDOS on the 2p levels of the O_4 site from which the O_{2c} atom is removed upon vacancy formation (red), and unoccupied PDOS on the total 4f levels of the Ce atoms (violet). Occupied PDOS on the 2p levels of the binding O_4 site and unoccupied PDOS on the 4f levels of one corner Ce atom for the free (blue) and connected (green) atoms. DOS and PDOS units are the number of states eV^{-1} $cell^{-1}$. The vertical lines indicate the average energy of the unoccupied 4f levels of all Ce atoms (violet), and free (blue) and connected (green) corner Ce atoms (see Table 1). Energies are with respect to the vacuum level, ε_{vacuum}. Filling denotes occupied levels. The dotted line indicates the separation between the two different scales in the vertical axis used to plot the black DOS and violet PDOS.

$\varepsilon_{4f}^{corner\ 2}$ with respect to the average energy of the total Ce 4f levels, ε_{4f} (vertical violet line), and the bandwidth of the PDOS on the Ce 4f levels, as measured by W_{4f} (Table 1).

Based on Fig. 2 and Table 1, we can assess the convergence of the electronic properties of the Ce_nO_{2n} (n = 38, 40, 80) NPs and their 1D and 2D assemblies as a function of the size and dimensionality. First of all, W_{4f} decreases across the series $Ce_{38}O_{76}$ > $Ce_{40}O_{80}$, 1D $Ce_{40}O_{80}$, $Ce_{80}O_{160}$ > $Ce_{40}O_{80}'$, 1D $Ce_{38}O_{76}$ > 1D $Ce_{80}O_{160}$, $Ce_{140}O_{280}$, 2D $Ce_{40}O_{80}$. This trend correlates with the number and type of corner Ce atoms. W_{4f} is the largest for the $Ce_{38}O_{76}$ NP with four corner Ce atoms, which are placed at the intersection between a Ce-terminated {100} facet and {111} facets. W_{4f} is the smallest for the structures with no corner Ce atoms ($Ce_{140}O_{280}$) or for the structures whose corner Ce atoms have completed their oxygen coordination sphere *via* the formation of the Ce–O_4 contacts (1D $Ce_{80}O_{160}$, 2D $Ce_{40}O_{80}$). Finally W_{4f} is intermediate for the structures, which have two ($Ce_{40}O_{80}$) or one (1D $Ce_{40}O_{80}$, $Ce_{80}O_{160}$) free corner Ce atoms of intersecting {111} facets.

At the same time ε_{4f} is essentially constant across the series, with the exception of 1D $Ce_{38}O_{76}$ (slightly stabilized by *ca.* 0.1 eV) and $Ce_{40}O_{80}'$ (slightly destabilized by *ca.* 0.1 eV). $\varepsilon_{4f}^{\text{corner 1}}$ and $\varepsilon_{4f}^{\text{corner 2}}$ for $Ce_{40}O_{80}$ and $Ce_{40}O_{80}'$, $\varepsilon_{4f}^{\text{corner 1}}$ for $Ce_{38}O_{76}$ and $Ce_{80}O_{160}$, and $\varepsilon_{4f}^{\text{corner 2}}$ for 1D $Ce_{40}O_{80}$ (vertical blue lines in Fig. 2) are noticeably downshifted with respect to ε_{4f}. On the other hand $\varepsilon_{4f}^{\text{corner 1}}$ for 1D $Ce_{80}O_{160}$, and $\varepsilon_{4f}^{\text{corner 1}}$ and $\varepsilon_{4f}^{\text{corner 2}}$ for 2D $Ce_{40}O_{80}$ (vertical green lines in Fig. 2) coincide with ε_{4f}. $\varepsilon_{4f}^{\text{corner 1}}$ for 1D $Ce_{38}O_{76}$ is slightly downshifted (*ca.* 0.1 eV) with respect to ε_{4f}.

Moreover, the shape of the PDOS on the 4f levels of the free and connected corner Ce atoms is different: it corresponds to a symmetric Gaussian distribution for the connected corner Ce atoms while it is rather distorted with respect to a Gaussian distribution for the free corner Ce atoms. This indicates that it is the free Ce corner atoms, which cause the deformation of the PDOS on the total 4f levels with respect to a symmetric Gaussian distribution as shown in Fig. 2.

The properties of the 4f levels for 1D $Ce_{38}O_{76}$ are different from those computed for 1D $Ce_{80}O_{160}$, 2D $Ce_{40}O_{80}$ and $Ce_{140}O_{280}$. This difference is related to the structure of the Ce_4–O_4 contact previously discussed, whose Ce–O bonds (251 pm) are elongated with respect to the average Ce–O bond length between six-coordinated Ce atoms and four-coordinated O atoms (230 pm) found in $Ce_{140}O_{280}$. As a result W_{4f} is larger and ε_{4f} is slightly red-shifted as compared to 1D $Ce_{80}O_{160}$, 2D $Ce_{40}O_{80}$ and $Ce_{140}O_{280}$. This shows that even local geometric effects appreciably influence the global electronic structure.

The formation of the Ce–O_4 and Ce_4–O_4 contacts has an opposite effect on the 2p levels of the O atoms of the contacts, which are shifted to lower energies after the contact is formed (Fig. 2).

The 1D and 2D nanoarrays depicted in Fig. 1 have additional O_4 sites at {100} facets, which are not involved in the Ce–O_4 or Ce_4–O_4 contacts, with two-coordinated oxygen atoms, O_{2c}. In Fig. 2 we report the occupied PDOS on the 2p levels of one of the equivalent O_4 sites, which do not form contacts, for the nanoarrays and their building blocks, and the occupied PDOS on the 2p levels of one of the equivalent O_4 sites for $Ce_{40}O_{80}'$ and $Ce_{140}O_{280}$. In particular we focus on the energy of the highest energy peak of the PDOS, $\varepsilon_{2p}^{O_{2c}}$, which is an important descriptor for the behavior of $E_f(O_{vac})$ for creation of an O_{2c} vacancy at these O_4 sites. We find that $\varepsilon_{2p}^{O_{2c}}$ is stabilized by 0.11–0.13 eV upon formation of one Ce–O_4 contact (1D Ce_nO_{2n} (n = 40, 80) *versus* their respective building blocks) and by twice as much (0.28 eV) upon formation of two Ce–O_4 contacts (2D $Ce_{40}O_{80}$ with respect to $Ce_{40}O_{80}$). In the case of the Ce_4–O_4 contact the $\varepsilon_{2p}^{O_{2c}}$ stabilization is even larger (0.38 eV), as eight new Ce–O bonds (two per O atom) are formed (Table 1).

Fig. 2 indicates that the electronic structure of 1D $Ce_{80}O_{160}$ and 2D $Ce_{40}O_{80}$ resembles more that of a $Ce_{140}O_{280}$ rather than that of their respective 0D building blocks. A shift of $\varepsilon_{2p}^{O_{2c}}$ towards lower energies and a decrease of W_{4f} with increasing dimensionality are found for 0D, 1D and 2D $Ce_{40}O_{80}$. Overall, this shows that the self-assembly of the Ce_nO_{2n} building blocks in 1D and 2D structures effectively corresponds to increasing the size of the building block.

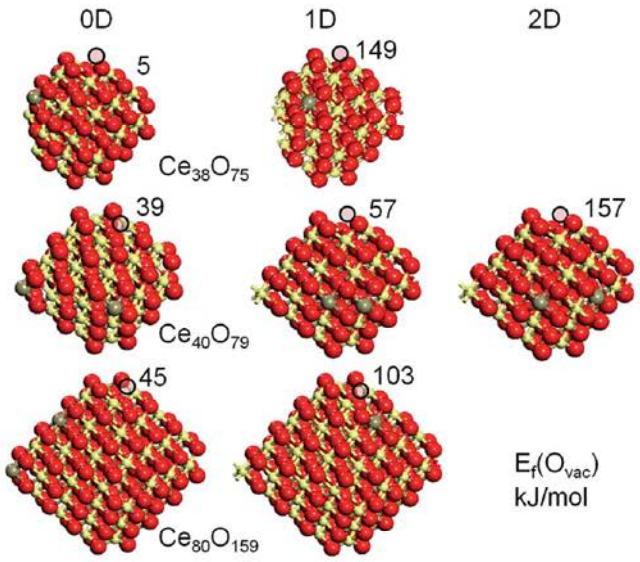

Fig. 3 Oxygen defective Ce_nO_{2n-1} NPs for the 0D, 1D and 2D structures displayed in Fig. 1, which contain one per NP, most easily formed O_{2c} vacancy at the top O_4 sites with the corresponding oxygen vacancy formation energies $E_f(O_{vac})$ [kJ mol^{-1}] calculated *vs.* 1/2 O_2 triplet state energy. Ce^{4+} cations – light beige spheres, Ce^{3+} cations – dark beige spheres, O^{2-} anions – red spheres, and the position of O_{vac} – black circles. As a result of the adopted orientation, only one Ce^{3+} cation is visible for 0D, 1D $Ce_{38}O_{75}$ and 1D $Ce_{80}O_{159}$.

Formation of oxygen vacancies in ceria nanoarchitectures

The O_4 sites, which do not take part in the Ce–O_4 or Ce_4–O_4 contacts, have been probed for their ability to release O_{2c} atoms (Fig. 3). The removal of such O_{2c} atoms was reported to require the least $E_f(O_{vac})$ in the $Ce_{21}O_{42}$, $Ce_{40}O_{80}'$ and $Ce_{80}O_{160}$ NPs in comparison with the facet, sub-facet and interior O atoms.[6,7] Depending on the configuration of the Ce^{3+} ions, formed upon O atom removal, $E_f(O_{vac})$ for a given NP size varies within a few tenths of an electronvolt.[6,7] The energetically most stable Ce^{3+} configuration is obtained upon localization of the two 4f excess electrons at corner or edge Ce atoms.[6,7] The computed most stable Ce^{3+} configurations are shown in Fig. 3 (see Fig. S2† for other low-energy Ce^{3+} configurations).

Previously[6,7] we showed that $E_f(O_{vac})$ is controlled by the energy separation between the occupied 2p levels of the O_{2c} atom, which is removed, and the unoccupied 4f levels of the Ce atoms, which receive the two excess electrons of the removed O_{2c} atom in the pristine systems. Accordingly, the $E_f(O_{vac})$ trends are discussed in terms of the $\varepsilon_{2p}^{O_{2c}}$ energies of the removed O_{2c} atoms and the average energies of the 4f levels of the Ce^{4+} cations, which become reduced upon O_{2c} atom removal, ε_{4f}^{I}, in the pristine stoichiometric structure. Larger W_{4f} values, *i.e.*, $\varepsilon_{4f}^{I} < \varepsilon_{4f}$, imply smaller $E_f(O_{vac})$ values. Concomitantly, lower $\varepsilon_{2p}^{O_{2c}}$ values imply larger $E_f(O_{vac})$.

In the $Ce_{40}O_{79}$ structure the two 4f excess electrons were localized separately at the two free corner Ce sites ($\varepsilon_{4f}^{\text{corner 1}} = \varepsilon_{4f}^{\text{corner 2}} = -3.97$ eV in pristine $Ce_{40}O_{80}$). The 1D $Ce_{40}O_{80}$ structure has one connected corner Ce atom ($\varepsilon_{4f}^{\text{corner 1}} = -3.68$ eV) and one free corner Ce atom ($\varepsilon_{4f}^{\text{corner 2}} = -4.05$ eV).

Therefore, in 1D $Ce_{40}O_{79}$ one 4f electron was localized at the free corner Ce atom, and the other 4f electron was localized at a nearby edge Ce site ($\varepsilon_{4f}^{edge} = -4.05$ eV, in 1D $Ce_{40}O_{80}$). The computed lowest-energy configuration for 2D $Ce_{40}O_{79}$ has both the Ce^{3+} cations at equivalent edge sites ($\varepsilon_{4f}^{edge} = -3.88$ eV in 2D $Ce_{40}O_{80}$). The $E_f(O_{vac})$ trend computed as a function of the dimensionality for these Ce^{3+} configurations, $Ce_{40}O_{80} \leq$ 1D $Ce_{40}O_{80} \ll$ 2D $Ce_{40}O_{80}$, is directly related to the $\varepsilon_{2p}^{O_{2c}}$ and W_{4f} values in these structures (Table 1). 2D $Ce_{40}O_{80}$ with the lowest $\varepsilon_{2p}^{O_{2c}}$, the smallest W_{4f}, and a well-shaped Gaussian 4f PDOS has the highest $E_f(O_{vac})$ value (157 kJ mol^{-1}) among the 0D, 1D and 2D $Ce_{40}O_{80}$ structures.

For 1D $Ce_{40}O_{79}$, we also inspected the stability of the Ce^{3+} configuration with one 4f electron at the connected corner Ce atom and the other at the free corner Ce atom. This configuration is less stable (by 45 kJ mol^{-1}, Fig. S2†) than the computed most stable configuration ($E_f(O_{vac}) = 57$ kJ mol^{-1}), indicating that the connected corner Ce atom may not be easily reduced. This increment is consistent with $|\varepsilon_{4f}^{edge} - \varepsilon_{4f}^{corner\ 1}| = 0.37$ eV in the pristine 1D $Ce_{40}O_{80}$ structure. For 2D $Ce_{40}O_{79}$, the Ce^{3+} configuration with the 4f electrons localized separately at the connected corner Ce atoms ($\varepsilon_{4f}^{corner\ 1} = \varepsilon_{4f}^{corner\ 2} = -3.85$ eV in the pristine 2D $Ce_{40}O_{80}$ structure) was found to be somewhat less stable (by 23 kJ mol^{-1}, Fig. S2†) than the computed most stable configuration. This increment is smaller than that obtained for 1D $Ce_{40}O_{79}$. It is consistent with $|\varepsilon_{4f}^{edge} - \varepsilon_{4f}^{corner\ 1}| + |\varepsilon_{4f}^{edge} - \varepsilon_{4f}^{corner\ 2}| = 0.06$ eV in 2D $Ce_{40}O_{80}$ being smaller than $|\varepsilon_{4f}^{edge} - \varepsilon_{4f}^{corner\ 1}| = 0.37$ eV in 1D $Ce_{40}O_{80}$. These results show that the electronic structure properties of the PDOS on the total 4f levels of the pristine structure influence directly the energy difference between different Ce^{3+} configurations. W_{4f} for 2D $Ce_{40}O_{80}$ is smaller than that for 1D $Ce_{40}O_{80}$. Correspondingly, the energy difference between different Ce^{3+} configurations spans a smaller energy range for 2D $Ce_{40}O_{80}$ as compared to 1D $Ce_{40}O_{80}$.

In $Ce_{80}O_{159}$ one 4f electron was localized at the available corner Ce atom ($\varepsilon_{4f}^{corner\ 1} = -4.24$ eV in $Ce_{80}O_{160}$) and the other 4f electron was localized at a nearby edge Ce atom ($\varepsilon_{4f}^{edge} = -3.90$ eV in $Ce_{80}O_{160}$). In 1D $Ce_{80}O_{159}$ one 4f electron was localized at a facet Ce site in the proximity of the vacancy ($\varepsilon_{4f}^{facet} = -3.84$ eV in 1D $Ce_{80}O_{160}$) and the other 4f electron was localized at an edge Ce atom ($\varepsilon_{4f}^{edge} = -3.90$ eV in 1D $Ce_{80}O_{160}$). Based on the $\varepsilon_{2p}^{O_{2c}}$ and W_{4f} values, larger $E_f(O_{vac})$ values are expected for 1D $Ce_{80}O_{160}$ as compared to $Ce_{80}O_{160}$. However, a somewhat smaller $E_f(O_{vac})$ increment (58 kJ mol^{-1}) between 0D $Ce_{80}O_{160}$ and 1D $Ce_{80}O_{160}$ than the expected one is found. This result may be related to the relaxation energy contribution to $E_f(O_{vac})$ for 1D $Ce_{80}O_{160}$. A significant energy gain is expected for localization at the facet site in the proximity of the vacancy. This is because the total Ce–O bond expansion of the seven Ce–O bonds of the facet Ce atom associated with the localization of the 4f electron at this site is particularly pronounced (90 pm). The creation of the O vacancy for 0D $Ce_{38}O_{76}$ is nearly energy-neutral (5 kJ mol^{-1}), but is significantly more difficult (149 kJ mol^{-1}) in 1D $Ce_{38}O_{76}$.

Overall, Fig. 3 shows that the self-assembly has direct consequences on $E_f(O_{vac})$. For each building block size, larger $E_f(O_{vac})$ values are computed for the 1D or 2D arrays with respect to the 0D building blocks. These changes in $E_f(O_{vac})$ are controlled by the effect of the creation of the Ce–O_4 and Ce_4–O_4 contacts on the electronic structure (Fig. 2 and Table 1), which corresponds to stabilization of $\varepsilon_{2p}^{O_{2c}}$ as well as a decrease of W_{4f}. The NPs or nanoarrays with corner Ce atoms or a Ce-terminated facet ($Ce_{38}O_{76}$, $Ce_{40}O_{80}$, 1D $Ce_{40}O_{80}$ and 0D $Ce_{80}O_{160}$), which have larger W_{4f} values and higher $\varepsilon_{2p}^{O_{2c}}$ energies, have smaller $E_f(O_{vac})$ as compared to the nanoarrays with no corner Ce atoms or a Ce-terminated facet (1D $Ce_{38}O_{76}$, 1D $Ce_{80}O_{160}$ and 2D $Ce_{40}O_{80}$), which instead have smaller W_{4f} values and lower $\varepsilon_{2p}^{O_{2c}}$ energies. A rather low $E_f(O_{vac})$ value was reported for $Ce_{40}O_{80}'$ (77 kJ mol^{-1}, Table 1),[6,7] which also exposes two corner Ce atoms. Overall we find a similar $E_f(O_{vac})$ ordering as for W_{4f}, implying that $E_f(O_{vac})$ and W_{4f} are interrelated.

To better understand the $E_f(O_{vac})$ changes induced by the NP self-assembly we also computed the energy for removal of an O_{2c} atom from the O_4 site of the $Ce_{140}O_{280}$ NP. The two excess Ce^{3+} cations were localized on edge Ce sites (Fig. 4). A small $E_f(O_{vac})$ difference (12 kJ mol^{-1} at most) is found between the various Ce^{3+} configurations. This result is similar to that discussed above for 2D $Ce_{40}O_{80}$ and depends on the narrow 4f PDOS bandwidth ($W_{4f} \sim 0.1$ eV). A second important observation is

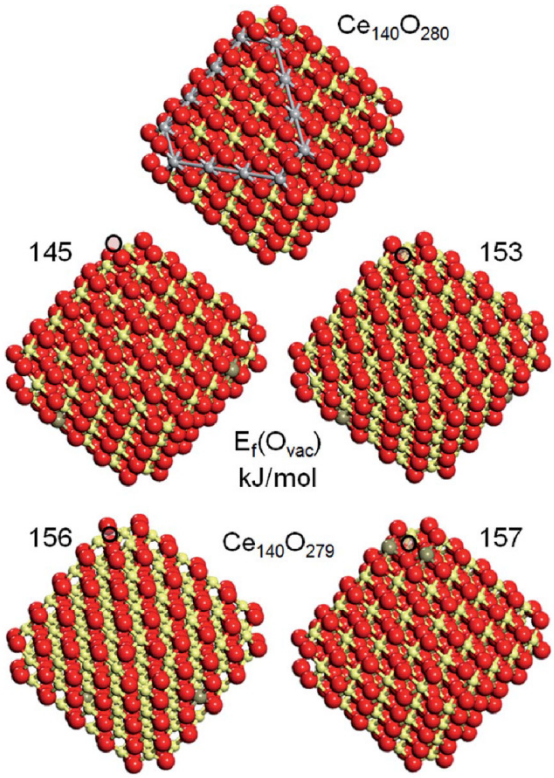

Fig. 4 Sketches of a stoichiometric ceria $Ce_{140}O_{280}$ NP and oxygen defective $Ce_{140}O_{279}$ NPs with an O_{2c} vacancy at the top O_4 site with the corresponding oxygen vacancy formation energies $E_f(O_{vac})$ [kJ mol^{-1}] calculated *vs.* 1/2 O_2 triplet state energy for various Ce^{3+} configurations. Ce^{4+} cations – light beige spheres, Ce^{3+} cations – dark beige spheres, O^{2-} anions – red spheres, the position of O_{vac} – black circles, and edges of one {111} facet – silver spheres.

that the lowest $E_f(O_{vac})$ value for $Ce_{140}O_{280}$ is similar though somewhat smaller than the lowest $E_f(O_{vac})$ value for 2D $Ce_{40}O_{80}$. As already mentioned, 2D $Ce_{40}O_{80}$ and $Ce_{140}O_{280}$ have similar electronic structures, with the most significant difference being a small shift (0.15 eV) towards lower energies for $\varepsilon_{2p}^{O_{2c}}$, which may explain the slightly larger $E_f(O_{vac})$ value computed for 2D $Ce_{40}O_{80}$. This is further evidence for the stringent resemblance between 2D $Ce_{40}O_{80}$ and $Ce_{140}O_{280}$.

$\varepsilon_{2p}^{O_{2c}}$ may differ from the 2p highest occupied molecular orbital (HOMO) energy, *e.g.*, the HOMO of Ce_nO_{2n} (n = 38, 40, 80) and 1D $Ce_{40}O_{80}$ in Fig. 2 is given by the 2p levels of the O_4 site, which forms the contact (cfr. highest energy peak in the blue and red filled PDOS). Moreover, several Ce atoms usually contribute to the 4f lowest unoccupied molecular orbital (LUMO), except for structures with corner Ce atoms. Here the LUMO essentially corresponds to one of the seven 4f levels of the corner Ce atom. Despite these differences, we find that the modulations of $E_f(O_{vac})$ can be nicely correlated with concomitant variations of the O 2p HOMO and Ce 4f LUMO energy difference, $\Delta\varepsilon$, in Table 1. Thus, $\Delta\varepsilon$ can also be considered as a practical descriptor of the facility to form O vacancies in CeO_2 nanostructures.

Table 2 Comparison of the lowest O atom vacancy formation energy, ($E_f(O_{vac})$), and the O 2p HOMO and Ce 4f LUMO energy difference, ($\Delta\varepsilon$), for various CeO_2 systems, calculated with the PW91+4 and HSE06 approaches

	$E_f(O_{vac})$, kJ mol^{-1}		$\Delta\varepsilon$, eV	
Model	PW91+4	HSE06	PW91+4	HSE06
CeO_2(111) regular[a]	251[d]	253[b,c,d]	2.01	3.17
Step I[a]	201[d]	213[d]	2.12	3.06
Step II[a,e]	216	228	1.77	2.77
Step III[a]	219[d]	228[d]	2.05	3.49
0D $Ce_{21}O_{42}$	161	198	1.91	3.19
0D $Ce_{40}O_{80}'$	77	135	1.49	2.83
0D $Ce_{40}O_{80}$	39	105	0.97	2.22
1D $Ce_{40}O_{80}$	57	117	1.15	2.46
2D $Ce_{40}O_{80}$	157	178	1.76	3.05

[a] See Fig. S2. [b] The PW91+4 $E_f(O_{vac})$ value computed for a $p(3 \times 4)$ CeO_2(111) surface unit cell with three CeO_2 layers employing the experimental/optimized (541/549 pm) lattice constant is 245/217 kJ mol^{-1}.[30] [c] A lower $E_f(O_{vac})$ value (218 kJ mol^{-1}) was reported[8] for a $p(4 \times 4)$ CeO_2(111) surface unit cell, which corresponds to a defect concentration Θ = 1/16 monolayer of O atoms. [d] The difference with respect to the values in ref. 31 is due to the lack of inclusion in this work of the aspheric gradient correction within the PAW sphere. [e] The position of one Ce^{3+} cation is different with respect to ref. 31.

Comparison between PW91+4 and HSE06 approaches

To corroborate the PW91+4 results, we evaluated $E_f(O_{vac})$ using the HSE06 functional[26,27] for 0D, 1D, and 2D $Ce_{40}O_{80}$ and $Ce_{40}O_{80}'$. To generalize our comparison, we also considered the HSE06 $E_f(O_{vac})$ data for regular[30,31] and three (I–III) vicinal stepped CeO_2(111) surface models,[31] and for $Ce_{21}O_{42}$.[6,7] For the extended systems, we considered O atoms with different coordination numbers. In particular, we computed $E_f(O_{vac})$ for removal of: a subsurface four-coordinated oxygen atom, O_{4c}, from a regular CeO_2(111) model; a three-coordinated oxygen atom, O_{3c}, from the step of a CeO_2(111) model with step type I; a two-coordinated oxygen atom, O_{2c}, from the step of CeO_2(111) models with step types II and III (Fig. S3†). These O_{vac} positions and associated Ce^{3+} configurations correspond to the most stable ones for the models employed.[31]

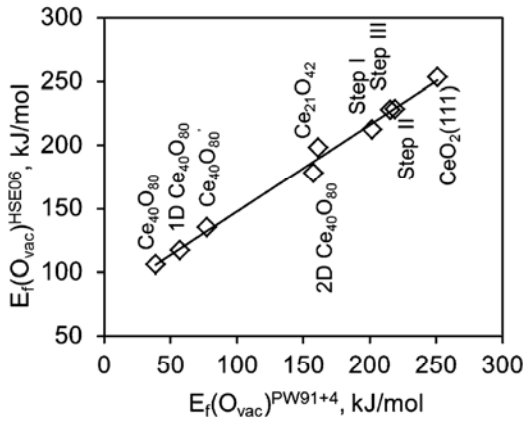

Fig. 5 Correlation between the oxygen vacancy formation energy computed with the HSE06 and PW91+4 functionals, $E_f(O_{vac})^{HSE06}$ and $E_f(O_{vac})^{PW91+4}$, for $Ce_{21}O_{42}$, $Ce_{40}O_{80}'$ and $Ce_{40}O_{80}$ NPs, 1D, and 2D $Ce_{40}O_{80}$ nanoarchitectures, regular and three vicinal CeO_2(111) surfaces. The fitted correlation (in kJ mol^{-1}): $E_f(O_{vac})^{HSE06} = 79 + 0.68\ E_f(O_{vac})^{PW91+4}$, $R^2 = 0.99$.

As shown in Fig. 5, the $E_f(O_{vac})$ values calculated with the PW91+4 approach correlate remarkably well ($R^2 = 0.99$) with the values obtained with the HSE06 hybrid functional. The difference between the $E_f(O_{vac})$ values predicted by the two approaches is somewhat dependent on the system. For $Ce_{21}O_{42}$, $E_f(O_{vac})^{HSE06}$ is 37 kJ mol^{-1} larger than $E_f(O_{vac})^{PW91+4}$ (Table 2). This difference is somewhat larger (~60–70 kJ mol^{-1}) for $Ce_{40}O_{80}$, $Ce_{40}O_{80}'$ and 1D $Ce_{40}O_{80}$. A smaller deviation (~20 kJ mol^{-1}) is computed for 2D $Ce_{40}O_{80}$. The HSE06 and PW91+4 schemes predict almost the same energy for O_{vac} formation for the regular and the three vicinal CeO_2(111) surfaces. This correlation validates the reliability of the PW91+4 $E_f(O_{vac})$ trends for the NPs and nanoarchitectures with different sizes and dimensionalities discussed within the present work.

The correlation is very useful as it can provide estimates with an acceptable uncertainty for $E_f(O_{vac})$ for systems that have too many atoms to be treated at the more expensive HSE06 level of theory. The HSE06 estimates for 0D, 1D $Ce_{80}O_{160}$ and $Ce_{140}O_{280}$ from the linear correlation in Fig. 5 are 110, 150 and 178 kJ mol^{-1}, respectively. The $E_f(O_{vac})^{HSE06}$ values for $Ce_{140}O_{280}$ and 2D $Ce_{40}O_{80}$ (178 kJ mol^{-1}, Table 2), although increased with respect to the other nanostructures, still remain smaller by 75 kJ mol^{-1} than the value for the regular CeO_2(111) surface. These values are also smaller by 35 kJ mol^{-1} than the $E_f(O_{vac})^{HSE06}$ value obtained for the vicinal CeO_2(111) surface with step type I (213 kJ mol^{-1}, Table 2). Thus, the O_{vac} formation is found to be greatly facilitated in Ce_nO_{2n} nanostructures compared with regular and vicinal CeO_2(111) surfaces. This facility to form O

vacancies in nanostructured CeO_2 is instrumental to understand the remarkable activity documented for these systems.[4,5]

Conclusions

In summary, the present work provides rationalization based on the electronic structure analysis for the variations of $E_f(O_{vac})$ values reported as a function of the size and dimensionality of the Ce_nO_{2n} (n = 38, 40, 80) NPs and their self-assemblies. The PW91+4 $E_f(O_{vac})$ trends have been verified based on HSE06 single-point energy calculations at PW91+4 optimized geometries for selected structures. This study shows that the presence of certain structural features can appreciably affect the global electronic structure, in particular with regard to the shape and bandwidth of the unoccupied DOS projected onto the Ce 4f levels, which ultimately impact on the $E_f(O_{vac})$ values. Our work identifies the corner Ce atoms as a structural motif essential for a significant reduction of $E_f(O_{vac})$. The remarkable electronic similarity between 1D $Ce_{80}O_{160}$, 2D $Ce_{40}O_{80}$ and $Ce_{140}O_{280}$ may have important implications. For instance, in theoretical studies, one may approach bigger NPs through computationally less demanding assembly of much smaller NPs.

We emphasize the model character of the present work, which is a first step in electronic structure investigations of ceria nanoarchitectures. Based on our findings the presence and absence of corner Ce atoms in ceria nanoarchitectures are predicted to significantly affect propensity to form O vacancies. The presence of such sites in ceria based catalysts will significantly affect their red-ox properties. Moreover another pivotal structural motif, the O_4 unit on small {100} facets, present in the studied nanoarrays has been recently identified experimentally as an abundant element in ceria based nanomaterials.[11] Thus, the outcome of this study appears to be relevant also for nanoarchitectures that are formed from larger building blocks or even for nanostructured ceria without clear regularity.

Acknowledgements

Financial support has been provided by the European Community (FP7-NMP.2012.1.1-1 project ChipCAT, Ref. N°310191), the Spanish MINECO (CTQ2012-34969, FIS2012-37549-C05-02, RYC-2011-09582) and the Generalitat de Catalunya (2014SGR97, 2014SGR301, XRQTC). SMK thanks the Spanish Ministerio de Educación for a pre-doctoral FPU grant AP2009-3379. MAS and KHL acknowledge funding from MOE/AcRF RG73/10. This work is a part of the COST Action CM1104 "Reducible oxide chemistry, structure and functions". Computer resources, technical expertise and assistance provided by the Red Española de Supercomputación are gratefully acknowledged.

Notes and references

1 C. Sun, H. Hong Li and L. Chen, *Energy Environ. Sci.*, 2012, **5**, 8475–8505.
2 *Catalysis by Ceria and Related Materials*, ed. A. Trovarelli and P. Fornasiero, Catalytic Science Series, Imperial College Press, London, U. K., 2nd edn, 2013, vol. 12.
3 S. T. Bromley, I. d. P. R. Moreira, K. M. Neyman and F. Illas, *Chem. Soc. Rev.*, 2009, **38**, 2657–2670.
4 S. Carrettin, P. Concepcion, A. Corma, J. M. L. Nieto and V. F. Puntes, *Angew. Chem., Int. Ed.*, 2004, **43**, 2538–2540.
5 J. Guzman, S. Carrettin and A. Corma, *J. Am. Chem. Soc.*, 2005, **127**, 3286–3287.
6 A. Migani, G. N. Vayssilov, S. T. Bromley, F. Illas and K. M. Neyman, *Chem. Commun.*, 2010, **46**, 5936–5938.
7 A. Migani, G. N. Vayssilov, S. T. Bromley, F. Illas and K. M. Neyman, *J. Mater. Chem.*, 2010, **20**, 10535–10546.
8 J. Paier, C. Penschke and J. Sauer, *Chem. Rev.*, 2013, **113**, 3949–3985.
9 G. N. Vayssilov, Y. Lykhach, A. Migani, T. Staudt, G. P. Petrova, N. Tsud, T. Skála, A. Bruix, F. Illas, K. C. Prince, V. Matolin, K. M. Neyman and J. Libuda, *Nat. Mater.*, 2011, **10**, 310–315.
10 Q. Fu, H. Saltsburg and M. Flytzani-Stephanopoulos, *Science*, 2003, **301**, 935–938.
11 A. Bruix, Y. Lykhach, I. Matolínová, A. Neitzel, T. Skála, N. Tsud, M. Vorokhta, V. Stetsovych, K. Ševčíková, J. Mysliveček, R. Fiala, M. Václavů, K. C. Prince, S. Bruyère, V. Potin, F. Illas, V. Matolín, J. Libuda and K. M. Neyman, *Angew. Chem., Int. Ed.*, 2014, DOI: 10.1002/anie.201402432.
12 H.-X. Mai, L.-D. Sun, Y.-W. Zhang, R. Si, W. Feng, H.-P. Zhang, H.-C. Liu and C.-H. Yan, *J. Phys. Chem. B*, 2005, **109**, 24380–24385.
13 S. Yang and L. Gao, *J. Am. Chem. Soc.*, 2006, **128**, 9330–9331.
14 N. Du, H. Zhang, B. Chen, X. Ma and D. Yang, *J. Phys. Chem. C*, 2007, **111**, 12677–12680.
15 X. Liu, K. Zhou, L. Wang, B. Wang and Y. Li, *J. Am. Chem. Soc.*, 2009, **131**, 3140–3141.
16 T. X. T. Sayle, M. Cantoni, U. M. Bhatta, P. S. Parker, S. R. Hall, G. Möbus, M. Molinari, D. Reid, S. Seal and D. C. Sayle, *Chem. Mater.*, 2012, **24**, 1811–1821.
17 Z. Tang and N. A. Kotov, *Adv. Mater.*, 2005, **17**, 951–962.
18 F. Viñes, F. Illas and K. M. Neyman, *Angew. Chem., Int. Ed.*, 2007, **46**, 7094–7097.
19 J. P. Perdew, J. A. Chevary, S. H. Vosko, K. A. Jackson, M. R. Pederson, D. J. Singh and C. Fiolhais, *Phys. Rev. B: Condens. Matter Mater. Phys.*, 1992, **46**, 6671–6687.
20 J. P. Perdew, J. A. Chevary, S. H. Vosko, K. A. Jackson, M. R. Pederson, D. J. Singh and C. Fiolhais, *Phys. Rev. B: Condens. Matter Mater. Phys.*, 1993, **48**, 4978.
21 J. P. Perdew and Y. Wang, *Phys. Rev. B: Condens. Matter Mater. Phys.*, 1992, **45**, 13244.
22 C. Loschen, J. Carrasco, K. M. Neyman and F. Illas, *Phys. Rev. B: Condens. Matter Mater. Phys.*, 2007, **75**, 035115; C. Loschen, J. Carrasco, K. M. Neyman and F. Illas, *Phys. Rev. B: Condens. Matter Mater.*, 2011, **84**, 199906(E).
23 V. I. Anisimov, F. Aryasetiawan and A. I. Lichtenstein, *J. Phys.: Condens. Matter*, 1997, **9**, 767–808.
24 S. L. Dudarev, G. A. Botton, S. Y. Savrasov, C. J. Humphreys and A. P. Sutton, *Phys. Rev. B: Condens. Matter Mater. Phys.*, 1998, **57**, 1505.

25 A. Migani, K. M. Neyman and S. T. Bromley, *Chem. Commun.*, 2012, **48**, 4199–4201.
26 J. Heyd, G. E. Scuseria and M. Ernzerhof, *J. Chem. Phys.*, 2003, **118**, 8207.
27 J. Heyd, G. E. Scuseria and M. Ernzerhof, *J. Chem. Phys.*, 2006, **124**, 219906.
28 J. Paier, M. Marsman, K. Hummer, G. Kresse, I. C. Gerber and J. G. Ángyán, *J. Chem. Phys.*, 2006, **124**, 154709.
29 J. Paier, M. Marsman, K. Hummer, G. Kresse, I. C. Gerber and J. G. Ángyán, *J. Chem. Phys.*, 2006, **125**, 249901.
30 A. Bruix, A. Migani, G. N. Vayssilov, K. M. Neyman, J. Libuda and F. Illas, *Phys. Chem. Chem. Phys.*, 2011, **13**, 11384–11392.
31 S. M. Kozlov and K. M. Neyman, *Phys. Chem. Chem. Phys.*, 2014, **16**, 7823–7829.
32 G. Kresse and J. Hafner, *Phys. Rev. B: Condens. Matter Mater. Phys.*, 1993, **47**, 558–561.
33 G. Kresse and J. Furthmüller, *Phys. Rev. B: Condens. Matter Mater. Phys.*, 1996, **54**, 11169–11186.
34 M. V. Ganduglia-Pirovano, J. L. F. Da Silva and J. Sauer, *Phys. Rev. Lett.*, 2009, **102**, 026101.
35 J. L. F. Da Silva, M. V. Ganduglia-Pirovano, J. Sauer, V. Bayer and G. Kresse, *Phys. Rev. B: Condens. Matter Mater. Phys.*, 2007, **75**, 045121.
36 G. Kresse and D. Joubert, *Phys. Rev. B: Condens. Matter Mater. Phys.*, 1999, **59**, 1758–1775.
37 R. F. W. Bader, *Atoms in Molecules*, Oxford University Press, Oxford, U. K., 1990.
38 D. J. Mowbray, A. Migani, G. Walther, D. M. Cardamone and A. Rubio, *J. Phys. Chem. Lett.*, 2013, **4**, 3006–3012.
39 S. J. Duclos, Y. K. Vohra, A. L. Ruoff, A. Jayaraman and G. P. Espinosa, *Phys. Rev. B: Condens. Matter Mater. Phys.*, 1988, **38**, 7755–7758.
40 L. Gerward and J. S. Olsen, *Powder Diffr.*, 1993, **8**, 127–129.
41 A. S. Barnard and A. I. Kirkland, *Chem. Mater.*, 2008, **20**, 5460–5463.
42 Z. L. Wang and X. D. Feng, *J. Phys. Chem. B*, 2003, **107**, 13563–13566.
43 T. X. T. Sayle, S. C. Parker and D. C. Sayle, *Chem. Commun.*, 2004, 2438–2439.
44 C. Loschen, S. T. Bromley, K. M. Neyman and F. Illas, *J. Phys. Chem. C*, 2007, **111**, 10142–10145.
45 C. Loschen, A. Migani, S. T. Bromley, F. Illas and K. M. Neyman, *Phys. Chem. Chem. Phys.*, 2008, **10**, 5730–5738.
46 The $Ce_{38}O_{76}$ structure is merely a sub-system of the $Ce_{40}O_{80}$ NP obtained without an attempt to approach the lowest-energy NP for this size. It has been included to account for the interaction between Ce and O terminated facets.
47 A. Migani, C. Loschen, F. Illas and K. M. Neyman, *Chem. Phys. Lett.*, 2008, **465**, 106–109.
48 $Ce_{140}O_{280}$ is derived from the perfect under-stoichiometric octahedral $Ce_{146}O_{280}$ bulk cut by removal of the excess six Ce corner atoms, which results in six O_4 sites and no corner Ce atoms.